DISSERTATION

DETERMINATION OF RELIABLE MINIMUM, DISPROOF-BASED PARTICLE FORMATION MECHANISMS: INVESTIGATION OF A SECOND-GENERATION $Ir(0)_n$ NANOPARTICLE SYSTEM

Submitted by

Christopher Breck Whitehead

Department of Chemistry

In partial fulfillment of the requirements

For the Degree of Doctor of Philosophy

Colorado State University

Fort Collins, Colorado

Spring 2021

Doctoral Committee:

Advisor: Richard Finke

Jamie Neilson
Alan Van Orden
Patrick Shipman

ABSTRACT

DETERMINATION OF RELIABLE MINIMUM, DISPROOF-BASED PARTICLE FORMATION MECHANISMS: INVESTIGATION OF A SECOND-GENERATION $Ir(0)_n$ NANOPARTICLE SYSTEM

A long-sought goal in particle formation is an understanding of the chemical reaction mechanism. The complete understanding of the associated processes (nucleation, growth, and agglomeration) will yield particle size and distribution control. Mechanistic control and knowledge will yield improvements in the development of renewable energy and catalytic materials. The current state of chemical reaction mechanisms and the direct methods to study them are presented in an in-depth literature review in Chapter II. The best, state-of-the-art case studies are examined and the minimum criteria for a reliable, disproof-based chemical mechanism are presented.

The experimental work presented in this dissertation centers on a second-generation $\{[(1,5\text{-COD})Ir^{I}\bullet HPO_4]_2\}^{2-}$ precursor to $Ir(0)_{\sim 150}(HPO_4^{2-})_x$ nanoparticle system. The exhaustive investigation of the reaction speciation and the dependence of Ir^{I} and HPO_4^{2-} concentrations on the reaction kinetics are presented in Chapter III. Based on the reaction kinetics and there experimentally determined nucleation step, the molecular mechanism of $Ir(0)_{\sim 150}(HPO_4^{2-})_x$ nanoparticle formation is elucidated. Next, in Chapter IV, the second-generation $\{[(1,5\text{-COD})Ir^{I}\bullet HPO_4]_2\}^{2-}$ precursor to $Ir(0)_{\sim 150}(HPO_4^{2-})_x$ nanoparticle system is monitored directly by X-ray absorption spectroscopy and small-angle X-ray scattering and indirectly by in-house cyclohexene reporter reaction, gas-liquid chromatography, proton nuclear magnetic resonance, and transmission electron microscopy. A total of 6 physical methods are used to follow the particle

formation kinetics. Finally, mechanism-enabled population balance modeling is applied as a final test of the proposed mechanism.

ACKNOWLEDGEMENTS

I would like to acknowledge my advisor, Prof. Rick Finke, for his time, effort, and passion in mentoring and inculcating me throughout my graduate journey. I am tremendously grateful for his tutelage and wholesome life advice. I would like to thank the numerous Finke Group members that have given their time to read paper drafts, participated in vigorous scientific debates, and allowed me to pet their dogs. I would especially like to express my gratitude to my colleague Carly Jewell for her steadfast reminders to practice self-care and for her artful logic skills. I would like to thank my undergraduate mentors (Profs. Holman, Williamson, Fisher, Kirk, Goodney, and Hobgood) for cultivating my passion for scientific discovery, for trusting me to teach their children how to swim, and for expanding my global awareness. I would like to acknowledge Leslie Shevlin for teaching me perseverance, leadership, and humility. Next-to-last, I would like to express my appreciation for the LGBTQ+ mentors I have had during my graduate career that taught me how to how to authentically navigate scientific spaces. Finally, I would like to thank my family for their unconditional love and support.

DEDICATION

Dedicated to Grandma Bev who taught me to live fervidly and love fiercely.

TABLE OF CONTENTS

I. INTRODUCTION

This dissertation follows a "journal's format", in which each chapter is a manuscript that has been prepared for submission or accepted for publication in a peer-reviewed scientific journal. Therefore, each major chapter follows the formatting guidelines of that journal. An overview is presented at the beginning of each chapter along with a footnote delineating the specific contributions by potential co-authors. The Supporting Information sections have been included as separate appendices for each chapter at the end of the dissertation. The following will provide a brief description of Chapters II–IV.

Chapter II is a literature review that serves two purposes. First, it provides important background details to place the original work of this dissertation in the context of the known literature. Second, it serves to provide a foundational knowledge of the minimum requirements for reliable, mechanistic investigation. This manuscript is being prepared for submission to an academic journal in the spring of 2021. The review consists of (i) a brief introduction to chemical reaction mechanisms, the state-of-the-art techniques for direct kinetics measurements, and the current gap in the nanoparticle formation literature; (ii) a background section on the minimum criteria for a chemical mechanism and why disproof-based, minimum mechanisms are of interest; (iii) six illustrative case studies that represent 6 state-of-the-art kinetics studies covering $Pd(0)_n$ nanoparticle formation studied by small-angle X-ray scattering (SAXS), $(ZnO)_n$ nanoparticle formation studied by tandem SAXS/WAXS/UV-Vis, $Rh(0)_n$ nanocube formation studied by X-ray absorption fine structure spectroscopy (XAFS), $(CdSe)_n$ nanocrystal formation studied by XAFS, $Ir(0)_n$ nanoparticle formation studied by XAFS and SAXS, and $Au(0)_n$ nanoparticle formation

studied by XAFS, SAXS, and XRD; (iv) a section on the current state of particle formation mechanisms; (v) a conclusion section, and finally (vi) an outlook section.

Chapter III describes the study and determination of the molecular nucleation mechanism of a second-generation, $\{[(1,5\text{-COD})Ir^{I}\bullet HPO_4]_2\}^{2-}$ precursor to $Ir(0)_{\sim 150}(HPO_4^{2-})_x$ nanoparticle system. This chapter was published in the journal *Chemistry of Materials* (Whitehead, C. B.; Finke, R. G. *Chem. Mater.* **2019**, *31*, 2848-2862. http://pubs.acs.org/doi/acs.chemmater.8b05335). The study details speciation, characterization, and in-house kinetics studies en route to a Ockham's razor-obeying minimum molecular nucleation mechanism starting from a bimetallic iridium precursor. The comprehensive minimum molecular mechanism yielded from this work allowed for the direct, synchrotron experiments addressed in the next chapter.

Chapter IV encompasses the study of the second-generation, $\{[(1,5\text{-COD})Ir^{I}\bullet HPO_4]_2\}^{2-}$ precursor to $Ir(0)_{\sim 150}(HPO_4)_x$ nanoparticle system by 2 direct (XAFS and SAXS) and 4 indirect (cyclohexene catalytic reporter reaction (CHCRR), gas-liquid chromatography (GLC), proton nuclear magnetic resonance (^{1}H NMR), and transmission electron microscopy (TEM)) for a total of 6 physical methods. Additionally, the proposed minimum mechanism is tested by mechanism-enabled population balance modeling (ME-PBM). This chapter is being prepared for submission to an *ACS* journal in the spring of 2021. The kinetics data from state-of-the-art, direct, synchrotron techniques are well-fit by the same minimal 2-step mechanism from Chapter III, and the resultant rate constants between direct and indirect techniques are in agreement within experimental error. Finally, ME-PBM is applied to the TEM-determined particle-size distribution (PSD) and the minimum mechanism is upgraded by the implied, needed additional steps.

Chapter V provides a concise summary of the results described in this dissertation. There are also six additional publications[1,2,3,4,5,6] (for a total of 9 papers) resulting from my graduate

career at Colorado State University. The first two first-author papers are a two-part[1,2] literature review of the 1950 LaMer model with Prof. Saim Özkar and Prof. Richard Finke. The third is a first-author perspective[3] on burst growth versus burst nucleation written with Prof. Murielle Watzky and Prof. Richard Finke. The last two papers are the initial mechanism-enabled population balance modeling papers[5,6] that include significant work by Dr. Derek Handwerk and Prof. Patrick Shipman, Prof. Saim Özkar, and Prof. Richard Finke.

REFERENCES

1. Whitehead, C. B.; Özkar, S.; Finke, R. G. LaMer's 1950 Model for Particle Formation of Instantaneous Nucleation and Diffusion-Controlled Growth: A Historical Look at the Model's Origins, Assumptions, Equations, and Underlying Sulfur Sol Formation Kinetics Data. *Chem. Mater.* **2019**, *31*, 7116–7132.

2. Whitehead, C. B.; Özkar, S.; Finke, R. G. LaMer's 1950 Model of Particle Formation: A Review and Critical Analysis of Its Classical Nucleation and Fluctuation Theory Basis, of Competing Models and Mechanisms for Phase-Changes and Particle Formation, and then of Its Application to Silver Halide, Semiconductor, Metal, and Metal-Oxide Nanoparticles. *Mater Adv.* **2021**, *2*, 186-235.

3. Whitehead, C. B.; Watzky, M. A.; Finke, R. G. "Burst Nucleation" vs Autocatalytic, "Burst" Growth In Near-Monodisperse Particle Formation Reactions. *J. Phys. Chem. C* **2020**, *124*, 24543-24554.

4. Finke, R. G.; Watzky, M. A.; Whitehead, C. B. Response to "Particle Size Is a Primary Determinant for Sigmoidal Kinetics of Nanoparticle Formation: A "Disproof" of the Finke–Watzky (F-W) Nanoparticle Nucleation and Growth Mechanism". *Chem. Mater.* **2020**, *32*, 3657-3672.

5. Handwerk, D. R.; Shipman, P. D.; Whitehead, C. B.; Özkar, S.; Finke, R. G. Mechanism-Enabled Population Balance Modeling of Particle Formation en Route to Particle Average Size and Size Distribution Understanding and Control. *J. Am. Chem. Soc.* **2019**, *141*, 15827–15839.

6. Handwerk, D. R.; Shipman, P. D.; Whitehead, C. B.; Özkar, S.; Finke, R. G. Particle Size Distributions via Mechanism-Enabled Population Balance Modeling. *J. Chem. Phys. C* **2020**, *124*, 4852-4880.

II. A REVIEW OF IN SITU SYNCHROTRON XAFS AND SAXS INVESTIGATIONS OF METAL, METAL-OXIDE, AND SEMICONDUCTOR NANOPARTICLE SYNTHESES EN ROUTE TO RELIABLE, DISPROOF-BASED, DELIBERATELY MINIMUM MECHANISMS FOR PARTICLE FORMATION

Overview[i]

Following a brief description of synchrotron X-ray absorption fine structure (XAFS) spectroscopy and small/wide angle X-ray scattering (SAXS/WAXS), the definition of and four criteria for attaining reliable, disproof-based chemical mechanisms of particle formation are given. A total of 64 papers using synchrotron techniques for mechanistic investigation have been analyzed en route to the selection of six illustrative case studies. Each case study is assessed using the four criteria provided, specifically the case histories of: (i) palladium nanoparticles studied using SAXS, (ii) zinc-oxide nanoparticles studied using SAXS/WAXS/UV-Vis, (iii) rhodium nanocubes examined using XAFS, (iv) cadmium-selenide nanocrystals studied by XAFS, (v) iridium nanoparticles studied by XAFS and SAXS, and (vi) gold nanoparticles studied by XAFS, SAXS, and XRD. Four tables are constructed that analyze in detail each paper, Tables S2.1-S2.4 of Appendix I. Six illustrative case studies are presented in greater detail in this chapter, and two tables are presented that summarize the current state of disproof-based, deliberately minimalistic

[i] This chapter provides background material on the current state-of-the-art for reliable mechanistic investigation. The chapter serves to place the original work of this dissertation in the context of the known literature. A version of this manuscript will be submitted for publication in the near future to an academic journal (expected spring of 2021). A list of abbreviations is provided in Appendix I that serves as the Supporting information of this Chapter II. This chapter was written by the author of this dissertation, C. B. Whitehead, with minimal edits and organization suggestions from the author's advisor. Minor changes were made to meet dissertation formatting guidelines.

particle formation mechanisms expressed in terms of the necessary pseudo-elementary steps. Finally, a Conclusions section with 9 takeaways and an Outlook section are also provided.

2.1. INTRODUCTION

Knowledge and understanding of chemical reaction mechanisms are critical to accomplishing the long-sought goal of synthetic control of especially particle size and size-distribution in particle formation science.[1,2,3,4] Complete understanding of the nucleation, growth, and agglomeration processes[5,6,7,8,9,10,11,12] promises to provide the desired size and distribution control in particle synthesis[13,14,15,16,17,18,19,20,21,22,23] just as mechanistic insights into other chemical and industrial processes have resulted in improvements in the fields of renewable energy, semiconductor synthesis, nanocatalysis, and many others.[24,25,26,27,28,29]

Due to the sub-nanoscale size (< 1 nm) of just-formed nuclei, it is very difficult to observe directly in real time the smallest, kinetically first-formed cluster(s), termed the kinetically effective nucleus (KEN)[30], which recent work shows can consist of just 2-3 atoms.[31,32] Hence, there is a need to use synchrotron-based spectroscopic techniques to monitor the nucleation, growth and any agglomeration of particles, notably synchrotron X-ray absorption fine structure (XAFS) spectroscopy (that provides oxidation state, coordination number, and associated structural information) as a function of time, and synchrotron small-angle X-ray scattering (SAXS) (that allows monitoring of particle radius and number of particles) in real-time.[33,34,35,36,37] These techniques can be used in tandem with each other or other methods, and they can be used to monitor directly particle formation reactions *in situ*.

However, significant gaps remain in the nanoparticle formation literature en route to a deeper understanding of (i) first, what constitutes a reliable, disproof-based chemical reaction mechanism; (ii) the experimental data needed to be able to claim such a mechanism; (iii) how such mechanisms differ from any other type of non-disproof-based model(s); (iv) the preferred

experimental methods for collecting the needed kinetics data; and then (v) what are the arguably best, prototype mechanistic case studies to date by synchrotron-based methods?

Hence herein we begin by discussing the requirements for a reliable, disproof-based chemical mechanism and then we present six case studies of particle formation monitored by synchrotron-based SAXS, XAFS or tandem SAXS/XAFS methods.[38,39,40,41,42,43] We systemically assess the results and strengths of each case study and, where needed, suggest additional studies en route to a reliable reaction mechanism. The goal is to use these six case studies as pedagogically valuable examples of how to most efficiently achieve reliable, disproof-based reaction mechanisms of for particle formation regardless of the exact type or composition of the resultant particles. Two summary tables that present the current state-of-the-art in terms of disproof-based, deliberately minimalistic (i.e.., Ockham's razor obeying) particle formation mechanisms are also provided and briefly discussed.

2.2. BACKGROUND

2.2.1. Key Requirements for a Minimum Chemical Mechanism

From classical physical-organic chemistry, the definition of a mechanism is well understood for at least 50 years.[44,45,46] Ideally, chemical mechanisms will have the following, minimal, requirements:[47,48]

1. A complete mass- and charge-balanced reaction stoichiometry, as that is what the proposed steps of the mechanism must add up to[49];
2. Kinetics data,[50,51] ideally using multiple, direct physical methods and handles;

3. Elementary, or if not pseudo-elementary,[52] step reactions that present the stepwise mechanism and add up to the experimentally established reaction stoichiometry all while crucially defining the rate constants, *and* the unambiguous words[53,54] one can use, to discuss the observed chemistry;
4. Critically, disproof-based quantitative comparison of the experimental data to how well (or poorly) postulated competing, alternative mechanisms are able to fit that data, all en route to an Ockham's razor-obeying, therefore deliberately minimalistic mechanism as the initial goal of mechanistic studies.[55,56,57,58]

Once one has the minimum, disproof-based chemical mechanism 'in hand', then one has a good start on a broader and more generalized understanding of the system. That mechanistic understanding of nucleation, growth, and agglomeration that are ubiquitous processes across nature can then be used to further control key properties of the system: particle size, particle-size distribution, catalytic activity, photochemical properties (that are often size and size-dispersion dependent, e.g., in semiconductor quantum dot nanoparticles), and so on.

Unfortunately, experimental kinetics and rate-law-backed mechanisms for nucleation are rare at the molecular and atomic level, save for a small handful of studies.[26,30,31,32,38,42] The precise mechanism of nucleation is critical as it starts off the particle-formation process; without the precise details of the nucleation process one cannot possibly claim to a complete nor reliable mechanism of particle formation. Growth and agglomeration are in a bit better shape,[59,60,61,62,63,64] but still not well supported kinetically and mechanistically—with, again, an experimental rate law for growth or agglomeration—so that there are needed advances there as well. Through the basic four requirements outlined above en route to a reliable mechanism illustrated via six case studies,

we hope to demystify how one can perform reliable mechanistic investigations that allow elucidation of the most probable particle formation process.

2.2.2. Why Disproof-Based, Minimum, Reliable Reaction Mechanisms Are an Important Goal

Even if one obtains powerful synchrotron-based evidence on a well-designed, important particle formation process, the broader application and impact of that sophisticated effort and impressive data *will have been wasted* until and unless one expresses that data in its most concise, most powerful form—*a reaction mechanism in the form of charge and mass balanced reactions that define the differential equations able to account quantitatively for the intermediate species as well as net process over time*. It is the more general application to other systems as well as quantitative predictability that is contained within generalized kinetics equations expressed in terms of generalized A, B, C…N species with rate constants defined by ideally elementary, or at least pseudo-elementary,[52] steps. Again, each of those steps must be mass- and charge-balanced, and those proposed mechanistic steps must add up to the observed, also fully mass- and charge-balanced, experimentally determined reaction stoichiometry. Note the power here of avoiding mistakes or proposing something foolish by making sure what one proposes obeys the Laws of Mass and Charge Balance. Additionally, if the rate constants are known—ideally as a function of temperature—then there is predictability from one set of starting conditions and temperature to another set of, for example, more optimized conditions.

Additionally, with the 2019 advent of Mechanism-Enabled Population Balance Modeling (ME-PBM)[65,66], that can track every particle in a proposed particle-formation pathway consisting of even thousands of elementary steps, disproof-based, deliberately minimum mechanisms are

(necessary and) sufficient to be able to predict both average particle sizes and particle-size distributions (PSDs), including the PSD shape. The available evidence to date also illustrates the ability of disproof-based ME-PBM to confirm—or more often to date to refute[65,66]—a proposed mechanism[65,66] en route to a refined mechanism. ME-PBM is also able *to extract rate constants* for the proposed, pseudo-elementary step mechanism *from PSD data.*[65,66] But, to exploit the full generality, predictability and for knowledge transfer to other systems or conditions, a reliable minimum reaction mechanism is required to start, as the name *Mechanism-Enabled* PBM indicates.

2.2.3. Literature Search and Paper Selection

A total of 69 papers were collected through a search of the literature via SciFinder and the Web of Science. Series of searches were performed over a period of more than 2 years, where various combinations of terms were cross referenced including, but not limited to: "XAFS", "SAXS", "in situ", "in operando", "tandem", "mechanism", "kinetics", "formation", "nanoparticle", and "nanocrystal". The 69 papers collected and analyzed in this publication are tabulated into four tables in Appendix I: Table S2.1, 5 entries (instructional, review articles on the general use of XAFS and SAXS in scientific research); Table S2.2, 22 entries (SAXS studies of nanoparticle formation); Table S2.3, 22 entries (XAFS studies of nanoparticle formation); and Table S2.4, 20 entries (Tandem techniques, with at least one being direct synchrotron XAFS or SAXS). Not unsurprisingly, transition-metal nanoparticles comprise the majority of papers tabulated as they often represent systems with fewer components that have been studied more extensively over a longer period of time.

The interested reader is strongly—*actually very strongly*—encouraged to study and analyze for themselves these four tables to understand the variety of systems covered, the status of the approaches, and the overall efforts at nanoparticle reaction development and associated mechanistic investigation summarized in Tables S2.1-S2.4 of Appendix I. Indeed, if Tables S2.1-S2.4 of Appendix I covered anything smaller than their current ~52 pages, we would have placed them upfront in this review. Self-study of Tables S2.1-S2.4 of Appendix I will generate the reader's own assessment and insights regarding the status of the field of particle formation synthesis, kinetics and mechanism using synchrotron methods. Papers that did not present, discuss, or claim a mechanism are not included even if they reported XAFS or SAXS data. In what follows we have selected 6 case studies for a closer look and critical analysis based, overall, on how they illustrate together the state-of-the-art in the field as well as what else is needed to attain reliable chemical mechanisms for the particle formation reactions. Our apologies in advance to authors of the many other interesting studies summarized in Tables S2.1-S2.4 that either space, or our approach and organization of this review, did not permit us to cover in detail in this chapter that follows. Also, not covered herein due to scope and space limitations are computational chemistry approaches and contributions that promise to be of increasing importance, perhaps especially with a deeper understanding of nucleation processes.[67,68] That said, computations not carefully connected to experimental results can lead to erroneous conclusions, even for much simpler chemical systems than particle formation reactions.[69]

2.3. SELECTED, ILLUSTRATIVE CASE STUDIES

The goal of the current review is to expedite the conversion of a growing body of powerful synchrotron-based spectroscopic studies and data now available (Tables S2.1-S2.4, by the multiple

expert investigators and studies), into the "causes" (the mechanisms) for those "effects" (the observables) as monitored by powerful, direct, *in-situ* synchrotron-based spectroscopies. In the following six sections of this review, six state-of-the-art kinetics case studies that utilize synchrotron techniques are summarized. These six case studies have been chosen as illustrative, often arguably top examples in the field of nanoparticle formation kinetics and mechanistic studies or at least synchrotron-based studies. Each will have several of the required pieces of information necessary to be able to claim a reliable mechanism, although an interesting observation is that each prototype system is missing one or more aspects that, ideally, will be added in the future to that system and study.

The six case studies are: (3.1) palladium nanoparticle formation monitored by SAXS[38]; (3.2) zinc-oxide nanoparticle formation monitored by SAXS/WAXS/UV-Visible[39]; (3.3) rhodium nanocube formation monitored by XAFS[40]; (3.4) cadmium-selenide nanocrystal formation monitored by XAFS[41]; (3.5) iridium nanoparticle formation monitored by XAFS and SAXS[42]; and (3.6) gold nanosphere and nanowire formation monitored by XAFS, SAXS, and XRD.[43] Each case study is organized by: (i) a summary of the system and techniques used to study it; (ii) a review of the key kinetics data; (iii) the authors' proposed formation model or mechanism; and (iv) an analysis of the case's results as compared to the four components required for establishing a minimum, disproof-based mechanism.

2.3.1. Case Study #1: Mechanistic Investigation of Palladium Nanoparticle Formation Using Small-Angle X-ray Scattering

Karim and coworkers, in 2017, published their detailed, disproof-based mechanistic investigation of palladium nanoparticle formation.[38] Spherical palladium nanoparticles were

prepared from Pd(II) acetate, $Pd(OAc)_2$, and trioctylphosphine (TOP) in a 50:50 solvent mixture of toluene and 1-hexanol at 100 ºC under nitrogen.[38,70] The formation kinetics were monitored by *in situ* SAXS, where a syringe pump was used to draw a small sample into the beam and then inject it back into the reaction solution after each measurement. The reaction was studied at palladium concentrations from 0.5 to 25 mM, hence a relatively wide factor of 50. The *tri*-octylphosphine, TOP, ligand-to-metal molar ratios (TOP:Pd) were studied at ratios of 1, 1.5, and 2. Finally, the end-time particle size and size distributions were collected *ex situ* using dark-field STEM. The generalized reaction stoichiometry, as given in ref 38, is reproduced below as eq 2.1.

$$Pd^{II}(TOP)(OAc)_2(solv) + R'CH_2OH \xrightarrow{N_2,} Pd^0 + TOP + 2AcOH + R'CHO + Solv \quad \text{(Eq 2.1)}$$

The authors directly monitored the Pd nanoparticle formation by *in situ* synchrotron SAXS experiments—with an eye towards their noting that SAXS counts as "two methods" if one monitors both the particle radius as well as the number of particles vs time[71], *vide infra*. By using a Schultz polydisperse spherical model, they were able to fit the SAXS data and extract the particle sizes and total number of particles simultaneously with respect to time.

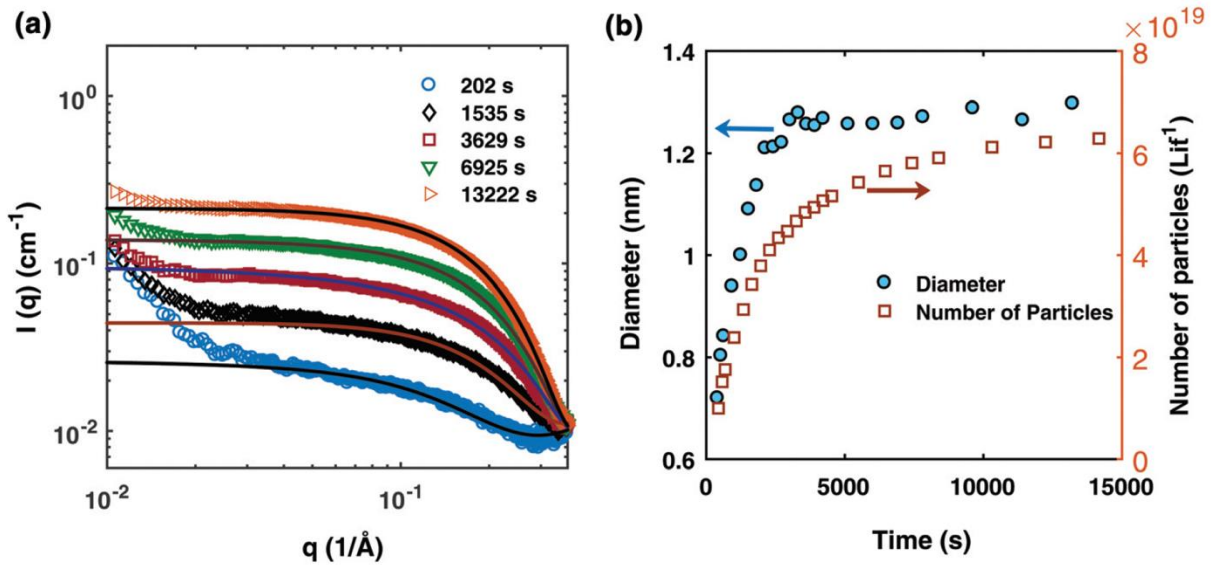

Figure 2.1. (a) SAXS data at different reaction times after absolute scaling with fitting by Schultz polydisperse spherical model; **(b)** particle size evolution (blue circles) and number of particles (open orange squares) plotted as a function of time (in seconds). The Pd nanoparticles were prepared from a solution of 10 mM $Pd(OAc)_2$, 20 mM TOP, in a 50:50 solution of toluene and 1-hexanol at 100 ºC. Figure reproduced with permission from ref 38. Copyright 2017 Royal Society of Chemistry.

The data display direct evidence of slow, continuous nucleation with fast growth, results in direct contradiction to the classical LaMer model of 1950 that postulates burst nucleation followed by diffusion-controlled growth.[38,63,64] Furthermore, the continuous increase in particles suggests that agglomeration, which would reduce the number of particles, is not involved in the $Pd(0)_n$-particle formation process under their conditions that include an excess of strongly coordinating *tri*-octylphosphine ligand. The authors hypothesized that, at a minimum, continuous nucleation, fast autocatalytic growth, and the incorporation of ligand effects will be needed for any kinetic model and associated minimum mechanism able to fit their SAXS data.

The authors proceeded by constructed a model relying on three assumptions: (i) that the fraction of surface versus core atoms can be ignored, which for particles smaller than 1.5 nm (as

seen in Figure 2.1) is a tenable assumption because the percentage of surface atoms is >75% of the total atoms[38]; (ii) that the growth and ligand binding to the particle surface is independent of particle size and ligand coverage, in this first model to be able to account for ligand effects. ("In the absence of experimental or theoretical information, the effects of size, polydispersity and ligand coverage on the rate constants are not included in the model."[38]); and (iii) that the ligand–metal precursor binding ratio is assumed to be 1 because isothermal titration calorimetry[72] shows, "the equilibrium binding constant for the second TOP binding ($A{\bullet}L + L \rightleftharpoons A{\bullet}L_2$) is around two orders of magnitude lower than the first binding"[38], where A is the Pd precursor and L is TOP.

By using their proposed mechanism under the above reasonable if not necessary assumptions for an initial, not over-parameterized model, the authors developed a kinetic model and associated minimum mechanism able to fit quantitatively their experimentally determined number of particles as a function of time data. The proposed kinetic model for nucleation, autocatalytic growth, and accompanying ligand effects used to fit the experimental data in Figure 2.2 is given in Scheme 2.1. The model was constructed using the minimum number of pseudo-elementary steps necessary to describe the reaction, that is, by ensuring that Ockham's razor[57] was obeyed.

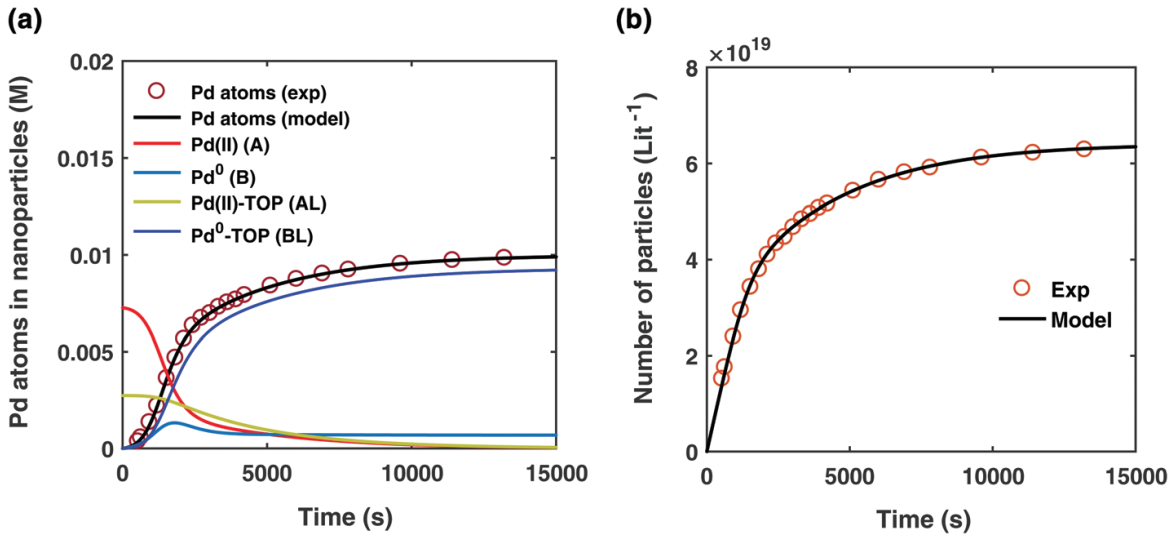

Figure 2.2. **(a)** Experimentally determined concentration of Pd atoms in nanoparticles (molarity, M) as a function of time (seconds, s) is plotted (red open circles) and fit with the kinetic model (black line) accounting for Pd atoms as total nanoparticles (B + B•L). The resultant rate constants are: $k_1 = 2.45 \times 10^{-5}$ s^{-1}, $k_2 = 8.5 \times 10^{-1}$ s^{-1} M^{-1}, $k_3 = 7.9 \times 10^{-3}$ s^{-1} M^{-1}, $k_4 = 2.1 \times 10^{-1}$ s^{-1} M^{-1}, $K_{eq,3} = 2.18 \times 10^{1}$ M^{-1}, and $K_{eq,4} = 1.27 \times 10^{3}$ M^{-1}. Based on the kinetic model rate constants, concentrations of A (red line), B (light blue line), A•L (green line), and B•L (dark blue line) were simulated as a function of time. **(b)** Experimentally determined number of particles as a function of time fit with the kinetic model. The reaction conditions for the experimental data were 10 mM $Pd(OAc)_2$, 50:50 toluene:hexanol solvent, TOP:Pd ratio of 2:1, and 100 °C reaction temperature. Figure reproduced with permission from ref 38. Copyright 2017 Royal Society of Chemistry.

Scheme 2.1. Karim and Co-Workers[38] 4-Step Ligand-Based Model for Particle Formation, Autocatalytic Surface Growth, Ligand–Precursor Interactions, and Ligand–Particle Interactions.

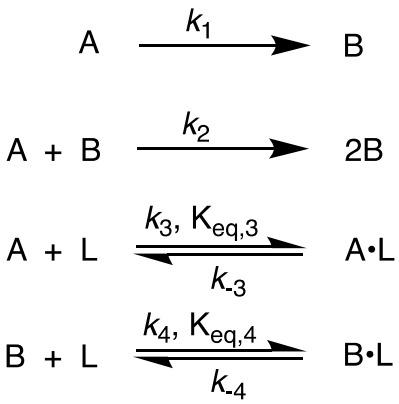

The model contains four pseudo-elementary steps defining the corresponding rate constants. The first step is nucleation including reduction (A → B, k_1), where Pd(II) is reduced to Pd(0) and $Pd(0)_n$ nuclei are formed. Note, as discussed elsewhere[30], under constant initial $[A]_{Total}$, higher-order nucleation nA → nB (=B_n) is kinetically hidden because $(d[A_0]/dt) / n = k_1[A_0]^n$, where $[A]_0$ is often constant to a ≥99.9% level during the induction period.[30] In the present case, unimolecular rate-determining Pd(II) → Pd(0) is arguably likely present given that the slow step is the release of A, that is A-L → A + L. The second step employed is autocatalytic surface growth (A + B → 2B, k_2)[73], where Pd(II) is reduced and added to the surface of the growing $Pd(0)_n$ particle. Next, the equilibrium between the Pd(II) precursor complex and the ligand, TOP, (A + L ⇌ A•L, k_3 and $K_{eq,3}$), and the equilibrium between the $Pd(0)_n$ particle and TOP (B + L ⇌ B•L, k_4 and $K_{eq,4}$) are included. The kinetic model's ability to account for the experimental data in Figure 2.2 demonstrates the value of obtaining simultaneous size *and* number of particles data by SAXS as Prof. Karim has insightfully emphasized.[71] The quantitative fits presented Figure 2.2 argue strongly that the ligand-based kinetics model, incorporating the species A, B, A•L, B•L, and L, is a satisfactory, quantitative kinetics model for describing this valuable $Pd(0)_n$ particle-formation system from the Karim laboratory.

The model can be further visualized using the pictorial representation provided by the authors shown in Figure 2.3:

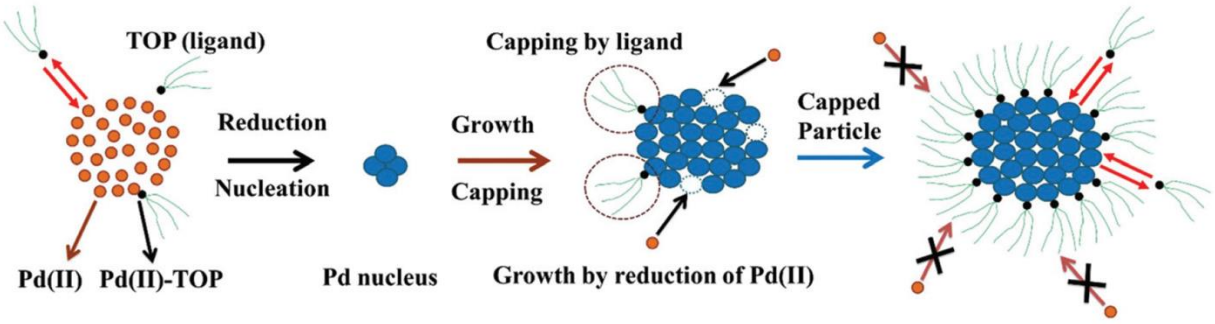

Figure 2.3. Schematic representation of the ligand-based model. The figure represents the 4 steps of the model: (1) reduction of Pd(II) to Pd(0) and the formation of the Pd nucleus (A → B); (2) autocatalytic growth of the Pd nucleus by further addition and reduction of Pd(II) (A + B → 2B); (3) reversible ligand binding with the precursor Pd(II) (A + L ⇌ A•L); and (4) reversible ligand binding to the particle surface (B + L ⇌ B•L). Orange circles are the unreduced Pd(II), small black circles with green tails are trioctylphosphine (TOP, ligand), and blue circles are reduced $Pd(0)_n$ particles. Figure reproduced with permission from ref 38. Copyright 2017 Royal Society of Chemistry.

Noteworthy here is that the Karim and co-authors' contribution is ahead of most in that they did not provide only the (useful) artistic rendering on the reaction in Figure 2.3 as the "mechanism" of the process as far too many XAFS or SAXS studies presently do. Figure 2.3 is, again, useful as a pictorial representation of the particle formation process. That said, artistic renderings such as Figure 2.3 cannot be used to quantitatively describe or predict particle size or size-distribution, for example, under other conditions. In this way, the Karim et al. study is noteworthy for its balanced reaction kinetic scheme in Scheme 2.1, its quantitative fitting of the SAXS data, and the resulting rate constants obtained.

Ideally, all reasonable alternative mechanisms should be considered and assessed en route to a reliable, disproof-based mechanism. In the SI of ref 38, five models were tested. Included in these models are mechanisms that did not include ligand steps (A → B and A + B → 2B), included only the A•L ligand step (A → B, A + B → 2B, and A + L ⇌ A•L), and included only the B•L ligand step (A → B, A + B → 2B, and B + L ⇌ B•L). These three models, the first of which is the

classic 2-Step mechanism of just A → B, A + B → 2B,[73] were unable to fit the data. Out of the 5 models tested, the only model capable of accounting for the experimental data was the four-step model presented in Scheme 2.1. Here, the authors disproved four alternative mechanisms en route to the Ockham's Razor[57] obeying mechanistic model in Scheme 2.1 that can quantitatively describe their $Pd(0)_n$ nanoparticle system.

Additionally, the authors demonstrated the applicability of their minimal ligand-based kinetic model to other literature systems that exhibit a particle-size dependence based on the ligand concentration. They found that their ligand-based kinetic model, that includes reversible ligand binding to the precursor ("A") and the particle surface ("B"), fit literature data sets for Pd/PVP[74] and Au/Thiol[75] systems as well—a valuable demonstration of the broader generality of their kinetics model.

The authors' work highlights one of the most important pieces of mechanistic investigation—the power of pseudo-elementary steps.[52] A pseudo-elementary step is defined as the composite of the underlying elementary steps.[52,73] Nanoparticle formation consists of at least hundreds (for smaller particles) to often thousands of elementary steps—and millions of elementary steps once one reaches micron-sized particles. In the case of Karim's Pd system, the final particles contain 100s of atoms in a mechanism that must, therefore, correspond minimally to hundreds of elementary steps. Yet, Karim and coworkers were able to describe the Pd nanoparticle formation[38] process, and the formation process of others' systems,[74,75] quantitatively using only 4 pseudo-elementary steps—a clear, powerful demonstration of the pseudo-elementary step concept.[52,73] As such, the Virginia Tech team demonstrate convincingly the value of the pseudo-elementary step approach and results to the kinetics and mechanisms of more complex reactions. A highly illustrative example where the pseudo-elementary step concept has been used

to elucidate a catalytic mechanism is available elsewhere.[49] A review of the pseudo-elementary step method for approaching the mechanism of complex reactions is in progress for readers wanting more information and will be published in due course.

In summary of this first case study, the authors used SAXS to simultaneously monitor the particle size and the total number of particles with time, and because of the connection of particle radius to total atoms of Pd, the concentration of Pd nanoparticle formation as a function of time. Their mechanistic model satisfies fully three of the four criteria for a reliable mechanistic study and partially satisfies the other of the four criteria. For criterion (i)—a complete, balanced reaction stoichiometry— "A" is a complex of the Pd starting material, $Pd(OAc)_2$, the solvent (toluene or pyridine), and/or hexanol,[38] so that the precise composition of "A" is not known unequivocally and hinders attaining a detailed understanding of the more intimate nucleation mechanism. The precise composition of the products, $Pd_nL_m(solvent)_a$, are not known. The authors' TEM studies show that an increase in solvent polarity results in an increase in particle size, yet literature studies[76,77] found the opposite trend, so that the exact composition of "A" and the resulting effect of the choice of solvent remain topics of interest and potential future study in this important and interesting system. Second, the authors fully satisfied criterion (ii)—collection of kinetics data—with their direct SAXS kinetics data that yields two observables, particle-size and concentration.[38,71] Finally, the authors also satisfied criteria (iii) and (iv)—(pseudo)-elementary steps that present the mechanism and disproof of all possible alternative hypotheses, respectively—with their development of a minimal, pseudo-elementary 4-step kinetic model. The model accurately describes the physical processes, the rate constants, and the correct words for describing unambiguously each pseudo-elementary step. Furthermore, the 4-step kinetic model proposed was the only mechanism out of several tested to account for the experimental data and

is an Ockham's Razor-obeying model. In sum, the excellent work[38] by Karim and coworkers is an important case study of nanoparticle formation employing SAXS monitoring and proper mechanistic model building. It is a "must-read" in our opinion for anyone pursuing reliable particle-formation mechanisms.

2.3.2. Case Study #2: Zinc-Oxide Nanoparticle Formation Investigated Using *In Situ* Stopped-Flow Microfluidic SAXS/WAXS/UV-Vis Experiments

A recent 2019 study by Förster and co-workers monitored the formation kinetics of ZnO nanoparticles using an *in situ* tandem SAXS/WAXS/UV-Vis stopped-flow microfluidic set-up.[39] The ZnO nanoparticles were prepared by mixing solutions of zinc oleate in THF and TBA^+OH^- (tetrabutylammonium hydroxide, 1 M in methanol) in THF using a Y-shaped Teflon mixer at high flow rates flowing into a quartz capillary. The proposed reaction stoichiometry is given as eq 2.2, that is, in-so-far as we can construct the balanced reaction stoichiometry given the data provided in ref 39.

$$n\,Zn(C_{18}H_{33}O_2)_2 + 2n\,(CH_3)_4N^+OH^- \xrightarrow{THF} (ZnO)_n\bullet(C_{18}H_{33}O_2^-)_x + n\,H_2O + 2n\,(CH_3)_4N^+ + 2n - x\,C_{18}H_{33}O_2^- \quad \text{(Eq 2.2)}$$

The authors report eq 2.3 with rate constant k_1 as a key chemical reaction that leads to the formation of the ZnO nanoparticle core.

$$Zn^{II} + 2\,OH^- \xrightarrow{k_1} ZnO + H_2O \quad \text{(Eq 2.3)}$$

The capillary of the stopped-flow microfluidic, for the *in situ* SAXS/WAXS/UV-Vis measurements and set-up in Figure 2.4, was heated using a copper heating tube integrated into the *in situ* capillary holder.[39] Experiments were conducted at two zinc concentrations, [Zn] = 160 mM and 53 mM, and two temperatures, T = 40 °C and 50 °C. The [TBA^+OH^-] was kept at 167 mM for all experiments.[39] Control experiments concluded that T = 30 °C and 60 °C were not optimal for monitoring ZnO nanoparticle formation kinetics.[39] SAXS/WAXS data were processed according to literature standards and particle radii versus time data were reported.[39]

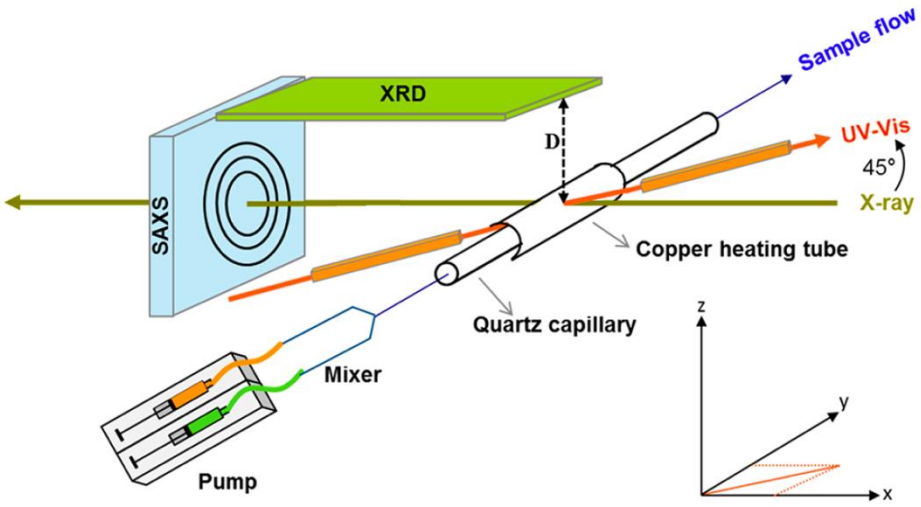

Figure 2.4. As noted by the authors,[39] "Schematic presentation of the *in situ* setup employed for real-time SAXS/WAXS/UV-Vis measurements during the formation of ZnO nanoparticles. The setup measures SAXS, WAXS, and the UV-Vis spectra simultaneously in the same sample volume."[39] Reproduced with permission from ref 39. Copyright 2019 American Chemical Society.

The authors analyzed their SAXS data under the four experimental conditions to determine the radii as a function of early time (0 – 1000 s), results reported in Figure 2.5.

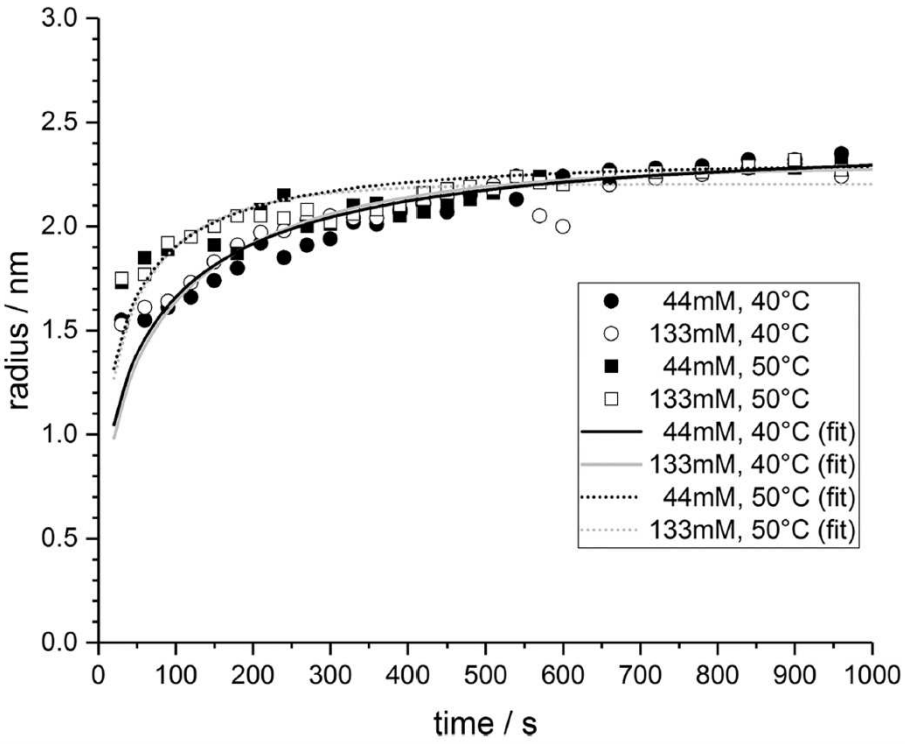

Figure 2.5. "Time evolution of the average ZnO nanoparticle radii determined from the fitted SAXS curves for two different concentrations and temperature during the first 1000 s of the nucleation and growth reaction. The solid lines are fits to a homogeneous nucleation and growth model."[39] Reproduced with permission from ref 39. Copyright 2019 American Chemical Society.

Based on the in situ SAXS data reported in Figure 2.5 and eq 2.3, a series of differential equations, eqs 2.4–2.8, were derived to describe the ZnO particle formation process, most of which are not of an elementary or pseudo-elementary step origin.

$$\frac{d[Zn^{2+}]}{dt} = \frac{d[OH^-]}{dt} = -k_1[Zn^{2+}][OH^-] \quad \text{(Eq 2.4)}$$

$$\frac{d[ZnO_N]}{dt} = \beta \frac{V}{v_0} exp\left[-\frac{\Delta G_c}{kT}\right] \quad \text{(Eq 2.5)}$$

$$\frac{d[ZnO_{PJ}]}{dt} = 4\pi R_j D N_A [ZnO] \frac{\left(1-\frac{[ZnO]_{sat}}{[ZnO]} exp\left[\frac{R_{cap}}{R_j}\right]\right)}{\left(1+\frac{D}{R_j k_{gr}}\right)} \quad \text{(Eq 2.6)}$$

$$\frac{d[ZnO]}{dt} = k_1[Zn^{2+}][OH^-] - \beta\frac{V}{v_0}exp\left[-\frac{\Delta G_c}{kT}\right] - \int_0^t 4\pi R_j D N_A [ZnO]\frac{\left(1-\frac{[ZnO]_{sat}}{[ZnO]}exp\left[\frac{R_{cap}}{R_j}\right]\right)}{\left(1+\frac{D}{R_j k_{gr}}\right)}h(t_j)dt_j$$

$J = 1, \ldots, N$ (Eq 2.7)

$$\left.\frac{d[P_j]}{dt}\right|_{t=t_j} = \beta\, exp\left[-\frac{\Delta G_c}{kT}\right]\delta[t-t_J] = h(t_J) \quad \text{(Eq 2.8)}$$

The terms in these equations are as follows: concentrations of precursors are $[Zn^{2+}]$ and $[OH^-]$; free solvated ZnO units are [ZnO]; ZnO units converted by nucleation are $[ZnO_N]$; ZnO units converted by growth are $[ZnO_{PJ}]$; particle concentrations are $[P_J]$; k_1 is the rate constant of the minimum chemical reaction back in eq 2.3; rate constant of the growth reaction is k_{gr}; volume of the spherical particle is V; Avogradro's constant is N_A; rate constant of the nucleation reaction is β; diffusion constant of the ZnO units is D; interfacial tension of the ZnO nanoparticles is γ; saturation concentration of ZnO is $[ZnO]_{sat}$; and the nucleation free enthalpy is ΔG_c.

The authors report that solving the set of "coupled differential equations yields the concentration $[P_J](t)$ and radii $R_J(t)$ of all particles J that have been formed during the nucleation process."[39] They solved the set of differential equations for each data set in Figure 2.5, which resulted in the fits given and values for the precursor rate constant (k_1), the growth rate constant (k_{gr}), the interfacial tension (γ), and the saturation concentration ($[ZnO]_{sat}$). However, even with at least 4 adjustable parameters, the fits appear to match only ca. 50% of the experimental data. This suggests that something important is missing from the model, a point which will be discussed more in a moment.

Next, the authors observed a change in the WAXS signal and UV-Vis peaks after 1 h, where higher-order Bragg reflections are identified, and a red-shift of the absorption edge is observed (Figure 2.6).[39]

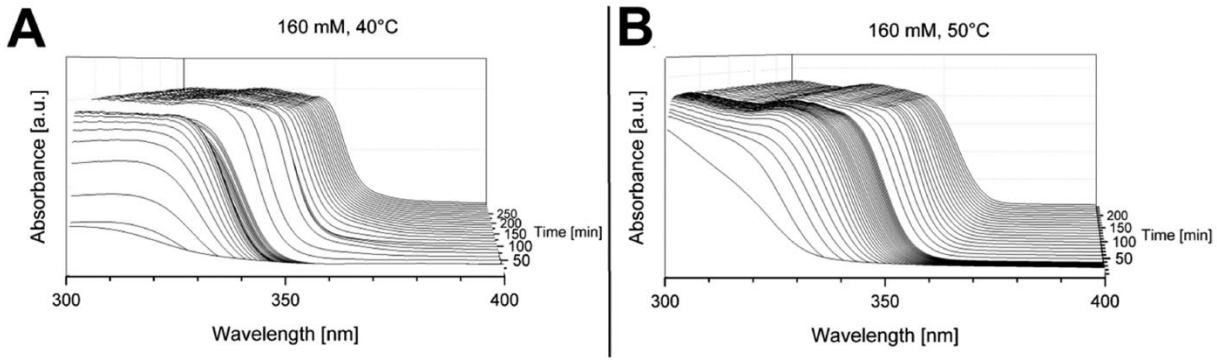

Figure 2.6. "UV-Vis spectra as a function of time recorded in situ during the formation of the ZnO nanoparticles at a concentration $[Zn^{2+}]_0$ = 0.133 mol/L at temperatures of 40 °C (A) and 50 °C (B)."[39] The red-shift of the absorption edge for both spectra is observed after 1 h, after which the primary nucleation and growth processes are hypothesized to have concluded as judged by the authors' interpretation of their SAXS data. Reproduced with permission from ref 39. Copyright 2019 American Chemical Society.

The overall particle-size by SAXS does not change significantly after 1 h, which suggests that a different type of growth process is occurring. The authors conclude that an increase in ZnO crystallinity is taking place during this "second growth phase", where the ZnO is observed to "develop full crystallinity."[39] Overall, the authors present expertly collected, high-quality kinetics data on the formation of ZnO. They collected it by multiple direct techniques using three direct physical methods, SAXS/WAXS and UV-Vis, reasons it merits selection as an important case study.

The authors' kinetics model partially satisfies two of the four minimum criteria for reliable mechanistic study. The first criterion was not met in that a complete, balanced reaction

stoichiometry was not provided.[39] We presented a possible mass- and charge-balanced formation reaction back in eq 2.2, but further characterization studies are warranted to elucidate the exact values for x and n in eq 2.2. Next, criterion (ii) was satisfied: the authors collected high-quality size versus time SAXS data and absorbance versus time UV-Vis data for the entire ZnO formation. The third criterion was partially satisfied as differential equations for the different processes were derived, but unfortunately pseudo-elementary steps for the reaction were not provided—there is no real chemical mechanism as a result of this careful, quantitative, expert work. The authors presented differential equations for nucleation and growth based on a single chemical reaction, eq 2.3. However, the differential equation for nucleation, eq 2.5, does not match that predicted by the coefficients in eq 2.3 (where eq 2.4 would have to have a squared, $[OH^-]^2$ dependence), but, instead, is based Classical Nucleation Theory (CNT). As a result, the $d[ZnO_N]/dt$ term is equal to a compilation of CNT-based constants and not the desired concentration terms (i.e., functions of $[Zn^{2+}]$, $[OH^-]$, and $[C_{18}H_{33}O_2^-]$) and associated rate constants corresponding to a mechanism composed of (pseudo)-elementary step reactions.[78] Lastly, criterion (iv) remains to be addressed in that other possible if not probable nucleation and growth models need to be tested to determine what model is best accounts for the formation of the observed "ZnO"—really more closer to $(ZnO)_n \bullet (C_{18}H_{33}O_2^-)_x$—nanoparticles.

In short, the authors study zinc oxide particle formation using state-of-the-art tandem *in situ* SAXS/WAXS and UV-Vis techniques. A single, non-disproof-based physical-chemical model is provided with at least 4 adjustable parameters that doesn't fully fit the observed kinetics data. Additional studies that would be welcome include: (i) writing out proposed pseudo-elementary steps for the reaction; (ii) obtaining a rate law in terms of $[Zn^{II}]$, $[OH^-]$, and $[C_{18}H_{33}O_2^-]$ as a minimum; and (iii) testing alternative models to determine the best, disproof-based model for ZnO

nanoparticle formation. A reliable, disproof-based mechanism for ZnO nanoparticle formation could result from just one set of additional studies based on this valuable, initial work.

2.3.3. Case Study #3: Mechanistic Analysis of Rhodium Nanoparticle Formation Using X-ray Absorption Fine Structure Spectroscopy

In 2012, Tanaka and coworkers published a noteworthy study on the formation of rhodium nanocubes.[40] The authors prepared the nanocubes from $RhCl_3 \bullet 3H_2O$ (0.2 mmol) in ethylene glycol (10 mL) with the bromide source tetradecyltrimethylammonium bromide (TTAB, 3.0 mmol) and poly(vinylpyrrolidone) (PVP, 3.0 mmol) at 130 ºC, eq 2.9.[40] The solution was stirred at room temperature under N_2 for 20-30 minutes, and then it was heated to 130 ºC within 3 minutes with vigorous stirring.[40] The proposed reaction stoichiometry from the experimental of ref 40 is given as eq 2.9 below, but is incomplete as it doesn't indicate the critical reductant, almost surely the ethylene glycol solvent, nor its oxidized products, initially glycolaldehyde one expects, then possibly higher oxidation to glycolic acid—depending in no small part on the (unspecified) amount of H_2O present in the system as required for the oxidation of glycoaldehyde to glycolic acid.

$$n\ RhCl_3 \xrightarrow[\text{Ethylene Glycol, } N_2,\ \Delta]{\text{[TTAB]}\ (C_{14}H_{29})N^+(CH_3)_3Br^-,\ \text{PVP}} Rh(0)_n \bullet \{Br^-(CH_3)_3C^+\} + 3Cl^- \qquad \text{(Eq 2.9)}$$

The reaction kinetics data were studied in real-time using dispersive X-ray absorption fine spectroscopy (DXAFS), which allows for microsecond data collection and easier measurement of subtle edge position shifts.[79] In addition, the authors used ex situ TEM, UV-vis, XRD, and MALDI-TOF MS to corroborate their DXAFS results,[40] a noteworthy total of five physical

methods for monitoring their $Rh(0)_n$ formation reaction. After 60 minutes, the authors reported final particle sizes of 5.2 ± 0.6 nm with 89.0% of particles cubic in shape.

To begin, the authors directly monitored the EXAFS intensity as a function of time, Figure 2.7.

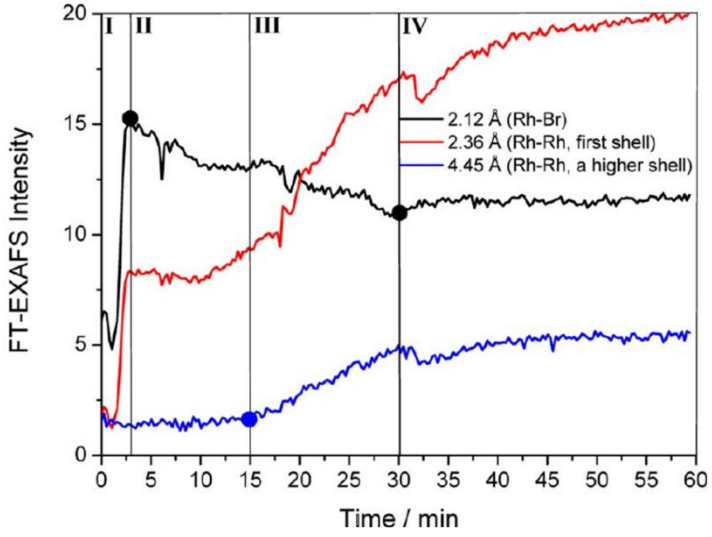

Figure 2.7. FT-EXAFS peak intensities as a function of time are shown for Rh-Br (black), Rh-Rh first coordination shell (red), and Rh-Rh higher-order coordination shells (blue). Overlain are four detectable stages for the formation of Rh nanocrystals for the $RhCl_3$–TTAB–PVP–EG system labeled by the authors as: ligand exchange (stage I), $Rh_{2\text{-}4}$ nuclei formation (stage II), nanocrystal growth (stage III), and transformation to high-quality nanocubes (stage IV). Figure reproduced with permission from ref 40. Copyright 2012 American Chemical Society.

The authors observed three points where the EXAFS data changed and thereby identified four "Stages" in the reaction. During the first stage (Stage I), they observed a sharp increase in Rh–Br bonds. The second stage (Stage II) was highlighted by a decrease in Rh–Br bonds, an increase in first shell Rh–Rh bonds, but no change in higher shell Rh–Rh bonds. In the third stage (Stage III), they saw a continued decrease in Rh–Br bonds, a sharp increase in first shell Rh–Rh bonds, and a steady increase in higher shell Rh–Rh bonds. The final stage (Stage IV) was characterized by a

leveling off for all species. The EXAFS intensity versus time data is consistent with four kinetic stages of the Rh particle formation process. Whether or not it requires three, four (or more) kinetic steps is not clear from just the raw data.

Next, the authors observed the Rh XANES K-edge as it evolved over time (Figure 2.8a–c) and separated it for the first three stages observed in Figure 2.7. In Figure 2.8a, they observed the signal of the reaction solution changes from being consistent with the $RhCl_3$ reference to being consistent with the $RhBr_3$ reference. The change suggests that in Stage I the Rh precursor undergoes a ligand exchange. In Figure 2.8b, the signal begins to show features consistent with the Rh foil reference, and in Figure 2.8c, significant changes are observed to suggest the formation of Rh nanoparticles.

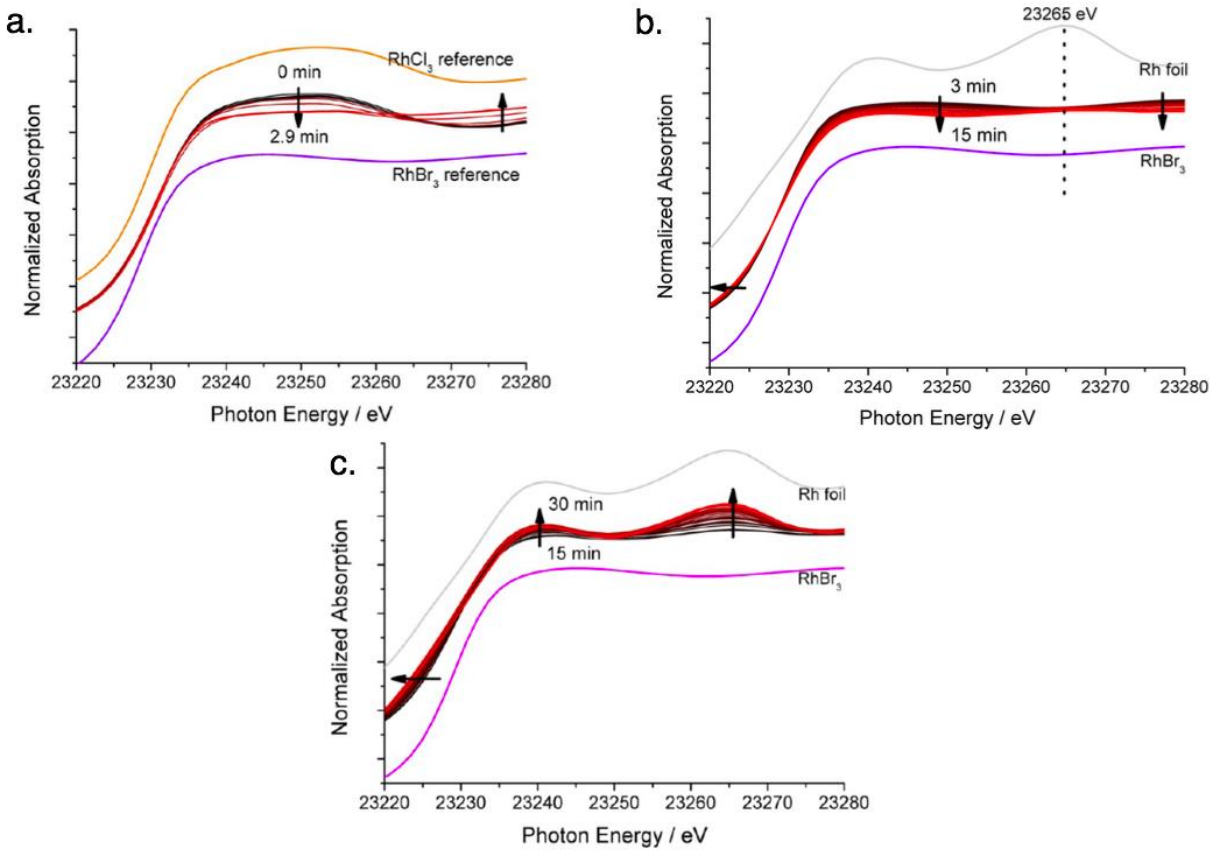

Figure 2.8. Rh K-edge XANES evolution for the $RhCl_3$–TTAB–PVP–EG system. **(a)** Stage I: chloro ligands substituted by bromo ligands, time 0 min to 3 min, with $RhCl_3$ and $RhBr_3$ reference spectra given. **(b)** Stage II: formation of $Rh_{2–4}$ nuclei, time 3 min to 15 min, with $RhBr_3$ and Rh foil reference spectra given. **(c)** Stage III: growth of nuclei to nanoparticles of size 5.2 ± 0.8, time 15 min to 30 min, with $RhBr_3$ and Rh foil reference spectra given. Arrows present in **(a)**–**(c)** indicate the direction of spectra change with time. Figure adapted with permission from ref 40. Copyright 2012 American Chemical Society.

The EXAFS and XANES data, from Figure 2.7 and 2.8 respectively, are interpreted by the authors as suggesting a four-stage process for formation of their Rh nanoparticles. To investigate their hypothesis, the authors sought to fit their kinetics data, the loss of $[Rh^{3+}]$ as a function of time (Figure 2.9). They used a known literature minimum mechanism, the 2-step mechanism of slow, continuous nucleation followed by autocatalytic surface growth,[73] to fit their kinetics data (green triangles in Figure 2.9).

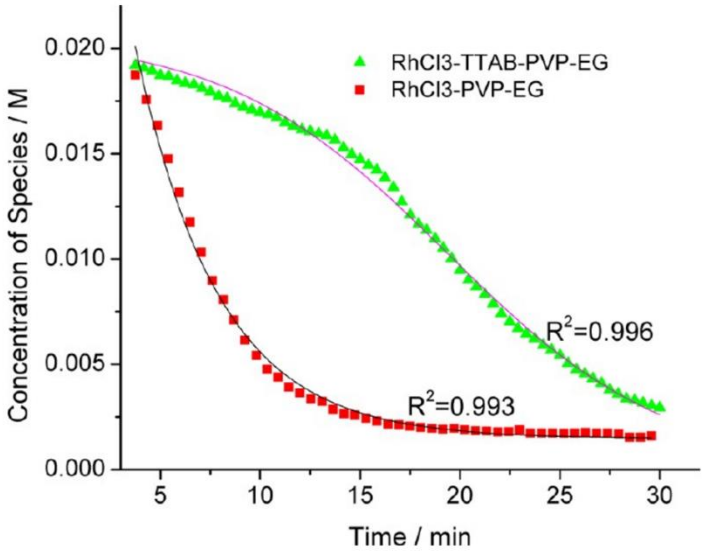

Figure 2.9. Loss of $[Rh^{3+}]$ as a function of time is plotted for $RhCl_3$–PVP–EG with the bromide TTAB (green triangles) and without the bromide source TTAB (red squares). The system without TTAB (red) was fit using a pseudo-first-order rate law. The system with TTAB (green) was fit using the 2-Step mechanism of slow continuous nucleation followed by autocatalytic surface growth (A ⟶ B with rate constant k_1 and A + B ⟶ 2B, rate constant k_2, where A = Rh^{3+} and B =

Rh^0). The fit yielded the following results: k_1 = 0.005 min^{-1} and k_2 = 8.77 min^{-1} M^{-1}. Figure reproduced with permission from ref 40. Copyright 2012 American Chemical Society.

The authors demonstrated in Figure 2.9 that bromide is critical to their prior equilibrium ligand exchange first stage. The reaction with*out* TTAB (red squares) was fit with an empirical power law[80]—and could not be fit (not shown) with a 2-step model.[73] However, the reaction with TTAB (green triangles) was fit at least roughly by the 2-step mechanistic model of continuous nucleation, A ⟶ B with rate constant k_1, and autocatalytic growth, A + B ⟶ 2B with rate constant k_2, where A = Rh^{3+} and B = Rh(0).[73]

However, the data in Figures 2.7–2.9, combined with mass spectrometry data in Figures S2.1–S2.3, led the authors to proposal the pictorial four-stage model for Rh nanocrystal formation shown in Figure 2.10.

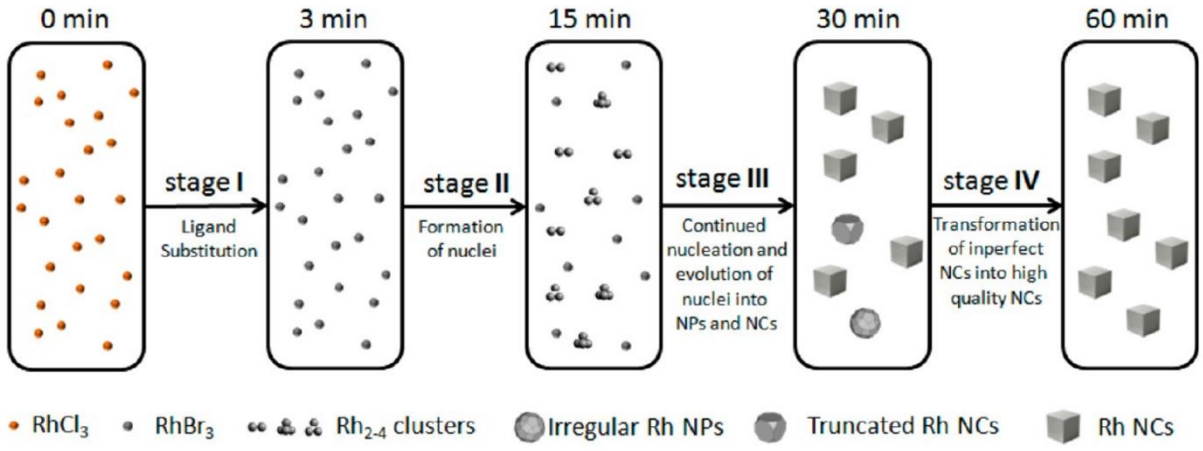

Figure 2.10. Schematic representation of the proposed four-stage formation process of Rh nanocrystals from $RhCl_3$ deduced from XAFS and MALDI-TOF experiments. Stage I is ligand substitution from chloro to bromo ligands. Stage II is the formation of Rh_{2-4} nuclei. Stage III is proposed to be continued nucleation and growth of nuclei into nanoparticles and cubic nanocrystals. Finally, Stage IV is a final growth stage where imperfect nanoparticles and nanocrystals transform into more crystalline nanocrystals. The authors note, "the Rh species shown in the five boxes represent the predominant but not the exclusive Rh species present, and the

chemical transformations illustrated under each arrow represent the major characteristic, but not necessarily the only process involved during each stage."[40] Figure reproduced with permission from ref 40. Copyright 2012 American Chemical Society.

Overall, the authors demonstrated the power of directly monitoring the loss of Rh^{3+} and the formation of Rh^0 with DXAFS while also employing *ex situ* MS and TEM. Their 4-stage pictoral model—while not a chemical mechanism—does satisfy two of the criteria and partially satisfies the other two criteria underlying reliable mechanistic studies. For criterion (i), the authors monitored the transformation of Rh species well throughout the reaction from Rh^{3+}–Cl to Rh^{3+}–Br and finally Rh^0. They identified, through MS, low molecularity nucleation, where the kinetically effective nucleation (KEN)[30] was observed to be $Rh_{2–4}$—an important result in its own right.

However, the complete, balanced reaction stoichiometry was not reported. The true nature of the final product remains unspecified, nominally something like "$Rh_nBr_a(PVP)_b$(glycolic acid)$_c$(ethylene glycol)$_d$", where the unknown coefficients *c* and *d* might be small enough to be negligible. Additionally, the Stage I ligand substitution reaction merits additional study—as does the simplification of just starting with preformed $RhBr_3$. The fully study of the exchange reaction and the proposed equilibrium constants are of interest as are controls of the effects of added H_2O on this reaction, almost surely important as glycolaldehyde is expected to be a kinetically more facile oxidant than ethylene glycol when the H_2O needed for the reaction converting glycolaldehyde plus H_2O to glycolic acid (and $2e^- / 2H^+$) is present. As for the second criterion (ii) of a reliable mechanistic study, the authors collected excellent, direct kinetics data (Figures 2.7 and 2.8). The Rh species were monitored by in situ XANES and EXAFS throughout the entire reaction. (iii) The third criterion of pseudo-elementary steps to describe the physical processes has been partially satisfied. Unfortunately, the authors then pretty much ignore the 2-step mechanism used in Figure 2.9 to fit their kinetics data and jump to the proposed a 4-stage representation in

Figure 2.10 that is ultimately just a pictorial restatement of their hypothesis of a 4-stage process. Finally, criterion (iv) has been accounted for as the authors disproved alternative hypotheses throughout their investigation. One example was the reaction with*out* TTAB (red squares) in Figure 2.9, where the control experiment produced different kinetics and further supported Stage I of the proposed 4-stage model. Additionally, the authors fit their kinetics data (in their supporting information[40]) with an additional literature mechanism, a 4-step model[81] of continuous nucleation, autocatalytic surface growth, bimolecular agglomeration, and autocatalytic agglomerative growth. They found that agglomerative growth is *not* a significant contributor to the growth of their nanocubes, evidence supportive of their proposed growth pathway (Stage III) and shape correction (Stage IV). Presumably, the 2-step mechanism used to fit their data corresponds to Stages II and III, but without writing out the precise pseudo-elementary steps, one does not know what steps are being fit in Figure 2.9.

Noteworthy is that the authors have been careful to not claim that they *know* the mechanism. Rather, they have offered their evidence and conclusions while working towards a disproof-based mechanism, but to date achieving a quite plausible model consistent with and supported by their data. Their study is a good example of acquiring high-quality, direct kinetics data from XAFS and corroborate it with other physical techniques. Welcome on this valuable system would be additional XAFS as well as SAXS studies (i) starting with $RhBr_3$ to avoid the ligand exchange, (ii) establishing the composition of the "Rh_nBr_a(PVP)$_b$(glycolic acid)$_c$(ethylene glycol)$_d$" products, (iii) establishing the role of water and the balanced reaction including the expected role of glycol as the reductant and the oxidized, glycolaldehyde / glycolic products—the effects of added, non-coordinating bases such as Proton Sponge™ need to also be examined because writing the balanced reaction reveals that H+ are produced in the particle-formation

proves. Then (iv) measuring the full rate law for the nucleation and growth processes ([$RhBr_3$], [Br^-], [glycol], [Base], [PVP], and any other dependencies will be needed, along critically with (v) expressing the results in pseudo-elementary step mechanisms that can be subjected to further disproof until, ideally, a single proposed mechanism remained, are also needed. The results of those studies promises to be a reliable mechanism for $Rh(0)_n$ and by extension to other particle formations starting with the common precursor of the metal-halide and using alcohol reductants.

2.3.4. Case Study #4: Early-Stage CdSe Nanocrystal Formation Studied by In Situ XAFS in a Microfluidic Cell

In 2011, Maeda and co-workers studied the early-time formation of $(CdSe)_n$ nanocrystals using XAFS and microfluidic cell.[41] The three reactant solutions (Cd, Se, and ligand) were mixed and measurements were taken a different points along the microfluidic cell that correspond to different time points in the reaction between 0.0 s and 8.1 s.[41] The cadmium reactant solution was prepared by heating $Cd(CH_3COO)_2$, oleic acid, and octadecene (ODE) at 453 K under Ar. The selenium reactant solution was prepared by dissolving selenium powder in trioctylphosphine (TOP or $P(C_8H_{17})_3$) and diluted by ODE. Ligand, dodecylamine ($CH_3(CH_2)_{11}NH_2$, DDA), solution was prepared by dissolving DDA in ODE. The solutions were combined, heated to 513 K, and monitored by XAFS. Figure 2.11 provides the schematic of the microfluidic cell with its UV-Vis and X-ray components.

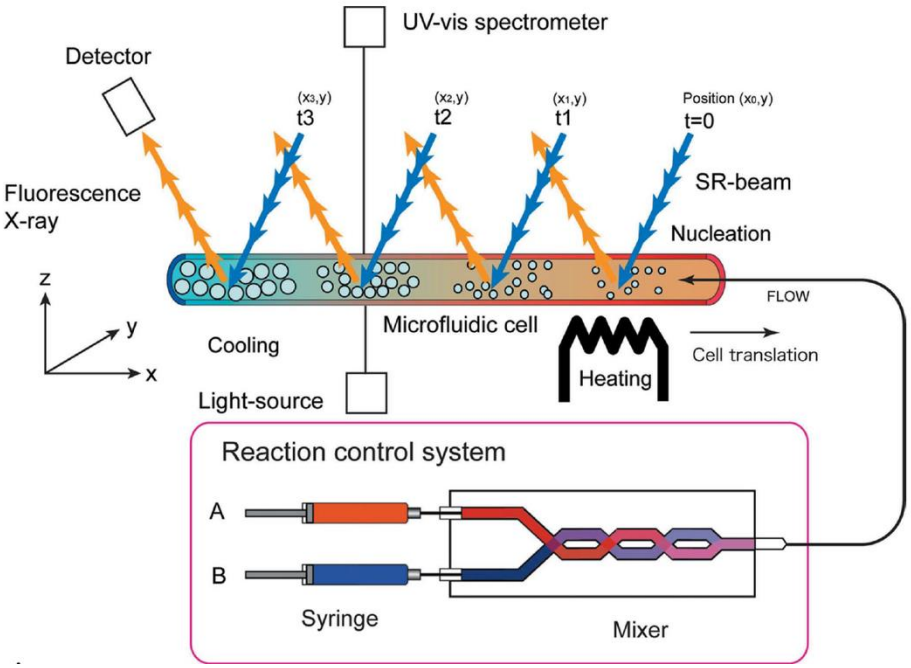

Figure 2.11. "Schematic principle of the *in situ* XAFS experimental set-up using a microfluidic cell. Fluorescence yield spectra record at positions (*x*,*y*) along a microreactor channel provide time-dependent XAFS spectra. In the present reaction, precursor flows (TOP-Se and Cd stock solution) are mixed before introducing to a heated microchannel."[41] Reproduced with permission from ref 41. Copyright 2011 International Union of Crystallography.

The proposed reaction stoichiometry, that is, as far as we can determine it from the data provided in ref 41, is given in eq 2.10.

$$n\,Cd(CH_3COO)_2 + n\,Se{=}P(C_8H_{17})_3 + n\,CH_3(CH_2)_{11}NH_2 \xrightarrow[\text{ODE, Ar,}]{\text{oleic acid}} (CdSe)_n{\bullet}(CH_3(CH_3)_{11}NH_2)_x + n\,P(C_8H_{17})_3 + 2n\,CH_3COO^- + n\text{-}x\,CH_3(CH_2)_{11}NH_2 \quad \text{(Eq 2.10)}$$

The Se, Cd, and DDA concentrations were 30 mM, 12 mM, and 5-10 wt%, respectively. XAFS measurements were collected at 0.0, 1.1, 1.4, 1.8, 2.4, 3.0, 5.0, and 8.1 s.[41] The data were processed

according to standard literature methods using the *ATHENA* and *ARTEMIS* modules.[82] Based on the UV-Vis, XANES, and EXAFS data, the kinetics, formation of amorphous nanoparticles, and the estimation of $(CdSe)_n$ yield were reported.[41]

The authors analyzed their XANES, EXAFS, UV-Vis and photoluminescence (PL) results to determine the early time (0.0 – 8.1 s) $(CdSe)_n$ formation behavior. The XANES results given in Figure 2.12a indicate the author's direct observation of formation of the $(CdSe)_n$ particles. Simultaneously, the authors used UV-Vis and PL spectroscopies (Figures 2.12b and 2.12c) to monitor directly both $(CdSe)_n$ particle formation and crystallinity.

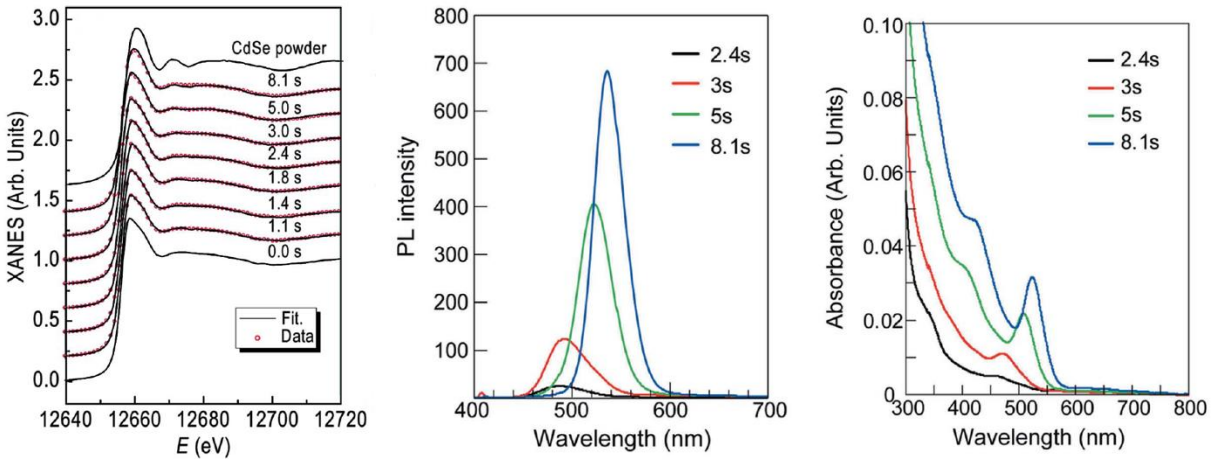

Figure 2.12. (a) Experimental XANES spectra collected from 0.0 – 8.1 s after "initiation of the reaction with the addition of 5 wt% DDA," where again DDA is dodecylamine.[41] Reference spectra of $(CdSe)_n$ were given for $(CdSe)_n$ powder crystals of 3 nm. "Open circles indicate simulated XANES spectra."[41] **(b)** Photoluminescence spectra of $(CdSe)_n$ nanoparticles in the presence of 5 wt% DDA.[41] **(c)** UV-vis absorbance spectra of the $(CdSe)_n$ nanoparticles for the same solution as (b). Reproduced with permission from ref 41. Copyright 2011 International Union of Crystallography.

By XANES, one can see the increase at ca. 12670 eV with time that is indicative of $(CdSe)_n$ particle formation, by comparison to authentic $(CdSe)_n$ powder. $(CdSe)_n$ particle formation is further supported by both the UV-Vis excitonic absorption at 350 nm and the PL peak at 365 nm.[41,83]

Notably, prior to 2.4 s, there no absorption or emission peaks are present, indicating a lack of crystalline $(CdSe)_n$. A closer observation of the PL spectra shows a red-shift with time interpreted as the loss of deep-trap states due to increased crystallinity.[41] The PL spectra also indicate that the particle shape is growing more symmetrical, the narrowing and increased symmetry of the peak supporting the interpretation of increased crystallinity.[84] Hence, at the earlier times of 2.4 and 3 s, amorphous $(CdSe)_n$ nanoparticles are most likely formed, but by 8.1 s they have increased crystallinity.

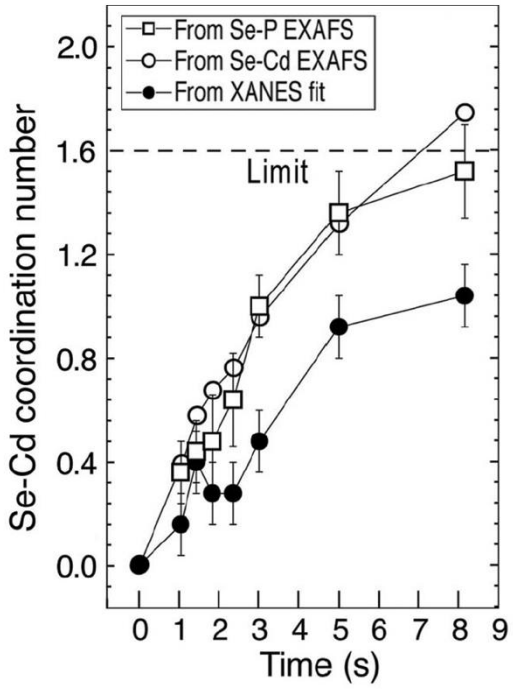

Figure 2.13. "Se–Cd coordination number as a function of elapsed time determined by EXAFS independently for the Se–P and Se–Cd pairs (open squares and open circles, respectively) compared with the value determined by the XANES fit (closed circles). The dashed line indicates the Se–Cd coordination limit. The reacted amount of Se and Cd during the reaction is assumed to be equal."[41] Reproduced with permission from ref 41. Copyright 2011 International Union of Crystallography.

The synchrotron EXAFS and XANES results were compiled in Figure 2.13, where the Se–Cd coordination number was independently determined three ways as a function of time. The two datasets collected by EXAFS are the same within error, which is consistent with "a two-component model" (i.e., "unreacted Se–TOP does not dissolve leaving Se^{2-} ions").[41] The authors remark that the XANES results are lower in average Se-Cd coordination number due to the reference used in processing the data.[41] Furthermore, the authors considered three possible alternative hypotheses for the difference between the EXAFS and XANES data en route to their final Se-Cd coordination numbers.[41] The $(CdSe)_n$ study[41] presented by Maeda and co-workers demonstrates an important approach to observing particle formation at early times. They have designed a direct, tandem UV-Vis and XAFS microfluidic technique and used it to monitor the formation of $(CdSe)_n$ during the important first 10 s of the reaction.

In future more detailed mechanistic studies, the exact reaction stoichiometry could be elucidated, thereby satisfying criterion (i) of a reliable mechanistic study. In that endeavor, the considerable literature in the semiconductor/quantum dot field, and the advances the field has made in the last decade, are likely to prove useful.[25,85,86,87,88,89] For example, the authors in this study claimed[41] that ODE was used because it is a non-coordinating solvent. However, a recent 2019 paper has demonstrated that ODE is not innocuous at temperatures greater than 393 K, where ODE will autopolymerizes and coat the nanoparticle in a manner that cannot be removed with standard purification methods.[90] Hence, at the temperature of the reaction[41] (513 K), ODE cannot be claimed to be a non-coordinating solvent.

Criterion (ii)—namely collecting kinetics data—was satisfied by the use of XANES, EXAFS, UV-Vis, and PL to address the kinetics of $(CdSe)_n$ nanoparticle formation. The use of a microfluidic device was effective in providing the early time points. That said, future studies are

needed to obtain the full rate law for particle formation. Criterion (iii) will also need to be addressed in future studies, that is, the need to write out the complete pseudo-elementary steps to describe the $(CdSe)_n$ particle-formation mechanism. Finally, regarding criterion (iv), the authors did apply a disproof-based method to a number of their experiments. Importantly, they did not overinterpreted their data, in our opinion, nor have they claimed more than they know about the precise $(CdSe)_n$ formation mechanism.

Overall, the authors provide a noteworthy initial study[41] using *in situ* XAFS to produce Se-Cd bond formation kinetics data and garner insights into the early time of $(CdSe)_n$ nanoparticle formation. Hopefully, (a) determination of a full rate law for particle formation, and (b) pseudo-elementary step construction consistent with that experimental rate law are future studies that the community can hopefully look forward to, based on the authors' *in situ* methodology.

2.3.5. Case Study #5: A Second-Generation $Ir(0)_n$ System Studied by XAFS, SAXS and Four Other Methods, Including Mechanism-Enabled Population Balance Modeling

In 2019 and 2021, extensive work on a second-generation $\{[(1,5\text{-COD})Ir^{I}\bullet HPO_4]_2\}^{2-}$ precursor to $Ir(0)_n\bullet(HPO_4^{2-})_x$ nanoparticle system[32,42] was reported, research that follows a series of papers since 1997 on a first-generation $\{(1,5\text{-COD})Ir^{I}\bullet POM\}^{8-}$ (POM = $P_2W_{15}Nb_3O_{62}^{9-}$, **p**oly**o**xo**m**etalate) precursor to $Ir(0)_n\bullet(POM^{9-})_m$ nanoparticle system.[31,73,81,91,92] Iridium nanoparticles in the *2nd-generation system* were prepared by combining $[(1,5\text{-COD})Ir^{I}(solv)_2]^{+}$ with 2–6 molar equivalents of $(Bu_4N)_2HPO_4$ in acetone. The exact composition of the iridium precursor and its solution dimeric resting state, $\{[(1,5\text{-COD})Ir^{I}\bullet HPO_4]_2\}^{2-}$, were established by using UV-vis, ^{1}H NMR, ESI-MS, and a Signer solution molecular weight apparatus.[32,93] The

experimentally determined, balanced reaction stoichiometry of the HPO_4^{2-}-stabilized $Ir(0)_{\sim 150}$ nanoparticles has been published[32] and is given in eq 2.11 in its more general form:

$$n\,[(1,5\text{-COD})Ir^{I}(NCCH_3)_2][BF_4] \;+\; n\,(Bu_4N)_2HPO_4 + n\,PS^{TM} \xrightarrow[\text{Acetone}]{2.5\ H_2}$$

$$Ir(0)_n\bullet(HPO_4^{2-})_x \;+\; (n - x)\,HPO_4^{2-} \;+\; n\,\bigcirc \;+\; n\,(Bu_4N^{+})(BF_4^{-})$$
$$+\; n\,Bu_4N^{+} + n\,PS^{TM}\text{–}H^{+} + 2n\,CH_3CN \qquad \text{(Eq 2.11)}$$

The prior equilibrium given in Scheme 2.2 was shown to be present by ^{1}H NMR, UV-vis, and Signer solution molecular weight studies.[32,93]

Scheme 2.2. Formation of a 1:2 $HPO_4^{2-}/Ir^{I}(1,5\text{-COD})^{+}$ Intermediate, **2**, and Then the Final 1:1 Diphosphate-Bridged Complex, **3**, Supported by the ^{1}H NMR Titration Studies. Reproduced with Permission from Ref 32. Copyright 2019 American Chemical Society.

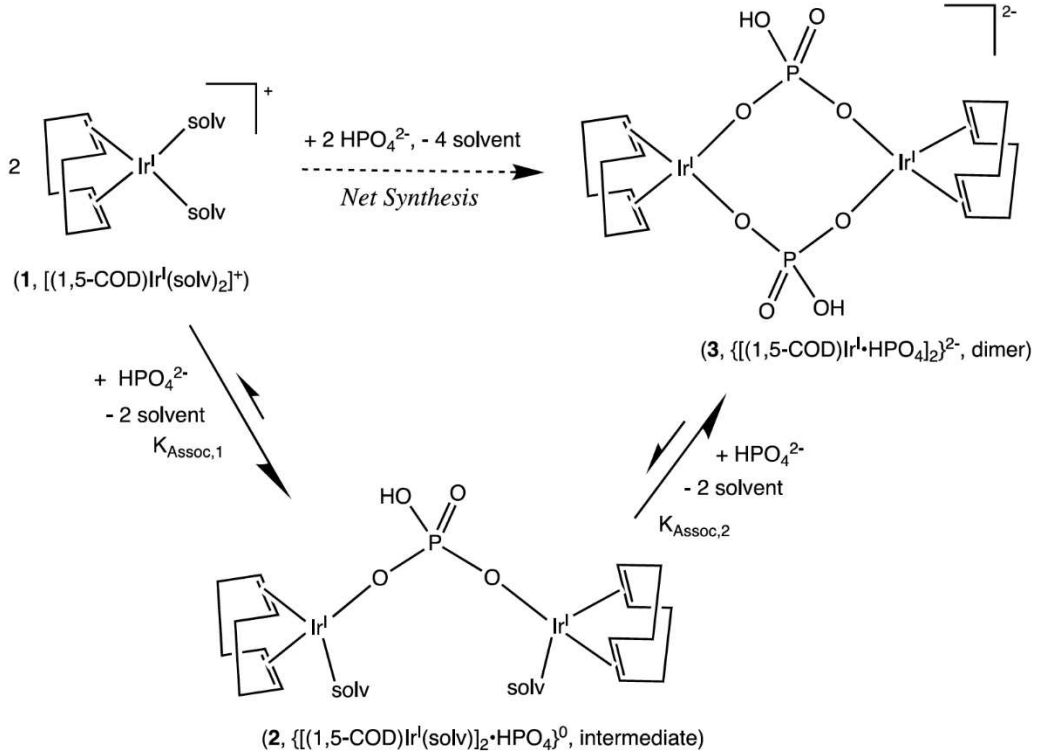

An indirect, but convenient cyclohexene hydrogenation catalytic reporter reaction (CHCRR)[73] that generates thousands of precise kinetics data points, was used for in-house monitoring of the $Ir(0)_n$ particle formation—and, importantly, to find optimized conditions for subsequent monitoring by the more direct methods of XAFS and SAXS, *vide infra*. (For a more extensive understanding of the CHCRR and its accompanying assumptions, please refer to references 32, 42, and 73, Appendix A of reference 73 providing the original derivation for the use of the CHCRR.) In addition, in-house GLC of the cyclooctane product, ^{1}H NMR, and UV-vis were used to monitor the reaction and check on the in-house CHCRR kinetics.

The reproducible sigmoidal kinetics curves obtained prior to the XAFS and SAXS studies were fit by the literature 1997 2-step mechanism[73] of slow, continuous nucleation (A → B, k_{1obs}) and autocatalytic surface growth (A + B → 2B, k_{2obs}). Reactions were run around a range of $[Ir_2]_{Initial}$ from 1.5 mM to 6.0 mM and at five different amounts of HPO_4^{2-} stabilizer, $[HPO_4^{2-}]_{Added}$. A total of 20 different combinations of $[Ir_2]_{Initial}$ and $[HPO_4^{2-}]_{Added}$ were studied and run in triplicate or more—an advantage of the in-house methods as a precursor to the XAFS and SAXS studies. Additionally, the dependence of the nucleation rate constant, k_{1obs}, on both the starting $[Ir_2]_{Initial}$ and importantly on the amount of $[HPO_4^{2-}]_{Added}$ were determined. These figures are reproduced below as figures 2.14a and 2.14b.[32]

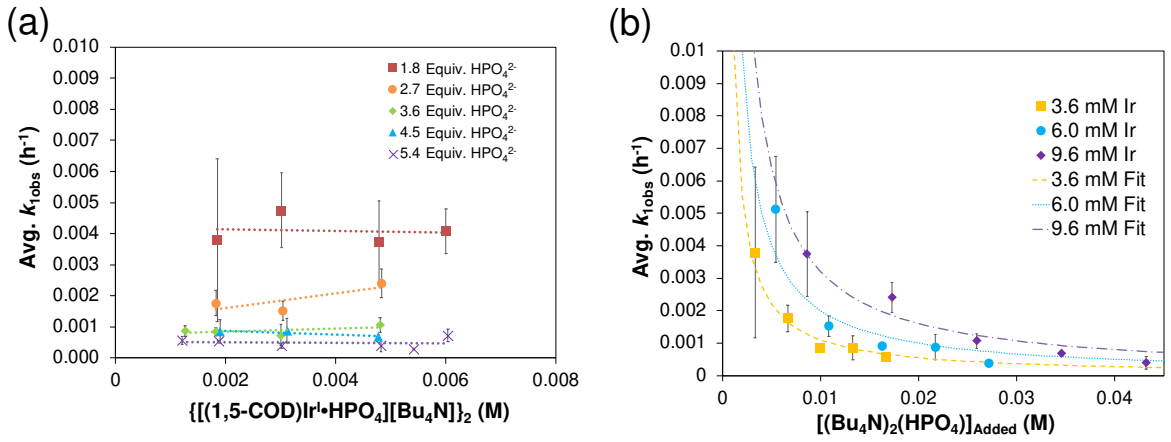

Figure 2.14. **(a)** Plot of k_{1obs} (h^{-1}) vs the initial {[(1,5-COD)Ir^{I}•HPO_4][Bu_4N]}$_2$ precursor concentration (M). Nucleation rate constants (k_{1obs}) were collected from 0.0015 – 0.006 M at five ratios of [$(Bu_4N)_2HPO_4$]:[Ir] (red squares = 1.8:1, orange circles = 2.7:1, green diamonds = 3.6:1, blue triangles = 4.5:1, and purples X's = 5.4:1). "The important result is the slope = 0 in each case within experimental error, indicating that there is no further dependence (that is, beyond the observed, first-order dependence) of k_{1obs} on the starting concentration of {[(1,5-COD)Ir^{I}•HPO_4][Bu_4N]}$_2$."[32] **(b)** Plot of k_{1obs} (h^{-1}) vs the added $(Bu_4N)_2HPO_4$ beyond a 1:1 ratio of [HPO_4^{2-}]:[Ir]. The starting iridium concentrations were 3.6 mM (yellow squares), 6.0 mM (blue circles), and 9.6 mM (purple diamonds). Data were fit based on a derivation for K_{Diss} (see Scheme 2.3 below) that is given in reference 32. Reproduced with permission from ref 32. Copyright 2019 American Chemical Society.

Figure 2.14a demonstrates that, for this 2nd-generation iridium nanoparticle formation, nucleation is first-order in the well-characterized, dimeric precursor {[(1,5-COD)Ir^{I}•HPO_4]$_2$}$^{2-}$, consistent with a small kinetically effective nucleus (KEN)[30] of just Ir(0)$_2$. Furthermore, the fit of the k_{1obs} nucleation rate constants versus the added [$(Bu_4N)_2(HPO_4)$] data to the proposed nucleation mechanism[32,42] given in Scheme 2.3 was the only mechanism of five nucleation mechanisms considered able to fit the data in Figure 2.14b. The kinetics analysis also reveal that {[(1,5-COD)Ir^{I}•HPO_4]$_2$}$^{2-}$ is not the active species that nucleates to Ir(0)$_2$, but instead indicates {[(COD)Ir^{I}(solv)]$_2$•HPO_4}^{0} (and possibly also (1,5-COD)Ir^{I}(solvent)$_2^+$ based on prior precedent[31]) as top candidates for a kinetically competent intermediate involved in nucleation (eq 2.13).

Scheme 2.3. Proposed Nucleation Mechanism[32] Involving the Dissociative Equilibrium from $\{[(1,5\text{-COD})Ir^{I}\bullet HPO_4][Bu_4N]_2\}$ in Acetone, Based on the $[HPO_4^{2-}]$ Dependence of the Kinetics and ^1H NMR Evidence for the Neutral, $\{[(COD)Ir^{I}(solv)]_2\bullet HPO_4\}^0$ Intermediate. Adapted and Reproduced with Permission from Ref 42. Copyright 2021 American Chemical Society.

$$\{[(COD)Ir^{I}\bullet HPO_4]_2\}^{2-} + 2\ solv \underset{}{\overset{K_{Diss}}{\rightleftharpoons}} \{[(COD)Ir^{I}(solv)]_2\bullet HPO_4\}^0 + HPO_4^{2-} \qquad \text{(Eq 2.12)}$$

$$\{[(COD)Ir^{I}(solv)]_2\bullet HPO_4\}^0 + HPO_4^{2-} \xrightarrow{k_{3,fast}} Ir(0)_2 + HPO_4^{2-} + 2\ \text{  } + 2\ H^+ + 2\ solv \qquad \text{(Eq 2.13)}$$

Noteworthy here is that multiple attempts over many years to obtain XAFS and SAXS kinetics data for the first-generation system failed due to the large, W-containing POM^{9-} stabilizer, the large ca. 1.5nm by 1.2 nm "cigar-shaped" POM^{9-} size obscuring SAXS monitoring of early time nucleation events and the W in the POM^{9-} (= $P_2W_{15}Nb_3O_{62}^{9-}$) interfering with the Ir-XANES. Hence, the $\{[(1,5\text{-COD})Ir^{I}\bullet HPO_4]_2\}^{2-}$ second generation system was developed specifically with XAFS and SAXS monitoring in mind and in order to check on the convenient, precise-data-generating, but indirect CHCRR kinetics method.

Synchrotron XAFS and SAXS experiments were conducted on the second-generation $\{[(1,5\text{-COD})Ir^{I}\bullet HPO_4]_2\}^{2-}$ precursor to $Ir(0)_n\bullet(HPO_4^{2-})_x$ nanoparticle system at initial Ir concentrations from 3.0 mM to 12.0 mM and at five Ir : HPO_4^{2-} stabilizer ratios of from 1:1.8 to 1:5.4.[42] The $Ir(0)_n$ nanoparticle formation reactions were run under the standard conditions of ~40 psig H_2 at 22 °C and with 1 molar equivalent of Proton Sponge per Ir present to absorb the H^+ produced in the balanced reaction, eq 2.11—and also prevents hydrogenation of the acetone solvent to 2-propanol by the highly catalytically active $Ir(0)_n$ nanoparticles,[94] experimental design

that takes advantage of the deep knowledge of the two $Ir(0)_n$ nanoparticle formation systems.[30,31,32,65,66,73,81,91,92,94]

Optimized conditions for the XANES ([Ir] = 0.005 M, 2.25 molar equiv HPO_4^{2-}) and SAXS ([Ir] = 0.009 M, 3.6 molar equiv HPO_4^{2-}) worked out with the in-house CHCRR were employed along with Tandem CHCRR kinetics data collected at the synchrotron simultaneously with (separate) XANES and SAXS studies done at different synchrotrons with separate collaborators.[42] Also collected was additional in-house CHCRR data (i.e., under the XANES and SAXS conditions[42]) as was gas-liquid chromatography quantification of the cyclooctane (COA) product formation vs time, again under the XANES and SAXS conditions. The composite data in terms of molar concentration of iridium (M) as a function of time (h) are given below in Figure 2.15.

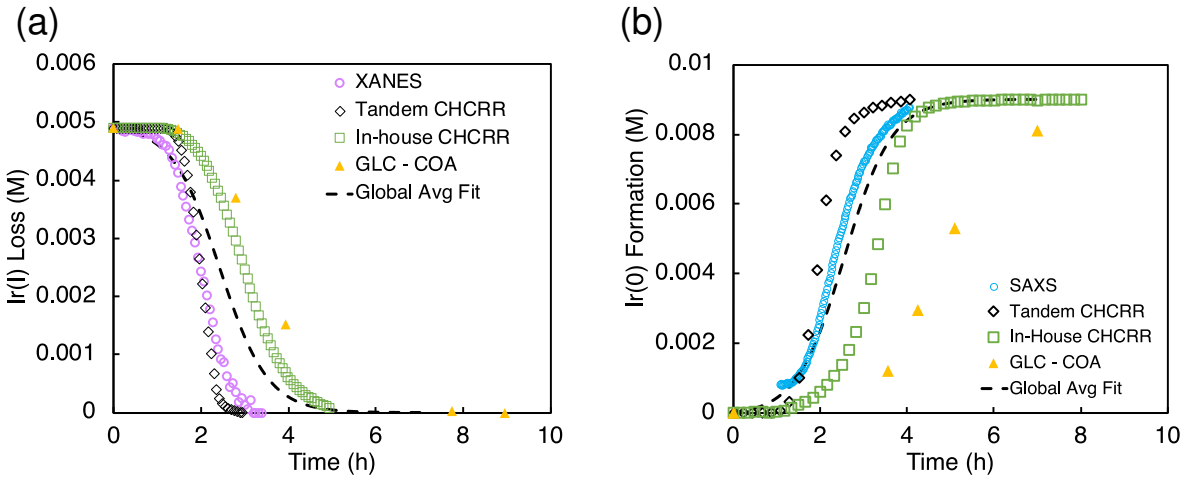

Figure 2.15. (a) XANES data (hollow purple circles), tandem CHCRR data collected at the synchrotron (hollow black diamonds), in-house CHCRR data collected under otherwise identical conditions (open green squares), and GLC of the cyclooctane product (solid yellow triangles) were fit with the 2-step mechanism[73] to yield a global average fit (dashed black line). Resultant rate constants are $k_{1obs(avg,XANES)} = (2.2 \pm 0.3) \times 10^{-2}$ h^{-1} and $k_{2obs(avg,XANES)} = (3.7 \pm 0.1) \times 10^{2}$ h^{-1} M^{-1}. **(b)** SAXS data (hollow blue circles), tandem CHCRR data collected at the synchrotron (hollow black diamonds), in-house CHCRR data collected under otherwise identical conditions (open green squares), and GLC of the cyclooctane produced (solid yellow triangles) were fit with the 2-step mechanism[73] to yield a global average fit (dashed black line). Resultant rate constants are

$k_{1obs(avg,SAXS)} = (1.7 \pm 0.2) \times 10^{-2}$ h^{-1} and $k_{2obs(avg,SAXS)} = (2.0 \pm 0.1) \times 10^{2}$ h^{-1} M^{-1}. Reproduced with permission from ref 42. Copyright 2021 American Chemical Society.

The k_{1obs} nucleation rate constants for the XANES, in-house CHCRR, and $GLC_{cyclooctane}$ datasets are equivalent within 1.6-fold. The Tandem CHCRR dataset to the XANES was determined to be an outlier statistically (>5σ) and experimentally (due, apparently, to small amounts of Ir(0) from X-ray radiolysis catalyzing and accelerating the CHCRR).[42] The k_{1obs} nucleation rate constants for the SAXS, Tandem CHCRR, in-house CHCRR, and $GLC_{cyclooctane}$ datasets all proved to be within a similar factor of 2. The Tandem CHCRR run simultaneously to the SAXS undercuts the synchrotron data some, but there was evidence of Ir(0) metal fouling found on the SAXS cell window[42], presumably due to actually well-precedented—but little discussed and certainly under recognized—X-ray radiolysis during such synchrotron studies.[95,96,97,98,99,100,101,102,103] There is compelling precedent in the well-studied $Ir(0)_n$ nanoparticle system that even trace amounts of adventitious Ir(0) hugely increase the nucleation and subsequent growth rates, sometimes resulting in complete elimination of the induction period of the typically sigmoidal kinetics curve.[73,92] A fundamental contribution from these particular synchrotron XANES and SAXS studies is, then, to raise a red flag concerning the involvement in X-ray-based methods that are more often than not assumed to be completely direct without artifacts. Relevant here is that Frenkel and collaborators have shown[95] that a photon flux of ~$3x10^{13}$ photons per second results in an estimated ~10^{15} solvated electrons[104] even when that radiolysis involves the improbable, highly energetic removal of an electron from divalent zinc, $Zn^{2+} + h\nu \rightarrow Zn^{3+} + e^{-}$. Of course, in particle formation systems exhibiting autocatalytic, exponential growth as is commonly seen, any trace nucleation events due to X-ray radiation-induced radiolysis will then be quickly magnified, exponentially.

The data from all the monitoring methods (XANES, SAXS, CHCRR, and GLC) were standardized, compiled, and analyzed as a single dataset containing 1,178 total data points. These data and the global fit using the 2-step mechanism are reproduced as Figure 2.16. The resultant, globally average, fit-determined rate constants yielded $k_{1obs,global\ avg} = (1.5 \pm 0.1) \times 10^{-2}$ and $k_{2obs,global\ avg} = (2.4 \pm 0.1) \times 10^{2}$ as relatively precise rate constants (±7% and ±4% error, respectively) that are believed to be reasonably accurate k_{1obs} and k_{2obs} rate constants as well.

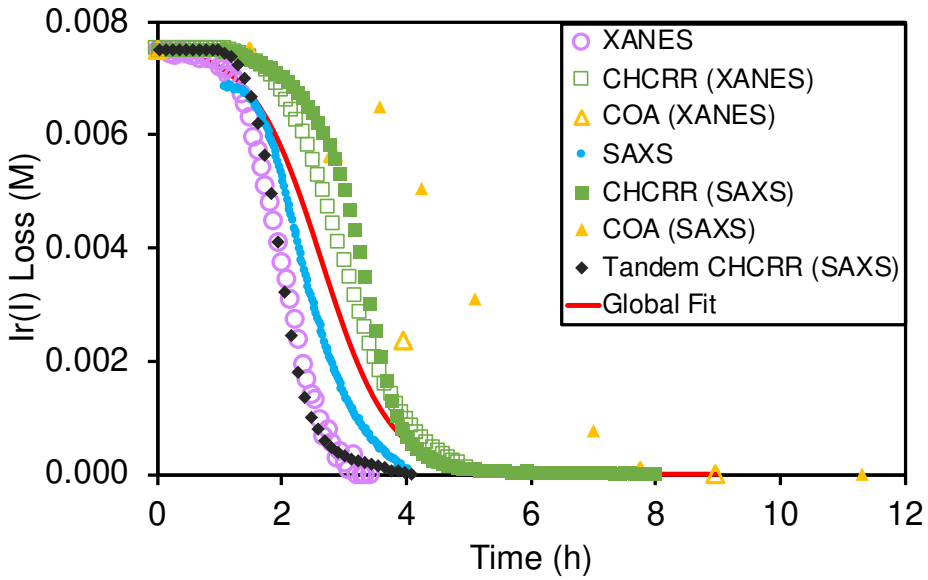

Figure 2.16. "The seven datasets are given: XANES as hollow purple circles, in-house CHCRR (under XANES conditions) as hollow green squares, COA (under XANES conditions) as hollow yellow triangles, SAXS as solid blue circles, in-house CHCRR (under SAXS conditions) as solid green squares, COA (under SAXS conditions) as solid yellow triangles, and Tandem CHCRR (simultaneous with SAXS measurements) as solid black diamonds. The solid red line represents the global fit to all seven datasets."[42] The resultant, globally average, fit-determined rate constants with fitting error are $k_{1obs,global\ avg} = (1.5 \pm 0.1) \times 10^{-2}$ and $k_{2obs,global\ avg} = (2.4 \pm 0.1) \times 10^{2}$. All datasets, as mentioned in ref 42, were standardized to 7.5 mM in Ir^{I}. Reproduced with permission from ref 42. Copyright 2021 American Chemical Society.

Overall, the XANES, SAXS, in-house CHCRR, and GLC methods all reported equivalent rate constants within either 1.6 of 2 orders of magnitude for XANES and SAXS, respectively, a

rare comparison of multiple in-house as well as synchrotron XANES plus SAXS particle formation monitoring methods. The composite kinetics data from all available experimental methods (XANES, SAXS, CHCRR, GLC, and ^{1}H NMR), were fit by the 2-step mechanism of slow, continuous nucleation (A → B, k_{1obs}) and autocatalytic surface growth (A + B → 2B, k_{2obs}). Therefore, all experimental methods, including the synchrotron XANES and SAXS, presently support the 2-step mechanism as the minimal mechanism to describe quantitatively $Ir(0)_n$ formation. What is interesting from the well-studied $Ir(0)_n$ nanoparticle systems is that, in both the first and second-generation systems now, that even with the addition of synchrotron XANES and SAXS and XAFS, the sum of all of the kinetics methods are insufficient to determine the true particle formation mechanism as demonstrated by ME-PBM analysis, discussed next.

Mechanism-enabled population balance modeling (ME-PBM) was first reported in 2019 and 2020 papers,[65,66] there for 1st-generation $Ir(0)_n$ nanoparticle system. Population balance modeling (PBM) tracks each and every particle in a proposed particle-formation pathway, consisting of even thousands of elementary steps. However, ME-PBM uniquely uses experimentally established minimum particle formation mechanisms to develop the ME-PBM code.[65,66] ME-PBM as a result is able to *predict* both average particle sizes and particle-size distributions (PSDs), including the *PSD shape*, from an input minimum mechanism. Relevant here is that there are now 5 classes of experimentally based minimum consisting of 96 distinct possible particle formation mechanisms that one can test as summarized later in a Table in Section 2.4.

ME-PBM is also able to inform the inverse problem of going from "observations / effects" back to "cause / a mechanism" whereby one tests and thereby refuting—or supporting—ideally all possible reasonable minimum mechanisms, while also extracting rate constants for the pseudo-elementary steps of that minimum mechanism from PSD data.[65,66] As alluded to above, in both the

first[65,66] and now second generation $Ir(0)_n$ nanoparticle systems, the ME-PBM analysis of the wealth of kinetics data otherwise buried in the PSD has led to disproof of the minimum mechanisms that were previously able to account for all of the experimental data (i.e., other than the PSD). Significantly, ME-PBM analysis of the PSD in the first generation $Ir(0)_n$ system also provided a new paradigm for how narrow PSDs can be formed[65,66]: smaller particle grow faster than larger particles, thereby catching up in size to them and resulting in near-monodisperse PSDs despite the inherently broadening effects of continuous nucleation.[65,66]

Hence, initial ME-PBM analysis of the TEM-determined PSDs in the second-generation $Ir(0)_n$ nanoparticle formation system was reported in the 2021 paper that also reported the XANES and SAXS studies.[42] Specifically, ME-PBM was used to analyze the end-time PSD at 10.0 h (shown as the black distribution in Figure 2.17), using to start the 2-step mechanism while also including the experimentally determined prior equilibrium (given back as eqs 2.12 and 2.13).

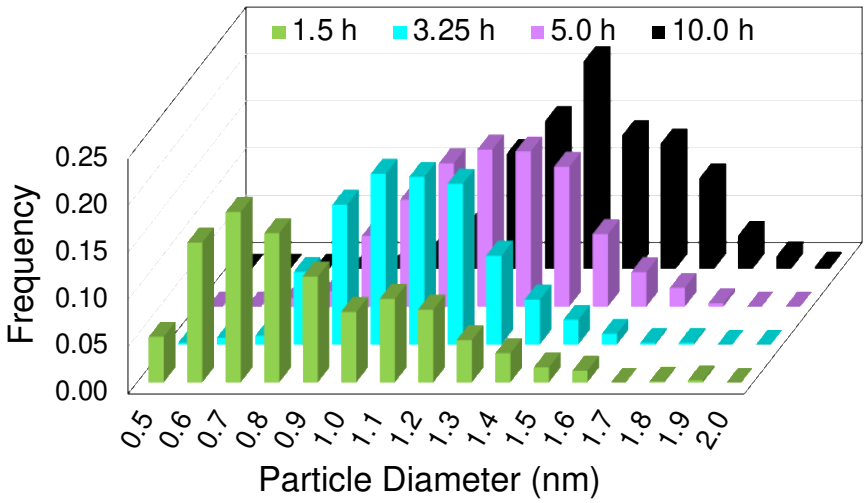

Figure 2.17. "Particle size distributions for the formation of $Ir(0)_n$ nanoparticles at 1.5 h (green), 3.25 h (teal), 5.0 h (purple), and 10.0 h (black). At each time point, a new reaction solution was prepared of 5.0 mM $[(1,5\text{-COD})Ir^{I}(NCCH_3)_2][BF_4]$ in the presence of 2.25 molar equiv of $(Bu_4N)_2HPO_4$ in 3.33 mL acetone and 0.67 mL cyclohexene at 22.0 ± 0.1 °C. Each data point

represents >450 measured particles; across the 4 samples >2700 particles were measured."[42] Reproduced with permission from ref 42. Copyright 2021 American Chemical Society.

The attempted fit using the 2-step mechanism consistent with the XANES, SAXS and all the other data to this point, along with the simulated $[A]_t$ loss curve from the resulting rate constants of that attempted fit, are reproduced as Figures 2.18a and 2.18b, respectively. The fit is obvious poor—no fit at all, really—*disproving the 2-step mechanism that was otherwise consistent with all of the XAFS, SAXS, and other kinetics data.*[42]

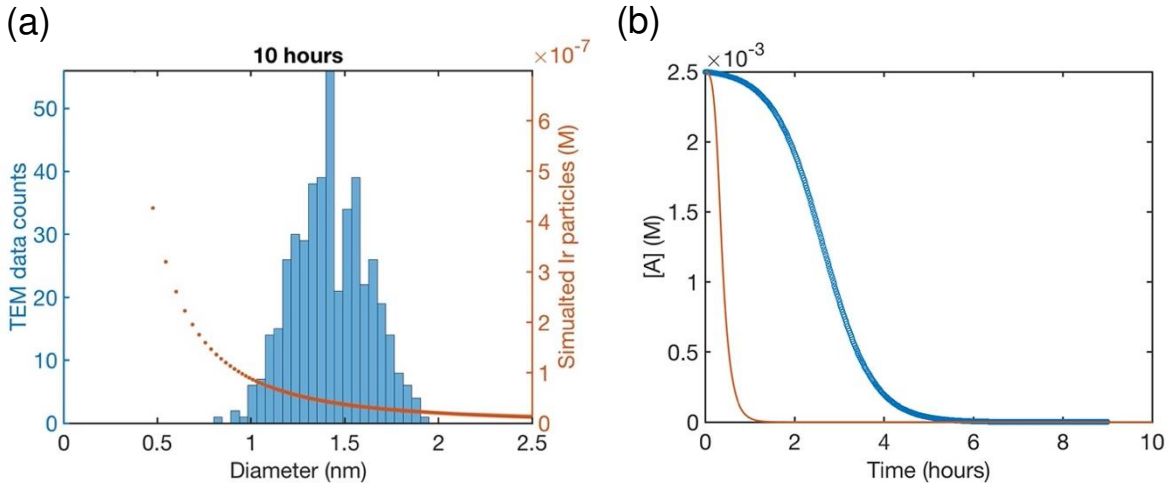

Figure 2.18. (a) Attempted fit to the end-time, 10.0 h histogram using ME-PBM built off of the 2-step mechanism with experimentally determined nucleation mechanism. The resultant fit-determined rate constants are as follows: $k_{+Diss} = 4.0 \times 10^{-1}$ h^{-1} M^{-2}, $k_{-Diss} = 3.7 \times 10^{4}$ h^{-1} M^{-1}, $k_1 = 6.6 \times 10^{-1}$ h^{-1}, $k_2 = 9.2 \times 10^{3}$ h^{-1} M^{-1}, meaningless rate constants given the poor fit. The Best Function Value (BFV)[65,66] is 90.0, indicating a poor fit (as lower BFVs indicate[65,66] better agreement between the experimental data and the attempted fit). However, the rate constants are provided as they are used to generate the predicted precursor loss curve discussed next. **(b)** Calculated precursor loss, $[A]_t$, using the "best-fit" rate constants parameters from the above attempted fit to the PSD, are co-plotted with the experimental global $[A]_t$ data from the simulated global fit of data from all the available methods. Reproduced with permission from ref 42. Copyright 2021 American Chemical Society.

Given the poor fit in Figure 2.18a, the authors considered 15 total minimal mechanisms—albeit only a fraction of the 96 possible mechanisms summarized via Table S2.5. The minimal mechanism the authors report as a current best-fit of the PSD is the 4-step mechanism given in Scheme 2.4 that contains slow, continuous nucleation ($A_{solv} \rightarrow B$, k_{1obs}), small particle growth ($A + B \rightarrow C$, k_{2obs}), bimolecular small particle agglomeration ($B + B \rightarrow C$, k_{3obs}), and large particle growth ($A + C \rightarrow 1.5C$, k_{4obs}), where A = $\{[(1,5\text{-COD})Ir^{I}\bullet HPO_4]_2\}^{2-}$, A_{solv} = $\{[(COD)Ir^{I}(solv)]_2\bullet HPO_4\}^{0}$, B = small $Ir(0)_m$, and C = large $Ir(0)_n$.

Scheme 2.4. Experimentally Determined Prior Equilibrium and the New 4-Step Mechanism of (i) Slow, Continuous Nucleation, (ii) Small Particle Growth, (iii) Bimolecular Small Particle Agglomeration, and (iv) Large Particle Growth. Reproduced with Permission from Ref 42. Copyright 2021 American Chemical Society.

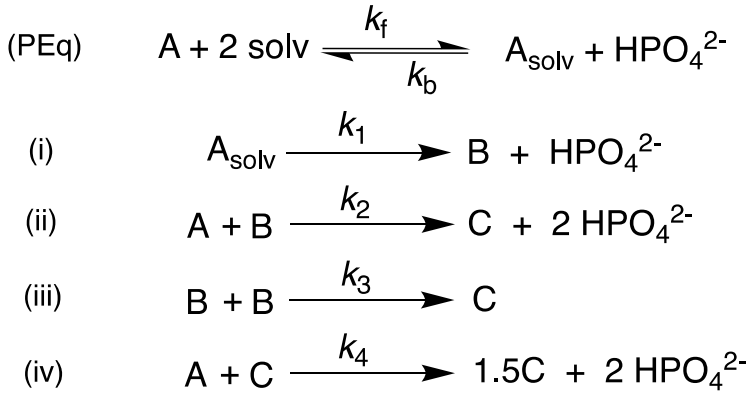

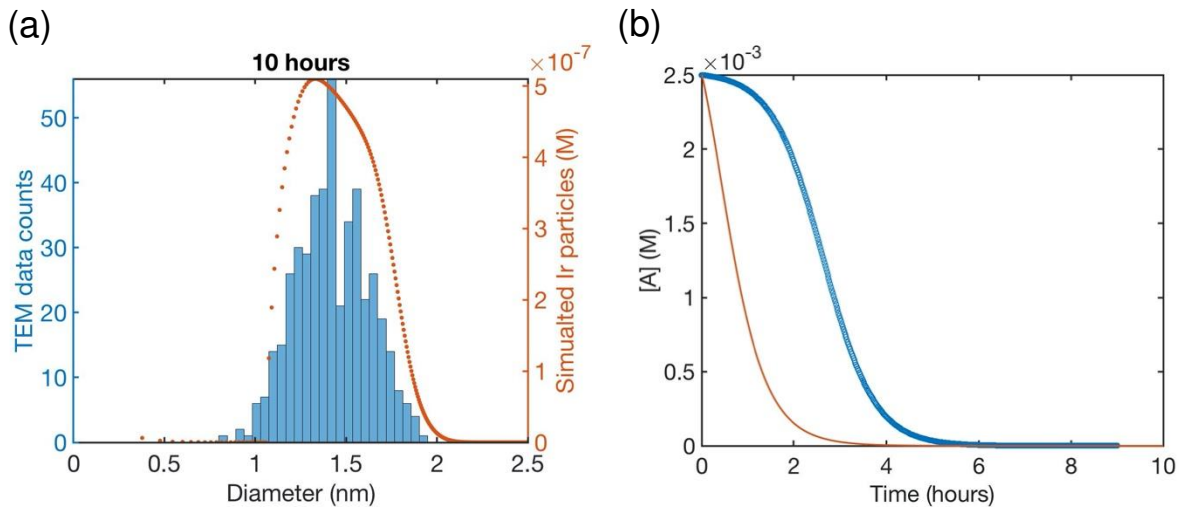

Figure 2.19. (a) Fit to the end-time, 10.0 h histogram using ME-PBM built off of the new 4-step mechanism with experimentally determined nucleation mechanism. The resultant fit-determined rate constants are as follows: $k_{+\text{Diss}} = 2.6 \times 10^{-1}$ h^{-1} M^{-2}, $k_{-\text{Diss}} = 2.2 \times 10^{4}$ h^{-1} M^{-1}, $k_1 = 2.2$ h^{-1}, $k_2 = 5.4 \times 10^{4}$ h^{-1} M^{-1}, $k_3 = 1.6 \times 10^{6}$ h^{-1} M^{-1}, $k_4 = 5.4 \times 10^{4}$ h^{-1} M^{-1}, and the B versus C cutoff value $M = 23$. The Best Function Value (BFV)[65,66] is 25.4, indicating an improved fit over the 2-step shown in Figure 2.18—as, again, a lower BFV indicate[65,66] better agreement between the experimental data and the attempted fit. **(b)** Calculated precursor loss, $[A]_t$, using the "best-fit" rate constants parameters from the above attempted fit to the PSD, are co-plotted with the experimental global $[A]_t$ data from the simulated global fit of data from all the available methods. Reproduced with permission from ref 42. Copyright 2021 American Chemical Society.

Although the authors demonstrate that the 4-step mechanism given in Scheme 2.4 can fit the PSD reasonably well, Figure 2.19a, the authors note that the fit to the experimental $[A]_t$ loss curve in Figure 2.18b "is poor" when compared to the simulated $[A]_t$ loss curve (i.e., the expected $[A]_t$ loss curve simulated using the rate constant parameters extracted from the PDS). This example illustrates both the mechanistic power, as well as the amount of work needed, when using ME-PBM as a now apparently "Gold-Standard Test" of ones proposed particle formation mechanism.[42,65,66] As the authors note, they "still have more work to do to uncover the more detailed, even closer to correct particle formation mechanism."[42]

Evaluating the second-generation $\{[(1,5\text{-COD})Ir^{I}\bullet HPO_4]_2\}^{2-}$ precursor to $Ir(0)_n\bullet(HPO_4^{2-})_x$ nanoparticle system[32,42] for how well it stacks up to the four criteria for establishing a minimum mechanism, provided are: (i) an experimentally determined, balanced reaction stoichiometry; (ii) extensive kinetics data by 4 methods including XANES and SAXS; (iii) (pseudo)-elementary reaction steps that make up the proposed mechanism and that add up to the experimental stoichiometry, define the rate constants, and provide defined, unambiguous words for describing the mechanism. Additionally, provided was (iv) disproof of 14 alternative (of 15 total), possible hypothesized mechanisms. Somewhat hidden behind the success of the $Ir(0)_n$ systems is the amount of synthesis and characterization of the first generation $\{(1,5\text{-COD})Ir^{I}\bullet POM\}^{8-}$ precursor[91,92] and then the second-generation $\{[(1,5\text{-COD})Ir^{I}\bullet HPO_4]_2\}^{2-}$ precursor[32,105,106] characterization of their nanoparticle products by as many applicable methods as possible,[91,92,106] and the care in establishing the balanced reaction stoichiometry[91,92,106] before beginning serious kinetics and mechanistic studies. Strict adherence to a disproof- and Ockham's razor-based approach, as rigorous mechanism demands, is another key underlying the $Ir(0)_n$ kinetics and mechanistic studies—as is a philosophical acceptance of the truism that all deliberately minimum mechanisms will eventually be upgraded ("disproved") as new methods, experiments, or data analyses (such as ME-PBM) become available.

2.3.6. Case Study #6: Investigation of Pre-Nucleation Clusters en Route to Gold Nanospheres and Nanowires by XAFS, SAXS, and HE-XRD.

The final case we will examine is a 2020 study by Ramamoorthy and co-workers. Those authors report their syntheses of gold nanospheres and nanowires by injecting the gold precursor and reductant into a T-micromixer and monitoring the formation by XAFS, SAXS, and HE-

XRD.[43] All experiments were performed at 20 mM $HAuCl_4 \cdot 3H_2O$ and 1 M triisopropylsilane (TIPS) in hexane. Three concentrations of ligand, oleylamine (OY), were used: 50 mM, 100 mM, and 400 mM. The reaction stoichiometry proposed by the authors is given as eq 2.14 with R = isopropyl.

$$2\,AuCl_4 + 3\,R_3SiH + 5\,C_{18}H_{35}NH_2 \xrightarrow{\text{Hexane}} 2\,Au(0) + 3\,R_3SiCl + 5\,C_{18}H_{35}NH_3^+Cl^- \quad \text{(Eq 2.14)}$$

The Au and OY solutions were mixed until complete dissolution before the addition of the TIPS solution. No temperatures were given for the reactions. In situ SAXS, XAFS, and HE-XRD experiments were carried out in a glass capillary, a poly(methyl methacrylate) (PMMA) cuvette, and a thin-walled glass capillary, respectively.[43] TEM and HE-XRD were used to characterize the resultant nanospheres at [OY] = 50 and 100 mM and nanowires at [OY] = 400 mM.[43] Finally, XPS was used to assess ligand binding to the metal surface.

First, the formation of nano*spheres* from the reactions with 50 mM and 100 mM OY (i.e., and not the nano*wires* formed under different conditions, *vide infra*) were investigated by XAFS and SAXS. In the following section, the nanospheres formed from the reaction with 50 mM OY is analyzed. The XAFS data were interpreted using linear combination analysis (LCA) that allowed for simultaneous determination of precursor concentration (Au^{III}), intermediate concentration (Au^{I}), and final product concentration (Au^{0}) as a function of time. The XAFS formation data as a function of time and an example of the LCA result are given as Figure 2.20a and 2.20b, respectively.

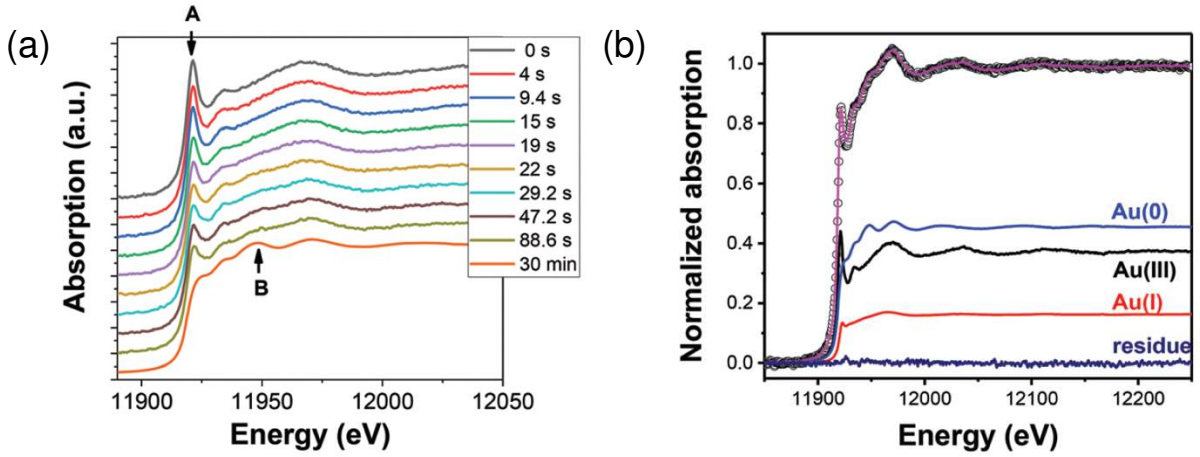

Figure 2.20. **(a)** In situ XAS spectra at the Au L_{III}-edge monitoring the formation of Au nanospheres from the gold precursor solution with [OY] = 50 mM. Spectra are given stepwise from 0 – 88.6 s and 30 min. The decrease in the intensity of the white line intensity at 11,921.2 eV is denoted by "A", and the increase in the signal corresponding to Au foil at 11,948.5 eV is denoted by "B". **(b)** The XAFS spectrum collected at 29.2 s, hollow circles, is given as a representative spectrum for linear combination analysis (LCA). The pink line is the LCA fit of the XAFS spectrum, which yields the three components: Au(III) precursor (black line), Au(I) intermediate species (red line), and resultant Au(0) nanospheres (blue line). Reproduced with permission from ref 43. Copyright 2020 Royal Society of Chemistry.

As CNT did not accurately describe the formation data, a new kinetic model had to be devised to fit the data. The authors constructed a multistep kinetic model to account for the induction period, nucleation, and for growth. The proposed nanosphere formation kinetic model is given as Scheme 2.5 and includes equilibrium expressions between reactive and non-reactive Au(III) and Au(I) species.

Scheme 2.5. Kinetic Model for the Formation of Au Nano*spheres* with [OY] = 50 mM. Reproduced with Permission from Ref 43. Copyright 2020 Royal Society of Chemistry.

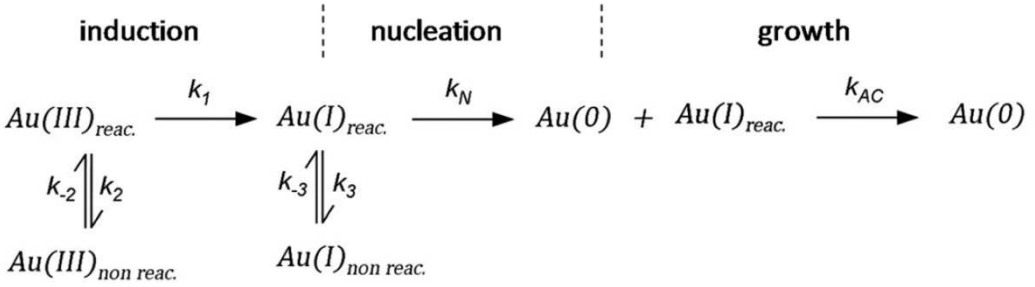

The proposed kinetic model contains two reduction steps: $Au(III)_{reac}$ to $Au(I)_{reac}$ with rate constant k_1 and $Au(I)_{reac}$ to Au(0) with rate constant k_N. That second step with k_N is the first step in the two-step nucleation/growth process. The final, autocatalytic process[73] involves Au(0) and $Au(I)_{reac}$ to form additional Au(0) with rate constant k_{AC}. The authors report that "a competition between reduction and complexation of the Au(III) and Au(I) by OY is described by two additional equilibrium during the induction stage. The two 'non-reactive' complexes are not directly involved in the reduction steps but serve as a reservoir for the 'reactive complexes'."[43]

Using the mass-balance expressions of $[Au(III)_{Total}] = [Au(III)_R] + [Au(III)_{NR}]$, $[Au(I)_{Total}] = [Au(I)_R] + [Au(I)_{NR}]$, and $[Au(0)] = 1 - [Au(III)_{Total}] - [Au(I)_{Total}]$, the authors inputted their model into MatLab as a series of ordinary differential equations (ODEs), eqs 2.15–2.18.

$$\frac{d[Au(III)_R]}{dt} = -(k_1 + k_2) \times [Au(III)_R] + k_{-2}[Au(III)_{NR}] \quad \text{(Eq 2.15)}$$

$$\frac{d[Au(III)_{NR}]}{dt} = k_2[Au(III)_R] - k_{-2}[Au(III)_{NR}] \quad \text{(Eq 2.16)}$$

$$\frac{d[Au(I)_{NR}]}{dt} = k_3[Au(I)_R] - k_{-3}[Au(I)_{NR}] \quad \text{(Eq 2.17)}$$

$$\frac{d[Au(I)_R]}{dt} = k_1[Au(III)_R] - k_3[Au(I)_R] + k_{-3}[Au(I)_{NR}] - k_N[Au(I)_R] - k_{AC}[Au(I)_R][Au(0)]$$

(Eq 2.18)

These equations were numerically integrated and used to fit the experimental kinetics data collected using the LCA of the XAFS signals resulting in 7 rate-constant parameters. The resultant fits produced Figure 2.21.

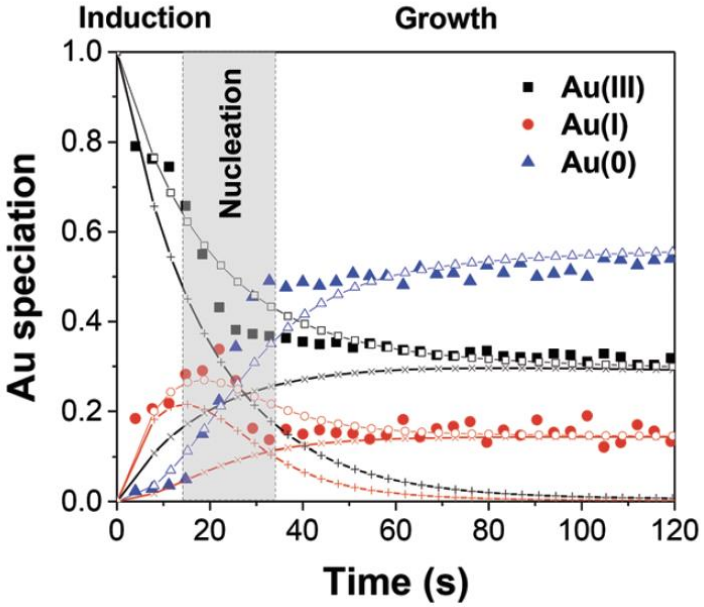

Figure 2.21. The Au(III), Au(I), and Au(0) concentrations determined by LCA analysis of the XAFS spectra (example given in Figure 2.20b) are given here from 0 – 120 s as filled black squares, filled red circles, and filled blue triangles, respectively. The best-fit lines from each Au species are given using the corresponding connected hollow shape. The black (+) represents the reactive Au(III) species, while the black (×) represent the non-reactive Au(III) species. The red (+) represents the reactive Au(I) species, while the red (×) represent the non-reactive Au(I) species. Reproduced with permission from ref 43. Copyright 2020 Royal Society of Chemistry.

The data are well-fit from 0 – 20 s and then again from 45 – 120 s. For all species of Au, there is a discrepancy between the data and the fit lines between 20 – 45 s, somewhat surprising given the

considerable flexibility of 7 variable rate-constant parameters, an indication that one or more of the assumed steps in the proposed model is incorrect (e.g., the assumed first-order nucleation) or that needed but unknown additional steps are missing.

Next, the formation of nano*wires* from the reaction with 400 mM OY were also investigated by XAFS and SAXS. The XAFS data were interpreted using LCA to simultaneous determine precursor concentration (Au^{III}), intermediate concentration (Au^{I}), and final product concentration (Au^{0}) as a function of time. The XAFS formation data as a function of time is given as Figure 2.22.

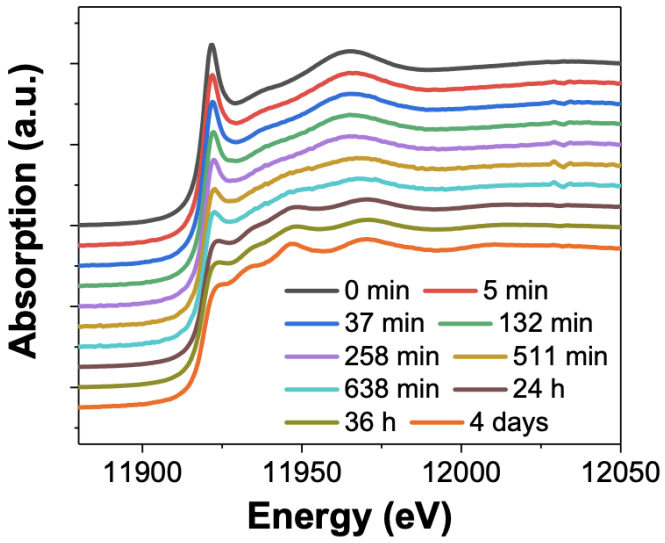

Figure 2.22. (a) In situ XAS spectra at the Au L_{III}-edge monitoring the formation of Au nanowires from the gold precursor solution with [OY] = 400 mM. Spectra are given from 0 min – 4 days. Reproduced with permission from ref 43. Copyright 2020 Royal Society of Chemistry.

Scheme 2.6. Kinetic Model for the Formation of Au Nano*wire*s with [OY] = 400 mM. Reproduced with Permission from Ref 43. Copyright Royal Society of Chemistry 2020.

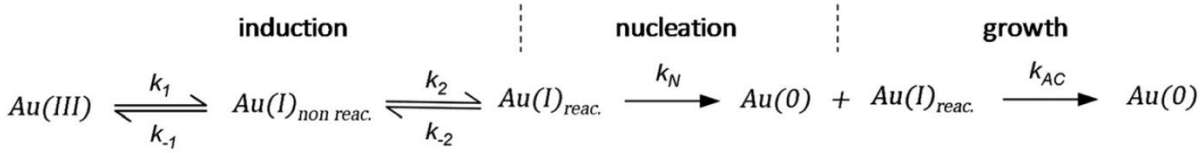

Using the kinetic model presented in Scheme 2.6 and the mass-balance expressions from before, the authors derived ODEs, reproduced below as equations 2.19–2.21, and associate 6 rate-constant parameters.

$$\frac{d[Au(III)]}{dt} = -k_1[Au(III)] + k_{-1}[Au(I)_{NR}] \quad \text{(Eq 2.19)}$$

$$\frac{d[Au(I)_{NR}]}{dt} = k_1[Au(III)] - k_{-1}[Au(I)_{NR}] - k_2[Au(I)_{NR}] + k_{-2}[Au(I)_R] \quad \text{(Eq 2.20)}$$

$$\frac{d[Au(I)_R]}{dt} = k_2[Au(I)_{NR}] - k_{-2}[Au(I)_R] - k_N[Au(I)_R] - k_{AC}[Au(I)_R][Au(0)] \quad \text{(Eq 2.21)}$$

Then, the authors used their ODEs to simultaneously fit the kinetics data for the three gold species: Au(III), Au(I), and Au(0). As seen in Figure 2.23, the data are all well-fit, not unexpectedly given the six rate constant fitting parameters.

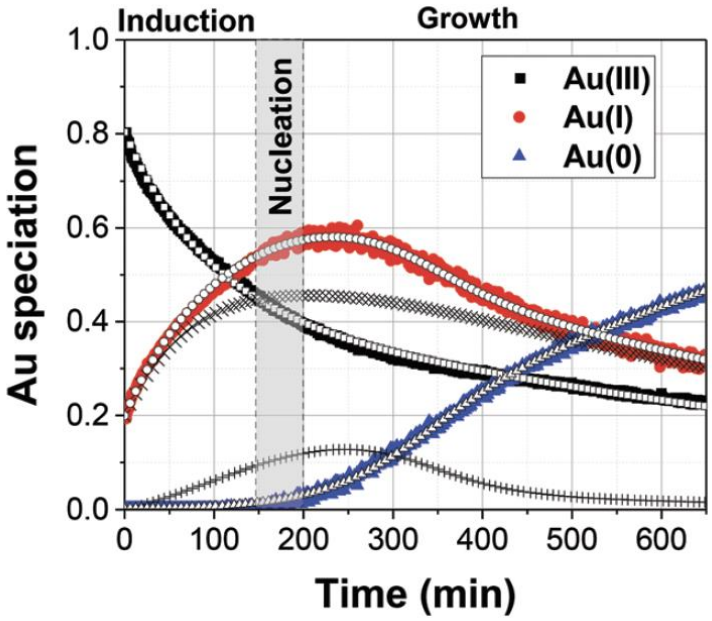

Figure 2.23. The Au(III), Au(I), and Au(0) concentrations determined by LCA analysis of the XAFS spectra are given here from 0 – 650 min as filled black squares, filled red circles, and filled

blue triangles, respectively. The best-fit lines from each Au species are given using the corresponding hollow shape. The black (+) represents the reactive Au(I) species, while the black (×) represent the non-reactive Au(I) species. Reproduced with permission from ref 43. Copyright 2020 Royal Society of Chemistry.

Next, and returning to the case with [OY] = 50 mM that formed nano*spheres*, the *in situ* SAXS patterns were closely analyzed during the first 38 s when the authors hypothesize pre-nucleation clusters (PNCs) are formed. Prior to nucleation at 38 s, it was observed that the scattering pattern changed. The scattering pattern shifts again following the onset of nucleation during the primarily growth period from 48 s – 30 min. These scattering patterns have been reproduced herein as Figure 2.24.

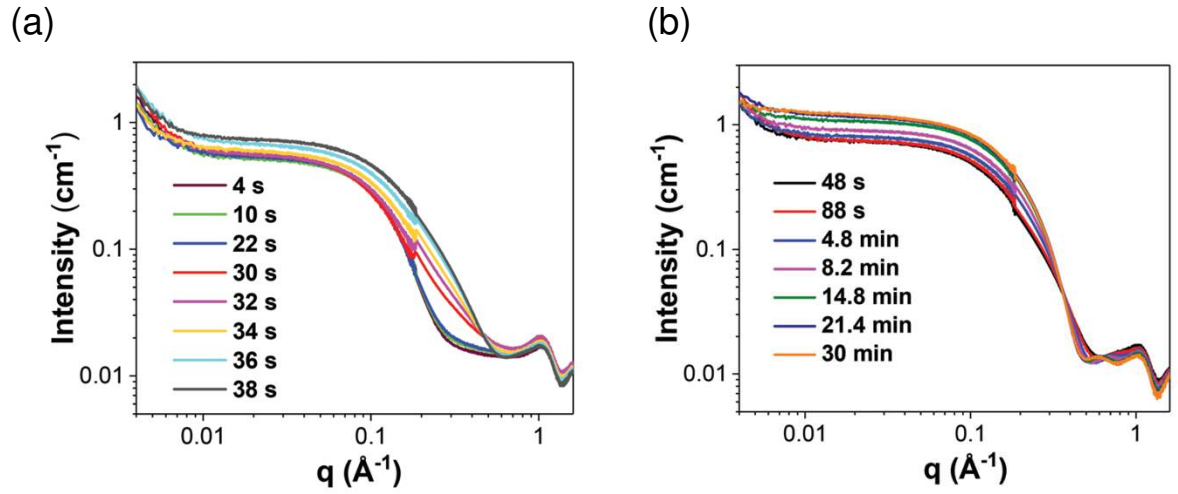

Figure 2.24. In situ SAXS patterns for the Au precursor system with [OY] = 50 mM from **(a)** 4 – 38 s, where it is believed that pre-nucleation clusters are formed and nucleation begins. Next, from **(b)** 48 s – 30 min, primarily growth is believed to occur. Reproduced with permission from ref 43. Copyright 2020 Royal Society of Chemistry.

These scattering patterns were fit, and the particle diameter versus time plotted. These data are presented in Figure 2.25 as diameter in nanometers versus time in seconds, where time is plotted on a log scale.

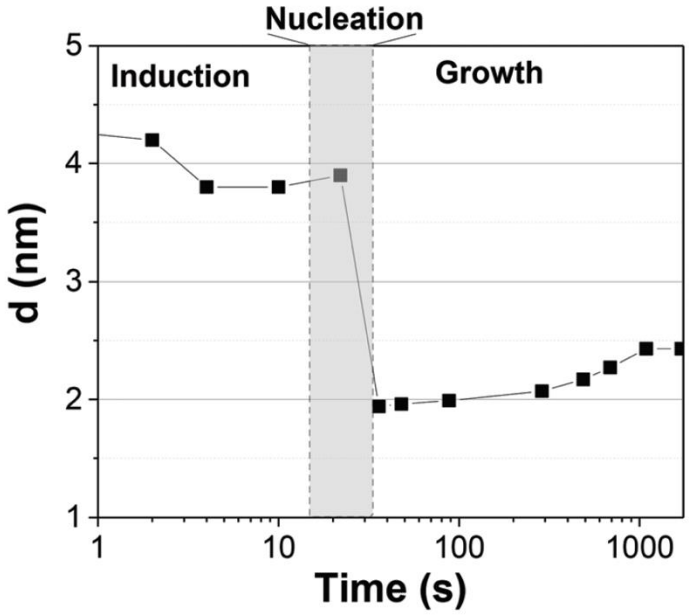

Figure 2.25. Mean particle diameter (nm) is given as a function of *log time* (s) for the Au precursor system with [OY] = 50 mM, as shown in Figure 2.24. In the induction period, the mean diameter was calculated "from the radius of gyration of the Au(III)–Au(I) pre-nucleation clusters".[43] In the growth period, the mean diameter was determined from the Au(0) nanospheres. The shaded region is believed to be the time period when primarily nucleation takes place. Reproduced with permission from ref 43. Copyright 2020 Royal Society of Chemistry.

Based on the data presented in Figure 2.25, the authors believe during the induction period that the SAXS scattering is reporting "the radius of gyration of the Au(III)–Au(I) pre-nucleation clusters"[43] and not of Au(0) nanospheres. Then, following what the authors have labelled as the nucleation period, the implication is that the SAXS is reporting the mean radius of the resultant Au(0) nanospheres.[43] Hence, it follows that the true nucleation kinetics are obscured by the much larger PNC, so that only growth data are what is primarily observed in the SAXS measurements. The authors did not attempt to fit the SAXS data with their kinetic model.

Overall, Ramamoorthy and co-workers have presented a valuable study on the formation of $Au(0)_n$ in which they directly monitor the formation of $Au(0)_n$ nanospheres or nanowires by *in*

situ XAFS, SAXS, and HE-XRD, as well as characterized the resultant particles with *ex situ* TEM.[43] Of perhaps special interest is the observation of PNCs. In terms of satisfying the four criteria for a reliable mechanistic investigation, for criterion (i) the authors have proposed a balanced reaction stoichiometry that was reproduced herein as eq 2.14. The exact composition of the pre-nucleation clusters would be a useful target for future studies. The authors discussed possible compositions of the Au-based PNCs, but the PNCs were not determined beyond aggregates of $\{(RNH_4^+)(AuCl_4^-)(OY)\}_n$, where R = isopropyl.[43] However, after nucleation has been initiated and growth has begun, the authors have been able to determine the Au speciation—*a non-trivial task*—and plot several Au species as a function of time, another non-trivial achievement. Criterion (ii) was also fully satisfied as the kinetics of $Au(0)_n$ were collected *in situ* by both EXAFS and SAXS over the entire reaction as Figures 2.20 – 2.24 document for both the nanospheres and the nanowires.

Criterion (iii), namely the task of constructing a pseudo-elementary step-based mechanism, has been partially satisfied. For the two cases—nanospheres and nanowires—the authors have presented proposed kinetic models reproduced herein as Schemes 2.5 and 2.6, respectively. They have used these kinetic models to write differential equations and then fit their kinetics data with those differential equations. In a future study once the composition of the PNC has been determined, then one will be able to write the exact pseudo-elementary step reactions that sum to the overall net $Au(0)_n$ formation mechanism. Missing at present is the experimentally determined *rate law for nucleation*. As for criterion (iv), only one alternative model was examined. The authors demonstrated that CNT was invalid for their $Au(0)_n$ formation system, but they did not report the disproof of any other alternative mechanistic models en route to their proposed kinetic models. A greater amount of disproof will be required to provide higher confidence in the resultant, proposed

mechanism. That said, we picked this system as an illustrative case history because it demonstrates state-of-the-art, *in situ* use of three separate synchrotron techniques: XAFS, SAXS, and HE-XRD that also identifies PNCs. Additional studies of this interesting system the community would likely welcome include those hinted at above: (i) determination of the composition(s) of the pre-nucleation clusters; (ii) further work on the experimental rate law especially of nucleation; and (iii) testing of additional reasonable alternative mechanistic models for formation of the gold nanosphere and nanowires.

2.4. CURRENT STATE OF PARTICLE FORMATION MECHANISMS

Prior to 1997,[73] Classical Nucleation Theory (CNT), Avrami's equation, and the LaMer physical-chemistry *models* dominated the particle formation literature.[63,64] However, modern techniques and advances indicate that each of these physical-chemical models have serious if not fatal weaknesses.[25,26,31,32,38,42,53,54,63,64,65,66,107,108] CNT was developed[109,110,111] in the late 1800s as a mathematical model for particle nucleation, but agrees with experiment best (if not only) within ca. $10^{\pm1}$ for gas-phase hydrocarbon or other weakly, reversibly associating systems at temperatures >300 K as demonstrated by El-Shall and co-workers noteworthy studies.[107,108] The Avrami model was developed in 1939[112,113,114] and has been modified several times,[115,116,117,118] but remains a semi-empirical treatment and equation that fails to yield physically relevant rate constants,[53,54,119] nor other physically unambiguously interpretable parameters.[119]

The LaMer model[120] postulating "burst" nucleation and "diffusion-controlled" growth was developed for sulfur sols and has since been used to try to explain hundreds of particle formation systems.[63,64,121] Yet, in its 70 years of existence, the LaMer mathematical model and equation has never been used to successfully fit kinetics data save his original case on $(S)_n$ sols.[120] The LaMer

hypothesis of "burst" nucleation and "diffusion-controlled" growth has been compellingly disputed[25,26,122,123,124,125,126,127] in three recent[63,64,121] reviews of 1,953 papers citing the LaMer model. Relevant here are the wise words of B. Peters that "The classic theories work poorly or not at all when applied beyond the validity of their assumptions."[128]

Little known is that Victor LaMer also published a stepwise mechanism for particle formation in 1952,[129] but never tested it with nor used it to explain experimental kinetics data for particle formation. Turkevich's 1953 "organizer mechanism"[130,131] merits mention in Table 2.1 as well, even though it lacks specific pseudo-elementary steps, because it is the early example of what are now termed PNCs (prenucleation clusters) as discussed in a 2021 review. Indeed, reading Turkvich's literature reveals he was often far ahead of his time in his intuition and understanding about particle synthesis, physical properties, and mechanism.

However, the first, disproof-based minimum mechanism for particle formation mechanism composed of specific pseudo-elementary steps (that also add up to an experimentally demonstrated balanced reaction to well-characterized products) did not appear until 1997,[73] the 2-step mechanism of continuous nucleation and autocatalytic surface growth listed in Table 2.1. This simplest version of particle formation has since been used to successfully fit homogeneous nanoparticle formation,[132] heterogeneous nanoparticle formation,[133] solid state kinetics,[134] dye aggregation,[135] protein aggregation,[136] and other "cooperative" autocatalytic phenomena in nature.[137] Six upgraded, minimum mechanisms for particle formation have since been reported[38,65,66,73,81,138,139,140,141] as summarized in Table 2.1, specific upgrades to the 2-step mechanism occurring 5 times as additional evidence for more complex pathways became available (entries 2, 3, 5, 6, and 7 – Table 2.1) along with disproof[55,56,58] of at least 21 additional alternatively mechanisms en route to those 6 of the 7 mechanisms in Table 2.1.[26,65,66,73,81,138,139,140,141] The 2005

crystal-growth model from Tsapatsis and co-workers[142] is also included in Table 2.1 because their model has proposed pseudo-elementary steps supported by Population Balance Modeling while disproving one alternative mechanism—and hence is really an early example of a mechanistic model partially tested by ME-PBM.

Table 2.1. Historical Summary of Pseudo-Elementary Step Mechanisms for Particle Formation. Reproduced with permission from ref 64. Copyright 2021 Royal Society of Chemistry.

YEAR	PERSON(S)	MECHANISM (A, B, and C formalism)	MECHANISM (in words), and COMMENTS
1952	**V. K. LaMer**[129]	$mA_1 \rightleftharpoons B_m$ $B_m + A_1 \rightleftharpoons B_{m+1}$ $B_{(i-1)} + A_1 \rightleftharpoons B_i$	Stepwise bimolecular addition leading to "burst nucleation" (NB: "diffusion-controlled growth"[120] was not included[129] as part of the scheme provided) [A_1 = "kinetically independent unit of phase *A"*, B_i = "embryo of phase *B* containing *i* units", and "*m* is usually 2, whereas *i* in the case of water vapor condensation is about 80—i.e., this reaction is of the 80th order"]
1953	**Turkevich,**[130,131] **Stevenson, Hillier**	No pseudo-elementary step mechanism was provided in refs 130 or 131.	Nucleating agents build up a *chemical* complex, organize macromolecularly, then undergo a molecular rearrangement to produce the metal nucleus, Turkevich's "organizer" mechanism / hypothesis—what can now be seen to be an early version of the Prenucleation Clusters postulate.
1997	**Finke, Watzky**[73]	$A \xrightarrow{k_1} B$ $A + B \xrightarrow{k_2} 2B$	Slow, kinetically continuous nucleation followed by typically fast, explosive autocatalytic surface growth. Important to note is that higher order n$A \xrightarrow{k_1} nB$ nucleations are covered by (i.e., can be hidden in) the pseudo-elementary first step, as the subsequent discovery of second-order and termolecular nucleations demonstrates.[30,31] [*A* = metal precursor, *B* = growing, metal(0) particle]
2004	**Hornstein, et al.**[138]	$A \xrightarrow{k_1} B$ $A + B \xrightarrow{k_2} 2B$ $\boldsymbol{B} + B \xrightarrow{k_3} C$	Evidence for bimolecular agglomeration as a 3rd step added to the 1997 2-step mechanism[73]

2005	**Besson, Finney, et al.**[81,139,140]	$A \xrightarrow{k_1} B$ $A + B \xrightarrow{k_2} 2B$ $B + B \xrightarrow{k_3} C$ $B + C \xrightarrow{k_4} 1.5\,C$ [A = metal precursor, B = small particles, C = larger particles]	Evidence for a 4th step of autocatalytic agglomeration where the smaller particles, B, and larger particles, C, agglomerate with a separate, k_4, rate constant
2005	**Drew, Katsoulakis, Tsapatsis**[142]	$A \xrightarrow{k_1} B$ $B \xrightarrow{k_2} C_1$ $B + C_i \xrightarrow{K_i} C_{i+1}$ $C_i + C_j \xrightarrow{K_{ij}} C_{i+j}$ [A = primary colloidal particles; B = growing crystal; C_1 = nucleated primary particles] [$b = n_{Ao}K_i/k_2$; $c = n_{Ao}K_{ij}/k_2$; n_{Ao} = initial number of fresh primary particles; n_i = particle density of crystal i; $y = \bar{n}/n_{Ao}$; $\tau = k_2 t$]	A proposed mechanism for *crystal* growth by aggregation of meta-stable nanoparticle precursors, one used with Population-Balance Modeling. Three alternative mechanisms were tested; shown is the author's preferred Mechanism II.
2014	**Kent, Mondloch, et al.**[141]	$A \xrightarrow{k_1} B$ $A + B \xrightarrow{k_2} 2B$ $B + B \xrightarrow{k_3} C$ $A + C \xrightarrow{k_4'} 1.5\,C$ [A = metal precursor, B = smaller particles, C = larger particles]	Evidence for a new 4th step of secondary autocatalytic growth where larger particles, C, growth with a separate, k_4', rate constant.
2017	**Karim, et al.**[38]	$A \bullet L \rightleftharpoons A + L$ $A \xrightarrow{k_1} B$ $A + B \xrightarrow{k_2} 2B$ $B \bullet L \rightleftharpoons B + L$ [A = metal precursor, B = growing particle, A•L = precursor with ligand, B•L = growing particle with ligand; both ligand steps have associated K_{eq} equilibrium constants]	Proposed four step mechanism, including two ligand binding equilibria steps, for the formation of metal nanoparticles, the first A•L step having additional precedent.[31,32] A set of 5 differential equations are reproduced in the Supporting Information.
2019	**Handwerk, Shipman, Whitehead, Özkar, et al.**[65,66]	$A \xrightarrow{k_1} B$ $A + B \xrightarrow{k_2} C$ $A + C \xrightarrow{k_3} 1.5C$	A new, 3-step mechanism, discovered by disproof-based *Mechanism-Enabled* Population-Balance Modeling, in which the $A + B \xrightarrow{k_2} 2B$ pseudo-elementary step of the 1997 2-step mechanism was expanded into two growth steps (or, alternatively, and as actually discovered[65,66] the 2nd and 3rd steps of the 2014 4-step mechanism are combined into a single, new 2nd step). Eleven alternative mechanisms were disproved. Quantitative fitting of

	Particle-Size Distributions (PSDs) was demonstrated, including the PSD shape. [*A* = metal precursor, *B* = smaller particles, *C* = larger particles]

Of considerable interest is what results if one takes just the 5 basic classes of mechanistic models in Table 2.1 that have been subjected to extensive disproof and therefore deemed to be more reliable,[65,66,73,81,138,139,140,141] and then combines them with 3 different precedented nucleation molecularities[30,31,32,73] and up to 3 different types of ligand binding steps based on A. Karim's groundbreaking[38] work (and other precedent for A•L to A + L dissociative steps[31,32]). Looking at the possible combinations, one now has 5 classes of ≥96 possible mechanisms that one can use to try to use in a disproof-based approach[55,56,58] to fitting one's particle formation data while striving for a disproof-based minimum mechanism for one's particle formation reaction.

Table 2.2. List of Possible Mechanisms for Testing From the Combinations of 5 Basic Mechanisms, up to 3 Types of Ligand Binding, and 3 Precedented Types of Nucleation[26,30,31,32,65,66,73,81,138,139,140,141]

Class	Mechanism	Unimolecular Nucleation	Bimolecular Nucleation	Termolecular Nucleation	Ligand Dependence
(I)	FW 2-Step	$A \rightarrow B$ $A + B \rightarrow 2B$	$2A \rightarrow 2B$ $A + B \rightarrow 2B$	$3A \rightarrow 3B$ $A + B \rightarrow 2B$	(i) $A \cdot L \rightleftharpoons A + L$ (ii) $B \cdot L \rightleftharpoons B + L$ (iii) with *A*·*L* and *B*·*L* steps
(II)	Classic 3-step with Bimolecular Agglomeration	$A \rightarrow B$ $A + B \rightarrow 2B$ $B + B \rightarrow C$	$2A \rightarrow 2B$ $A + B \rightarrow 2B$ $B + B \rightarrow C$	$3A \rightarrow 3B$ $A + B \rightarrow 2B$ $B + B \rightarrow C$	(i) $A \cdot L \rightleftharpoons A + L$ (ii) $B \cdot L \rightleftharpoons B + L$ (iii) $C \cdot L \rightleftharpoons C + L$ (iv) with *A*·*L* and *B*·*L* steps (v) with *A*·*L* and *C*·*L* steps (vi) with *B*·*L* and *C*·*L* steps
(III)	New, Handwerk et al. 3-Step	$A \rightarrow B$ $A + B \rightarrow C$ $A + C \rightarrow 1.5C$	$2A \rightarrow 2B$ $A + B \rightarrow C$ $A + C \rightarrow 1.5C$	$3A \rightarrow 3B$ $A + B \rightarrow C$ $A + C \rightarrow 1.5C$	(i) $A \cdot L \rightleftharpoons A + L$ (ii) $B \cdot L \rightleftharpoons B + L$ (iii) $C \cdot L \rightleftharpoons C + L$ (iv) with *A*·*L* and *B*·*L* steps (v) with *A*·*L* and *C*·*L* steps (vi) with *B*·*L* and *C*·*L* steps
(IV)	4-Step with B + C Agglomerative Growth	$A \rightarrow B$ $A + B \rightarrow 2B$ $B + B \rightarrow C$ $B + C \rightarrow 1.5C$	$2A \rightarrow 2B$ $A + B \rightarrow 2B$ $B + B \rightarrow C$ $B + C \rightarrow 1.5C$	$2A \rightarrow 2B$ $A + B \rightarrow 2B$ $B + B \rightarrow C$ $B + C \rightarrow 1.5C$	(i) $A \cdot L \rightleftharpoons A + L$ (ii) $B \cdot L \rightleftharpoons B + L$ (iii) $C \cdot L \rightleftharpoons C + L$ (iv) with *A*·*L* and *B*·*L* steps (v) with *A*·*L* and *C*·*L* steps (vi) with *B*·*L* and *C*·*L* steps
(V)	4-Step with A + C Secondary Autocatalytic Surface Growth	$A \rightarrow B$ $A + B \rightarrow 2B$ $B + B \rightarrow C$ $A + C \rightarrow 1.5C$	$2A \rightarrow 2B$ $A + B \rightarrow 2B$ $B + B \rightarrow C$ $A + C \rightarrow 1.5C$	$3A \rightarrow 3B$ $A + B \rightarrow 2B$ $B + B \rightarrow C$ $A + C \rightarrow 1.5C$	(i) $A \cdot L \rightleftharpoons A + L$ (ii) $B \cdot L \rightleftharpoons B + L$ (iii) $C \cdot L \rightleftharpoons C + L$ (iv) with *A*·*L* and *B*·*L* steps (v) with *A*·*L* and *C*·*L* steps (vi) with *B*·*L* and *C*·*L* steps

2.5. CONCLUSIONS

Synchrotron X-ray radiation-based methods of XAFS and SAXS are powerful, largely direct methods for observing particle formations across every area of nature and science where particles are formed. Often, one wants to be able to control size and size-dispersion to optimize properties and applications of those particles, and this is where a detailed, quantitative, experimentally based mechanisms become important. Key takeaways, from the analysis of 69 synchrotron-based particle formation papers summarized in Table S2.1-S2.4 of Appendix I and the 6 case studies examined in detail in this review, are as followed:

- Employing Synchrotron X-ray radiation-based experiments provides powerful, largely direct particle formation kinetics data. Indeed, Tables S2.1-S2.4 of Appendix I document the wealth of typically expert obtained, in situ, many times creative, tandem-methods monitoring of particle formation reactions. One caveat here, that merits closer attention in the future, is that X-ray radiation induced radiolysis can initiate nucleation events that then quickly magnify the loss of precursor by exponential, autocatalytic growth.
- Four *minimum* criteria one needs to be able to claim a chemical mechanism of particle formation for a given system are[63]: (i) a complete mass- and charge-balanced, experimentally determined reaction stoichiometry; (ii) kinetics data, ideally the full rate law for nucleation, growth and any agglomeration that might be present; (iii) postulation of pseudo-elementary step-based mechanisms that add up to the observed reaction stoichiometry and then writing down the differential equations corresponding to each mechanism; and (iv) disproof of ideally all reasonable alternative mechanistic hypotheses by checking each mechanism against the observed kinetics data en route to an Ockham's

razor obeying, experimentally supported, disproof-based proposed minimum mechanism of particle formation for the system at hand.

- Even a brief survey of Tables S2.2-S2.4 of Appendix I, that we hope the reader has done for themselves, teaches several other important points: (i) at least ~94% of the time, the systems examined are not well defined, without for example even a complete, balanced reaction stoichiometry having been determined. In that sense, more in-house, more "synthetic" efforts before "synchrotron spectroscopic" efforts—*actually, much, much more*—would, in many cases, have provided better defined systems worthier of the sophisticated, expert, often creative synchrotron XAFS and SAXS efforts one finds listed in Tables S2.2-S2.4 of Appendix I. Put another way, one can view all 64 cases in Tables S2.2-S2.4 as using synchrotron radiation methods to examine particle formation systems directly and see what insights can be obtained. That is fine, but one should not claim that a mechanism has resulted from those largely survey studies. (ii) In 4 of the 64 cases in Tables S2.2-S2.4 of Appendix I, all four of the requirements (i)-(iv) for a reliable mechanism are missing; in 38 of the 64 cases (59% of the time) in Tables S2.2-S2.4 of Appendix I, three of the four requirements are missing; in 16 cases (25% of the time) two of (i)-(iv) are missing; and in only 4 cases (6% of the time) are just one of requirements (i)-(iv) for a reliable mechanism missing.
- Worth emphasizing is that the required but missing first component in, then, ca. 94% of particle formation studies examined by this review is the balanced reaction stoichiometry. Without a balanced reaction stoichiometry, the pseudo-elementary steps of the proposed mechanism—*that must add up to that net reaction stoichiometry*—cannot be reliably nor

unequivocally determined. Even for the 6 studies in this chapter, only 1 completely has and 2 more partially have an experimentally determined, balanced reaction stoichiometry.

- Also missing in 61 of 64 examples in Tables S2.2-S2.4 and in 3 of the 6 cases in this chapter is *a full, experimentally determined rate law for nucleation and growth*. One cannot possibly have a reliable reaction mechanism without the full rate law. Rate laws for *nucleation* are especially rare, being present in arguably only 1 case of the 64 total studies covered in this review.
- Too often presently mechanisms are claimed based on *qualitative* data or 'snapshots' of what size particles are present at what times. These qualitative *pictorial or schematic models or just word-based "mechanisms"*[143,144,145,146,147,148,149,150,151] should not be confused with disproof-based, minimum *mechanisms* expressed in balanced reactions as detailed in Tables 2.1 and 2.2.
- One should *expect*, and indeed hope, that one's initial, minimum mechanism will one day be disproved, replaced by a more complex, experimentally further supported pathway. This is the expectation of minimal, disproof-based mechanisms, where, as time progresses, and techniques improve, new insights and new details become possible as new methods, additional experimentation, or applicable computations become available. Relevant here are recommend articles by Platt,[55] Chamberlain,[56] Scott,[58] and Weinfurt[152] on employing a proper disproof-based scientific method and avoiding the >400-year-old problem in science of "idols and false notions"[152].
- Presently, one can write 5 primary classes of pseudo-elementary-step based, minimum mechanisms, that include 3 precedented types of nucleation and 3 precedented types of

ligand binding, for a total of ≥96 possible mechanisms now available to test out on one's experimental data.

- Mechanism-Enabled Population Balance Modeling has recently emerged as a must-use tool to test one's mechanism, specifically to see if the proposed mechanism can quantitatively account for the proposed particle-size distribution, including its shape.

6. OUTLOOK

The future is bright for synchrotron-based experimental methods en route to reliable, disproof-based chemical mechanisms for particle formation. Efforts that will enhance that bright future include a focus on the four requirements outlined herein for obtaining a reliable reaction mechanism, starting with establishment of a balanced reaction stoichiometry. The combination of complimentary, in-house physical methods with synchrotron-based methods will expedite and make more efficient the use of limited synchrotron beam time. A focus on establishing the full rate law for especially nucleation, but also growth as well as any agglomeration, is also needed. Testing the known mechanisms in Table 2.2 against one's experimental data, before postulating additional mechanisms, and using ME-PBM in conjunction with PSD data—as the present, apparent "Gold standard / acid test" of any proposed mechanism—promise to aid rapid mechanistic progress. Computational chemistry[67,68] employed skeptically[69] is expected to play an important role, too. Indeed, it appears that the particle-formation community is on the cusp of significant mechanistic breakthroughs for a multitude of systems that produce particles throughout nature, in no small part to the continued expert, creative use of powerful synchrotron methods!

REFERNCES

1. Chow, A. H. L.; Tong, H. H. Y.; Chattopadhyay, P.; Shekunov, B. Y. Particle engineering for pulmonary drug delivery. *Pharm. Res.* **2007**, *24*, 411-437.

2. Vehring, R. Pharmaceutical Particle Engineering *via* Spray Drying. *Pharm. Res.* **2008**, *25*, 999-1022.

3. Baldelli, A.; Boraey, M. A.; Nobes, D. S.; Vehring, R. Analysis of the Particle Formation Process of Structured Microparticles. *Mol. Pharmaceutics* **2015**, *12*, 2562-2573.

4. Koehler, J. M.; Visaveliya, N.; Knauer, A. Controlling formation and assembling of nanoparticles by control of electrical charging, polarization, and electrochemical potential. *Nanotechnol. Rev.* **2014**, *3*, 553-568.

5. Kashchiev, D. *Nucleation: Basic Theory with Applications*; Butterworth-Heinemann: Oxford, U.K., 2000.

6. Oxtoby, D. W. Homogeneous nucleation: theory and experiment. *J. Phys.: Condens. Matter* **1992**, *4*, 7627–7650.

7. Nucleation—a Transition State to the Directed Assembly of Materials. *Faraday Discussions*; Royal Society of Chemistry: U.K., 2015; Vol. *179*, pp 9–154.

8. Erdemir, D.; Lee, A. Y.; Myerson, A. S. Nucleation for Crystals from Solution: Classical and Two-Step Models. *Acc. Chem. Res.* **2009**, *42*, 621-629. Note the "Two-Step Model" referred to in this work is distinct from and should not be confused with the FW 2-step mechanism.[70]

9. Zhang, T. H.; Liu, X. Y. Nucleation: What Happens at the Initial Stage? *Angew. Chem., Int. Ed.* **2009**, *48*, 1308-1312.

10. Morris, A. M.; Watzky, M. A.; Finke, R. G. Protein aggregation kinetics, mechanism, and curve-fitting: a review of the literature. *Biochim. Biophys. Acta, Protein Proteomics* **2009**, *1794*, 375-397.

11. Zhang, R. Getting to the Critical Nucleus of Aerosol Formation. *Science* **2010**, *328*, 1366-1367.

12. Finney, E. E.; Finke, R. G. Nanocluster nucleation and growth kinetic and mechanistic studies: A review emphasizing transition-metal nanoclusters. *J. Colloid Interface Sci*. **2008**, *317*, 351-374.

13. Schmid, G. Large Clusters and Colloids. Metals in the Embryonic State. *Chem. Rev.* **1992**, *92*, 1709-1727.

14. Vargaftik, M. N.; Nagorodnikov, V. P.; StoIarov, I. P.; Moiseev, I. I.; Likholobov, V. A.; Kotchubey, D. I.; Chuvilin, A. L.; Zaikovsky, V. I.; Zamaraev, K. I.; Timofeeva, G. I. A novel giant palladium cluster. *J. Chem. Soc., Chem. Commun.* **1985**, 937-939.

15. Ahmadi, T. S.; Wang, Z. L.; Green, T. C.; Henglein, A.; El-Sayed, M. A. Shape-Controlled Synthesis of Colloidal Platinum Nanoparticles. *Science* **1996**, *272*, 1924-1926.

16. Aiken, J. D.; Finke, R. G. A review of modern transition-metal nanoclusters: their synthesis, characterization, and applications in catalysis. *J. Mol. Catal. A: Chem.* **1999**, *145*, 1-44.

17. Vidoni, O.; Philippot, K.; Amiens, C.; Chaudret, B.; Balmes, O.; Malm, J. O.; Bovin, J. O.; Senocq, F.; Casanove, M. J. Novel Spongelike Ruthenium Particles of Controllable Size Stabilized Only by Organic Solvents. *Angew. Chem., Int. Ed.* **1999**, *38*, 6736-6738.

18. Pelzer, K.; Vidoni, O.; Philippot, K.; Chaudret, B.; Colliere, V. Organometallic Synthesis of Size-Controlled Polycrystalline Ruthenium Nanoparticles in the Presence of Alcohols. *Adv. Funct. Mater.* **2003**, *13*, 118-126.

19. Ott, L. S.; Finke, R. G. Transition-metal nanocluster stabilization for catalysis: A critical review of ranking methods and putative stabilizers. *Coord. Chem. Rev.* **2007**, *251*, 1075-1100.

20. Jin, R. Quantum sized, thiolate-protected gold nanoclusters. *Nanoscale* **2010**, *2*, 343-362.

21. AbdulHalim, L. G.; Kothalawala, N.; Sinatra, L.; Dass, A.; Bakr, O. M. Neat and Complete: Thiolate-Ligand Exchange on a Silver Molecular Nanoparticle. *J. Am. Chem. Soc.* **2014**, *136*, 15865-15868.

22. Goswami, N.; Yao, Q.; Chen, T.; Xie, J. Mechanistic exploration and controlled synthesis of precise thiolate-gold nanoclusters. *Coord. Chem. Rev.* **2016**, *329*, 1-15.

23. Hosier, C. A.; Ackerson, C. J. Regiochemistry of Thiolate for Selenolate Ligand Exchange on Gold Clusters. *J. Am. Chem. Soc.* **2019**, *141*, 309-314.

24. Lee, J. M.; Kraynak, L. A.; Prieto, A. L. A Directed Route to Colloidal Nanoparticle Synthesis of the Copper Selenophosphate Cu_3PSe_4. *Angew. Chem., Int. Ed.* **2020**, *59*, 3038-3042.

25. McMurtry, B. M.; Qian, K.; Teglasi, J. K.; Swarnakar, A. K.; De Roo, J.; Owen, J. S. Continuous Nucleation and Size Dependent Growth Kinetics of Indium Phosphide Nanocrystals. *Chem. Mater.* **2020**, *32*, 4358-4368.

26. Mozaffari, S.; Li, W.; Dixit, M.; Seifert, S.; Lee, B.; Kovarik, L.; Mpourmpakis, G.; Karim, A. M. The role of nanoparticle size and ligand coverage in size focusing of colloidal metal nanoparticles. *Nanoscale Adv.* **2019**, *1*, 4052-4066.

27. Rossi, L. M.; Nangoi, I. M.; Costa, N. J. S. Ligand-Assisted Preparation of Palladium Supported nanoparticles: a Step toward Size Control. *Inorg. Chem.* **2009**, *48*, 4640-4642.

28. Somorjai, G. A.; Park, J. Y. Colloid Science of Metal Nanoparticle Catalysts in 2D and 3D Structures. Challenges of Nucleation, Growth, Composition, Particle Shape, Size Control and Their Influence on Activity and Selectivity. *Top. Catal.* **2008**, *49*, 126-135.

29. Lai, R.; Pu, C.; Peng, X. On-Surface Reactions in the Growth of High-Quality CdSe Nanocrystals in Nonpolar Solutions. *J. Am. Chem. Soc.* **2018**, *140*, 9174-9183.

30. Laxson, W. W.; Finke, R. G. Nucleation is Second Order: An Apparent Kinetically Effective Nucleus of Two for $Ir(0)_n$ Nanoparticle Formation from $[(1,5\text{-COD})Ir^{I}\bullet P_2W_{15}Nb_3O_{62}]^{8-}$ Plus Hydrogen. *J. Am. Chem. Soc.* **2014**, *136*, 17601-17615.

31. Özkar, S.; Finke, R. G. Nanoparticle Nucleation Is Termolecular in Metal and Involves Hydrogen: Evidence for a Kinetically Effective Nucleus of Three $\{Ir_3H_{2x}\bullet P_2H_{15}Nb_3O_{62}\}^{6-}$ in $Ir(0)_n$ Nanoparticle Formation From $[(1,5\text{-COD})Ir^{I}\bullet P_2W_{15}Nb_3O_{62}]^{8-}$ Plus Dihydrogen. *J. Am. Chem. Soc.* **2017**, *139*, 5444-5457.

32. Whitehead, C. B.; Finke, R. G. Nucleation Kinetics and Molecular Mechanism in Transition-Metal Nanoparticle Formation: The Intriguing, Informative Case of a Bimetallic Precursor, $\{[(1,5\text{-COD})Ir^{I}\bullet HPO_4]_2\}^{2-}$. *Chem. Mater.* **2019**, *31*, 2848-2862.

33. Li, T.; Senesi, A. J.; Lee, B. Small Angle X-ray Scattering for Nanoparticle Research. *Chem. Rev.* **2016**, *116* 11128-11180.

34. Chu, B.; Liu, T. Characterization of nanoparticles by scattering techniques. *J. Nanopart. Res.* **2000**, *2*, 29-41.

35. Goyal, P. S.; Aswal, V. K. Use of SANS and SAXS in study of nanoparticles. *Int. J. Nanosci. Ser.* **2005**, *4*, 987-994.

36. Bentrup, U. Combining *in situ* characterization methods in one set-up: looking with more eyes into the intricate chemistry of the synthesis and working of heterogeneous catalysts. *Chem. Soc. Rev.* **2010**, *39*, 4718-4730.

37. Sun, Y.; Ren, Y. In Situ Synchrotron X-Ray Techniques for Real-Time Probing of Colloidal Nanoparticles Synthesis. *Part. Part. Syst. Charact.* **2013**, *30*, 399-419.

38. Mozaffari, S.; Li, W.; Thompson, C.; Ivanov, S.; Seifert, S.; Lee, B.; Kovarik, L.; Karim, A. M. Colloidal nanoparticle size control: experimental and kinetic modeling investigation of the ligand–metal binding role in controlling the nucleation and growth kinetics. *Nanoscale* **2017**, *9*, 13772-13785.

39. Herbst, M.; Hofmann, E.; Förster, S. Nucleation and Growth Kinetics of ZnO Nanoparticles Studied by in Situ Microfluidic SAXS/WAXS/UV-Vis Experiments. *Langmuir* **2019**, *35*, 11702-11709.

40. Yao, S.; Yuan, Y.; Xiao, C.; Li, W.; Kou, Y.; Dyson, P. J.; Yan, N.; Asakura, H.; Teramura, K.; Tanaka, T. Insights into the Formation Mechanism of Rhodium Nanocubes. *J. Phys. Chem. C* **2012**, *116*, 15076-15086.

41. Oyanagi, H.; Sun, Z. H.; Jiang, Y.; Uehara, M.; Nakamura, H.; Yamashita, K.; Zhang, L.; Lee, C.; Fukano, A.; Maeda, H. *In situ* XAFS experiments using a microfluidic cell: application to initial growth of CdSe nanocrystals. *J. Synchrotron Rad.* **2011**, *18*, 272-279.

42. Whitehead, C. B.; Handwerk, D. R.; Li, Y.; Frenkel, A.; Ingham, B.; Kirby, N. M.; Finke, R. G. Nanoparticle Formation Kinetics, Mechanisms and Resultant Rate Constants: Examination of a Second-Generation $Ir(0)_n$ Particle Formation System by XANES, SAXS, TEM, and Mechanism-Enabled Population Balance Modeling. **2021**, *In Final Preparation (See Chapter IV).*

43. Ramamoorthy, R. K.; Yildirim, E.; Barba, E.; Roblin, P.; Vargas, J. A.; Lacroix, L.-M.; Rodriguez-Ruiz, I.; Decorse, P.; Petkov, V.; Teychené, S.; Viau, G. The role of pre-nucleation clusters in the crystallization of gold nanoparticles. *Nanoscale* **2020**, *12*, 16173-16188.

44. Tidwell, T. T. The First Century of Physical Organic Chemistry: A Prologue. *Pure Appl. Chem.* **1997**, *69*, 211-213.

45. Anslyn, E. V.; Dougherty, D. A. *Modern Physical Organic Chemistry*; University Science Books: Sausalito, CA, 2006.

46. Lowry, T. H.; Richardson, K. S. *Mechanism and Theory in Organic Chemistry*, 3rd ed.; Harper & Row: New York, 1987.

47. Halpern, J.; Kim, S.–H.; Leung, T. W. Cobalt–Carbon Bond Dissociation Energy of Coenzyme B_{12}. *J. Am. Chem. Soc.* **1984**, *106*, 8317–8319.

48. Hay, B. P.; Finke, R. G. Thermolysis of the Co–C Bond of the Adensylcobalamin. 2. Products, Kinetics, and Co–C Bond Dissociation Energy in Aqueous Solution. *J. Am. Chem. Soc.* **1986**, *108*, 4820–4829.

49. Smith, S. E.; Sasaki, J. M.; Bergman, R. G.; Mondloch, J. E.; Finke, R. G. Platinum-Catalyzed Phenyl and Methyl Group Transfer from Tin to Iridium: Evidence for an Autocatalytic Reaction Pathway with an Unusual Preference for Methyl Transfer. *J. Am. Chem. Soc.* **2008**, *130*, 1839-1841.

50. Frost, A. A.; Pearson, R. G. *Kinetics and Mechanism. A Study of Homogeneous Chemical Reactions*, 2nd ed.; Wiley & Sons: New York, 1961.

51. Espenson, J. H. *Chemical Kinetics and Reactions Mechanisms*, 2nd ed.; McGraw-Hill: New York, 1995.

52. Field, R. J.; Noyes, R. M. Oscillations in chemical systems. 19. Mechanisms of chemical oscillators: Conceptual bases. *Acc. Chem. Res.* **1977**, *10*, 214-221. Please also see references cited therein.

53. Finney, E. E.; Finke, R. G. Is There a Minimal Chemical Mechanism Underlying Classical Avrami-Erofe'ev Treatments of Phase Transformation Kinetic Data? *Chem. Mater.* **2009**, *21*, 4692-4705.

54. Finney, E. E.; Finke, R. G. Fitting and Interpreting Transition-Metal Nanocluster Formation and Other Sigmoidal Kinetic Data: A More Thorough Testing of Dispersive Kinetics vs Chemical-Mechanism-Based Equations and Treatments for 4-Step Type Kinetic Data. *Chem. Mater.* **2009**, *21*, 4468-4479.

55. Platt, J. R. Strong Inference. *Science* **1964**, *146*, 347–353.

56. Chamberlain, T. C. Studies for Students. The Method of Multiple Working Hypotheses. *J. Geology* **1897**, *5*, 837–848.

57. Hoffmann, R.; Minkin, V. I.; Carpenter, B. K. Ockham's Razor and chemistry. *Bull. Soc. Chim. Fr.* **1996**, *133*, 117-130.

58. Scott, S. L. The Burden of *Dis*proof. *ACS Catal.* **2019**, *9*, 4706-4708.

59. Drews, T. O.; Katsoulakis, M. A.; Tsapatsis, M. A Mathematical Model for Crystal Growth by Aggregation of Precursor Metastable Nanoparticles. *J. Phys. Chem. B* **2005**, *109*, 23879-23887.

60. Dill, E. D.; Josey, A. A.; Folmer, J. C. W.; Hou, F.; Martin, J. D. Experimental Determination of the Crystallization Phase-Boundary Velocity in the Halozeotype CZX-1. *Chem. Mater.* **2013**, *25*, 3932-3940.

61. Plummer, L. K.; Crockett, B. M.; Pennel, M. K.; Jansons, A. W.; Kosela, K. M.; Hutchison, J. E. Influence of Monomer Flux and Temperature on Morphology of Indium Oxide Nanocrystals during a Continuous Growth Synthesis. *Chem. Mater.* **2019**, *31*, 7638-7649.

62. Woehl, T. J.; Park, C.; Evans, J. E.; Arslan, I.; Ristenpart, W. D.; Browning, N. D. Direct Observation of Aggregative Nanoparticle Growth: Kinetic Modeling of the Size Distribution and Growth Rate. *Nano Lett.* **2014**, *14*, 373-378.

63. Whitehead, C. B.; Özkar, S.; Finke, R. G. LaMer's 1950 Model for Particle Formation of Instantaneous Nucleation and Diffusion-Controlled Growth: A Historical Look at the Model's Origins, Assumptions, Equations, and Underlying Sulfur Sol Formation Kinetics Data. *Chem. Mater.* **2019**, *31*, 7116–7132.

64. Whitehead, C. B.; Özkar, S.; Finke, R. G. LaMer's 1950 Model of Particle Formation: A Review and Critical Analysis of Its Classical Nucleation and Fluctuation Theory Basis, of Competing Models and Mechanisms for Phase-Changes and Particle Formation, and then of Its Application to Silver Halide, Semiconductor, Metal, and Metal-Oxide Nanoparticles. *Mater Adv.* **2021**, *2*, 186-235.

65. Handwerk, D. R.; Shipman, P. D.; Whitehead, C. B.; Özkar, S.; Finke, R. G. Mechanism-Enabled Population Balance Modeling of Particle Formation en Route to Particle Average Size and Size Distribution Understanding and Control. *J. Am. Chem. Soc.* **2019**, *141*, 15827–15839.

66. Handwerk, D. R.; Shipman, P. D.; Whitehead, C. B.; Özkar, S.; Finke, R. G. Particle Size Distributions via Mechanism-Enabled Population Balance Modeling. *J. Chem. Phys. C* **2020**, *124*, 4852-4880.

67. Kathmann, S. M.; Schenter, G. K.; Garrett, B. C. Understanding the Sensitivity of Nucleation Kinetics. *J. Chem. Phys.* **2002**, *116*, 5046-5057.

68. Kathmann, S. M.; Schenter, G. K.; Garrett, B. C.; Chen, B.; Siepmann, J. I. Thermodynamics and Kinetics of Nanoclusters Controlling Gas-to-Particle Nucleation. *J. Phys. Chem. C* **2009**, *113*, 10354-10370. See also the references 16 and 25-37 therein concerning DFT studies that strive to go beyond Classical Nucleation Theory.

69. Plata, R. E.; Singleton, D. A. A Case Study of the Mechanism of Alcohol-Mediated Morita Baylis Hillman Reactions. The Important of Experimental Observations. *J. Am. Chem. Soc.* **2015**, *137*, 3811-3826.

70. Karim, A. M.; Al Hasan, N.; Ivanov, S.; Siefert, S.; Kelly, R. T.; Hallfors, N. G.; Benavidez, A.; Kovarik, L.; Jenkins, A.; Winans, R. E.; Datye, A. K. Synthesis of 1 nm Pd Nanoparticles in a Microfluidic Reactor: Insights from in Situ X-ray Absorption Fine Structure Spectroscopy and Small-Angle X-ray Scattering. *J. Chem. Phys. C* **2015**, *119*, 13257-13267.

71. Private correspondence with Professor Ayman Karim of Virginia Polytechnic Institute and State University.

72. Moschetta, E. G.; Gans, K. M.; Rioux, R. M. Characterization of sites of different thermodynamic affinities on the same metal center via isothermal titration calorimetry. *J. Catal.* **2013**, *302*, 1-9.

73. Watzky, M. A.; Finke, R. G. Transition Metal Nanocluster Formation Kinetic and Mechanistic Studies. A New Mechanism When Hydrogen Is the Reductant: Slow, Continuous Nucleation and Fast Autocatalytic Surface Growth. *J. Am. Chem. Soc.* **1997**, *119*, 10382-10400.

74. Teranishi, T.; Miyake, M. Size Control of Palladium Nanoparticles and Their Crystal Structures. *Chem. Mater.* **1998**, *10*, 594-600.

75. Hostetler, M. J.; Wingate, J. E.; Zhong, C.-J.; Harris, J. E.; Vachet, R. W.; Clark, M. R.; Londono, J. D.; Green, S. J.; Stokes, J. J.; Wignall, G. D.; Glish, G. L.; Porter, M. D.; Evans, N. D.; Murray, R. W. Alkanethiolate Gold Cluster Molecules with Core Diameters from 1.5 to 5.2 nm: Core and Monolayer Properties as a Function of Core Size. *Langmuir* **1998**, *14*, 17-30.

76. Wu, B.-H.; Yang, H.-Y.; Huang, H.-Q.; Chen, G.-X.; Zheng, N.-F. Solvent effect on the synthesis of monodisperse amine-capped Au nanoparticles. *Chin. Chem. Lett.* **2013**, *24*, 457-462.

77. Jiang, Y.; Huang, Y.; Cheng, H.; Liu, Q.; Xie, Z.; Yao, T.; Jiang, Z.; Huang, Y.; Bian, Q.; Pan, G.; Sun, Z.; Wei, S. Solvent Influence on the Role of Thiols in Growth of Thiols-Capped Au Nanocrystals. *J. Phys. Chem. C* **2014**, *118*, 714-719.

78. Further, given the discussion *vide supra* in the Background section concerning CNT's inapplicability to strong bonding systems, alternative mechanisms need to be tests and disproven en route to claiming an understanding of ZnO particle-formation mechanism.

79. Nayak, C.; Jha, S. N.; Bhattacharyya, D. In Situ X-Ray Absorption Spectroscopy to Study Growth of Nanoparticles. In *In-Situ Characterization Techniques for Nanomaterials*; Kumar, C. S. S. R., Ed.; Springer-Verlag GmbH, Berlin Heidelberg, 2018; pp 189-222.

80. Asakura, H.; Teramura, K.; Shishido, T.; Tanaka, T.; Yan, N.; Xiao, C.; Yao, S.; Kou, Y. *In situ* time-resolved DXAFS study of Rh nanoparticle formation mechanism in ethylene glycol at elevated temperature. *Phys. Chem. Chem. Phys.* **2012**, *14*, 2983-2990.

81. Besson, C.; Finney, E. E.; Finke, R. G. Nanocluster Nucleation, Growth and Then Agglomeration Kinetic and Mechanistic Studies: A More General, Four-Step Mechanism Involving Double Autocatalysis. *Chem. Mater.* **2005**, *17*, 4925-4938.

82. Ravel, B.; Newville, M. ATHENA, ARTEMIS, HEPHAESTUS: data analysis for X-ray absorption spectroscopy using IFEFFIT. *J. Synchrotron Rad.* **2005**, *12*, 537-541.

83. Leatherdale, C. A.; Woo, W.-K.; Mukulec, F. V.; Bawendi, M. G. On the Absorption Cross Section of CdSe Nanocrystal Quantum Dots. *J. Phys. Chem. B* **2002**, *106*, 7619-7622.

84. Jia, X.; Zhang, P.; Lin, Z.; Anthony, R.; Kortshagen, U.; Huang, S.; Puthen-Veettil, B.; Conibeer, G.; Perez-Wurfl, I. Accurate determination of the size distribution of Si nanocrystals from PL spectra. *RSC Adv.* **2015**, *5*, 55119-55125.

85. Houtepen, A. J.; Hens, Z.; Owen, J. S.; Infante, I. On the Origin of Surface Traps in Colloidal II–VI Semiconductor Nanocrystals. *Chem. Mater.* **2017**, *29*, 752-761.

86. Owen, J. S.; Park, J.; Trudeau, P.-E.; Alivisatos, A. P. Reaction Chemistry and Ligand Exchange at Cadmium–Selenide Nanocrystal Surfaces. *J. Am. Chem. Soc.* **2008**, *130*, 12279-12281.

87. Kovalenko, M. V.; Manna, L.; Cabot, A.; Hens, Z.; Talapin, D. V.; Kagan, C. R.; Klimov, V. I.; Rogach, A. L.; Reiss, P.; Milliron, D. J.; Guyot-Sionnest, P.; Konstantataos, G.; Parak, W. J.; Hyeon, T.; Korgel, B. A.; Murray, C. B.; Heiss, W. Prospects of nanoscience with nanocrystals. *ACS Nano* **2015**, *9*, 1012-1057.

88. De Roo, J.; De Keukeleere, K.; Hens, Z.; Van Driessche, I. From ligands to binding motifs and beyond; the enhanced versatility of nanocrystal surfaces. *Dalton Trans*. **2016**, *45*, 13277-13283.

89. Reiss, P.; Carrière, M.; Lincheneau, C.; Vaure, L.; Tamang, S. Synthesis of Semiconductor Nanocrystals, Focusing on Nontoxic and Earth-Abundant Materials. *Chem. Rev.* **2016**, *116*, 10731-10819.

90. Dhaene, E.; Billet, J.; Bennett, E.; Van Driessche, I.; De Roo, J. The Trouble with ODE: Polymerization during Nanocrystal Synthesis. *Nano Lett.* **2019**, *19*, 7411-7417.

91. Lin, Y.; Finke, R. G. Novel Polyoxoanion and Bu_4N^+ Stabilized, Isolable, and Redissolvable, 20-30 Å $Ir_{\sim 300\text{-}900}$ Nanoclusters: The Kinetically Controlled Synthesis, Characterization, and Mechanism of Formation of Organic Solvent-Soluble, Reproducible Size, and Reproducible Catalytic Activity Metal Nanoclusters. *J. Am. Chem. Soc.* **1994**, *116*, 8335-8353.

92. Lin, Y.; Finke, R. G. A More General Approach to Distinguishing "Homogeneous" from "Heterogeneous" Catalysis: Discovery of Polyoxoanion- and Bu_4N^+-Stabilized, Isolable and Redissolvable, High Reactivity $Ir_{\sim 190\text{-}450}$ Nanocluster Catalysts. *Inorg. Chem.* **1994**, *33*, 4891-4910.

93. Clark, E. P. Signer Method for Determining Molecular Weights. *Ind. Eng. Chem., Anal. Ed.* **1941**, *13*, 821-821.

94. Özkar, S.; Finke, R. G. Iridium(0) Nanocluster, Acid-Assisted Catalysis of Neat Acetone Hydrogenation at Room Temperature: Exceptional Activity, Catalyst Lifetime, and Selectivity at Complete Conversion. *J. Am. Chem. Soc.* **2005**, *127*, 4800-4808.

95. Dias, E. T.; Gill, S. K.; Liu, Y.; Halstenberg, P.; Dai, S.; Huang, J.; Mausz, J.; Gakhar, R.; Phillips, W. C.; Mahurin, S.; Pimblott, S. M.; Wishart, J. F.; Frenkel, A. I. Radiation-Assisted Formation of Metal Nanoparticles in Molten Salts. *J. Phys. Chem. Lett.* **2021**, *12*, 157-164.

96. Ma, J.; Zou, Y.; Jiang, Z.; Huang, W.; Li, J.; Wu, G.; Huang, Y.; Xu, H. An in situ XAFS study—the formation mechanism of gold nanoparticles from X-ray-irradiated ionic liquid. *Phys. Chem. Chem. Phys.* **2013**, *15*, 11904-11908.

97. Bharti, A.; Bhardwaj, R.; Agrawal, A. K.; Goyal, N.; Gautam, S. Monochromatic X-Ray Induced Novel Synthesis of Plasmonic Nanostructure for Photovoltaic Application. *Sci. Rep*. **2016**, *6*, 22394.

98. Grand, J.; Ferreira, S. R.; de Waele, V.; Mintova, S.; Nenoff, T. M. Nanoparticle Alloy Formation by Radiolysis. *J. Phys. Chem. C* **2018**, *122*, 12573-12588.

99. Quinson, J.; Jensen, K. M. Ø. From platinum atoms in molecules to colloidal nanoparticles: A review on reduction, nucleation and growth mechanisms. *Adv. Colloid Interface Sci.* **2020**, *286*, 102300.

100. Remita, S.; Fontaine, P.; Lacaze, E.; Borensztein, Y.; Sellame, H.; Farha, R.; Rochas, C.; Goldmann, M. X-ray radiolysis induced formation of silver nano-particles: A SAXS and UV-visible absorption spectroscopy study. *Nuc. Instr. Meth. B* **2007**, *263*, 436-440.

101. Bondaz, L.; Fontaine, P.; Muller, F.; Pantoustier, N.; Perrin, P.; Morfin, I.; Goldmann, M.; Cousin, F. Controlled Synthesis of Gold Nanoparticles in Copolymers Nanomolds by X-ray Radiolysis. *Langmuir* **2020**, *36*, 6132-6144.

102. Yamaguchi, A.; Fukuoka, T.; Okada, I.; Ishihara, M.; Sakurai, I.; Utsumi, Y. Caltrop Particles Synthesized by Photochemical Reaction Induced by X-Ray Radiolysis. *J. Synchrotron Radiat.* **2017**, *24*, 653-660.

103. Stachowski, T. R.; Snell, M. E.; Snell, E. H. SAXS studies of X-ray induced disulfide bond damge: Engineering high-resolution insight from a low-resolution technique. *Plos One* **2020**, *15*, 0239702. DOI: 10.1371/journal.pone.0239702.

104. The ~10^{15} solvated electrons results from the rough estimation reported in the Supporting Information of reference 95. Therein, it is calculated that 1 photon of 8 keV energy results in the formation of ~300 absorbed electrons. Hence, given the observed complete absorption of radiation in the system examined, it was calculated that (300 absorbed electrons / photon) x (~3x10^{13} photons / second) = ~10^{15} solvated electrons per second are produced.

105. Özkar, S.; Finke, R. G. The hydrogenphosphate complex of (1,5-cyclooctadiene)iridium(I), $\{[Bu_4N][(1,5\text{-COD})Ir{\bullet}HPO_4]\}_n$: synthesis, spectroscopic characterization, and ES-MS of a new, preferred precursor to HPO_4^{2-} and Bu_4N^+ stabilized $Ir(0)_n$ nanoclusters. *J. Organomet. Chem.* **2004**, *689*, 493–501.

106. Özkar, S.; Finke, R. G. Transition-Metal Nanocluster Stabilization Fundamental Studies: Hydrogen Phosphate as a Simple, Effective, Readily Available, Robust, and Previously Unappreciated Stabilizer for Well-Formed, Isolable, and Redissolvable Ir(0) and Other Transition-Metal Nanoclusters. *Langmuir* **2003**, *19*, 6247-6260.

107. Rusyniak, M.; Abdelsayed, V.; Campbell, J.; El-Shall, M. S. Vapor Phase Homogeneous Nucleation of Higher Alkanes: Dodecane, Hexadecane, and Octadecane. 1. Critical Supersaturation and Nucleation Rate Measurements. *J. Phys. Chem. B* **2011**, *105*, 11866-11872.

108. Rusyniak, M.; El-Shall, M. S. Vapor Phase Homogeneous Nucleation of Higher Alkanes: Dodecane, Hexadecane, and Octadecane. 2. Corresponding States and Scaling Law Analysis. *J. Phys. Chem. B* **2001**, *105*, 11873-11879.

109. Gibbs, J. W. On the Equilibrium of Heterogeneous Substances. *New Haven Transactions of Connecticut Academy of Arts and Sciences* **1874**, *III*, 343-523.

110. Volmer, M. *Kinetik der Phasenbildung*. Verlag von Theordor Steinkopff: Leipzig, 1939.

111. Becker, R.; Döring, W. Kinetische Behandlung der Keimbildung in übersättigten Dampfen. *Ann. Phys.* **1935**, *24*, 719-752.

112. Avrami, M. Kinetics of Phase Change. I. General Theory. *J. Chem. Phys.* **1939**, *7*, 1103-1112.

113. Avrami, M. Kinetics of Phase Change. II. Transformation-Time Relations for Random Distribution of Nuclei. *J. Chem. Phys.* **1940**, *8*, 212-224.

114. Avrami, M. Kinetics of Phase Change. III. Granulation, Phase Change, and Microstructure. *J. Chem. Phys.* **1941**, *9*, 177-184.

115. Kolmogorov, A. N. On the Statistical Theory of Metal Crystallization. *Bull. Acad. Sci. USSR Phys. Ser.* **1937**, *3*, 555-560.

116. Johnson, W. A.; Mehl, R. F. Reaction Kinetics in Processes of Nucleation and Growth. *Trans. AIME* **1939**, *135*, 416-458.

117. Erofe'ev, B. A. A Generalized Equation of Chemical Kinetics and its Application in Reactions Involving Solids. *Dokl. Akad. Sci. USSR* **1946**, *52*, 511-514.

118. Dill, E. D.; Josey, A. A.; Folmer, J. C. W.; Hou, F.; Martin, J. D. Experimental Determination of the Crystallization Phase-Boundary Velocity in the Halozeotype CZX-1. *Chem. Mater.* **2013**, *25*, 3932-3940.

119. Finke, R. G.; Watzky, M. A.; Whitehead, C. B. Response to "Particle Size Is a Primary Determinant for Sigmoidal Kinetics of Nanoparticle Formation: A "Disproof" of the Finke–

Watzky (F-W) Nanoparticle Nucleation and Growth Mechanism". *Chem. Mater.* **2020**, *32*, 3657-3672.

120. LaMer, V. K.; Dinegar, R. H. Theory, Production and Mechanism of Formation of Monodispersed Hydrosols. *J. Am. Chem. Soc.* **1950**, *72*, 4847–4854.

121. Whitehead, C. B.; Watzky, M. A.; Finke, R. G. "Burst Nucleation" vs Autocatalytic, "Burst" Growth In Near-Monodisperse Particle Formation Reactions. *J. Phys. Chem. C* **2020**, *In Press.* DOI: 10.1021/acs.jpcc.0c06875.

122. Harada, M.; Inada, Y. In Situ Time-Resolved XAFS Studies of Metal Particle Formation by Photoreduction in Polymer Solutions. *Langmuir* **2009**, *25*, 6049-6061.

123. LaGrow, A. P.; Ingham, B.; Toney, M. F.; Tilley, R. D. Effect of Surfactant Concentration and Aggregation on the Growth Kinetics of Nickel Nanoparticles. *J. Phys. Chem. C* **2013**, *117*, 16709-16718.

124. Kytsya, A.; Hazylyak, L.; Hrynda, y.; Horechyy, A.; Medvedevdkikh, Y. The Kinetic Rate Law for the Autocatalytic Growth of Citrate-Stabilized Silver Nanoparticles. *Int. J. Chemical Kinetics* **2015**, *47*, 351-360.

125. Sergievskaya, A. P.; Tatarchuk, V. V.; Makotchenko, E. V.; Mironov, I. V. Formation of gold nanoparticles during the reduction of $HAuBr_4$ in reverse micelles of oxyethylated surfactant: Influence of gold precursor on the growth kinetics and properties of the particles. *J. Mater. Res.* **2015**, *30*, 1925-1933.

126. Harada, M.; Kizaki, S. Formation Mechanism of Gold Nanoparticles Synthesized by Photoreduction in Aqueous Ethanol Solution of Polymers Using In Situ Quick Scanning X-ray Absorption Fine Structure and Small-Angle X-ray Scattering. *Cryst. Growth Des.* **2016**, *16*, 1200-1212.

127. Yang, T.–H.; Peng, H.–C.; Zhou, S.; Lee, C.–T.; Bao, S.; Lee, Y.–H.; Wu, J.–M.; Xia, Y. Toward a Quantitative Understanding of the Reduction Pathways of a Salt Precursor in the Synthesis of Metal Nanocrystals. *Nano Lett.* **2017**, *17*, 334-340.

128. Peters, B. Common Features of Extraordinary Rate Theories. *J. Phys. Chem. B* **2015**, *119*, 6349-6356.

129. La Mer, V. K. Nucleation in Phase Transitions. *Ind. Eng. Chem.* **1952**, *44*, 1270-1277.

130. Turkevich, J.; Stevenson, P. C.; Hillier, J. A Study of the Nucleation and Growth Processes in the Synthesis of Colloidal Gold. *Discuss. Faraday Soc.* **1951**, *11*, 55-75.

131. Turkevich, J.; Stevenson, P. C.; Hillier, J. The Formation of Colloid Gold. *J. Phys. Chem.* **1953**, *57*, 670-673.

132. Bayram, E.; Linehan, J. C.; Fulton, J. L.; Roberts, J. A. S.; Szymczak, N. K.; Smurthwaite, T. D.; Özkar, S.; Balasubramanian, M.; Finke, R. G. Is it Homogeneous or Heterogeneous Catalysis Derived from $[RhCp^*Cl_2]_2$? *In Operando* XAFS, Kinetic, and Crucial Kinetic Poisoning Evidence for Subnanometer Rh_4 Cluster-Based Benzene Hydrogenation Catalysis. *J. Am. Chem. Soc.* **2011**, *133*, 18889-18902.

133. Mondloch, J. E.; Wang, Q.; Frenkel, A. I.; Finke, R. G. Development Plus Kinetic and Mechanistic Studies of a Prototype Supported-Nanoparticle Heterogeneous Catalyst Formation System in Contact with Solution: Ir(1,5-COD)Cl/γ-Al_2O_3 and Its Reduction by H_2 to $Ir(0)_n$/γ-Al_2O_3. *J. Am. Chem. Soc.* **2010**, *132*, 9701-9714.

134. Tong, F.; Hanson, M. P.; Bardeen, C. Analysis of reaction kinetics in the photochemical molecular crystal 9-methylanthracene using an extended Finke-Watzky model. *Phys. Chem. Chem. Phys.* **2016**, *18*, 31936-31945.

135. Avinash, M. B.; Sandeepa, K. V.; Govindaraju, T. Emergent Behaviors in Kinetically Controlled Dynamic Self-Assembly of Synthetic Molecular Systems. *ACS Omega* **2016**, *1*, 378-387.

136. Morris, A. M.; Watzky, M. A.; Agar, J. N.; Finke, R. G. Fitting neurological protein aggregation kinetic data via a 2-step, minimal/"Ockham's razor" model: the Finke-Watzky mechanism of nucleation followed by autocatalytic surface growth. *Biochemistry* **2008**, *47*, 2413-2427.

137. Oladoja, N. A. A critical review of the applicability of Avrami fractional kinetic equation in adsorption-based water treatment studies. *Desalin. Water Treat.* **2015**, *57*, 15813-15825.

138. Hornstein, B. J.; Finke, R. G. Transition-Metal Nanocluster Kinetic and Mechanistic Studies Emphasizing Nanocluster Agglomeration: Demonstration of a Kinetic Method That Allows Monitoring All Three Phases of Nanocluster Formation and Aging. *Chem. Mater.* **2004**, *16*, 139-150. (See also the addition / correction: *Chem. Mater.* **2004**, *16*, 3972.)

139. Besson, C.; Finney, E. E.; Finke, R. G. A Mechanism for Transition-Metal Nanoparticle Self-Assembly. *J. Am. Chem. Soc.* **2005**, *127*, 8179-8184.

140. Finney, E. E.; Finke, R. G. The Four-Step, Double-Autocatalytic Mechanism for Transition-Metal Nanocluster Nucleation, Growth and Then Agglomeration: Metal, Ligand, Concentration, Temperature, and Solvent Dependency Studies. *Chem. Mater.* **2008**, *20*, 1956-1970.

141. Kent, P. D.; Mondloch, J. E.; Finke, R. G. A Four-Step Mechanism for the Formation of Supported-Nanoparticle Heterogeneous Catalysts in Contact with Solution: The Conversion of Ir(1,5-COD)Cl/γ-Al_2O_3 to $Ir(0)_{\sim 170}$/γ-Al_2O_3. *J. Am. Chem. Soc.* **2014**, *136*, 1930-1941.

142. Drews, T. O.; Katsoulakis, M. A.; Tsapatsis, M. A Mathematical Model for Crystal Growth by Aggregation of Precursor Metastable Nanoparticles. *J. Phys. Chem. B* **2005**, *109*, 23879-23887.

143. Koerner, H.; MacCuspie, R. I.; Park, K.; Vaia, R. A. In Situ UV/Vis, SAXS, and TEM Study of Single-Phase Gold Nanoparticle Growth. *Chem. Mater.* **2012**, *24*, 981–995.

144. Yao, T.; Sun, Z.; Li, Y.; Pan, Z.; Wei, H.; Xie, Y.; Nomura, M.; Niwa, Y.; Yan, W.; Wu, Z.; Jiang, Y.; Liu, Q.; Wei, S. Insights into Initial Kinetic Nucleation of Gold Nanocrystals. *J. Am. Chem. Soc.* **2010**, *132*, 7696-7701.

145. Tanaka, T.; Ohyama, J.; Teramura, K.; Hitomi, Y. Formation mechanism of metal nanoparticles studied by XAFS spectroscopy and effective synthesis of small metal nanoparticles. *Catalysis Today* **2012**, *183*, 108–118.

146. Liu, Y.; Qian, L.; Zhao, X.; Wang, J.; Yao, L.; Xing, X.; Mo, G.; Cai, Q.; Chen, Z.; Wu, Z. Synthesis and formation mechanism of self-assembled 3D flower-like Bi/□-Fe_2O_3 composite particles. *CrystEngComm* **2019**, *21*, 2799–2808.

147. Saeki, M.; Matsumura, D.; Yomogida, T.; Taguchi, T.; Tsuji, T.; Saitoh, H.; Ohba, H. In Situ Time-Resolved XAFS Studies on Laser-Induced Particle Formation of Palladium Metal in an Aqueous/EtOH Solution. *J. Phys. Chem. C* **2019**, *123*, 817–824.

148. Wang, J.; Winans, R. E.; Anderson, S. L.; Seifert, S.; Lee, B.; Chupas, P. J.; Ren. Y.; Lee, S.; Liu, Y. In Situ Small-Angle X-ray Scattering from Pd Nanoparticles Formed by Thermal Decomposition of Organo-Pd Catalyst Precursors Dissolved in Hydrocarbons. *J. Phys. Chem. C* **2013**, *117*, 22627–22635.

149. Asakura, H.; Teramura, K.; Shishido, T.; Tanaka, T.; Yan, N.; Xiao, C.; Yao, S.; Kou, Y. *In situ* time-resolved DXAFS study of Rh nanoparticle formation mechanism in ethylene glycol at elevated temperature. *Phys. Chem. Chem. Phys.* **2012**, *14*, 2983–2990.

150. Yao, T.; Liu, S.; Sun, Z.; Li, Y.; He, S.; Cheng, H.; Xie, Y.; Liu, Q.; Jiang, Y.; Wu, Z.; Yan, W.; Wei, S. Probing Nucleation Pathways for Morphological Manipulation of Platinum Nanocrystals. *J. Am. Chem. Soc.* **2012**, *134*, 9410-9416.

151. Bhattacharyya, K. X.; Pradel, C.; Lecante, P.; Mézailles, N. Mechanistic Investigations of the Synthesis of Size-Tunable Ni Nanoparticles by Reduction of Simple Ni^{II} Diamide Precursors. *Chem. Eur. J.* **2017**, *23*, 9352-9361.

152. Weinfurt, K. P. Vanquishing false idols, then and now. *Science* **2020**, *367*, 1312.

III. NUCLEATION KINETICS AND MOLECULAR MECHANISM IN TRANSITION-METAL NANOPARTICLE FORMATION: THE INTRIGUING, INFORMATIVE CASE OF A BIMETALLIC PRECUSOR, $\{[(1,5\text{-COD})Ir^{I}\bullet HPO_4]_2\}^{2-}$

Overview[ii]

Following a summary of the relevant literature on nucleation and applicable nucleation and growth models and mechanisms, the kinetics and molecular mechanism of nucleation are investigated in molecular detail starting from $[(1,5\text{-COD})Ir^{I}(NCCH_3)_2][BF_4]$, **1**, which upon addition of HPO_4^{2-} to **1** forms a neutral, phosphate-bridged species, $\{[(1,5\text{-COD})Ir^{I}(NCCH_3)]_2\bullet HPO_4\}^0$, **2**, en route to $\{[(1,5\text{-COD})Ir^{I}\bullet HPO_4]_2[Bu_4N]_2\}$, **3**. Post a list of the seven advantages of the $\{[(1,5\text{-COD})Ir^{I}\bullet HPO_4]_2\}^{2-}$ precatalyst as a novel bimetallic precursor for kinetic and mechanistic studies of nucleation, six important, previously unanswered questions are raised about the ill-understood but exceedingly broad and important topic of nucleation. ^{1}H NMR solution speciation and Signer apparatus solution molecular weight studies establish that in situ prepared $\{[(1,5\text{-COD})Ir^{I}\bullet HPO_4]_2\}^{2-}$, **3**, exists predominantly in its indicated, dimeric form. The NMR studies also identify $\{[(1,5\text{-COD})Ir^{I}(NCCH_3)]_2\bullet HPO_4\}^0$, **2**, as an important, meta-stable species with one less HPO_4^{2-}, formed in a dissociative equilibrium of **3** to **2** plus HPO_4^{2-}. Kinetic studies reveal a first-order dependence of nucleation on the concentration of **3** and hence rule out

[ii] This chapter details the preparation, characterization, and kinetics study of a second-generation iridium nanoparticle system. A molecular mechanism of nucleation was elucidated. This chapter contains the complete published manuscript (Whitehead, C. B.; Finke, R. G. *Chem. Mater.* **2019**, *31*, 2848–2862. https://pubs.acs.org/doi/abs/10.1021/acs.chemmater.8b05335) which has been reproduced with permission. The article is licensed under the American Chemical Society, and further permission requests related to the article should be directed to the ACS. The project described in this chapter was conceived by the PI, Prof. Finke. The author of this dissertation, C. B. Whitehead, conducted *all* experiments and data analysis. Writing was done by the author with helpful, pedagogical editing by the advisor, as this manuscript was the student's first publication. Minor changes to the manuscript have been made to meet dissertation formatting requirements. The supporting information can be found in Appendix II.

the higher-order dependence implied by classical nucleation theory. Additional kinetic studies reveal a telling, inverse, quadratic dependence on added HPO_4^{2-}, results that unveil the previously unavailable insights that a simple bimetallic, Ir_2 precursor is sufficient to enable low molecularity nucleation via $\{[(1,5\text{-COD})Ir^{I}(NCCH_3)]_2 \bullet HPO_4\}^0$, **2**, as a kinetically competent intermediate, a unique example of a nucleation mechanism known in molecular detail from a precisely defined molecular precursor that also includes spectroscopic detection of a kinetically competent intermediate. The results with $\{[(1,5\text{-COD})Ir^{I}\bullet\mathbf{HPO_4}]_2\}^{2-}$ in comparison to previous results with $\{[(1,5\text{-COD})Ir^{I}\bullet\mathbf{POM}\}^{8-}$ (**POM** = the **p**oly**o**xo**m**etalate $P_2W_{15}Nb_3O_{62}^{9-}$) allow insights into the details of nucleation, notably that Ir_2 vs Ir_3 kinetically effective nuclei are controlled by the different $\mathbf{HPO_4}^{2-}$ and $\mathbf{POM}^{8-}$ anion's surface charge and resultant **2** vs **3** $Ir^{I}(1,5\text{-COD})^+$ moieties they are able to bind to achieve surface-charge neutrality. The state-of-the-art nucleation results allow a total of nine insights, conclusions, and two new working hypotheses, insights that promise to help drive a deeper understanding of nucleation, not just in transition-metal nanoparticle formation but hopefully more broadly across nature.

3.1. INTRODUCTION

Nucleation Background

Nucleation[1,2,3,4,5,6,7,8,9,10] is that crucial, initial, presently ill-understood chemical process that governs nanoparticle formation and all other phase changes in nature. Nucleation is central to the resultant size and size-distribution of the nanoparticles that are formed and, hence, to the critical size-dependent properties of nanoparticles. Historically, key theories and models for nucleation have been classical nucleation theory[1,3,4] (CNT) and LaMer's associated model[11,12] of putative, thermodynamically controlled "instantaneous (burst)" nucleation and "diffusion-controlled" growth. However, neither of these often-cited models predict or make physical sense, for cases where nucleation is *slow and continuous and growth autocatalytic* (*vide infra*), nor for the evolving alternative hypothesis of kinetically controlled, *low, ≤2–3-molecularity, nucleation*.[13,14]

Finke-Watzky (FW) 2-Step Mechanism for Nanoparticle Formation Consisting of Slow, Continuous Nucleation and Fast, Autocatalytic Surface Growth

In 1997 and hence approaching 50 years after LaMer's model, the first *mechanism* of nanoparticle formation[15,16] appeared consisting of slow, continuous nucleation, A → B (rate constant k_1), and autocatalytic surface growth, A + B → 2B (rate constant k_2)—a mechanism now known to be much more broadly applicable across nature (*vide infra*). In this deliberately minimalistic, Ockham's razor obeying, disproof-based mechanism, A is nominally the precursor or precatalyst, $\{[(1,5\text{-COD})Ir^{I}\bullet HPO_4]_2\}^{2-}$, in the present work and B represents the growing nanoparticle, $Ir(0)_n$. The two pseudo-elementary step, minimalistic mechanism is known as the Finke-Watzky (FW) 2-step mechanism[15] and has found a broad and still expanding appeal in over

530 SciFinder citations at present, including to the following nanoparticle formation systems: Ir(0),[15,17,18] Rh(0),[19,20,21,22] Pt(0),[18,23] Ru(0),[24] Pd(0),[25,26] Ni(0),[27] Ag(0),[28,29] and Au(0)[30] nanoparticles. Direct X-ray absorption fine structure (XAFS) support for the 2-step mechanism exists in the cases of Rh(0)[22] and Pt(0)[23] nanoparticles, and direct small-angle X-ray scattering (SAXS) support for the 2-step mechanism exists in the case of important work on Ni(0) nanoparticle formation.[22,27] Additional application of the FW 2-step mechanism includes: homogeneous catalyst formation,[31,32,33] heterogeneous catalyst formation,[34,35,36] protein aggregation,[37,38,39,40] solid-state kinetics,[41,42] dye aggregation,[43] and other areas of nature showing "cooperative", autocatalytic phenomena.[44] Clearly, nucleation is *slow and continuous*,[15] A → B, in many cases in nature, the opposite of Classical Nucleation Theory and the LaMer model that posits putative "instantaneous (burst)" nucleation and "diffusion-controlled" growth.

However, the more intimate kinetic and mechanistic details of the deliberately minimalistic nucleation step, A → B (rate constant k_1) are only now being uncovered.[13,14] In the case of the FW 2-step mechanism, it has been known from the beginning[15] that higher molecularity nucleation, for example, possible nA → B_n, irreversible nucleation (rate constant $k_{1(\text{obs},n\text{-molecular})}$), will be hidden in the simpler unimolecular A → B formulation because [A] is often constant (=$[A]_0$) to a ≥99.9% level[13] during the induction period. This, in turn, means that $k_1[A]_0 = k_{1(\text{obs},n\text{-molecular})}[A]_0^n$, so that the apparent rate constant of unimolecular nucleation, k_1, would in the case of second- or higher-order nucleation be $k_1 = k_{1(\text{obs},n\text{-molecular})}[A]_0^{n-1}$ = a constant. Important to note is that even in the case of higher order (and implied higher molecularity) nucleation, the FW 2-step *unimolecular* nucleation mechanism can still be used to fit to higher molecularity nucleation kinetics data, n > 1. This means that studies of k_1 vs $[A]_0$ must be done to test for the possibility of such higher-order

nucleation. It is just such studies that are reported herein for the first time for an intriguing dimeric $\{[(1,5\text{-COD})Ir^{I}\bullet HPO_4]_2\}^{2-}$ precatalyst.

Note also that the dimeric $\{[(1,5\text{-COD})Ir^{I}\bullet HPO_4]_2\}^{2-}$ precursor raises the interesting and never-before-answered question of will a *bimetallic* precatalyst show ½ order (implying unimolecular, Ir_1), or first-order (implying bimolecular, Ir_2), or some higher order *n* (implying 2*m* molecular) nucleation? Or, since net termolecular, Ir_3, nucleation has recently been documented, when starting from the closely related $\{(1,5\text{-COD})Ir^{I}\bullet\mathbf{POM}]\}^{8-}$ ((**POM** = the **p**oly**o**xo**m**etalate $P_2W_{15}Nb_3O_{62}^{9-}$) nanoparticle precursor system, will a 3/2 order in $\{[(1,5\text{-COD})Ir^{I}\bullet\mathbf{HPO_4}]_2\}^{2-}$ be obtained indicating an unexpected, but conceivable, strict requirement for an Ir_3, termolecular nucleation? Such fundamental questions about nucleation have never been previously asked nor answered in the literature.

Classical Nucleation Theory

The study herein of $\{[(1,5\text{-COD})Ir^{I}\bullet HPO_4]_2\}^{2-}$ also provides a further check on Classical Nucleation Theory (CNT): is its *thermodynamically controlled, reversible, and hence implied higher order* $n\text{A} \rightarrow \text{B}_n$ nucleation actually observed experimentally? Or, alternatively, is CNT *simply inapplicable* for systems that form relatively strong, Ir–Ir bonds in the $Ir(0)_n$ nanoparticle and where individual Ir(0) atoms have lost their identity? A careful reading of CNT literature teaches that CNT was both designed for, and experimentally should only be applied to, *very weakly intermolecular bonding systems* where the molecular integrity of the associating entity is preserved,[13,45,46] for example, the reversible association of hydrocarbons, RH, in the gas phase, $n\text{RH} \rightarrow (\text{RH})_n$.[45,46] There, the RH•••RH *inter*molecular associations are much weaker than the RH *intra*-atomic bonding so that the chemical individuality and identity of each, relatively stable,

relatively low-energy RH is retained in a $(RH)_n$ cluster. As such, $(RH)_n$ nucleation is completely different than that for an $Ir(0)_n$ or other $M(0)_n$ transition-metal nanoparticle, where once $M(0)_n$ is formed, the identity of each *n* individual, high-energy, relatively unstable M(0) atom is lost in the relatively strongly M–M bonded, $M(0)_n$ nanoparticle.

Recent Evidence for Low, Bi-to Ter-Molecular, Irreversible Nucleation Involving Ir–H Intermediates

In a 2014 *JACS* paper and for the prototype system beginning with A = $\{(1,5\text{-COD})Ir^{I}\bullet\mathbf{POM}\}^{8-}$ under H_2 reductive conditions (**POM** = $P_2W_{15}Nb_3O_{62}^{9-}$), to form B = $Ir(0)_{\sim 300}$ nanoparticles stabilized by the $P_2W_{15}Nb_3O_{62}^{9-}$ polyoxometalate anion, *nucleation was shown to be overall second order in [A].*[13] Additionally, in that 2014 paper, the new concept of a Kinetically Effective Nucleus (KEN) was proposed[13] to supplant the outdated, never actually observed (nor unobservable by definition, as it is the highest energy species) "critical nucleus" of CNT.[1,3,5] Furthermore, the concept of a First-Observable Cluster (FOC) was presented, where the FOC is that first cluster detected (detectable) by whatever physical method being employed.[13] When claims of observation of the critical nucleus of CNT are made, it is argued elsewhere that what is actually being detected, instead, is the FOC.[13] Note that an *apparent* KEN of 2, that is, a species containing Ir_2, is what was implied by the observed, *apparent* second-order kinetics in the $\{(1,5\text{-COD})Ir^{I}\bullet POM\}^{8-}$ starting material.[13] Evidence exists that low, bimolecular (to termolecular, *vide infra*) nucleation may be more common in other systems across nature, results that conflict with and convincingly disprove CNT for those specific cases.[47.48.49]

Interestingly, in a follow-up 2017 paper,[14] nucleation in the classic $\{(1,5\text{-COD})Ir^{I}\bullet POM\}^{8-}$, which exhibits an observed second-order rate law in the starting $\{(1,5\text{-COD})Ir^{I}\bullet POM\}^{8-}$ complex,

was shown to actually be *termolecular in Ir* and involve H_2, with termolecular nucleation in Ir "hiding" under the apparent second-order kinetics in A.[14] The net termolecular, Ir_3, was uncovered by the inverse, ca. $1/[POM^{9-}]^2$, dependence of the nucleation kinetics indicating dissociation of the POM^{9-} from the starting $\{(1,5\text{-COD})Ir^{I}\bullet POM\}^{8-}$ complex and participation of **2** of the cationic (and hence more easily reducible), $Ir^{I}(1,5\text{-COD})^{+}$ fragments in the nucleation mechanism.[14] In that *strong Ir–Ir and Ir–H bonding system*,[14] the implied KEN proved experimentally to be $\{Ir_3H_{2x}POM\}^{6-}$, that is, to involve *just 3 Ir*, as well as Ir–H bonds, and to be *irreversibly formed,*[14] a disproof of any applicability of Classical Nucleation Theory to that prototype transition-metal, $Ir(0)_n$ nanoparticle formation system.

Effects of Dust on Ostensibly "Homogeneous", albeit Actually Dust-Mediated, Heterogeneous Nucleation

A second 2017 paper[50] studying the same prototype $\{(1,5\text{-COD})Ir^{I}\bullet POM\}^{8-}$ system revealed the important effects of dust on the nucleation process. Specifically and quoting key results therein,[50] the following was found: "the nucleation apparent rate 'constant' $k_{1obs(bimol)}$ is slowed by a factor of ~5 to ~7.6, depending on the precise experiment and its conditions, just by filtration of the precatalyst solution using a 0.20 μm filter *and* rinsing the glassware surface with 0.20 μm filtered propylene carbonate solvent." It was also shown by five lines of evidence that, to quote, "the filterable component of the solution, which is having the nucleation rate-enhancing, and size-dispersion broadening effects, is dust."[50] Remarkably, the filtration was also found to narrow the resulting size distribution by a factor of 2.4-fold (from ±19% to a relatively narrow ±8%), results the could be rationalized by a reduced nucleation rate constant, k_1, but an unchanged autocatalytic growth rate constant, k_2.[50]

Strengths but Also Key Limitations of the Classic $\{(1,5\text{-COD})Ir^{I}\bullet POM\}^{8-}$ System That Have Led to the Present Studies of the $\{[(1,5\text{-COD})Ir^{I}\bullet HPO_4]_2\}^{2-}$ System

The classic $\{(1,5\text{-COD})Ir^{I}\bullet\mathbf{POM}\}^{8-}$ nanoparticle formation system has exhibited a number of major advantages, a few key ones of which are as follows: (i) it starts from a compositionally precisely characterized, reproducible precursor, $\{(1,5\text{-COD})Ir^{I}\bullet POM\}^{8-}$;[51] (ii) the resultant $Ir(0)_n\bullet POM$ stabilized nanoparticles are reproducibly formed and well-stabilized by the "Gold Standard" POM^{9-} stabilizer;[52,53] (iii) the kinetics of nanoparticle formation occur at a convenient rate at room temperature, under an initial 40 psig of H_2, and exhibit reproducible kinetics;[15] (iv) the nanoparticle formation kinetics can be monitored (indirectly, but in real time) by a cyclohexene catalytic reporter reaction and (more directly) by the evolution of cyclooctane by gas chromatography or NMR;[15] and (v) the $\{(1,5\text{-COD})Ir^{I}\bullet POM\}^{8-}$ system operates via the dissociative K_{eq} in eq 3.1 that, it turns out, reports on the more detailed nucleation mechanism, all of which have allowed for the first determination of the KEN for a transition-metal nanoparticle nucleation reaction.[14]

$$\{(1,5\text{-COD})Ir^{I}\bullet POM\}^{8-} + 2\ solv \underset{}{\overset{K_{Diss}}{\rightleftharpoons}} [(1,5\text{-COD})Ir^{I}(solv)_2]^{+} + POM^{9-} \qquad \text{(Eq 3.1)}$$

However, three disadvantages of the $\{(1,5\text{-COD})Ir^{I}\bullet\mathbf{POM}\}^{8-}$ system, which have led to the current $\{[(1,5\text{-COD})Ir^{I}\bullet\mathbf{HPO_4}]_2\}^{2-}$ system examined herein, are: (a) the presence of the $P_2W_{15}Nb_3O_{62}^{9-}$ polyoxometalate has preluded Ir XAFS, in at least our hands and post several attempts, due to overlap of the W L_2 edge with the preferred Ir L_3 edge. This necessitates collecting XAFS at the Ir L_1 edge, which, in turn, greatly decreased the XAFS signal, again, at least in studies

we have tried. XAFS in the $\{(1,5\text{-COD})Ir^{I}\bullet POM\}^{8-}$ system is also confounded by the large ratio of 15 W to 1 Ir that decreases the sample transmittance. (b) A second main disadvantage of the $\{(1,5\text{-COD})Ir^{I}\bullet POM\}^{8-}$ system is that SAXS studies of $\{(1,5\text{-COD})Ir^{I}\bullet POM\}^{8-}$ are insensitive to the small, growing $Ir(0)_n$ core and hence non-optimum during the crucial nucleation process when $Ir(0)_n$ is smaller (or even when comparable) to the relatively large, ca. 1.2 nm x 1.5 nm, size of the POM^{9-}. This is a major limitation presently given that SAXS data are proving key for Population Balance Modeling (PBM) studies of size and size-distributions versus time, efforts currently in progress. A third disadvantage of the otherwise valuable $\{(1,5\text{-COD})Ir^{I}\bullet POM\}^{8-}$ system is that (c) synthesis of the $P_2W_{15}Nb_3O_{62}^{9-}$ is multistep, time-consuming, and can prove troublesome in the hands of inexperienced synthetic researchers.[54] These three limitations of the otherwise classic $\{(1,5\text{-COD})Ir^{I}\bullet\mathbf{POM}\}^{8-}$ system have led us to the present studies of present $\{[(1,5\text{-COD})Ir^{I}\bullet\mathbf{HPO_4}]_m\}^{m-}$ (m = 2) addressing each of the above limitations and providing a number of other advantages of this second-generation $Ir(0)_n$ nanoparticle formation system.

Prior Studies of $\{[(1,5\text{-COD})Ir^{I}\bullet HPO_4]_m\}^{m-}$

Previous studies from our lab reported that HPO_4^{2-} can serve as an effective stabilizer for $Ir(0)_n$ nanoparticles formed from the isolated complex,[17,55,56] $\{[(1,5\text{-COD})Ir^{I}\bullet HPO_4]_m\}^{m-}$. Characterization of the isolated complex included ^1H, ^{13}C, and ^{31}P NMR, elemental analysis, and electrospray ionization mass spectrometry (ESI-MS) that provided suggestive, albeit not definitive evidence, that m = 2. Hence, the more general m-based formulation was reported previously, $\{[(1,5\text{-COD})Ir^{I}\bullet HPO_4]_m\}^{m-}$.[17,55,56] Noteworthy as cited in the 2004 study,[56] the O–O distance in HPO_4^{2-} is expected to be between ca. 2.5 Å, whereas a single Ir bound to a bidentate oxo ligand such as HPO_4^{2-} requires an O–O distance between 2.8 and 3.3 Å (depending on the Ir–O

distance).[56] Hence, an $m = 1$ bidentate phosphate-to-iridium *monomer complex is not physically possible*. The results obtained herein start by obtaining compelling support for a dimer, $m = 2$, formulation of **3** in solution, and, in turn, the use of the second-generation precursor **3** in addressing the six questions posed next.

Focus of Chapter III

At least six important questions remain en route to a better understanding of the nucleation of transition-metal and other nanoparticles:

(i) Is the recent result of low, ≤2–3, molecularity nucleation[13,14] an isolated finding or a more general result?

(ii) What is the effect, if any, on the molecularity of nucleation when starting with the novel dimeric A_2-type precatalyst system, $\{[(1,5\text{-COD})Ir^{I}\bullet HPO_4]_2\}^{2-}$, examined herein? Via what reaction order and then by what more detailed mechanism is nucleation achieved by such a previously unstudied A_2 complex?

(iii) Does the use of a precursor containing the $Ir^{I}(1,5\text{-COD})^{+}$ moiety as in $\{[(1,5\text{-COD})Ir^{I}\bullet\mathbf{HPO_4}]_2\}^{2-}$ automatically require and result in a termolecular, Ir_3-containing kinetically effective nucleus as found for the $\{(1,5\text{-COD})Ir^{I}\bullet\mathbf{POM}\}^{8-}$ system? Or, is the presence of 2 Ir in the bimetallic $\{[(1,5\text{-COD})Ir^{I}\bullet\mathbf{HPO_4}]_2\}^{2-}$ precursor sufficient to initiate nucleation? Putting this another way, is nucleation from the same $Ir^{I}(1,5\text{-COD})^{+}$ component changed by the presence of a $\mathbf{HPO_4^{2-}}$ vs $\mathbf{POM^{9-}}$ counter polyanion?

(iv) Is a dissociative equilibrium also operative for the dimeric $\{[(1,5\text{-COD})Ir^{I}\bullet\mathbf{HPO_4}]_2\}^{2-}$ precatalyst system, as seen for the $\{(1,5\text{-COD})Ir^{I}\bullet\mathbf{POM}\}^{8-}$ system? How, then, does the molecularity of nucleation and overall nucleation mechanism beginning with

{[(1,5-COD)Ir^{I}•**HPO_4**]$_2$}$^{2-}$ compare to the termolecular, Ir_3 mechanism uncovered recently when starting with the classic {(1,5-COD)Ir^{I}•**POM**}$^{8-}$ system?

(v) What other physical insights result about the preferred molecularity and the more intimate mechanism of nucleation?

(vi) Additionally and significantly, is the apparent paradigm shift[13,14] away from higher molecularity of nucleation, as postulated by Classical Nucleation Theory, further supported by demonstration of low, ≤2–3 molecularity nucleation for the case of the novel A_2 = {[(1,5-COD)Ir^{I}•**HPO_4**]$_2$}$^{2-}$ precursor? If so, then that is an important, potentially far-reaching physical insight and apparent paradigm shift away from CNT.

Herein, we report that starting from [(1,5-COD)$Ir^{I}$$(NCCH_3)_2$][$BF_4$], **1**, upon addition of HPO_4^{2-}, a neutral phosphate-bridged species, {[(1,5-COD)$Ir^{I}$$(NCCH_3)$]$_2$•$HPO_4$}^{0}, **2**, is formed en route to {[(1,5-COD)Ir^{I}•HPO_4]$_2$[Bu_4N]$_2$}, **3**, as a novel dimer for kinetic and mechanistic studies of nucleation to answer the six questions, (i)–(vi), listed above. By first demonstrating herein that **3** is a dimer, m = 2, we have been able to exploit what turn out to be *seven advantages* of {[(1,5-COD)Ir^{I}•**HPO_4**]$_2$}$^{2-}$ as a precise, molecularly well-defined, nanoparticle precursor, advantages listed in a footnote for the interested reader.[57] Important to note here is that establishment of the detailed kinetics and mechanism of nucleation, from a precisely defined precursor, is exceedingly rare,[14] even considering the importance of nucleation and hence the resultant wealth of studies broadly across nature attempting to understand nucleation at the molecular level.[1–8]

3.2. EXPERIMENTAL

Materials

All solvents and compounds used were stored in a drybox prior to use. Acetone (Aldrich, for high-performance liquid chromatography (HPLC), 99.9%) was sparged with argon for ≥10 min before use. Cyclohexene was distilled over Na metal and benzophenone, under argon and then stored in the drybox. Ethyl acetate (Aldrich, ≥99.8%, <0.05% H_2O), acetonitrile (Aldrich, 99.8%, anhydrous, H_2O content <0.001%), benzene (Aldrich, anhydrous, 99.8%, stored under inert atmosphere), dichloromethane (HPLC grade, stored over molecular sieves), and tributylamine (Acros Organics, 99%) were degassed prior to storage and use in the drybox. The following were brought into the drybox as received: $(Bu_4N)H_2PO_4$ (Aldrich, powder), $AgBF_4$ (Aldrich, white powder), diethyl ether (Aldrich, anhydrous, HPLC grade), Proton-Sponge (Aldrich, 99%), and $[(1,5\text{-COD})Ir^{I}Cl]_2$ (STREM, 99%), ferrocene (Aldrich Chemical Company, Inc.), Decane (Sigma Aldrich), $(Bu_3NH)_2(H_2P_2O_7)$ (Sigma-Aldrich), and $(Bu_4N)^+(BF_4)^-$ (Aldrich, 99%). Outside of the drybox, $Bu_4N^+OH^-$ (Aldrich, 40% by mass in H_2O) was stored between 8 and 10 °C in the refrigerator. Deuterated solvents were purchased from Cambridge Isotope Laboratories: chloroform-d_1 (99.8%), acetonitrile-d_3 (99.8%), and acetone-d_6 (99.5%). Argon (>99.9% purity) and H_2 (>99.5% purity) were purchased from Airgas. H_2 gas was passed through O_2- and H_2O-scavenging traps (Trigon Technologies) prior to use.

Analytical Procedures

Unless otherwise stated, all synthetic work and reaction solution preparation were conducted in an oxygen- and moisture-free Vacuum Atmospheres nitrogen drybox environment (<1 ppm O_2, as monitored by a Vacuum Atmospheres, continuous O_2-level monitor). All air-

sensitive samples were stored double bottled inside the drybox. All glassware was dried at ~160 °C for 2 days to remove residual moisture before being transferred immediately into the drybox antechamber where they cooled under the vacuum of the antechamber and then inside the drybox. NMR (^{1}H, ^{13}C, ^{19}F, and ^{31}P) experiments were collected on either a Varian Inova 400 MHz or a Bruker Neo 400 MHz spectrometers at ~25 °C. Transmission electron microscopy (TEM) experiments were examined on a JEOL JEM2100F Transmission Electron Microscope. UV-Visible spectra were collected on an Agilent (Cary) UV–Visible spectrophotometer. Gas–liquid chromatography (GLC) was conducted using a Hewlett-Packard 5890 series II GC with a flame ionization detector equipped with a 30 m (0.25 mm i.d., 25 μm film) Dowex DB-1 column and coupled to a Hewlett-Packard 3395 integrator. Electrospray ionization time-of-flight liquid chromatography–mass spectrometry (ESI TOF LC–MS) were conducted in both positive and negative modes on an Agilent 6220 TOF LC/MS interfaced to an Agilent 1200 HPLC with an electrospray source.

Preparation of the Precursor Iridium Solvate Complex, $[(1,5\text{-}C_8H_{12})Ir^{I}(NCCH_3)_2][BF_4]$

The synthesis was prepared based on literature methods with small modifications.[17,58] In a N_2-atmosphere drybox, 2.006 g (3.00 mmol) of $[(1,5\text{-COD})Ir^{I}Cl]_2$ was dissolved into 43 mL of CH_2Cl_2 in a 100 mL round-bottomed flask. The solution was dark red. After 5 min of stirring, 10 mL of CH_3CN was added to the solution. The solution turned yellow and was stirred for 10 minutes. An extended stirring time of ca. 5 min was necessary to dissolve solid residue on the sides of the flask. Next, 1.176 g (6.04 mmol) of $AgBF_4$ was added to the solution. A white-gray precipitate of AgCl appeared immediately upon addition of $AgBF_4$. The solution was stirred for 5 min to ensure reaction completion. The solution was vacuum-filtered through a Whatman #2 paper

to collect the white-gray precipitate. The yellow filtrate was slowly poured into ~200 mL of diethyl ether, which caused instantaneous precipitation of fine yellow crystals of [(1,5-C_8H_{12})$Ir^I(NCCH_3)_2$][BF_4]. The crystals were collected under vacuum on a 30 mL glass frit, washed with one aliquot of ~10 mL of ether, and left for 5 min to dry. The crystals were transferred to a 20 mL vial, placed in a small vacuum chamber, and dried for 9 h (1.91 g, 4.07 mmol, 68% yield, with additional syntheses producing 75% and 80% yields). The [(1,5-C_8H_{12})$Ir^I(NCCH_3)_2$][BF_4] product and its purity were confirmed by ^{1}H NMR peaks that matched literature spectral data.[58] Experimental values (400 MHz, CD_2Cl_2, 25 ºC): 1.79 (m, C*H*$_2$), 2.30 (m, C*H*$_2$), 2.52 (s, C*H*$_3$), 4.28 (s, br, C*H*), and 5.32 (s, solvent). Literature values (360 MHz, CD_2Cl_2, 22 ºC): 1.78 (m, C*H*$_2$), 2.29 (m, C*H*$_2$), 2.53 (s, C*H*$_3$), 4.27 (s, C*H*).[58]

Preparation of $(Bu_4N)_2HPO_4$

The preparation of $(Bu_4N)_2HPO_4$ was accomplished by a literature method with modification to the critical water removal/drying step.[17] First, 254.8 mg (0.75 mmol) of $(Bu_4N)H_2PO_4$ were dissolved in 4 mL of CH_3CN. After stirring for 5 min, 0.50 mL $Bu_4N^+OH^-$ (40% by mass in water) was added dropwise over 15 s. The clear solution was stirred for 4.0 h and then placed under vacuum (~125 mmHg), in a small vacuum chamber within the drybox, at ~30 °C (temperature of drybox environment) to remove CH_3CN and H_2O. After 8–12 h, the vial was removed from the vacuum chamber to scrape the sides and break up large aggregates before being placed back under vacuum for an additional 12–24 h. The identity of the $(Bu_4N)_2HPO_4$ product was confirmed using ^{1}H, ^{13}C, and ^{31}P NMR in acetonitrile-*d*$_3$. These peak assignments can be found in the Appendix II. The purity was ≥92–97% for all samples used as part of this work as judged by both ^{1}H and ^{31}P NMR.

A minor, always ≤3–8% impurity of the Bu_4N^+ salt of pyrophosphate, $(Bu_4N)_4(P_2O_7)$, results from the well-precedented dehydration reaction,[59,60,61,62] 2 HPO_4^{2-} → $\{O_3P–O–PO_3)^{4-}$ + H_2O, under the conditions specified in the $(Bu_4N)_2HPO_4$ preparation section directly above. The precise, ≤3–8% amount of $(Bu_4N)_4(P_2O_7)$ is dependent on the drying method and especially the time and temperature under vacuum. The $(Bu_4N)_4(P_2O_7)$ was detected by ^{31}P NMR (and ^1H NMR at δ = 0.90 ppm): (^{31}P: 162 MHz, CD_3CN, 25 ºC) δ: -8.73 (s, $P_2O_7^{4-}$) and 2.34 (s, HPO_4^{2-}) ppm; (^1H: 400 MHz, CD_3CN, 25 ºC) δ: 0.90 (t, C*H*$_3$), 0.98 (t, C*H*$_3$), 1.33 (m, C*H*$_2$), 1.38 (m, C*H*$_2$), 1.62 (m, C*H*$_2$), 1.95 (br, solvent), 2.35 (t, C*H*$_2$), and 3.15 (t, C*H*$_2$) ppm. Spectra and additional discussion are provided in Appendix II.

Control experiments (summarized in Appendix II) were performed in which the $(Bu_4N)_2HPO_4$ was excessively dried to force the formation of deliberately enhanced amounts of $(Bu_4N)_4(P_2O_7)$. Nucleation and growth kinetics studies using the catalytic reporter reaction were run using $(Bu_4N)_2HPO_4$ that contained 10, 15, and 19.5% of $(Bu_4N)_4(P_2O_7)$. Those control experiments demonstrate that the low, ≤3–8% levels of $(Bu_4N)_4(P_2O_7)$ present by ^{31}P NMR in the as-prepared $(Bu_4N)_2HPO_4$ ligand and nanoparticle stabilizer do not affect the reaction kinetics within experimental error as judged by k_1 rate constants being equivalent within experimental error across the series of a nearly 2-fold increase in the amount of $(Bu_4N)_4(P_2O_7)$.

Initial Investigation of the Solution Speciation of $\{[(1,5\text{-COD})Ir^I•HPO_4][Bu_4N]\}_m$ Using UV–Visible Spectroscopy

Solutions for UV–visible spectroscopy experiments were prepared in the drybox from stock solutions of $[(1,5\text{-COD})Ir^I(NCCH_3)_2][BF_4]$ and $(Bu_4N)_2HPO_4$ in acetone. Precise amounts of these stock solutions were measured and transferred to a new, clean 1 dram vial via disposable 1.0 mL

syringes. Acetone was used to raise the total volume of the sample to 2.0 mL. Samples were prepared and measured at 0.0, 0.1, 0.2, 0.3, 0.4, 0.5, 0.6, 0.7, 0.8, and 0.9 molar equiv of $(Bu_4N)_2HPO_4$ vs equivalents of Ir. Samples were transferred from the 1 dram vial to an airtight cuvette via a disposable polyethylene pipette. The cuvette was transferred out of the drybox and immediately taken to the UV-visible spectrophotometer for measurement. The background spectrum was collected using just acetone. Results from this experiment can be found in the first figure in the Results and Discussion.

Two ^{1}H NMR Spectroscopy Titrations of $[(1,5\text{-COD})Ir^I(NCCH_3)_2][BF_4]$ with $(Bu_4N)_2HPO_4$: Evidence of Formation of a 1:1, $\{[(1,5\text{-COD})Ir^I{\bullet}HPO_4]_m\}^{m-}$ Complex

A 1.0 mM iridium stock solution of 6.1 mg of $[(1,5\text{-COD})Ir^I(NCCH_3)_2][BF_4]$ in 13 mL acetone-d_6 was prepared. A separate, more concentrated, stock solution of $(Bu_4N)_2HPO_4$ was prepared so that 5 μL would be equal to 0.1 molar equiv of $(Bu_4N)_2HPO_4$. Samples of 0.4 mL of the iridium stock solution were combined with the appropriate number of 5 μL aliquots of $(Bu_4N)_2HPO_4$ stock solution to yield samples containing 0.0, 0.2, 0.4, 0.5, 0.6, 0.7, 0.9, 1.1, 1.4, and 1.8 molar equiv of $(Bu_4N)_2HPO_4$. Each sample was prepared from the stock solutions in the N_2 drybox environment, sealed with a septum top, and then removed from the drybox for immediate measurement by ^{1}H NMR. The distinct signals at δ 1.01 (t, CH_3), 1.47 (m, CH_2), 1.86 (m, CH_2) and 3.49 (t, CH_2) ppm characteristic of tetrabutylammonium were integrated. The broad signals at 3.7 (br, C*H*), 4.0 (br, C*H*), and 4.3 (br, C*H*) were integrated and assigned to the vinyl protons on the cycloocta-1,5-diene of the iridium precursor[58], $[(1,5\text{-COD})Ir^I(NCCH_3)_2][BF_4]$. The vinyl proton integration was converted into a total percentage of iridium in three forms: precursor, **1**, $[(1,5\text{-COD})Ir^I(NCCH_3)_2][BF_4]$ (δ = 4.3 ppm), bridged, **2**, (δ = 4.0 ppm; see the bridged complex

in the scheme presented in the Results and Discussion), and dimer, **3**, (δ = 3.7 ppm). A plot of the data is provided in the Results and Discussion section.

A ^{1}H NMR titration study was also conducted, in the exact same manner as stated directly above but with the following modifications to cover in greater detail the narrower range of 0.0, 0.1, 0.2, 0.3, 0.4, 0.5, 0.6, 0.7, 1.0, and 1.3 molar equiv of $(Bu_4N)_2HPO_4$. Only the signal at 4.3 ppm (indicative of the vinyl protons of the cycloocta-1,5-diene bound to Ir) was integrated, then converted to concentration of **1** and analyzed. The resulting Figure S3.4 can be found in Appendix II.

Signer Solution Molecular-Weight Apparatus

A Signer MW apparatus was constructed in-house based on the specifications given in the original publication from 1941 by Clark;[63] an image of the apparatus is provided in Figure S3.5, Supporting Information. The apparatus was cleaned with water and acetone and dried an oven at ~165 °C for ≥2 days. Ferrocene was used as the nonvolatile reference compound because it is a nonelectrolyte and is soluble in the solvent of interest, acetone. Each solution was prepared in acetone using volumetric glassware. For ferrocene, 2.6 mg was dissolved into 2.0 mL of acetone to achieve a 6.99 mM solution. Next, 6.2 mg of $[(1,5\text{-COD})Ir^{I}(NCCH_3)_2][BF_4]$, **1**, and 7.6 mg of $(Bu_4N)_2HPO_4$ were added into 2.0 mL of acetone to achieve 6.6 mM of each. To one bulb of the Signer apparatus, 0.5 mL of the solution of **1** of unknown MW was added; then, 0.5 mL of the standard reference compound (ferrocene) solution was added to the other bulb. The apparatus was placed horizontally, with the bridge up to ensure the two solutions did not mix for 10 days to allow the system's vapor pressure to equilibrate (see Appendix II for a picture of the Signer apparatus). Every 2–3 days, the apparatus was turned vertical and the volume changes of each side of the

Signer apparatus were measured. Once equilibration was reached, the ending volumes for each solution were used in eq 3.2 to calculate the unknown's (*X*'s, eq 3.2) solution molecular weight. Equation 3.2 is derived from Raoult's Law, as detailed elsewhere[63], in which "stnd" is the known MW standard chosen, in our case, ferrocene.

$$MW(\boldsymbol{X}) = \frac{mass(\boldsymbol{X}) \times MW(stnd) \times volume(stnd)}{mass(stnd) \times volume(\boldsymbol{X})} \quad \text{(Eq 3.2)}$$

Electrospray Ionization Time-of-Flight Liquid Chromatography–Mass Spectrometry Experiments on 1 Formed in Situ

Preparation of **1** *in situ* was carried out in the drybox by adding equal molar amounts of 6.0 mM [(1,5-COD)$Ir^{I}(NCCH_3)_2$][BF_4] (2.8 mg) and $(Bu_4N)_2HPO_4$ (3.7 mg) by weighing these out in a 1 dram glass vial and then adding 1.0 mL acetone. The vial was septum-capped to ensure air-free transfer of the sample, which was accomplished by a gas-tight syringe. Both positive and negative electrospray ionization time-of-flight liquid chromatography–mass spectrometry (TOF ESI LC–MS) were obtained within an hour of preparation of the sample. A control experiment showed that **1** is readily soluble in the mobile phase employed, MeOH. Analysis of the mass spectrum was conducted with the aid of Agilent's LC/MS Chemstation Software. Detailed results are available in Table S3.1 in Appendix II.

Standard Conditions for $Ir(0)_n$ Nanoparticle Formation Kinetics Experiments with Concomitant Cyclohexene Hydrogenation Serving as the Reporter Reaction

All nanoparticle formation and hydrogenation reactions were carried out using a custom-built pressurized hydrogenation apparatus using a Fischer-Porter (F–P) pressure bottle.[15]

Nanoparticle formation was monitored indirectly but in real time by the well-precedented cyclohexene hydrogenation catalytic reporter reaction[15,16,18,35,64] shown in Scheme S3.2 in Appendix II. Precatalyst solutions of $[(1,5\text{-COD})Ir^{I}(NCCH_3)_2][BF_4]$ plus $(Bu_4N)_2HPO_4$ were prepared in a drybox, where the required amount of $[(1,5\text{-COD})Ir^{I}(NCCH_3)_2][BF_4]$ (10.8 μmol for a 3.6 mM solution) was weighed in a disposable 1 dram glass vial along with 1.0 molar equiv of Proton-Sponge (1,8-bis(dimethylamino)naphthalene) and 1.8, 2.7, 3.6, 4.5, or 5.4 molar equiv of $(Bu_4N)_2HPO_4$. The solids were dissolved in 2.5 mL of acetone (added via a 5.0 mL gas-tight syringe). Using a 1.0 mL gas-tight syringe, 0.5 mL of cyclohexene was then added to the solution. The faint, air-sensitive yellow solution was transferred while still in the drybox to a new, 22 x 175 mm Pyrex culture tube containing a new 5/16 x 5/8 in. Teflon-coated stir bar via a disposable polyethylene pipette. The culture tube with the solution of $[(1,5\text{-COD})Ir^{I}(NCCH_3)_2][BF_4]$ and $(Bu_4N)_2HPO_4$ were placed in a F–P bottle modified with Swagelock poly(tetrafluoroethylene)-sealed Quick-Connects, sealed, transferred out of the drybox, and attached with the Quick-Connects of the hydrogenation line and its computer-interfaced Omega PX621 pressure transducer. The F–P bottle was placed in a 500 mL jacketed reaction flask containing dimethyl silicon fluid (Thomas Scientific) that was held at 22 °C by a thermostatic recirculating water bath (VWR). Prior to attachment, the hydrogenation line was kept under vacuum. After attachment, the hydrogenation line was filled with H_2 gas at ~40 psig. Quick purges were performed every 15 s for 3.5 min (14 purges). Following the purge, the F–P bottle was pressurized to ~40 psig H_2 over 30 s before stirring (~900 rpm) was initiated (all as before)[15,50,64,65,66] and pressure uptake data (measurements every minute) were collected using LabView 8.2.[15] Hydrogenation reactions were obtained by monitoring the loss of H_2 pressure versus time (6–18 h depending on the concentration of iridium and how many equivalents of $(Bu_4N)_2HPO_4$ were present). As before, a correction[67] for

the initial vapor pressure of acetone was applied to the data. This correction was determined by collecting pressure versus time data for 24 h on a sample of 2.5 mL acetone and 0.5 mL cyclohexene to determine the background pressure considerations of the solvent vapor pressure over the course of the hydrogenation reaction time.[67] The H_2 loss data was converted to cyclohexene loss as before[15] and using the known, 1:1 H_2 to cyclohexene hydrogenation reaction stoichiometry. The resultant data were then processed using Microsoft Excel, Origin 7, and COPASI.[13,68] Specifically, rate constants (k_{1obs} and k_{2obs}) were extracted by fitting the cyclohexene consumption data to the integrated rate equation, eq S3.10, for the FW 2-step mechanism by nonlinear least-squares fitting using Origin 7 while using just the first half of the cyclohexene consumption data (to ensure that the assumptions underlying the reporter-reaction method remain valid[15]). The curve-fit values for k_{2obs} were corrected by the [cyclohexene]/[Ir] ratio as the mathematics of the reporter reaction require (see elsewhere for details).[15]

Control Experiment Testing for the Impact of Laboratory Dust on the Nucleation Kinetics

Control experiments to account for the effects of dust were carried out following the previously described (*vide supra*) experimental process to remove dust, an experimental protocol that follows our 2017 work[50] but with a few modifications to adapt it to the present system. Specifically, all solvent (acetone) was passed through a 0.20 μm syringe filter from Scientific Strategies. The 22 x 175 mm Pyrex culture tube was then rinsed with ~2 mL of filter solvent, which was subsequently discarded. Next, after the precatalyst and $(Bu_4N)_2HPO_4$ had been dissolved completely into 2.55 mL of prefiltered acetone, the reaction solution was filtered through a new 0.20 μm filter and added to the filtered-solvent-rinsed culture tube. An approximate end volume of 3.0 mL, as used in all the standard kinetics studies already described, was achieved by adding

0.55 mL of cyclohexene to the 2.55 mL of acetone employed, which brought the total initial volume to 3.10 mL. Due to the additional filter steps and inherent loss of solvent to the filter and evaporation, the final resultant volume was the desired, ~3.0 mL. Duplicated measurements of $[(1,5\text{-COD})Ir^{I}(NCCH_3)_2][BF_4]$ at 3.6, 6.0, and 9.6 mM with 5.4 molar equiv of $(Bu_4N)_2HPO_4$ were carried out, and then compared to the rate constants from the same unfiltered experiments, the results of which are summarized in Figures S3.7 and S3.8, Appendix II.

Cyclooctane (COA) Evolution Kinetics and Confirmation of the $[(1,5\text{-COD})Ir^{I}(NCCH_3)][BF_4]$ Conversion Stoichiometry by Gas–Liquid Chromatography

The procedure employed is similar to previous publications.[15,66] Specifically, samples of $[(1,5\text{-COD})Ir^{I}(NCCH_3)][BF_4]$ plus $(Bu_4N)_2HPO_4$ with 1 molar equiv of Proton-Sponge were prepared in a drybox as detailed in the section above entitled "*Standard Conditions for Ir(0)$_n$ Nanoparticle Formation Kinetics Experiments with Concomitant Cyclohexene Hydrogenation Serving as the Reporter Reaction*". Prior to transfer of the reaction solution from the 1 dram vial to the new culture tube, 3 μL of decane (as an internal standard) were added to the solution. The solution was thoroughly mixed, transferred into the culture tube, and a standard conditions hydrogenation experiment was carried out. At specific, predetermined times during the hydrogenation, the stirring was stopped, the H_2 pressure was released from the F–P bottle (while keeping a positive H_2 pressure of ≥10 psig), and an aliquot (≤0.05 mL) was taken for gas–liquid chromatography (GLC) using a 9 in. needle attached to a gas-tight syringe. Before extracting the aliquot, the needle was rinsed 10 times with acetone and dried using compressed air. After extraction of the aliquot, the F–P bottle was resealed, purged five times in 5 s intervals, allowed to repressurize for 25 s (to reach 40 psig), and then stirring resumed was at ~900 rpm.

The amount of cyclooctane (COA) evolved over time was determined by analyzing the relative peak area of COA vs the relative peak area of the decane internal standard. A calibration curve of known amounts of authentic COA and decane was obtained and then used to determine the equivalents of COA evolved versus the total, initial iridium in the sample. The equivalents of COA were divided by the equivalents of initial iridium vs time values, and then, each were multiplied by the initial $[Ir]_0$ concentration to yield $[COA]_t$ values, plotted versus time. The data were then fit using the same analytic function corresponding to the FW 2-step mechanism of slow, continuous nucleation and autocatalytic surface growth, eq S3.10.

Time-Resolved ^{1}H NMR and GLC Cyclooctane Product Quantification

Reaction solutions were prepared as previously stated in the section directly above. At predetermined times during the reaction, the F–P bottle was sealed, removed from the hydrogenation line, and returned to the drybox. Therein, the H_2 pressure was released and a 1.0 mL aliquot collected, placed in a 1 dram vial, and 1 μL of decane (internal standard) was added prior to GC analysis. This sample was capped, removed from the drybox, and analyzed by GC via the protocol described directly above.

For ^{1}H NMR sample preparation, a 0.1 mL aliquot of the original reaction solution that had been transferred back into the drybox was placed in a standard 5 mm o.d. NMR tube and diluted with 0.9 mL of acetone-d_6 to yield a final volume of 1.0 mL. A 10 μL aliquot of benzene was added as an internal standard. The sample tube was sealed with a septum top, removed from the drybox, and a ^{1}H spectrum was obtained on a 400 MHz NMR spectrometer. Spectra were analyzed using the program TopSpin 3.5pl7 for Mac OS X. The primary reference peak was tetramethylsilane (TMS) that came in the acetone-d_6 (0.05% v/v TMS). The analysis and

integration relative to the benzene internal standard focused on the peaks characteristic of the cyloocta-1,5-diene bound to iridium (δ = 4.3, 4.0, and 3.7 ppm, for **1**, **2**, and **3**, respectively) and the hydrogenated product, cyclooctane (δ = 1.4 ppm). The concentration of cyclooctane versus time data was analyzed using the FW 2-step mechanism to determine nucleation and growth rate constants and compared to the rate constants collected by GLC analysis. The results are given in Figure S3.9 of Appendix II.

Transmission Electron Microscopy Grid Preparation and Average Particle Size Determination

The solutions used in the following transmission electron microscopy experiments were prepared using the same procedures described above for standard condition nanoparticle formation and concomitant cyclohexene hydrogenation experiments. All solutions for TEM were prepared with 6.0 mM in Ir and 5.4 molar equiv of $(Bu_4N)_2HPO_4$. These specific excess $(Bu_4N)_2HPO_4$ conditions produced readily reproducible kinetics results and, hence, were used for analysis by TEM. To collect TEM samples, the hydrogenation reaction was stopped at predetermined times by stopping the stirring and releasing the H_2 pressure down to ~5 psig to maintain a small positive pressure, quickly resealing the F–P bottle, disconnecting it from the hydrogenation line via its Quick-Connects, and then bringing the F–P bottle back into the drybox. In the drybox, the remaining H_2 pressure was released from the F–P bottle and the solution was transferred into a new and clean 20 mL scintillation vial. A small, ≤0.5 mL amount of the solution was transferred to a new 20 mL scintillation vial and diluted 20-fold by 2-butanone. The use of the 2-butanone and 1:20 dilution prevents aggregation of the nanoparticles on the grids, ostensibly because butanone has a higher boiling point and lower volatility than acetone, so that evaporation of the 1:20 solvent

mixture from the surface of the grid is slower and resulted in usable micrographs without noticeable aggregation of particles (whereas using just acetone gave clumped, aggregated nanoparticles that could not be readily analyzed for their size distribution by TEM). Silicon nitride grids were used and prepared by placing a 1.0 μL aliquot of the 1:20 solution on the grid via a micropipette and allowing excess liquid to evaporate. The grids were fully dried in the drybox environment at ~30 °C for a minimum of 2 h prior to being analyzed by TEM. Controls showed that Cu/C TEM grids could not be used with scanning TEM (STEM), at least on our instrument, because contamination from the organic coating on the Cu–C grids resulted in obscured TEM images.

Micrographs of dark-field scanning TEM (STEM) were collected at three or more locations on the TEM grid to ensure each given micrograph was representative of the entire sample. For each sample, ≥200 particles were measured for their size (with some samples having up to 1000 particles measured) because measuring ≥200 particles proved necessary to obtain a reproducible average size. The open source software ImageJ, a National Institutes of Health sponsored image processing platform (http://rsbweb.nih.gov/ij/), was used as previously detailed.[69]

3.3. RESULTS AND DISCUSSION

Evidence for the Solution Speciation of $[(1,5\text{-COD})Ir^{I}(NCCH_3)_2][BF_4]$ Titrated with $(Bu_4N)_2HPO_4$

Three different techniques were employed to study the solution speciation as a function of the $HPO_4^{2-}/Ir^{I}(1,5\text{-COD})^{+}$ ratio: initially UV–visible spectroscopy, then ^{1}H NMR spectroscopy, and importantly a Signer apparatus solution molecular weight (MW) determination in acetone. The combined results establish $m = 2$ for the 1:1 complex, $\{[(1,5\text{-COD})Ir^{I}\bullet HPO_4]_m\}^{m-}$, that is for {[(1,5-

COD)Ir^{I}•HPO_4]$_2$}$^{2-}$, complex **3**, as detailed in what follows.

Initial Investigation of the Solution Speciation by UV-visible Spectroscopy

An initial probe of the solution speciation of [(1,5-COD)$Ir^{I}(NCCH_3)_2$][BF_4], **1**, titrated first with 0–0.5 equiv $(Bu_4N)_2HPO_4$ per equivalent of Ir, and then with 0–0.9 equiv of $(Bu_4N)_2HPO_4$ per equivalent of Ir, all in acetone, is shown in Figures 3.1a and 3.1b, respectively. Clear changes are observed at 346, 376, and 408 nm, indicating the documented complexation of HPO_4^{2-} to the Ir^{I}(1,5-COD)$^+$ moiety.[56] The lack of clean isosbestic points in either Figure 3.1a or Figure 3.1b implies a mixture of ≥3 species is present.

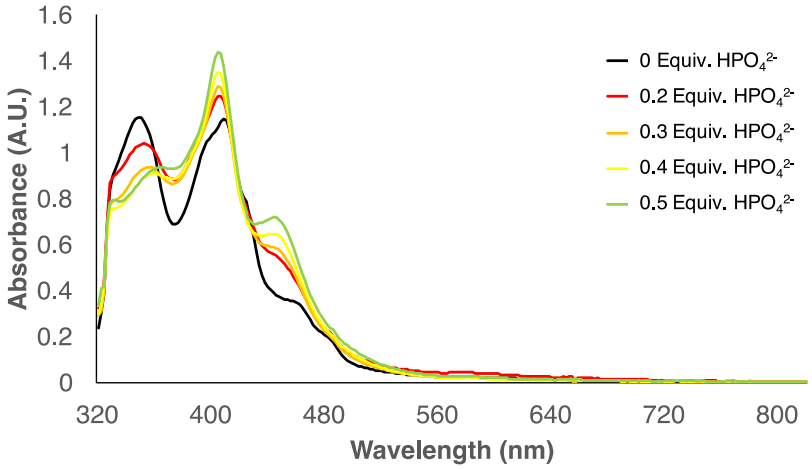

(a)

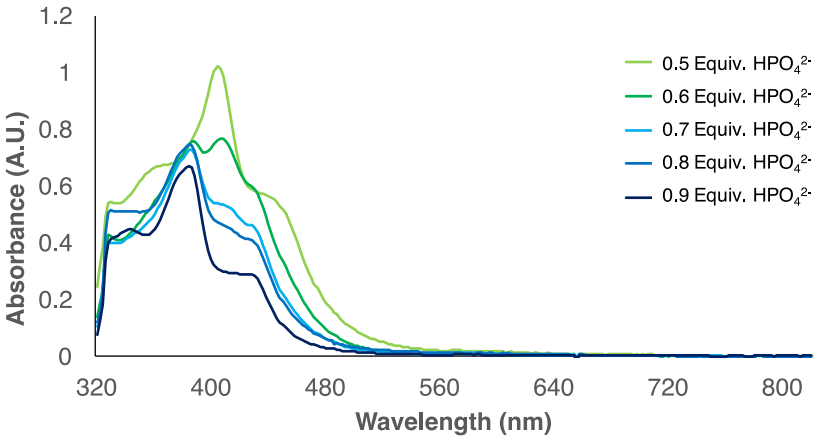

(b)

Figure 3.1. (a) UV–visible spectra of mixtures of 1.0 mM [(1,5-COD)$Ir^{I}(NCCH_3)_2$][BF_4], **1**, titrated with 0.0–0.5 molar equiv of added $(Bu_4N)_2HPO_4$. **(b)** UV–visible spectra of mixtures of 0.5 mM [(1,5-COD)$Ir^{I}(NCCH_3)_2$][BF_4] titrated with 0.5–0.9 molar equiv of added $(Bu_4N)_2HPO_4$. Primary changes to the spectra are observed at 346, 376, and 408 nm, but no clean isosbestic points are observed consistent with the presence of ≥3 distinct species. The small differences between the spectra top (a) and bottom (b) spectra at 0.5 added molar equiv of $(Bu_4N)_2HPO_4$ can be attributed to 1.0 vs 0.5 mM concentration difference in the two experiments.

Investigation of the Solution Speciation via ^{1}H NMR Spectroscopy

Two ^{1}H NMR-monitored titrations were conducted using 1.0 mM [(1,5-COD)$Ir^{I}(NCCH_3)_2$][BF_4], with added molar equivalents of $(Bu_4N)_2HPO_4$ ranging from 0.0 to 1.8. The first titration monitored only the loss of [(1,5-COD)$Ir^{I}(NCCH_3)_2$][BF_4], **1**, whereas the second, more detailed titration monitored the loss of **1**, the appearance and subsequent loss of [(1,5-COD)$Ir^{I}(NCCH_3)$]$_2$[HPO_4], **2**, and the appearance of {[(1,5-COD)Ir^{I}•HPO_4][Bu_4N]}$_2$, **3**. The first titration can be found in Figure S3.4 (Appendix II), whereas the second, more in-depth titration is shown in Figure 3.2. A close inspection of the ^{1}H NMR reveals that the vinyl protons of the cycloocta-1,5-diene bound to iridium produces *three distinct signals*, as seen in Figure S3.3a–c in Appendix II. Upon integration of those signals versus the benzene internal standard, the percentage of each iridium species was determined at each of the 0.0–1.8 equiv increasing ratios of added $(Bu_4N)_2HPO_4$. The deduced solution speciation is shown in Scheme 3.1, whereas Figure 3.2

illustrates the relative percentages of each of the three species provided by the integration of their respective cycloocta-1,5-diene vinylic protons.

Scheme 3.1. Formation of a 1:2 $HPO_4^{2-}/Ir^I(1,5\text{-COD})^+$ Intermediate, **2**, and Then the Final 1:1 Diphosphate-Bridged Complex, **3**, Supported by the ^1H NMR Titration Studies

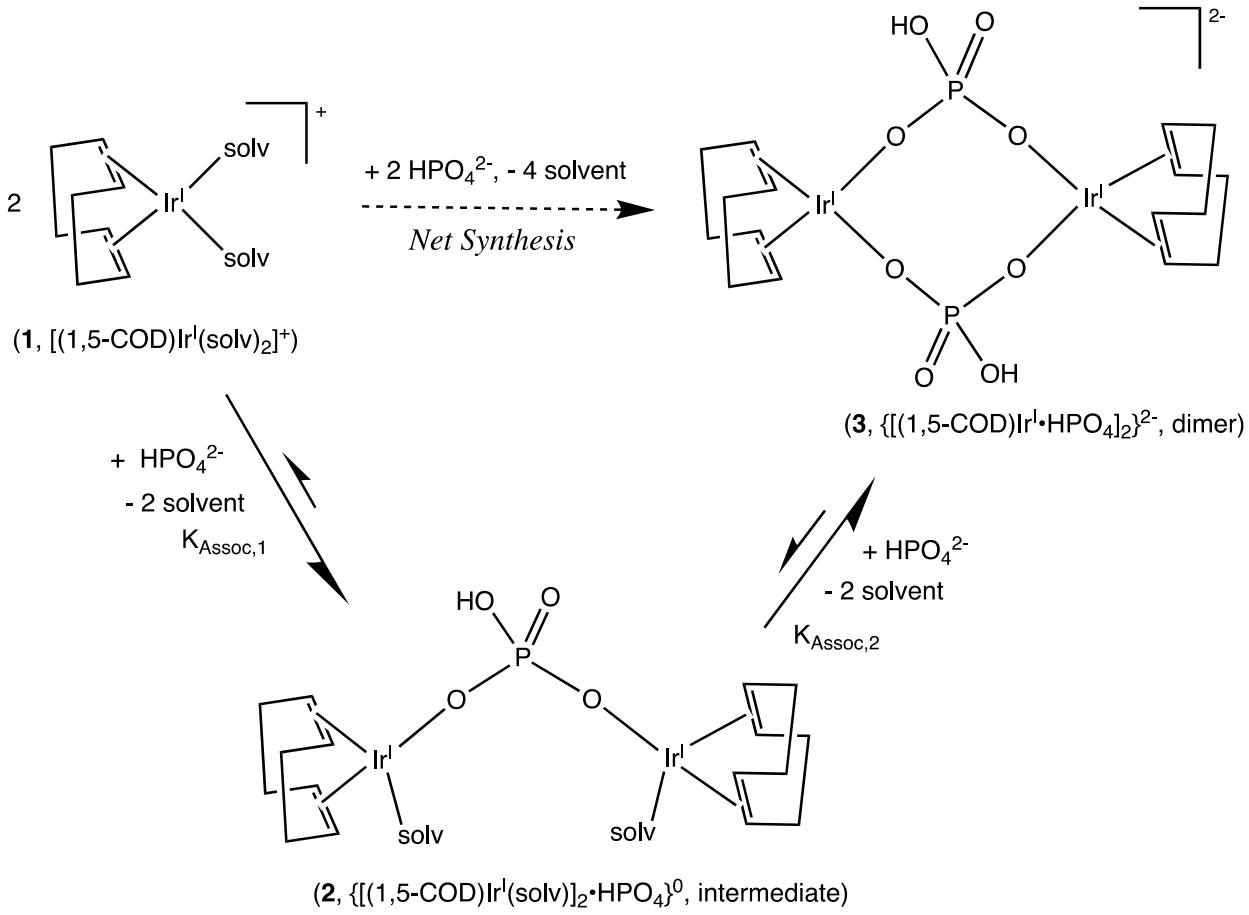

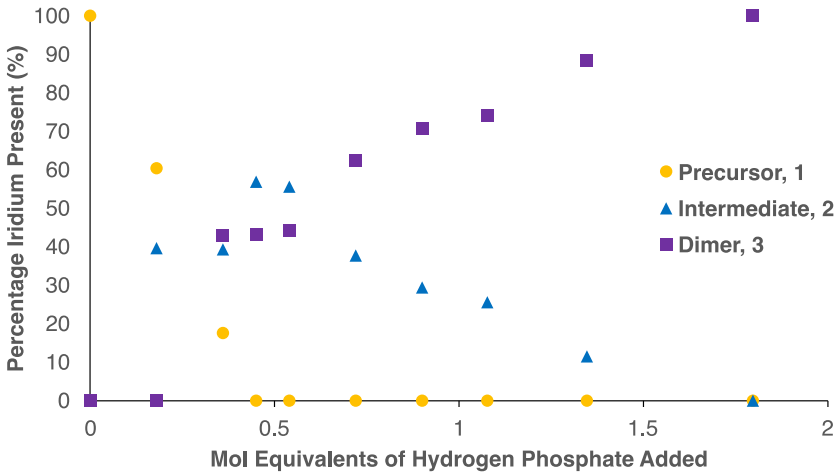

Figure 3.2. Results of the ^{1}H NMR titration of 1.0 mM [(1,5-COD)Ir^{I}(NCCH$_3$)$_2$][BF$_4$], **1**, with added molar equivalents of (Bu$_4$N)$_2$HPO$_4$ from 0.0 to 1.8 molar equiv in acetone-d_6. The vinyl protons of the solvate complex [(1,5-COD)Ir^{I}(NCCH$_3$)$_2$]$^{+}$, **1**, appear at 4.3 ppm; the vinyl protons for the neutral bridged species, {[(1,5-COD)Ir^{I}(NCCH$_3$)]$_2$•HPO$_4$}^{0}, **2**, appear at ~4.0 ppm, whereas the vinyl protons for the dicationic 1:1 complex, {[(1,5-COD)Ir^{I}•HPO$_4$][Bu$_4$N]}$_2$, **3**, appear at ~3.7 ppm. Rough, semiquantitative estimates can be made of $K_{Assoc,1} \approx 10^3$–10^4 M^{-1} and $K_{Assoc,2} > 10^2$ M^{-1}, Scheme 3.1, as detailed in Appendix II for the interested reader. Representative NMR are also provided in Appendix II as Figure S3.3a–c.

Important to start with in Figure 3.2 is that the precursor **1** loss (yellow circles) shows a linear decrease until zero is reached at ~0.5 equiv of (Bu$_4$N)$_2$HPO$_4$ per equivalent of (1,5-COD)Ir^{I}(NCCH$_3$)$_2$)$^{+}$, that is, at a 1:2 ratio consistent with the formulation of **2** as {[(1,5-COD)Ir^{I}(NCCH$_3$)]$_2$•HPO$_4$}^{0}. Next, the loss of **2** (blue triangles) is apparent with the growth of what is formulated as the 1:1 complex, **3** (purple squares). Note also that little **3** is formed until one is past the ca. 0.5 equiv of (Bu$_4$N)$_2$HPO$_4$ per equivalent of [(1,5-COD)Ir^{I}(NCCH$_3$)$_2$]$^{+}$ point in Figure 2. Scheme 3.1 is drawn with the 1:2 complex, **2**, being on path to the final 1:1 complex, **3**, an interpretation that will supported by kinetics studies as a function the [HPO$_4^{2-}$] concentration provided in a subsequent section. But first, evidence is provided in the next section supporting the dimeric form of **3** in acetone via a solution molecular weight measurement.

Signer Apparatus Solution Molecular Weight Evidence That 3 is a Dimer in Acetone

Because our prior studies by four mass spectrometry methods (ESI-MS, fast atom bombardment mass spectrometry, matrix-assisted laser desorption ionization-time-of-flight, and electron ionization mass spectrometry) yielded only suggestive, albeit not definitive, evidence at the time for the aggregation state and hence molecular weight (MW) of **3** as a dimer[56] and because what we really need is *the solution speciation* of the resting form of the complex, **3**, *in acetone* where the kinetics will be obtained, a Signer MW apparatus was used to determine the average solution molecular weight of **3** *in acetone*.[63] The Signer MW apparatus employs the colligative properties of the solute at a constant temperature to determine the solution MW of an unknown complex via a known MW standard (in this case ferrocene[70]), all via eq 3.2a based on Raoult's Law.[71] The Signer, colligative properties MW method is a number-average method; that is, it yields a number-averaged molecular weight of all the solute species in solution, as seen in eq 3.3. In eq 3.3, MW_{Observed} is the observed molecular weight calculated from the Signer whereas the denominator is the sum of the average molecular weights of all the species present in the solution multiplied by α, a weighting factor to account for the percentage of the given species in solution (see Appendix II for details).

$$MW(\mathbf{3}) = \frac{mass(\mathbf{3}) \times MW(stnd) \times volume(stnd)}{mass(stnd) \times volume(\mathbf{3})} \qquad \text{(Eq 3.2a)}$$

$$m = \frac{MW_{Observed}}{\sum_i \alpha_i \times MW_{avg,i}} \qquad \text{(Eq 3.3)}$$

Using the Signer MW apparatus for a 1:1, $\{[(1,5\text{-COD})Ir^{I}\bullet HPO_4]_m\}^{m-}$ complex at 6.6 mM as the unknown, an apparent solution molecular weight of *1070 g/mol* was obtained using eq 3.2a

(full details of that determination are provided in Appendix II). This compares to (i) a nominal combined MW of 1278 g/mol for the intact dimer, $\{[(1,5\text{-COD})Ir^{I}\bullet HPO_4][Bu_4N]\}_2$, plus two $[Bu_4N^+][BF_4^-]$ produced as a result of its *in situ* preparation, and with the assumption of tight-ion pairing between the anion and Bu_4N^+ cations in both $\{[(1,5\text{-COD})Ir^{I}\bullet HPO_4][Bu_4N]\}_2$ and two $[Bu_4N^+][BF_4^-]$. The Signer MW results were further analyzed via eq 3.3 at the other limit of no ion-pairing (thereby giving the maximum possible number of species in solution). Importantly, *no matter what model of the solution speciation that was used, an m value between m = 1.8 to 2.3 resulted*, fully consistent with and supportive of a $m = 2$ formulation of $\{[(1,5\text{-COD})Ir^{I}\bullet HPO_4]_2\}^{2-}$, **3**, in acetone solution where the kinetics will be performed, *vide infra*. Significantly, then, the dimer, $\{[(1,5\text{-COD})Ir^{I}\bullet HPO_4]_2\}^{2-}$, **3**, is established as the dominant resting species in acetone solution at 22 °C.

The ^1H NMR titration back in Figure 3.2 also establishes that **3** can be in a dissociative equilibrium with HPO_4^{2-} and the bridged intermediate, $\{[(1,5\text{-COD})Ir^{I}(NCCH_3)]_2\bullet HPO_4\}^0$, **2**, Scheme 3.1, *vide supra*. Hence, kinetics studies of nucleation beginning with **3** and armed with the knowledge that **2** is a potential intermediate in the nucleation process, were performed next.

Kinetics Studies of Nucleation of $Ir(0)_n$ Nanoparticles

The kinetics or $Ir(0)_n$ nanoparticle formation were studied next at between 1.8 and 5.4 molar equiv of $(Bu_4N)_2HPO_4$ versus $[(1,5\text{-COD})Ir^{I}(NCCH_3)_2][BF_4]$, **1**, that is, under conditions where we have established that the dimer, $\{[(1,5\text{-COD})Ir^{I}\bullet HPO_4]_2\}^{2-}$, **3**, is the predominant resting form. The first main objective of the kinetics studies is to establish unequivocally the molecularity of nucleation when starting from a *bimetallic* Ir_2 precursor; is the nucleation first, three-halves, second, or higher order n in **3**, implying an Ir_2, Ir_3, Ir_4, or Ir_{2n} molecularity of nucleation?

A typical cyclohexene hydrogenation reporter-reaction monitoring of the formation of $Ir(0)_n$ nanoparticles is shown in Figure 3.3, along with the curve-fit to the FW 2-step mechanism of slow, continuous nucleation (rate constant k_1) and autocatalytic surface growth (rate constant k_2).

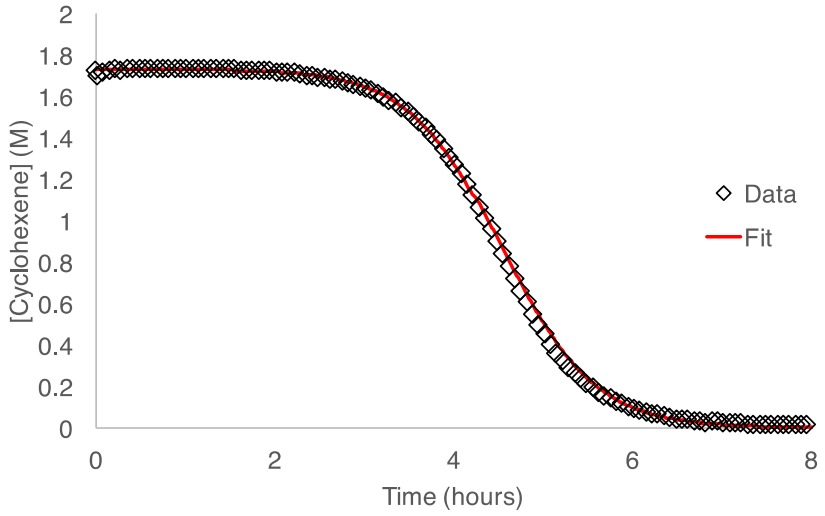

Figure 3.3. Representative, reproducible sigmoidal kinetics for *in situ* prepared $\{[(COD)Ir^{I}\bullet HPO_4][Bu_4N]\}_2$, **1**, with 5.4 molar equiv of added $(Bu_4N)_2HPO_4$ and 1 mol equivalent of Proton-Sponge per Ir present in acetone under an initial 40 psig H_2 and at [Ir] = 6.0 mM. The catalytic reporter reaction[13,14,15] (Scheme S3.2 of Appendix II) used 1.65 M cyclohexene. Shown is every fourth data point and the curve-fit of the data to the FW 2-step mechanism.[15]

Evidence that Nucleation is First Order in the Dimer, $\{[(1,5\text{-}COD)Ir^{I}\bullet HPO_4][Bu_4N]\}_2$, 3, and Hence Net Bimoleculear with a Kinetically Effective Nucleus of 2, Ir_2

Figure 4 shows the key result of searching for a higher, beyond first-order dependence in [A], where A is the precursor (herein A = the dimer $\{[(1,5\text{-}COD)Ir^{I}\bullet HPO_4][Bu_4N]\}_2$, **3**) in the A → B (rate constant k_{1obs}) formally nucleation step of the FW 2-step mechanism.[15] Figure 4 shows the k_{1obs} rate constant from fits to the FW 2-step mechanism versus starting concentration of $\{[(1,5\text{-}COD)Ir^{I}\bullet HPO_4][Bu_4N]\}_2$, **3**, performed in triplicate at each point of the five different

concentrations of $(Bu_4N)_2HPO_4$ stabilizer (1.8–5.4 molar equiv). In intriguing contradistinction to the additional, linear k_{1obs} vs $[A]^1$ and hence overall *second-order* dependence recently observed when starting with the *monometallic*, $\{(1,5\text{-COD})Ir^I\bullet\mathbf{POM}\}^{8-}$ (**POM** = $P_2W_{15}Nb_3O_{62}^{9-}$ polyoxometalate) precatalyst, in the current case starting with $\{[(1,5\text{-COD})Ir^I\bullet\mathbf{HPO_4}][Bu_4N]\}_2$ = A, *there is clearly no additional (e.g., additional first-order) dependence on A*, even though the data are noisy, not unexpectedly.[13,14,15] *Put in other terms, the previously unknown finding is that when starting with the bimetallic* $\{[(1,5\text{-COD})Ir^I\bullet HPO_4]_2\}^{2-}$ *precursor, nucleation is simple first order in that bimetallic precatalyst, corresponding to an overall bimolecular KEN[14] of 2,* Ir_2.

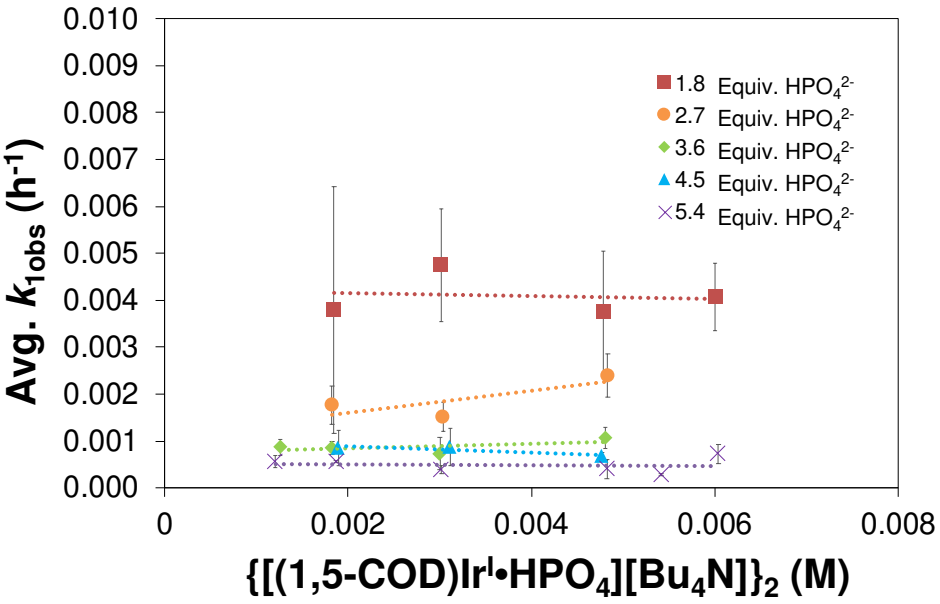

Figure 3.4. A plot of k_{1obs} (h^{-1}) vs the initial $\{[(1,5\text{-COD})Ir^I\bullet HPO_4][Bu_4N]\}_2$ precatalyst concentration (M). Nucleation rate constants were collected across a range of precatalyst concentrations at five different concentration ratios of $[(Bu_4N)_2HPO_4]$:[Ir] (red squares = 1.8:1, orange circles = 2.7:1, green diamonds = 3.6:1, blue triangles = 4.5:1, and purple X's = 5.4:1). The linear fits to a line $y = mx + b$ are as followed: 1.8 equiv (y = -0.0305x + 0.0042), 2.7 equiv (y = 0.2317x + 0.0011), 3.6 equiv (y = 0.0513x + 0.0007), 4.5 equiv (y = -0.0636x + 0.001), and 5.4 equiv (y = -0.0514x + 0.0006). The important result is that $m = 0$ in each case within experimental error, indicating that there is no further dependence (that is, beyond the observed, first-order dependence) of k_{1obs} on the starting concentration of $\{[(1,5\text{-COD})Ir^I\bullet HPO_4][Bu_4N]\}_2$.

The kinetics results shown are further supported by experiments monitoring the evolution of the reaction more directly via the cyclooctane in the reaction (from the hydrogenation of cylcoocta-1,5-diene in) by two techniques, gas–liquid chromatography (GLC) and ^{1}H NMR. The results from these studies were fit to the FW 2-step mechanism and are summarized in Figure S3.9 (Appendix II) for the interested reader. The main result is that they confirm in a general way the kinetics seen in Figure 3.4.

In short, the kinetics in Figure 3.4 and Figure S3.9 provide *prima facie* kinetic evidence that nucleation is *first-order* with respect to the $\{[(1,5\text{-COD})Ir^{I}\bullet HPO_4]_2\}^{2-}$ *bimetallic* precursor. These results, in turn, provide novel physical insights answering three of the key questions posed as part of the present studies, specifically the following: (i) establishing the interesting physical insight that a Ir^{I}_2 precursor is sufficient to nucleate $Ir(0)_n$ nanoparticle formation under H_2 reduction conditions; (ii) providing just the second example, backed by the needed kinetics studies, that at least $Ir(0)_n$ nanoparticle nucleation is a low, ≤2 order, ≤2–3 molecular, kinetically controlled process;[13,14] and (iii) reporting the previously unknown, interesting finding that, upon changing the associate polyanion and form of the otherwise identical $Ir^{I}(1,5\text{-COD})^{+}$-containing precursor from monometallic $[(1,5\text{-COD})Ir^{I}\bullet\mathbf{POM}\}^{8-}$ to the bimetallic $\{[(1,5\text{-COD})Ir^{I}\bullet\mathbf{HPO_4}]_2\}^{2-}$, nucleation changes from net termolecular in Ir (Ir_3) to overall bimolecular in Ir (Ir_2). Stating this last insight a different way, low-molecularity nucleation (Ir_n, $n \leq 2$–3) is kinetically sufficient to initiate the nanoparticle formation reaction, but is *not* a constant $n = 2$ or 3, even for closely related complexes containing the identical $Ir^{I}(1,5\text{-COD})^{+}$ component. The next section digs more deeply into the intimate mechanism of nucleation to see if we can understand this interesting difference between the two, $\mathbf{HPO_4^{2-}}$ versus $\mathbf{POM^{9-}}$ containing nanoparticle precursor systems. We can, and

it turns out that their different *surface* charges look to be a key factor, *vide infra*.

Further Insights into the Nucleation Mechanism: The Effects of Added HPO_4^{2-} on the Nucleation Kinetics

Given that more detailed, physical insights into nucleation mechanisms are virtually unknown precisely at the molecular level,[14] the nucleation kinetics and associated mechanism were investigated in more detail by probing the rate constant (k_{1obs}) as a function of the concentration of added hydrogen phosphate, $(Bu_4N)_2HPO_4$, that is, beyond a 1:1 ratio of HPO_4^{2-} to Ir and at each of the three total Ir concentrations of 3.6, 6.0, and 9.6 mM. Each data point in Figure 3.5 represents the average of three to four experimental runs leading to the error bars shown. The key questions being probed here are: (a) Is there a $[HPO_4^{2-}]$ dependence in the rate law, thereby giving deeper physical insight into the nucleation mechanism and kinetically effective nucleus (KEN) for the nucleation process? (b) Is $\{[(1,5\text{-COD})Ir^{I}(NCCH_3)]_2 \bullet HPO_4\}^0$, **2**, a kinetically competent intermediate or just an off-path species that can be detected in solution?

The data in Figure 3.5 reveal that k_{1obs} decreases in an apparent quadratic fashion with added $(Bu_4N)_2HPO_4$, quantitatively consistent with and highly supportive of a dissociative equilibrium[14] in which the dominant resting form of the precatalyst, $\{[(1,5\text{-COD})Ir^{I} \bullet HPO_4][Bu_4N]\}_2$, loses $(Bu_4N)_2HPO_4$, to form (by mass balance) *the ^{1}H NMR-detected $\{[(1,5\text{-COD})Ir^{I}(NCCH_3)]_2 \bullet HPO_4\}^0$, **2**,* Scheme 3.2. The implication is that the resultant neutral species $\{[(1,5\text{-COD})Ir^{I}]_2 \bullet HPO_4\}^0$, **2**, observed directly by ^{1}H NMR is a kinetically competent nucleation intermediate en route to the $Ir(0)_n$ nanoparticle product, Scheme 3.2. This is an *extremely rare is not unprecedented example of direct spectroscopic plus kinetics evidence of the intimate mechanism of nucleation, including for a key intermediate in the nucleation process*.

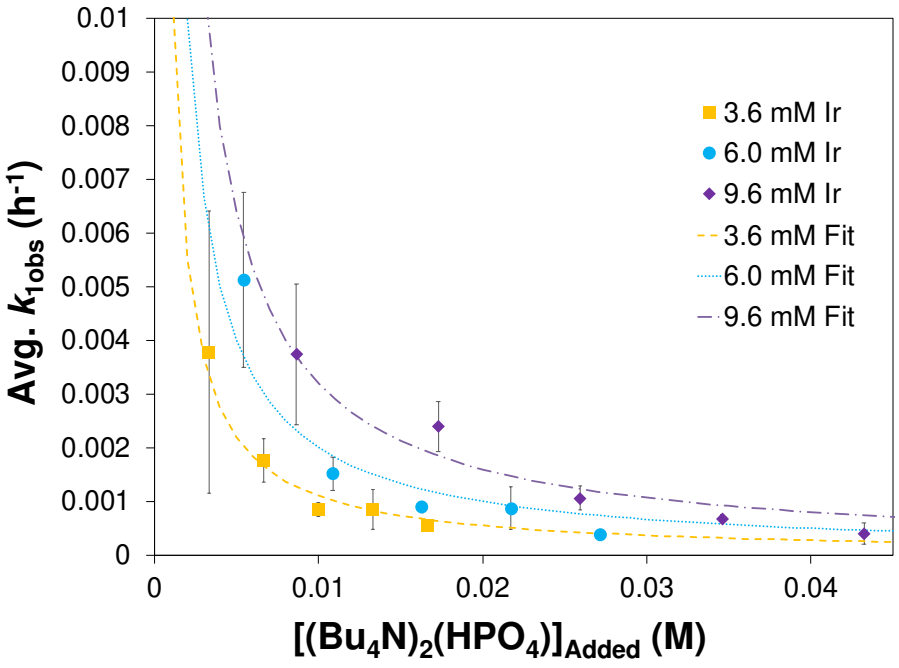

Figure 3.5. A plot of the nucleation rate constant (k_{1obs}) vs the added $(Bu_4N)_2HPO_4$ beyond a 1:1 ratio of $[HPO_4^{2-}]$ / [Ir]. The starting iridium concentrations were 3.6 mM (yellow squares), 6.0 mM (blue circles), and 9.6 mM (purple diamonds). The lines shown are fits to eq 3.10, derived for the dissociative equilibrium and more detailed mechanism provided in Scheme 3.2.

Scheme 3.2. Proposed More Intimate Nucleation Mechanism Involving a Dissociative Equilibrium from$\{[(1,5\text{-COD})Ir^{I}\bullet HPO_4][Bu_4N]\}_2$, Represented as $[Ir^{I}\bullet HPO_4\bullet Bu_4N]_2$, and in Acetone

$$[Ir^{I}\bullet HPO_4\bullet Bu_4N]_2 \underset{}{\overset{K_{Diss}}{\rightleftharpoons}} [Ir_2\bullet HPO_4]^0 + [(Bu_4N)_2HPO_4]^0$$

$$(A_2 - x) \qquad (x) \qquad (B_0 + x)$$

$$K_{Diss} = \frac{[((COD)Ir)_2HPO_4][(Bu_4N)_2HPO_4]}{[A_2]} = \frac{(x)(B_0+x)}{(A_2-x)} \qquad \text{(Eq 3.4)}$$

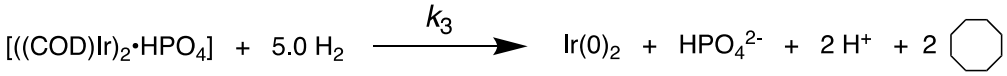

(Eq 3.5)

In the mechanism outlined in Scheme 3.2, B_0 is the added, excess $(Bu_4N)_2HPO_4$ beyond that contained in the starting, A_2 dimer, $[Ir^I•HPO_4•Bu_4N]_2$. The formation of the $\{[(1,5\text{-}COD)Ir^I(solv)]_2•HPO_4\}^0$ intermediate can then proceed forward under H_2 gas according to the proposed pseudoelementary,[15] rate-determining step, shown in eq 3.5 that is part of Scheme 3.2. On the basis of eq 3.5, the differential rate equation is eq 3.6, where $k_{3obs} = k_3[H_2]^y$ for constant and excess H_2. From the overall stoichiometry implied by Scheme 3.2 and its relevant part of $A_2 \rightarrow Ir(0)_2$, plus for the rate-determining step of eq 3.5, we can write eq 3.6:

$$-\frac{d[A_2]}{dt} = +\frac{d[Ir(0)_2]}{dt} = k_3\left[\left((COD)Ir\right)_2HPO_4\right][H_2]^y = k_{3obs}\left[\left((COD)Ir\right)_2HPO_4\right] = k_{3obs}(x) \quad \text{(Eq 3.6)}$$

Next, it is necessary to write an expression for $\{[(1,5\text{-}COD)Ir]_2•HPO_4]\}_t$ and we can write that in terms of our K_{Diss} defined in Scheme 3.2 eq 3.4, which simplifies to eq 3.7

$$x^2 + (B_0 + K_{Diss})x - K_{Diss}[A_2] = 0 \quad \text{(Eq 3.7)}$$

As eq 3.7 has the general form of a quadratic equation, the solution can be solved using the positive root of the quadratic equation, eq 3.8.

$$x = \frac{\left\{-(B_0+K_{Diss})+\left[(B_0+K_{Diss})^2+4K_{Diss}[A_2]\right]^{\frac{1}{2}}\right\}}{2} \quad \text{(Eq 3.8)}$$

Next, eq 3.8 can be plugged into eq 3.6 and that result into eq 3.9, where k_{1obs} is defined by eq S3.9 of Appendix II (for the nucleation step of the FW 2-step mechanism presented there) and where [A] in eq S3.9 is [A] = [A_2]. This then yields the expression for k_{1obs}, eq 3.10

$$\left[-\frac{d[A]}{dt}\right]_{nucleation} = \left[-\frac{d[A_2]}{dt}\right]_{nucleation} = k_{1obs}[A_2] \qquad \text{(Eq 3.9)}$$

$$k_{1obs} = \frac{k_{3obs}}{2[A_2]} \times \left(-(B_0 + K_{Diss}) + \left((B_0 + K_{Diss})^2 + (4K_{Diss}[A_2])\right)^{\frac{1}{2}}\right) \qquad \text{(Eq 3.10)}$$

Equation 3.10 was then used to curve-fit (by nonlinear least squares) the k_{1obs} vs B_0 data shown in Figure 3.5. The individual results from the various fits are tabulated in Appendix II, along with rough estimates of the K_{Diss} values (~10^{-6}) in acetone at 22 °C.

In short, the kinetics, as well as the identification of **2** by ^{1}H NMR, support the more intimate nucleation mechanism shown in Scheme 3.2 in which the neutral (therefore presumably more readily reduced by H_2) *bimetallic intermediate {[(1,5-COD)Ir^I(solv)]$_2$•HPO$_4$}^{0}*, **2**, is the kinetically dominant nucleation intermediate. As noted in the Introduction (section 3.1), such physical insights into nucleation, its preferred (low) molecularity, and its intimate mechanism involving a kinetically competent intermediate, **2**, are virtually unknown.[14]

Hypothesis for the Change from an Ir_2 to Ir_3 Kinetically Effective Nucleus

Reflection on the above results allows a rational explanation and a more general hypothesis going forward for why the molecularity or nucleation changes from Ir_2 to Ir_3, even for the closely related {[(1,5-COD)Ir^I•**HPO$_4$**]$_2$}$^{2-}$ versus [(1,5-COD)Ir^I•**POM**}$^{8-}$ precursors with their common Ir^I(1,5-COD)$^+$ component. Specifically, the *dianionic* **HPO$_4^{2-}$** can bind *two* Ir^I(1,5-COD)$^+$ whereas

the *trianionic surface-charged* POM is able to bind *three* $Ir^{I}(1,5\text{-COD})^{+}$ en route to *the kinetically fastest* nucleation in the case, via Ir_2 and Ir_3, respectively. The *trianionic surface charge* of the **POM^{9-}** polyoxoanion can be seen by rewriting $P_2W_{15}Nb_3O_{62}^{9-}$ as it actually structurally exists, $\{(\mathbf{Nb_3O_9^{3-}})(W_{15}O_{45})^{0}(PO_4)_2^{6-}\}$.) Moreover, the presence of a $Ir^{I}(1,5\text{-COD})^{+}$ dissociative equilibria in both systems allows the self-assembly formation of the kinetically preferred $\{\mathbf{Ir^{I}_2{\bullet}HPO_4}\}^{0}$ and $\{\mathbf{Ir^{I}_3{\bullet}POM}\}^{6-}$ (structurally $\{[Ir^{I}_3(W_{15}Nb_3O_{54})^{3-}]^{0}(PO_4)_2\}^{6-}$) in each case, both of which *are effectively neutral on their surfaces* and both of which have self-assembled the maximum number of mono-cationic $Ir^{I}(1,5\text{-COD})^{+}$ that their anionic *surface* charge allows.

An important hypothesis going forward, and which merits further testing in other systems, is apparent from the above findings: *an m– charged anion with m+ of positively charged nanoparticle precursor may more generally be a kinetically preferred nucleation precursor and/or intermediate.* Additionally, mineral (inorganic) dust that can be anionic on its surface, $dust^{m-}$ (basically $Si_aAl_bO_c(OH)_d^{m-}$; see the first Table elsewhere[50]), plausibly operates in a similar way to enhance nucleation with at least cationic nanoparticle precursors.[50]

Control Experiment Quantitating the Impact of Laboratory Dust on the Nucleation Kinetics

In light of the above hypothesis about dust and given our 2017 report that the removal of dust by 0.2 μm filtration reduces the observed k_1 nucleation rate constant in the $\{(1,5\text{-COD})Ir^{I}{\bullet}\mathbf{POM}\}^{8-}$ system by a factor of ~5–7.6,[50] as a control, we examined the effects of 0.2 μm filtration (of all solvent, solutions, and rinsing all glassware with filtered solvents) and the accompanying dust removal[50] on the kinetics of nucleation of the $\{[(1,5\text{-COD})Ir^{I}{\bullet}\mathbf{HPO_4}]_2\}^{2-}$ system.

Figures S3.6 and S3.7 of Appendix II reveal that the expected slowing of k_{1obs} with 0.2 μm

filtration is seen, albeit at a somewhat lower, ~1.5–5-fold level of reduction in k_{1obs} for the $\{[(COD)Ir^{I}\bullet HPO_4][Bu_4N]\}_2$ system. The implication and important finding is that nucleation has a heterogeneous, dust-mediated component, not unexpectedly given that the first demonstration of dust effects on nucleation date back more than 100 years (see the discussion and references of that 2017 paper[50]). Further studies of dust, and as a function of the different countercations and their amounts, will be needed, however, to understand the more intimate mechanism of dust's effect(s) on nucleation.

These controls and their results add to the growing list since 1994 studies[51] of the nonzero, sometimes dramatic, effects on nucleation[50,51,65] of dust,[50] water,[51] O_2,[51] trace solvents used in syntheses (such as EtOAc[65]), and other impurities. Summarized in the Supporting Information are additional controls revealing the dramatic effects of additives such as the diprotonated $(Bu_3NH)_2(H_2P_2O_7)$ on the nucleation kinetics of the parent system. The above factors are among the reasons nucleation rate constants are notoriously hard to measure reproducibly and precisely.[13,14,15]

Time-Resolved Transmission Electron Microscopy (TR-TEM) and Associated Particle Size Distribution

It is of fundamental interest to know the particle size and size distribution that results from the nanoparticle nucleation mechanism back in Scheme 3.2, particle size distributions that are invaluable for in-progress Population Balance modeling. Figure 3.6 depicts the $Ir(0)_n$ particle diameter distribution at 11.5 h, the end of the reaction (as judged by the evolution of 1.0 equiv cyclooctane per Ir from the $Ir^{I}(1,5\text{-}COD)^{+}$ containing precursor). The average particle size at the end of the reaction is 1.5 ± 0.2 nm, for a polydispersity of ±13%, hence near-monodisperse (≤

±15% by the published definition of near-monodisperse).[19]

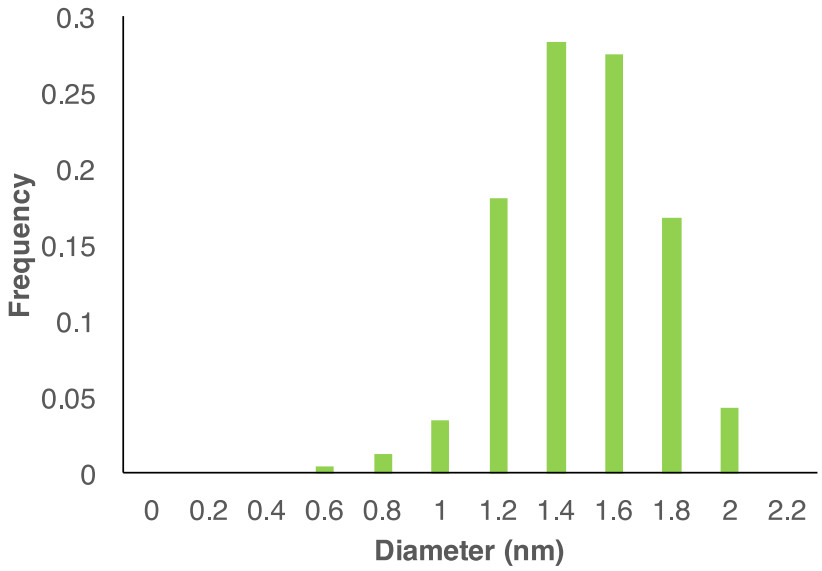

Figure 3.6. Histogram of the particle size distribution of $Ir(0)_n$ nanoparticles collected at the end of the reaction (11.5 h) for a standard 6.0 mM $[(COD)Ir(NCCH_3)_2][BF_4]$ in acetone in the presence of 5.4 molar equiv of $(Bu_4N)_2HPO_4$ and 0.5 mL of 1.65 M cyclohexene at 22.0 ± 0.1 ºC. Particle diameters were measured for 233 particles and plotted against frequency (normalized counts). The average particle size at the end of the reaction is 1.5 ± 0.2 nm with a polydispersity of ±13%.

A more detailed analysis was performed on all eight TEM samples that were collected. Representative TEM micrographs are provided in Appendix II for interested readers. Shown below in Figure 3.7 are the particle size distributions from specific samples at the beginning (1.0 h), middle (2.25 and 6.25 h), and end (11.5 h) of the reaction. The size distribution at 1.0 h is skewed far to the left toward smaller sizes, as would be expected during the induction period, wherein primarily nucleation and initial autocatalytic growth are taking place. The average size at 1.0 h is 0.7 ± 0.2 nm, with a polydispersity at that time of ±29%. As the reaction progresses to 2.25 and 6.0 h, the beginning of the growth period and halfway through the evolution of cyclooctane, respectively, the distributions have shifted to be centered at 1.1 and 1.2 nm *with narrowed*

polydispersities of ±18% and ±17%, respectively. Finally, at the end of the growth period, at 11.5 h, the distribution has centered at the end size of 1.5 ± 0.2 nm with *a further narrowed polydispersity* of ±13%, as also shown back in Figure 3.6. The average diameters vs time are tabulated in Table 3.1.

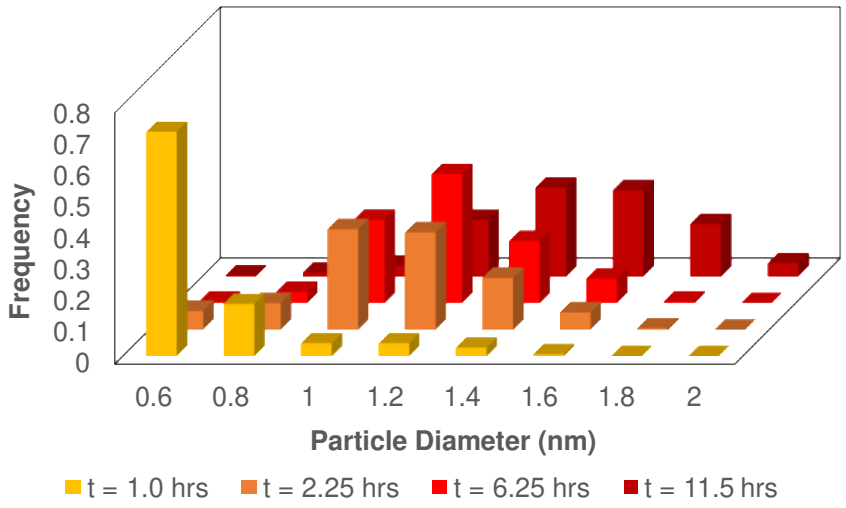

Figure 3.7. Particle size distributions for the reaction at four specific times: beginning of the reaction (yellow), at the start of the autocatalytic growth (orange), halfway through evolution of the cyclooctane (red), and at the end of the reaction when 1.0 equiv of cyclooctane has been evolved (burgundy). At each time point, a new reaction was prepared of 6.0 mM $[(COD)Ir^{I}(NCCH_3)_2][BF_4]$ in the presence of 5.4 molar equiv of $(Bu_4N)_2HPO_4$ and 0.5 mL of 1.65 M cyclohexene at 22.0 ± 0.1 °C in acetone. Across all the samples collected, >1900 nontouching particles were measured. As the size increases, the distribution narrows from an initially observed polydispersity of ±29%, to ±17–18%, to a final polydispersity of ±13%.

Table 3.1. Evolution of the Average Particle Diameter (nm) for 6.0 mM $[(COD)Ir^{I}(NCCH_3)_2][BF_4]$ with 5.4 Molar Equivalents $(Bu_4N)_2HPO_4$ as a Function of the Reaction Time

Time (hours)	1.0	2.25	4.5	4.8	6.25	6.5	8.25	11.5
Avg. Diameter (nm)	0.7 ± 0.2	1.1 ± 0.2	1.1 ± 0.3	1.4 ± 0.3	1.2 ± 0.2	1.3 ± 0.2	1.3 ± 0.2	1.5 ± 0.2

The diameter vs time data in Table 3.1 can be analyzed quantitatively using an equation derived from the FW 2-step mechanism for the D_t (diameter as a function of time) in terms of the D_f (final particle diameter).[72] That plot, and a brief discussion of the resultant rate constants for nucleation, k_{1obs}, and autocatalytic surface growth, k_{2obs}, are provided along with Figure S3.11 in Appendix II. It is likely that a surface–ligand binding effect, as recently precedented in the important work of Prof. A. Karim and his students (for $Pd(0)_m$ particle formation in the presence of $P(Octyl)_3$),[26] is important in the observed size-narrowing as a function of time, as seen in the data in Table 3.1. The needed SAXS, XAFS, and population balance modeling efforts of the $\{[(1,5\text{-COD})Ir^{I}\bullet HPO_4]_2\}^{2-}$ system reported herein are nearing completion and will be reported in due course.

3.4. CONCLUSIONS

Six questions were raised in the Introduction; each of those has been answered via the present investigation of the detailed kinetics and molecular mechanism of nucleation of the well-defined, bimemetallic precatalyst system, $\{[(1,5\text{-COD})Ir^{I}\bullet HPO_4]_2\}^{2-}$, while exploiting the seven advantages[57] this novel system provides. Specifically, the following at least nine insights and conclusion, plus two working hypotheses meriting future, additional investigation, have resulted from the present studies:

- Overall nucleation is first-order in the dimeric, A_2-type precatalyst system $\{[(1,5\text{-COD})Ir^{I}\bullet HPO_4]_2\}^{2-}$. These kinetics in turn reveal a simple molecularity in Ir of 2, that is Ir_2, in the rate-determining transition state of nucleation. Put another way, a simple binuclear Ir_2 complex is sufficient to nucleate the formation of $Ir(0)_n$ nanoparticles via a Kinetically Effective Nucleus[13] of Ir_2, really $Ir_2H_x(\mathbf{HPO_4})_1\bullet$dust (analogous to the

previously reported Ir_3H_x(**POM**)$_1$•dust),[14] if one starts with both those Ir in the same, Ir_2-containing, bimetallic complex $\{[(1,5\text{-COD})Ir^{I}\bullet\mathbf{HPO_4}]_2\}^{2-}$. Further, the role of the metal hydrides (M–H) in nucleation of at least transition-metal nanoparticles has growing precedent.[14,73]

- Low, ≤2-3 molecularity nucleation is therefore demonstrated and fully supported by the present studies. Low molecularity nucleation[13,14] is in at least strong-bonding systems is *a major paradigm shift in nucleation theory*,[13,14] one that is gaining more and more support as a more general result across nature (see the discussion and references elsewhere[13,14]). Put another way, low-molecularity nucleation in strong bonded systems is an important, paradigm-shifting working hypothesis going forward as a result of this and other recent work.[13,14]
- Dust, and other additives (e.g., the diprotonated $H_2P_2O_7^{2-}$ data provided in the Supporting Information) have significant effects on the nucleation kinetics. The up to 5-fold effect on the nucleation rate constant k_{1obs}, vs when the amount of dust is lowered by microfiltration, means that nucleation in even the present molecularly precise, $\{[(1,5\text{-COD})Ir^{I}\bullet HPO_4][Bu_4N]\}_2$ precursor system should be considered as being heterogeneous. Nucleation is, indeed "almost always heterogeneous" (see p. 542 of the proceedings of a 2015 workshop of experts on nucleation[8]).
- Equilibrium-thermodynamics-based Classical Nucleation Theory (CNT), with its theoretical concept of *reversible* $n\text{A} \rightleftharpoons \text{A}_n$ to form an A_n (n>>2–3) "Critical Nucleus", is once again disproven for strong-bonding, irreversibly forming systems,[13,14] such a transition-metal nanoparticle formation. Nucleation is typically under kinetic control, not the equilibrium/thermodynamic control posited by CNT and its reversible assembly of nA

$\rightleftharpoons A_n$, n>>2–3. This is why CNT works only for very weakly bonded, reversibly associating systems that it was designed for, such as $n(RH) \rightleftharpoons (RH)_n$ in the gas phase.[45,46]

Intriguingly, in the 2015 workshop on nucleation[8] already noted, Classical Nucleation Theory was used to (try to) explain or rationalize most talks and their associated papers. Yet the summary of the workshop concluded "Classical Nucleation Theory does not adequately explain the (in that case) crystal nucleation process" (see p. 543[8]). *Note, then, that the problem is NOT with CNT*. Instead, the problem is with continued application in the literature of CNT to systems for which CNT was never intended, an unfortunately too common problem in the literature of the misapplication of classical theories that "work poorly, or not at all, when applied beyond the validity of their assumptions".[74] CNT is *simply not applicable to strong bonded systems* involving high-energy, unstable Ir–H/Ir(0) containing species,[14] as is the case for transition-metal nanoparticle formation. *Nor is CNT applicable to the large majority of other systems throughout nature that are also not relatively weakly bonded, lower energy, meta- to stable species, such as*[10] *$(RH)_n$, $(H_2O)_n$, $(N_2)_n$, $(Ar)_n$, and so on, wherein the application of CNT was intended and therefore makes sense.*

- The more intimate mechanism of nucleation beginning with the dimeric precatalyst, $\{[(1,5\text{-COD})Ir^{I}\bullet HPO_4][Bu_4N]\}_2$, involves a dissociate equilibrium, K_{Diss}, to form $(Bu_4N)_2HPO_4$ and $\{[(1,5\text{-COD})Ir^{I}(solv)]_2\bullet HPO_4\}^0$, the latter as a kinetically competent nucleation intermediate therefore apparently more readily reducible by H_2, a rare, detailed mechanistic/physical insight into (molecular) nucleation.[14]
- Importantly, the intimate mechanism of nucleation is influenced by the choice of counteranion, the $Ir^{I}(1,5\text{-COD})^+$ component itself not being sufficient to establish the molecularity of nucleation. Instead and interestingly, the $Ir^{I}(1,5\text{-COD})^+$ dissociative

equilibria present in both the $\{[(1,5\text{-COD})Ir^{I}\bullet\mathbf{HPO_4}]_2\}^{2-}$ and[14] $[(1,5\text{-COD})Ir^{I}\bullet\mathbf{POM}\}^{8-}$ systems provides a facile pathway for formation of the kinetically preferred $\{Ir^{I}_{\mathbf{2}}\bullet\mathbf{HPO_4}\}^{0}$ and $\{Ir^{I}_{\mathbf{3}}\bullet\mathbf{POM}\}^{\mathbf{6-}}$ in those two related, but kinetically distinct, cases. However, the two cases are unified by the observation that both have bound the maximum number of $Ir^{I}(1,5\text{-COD})^{+}$ their surface charges permit, that is the number (2 vs 3, respectively) of $Ir^{I}(1,5\text{-COD})^{+}$ needed to yield *effectively neutral surface charges*.

- Hence, a previously unavailable, second working hypothesis meriting additional experimental testing in other systems emerges, namely, *that an m– charged anion binding a total of m+ of positively charged nanoparticle precursor may more generally be a kinetically preferred nucleation precursor and/or intermediate.* A second, related working hypothesis is that mineral (inorganic) dust of general formula $Si_aAl_bO_c(OH)_d^{m-}$ = $Dust^{m-}$ (see the first Table elsewhere[50]) may well enhance nucleation by a similar mechanism, at least when binding cationic nanoparticle precursors.[50] These results tie more broadly into the growing concept of a *dense prenucleation phase/prenucleation clusters*[8,9,75] as a critical part of nucleation across nature anytime that a denser phase can be achieved. The present and our prior[13,14] work show that the low end of these kinetically competent clusters[13] can be an A_n of n = just 2–3.
- Valuable TEM vs time size and size-dispersion data were gathered that will be valuable in ongoing efforts at Population Balance Modeling (PBM) to connect the size and size distributions to the nucleation and autocatalytic growth mechanism. Critical to those efforts is the unprecedented level of knowledge *of the intimate mechanism of nucleation* provided by the present and our 2017[14] studies. Without such knowledge of the true nucleation

mechanism, *all* prior PBM studies of *all* systems across nature, which often relied on inapplicable CNT, are arguably flawed!

- Also, and while not part of the present studies, the $\{[(1,5\text{-COD})Ir^{I}\bullet HPO_4][Bu_4N]\}_2$ system has, as anticipated,[57] permitted successful synchrotron SAXS and XAFS experiments, results which are being prepared for a separate publication, along with the needed PBM necessary to describe quantitatively the evolution of the size distribution.

Overall, then, the present studies provide a prototype example of the insights possible into nucleation when starting from a precisely molecularly defined precursor: one where the kinetics separating nucleation from growth can be obtained, and one where multiple advantages of a molecularly precisely defined system are available.[57] It is hoped that the present system and example will help inspire analogous, detailed studies into nucleation phenomena for other, molecularly precise precursor systems testing and refining as needed the findings and two working hypotheses uncovered by the present studies.

REFERENCES

1. Volmer, M.; Weber, A. Z. Nucleus formation in supersaturated systems, *Z. Phys. Chem.* **1926**, *119*, 277–301.

2. Tohmfor, G.; Volmer, M. Die Keimbildung unter dem Einfluß elektrischer Ladungen. *Ann. Phys.* **1938**, *425*, 109–131.

3. Volmer, M.; *Kinetik der Phasenbildung*; Steinfopff: Leipzig, 1939.

4. Becker, R.; Döring, W. Kinetische Behandlung der Keimbildung in übersaettigten Daepfern. *Ann. Phys.* **1935**, *416*, 719–752.

5. Kashchiev, D. *Nucleation: Basic Theory with Applications*; Butterworth-Heinemann: Oxford, U.K., 2000.

6. Oxtoby, D. W. Homogeneous nucleation: theory and experiment, *J. Physics: Condensed Matter* **1992**, *4*, 7627–7650.

7. Zhang, T. H.; Liu, X. Y. Nucleation: What Happens at the Initial Stage? *Angew. Chem., Int. Ed.* **2009**, *48*, 1308–1312.

8. Erdemir, D.; Lee, A. Y.; Myerson, A. S. Nucleation for Crystals from Solution: Classical and Two-Step Models. *Acc. Chem. Res.* **2009**, *42*, 621–629. Note the "Two-Step Model" referred to in this work and associated literature, involving an amorphous, prenucleation, dense phase and/or clusters, is distinct from and should not be confused with the FW 2-step mechanism[15] of continuous nucleation and autocatalytic surface growth.

9. Nucleation—a Transition State to the Directed Assembly of Materials. *Faraday Discussions*; Royal Society Of Chemistry: U.K., 2015; Vol. *179*, 9–154.

10. Zhang, R.; Khalizov, A.; Wang, L.; Hu, M.; Xu, W. Nucleation and Growth of Nanoparticles in the Atmosphere. *Chem. Rev.* **2012**, *112*, 1957–2011. The "strongly associated" systems in this review correspond in a general way to what we denote as "strongly bonded" systems in the present and prior[13] research.

11. LaMer, V.; Dinegar, R. Theory, Production and Mechanism of Formation of Monodispersed Hydrosols. *J. Am. Chem. Soc.* **1950**, *72*, 4847–4854.

12. Zaiser, E. M.; LaMer, V. K. The kinetics of the formation and growth of monodispersed sulfur hydrosols. *J. Colloid Sci.* **1948**, *3*, 571–598.

13. Laxson, W. W.; Finke, R. G. Nucleation is Second Order: An Apparent Kinetically Effective Nucleus of Two for $Ir(0)_n$ Nanoparticle Formation from $[(1,5\text{-COD})Ir^{I}\bullet P_2W_{15}Nb_3O_{62}]^{8-}$ Plus Hydrogen. *J. Am. Chem. Soc.* **2014**, *136*, 17601–17615, and references therein.

14. Özkar, S.; Finke, R. G. Nanoparticle Nucleation Is Termolecular in Metal and Involves Hydrogen: Evidence for a Kinetically Effective Nucleus of Three $\{Ir_3H_{2x}\bullet P_2W_{15}Nb_3O_{62}\}^{6-}$ in $Ir(0)_n$ Nanoparticle Formation From $[(1,5\text{-COD})Ir^{I}\bullet P_2W_{15}Nb_3O_{62}]^{8-}$ Plus Dihydrogen. *J. Am. Chem. Soc.* **2017**, *139*, 5444–5457, and references therein.

15. Watzky, M. A.; Finke, R. G. Transition Metal Nanocluster Formation Kinetic and Mechanistic Studies. A New Mechanism When Hydrogen Is the Reductant: Slow, Continuous Nucleation and Fast Autocatalytic Surface Growth. *J. Am. Chem. Soc.* **1997**, *119*, 10382–10400.

16. Watzky, M. A.; Finke, R. G. Nanocluster Size-Control and "Magic Number" Investigations. Experimental Tests of the "Living-Metal Polymer" Concept and of Mechanism-Based Size-Control Predictions Leading to the Syntheses of Iridium(0) Nanoclusters Centering about Four Sequential Magic Numbers. *Chem. Mater.* **1997**, *9*, 3083–3095.

17. Özkar, S.; Finke, R. G. Transition-Metal Nanocluster Stabilization Fundamental Studies: Hydrogen Phosphate as a Simple, Effective, Readily Available, Robust, and Previously Unappreciated Stabilizer for Well-Formed, Isolable, and Redissolvable Ir(0) and Other Transition-Metal Nanoclusters. *Langmuir*, **2003**, *19*, 6247–6260.

18. Besson, C.; Finney, E. E.; Finke, R. G. A Mechanism for Transition-Metal Nanoparticle Self-Assembly. *J. Am. Chem. Soc.* **2005**, *127*, 8179–8184.

19. Aiken, J. D., III; Finke, R. G. Nanocluster Formation Synthetic, Kinetic, and Mechanistic Studies. The Detection of, and Then Methods to Avoid, Hydrogen Mass-Transfer Limitations in the Synthesis of Polyoxoanion- and Tetrabutylammonium-Stabilized, Near-Monodisperse 40 ± 6 Å Rh(0) Nanoclusters. *J. Am. Chem. Soc.* **1998**, *120*, 9545–9554.

20. Weddle, K. S.; Aiken, J. D., III, Finke, R. G. Rh(0) Nanoclusters in Benzene Hydrogenation Catalysis: Kinetic and Mechanistic Evidence that a Putative $[(C_8H_{17})_3NCH_3]^+[RhCl_4]^-$ Ion-Pair Catalyst is Actually a Distribution of Cl^- and $[(C_8H_{17})_3NCH_3]^+$ Stabilized Rh(0) Nanoclusters. *J. Am. Chem. Soc.* **1998**, *120*, 5653–5666.

21. Hagen, C. M.; Widegren, J. A.; Maitlis, P. M.; Finke, R. G. Is it Homogeneous or Heterogeneous Catalysis? Compelling Evidence for Both Types of Catalysts Derived from $[Rh(\eta^5\text{-}C_5Me_5)Cl_2]_2$ as a Function of Temperature and Hydrogen Pressure. *J. Am. Chem. Soc.* **2005**, *127*, 4423–4432.

22. Harada, M.; Inada, Y. In Situ Time-Resolved XAFS Studies of Metal Particle Formation by Photoreduction in Polymer Solutions. *Langmuir* **2009**, *25*, 6049–6061.

23. Harada, M.; Yosihiko, K. Nucleation and Aggregative Growth Process of Platinum Nanoparticles Studied by in Situ Quick XAFS Spectroscopy. *Langmuir* **2012**, *28*, 2415–2428.

24. Hagen, C. M.; Vieille-Petit, L.; Laurenczy, G.; Süss-Fink, G.; Finke, R. G. Supramolecular Triruthenium Cluster-Based Benzene Hydrogenation Catalysis: Fact or Fiction? *Organometallics*, **2005**, *24*, 1819–1831.

25. Wojnicki, M.; Fitzner, K.; Luty-Blocho, M. Kinetic Studies of Nucleation and Growth of Palladium Nanoparticles. *J. Colloid Interface Sci.* **2016**, *465*, 190–199.

26. Mozaffari, S.; Li, W.; Thompson, C.; Ivanov, S.; Seifert, S.; Lee, B.; Kovarik, L.; Karim, A. M. Colloidal nanoparticle size control: experimental and kinetic modeling investigation of the ligand-metal binding role in controlling the nucleation and growth kinetics. *Nanoscale* **2017**, *9*, 13772–13785.

27. LaGrow, A. P.; Ingham, B.; Toney, M. F.; Tilley, R. D. Effect of Surfactant Concentration and Aggregation on the Growth Kinetics of Nickel Nanoparticles. *J. Phys. Chem. C* **2013**, *117*, 16709–16718.

28. Kytsya, A.; Bazylyak, L.; Hrynda, Y.; Horechyy, A.; Medvedevdkikh, Y. The Kinetic Rate Law for the Autocatalytic Growth of Citrate-Stabilized Silver Nanoparticles. *Int. J. Chem. Kinet.* **2015**, *47*, 351–360.

29. Tatarchuk, V. V.; Sergievskaya, A. P.; Korda, T. M.; Druxhinina, I. A.; Zaikovsky, V. I. Kinetic Factors in the Synthesis of Silver Nanoparticles by Reduction of Ag^+ with Hydrazine in Reverse Micelles of Triton N-42. *Chem. Mater.* **2013**, *25*, 3570–3579.

30. Harada, M.; Kizaki, S. Formation Mechanism of Gold Nanoparticles Synthesized by Photoreduction in Aqueous Ethanol Solutions of Polymers Using in Situ Quick Scanning X-ray Absorption Fine Structure and Small-Angle X-ray Scattering. *Cryst. Growth. Des.* **2016**, *16*, 1200–1212.

31. Yin, C. X.; Finke, R. G. Kinetic and Mechanistic Studies of Vanadium-Based, Extended Catalytic Lifetime Catechol Dioxygenases. *J. Am. Chem. Soc.* **2005**, *127*, 13988–13996.

32. Bayram, E.; Linehan, J. C.; Fulton, J. L.; Roberts, J. A. S.; Szymczak, N. K.; Smurthwaite, T. D.; Özkar, S.; Balasubramanian, M.; Finke, R. G. Is it Homogeneous or Heterogeneous Catalysis Derived from $[RhCp^*Cl_2]_2$? *In Operando* XAFS, Kinetic, and Crucial Kinetic Poisoning Evidence for Subnanometer Rh_4 Cluster-Based Benzene Hydrogenation Catalysis. *J. Am. Chem. Soc.* **2011**, *133*, 18889–18902

33. Smith, S. E.; Sasaki, J. M.; Bergman, R. G.; Mondloch, J. E.; Finke, R. G. Platinum-Catalyzed Phenyl and Methyl Group Transfer from Tin to Iridium: Evidence for an Autocatalytic Reaction Pathway with an Unusual Preference for Methyl Transfer. *J. Am. Chem. Soc.* **2008**, *130*, 1839–1841.

34. Mondloch, J. E.; Wang, Q.; Frenkel, A. I.; and Finke, R. G. Development Plus Kinetic and Mechanistic Studies of a Prototype Supported-Nanoparticle Heterogeneous Catalyst Formation System in Contact with Solution: Ir(1,5-COD)Cl/γ-Al_2O_3 and Its Reduction by H_2 to $Ir(0)_n$/γ-Al_2O_3. *J. Am. Chem. Soc.* **2010**, *132*, 9701–9714.

35. Mondloch, J. E.; Finke, R. G. Supported-Nanoparticle Heterogeneous Catalyst Formation in Contact with Solution: Kinetics and Proposed Mechanism for the Conversion of Ir(1,5-COD)Cl/γ-Al_2O_3 to $Ir(0)_{\sim 900}$/γ-Al_2O_3. *J. Am. Chem. Soc.* **2011**, *133*, 7744–7756.

36. Mondloch, J. E.; Bayram, E.; Finke, R. G. A Review of the Kinetics and Mechanisms of Formation of Supported-Nanoparticle Heterogeneous Catalysts. *J. Mol. Catal. A.* **2012**, *355*, 1–38.

37. Morris, A. M.; Watzky, M. A.; Agar, J. N.; Finke, R. G. Fitting neurological protein aggregation kinetic data via a 2-step, minimal/"Ockham's razor" model: the Finke-Watzky mechanism of nucleation followed by autocatalytic surface growth. *Biochemistry* **2008**, *47*, 2413–2427.

38. Watzky, M. A.; Morris, A. M.; Ross, E. D.; Finke, R. G. Fitting yeast and mammalian prion aggregation kinetic data with the Finke-Watzky two-step model of nucleation and autocatalytic growth, *Biochemistry* **2008**, *47*, 10790–10800.

39. Morris, A. M.; Finke, R. G. α-Synuclein aggregation variable temperature and variable pH kinetic data: a re-analysis using the Finke-Watzky 2-step model of nucleation and autocatalytic growth. *Biophys. Chem.* **2009**, *140*, 9–15.

40. Morris, A. M.; Watzky, M. A.; Finke, R. G. Protein aggregation kinetics, mechanism, and curve-fitting: a review of the literature. *Biochem. Biophys. Acta, Proteins Proteomics* **2009**, *1794*, 375–397.

41. Finney, E. E.; Finke, R. G. Fitting and Interpreting Transition-Metal Nanocluster Formation and Other Sigmoidal-Appearing Kinetic Data: A More Thorough Testing of Dispersive Kinetic vs Chemical-Mechanism-Based Equations and Treatments for 4-Step Type Kinetic Data. *Chem. Mater.* **2009**, *21*, 4468–4479.

42. Tong, F.; Hanson, M. P.; Bardeen, C. Analysis of reaction kinetics in the photochemical molecular crystal 9-methylanthracene using an extended Finke-Watzky model. *Phys. Chem. Chem. Phys.* **2016**, *18*, 31936–31945.

43. Avinash, M. B.; Sandeepa, K. V.; Govindaraju, T. Emergent Behaviors in Kinetically Controlled Dynamic Self-Assembly of Synthetic Molecular Systems. *ACS Omega*, **2016**, *1*, 378–387.

44. Oladoja, N. A. A critical review of the applicability of Avrami fractional kinetic equation in adsorption-based water treatment studies. *Desalin. Water Treat.* **2015**, *57*, 15813–15825.

45. Rusyniak, M.; Abdelsayed, V.; Campbell, J.; El-Shall, M. S., Vapor Phase Homogeneous Nucleation of Higher Alkanes: Dodecane, Hexadecane, and Octadecane. 1. Critical Supersaturation and Nucleation Rate Measurements. *J. Phys. Chem. B* **2001**, *105*, 11866–11872.

46. Rusyniak, M.; El-Shall, M. S., Vapor Phase Homogeneous Nucleation of Higher Alkanes: Dodecane, Hexadecane, and Octadecane. 2. Corresponding States and Scaling Law Analysis. *J. Phys. Chem. B* **2001**, *105*, 11873–11879.

47. Henglein, A.; Giersig, M. Formation of Colloidal Silver Nanoparticles: Capping Action of Citrate. *J. Phys. Chem. B* **1999**, *103*, 9533–9539.

48. Yao, S.; Yuan, Y.; Xiao, C.; Li, W.; Kou, Y.; Dyson, P. J.; Yan, N.; Asakura, H.; Teramura, K.; Tanaka, T. Insights into the Formation Mechanism of Rhodium Nanocubes. *J. Phys. Chem. C* **2012**, *116*, 15076–15086.

49. Meisl, G.; Yang, X.; Hellstrand, E.; Frohm, B.; Kirkegaard, J. B.; Cohen, S. I. A.; Dobson, C. M.; Linse, S.; Knowles, T. P. J. Differences in nucleation behavior underlie the contrasting aggregation kinetics of the Aβ40 and Aβ42 peptides. *Proc. Natl. Acad. Sci. U.S.A.* **2014**, *111*, 9384–9389.

50. Özkar, S.; Finke, R. G., Dust Effects On Nucleation Kinetics and Nanoparticle Product Size Distributions: Illustrative Case Study of a Prototype $Ir(0)_n$ Transition-Metal Nanoparticle Formation System. *Langmuir* **2017**, *33*, 6550–6562.

51. Lin, Y.; Finke, R. G. Novel Polyoxoanion- and Bu_4N^+-Stabilized, Isolable, and Redissolvable, 20—30-Å $Ir_{\sim 300\text{-}900}$ Nanoclusters: The Kinetically Controlled Synthesis, Characterization, and Mechanism of Formation of Organic Solvent-Soluble, Reproducible Size, and Reproducible Catalytic Activity Metal Nanoclusters. *J. Am. Chem. Soc.* **1994**, *116*, 8335–8353.

52. Özkar, S.; Finke, R. G. Nanocluster Formation and Stabilization Fundamental Studies: Ranking Commonly Employed Anionic Stabilizers via the Development, Then Application, of Five Comparative Criteria. *J. Am. Chem. Soc.* **2002**, *124*, 5796–5810.

53. Ott, L. S.; Finke, R. G. Transition-metal nanocluster stabilization for catalysis: A critical review of ranking methods and putative stabilizers. *Coord. Chem. Rev.* **2007**, *251*, 1075–1100.

54. Laxson, W. W.; Özkar, S.; Finke, R. G. Triniobium, Wells-Dawson-Type Polyoxoanion, $[(n\text{-}C_4H_9)_4N]_9P_2W_{15}Nb_3O_{62}$: Improvements in the Synthesis, Its Reliability, the Purity of the Product, and the Detailed Synthetic Procedure. *Inorg. Chem.* **2014**, *53*, 2666–2676.

55. Özkar, S.; Finke, R. G. Molecular insights for how preferred oxoanions bind to and stabilize transition-metal nanoclusters: A tridentate, C_3 symmetry, lattice size-matching binding model. *Coord. Chem. Rev.* **2004**, *248*, 135–146.

56. Özkar, S.; Finke, R. G. The hydrogenphosphate complex of (1,5-cyclooctadiene)iridium(I), $\{[Bu_4N][(1,5\text{-}COD)Ir{\bullet}HPO_4]\}_n$: synthesis, spectroscopic characterization, and ES-MS of a new, preferred precursor to HPO_4^{2-} and Bu_4N^+ stabilized $Ir(0)_n$ nanoclusters. *J. Organomet. Chem.* **2004**, *689*, 493–501.

57. The advantages of $\{[(1,5\text{-}COD)Ir^{I}{\bullet}HPO_4]_2[Bu_4N]_2\}$, **3**, as a nanoparticle precatalyst and for kinetic and mechanistic studies, include: (i) $(Bu_4N)_2HPO_4$ is readily prepared from commercially available, inexpensive $(Bu_4N)H_2PO_4$ by the addition of $Bu_4N^+OH^-$; (ii) HPO_4^{2-} has a valuable, direct ^{31}P NMR handle (as exploited in the present work); (iii) HPO_4^{2-} ranks only slightly below the "Gold Standard" $P_2W_{15}Nb_3O_{62}^{9-}$ polyanionic system as a stabilizer so that (iv) clean, reproducible $Ir(0)_n$ nanoparticle formation, with no bulk-metal formation, is seen using $(Bu_4N)_2HPO_4$; (v) reproducible, sigmoidal kinetics of nanoparticle formation are exhibited that can be accounted for by the FW 2-step mechanism that occurs at convenient rates using an easily implemented, *in situ* generation of $\{[(1,5\text{-}COD)Ir^{I}{\bullet}HPO_4][Bu_4N]\}_2$; and (vi) this in situ synthesis and system allows kinetics studies wherein the Ir^{I}/HPO_4^{2-} ratio can be readily changed to

optimize both the stability of the system and the nanoparticle formation kinetics, to probe, as it turns out, a dissociative K_{eq} that allows insights into the more intimate nucleation mechanism. Additionally, (vii) the $\{[(1,5\text{-COD})Ir^{I}\bullet HPO_4]_2\}^{2-}$ system has permitted successful synchrotron SAXS and XAFS experiments, and those data have allowed Population Balance Modeling (PBM) connecting the observed size and size distribution to the nanoparticle formation mechanism in a system where the nucleation mechanism is known (i.e., and where therefore and, for example, inapplicable Classical Nucleation Theory does not have to be relied upon). The SAXS, XAFS, and PBM studies will be reported separately in due course.

58. Day, V. W.; Klemperer, W. G.; Main, D. J. Niobotungstate, $Nb_2W_4O_{19}^{4-}$ and triphosphate, $P_3O_9^{3-}$, complexes of (cyclooctadiene)iridium(I): synthesis, structure, and stability of tetra-*n*-butylammonium salts of $\{[(C_8H_{12})Ir]_5(Nb_2W_4O_{19})_2\}^{3-}$, $\{[(C_8H_{12})Ir]_2H(Nb_2W_4O_{19})_2\}^{5-}$, and $[(C_8H_{12})Ir(P_3O_9)]^{2-}$. *Inorg. Chem.* **1990**, *29*, 2345–2355.

59. Cotton, F. A.; Wilkinson, G. *Advanced Inorganic Chemistry,* 5th ed.; John Wiley & Sons: New York, 1988.

60. Van Wazer, J. R.; Griffith, E. J.; McCullough, J. F. Hydrolysis of Condensed Phosphates. *J. Am. Chem. Soc.* **1952**, *74*, 4977–4978.

61. Ramirez, F.; Marecek, J. F. Oxyphosphorane and monomeric metaphosphate ion intermediates in phosphoryl transfer from 2,4-dinitrophenyl phosphate in aprotic and protic solvents. *J. Am. Chem. Soc.* **1979**, *101*, 1460–1465.

62. Guthrie, J. P. Hydration and dehydration of phosphoric acid derivatives: free energies of formation of the pentacoordinate intermediates for phosphate ester hydrolysis and of monomeric metaphosphate. *J. Am. Chem. Soc.* **1977**, *99*, 3991–4001.

63. Clark, E. P. Signer Method for Determining Molecular Weights. *Ind. Eng. Chem., Anal. Ed.* **1941**, *13*, 820–821.

64. Mondloch, J. E.; Finke, R. G. Kinetic Evidence for Bimolecular Nucleation in Supported-Transition-Metal-Nanoparticle Catalyst Formation in Contact with Solution: The Prototype Ir(1,5-COD)Cl/γ-Al_2O_3 to $Ir(0)_{\sim 900}/\gamma$-Al_2O_3 System. *ACS Catal.* **2012**, *2*, 298–305.

65. Kent, P.; Mondloch, J. E.; Finke, R. G. Synthesis of Heterogeneous $Ir^0_{\sim 600\text{-}900}/\gamma$-$Al_2O_3$ in One Pot From the Precatalyst Ir(1,5-COD)Cl/γ-Al_2O_3: Discovery of Two Competing Trace "Ethyl Acetate Effects" on the Nucleation Step and Resultant Product. *ACS Catal.* **2016**, *6*, 5449–5461.

66. Kent, P. D.; Mondloch, J. E.; Finke, R. G. A Four-Step Mechanism for the Formation of Supported-Nanoparticle Heterogeneous Catalysts in Contact with Solution: The Conversion of Ir(1,5-COD)Cl/γ-Al_2O_3 to Ir(0)$_{\sim 170}$/γ-Al_2O_3. *J. Am. Chem. Soc.* **2014**, *136*, 1930–1941.

67. Widegren, J. A.; Aiken, J. D., III; Özkar, S.; Finke, R. G. Additional Investigations of a New Kinetic Method To Follow Transition-Metal Nanocluster Formation, Including the Discovery of Heterolytic Hydrogen Activation in Nanocluster Nucleation Reactions. *Chem. Mater.* **2001**, *13*, 312–324.

68. Hoops, S.; Sahle, S.; Gauges, R.; Lee, C.; Pahle, J.; Simus, N.; Singhal, M.; Xu, L.; Mendes, P.; Kummer, U. COPASI-a COmplex PAtheway SImulator. *Bioinformatics* **2006**, *22*, 3067–3074.

69. Woehrle, G. H.; Hutchison, J. E.; Özkar, S.; Finke, R. G. Computer Based Analysis of Nanoparticle Transmission-Electron Microscopy Data Using a Public Domain Image-Processing Program, Image. *Turk. J. Chemistry,* **2006**, 30, 1–13.

70. Miller, S. A.; Tebboth, J. A.; Tremaine, J. F. 114. Dicyclopentadienyliron. *J. Chem. Soc.* **1952**, 632–635.

71. Ramsay, W. XLIX.—The molecular weights of the metals. *J. Chem. Soc., Trans.* **1889**, *55*, 521–536.

72. Watzky, M. A.; Finney, E. E.; Finke, R. G. Transition-Metal Nanocluster Size vs Formation Time and the Catalytically Effective Nucleus Number: A Mechanism-Based Treatment. *J. Am. Chem. Soc.* **2008**, *130*, 11959–11969.

73. Ben-Eliyahu, Y.; Brill, M.; Mintz, M. H. Hydride nucleation and formation of hydride growth centers on oxidized metallic surface—kinetic theory. *J. Chem. Phys.* **1999**, *111*, 6053–6060.

74. Peters, B. Common Features of Extraordinary Rate Theories. *J. Phys. Chem. B* **2015**, *119*, 6349–6356. The indicated quote is taken from p. 6354.

75. ten Wolde, P. R.; Frenkel, D. Enhancement of Protein Crystal Nucleation by Critical Density Fluctuations. *Science* **1997**, *277*, 1975–1978.

IV. NANOPARTICLE FORMATION KINETICS, MECHANISMS, AND ACCURATE RATE CONSTANTS: EXAMINATION OF A SECOND-GENERATION IR(0)N PARTICLE FORMATION SYSTEM BY FIVE MONITORING METHODS PLUS INITIAL MECHANISM-ENABLED POPULATION BALANCE MODELING

Overview[3]

The kinetics and mechanism of a second-generation iridium, bimetallic $\{[(1,5\text{-COD})Ir^{I}\bullet HPO4]_2\}^{2-}$ nanoparticle precursor system that produces $Ir(0)_{\sim 150}\bullet(HPO_4)_x$ nanoparticles are investigated herein. Specifically, a list of seven open questions is addressed via a total of five experimental techniques used to monitor the kinetics of the $\{[(1,5\text{-COD})Ir^{I}\bullet HPO4]_2\}^{2-}$ system plus Mechanism-Enabled Population Balance Modeling (ME-PBM), hence six total methods. To start, an indirect but in-house cyclohexene catalytic reporter reaction (CHCRR) monitoring method is used to follow the formation of the catalytically active $Ir(0)_n$. Next, gas-liquid chromatography (GLC) is used to quantify the amount of cyclooctane product formed vs time as a second way to monitor the loss of the $\{[(1,5\text{-COD})Ir^{I}\bullet HPO4]_2\}^{2-}$ precatalyst. Synchrotron X-ray absorption near-edge structure (XANES) is used next to more directly monitor the reduction of Ir^{I} to Ir^{0} and small-angle X-ray scattering (SAXS) is employed in separate experiments at a second synchrotron to monitor the formation of $Ir(0)_n$ vs time. Transmission Electron Microscopy

[3] This chapter furthers the mechanistic investigation of a second-generation iridium nanoparticle system, originally introduced in Chapter III. The synchrotron XANES and SAXS datasets were collected by a previous graduate student, Patrick Kent, and the data processing for these datasets was done by collaborators: Dr. Yuanyuan Li and Prof. Anatoly Frenkel (XANES) and Drs. Bridget Ingham and Nigel Kirby (SAXS). All XANES and SAXS data analysis was conducted by the author of this dissertation, C. B. Whitehead, as were all in-house experiments and data analyses. Writing was done by the author with writing and organization suggestions and edits by the advisor. A version of this manuscript will be submitted for publication in the near future to an ACS journal (expected spring of 2021). Minor changes were made to meet dissertation formatting guidelines. The supporting information can be found in Appendix III.

(TEM) on reaction aliquots is used to determine the particle-size distribution (PSD) vs time. The experimental kinetics data are then fit and analyzed to start using a minimal, 2-step mechanism of nucleation, $A \rightarrow B$ (rate constant k_1), and autocatalytic growth, $A + B \rightarrow 2B$ (rate constant k_2). How well the rate constants agree between the various methods is addressed as is the overall estimated accuracy of the kinetics in light of the multiple methods employed to monitor the particle-formation kinetics. ME-PBM is then used to analyze the TEM PSD data vs time, specifically to answer the question of whether or not the minimum mechanism consistent with all the kinetics data from the five physical methods can explain the observed PSD? An important finding is that it cannot. A Discussion section returns to the seven primary questions posed in the Introduction and includes 16 recommendations for future studies. A Conclusions section is also provided.

4.1. INTRODUCTION

Metal nanoparticles are known for their catalytic[1,2,3,4,5,6] and medicinal[7,8] applications. These properties are connected to the particle size and size distributions, which can be tuned through ligands[9,10,11] and reaction conditions[12,13]. To control the final particle size and size distribution, one needs to fully understand the particle-formation processes—that is, the mechanism—of nucleation, growth, and any possible agglomeration.

Minimal, Disproof-Based Mechanisms for Particle Formation.

Deliberately minimalist (i.e., Ockham's razor[14] obeying), disproof-based[15,16,17] mechanisms for particle formation are of considerable current interest because such mechanisms can inform rational particle syntheses. Mechanism-designed syntheses can, in turn, control particle size and size distributions[18,19] of interest in a myriad of nanoparticles and nanocrystals applications.[20,21,22,23,24] For this reason the kinetics and mechanisms of particle formations,[25,26,27,28,29,30,31,32,33] as well as the use of multiple, ideally direct physical methods[34,35,36,37,38,39,40,41,42] to follow the particle formations in real time, continue to be of intense current interest.[26,27,28,29,30,31,32,33] Despite this interest, the work that follows is an example of only a few studies in the literature where ≥3 multiple, direct or indirect methods are used to follow the kinetics of nanoparticle nucleation and growth[43,44] and only the second example where the powerful, mechanism-checking tool of Mechanism-Enabled Population Balance Modeling (ME-PBM) is employed.[18,19]

A First-Generation, Extensively-Studied $\{(1,5\text{-COD})Ir^{I}\bullet POM\}^{8-}$ Nanoparticle Formation System.

Extensive study of a first-generation $\{(1,5\text{-COD})Ir^{I}\bullet POM\}^{8-}$ precursor system[45,46] (POM = polyoxometalate) is responsible for the minimum, disproof-based kinetics and mechanisms summarized in Scheme 4.1. The $\{(1,5\text{-COD})Ir^{I}\bullet POM\}^{8-}$ precursor system self-assembles *n* equivs of $\{(1,5\text{-COD})Ir^{I}\bullet POM\}^{8-}$ under H_2 typically in acetone (alternatively sometimes in propylene carbonate[47]) solvent to yield well-formed, highly (polyoxometalate) stabilized $Ir(0)_n\bullet(POM^{9-})_x$ nanoparticles, such as $Ir(0)_{\sim 300}\bullet(POM^{9-})_x$ ($x \sim 17$)[45] in acetone, where POM is POM^{9-} = $P_2W_{15}Nb_3O_{62}^{9-}$, eq 4.1, the experimentally established, balanced reaction stoichiometry.[45,46]

$$n\,\{(1,5\text{-COD})Ir^{I}\bullet POM\}^{8-} + 2.5n\,H_2 \longrightarrow Ir(0)_{\sim n}\bullet(POM^{9-})_x + (n - x)\,POM^{9-} + n\,\text{  } + n\,H^{+} \quad \text{(Eq 4.1)}$$

The custom-built[48] sterically bulky, highly-negative charged, "electrosteric"[49] POM^{9-} "Gold standard"[49] nanoparticle stabilizer affords five outstanding features and five advantages[50] to the $Ir(0)_n\bullet(POM^{9-})_x$ nanoparticle system (for additional discussion, see p 2850 elsewhere[64]). However, despite the positives of the $\{(1,5\text{-COD})Ir^{I}\bullet POM\}^{8-}$ precursor and resultant $Ir(0)_n\bullet(POM^{9-})_x$ nanoparticle system, two significant *limitations* of this classic system (discussed more elsewhere[64]) directly relevant to the present contribution are that: (i) the large, ca. 1.2 nm width by ca. 1.5 nm length of the cigar-shaped POM, $P_2W_{15}Nb_3O_{62}^{9-}$, interferes with SAXS observation of early nucleation events. Those early nucleation clusters can easily be below 1.0 nm, as for example as modeled by a crystallographically characterized tetra-iridium hydride, $Ir_4H_4(1,5\text{-COD})_4$ cluster[51,52] that is 0.8 ± 0.1 nm by SAXS observation control experiments (performed in collaboration with Prof. A. Karim and his group[9,32,39]). An additional limitation of the $\{(1,5\text{-COD})Ir^{I}\bullet POM\}^{8-}$ system is (ii) that the W in the POM interferes with the Ir XAFS

(specifically, the overlap of the W L_2-edge with the preferred Ir L_3-edge). Hence, there was a need to develop a second-generation $Ir(0)_n$ nanoparticle system that retained the multiple advantages of the $Ir^I(1,5\text{-COD})^+$ precursor system, yet replaced the POM^{9-} polyoxometalate stabilizer by a smaller but still effective polyanionic stabilizer. Those studies were started back in 2003 and will be summarized in a moment, after some additional, necessary background material is covered.

The Cyclohexene Catalytic Hydrogenation Reporter Reaction Methodology

In 1994, we developed[45,46] a way to monitor in-house—and hence routinely and rapidly albeit *indirectly*—the formation of $Ir(0)_n$ and other catalytically active nanoparticles shown in the equations below, a method we expanded and refined in a 1997 paper.[53] The method involves exploiting the perhaps most important concept in studying modern, complex, multi-step reactions kinetically and mechanistically, namely the pseudo-elementary step (PEStep) concept.[53,54] In a pseudo-elementary step, multiple steps—sometimes thousands of steps, as in the case of nanoparticle formation—are summed and thereby condensed into and represented kinetically by composite, "pseudo-elementary"[53,54] steps such as the A → B and A + B → 2B two-step minimum mechanism[53] shown in Scheme 4.1. There, the PEStep concept,[53,54] and fast cyclohexene hydrogenation catalysis by the resultant $Ir(0)_n$ nanoparticles, is used to monitor the nanoparticle formation reaction indirectly, but in real time and with thousands of data points from a high-precision, ± 0.01 psig pressure transducer monitoring the loss of H_2 as detailed in Scheme 4.1.

Scheme 4.1. Fast Cyclohexene Hydrogenation Catalytic Reporter Reaction (CHCRR) Monitoring Method and a Minimalistic 2-Step Mechanism[53] Used as a Starting Point for the Analysis of the Kinetics Data

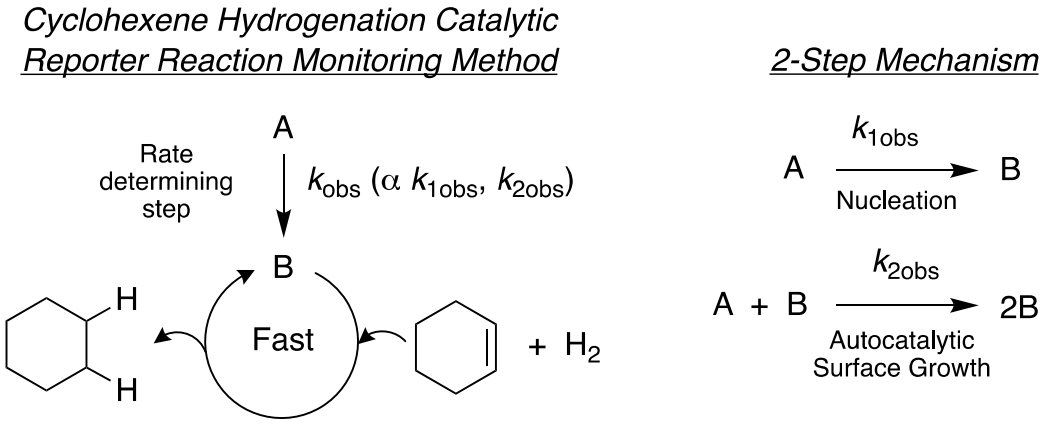

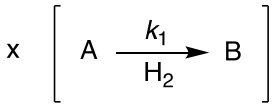

(Eq 4.2)

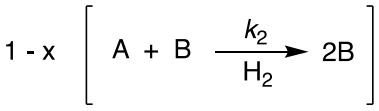

(Eq 4.3)

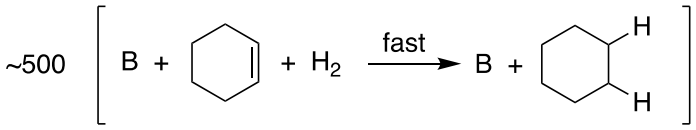

(Eq 4.4)

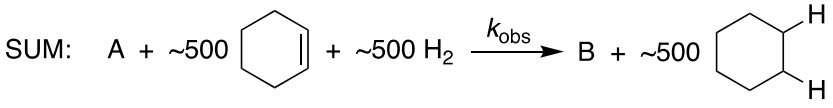

(Eq 4.5)

The mathematical derivation and details behind the use of the above pseudo-elementary steps have been available since 1997.[53] The key part for monitoring the catalytically active particle formation is that eq 4.5 allows one to write the differentials shown in eq 4.6 (i.e., under certain conditions[53],

notably an excess of cyclohexene and H_2 compared to A). Equation 4.6 teaches that one can in turn monitor the loss of H_2 by a pressure transducer due to the fast catalytic hydrogenation of cyclohexene, yet actually *be following kinetically the slow steps of nanoparticle formation*. In the above case in eq 4.1, the slow steps are nucleation (represented minimalistically by the PEStep A → B) and autocatalytic surface-growth (represented minimalistically by the PEStep A + B → 2B). Normally, the excess of cyclohexene to Ir precursor is 500-1500 equivalents, shown as 500 in the denominator of eq 4.6 because that will apply to the studies examined in the present work.

$$\frac{\left(-\frac{d[A]}{dt}\right)}{1} = \frac{\left(+\frac{d[B]}{dt}\right)}{1} = \frac{\left(-\frac{d[Cyclohexene]}{dt}\right)}{500} = \frac{\left(+\frac{d[Cyclohexane]}{dt}\right)}{500} \qquad \text{(Eq 4.6)}$$

That the pseudo-elementary step and CHCRR monitoring methods work at least semi-quantitatively was confirmed first in[53] 1997, and many times since,[55] by (i) control experiments showing that the kinetics are zero-order in cyclohexene (i.e., $[cyclohexene]^0$), so that the hydrogenation reporter reaction step must be fast compared to the nanoparticle formation PESteps of A → B and A + B → 2B. These two PESteps are, then, actually controlling the observed kinetics. Additionally, (ii) controls were done independently monitoring the reaction somewhat more directly via the evolution of cyclooctane (see eq 4.1, *vide supra*), controls that confirm the sigmoidal shape of the kinetic curves and also yielded rate constants within experimental error of those from the CHCRR.[53]

The CHCRR kinetics methodology has since allowed ≥1500 kinetics experiments to be done routinely and in-house by 11 different researchers over a period of ≥23 years. Even though the pseudo-elementary step and CHCRR methodologies have been available since 1997 and have been used and discussed many times before,[53,64] details are presented in Appendix III as a

convenience to the reader who might not be familiar with, or wants to brush up on, the CHCRR and pseudo-elementary step methodologies. We will see that the results obtained herein document that such in-house methods, even if indirect, can be an important addition to and compliment of synchrotron-radiation-based methods.

For some time now, we have had studies in progress striving to test the CHCRR methodology and resultant mechanisms even further, especially as presented herein by more direct, synchrotron-radiation-based methods. In that regard, the present contribution is the result of the multi-year effort that started in 2003 with the synthesis and development of a second generation $\{[(1,5\text{-COD})Ir^{I}\bullet HPO4]_2\}^{2-}$ system[56], *vide infra*, employed herein that over comes the two main limitations of the first-generation $\{(1,5\text{-COD})Ir^{I}\bullet POM\}^{8-}$ system by allowing the use of synchrotron XAFS and SAXS methods. The present contribution is also the result of two separate collaborations using synchrotrons on two continents as well as our on-going collaboration with mathematicians in developing and employing ME-PBM. Perhaps the most interesting question addressed herein is whether or not the 5 physical methods, including 2 synchrotron methods, are sufficient to obtain the more detailed, reliable nanoparticle formation mechanism in a second-generation system studied at the state-of-the-art that includes 5 physical methods, rare knowledge of the nucleation mechanism, as well as checking by ME-PBM.

The Minimum, Disproof-Based Mechanisms for Particle Formation

The primary pseudo-elementary step-based minimum mechanisms for particle formation[47,53,55,57,58,59,60,61,62,63,64] needed to enable ME-PBM and that have been discovered over time using the first generation $\{(1,5\text{-COD})Ir^{I}\bullet POM\}^{8-}$ precursor to $Ir(0)_n\bullet(POM^{9-})_x$ system are shown in Scheme 4.2,[18] illustrated there for that prototype, 1st-generation $Ir(0)_n$ nanoparticle

system. The proposed mechanisms are based on experimentally established, full, balanced reaction stoichiometries (e.g., Scheme 4.2), TEM product vs time data, extensive CHCRR kinetics data, and multiple controls and checks where possible such as cyclooctane evolution kinetics data obtained by GLC.

Scheme 4.2. Deliberately Minimalistic, Ockham's Razor-Obeying Mechanistic Pseudo-Elementary Steps[53,54] for Particle Formation in A (= Precursor), B (= on average "smaller particles"), and C (= on average "larger particles") Generalized Form; Adapted from reference 18 with Permission. Copyright 2019 American Chemical Society.

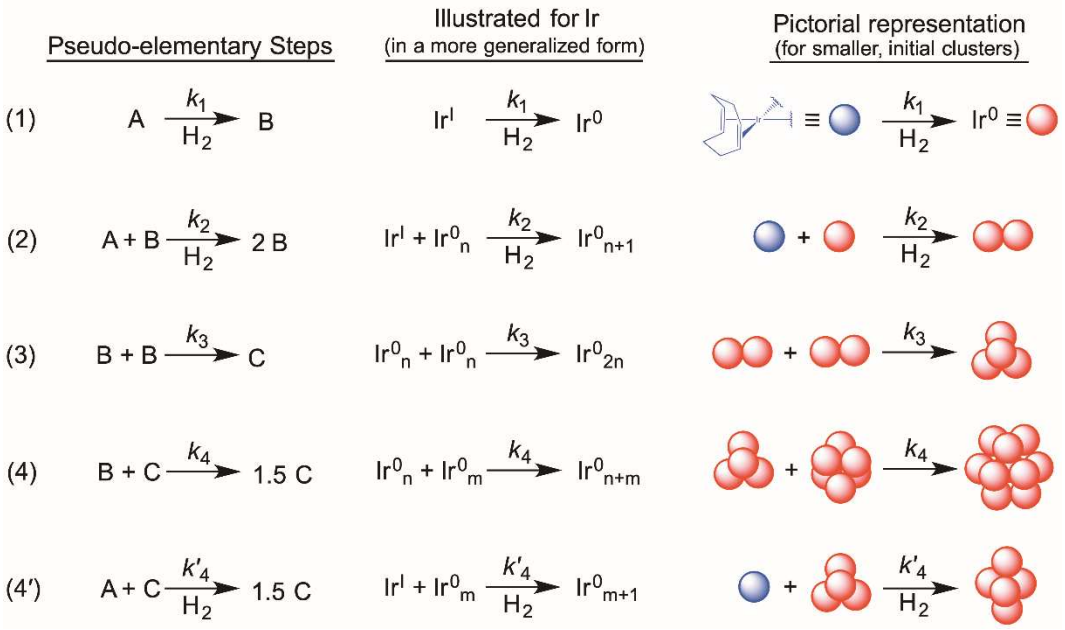

The pseudo-elementary steps presented in Scheme 4.1 were uncovered through the extensive study of the first-generation Ir system,[47,53,55,57,58,59,60,61,62,63,64] and specifically by: (i) elucidating the reaction speciation; (ii) establishing experimentally the balanced reaction stoichiometry; (iii) collecting the TEM-based particle-size distribution; (iv) monitoring the loss of the $Ir^{I}(1,5\text{-COD})^{+}$-containing precursor vs time by GLC (of the hydrogenated cyclooctane formed, as shown eq 4.1); and notably (v) collecting extensive kinetics studies by the CHCRR kinetics

methodology with checking by GLC monitored kinetics, as detailed in Appendix III and utilized herein, *vide infra*.

The significance of the minimum mechanisms in Scheme 4.2 is that they are the first of their kind, and also the first *mechanistic alternatives* to the unsupported[65,66] 1950 LaMer model[67] for particle formation postulating "instantaneous / burst nucleation" and then "diffusion-controlled growth". The minimum mechanisms in Scheme 4.1 serve as the working mechanistic hypotheses going forward for further attempted disproof and *the expected, normal refinement to more complex mechanisms* as is the fate of all Ockham's razor obeying, deliberately initially minimalistic mechanisms (i.e., and once additional data our new methods become available); see the section 2.6 in a recent review[65] for more on this and related points ("2.6. The Critical Difference between a Physical Chemical Model and a Physical Organic Chemistry-Type, Chemical Equation- and Disproof-Based, Reaction Mechanism"[65]). If one writes out the combinations of the PESteps in Scheme 4.1, a new 3-step mechanism discovered by ME-PBM[18,19] (*vide infra*), and includes A. Karim's important ligand-based PEStesp[32,39], along with the established first[53], second[62], and third (termolecular) and "alternative termolecular"[47] nucleation mechanisms, one now has 5 classes containing at least 96 individual mechanisms to try to account quantitatively for one's particle formation reactions.

The simplest, discovered-first, 2-step mechanism[53] contained within Scheme 4.2 and explicitly given back in Scheme 4.1, namely that of A → B (rate constant k_1) and A + B → 2B (rate constant k_2), is especially well-tested in a number of other particle-formation and growth systems across nature, including homogeneous catalyst formation,[68,69,70] heterogeneous catalyst formation,[71,72,73,74] protein aggregation,[75,76,77] solid-state kinetics,[78,79] dye aggregation,[80] and other areas of nature showing "cooperative", autocatalytic phenomena.[81] The use to date of pretty much

any and all applicable physical methods in those >560 citations of the 1997 paper[53] documents that the 2-step mechanism is the best-tested, best-supported, and currently most accepted kinetics model for the *initial* treatment of particle-formation kinetics data at the pseudo-elementary step level for a broad variety of nucleation and growth systems across nature.[43-53,55-81] *However*, it is not yet clear which physical methods are both necessary and sufficient to yield a reliable particle formation mechanism? Additionally, not yet addressed are which physical methods in what combinations are needed to yield what level of precision and especially accuracy in the resultant rate constants?

Mechanism-Enabled Population Balance Modeling: Elucidation of a New, 3-Step Minimum Mechanism in the Original A = {(1,5-COD)Ir^{I}•POM}$^{8-}$ System.

The minimum mechanisms in Scheme 4.2 were further tested in[18] 2019 and[19] 2020 via the development of Mechanism-Enabled Population Balance Modeling (ME-PBM).[18,19] The underlying basis of population-balance modeling (PBM)[82,83,84,85,86,87] is not hard to understand: PBM is a method applicable to any system of countable entities[82] where "a distribution of properties changes in time and perhaps also in space".[84] As described in our 2020 ME-PBM paper, "…for every particle in the dynamic particle distribution ('population') one is simply keeping track of the evolving particle population using the law of mass balance on each and every particle size, thereby, determining the PSD as a function of time, including the key final PSD."[19] Hence, the accumulation of particles of any given size is equal to the input of particles to that size minus the output of particles from that size.[19]

Mechanism-Enabled-PBM builds off of and expands classic PBM by using deliberately minimalistic, extensively disproof-based[15,16] mechanisms of particle formation and agglomeration

(e.g., as back in Scheme 4.1) to guide the construction of the computer code of an also deliberately minimalistic, Ockham's razor-obeying (ME)-PBM. That code takes the minimum mechanisms contained within Scheme 4.2 or the new 3-step mechanism[18,19], one at a time, and uses each mechanism to develop a population-balance modeling code in MATLAB corresponding to—*or more correctly limited by*[18,19]—the minimum PEStep mechanism being used as input and, thereby, being tested in that specific ME-PBM. The resulting computer code is then used (i) to attempt to fit experimental particle-size distribution (PSD) data without any input assumptions about the underlying rate constant parameters or the PSD shape; and therefore (ii) to test the input minimum mechanism in its coded form. The key questions being addressed are (a) "Can the ME-PBM corresponding to a given, minimum mechanism fit the experimental PSD data?"[18,19], and (b) which specific mechanism and corresponding ME-PBM yields the best fit to the experimental PSD?

In our initial ME-PBM studies of the first-generation $\{(1,5\text{-COD})Ir^{I}\bullet POM\}^{8-}$ system, twelve total possible mechanisms were considered[18,19] constructed from the steps in Scheme 4.2 as well as three different, experimentally established nucleation mechanisms,[47,53,62,64] hence a range of 36 possible mechanisms. That work showed *that obtaining a good fit to the PSD is by no means trivial*. Instead, a good fit to the PSD and its shape is a stringent test of the input mechanism as well as the resultant code, requiring input of both the correct nucleation mechanism and an overall correct pseudo-elementary step mechanism ME-PBM code. However, once the "correct" nucleation and growth mechanism were employed in an also error-free code, the resultant *Mechanism-Enabled*-PBM code was able (iii) to fit the PSD, and also (iv) *serve as a check on the proposed mechanism*, as well as somewhat amazingly (v) *extract rate constants from that information-rich PSD*. In addition, in the current ME-PBM model and code, a cut-off parameter, *M*, is obtained that is used to define the "smaller", B, from the "larger", C, particles[18,19], Scheme

4.2, *vide supra*. The ME-PBM derived fit of the PSD, including the PSD shape, proved excellent, all with no prior input to the PSD shape.[18,19] Noteworthy here is that the ME-PBM-based excellent, *quantitative accounting* of the PSD results supports in at least a general way the CHCRR kinetics methodology[47,53-63] used to obtain those minimum mechanisms (i.e., back in Scheme 4.2) as well as the nucleation mechanisms used as input[47,53,62] to the ME-PBM.

The resultant rate constants from ME-PBM fitting of the PSD can then be used (vi) to predict a precursor, A-loss kinetics curve for comparison to the experimental CHCRR curve, the right-most part of Figure 4.1. This illustrates a limit of our current knowledge as well as an impetus for the present synchrotron-based and ME-PBM studies: as shown in the right-most part of Figure 4.1, the predicted A loss curve from the ME-PBM derived rate-constants (from the PSD analysis) vs the experimental CHCRR curves are both sigmoidal, *but not identical*. Hence, additional checking of the CHCRR kinetics by the more direct methods of XANES and SAXS, plus a better understanding of any differences between the various kinetics monitoring methods, are two additional, sub-goals of the present studies.

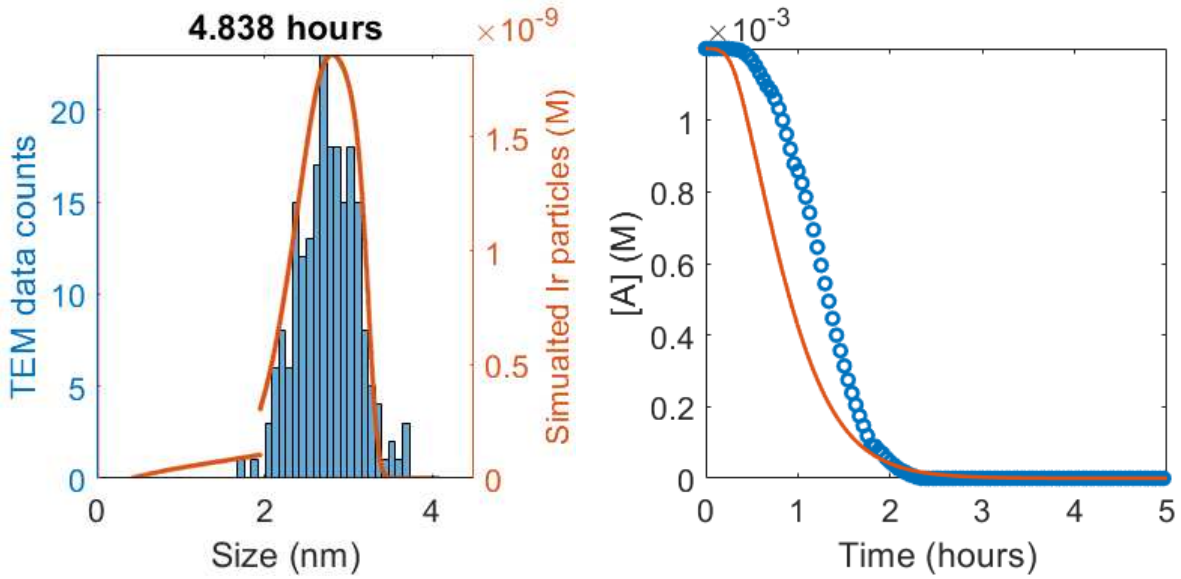

Figure 4.1. Fit of the final, 4.838 h histogram for formation of what are on-average $Ir(0)_{\sim 730}$ nanoparticles in that particular study from ~730 equivs of $\{(1,5\text{-COD})Ir^{I}\bullet POM\}^{8-}$ under H_2 in acetone solvent at 22 °C to yield the final, $Ir(0)_{\sim 730}\bullet(POM^{9-})_x$ nanoparticles. The resultant fit-determined rate constants (that refer to the detatiled kinetics scheme and rate-constant nomeclature in a 2019 ME-PBM paper[19]) are $k_{1alt} = 6.55 \times 10^4\ M^{-2}\ h^{-1}$, $k_2 = 1.65 \times 10^4\ M^{-1}\ h^{-1}$, and $k_3 = 5.63 \times 10^3\ M^{-1}\ h^{-1}$, and B vs C particle-size cut-off, $M = 274$. The fit to the PSD to the left including its shape is excellent, without any prior assumptions about the PSD shape. The computed curve shown to the right for the loss of the precursor A = $\{(1,5\text{-COD})Ir^{I}\bullet POM\}^{8-}$ (i.e., using the rate constants from the fit to the PSD) has the proper sigmoidal shape, but undercuts the CHCRR kientics curve by more than experimental error.

In a very important finding, the ME-PBM was also able to inform the "inverse problem" of what exact minimum mechanism is causing the observables by[18,19] providing a previously unconceived 3-step mechanism. In that new, net 3-step mechanism (that will be important in the present studies, *vide infra*), the A + B → 2B autocatalytic growth step of the 2-step mechanism had to be expanded into two steps, A + B → C (rate constant k_2) and A + C → 1.5C (rate constant k_3), in order to account for the PSD.[18,19] The ME-PBM fit to the observed PSD revealed the seminal insight that $k_2 > k_3$, that is, the finding that "smaller particles grow faster than larger particles"[18,19] *thereby catching up in size with the larger particles* by the end of the reaction.[18,19] This "smaller grow faster than larger" insight in turn provides a *paradigm shift* in the understanding of how narrow PSDs can be formed: there is no need for (unphysical; experimentally unsupported[65,66]) "instantaneous / burst" nucleation as postulated in the 1950 LaMer model[67] for forming putatively "monodisperse" particles. Instead, *near*-monodisperse, (by definition[88] ≤±15%) PSDs can be formed despite the broadening effect of continuous nucleation[53] because the smaller particles grow faster than the larger ones, in the end catching up with them in size.[18,19] The interested reader is referred to two full papers for further details and additional insights and conclusions from the initial application of ME-PBM to the classic $\{(1,5\text{-COD})Ir^{I}\bullet POM\}^{8-}$ precursor and resultant $Ir(0)_n\bullet(POM^{9-})_x$ system.[18,19] It is perhaps obvious why

ME-PBM will be—has to be—employed as part of the present work: it is a now-required test[18,19] of any proposed particle-formation mechanism(s). Can the proposed mechanism yield a ME-PBM able to account quantitatively for the PSD, including its shape? If not, then the proposed mechanism must be incorrect in one or more step(s).

A Second-Generation, $\{[(1,5\text{-COD})Ir^{I}\bullet HPO_4]_2\}^{2-}$, Iridium Nanoparticle System

As noted earlier, we began the development of a second-generation system back in 2003 involving HPO_4^{2-} as a smaller, simpler nanoparticle stabilizer.[56] Work since then, that serves as a foundation for the present studies, include: the synthesis[56,89] of the bimetallic nanoparticle precursor, $\{[(1,5\text{-COD})Ir^{I}\bullet HPO4]_2\}^{2-}$, and the experimentally determined, balanced reaction stoichiometry under H_2 for the formation of HPO_4^{2-}-stabilized $\{Ir(0)_n\bullet(HPO_4)_x\}^{-2x}$ nanoparticles in acetone solvent, eq 4.7.[56,89] Also available are the characterization[56] of the resultant $\{Ir(0)_n\bullet(HPO_4)_x\}^{-2x}$, average $n \sim 150$ nanoparticles as well as the TEM-determined particle-size distributions (PSDs) vs time[64]—PSDs begging for analysis by ME-PBM, *vide infra*.

$$75\ \{[(1,5\text{-COD})Ir^{I}\bullet HPO_4]_2\}^{2-} + 375\ H_2 \longrightarrow Ir(0)_{\sim 150}\bullet(HPO_4^{2-})_x + (150 - x)\ HPO_4^{2-} + 150\ \text{[cyclooctane]} + 75\ H^+ \quad \text{(Eq 4.7)}$$

Although the second-generation $\{[(1,5\text{-COD})Ir^{I}\bullet\mathbf{HPO_4}]_2\}^{2-}$ nanoparticle precursor system provides seven advantages as listed in a footnote,[90] including allowing us to use the direct monitoring methods of XANES and SAXS, one *disadvantage* of even this second-generation system in comparison to the classic $P_2W_{15}Nb_3O_{62}^{9-}$ POM system merits mention upfront: HPO_4^{2-}

is a somewhat less effective stabilizer compared to the large, polyanionic POM^{9-}. Hence, at least two molar equivalents of HPO_4^{2-} are required to avoid the formation of bulk Ir(0) metal.[49,56] This in turn implies that some agglomeration of the resultant $Ir(0)_n\bullet(HPO_4^{2-})_x$ particles is at least possible if not expected, so that the present studies should and will check for agglomeration via the kinetics, PSDs, SAXS and ME-PBMs—in the latter separate ME-PBMs first without, and then with, bimolecular agglomeration, B + B → C, as shown back in Scheme 4.2.

More Intimate Nucleation Mechanism for the $\{[(1,5\text{-COD})Ir^{I}\bullet HPO_4]_2\}^{2-}$ Precursor / $Ir(0)_n\bullet(HPO_4^{2-})_x$ Nanoparticle System Obtained via the CHCRR Methodology

Although CHCRR monitored sigmoidal kinetics of formation of $\{Ir(0)_n\bullet(HPO_4)_x\}^{-2x}$ nanoparticles from the A = $\{[(1,5\text{-COD})Ir^{I}\bullet HPO_4]_2\}^{2-}$ precursor are well-fit by the simple A → B, then A + B → 2B 2-step mechanism,[64] we have shown previously that the constant [A] in the induction period hides higher-order, more complex nucleation mechanisms until and unless one goes looking for them with additional kinetics studies.[47,62,64] The needed studies uncovering the more intimate, molecular nucleation mechanism—that is needed for the ME-PBM—have already been performed for the $\{[(1,5\text{-COD})Ir^{I}\bullet HPO_4]_2\}^{2-}$ precursor system. Specifically, varying [A] and $[HPO_4^{2-}]$ concentration studies allowed the identification[64] of a once-again[47,62] low-molecularity nucleation mechanism, one now first-order in the bimetallic $\{[(1,5\text{-COD})Ir^{I}\bullet HPO_4]_2\}^{2-}$ precursor, but also involving a dissociative prior equilibrium, K_{Diss},[64] Scheme 4.3, now of a HPO_4^{2-} dianion. That dissociative prior equilibrium forms a neutral intermediate, $\{[(1,5\text{-COD})Ir^{I}]_2\bullet HPO_4\}^0$, that the results suggest is kinetically more readily reducible to Ir(0) by H_2, Scheme 4.3, than is the dianionic precursor $\{[(1,5\text{-COD})Ir^{I}\bullet HPO_4]_2\}^{2-}$. That easier reduction makes chemical sense as the intermediate, $\{[(1,5\text{-COD})Ir^{I}]_2\bullet HPO_4\}^0$, is less negatively charged as well as has a more open

structure,[64] features consistent with its more facile reduction to $Ir(0)_n$, likely via precedented $(Ir\text{-}H)_m$ hydride intermediates[47,64].

Scheme 4.3. Published More Intimate Nucleation Mechanism[64] Involving a Dissociative Equilibrium from $\{[(COD)Ir^{I}\bullet HPO_4]_2\}^{2-}$ in Acetone, Based on the $[HPO_4^{2-}]$ Dependence of the Kinetics and ^1H NMR Evidence for the Neutral, $\{[(COD)Ir^{I}(solv)]_2\bullet HPO_4\}^0$ Intermediate.

$$\{[(COD)Ir^{I}\bullet HPO_4]_2\}^{2-} + 2\ solv \underset{}{\overset{K_{Diss}}{\rightleftharpoons}} \{[(COD)Ir^{I}(solv)]_2\bullet HPO_4\}^0 + HPO_4^{2-} \quad \text{(Eq 4.8)}$$

$$\{[(COD)Ir^{I}(solv)]_2\bullet HPO_4\}^0 + HPO_4^{2-} \xrightarrow{k_{3,fast}} Ir(0)_2 + HPO_4^{2-} + 2\ \text{  } + 2\ H^+ + 2\ solv \quad \text{(Eq 4.9)}$$

The effects of common room dust on the nucleation, in the A = $\{[(1,5\text{-}COD)Ir^{I}\bullet\mathbf{HPO_4}]_2\}^{2-}$ system[64] (and also before in the A = $\{(1,5\text{-}COD)Ir^{I}\bullet\mathbf{POM}\}^{8-}$ system[63]) are available as part of our prior studies. Such detailed, approaching molecular-level, knowledge of a nucleation mechanism including the quantitative effects of the common impurity of dust is rare.[47,62] Noteworthy here is that measuring precise much less accurate nucleation kinetics and associated rate constants is notoriously difficult to even $\pm 10^1$. Hence, ideally doing better than $\pm 10^1$, while using multiple, complimentary physical methods, is another, state-of-the-art goal of the present contribution.

Specific Questions Addressed in the Present Study.

With the required background now in hand, we can summarize the focus of the present study by listing the seven specific questions addressed herein:

(1) Are synchrotron-based methods alone, specifically XANES and SAXS, sufficient in the present example to obtain the ostensibly "correct" mechanism according to all the available data? Are synchrotron XANES and SAXS direct methods pretty much fool-proof, or do these generally powerful methods also have limitations?

(2) Does the application of ME-PBM to the TEM-determined PSDs support or refute the best fitting mechanism? Is our recent conclusion, that ME-PBM is a "must use" tool[18,19] prior to publishing any particle formation mechanism, supported[18,19] or refuted?

(3) Will XANES and SAXS obtained kinetics data for the $\{[(1,5\text{-COD})Ir^{I}\bullet HPO_4]_2\}^{2-}$ precursor / $Ir(0)_n\bullet(HPO_4^{2-})_x$ nanoparticle system both be (i) sigmoidal as expected, (ii) well-fit by the 2-step mechanism as is found for the CHCRR and GLC-derived kinetics data? That is, will there (iii) be at least semi-quantitative agreement between the CHCRR, GLC and the more direct kinetic methods of XANES and SAXS?

(4) What level of *quantitative agreement* is there between the rate constants obtained by CHCRR, GLC, XANES and SAXS monitoring methods? What is the implied level of precision and, ideally, accuracy of the resultant rate constants? If there is any disagreement between the various physical methods beyond experimental error, then what is (are) the source(s) of that error?

(5) When looking in more detail at the now well-established, prototype $Ir^{I}(1,5\text{-COD})^{+}$-containing precursor systems,[45-47,50-53,55-64,88-90,91,92,93,94,95,96] what are the known, primary sources of experimental error in measuring accurate nucleation and growth rate constants? What more generally are the error bars on the nucleation and growth rate constants and how do those error bars compare to the most at least precise nucleation and growth kinetics in the literature?[97,98]

(6) What, then, is (are) deemed to be "best" physical method(s) for monitoring especially the notoriously hard to measure nucleation step(s)[62] and to obtain accurate rate constants? What are the strengths and weaknesses of each method, and how can they be used in a complimentary fashion? What roles do indirect, but in-house and hence convenient, methods such as the CHCRR have in comparison to the XANES and SAXS monitoring methods?

(7) Finally, what additional studies are recommended going forward en route towards an even more detailed understanding of particle formation nucleation, growth, and agglomeration across nature?

4.2. EXPERIMENTAL SECTION

Materials.

All solvents and compounds used were stored in a Vacuum Atmospheres inert (N_2) atmosphere drybox (<1.0 ppm O_2, as monitored by a Vacuum Atmospheres continuous O_2-level monitor) prior to use unless otherwise indicated. The following were brought into the drybox as received: $[(1,5\text{-COD})Ir^{I}Cl]_2$ (STREM, 99%), $(Bu_4N)H_2PO_4$ (Aldrich, powder), Proton-Sponge (Aldrich, 99%), $AgBF_4$ (Aldrich, white powder), decane (Sigma-Aldrich), and diethyl ether (Aldrich, anhydrous, high-performance liquid chromatography (HPLC) grade). Outside of the drybox, acetone (Aldrich, for HPLC, 99%) was sparged with argon for ≥10 min, then immediately sealed and transferred into the drybox. Cyclohexene was distilled over Na metal and benzophenone under argon, and then stored in the drybox. Ethyl acetate (Aldrich ≥99.8%, <0.05% H_2O), acetonitrile (Aldrich, 99.8%, anhydrous, H_2O content <0.001%), benzene (Aldrich, anhydrous, 99.8%, stored under inert atmosphere), 2-butanone (Aldrich, ≥99.0 purity) and

dichloromethane (HPLC grade, stored over 4 Å molecular sieves) were degassed as needed prior to storage and use in the drybox. Outside of the drybox, $Bu_4N^+OH^-$ (Aldrich, 40% by mass in H_2O) was stored between 8 and 10 °C in the refrigerator. Deuterated solvents were purchased from Cambridge Isotope Laboratories: chloroform-d_1 (99.8%), acetonitrile-d_3 (99.8%), and acetone-d_6 (99.5%). Argon (>99.9% purity) and H_2 (>99.5% purity) were purchased from Airgas. H_2 has was passed through O_2- and H_2O-scavenging traps (Trigon Technologies) prior to use. Silicon nitride grids (20 nm window thickness) for Transmission Electron Microscopy (TEM) were purchased from TEM Windows and used as received.

Analytical Procedures.

Unless otherwise stated, all synthetic works and reaction solution preparations were conducted in an oxygen- and moisture-free Vacuum Atmospheres nitrogen drybox environment (<1 ppm O_2, as monitored by a Vacuum Atmospheres continuous O_2-level monitor). All air-sensitive samples were stored double bottled inside the drybox. All glassware were dried at ~160 °C for 48 hours to remove residual moisture before being transferred immediately into the drybox antechamber where they cooled under the vacuum of the antechamber and then inside the drybox. **Cyclohexene Hydrogenation Catalytic Reporter Reaction (CHCRR)** experiments were conducted using an in-house, custom hydrogenation set-up detailed *vide infra*. **Gas-liquid chromatograph (GLC)** was conducted using a Hewlett-Packard 5890 series II GC with a flame ionization detector equipped with a 30 m (0.25 mm i.d., 25 μm film) Dowex DB-1 column and coupled to a Hewlett-Packard 3395 integrator. **Transmission electron microscopy (TEM)** experiments were examined with a JEOL JEM2100F transmission electron microscope using silicon nitride grids. **NMR (^{1}H, ^{13}C, and ^{31}P)** experiments were collected on either a Varian Inova

400 MHz or a Bruker Neo 400 MHz spectrometer at 25 °C. **Synchrotron X-ray Absorbance Fine Structure (XAFS)** experiments were performed at the Stanford Synchrotron Radiation Lightsource (SSRL) at beamline 2-2. **Synchrotron Small-Angle X-ray Scattering** (**SAXS)** patterns were collected at the Australian Synchrotron at the SAXS/WAXS beamline.

Preparation of the Iridium Solvate Precursor Complex, $[(1,5\text{-}C_8H_{12})Ir^I(NCCH_3)_2][BF_4]$ and the Stabilizer, $(Bu_4N)_2HPO_4$.

The synthesis of $[(1,5\text{-}C_8H_{12})Ir^I(NCCH_3)_2][BF_4]$ was prepared on the basis of literature methods with small modifications.[96,99] The preparation and characterization details are summarized in the Experimental Section of reference 64. Below is an abridged summary from a comprehensive report available to the interested reader.[64] In a N_2-atmosphere drybox, 3.00 mmol of $[1,5\text{-COD})Ir^ICl]_2$ was dissolved into 43 mL of CH_2Cl_2. After 5 min of stirring, 10 mL of CH_3CN was added to the solution. The solution was stirred for 10 min and turned yellow, and 6.04 mmol of $AgBF_4$ was added to the solution. A white-gray precipitate of AgCl appeared immediately and the solution was stirred for 5 min before it was vacuum-filtered through a Whatman #2 paper. The yellow filtrate was slowly poured into ~200 mL of diethyl ether. Precipitation of fine yellow crystals of $[(1,5\text{-}C_8H_{12})Ir^I(NCCH_3)_2][BF_4]$ occurred instantaneously, and the crystals were collected under vacuum using a 30 mL glass frit. The crystals were transferred and dried in a 20 mL vial under vacuum for 9 h. The synthesis resulted in an 80% yield and exhibited ^1H NMR peaks that matched literature spectral data[99] provided in reference 64.

The preparation of $(Bu_4N)_2HPO_4$ from $(Bu_4N)H_2PO_4$ and $Bu_4N^+OH^-$ in CH_3CN has been extensively studied and reported on by our research group.[64,96] In particular, the Supporting Information of reference 64 contains a series of important control experiments regarding the purity

and identity of the trace impurity, $(Bu_4N)_{4-x}(H_xP_2O_7)$, in the preparation of $(Bu_4N)_2HPO_4$. Briefly, equal molar amounts of $(Bu_4N)H_2PO_4$ and $Bu_4N^+OH^-$ (0.75 mmol and 0.50 mL, respectively) were combined in 4 mL of CH_3CN, stirred for 4.0 h, and placed under vacuum (~125 mmHg) at ~30 °C (temperature of the drybox environment) to remove CH_3CN and H_2O. Total drying time was ~24 h. The purity was ≥92–97%, as determined by ^1H and ^{31}P NMR. A ≤3–8% impurity of $(Bu_4N)_{4-x}(H_xP_2O_7)$ resulted from the well-precedented dehydration reaction[100,101,102,103] that occurs as a function of the drying time the solution spends under vacuum. Three control experiments available in reference 64 demonstrate that the impurity does not affect the reaction kinetics within experimental error.[64] Specifically, (i) increasing the length of drying time resulted in a maximum 10% $(Bu_4N)_{4-x}(H_xP_2O_7)$ impurity, which did not change the k_1 rate constant from when 3-8% impurity was present. Additionally, (ii) deprotonation of the commercially-available $(Bu_3NH)_2(H_2P_2O_7)$ to $(Bu_3NH)_{4y+3x}(P_2O_7)_y(HP_2O_7)_x$ was then added to the reaction mixture at 0.1, 0.2, 0.5, and 1.0 molar equivalent,[64] but did not change the observed kinetics until ≥0.2 molar equivalents (≥20%) were added. Finally, (iii) the kinetics with 0.00, 0.10, 0.25, 0.35, 0.50, and 2.00 molar equivalents of the commercially available diprotonated salt, $(Bu_3NH)_2(H_2P_2O_7)$, were measured, and once again the kinetics only changed when ≥0.25 molar equivalents (≥25%) were added.[64] Hence, at the levels (3-8%) of $Bu_4N)_{4-x}(H_xP_2O_7)$ present in the reaction, no observable effects on the reaction or the kinetics are seen within experimental error as detailed in the supporting information available elsewhere.[64]

Tandem In Situ X-ray Absorption Fine Structure (XAFS) Spectroscopy and Cyclohexene Hydrogenation Catalytic Reporter Reaction (CHCRR) to Monitor Iridium Nanoparticle Formation.

XAFS experiments were performed at the Stanford Synchrotron Radiation Lightsource (SSRL) at Beamline 2-2.[104] A double-crystal Si (220) monochromator was used to collect Ir L_3-edge (11,215 eV) data in transmission mode with a scan duration of 4 min. Reference Ir foil was used for energy calibration. Raw XAFS data files were processed and analyzed in Athena, within the IFEFFIT software package,[105] all in accordance with literature standards in the field of XAFS spectroscopy. Quantitative analysis of Ir L_3-edge XANES were performed by doing a linear combination fit of the change from 11172.5-11312.5 eV with standards as the first and last scans to yield weights of the initial and final phases.[106,107] Experiments were run in a Fischer-Porter (F–P) pressure bottle modified with two windows cut into the borosilicate, each covered with 0.127 mm Kapton film. Culture tube inserts were likewise cut and covered with 0.0254 mm Kapton film. Samples were prepared as detailed in the next section. Concomitantly, hydrogen pressure kinetics were recorded via the Omega pressure transducer. Specifically, reaction solutions were prepared at 5.0 mM $[(1,5\text{-COD})Ir^{I}(NCCH_3)_2][BF_4]$ (20.0 μmols in Ir), 5.0 mM Proton-Sponge (20.0 μmols), and three different HPO_4^{2-} loadings: 1.8, 2.25, and 2.7 molar equivalents per mol of Ir (36.0, 45.0, and 54.0 μmols in HPO_4^{2-}, respectively). Reaction solutions were prepared in 3.33 mL of acetone and 0.67 mL cyclohexene for a total solution volume of 4.0 mL. The F–P pressure bottle was initially pressurized with ~55 psig H_2 gas.

Extended X-ray absorption fine structure (EXAFS) data were collected on the $Ir(0)_n$ product. The Figure S4.1 of Appendix III coplots the Ir(0) black standard along with the $Ir(0)_n$ nanoparticle products from each XAFS experiment that all resemble closely the spectrum of Ir(0) black. Because somewhat accelerated nucleation and growth is observed in our XAFS (XANES) studies (and fouling on the cell windows in our SAXS studies), *vide infra*, precedented X-ray induced radiolysis in XAFS[108,109,110,111,112] and SAXS[113,114,115,116] will be a topic examined in the

Results and Discussion sections. Relevant here is that recent work[106] from one of us shows that a photon flux of ~$3x10^{13}$ photons per second results in an estimated ~10^{15} solvated electrons[117] even when that radiolysis involves the otherwise energetic process, $Zn^{2+} + h\nu \rightarrow Zn^{3+} + e^-$.

Standard Conditions for $Ir(0)_n$ Nanoparticle Formation Kinetics Experiments with Concomitant Cyclohexene Hydrogenation Serving as the Reporter Reaction.

$$n\,[(1,5\text{-COD})Ir^{I}(NCCH_3)_2][BF_4] \;+\; n\,(Bu_4N)_2HPO_4 + n\,PS^{TM} \xrightarrow[\text{Acetone}]{2.5\ H_2}$$

$$Ir(0)_n\bullet(HPO_4^{2-})_x \;+\; (n - x)\,HPO_4^{2-} \;+\; n\ \bigcirc \;+\; n\,(Bu_4N^+)(BF_4^-)$$
$$+\; n\,Bu_4N^+ + n\,PS^{TM}\text{–}H^+ + 2n\,CH_3CN \qquad \text{(Eq 4.10)}$$

Precatalyst solution of 6.0 mM Ir and ~4 molar equiv HPO_4^{2-} was prepared in a drybox by dissolving 8.4 mg $[(1,5\text{-COD})Ir^{I}(NCCH_3)_2][BF_4]$, 42.1 mg $(Bu_4N)_2HPO_4$, and 3.9 mg Proton-Sponge™, (1,8-bis(dimethylamino)naphthalene), in 2.5 mL acetone. The 2.5 mL precatalyst solution plus 0.5 mL of cyclohexene were transferred, while still in the drybox, to a new, 22 × 175 mm^2 Pyrex culture tube containing a new Teflon-coated 5/16 × 5/8 $in.^2$ stir bar via a disposable polyethylene pipette. All non-synchrotron nanoparticle formation and hydrogenation reactions were carried out using a custom-build pressurized hydrogenation apparatus using a Fischer–Porter (F–P) pressure bottle.[53] Nanoparticle formation was monitored indirectly but in real time by the well-precedented cyclohexene hydrogenation catalytic reporter reaction (CHCRR)[53,58,91,92,93] shown in Scheme 4.1. The culture tube with the precatalyst solution was placed in a F–P bottle modified with Swagelok poly(tetrafluoroethylene)-sealed quick-connects, sealed, transferred out of the drybox, and attached with the quick-connects of the hydrogenation line and its computer-interfaced Omega PX621 pressure transducer. Prior to attachment, the hydrogenation line was

kept under vacuum. After attachment, the hydrogenation line was filled with ~55 psig H_2 gas for experiments under SAXS conditions and ~40 psig H_2 gas for experiments under SAXS conditions. The F–P bottle was immersed in a 500 mL water-jacketed reaction flask held at 22 °C by a thermostatic recirculating temperature-control bath (VWR) filled with dimethyl silicon fluid (Thomas Scientific). A total of 14 quick purges with H_2 gas were performed over 3.5 min (1 every 15 s).[53,61,91,92] Following the fourteenth purge, the F–P bottle was pressurized to ~40 psig H_2 over 30 s before vigorous stirring (~900 rpm; to avoid H_2 gas-to-solution mass transfer limitations[118]) was initiated and pressure uptake data were collected every minute using LabView 8.2 (all as before).[53,64] As before, a required correction[55,64] for the initial vapor pressure of acetone and cyclohexene was applied to the data—a correction detailed in the next section. The H_2 loss data was converted to equivalent cyclohexene loss data using the experimentally established, 1 H_2 to 1 cyclohexene reaction stoichiometry.[53,64]

Temperature Re-equilibration and Acetone Solvent Plus Cyclohexene Vapor-Pressure Correction.

Experimentally, after the H_2 pressure flushes, unavoidable cooling by some evaporation, and then pressurization of the F–P bottle to an initial ~40 psig as detailed in the "Standard Conditions…" section just above, the measured pressure *increases* initially[55] by ca. 3 psig before showing a sigmoidal H_2-loss curve, see Figure S4.2 of Appendix III. Hence, the usual[55] correction for this pressure increase due to rewarming of the F–P bottle and solution and any acetone solvent and cyclohexene vapor-pressure additions was made by running the precedented control[55] experiment of combining 2.5 mL of acetone and 0.5 mL of cyclohexene in a new 22 × 175 mm^2 Pyrex culture tube containing a new Teflon-coated 5/16 × 5/8 $in.^2$ stir bar, placing the culture tube

in the F–P bottle, connecting the F–P-bottle to the hydrogenation line, and starting the experiment by the same series of H_2 flushes and then repressurizing to an initial ~40 psig as already described. Triplicate experiments were run to determine the difference between the F–P bottle filled with only H_2 gas and with the solvent mixture, as seen in Figure S4.2. Then, a point-by-point subtraction / correction for the observed pressure increase was applied to the experimental CHCRR H_2-loss data resulting in the final data for that kinetics run, Figure S4.3 as an example. This 19-year-old result and procedure[55] is, however, re-emphasized here because one of the questions addressed by the present work is the precision and accuracy of the nucleation and growth rate constants. The above necessary treatment of the H_2-loss data expands the ±0.05 psig precision-based error in Figure S4.2 as a typical example, ca. 43.00(±0.05) psig – 27.00 (±0.05) psig = 16.00 (± 0.07) psig, hence ±0.07/16 = 0.43%, a negligible source of error compared to the other sources of experimental error (e.g., as will be discussed in the Results and Discussion sections).

Kinetics Data Analysis Using COPASI Numerical Integration.

The resultant data from the CHCRR, as well as that from GLC, XANES, or SAXS monitoring (*vide infra*), were processed using Microsoft Excel, Origin 7, and COPASI.[62,119] Specifically and using the integrated rate equation for the 2-step mechanism, eq 4.11, rate constants (k_{1obs} and k_{2obs}) were extracted by fitting the cyclohexene consumption data. Origin 7 was used to perform the nonlinear least-squares fitting.

$$[A]_t = \frac{\frac{k_{1obs}}{k_{2obs}} + [A]_0}{1 + \frac{k_{1obs}}{k_{2obs}[A]_0} * \exp[(k_{1obs} + k_{2obs}[A]_0)t]} \qquad \text{(Eq 4.11)}$$

As before, only the first half of the cyclohexene consumption data was fit to ensure that the assumptions underlying the CHCRR, notably a zero-order excess of cyclohexene, remain vaild.[53] The curve-fit values of k_{2obs} were corrected by the ratio of [cyclohexene]/[Ir] as the mathematics of the CHCRR require (see elsewhere[53] for details).

Time-Resolved Gas–Liquid Chromatography (GLC) of Cyclooctane (COA) Product: Quantification and Kinetics.

The procedure employed is identical to our previous publication on the $\{[(1,5\text{-COD})Ir^{I}\bullet HPO_4]_2\}^{2-}$ system.[64] Specifically, samples were prepared as detailed in the section above entitled "Standard Conditions for $Ir(0)_n$ Nanoparticle Formation Kinetics Experiments with Concomitant Cyclohexene Hydrogenation Serving as the Reporter Reaction" given on p. 2852 in ref 64. At specific, predetermined times during the hydrogenation, the stirring was stopped, the H_2 pressure was reduced to ~10 psig H_2, and the F–P bottle was returned to the drybox. Inside the drybox, the reaction solution was transferred to a 1-dram vial, where 3 μL of decane were added as an internal standard for the GLC. Approximately 0.5 mL of the reaction solution with the decane (internal standard) was transferred to a different, clean 1-dram vial, removed from the drybox, and used for GLC analysis. A 2 μL sample was injected into the chromatograph. The amount of cyclooctane (COA) was determined by analyzing the relative peak area of COA versus the relative peak area of the decane (internal standard). A calibration curve of known amounts of authentic COA and decane was obtained and then used to determine the equivalents of COA evolved versus the total initial iridium in the sample. The equivalents of COA were divided by the equivalents of initial iridium, and then multiplied by the initial $[Ir]_0$ concentration to yield $[COA]_t$

values plotted as a function of time. The data were then fit using the analytic equation for the 2-step mechanism of slow, continuous nucleation and autocatalytic surface growth, eq 4.11.

In Situ Small-Angle X-ray Scattering and Tandem CHCRR Monitoring of $Ir(0)_n$ Nanoparticle Formation.

Small-angle X-ray scattering (SAXS) was conducted at the Australian Synchrotron at the SAXS/WAXS beamline.[104] Data were collected by a Pilatus-1M detector with a sample-camera length of 0.6 m, collecting photon energy at 18 keV, and an integration time of 5 s. A custom-built reaction cell was built to allow for SAXS as well as tandem CHCRR H_2 pressure loss monitoring of the $Ir(0)_n$ nanoparticle formation reaction; an image of the cell is provided in Figure S4.3, Appendix III. The custom-built reaction cell has modular gas fittings, and it also uses the same quick-connect fittings as the F–P bottle to interface the H_2 line and pressure transducer. The beamline's peristaltic pump system was similarly assembled from Hamilton modular components with syringe pump operations programmed into beamline control. Concomitantly, hydrogen pressure kinetics were recorded via the Omega pressure transducer. Reaction solutions were prepared in an inert atmosphere drybox with an O_2-level ≤5.0 ppm. Each sample consisted of the followed: 54.0 μmols $[(1,5\text{-COD})Ir^{I}(NCCH_3)_2][BF_4]$, 216 μmols $(Bu_4N)_2HPO_4$, 54.0 μmols Proton-Sponge, 5 mL acetone, and 1 mL cyclohexene. The reaction solution (at 9.0 mM Ir and 3.6 molar equivalents HPO_4^{2-} per mol Ir) was transferred into the cell, sealed, taken out of the drybox, and placed in the beam path. Every 76 s, 1 mL of solution as drawn by the peristaltic pump system up to a 1 mm quartz capillary before being returned to the continuously stirred solution. Background measurements were collected to subtract the scattering of both the capillary and solvent, as they were observed to contribute significantly at early reaction times. Despite the

background subtraction, $Ir(0)_n$ particle scattering was convoluted with the solvent scattering at less than 1.0 h and small particle sizes so that usable data resulted only after the first ca. 1 h as detailed in the Results section covering the SAXS experiments.

SAXS Data Processing and Analysis.

The SAXS data processing and analysis were done in accordance with literature standards in the field of small-angle scattering. The SAXS data analysis equation[120,121] employed is given in eq 4.12 where $I(q)$ is the scattering intensity, N is the total number of particles, $\Delta\rho$ is the electron density contrast between the scattering object and the surround matrix, $n(r)$ is the size distribution, $V(r)$ is the volume of an individual particle, $f(qr)$ is the form factor describing the particle shape, and $S(qr)$ is the structure factor describing the particle-particle interactions.

$$I(q) = N(\Delta\rho)^2 \int n(r)V(r)^2 f(qr)^2 S(qr)dr \qquad \text{(Eq 4.12)}$$

To obtain the size distribution as a function of time, several standard assumptions were made. First, due to the low concentration of the sample, particle-particle interactions are assumed to be negligible, so that $S(qr) = 1$. Next, a spherical form factor is assumed. The form is represented as

$$f(qr) = \frac{3[\sin(qr) - qr\cos(qr)]}{(qr)^3} \qquad \text{(Eq 4.13)}$$

and the volume as $V(r) = (4/3)\pi r^3$. Due to the raw SAXS data not being on an absolute scale, the constant prefactor, $N(\Delta\rho)^2$ becomes meaningless, other than as a factor that is proportional to the

number of particles. Next, three distribution functions were compared: log-normal, Gaussian, and Schulz, which are represented respectively as eqs 4.14, 4.15, and 4.16.

$$n(r) = \frac{exp\left(-\frac{1}{2\sigma^2}\left(ln\left(\frac{r}{r_0}\right)\right)^2\right)}{\sqrt{2\pi}*r\sigma} \quad \text{(Eq 4.14)}$$

$$n(r) = \frac{exp\left(-\frac{(r-r_0)^2}{2w^2}\right)}{\sqrt{2\pi}*w} \quad \text{(Eq 4.15)}$$

$$n(r) = Z^Z X^{Z-1} \frac{\exp(-XZ)}{r_0 \Gamma(Z)} \quad \text{(Eq 4.16)}$$

where $w = \sigma r_0$, $Z = \frac{1}{\sigma^2}$, $X = \frac{r_0}{r}$, and $\Gamma(x)$ is the gamma function. Fitting with each distribution function yielded little difference, as shown in Figure S4.4, Appendix III, where the mode of the distributions lies at a radius of approximately 7.5 Å. Ultimately, the Gaussian distribution function was used in the fittings for this report.

Intensity (arb. units) versus q ($Å^{-1}$) data were processed using the Irena software package. Initial attempts to use the full q-range, with the second form factor oscillation, gave rise to an erroneous peak at small particles size. Hence, the q-range fit was limited to the primary form factor feature. The experimental data were fit from the latest times to the earliest times. At 1.5 h and earlier, the dispersion parameter (σ) was fixed at 0.3 (once the intensity of the second form factor feature dropped below 10% of the initial scan). Data before 0.72 h were not fit because the total intensity was less than 10% of the initial scan. Overall, the number of particles, total volume, and pressure transducer signal were collected as a function of time.

Solvent background control scans before and after the reaction revealed some fouling of the cell window due to apparent $Ir(0)_n$ formation. Again, precedented X-ray induced radiolysis is one possible source of this fouling as will be discussed in the Results and Discussion sections.[111,112,113,114]

Time-Resolved Transmission Electron Microscopy Sampling, Grid Preparation, and then Particle-Size Determination.

The procedure employed is identical to our previous publication on the $\{[(1,5\text{-COD})Ir^{I}\bullet HPO_4]_2\}^{2-}$ system.[64] Specifically, samples were prepared as detailed in the section above entitled "Standard Conditions for $Ir(0)_n$ Nanoparticle Formation Kinetics Experiments with Concomitant Cyclohexene Hydrogenation Serving as the Reporter Reaction". All precatalyst solutions for TEM were prepared under XAFS conditions of 5.0 mM $[(1,5\text{-COD})Ir^{I}(NCCH_3)_2][BF_4]$ (20 μmols Ir), 2.25 molar equivalents $(Bu_4N)_2HPO_4$ (45 μmols), and 5.0 mM Proton-Sponge (20 μmols), 3.33 mL acetone, and 0.67 mL cyclohexene. The initial hydrogen pressure employed was 55 psig. At five specific, predetermined times during the hydrogenation (0.75, 1.5, 3.25, 5.0, and 11.0 h), the stirring was stopped, the H_2 pressure was reduced to ~10 psig H_2, and the F–P bottle was returned to the drybox. In the drybox, the remaining H_2 was released from the F–P bottle and the solution was transferred into a new and clean 20 mL scintillation vial. A small, ~0.5 mL aliquot of the solution was transferred to a new 20 mL scintillation vial and was approximately diluted 20-fold by 2-butanone. The use of 2-butanone and the ~1:20 dilution mitigate against aggregation of the nanoparticles on the grids (a valuable experimental "trick" discovered previously via consider experimental effort[64]) for minimizing particle aggregation due to preparation of the TEM grids. Silicon nitride grids were used and

prepared by placing a 1.0 μL aliquot of the 1:20 solution on the grid via a micropipette and allowing excess liquid to evaporate. The grids were fully dried in the drybox environment at ~30 °C for a minimum of 12 h prior to being analyzed by TEM.

Micrographs of dark-field Scanning TEM (STEM) were collected at three or more locations on the TEM grid to ensure each given micrograph was representative of the entire sample. For each sample ≥350 particles were measured for their size. Measuring 200 particles, at a minimum, is necessary for obtaining a reproducible and statistically-relevant average size. Across the 5 samples, 3054 particles were measured. The open-source software ImageJ, a National Institutes of Health sponsored image processing platform (http://rsbweb.nih.gov/ij/), was used to measure particles sizes, as previously detailed.[122]

Mechanism-Enabled Population Balance Modeling (ME-PBM).

ME-PBM was accomplished using a system of ordinary differential equations (ODEs) based on the experimental mechanism as detailed in references 18 and 19. Briefly, ODEs were derived for each pseudo-elementary step in the mechanism and solved using MATLAB's *ode15s* function. The PSDs were fit using MATLAB and the *patternsearch* algorithm. All fittings and simulations were performed on an early 2015 MacBook Pro with an Intel Core i5 processor at 2.7 GHz and 8 GB 1867 MHz DDR3 RAM. The code is freely available on github at the following link: https://github.com/drhandwerk/pbm.

Each mechanism was studied by running 100 iterations of the *patternsearch* algorithm unless the algorithm converged earlier. Fittings were done to the final, end-time histogram, and the integral L^1 norm was used as the objective function with the *trapz* function after interpolating the experimental data and the simulated solution to be on the same domain via *griddedInterpolant*.

The best function value (BFV) is the last result of the objective function with smaller BFVs indicating better agreement between the experimental data and the fit (i.e., smaller BFVs equal better fits). BFVs are reported in all ME-PBM figure captions. The pseudo-elementary step mechanisms employed are given in the Results section of the main text followed by the resulting histogram fit and simulated precursor vs time curve. The systems of ODEs used for each ME-PBM are reported in Appendix III.

Is a Volume vs Surface-Area Correction of the ME-PBM, or Perhaps Any of the Data or Resultant Rate Constants from Any of the Methods of Monitoring the Reaction, Needed to Be Able to Compare the ME-PBM to the Experimental Results?

A question that comes up is if either the ME-PBM, or perhaps any of the experimental data or k_2 rate constants from the various CHCRR, GLC, XANES or SAXS monitoring of the nanoparticle formation reaction, require a volume vs surface area correction? This question arises because the simple 2-step mechanism, A → B, A + B → 2B, as written refers to the *total volume* or *total number* (i.e., also *total concentration*) of B, eq 4.17, yet physically nanoparticle growth (i.e., non-aggregative growth) occurs *only the surface atoms of the particle—that is, only surface Ir(0) atoms can participate in surface autocatalytic growth*, eq 4.18 (or for example in the CHCRR, which is also a surface-catalysis phenomena):

$$-\frac{d[A]}{dt} = +\frac{d[B]}{dt} = k_1[A] + k_{2,T}[A][B]_{Total} \qquad \text{B}_{\text{Total}} \text{ equation, } k_{2,\text{T}} \quad \text{(Eq 4.17)}$$

(where T = total is the total volume or equivalently total number (i.e., total concentration) of B)

$$-\frac{d[A]}{dt} = +\frac{d[B]}{dt} = k_1[A] + k_{2,s}[A][B]_s \qquad \text{B}_{\text{Surface}} \text{ equation, } k_{2,\text{s}} \quad \text{(Eq 4.18)}$$

(where S = surface atoms)

As derived and explained in detail in Appendix III, with a bit of thought several things become apparent, most importantly that: (i) because the particles are growing physically by *surface* growth, all of the physical methods employed are ultimately measuring $[B]_{Surface}$ and, hence, $k_{2,s}$ (and not $k_{2,T}$). However, (ii) the ME-PBM is a total particle number balance, that is a total volume or (total) concentration of product, B, based model. Hence, (only) the ME-PBM needs to be corrected to account for the difference between the ratio of surface monomers / total monomers, as function of the total monomer number, *j*, for the purposes of the ME-PBM (and as coded, as *n* for example was already used for another variable in the code). Just such a *r(j)* = surface monomers / total monomers function is part of the ME-PBM.

The end result is that the kinetics curves and resultant k_2 values from all the physical methods and the ME-PBM are directly comparable as reported, and yield a $k_2 = k_{2,surface}$ value. A table of each method and what k_2 growth constant that method measures (Table S4.3), a derivation and additional equations and discussion are provided in Appendix III.

Effects of Authentic *tetra*-Iridium-Hydride Cluster, $Ir^{I}_4H_4$(1,5-COD)$_4$, On the Particle Formation Reaction: Does Addition of This Model of a Small, Kinetically Effective Nucleus (KEN)[62] Accelerate the Particle-Formation Reaction As Expected?

In the first of two sets of intriguing control experiments, a normal $\{[(COD)Ir^{I}\bullet HPO_4]_2\}^{2-}$ (0.003 M) in 2.5 mL of acetone and 0.5 mL of 1.65 M cyclohexene $Ir(0)_n$ particle formation reaction was run, first, without, and then in a second independent experiment with, the crystallographically (as well as NMR, IR, mass spectrometry, UV-vis, and XAFS) characterized[51,52] , discrete, *tetra*-iridium-hydride cluster, $Ir^{I}_4H_4$(1,5-COD)$_4$ (9×10^{-5} M, 0.25 μmols = ~1.5% by wt in Ir vs $\{[(COD)Ir^{I}\bullet HPO_4]_2\}^{2-}$), added in the second experiment. Both

particle formations and associated CHCRRs were conducted as usual at 22.0 ± 0.1 °C and initial 40 psig H_2. The results of these experiments are given in Figure S4.6 of Appendix III.

Because the above reaction with no added $Ir^I_4H_4(1,5\text{-COD})_4$ produced faster rate constants than normally seen in a set of 12 repeat Standard Conditions $Ir(0)_n$ formation reactions and because COVID-19 restrictions limited our ability to repeat these particular non-essential but interesting control experiments, a second, independent set of two additional $Ir(0)_n$ particle formation control reactions that we could do were performed and proved quite interesting. Those experiments employed $[(COD)Ir^ICl]_2$ (0.003 M) as the precursor with 3 molar equivalents of $(Bu_4N)^+Cl^-$ added to slow the reaction kinetics to a range of *days* rather than hours. The two kinetics runs were performed analogous to those above, without to start and then with, $Ir^I_4H_4(1,5\text{-COD})_4$ (1×10^{-4} M, 0.41 μmols = ~2% by wt in Ir), all under the otherwise identical conditions as above including 22.0 ± 0.1 °C and initial 40 psig H_2. The results of these two additional control experiments are given as Figure S4.7 of Appendix III. Most intriguingly, the reaction without $Ir^I_4H_4(1,5\text{-COD})_4$ took >5 days (≥120 hrs), whereas the reaction *with* $Ir^I_4H_4(1,5\text{-COD})_4$ went to completion within 1 h, an acceleration of more than 10^2.

4.3. RESULTS

Monitoring of the Ir^I to Ir^0 Conversion by X-ray Absorption Near Edge Structure Spectroscopy as Well as by Tandem CHCRR Monitoring

X-ray absorption near edge structure (XANES) spectroscopy was used to monitor the Ir^I to Ir^0 conversion for the $\{[(COD)Ir^I{\bullet}HPO_4]_2\}^{2-}$ system at 5.0 mM Ir and 1.8, 2.25, and 2.7 equivalents of HPO_4^{2-} at the SSRL in a modified Fisher-Porter bottle pressure cell that also allowed tandem monitoring by the indirect CHCRR method. EXAFS data were obtained for the

final $Ir(0)_n$ nanoparticle product (Figure S4.1 of Appendix III). The 4 min-per-scan, XANES kinetics experiments with 5.0 mM and 2.25 equiv HPO_4^{2-} are given below as Figure 4.2.

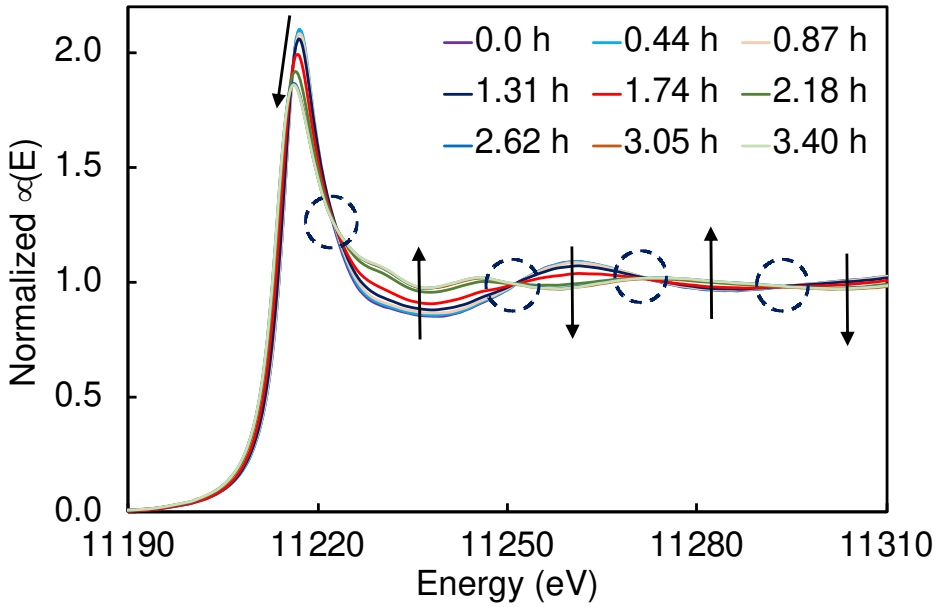

Figure 4.2. XAFS spectra evolution—normalized μ(E) vs energy (eV)—of the Ir L_3-edge as a function of reduction time with 5.0 mM $[(COD)Ir^{I}(NCCH_3)_2][BF_4]$ and 2.25 molar equivalents of $(Bu_4N)_2HPO_4$. The XAFS shows four tight isosbestic points at 11222.7, 11251.2, 11271.9, and 11293.5 eV. A total of 40 spectra were collected over 3.40 h, but only every fifth spectrum is given for visual clarity.

Each spectrum from Figure 4.2 was processed as described in the Experimental section, *vide supra*, to yield the amount of iridium as Ir^{I} vs Ir^{0} as a function of time, Figure 4.3. Concurrently with the XANES measurements, tandem CHCRR data were collected. Next and upon return from the synchrotron, identical but in-house CHCRR experiments were conducted. Further, in-house cyclooctane (COA) evolution by gas-liquid chromatography (GLC) was performed. The four techniques—XANES, Tandem CHCRR, in-house CHCRR, and in-house GLC—are coplotted in Figure 4.3 along with their COPASI-based fits to the 2-step mechanism via eq 4.11, *vide supra*.

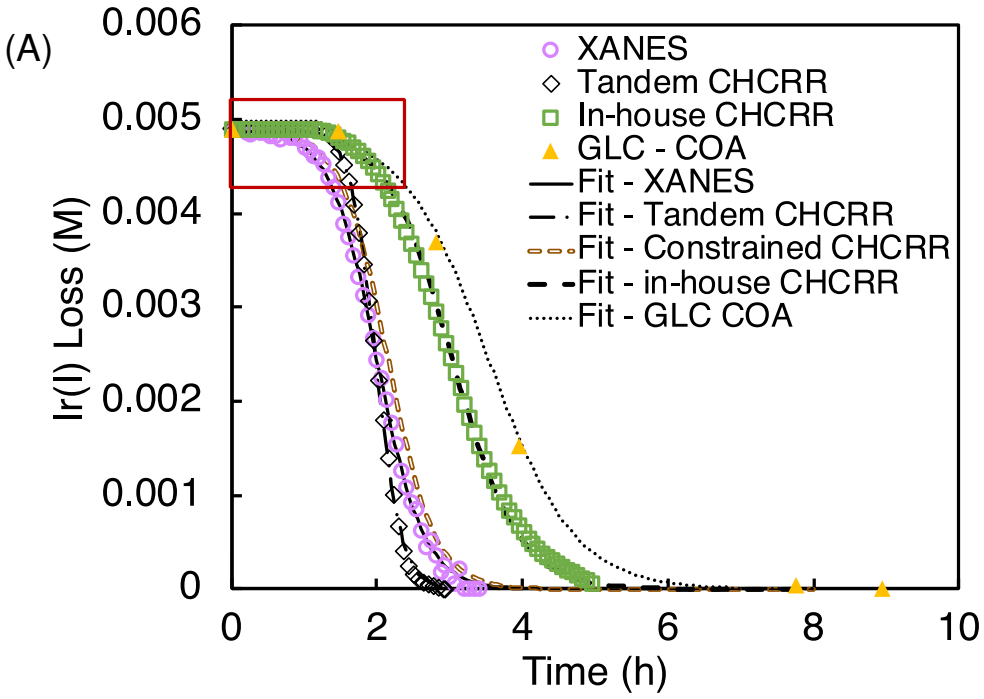
(A)
0.006
0.005
0.004
0.003
0.002
0.001
0
Ir(I) Loss (M)
0
2
4
6
8
10
Time (h)
XANES
Tandem CHCRR
In-house CHCRR
GLC - COA
Fit - XANES
Fit - Tandem CHCRR
Fit - Constrained CHCRR
Fit - in-house CHCRR
Fit - GLC COA

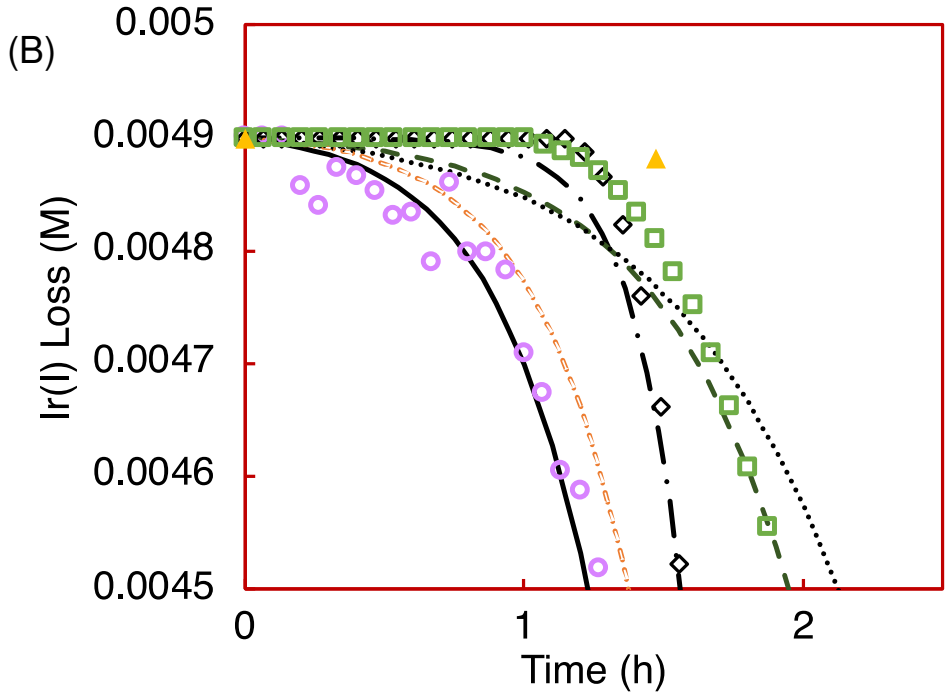
(B)
0.005
0.0049
0.0048
0.0047
0.0046
0.0045
Ir(I) Loss (M)
0
1
2
Time (h)

Figure 4.3. **(A)** XANES (open purple circles), Tandem CHCRR (black open diamonds), in-house CHCRR (open green squares), and $GLC_{cyclooctane}$ (solid gold triangles) kinetics data are co-plotted with their fits to the FW 2-step mechanism (solid, dot-dashed, dashed, and dotted lines, respectively). An additional fit line (brown hallow dash) is given for when k_{2obs} is constrained to the XANES fit value and k_{1obs} is allowed to vary. **(B)** A closer look at the first two hours of the reaction where the majority of nucleation is observed to take place. Experiments were conducted at 5.0 mM $[(COD)Ir^{I}(NCCH_3)_2][BF_4]$ and 2.25 molar equivalents of $(Bu_4N)_2HPO_4$. Additional experiments, with similar kinetic profiles, were conducted at 1.8 and 2.7 molar equivalents of $(Bu_4N)_2HPO_4$ and are reported in Table 4.1. Rate constants for all four experiments under XANES conditions are reported below in Table 4.1. Only every fifth data point from the in-house CHCRR is shown to avoid cluttering the already busy figure.

Table 4.1. Rate Constants from Synchrotron X-ray Absorbance Near-Edge Structure, Tandem CHCRR at Synchrotron, In-House CHCRR, and In-House Cyclooctane Evolution at 5.0 mM $[(1,5\text{-}COD)Ir^{I}(NCCH_3)_2][BF_4]$ and 2.25 Molar Equivalents $(Bu_4N)_2HPO_4$

Methods	k_{1obs} (h^{-1})	k_{2obs} (h^{-1} M^{-1})
XANES[a]	$(6.2 \pm 0.3)\times10^{-3}$	634 ± 5
[Tandem CHCRR[a,c]	$(6.6 \pm 0.3)\times10^{-5}$	1170 ± 6]
[Tandem CHCRR[a,d] (*Reanalyzed* with k_{2obs} constrained)[d]	$(3.9 \pm 0.8)\times10^{-3}$	[634][c]]
Triplicate In-House CHCRR[b]	$(5 \pm 1)\times10^{-3}$	331 ± 28
$GLC_{cyclooctane}$[a]	$(4.2 \pm 0.7)\times10^{-3}$	290 ± 10

[a] Reported rate constant error for k_1 and k_2 is the fitting error.
[b] Reported rate constant error for k_1 and k_2 is the standard error from 3 replicate measurements.
[c] This Tandem CHCRR entry is an outlier according to a z-test of $>\pm3\sigma$ ($>5\sigma$ is observed, *vide infra*) when comparing the triplicate in-house CHCRR and the Tandem CHCRR. A z-test between the XANES and the Tandem CHCRR yielded the same result and, again, a z-tests of k_{1obs} $>5\sigma$, $\sigma = \pm0.001$).
[d] This entry constrains k_{2obs} to the value seen for the tandem XANES of k_{2obs} = 634 h^{-1} M^{-1} to see if the data can still be fit and to see what k_{1obs} value results.

The kinetics curves for all four methods and all five entries in Table 4.1 are sigmoidal, semi-quantitatively similar, but certainly not identical. The Tandem CHCRR, in-house CHCRR,

and $GLC_{cyclooctane}$ monitoring experimental curves are flat within experimental error during the majority of the induction period. Noteworthy is that the *XANES begins an immediate, if slight, downward slope* at the start of the reaction. All four experiments exhibit a sharp downward turn following the induction period and, again, overall sigmoidal shape as expected.

Notable is that the Tandem CHCRR reaction (i.e., done at the same time as the XANES, in the same XAFS-modified Fisher-Porter bottle cell as described in the Experimental section) is distinct from both the (Tandem) XANES and the in-house CHCRR, resulting in an apparent 10^2 difference in k_{1obs} and a 2-fold difference in (compensating, correlated variable[123]) k_{2obs}, Table 4.1. Application of a z-test results in a >5σ difference between the Tandem CHCRR data and either the XANES or the in-house CHCRR data, meaning that the Tandem CHCRR is a statistical outlier by >3σ. If one refits the Tandem CHCRR kinetics with k_{2obs} constrained to the $k_{2obs} = 634\ h^{-1}\ M^{-1}$ from fitting the XANES data, the (compensating, correlated variable[121]) k_{1obs} falls back in line with $k_{1obs} \approx 10^{-3}\ h^{-1}$ values in Table 4.1—although the predicted curve shifts as expected to be more like the XANES curve and is a poorer fit to the CHCRR curve, Figure S4.8 of Appendix III.

When one compares the resultant rate constants from fitting the datasets with the 2-step mechanism (as shown in Table 4.1) but now excluding the Tandem CHCRR >5σ outlier, the XANES, *in-house* CHCRR, and $GLC_{cyclooctane}$ k_{1obs} values are all in at least broad agreement of a factor of ~1.6 fold by just ratioing the largest vs and smallest k_{1obs} entry in Table 4.1 (or, statistically, by a factor of ~1.5 σ, $\sigma = 0.001$ for k_{1obs}). This level of (broad) agreement of k_{1obs} within a fact of ~1.5 (post discarding the Tandem CHRRR outlier) is actually not too bad given that nucleation rate constants are notoriously hard to measure, even to $\pm 10^1$.[63,98,135] The k_{2obs} values are similarly in broad agreement within a range of factor of ~2.2 between the larges vs smallest k_{2obs} value (or, statistically, by a factor of ~1.8 σ, $\sigma = 188$ for k_{2obs}). The average k_{2obs} in Table

4.1 is k_{2obs} = (418 ± 66) h^{-1} M^{-1} and hence approaching error bars closer to what a small molecule chemist might be more comfortable with.

Even though the in-house and Tandem CHCRR are ostensibly the same monitoring method, it seems inescapable that there is some difference in conditions of the two separate experiments despite every effort to keep solvent, cyclohexene, temperature and other conditions identical and despite the effort to construct a near-identical reaction vessel out of a Fisher-Porter pressure bottle (i.e., that differs only in its necessary Kapton windows needed to allow the XANES experiments, as detailed in the Experimental section).

One obvious difference is that the XANES sample is irradiated with high energy X-ray radiation; hence, the possibility exists of well-precedented X-ray induced radiolysis[106,107,108,109,110] being an unwelcome component of the synchrotron X-ray-based methods. Radiolysis can knock electrons off of even Zn^{2+} in ionic liquids or melts to yield e^- (and Zn^{3+})[106,115]. Solvated e^- are strong reductants of course and could easily add to or even start Ir^I reduction, thereby speeding up both nucleation and autocatalytic, exponential, "explosive" growth—consistent with the observed, accelerated sigmoidal kinetics curve CHCRR Tandem to the XANES (as well as the accelerated CHCRR Tandem to the SAXS in the next section). Overall, radiolysis plus at least three other possibilities exist for the quantitative differences in the k_{1obs} and k_{2obs} values seen in Table 4.1. Those possibilities are summarized in a footnote[124] for now, as it will prove useful to have in hand all of the kinetics data obtained by all of the monitoring methods, as well as the average of those k_{1obs} and k_{2obs} values, before addressing possible sources of error in individual measurements by the different methods in the Discussion section.

Monitoring $Ir(0)_{\sim 150}\bullet(HPO_4^{2-})_x$ Nanoparticle Formation by Small Angle X-Ray Scattering

The kinetics of nanoparticle formation were also monitored by *in situ* SAXS in separate experiments done at a separate synchrotron facility with different expert collaborators as detailed in the Experimental section. Note that in the SAXS results shown in Figure 4.4, the concentration of the iridium precursor was necessarily increased from the value in the XANES experiments of 5.0 mM to 9.0 mM in the SAXS experiments in order to better observe particle formation at early times—which we will see still proved insufficient to allow scattering beyond the solvent background sufficient to allow observation of particles smaller than ca. 0.8 nm. The amount of stabilizer was also increased (from 2.25 molar equivalents vs Ir to 3.6 equivs) to slow the reaction to an observable rate at early times, something that is an advantage of the $Ir^{I}(1,5\text{-COD})^{+}$ / HPO_4^{2-} system, namely the ability to prepare in situ and thereby tune the system and its kinetics for the monitoring method at hand. We will, however and in turn, see that the extra equivalents of the HPO_4^{2-} stabilizer has the expected slowing effect on the CHCRR, presumably due to ligand capping of the $Ir(0)_n$ product particles. Additionally, the *in situ* SAXS were necessarily conducted using a custom-built SAXS cell able to handle the H_2 gas reactant, Figure S4.3 of Appendix III, a reactor different than the F-P bottle used in the XAFS and Tandem CHCRR. The different cell and somewhat different reaction conditions naturally comes with the different monitoring methods as one strives to optimize each physical method for the problem at hand.

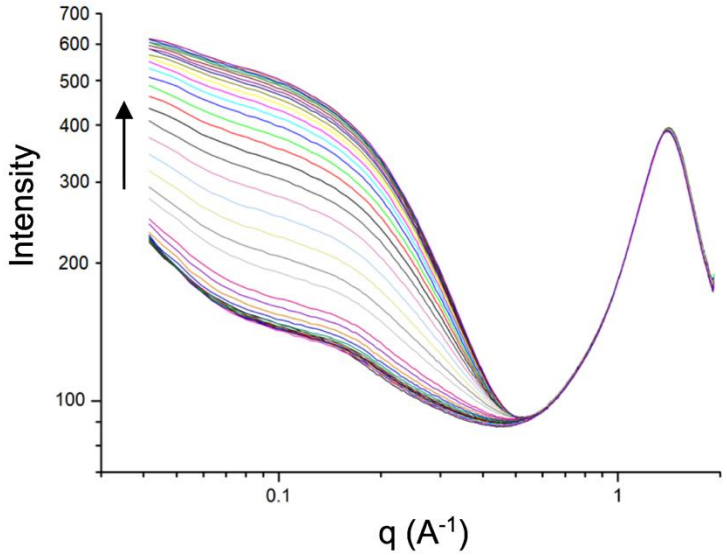

Figure 4.4. Evolution of the scattering intensity by SAXS with intensity plotted against q ($Å^{-1}$). Samples were prepared at 9.0 mM $[(COD)Ir^{I}(NCCH_3)_2][BF_4]$ and 3.6 molar equivalents of $(Bu_4N)_2HPO_4$ in 5.0 mL acetone and 1.0 mL cyclohexene. Data were collected every 76 s over 4 h with the first 1 h proving to be unusable due to solvent interference with small particle scattering.

The intensity versus q data was processed using eq 4.12, described *vide supra* in the Experimental section. The kinetics of nanoparticle volume were extracted from the data and are displayed as smooth, ascending, Ir(0) *formation* concentration versus time sigmoidal kinetics curves, Figure 4.5, because SAXS monitors the formation of $Ir(0)_n$. These formation kinetics were fit by the 2-step mechanism, eq 4.11, as displayed as Figure 4.5.

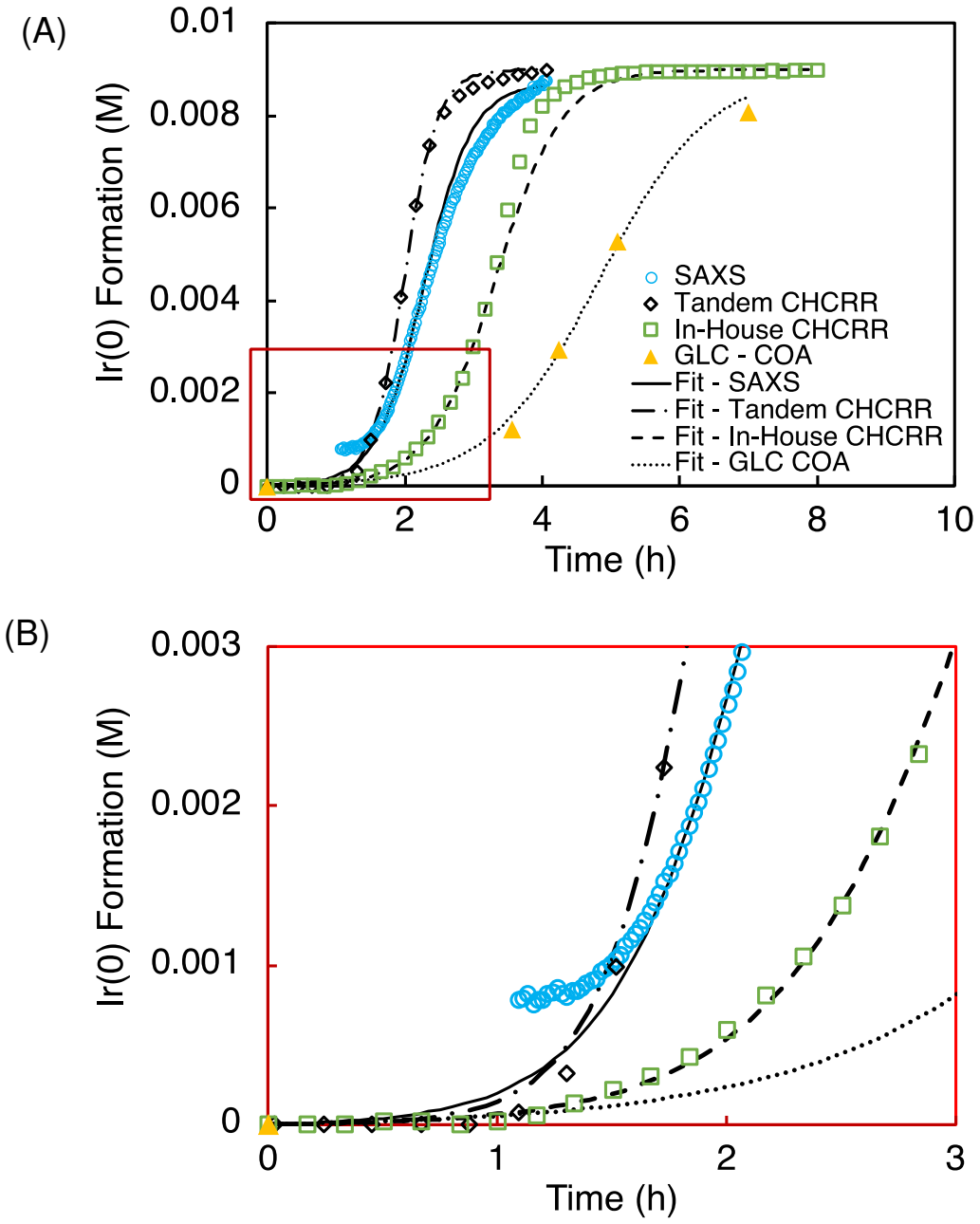

Figure 4.5. (A) SAXS (open blue circles), simultaneously collected Tandem CHCRR (open black diamonds), in-house CHCRR (open green squares), and cyclooctane evolution (solid gold triangles) kinetics data are plotted with their fits to the 2-step mechanism (solid, dot-dashed, dashed, and dotted lines, respectively). **(B)** A closer look at the first three hours of the reaction where the majority of nucleation is observed to take place. Experiments were conducted at 9.0 mM $[(COD)Ir^{I}(NCCH_3)_2][BF_4]$ and 3.6 molar equivalents of $(Bu_4N)_2HPO_4$. Rate constants for all four experiments under XANES conditions are reported below in Table 4.3. For both CHCRR datasets, only every tenth data point is given for visual clarity.

All the curves are sigmoidal and once again in at least broad agreement, save the cyclooctane evolution monitored by GLC that is slowed noticeably and, hence, a bit of an outlier, as discussed more in a moment. Once again, the synchrotron-based data (i.e., now SAXS rather than XANES) comes a bit faster and hence before the in-house CHCRR. Also noticeable is that the Tandem CHCRR done in concert with the SAXS is visually rather different—appearing sooner (faster) than the in-house CHCRR and even undercutting the SAXS data, much like the Tandem CHCRR to the XANES undercut that data back in Figure 4.3. During the SAXS some visually observable fouling of the cell windows occurred as the experiment progressed, presumably insoluble $Ir(0)_n$ formation and plating. Hence, once again X-ray radiolysis-produced e^- reduction and $Ir(0)_n$ formation is possible and, in the case of SAXS, there is visible evidence consistent with some decomposition in the intense x-ray beam.

The expanded part of the kinetics curves showing just the first ca. 3 h, Figure 4.5B, reveals the issue of solvent scattering dominating the signal in the first, ca. 1 hour. This means that nucleation is not well captured by these particular SAXS experiments, which also means that we were unable to obtain a reliable number of particles vs time, an otherwise very valuable part of the SAXS method.

Table 4.2. Rate Constants from Synchrotron Small-Angle X-ray Scattering, Tandem CHCRR, In-House CHCRR, and Cyclooctane Evolution at 9.0 mM [(1,5-COD)$Ir^{I}(NCCH_3)_2$][BF_4] and 3.6 Molar Equivalents $(Bu_4N)_2HPO_4$

Methods	k_{1obs} (h^{-1})	k_{2obs} (h^{-1} M^{-1})
SAXS[a]	$(4 \pm 2)\times10^{-3}$	332 ± 3
Tandem CHCRR[a]	$(1.1 \pm 0.2)\times10^{-3}$	460 ± 3
Triplicate In-House CHCRR[b]	$(2.4 \pm 0.5)\times10^{-3}$	401 ± 85
$GLC_{cyclooctane}$[a]	$(2.9 \pm 0.8)\times10^{-3}$	138 ± 7

[a] Reported rate constant error for k_1 and k_2 is the fitting error.
[b] Reported rate constant error for k_1 and k_2 is the standard error from 3 replicate measurements.

Looking at the results quantitatively by fitting to the 2-step mechanism, the k_{1obs} values in Table 4.2 are all within a factor of 2 of one another, thereby paralleling what was seen for the XANES k_{1obs} values back in Table 4.1. Additionally, the average k_{1obs} for the data in Table 4.2 is $k_{1obs} = (2.6 \pm 1.2) \times 10^{-3}$ h^{-1}, also within a factor of 2 of the average k_{1obs} back in Table 4.1 of $k_{1obs} = (5.2 \pm 0.7) \times 10^{-3}$ h^{-1} (and after discarding the Tandem CHCRR outlier back in Table 4.1). Once again the ~2-fold agreement is not what would make a small molecule chemist happy, but is actually 5-fold better (i.e., only 1/5th of the error) of the $\pm10^1$ that is often seen for nucleation rate constants.[62,98,135]

The k_{2obs} in Table 4.2 are in general agreement, now within a factor of ca. 40% (the first vs second k_{2obs} entries in Table 4.2), other than the cyclooctane evolution k_{2obs} (which is a factor of ~3.3 off from the largest k_{2obs} in Table 4.2, beyond what is normally seen in comparison to the in-house CHCRR for example). The average k_{2obs} for the SAXS data in Table 4.2 is $k_{2obs} = (332 \pm 120)$ h^{-1} M^{-1}, an average k_{2obs} value that is pleasingly within 25% of (and thereby well within

experimental error of) the average k_{2obs} in Table 4.1 of k_{2obs} = (418 ± 66) h^{-1} M^{-1}, and post discarding the Tandem CHCRR outlier back in Table 4.1.

Global Fitting of the XANES Table 4.1, Then SAXS Table 4.2, and Then Combined Tables 4.1 and 4.2 Data to Obtain $k_{1obs,avg}$ and $k_{2obs,avg}$ and $k_{1obs,global\ avg}$ and $k_{2obs,global\ avg}$ Rate Constants

Overall, from the SAXS plus the XANES kinetics, along with the supporting CHCRR and GLC kinetics, one can conclude that: (i) the basic sigmoidal shape is seen in all kinetics curves, (ii) that a minimal 2-step mechanism can be used to extract nucleation k_{1obs} and autocatalytic surface growth k_{2obs} rate constants, but (iii) that individual kinetic runs monitored by different methods can produce k_{1obs} as well as k_{2obs} values that differ by up to a factor of ~2 or a bit more.

As a zeroth-order treatment of the kinetics data, one can compute the average of all the results in Table 4.1 for k_{1obs} and then k_{2obs} (again sans the entry 2 outlier) and then, separately, all of the k_{1obs} and then k_{2obs} data in Table 4.2. For the Table 4.1 data, a global average $k_{1obs(avg,Table4.1)}$ = (2.2 ± 0.3) × 10^{-2} h^{-1} and $k_{2obs(avg,Table4.1)}$ = (3.7 ± 0.1) × 10^{2} h^{-1} M^{-1}. For the Table 4.2 data, the global average $k_{1obs(avg,Table4.2)}$ = (1.7 ± 0.2) × 10^{-2} h^{-1} and $k_{2obs(avg,Table4.2)}$ = (2.0 ± 0.1) × 10^{2} h^{-1} M^{-1}. Plots of the Table 4.1 and then Table 4.2 experimental data in comparison to the global average fits are shown in Figure 4.6. A summary of the global fit k_{1obs} and k_{2obs} values is shown in Table 4.3, along with the results of a global fit to all the kinetics data from Tables 4.1 and 4.2 combined.

(A) (B)

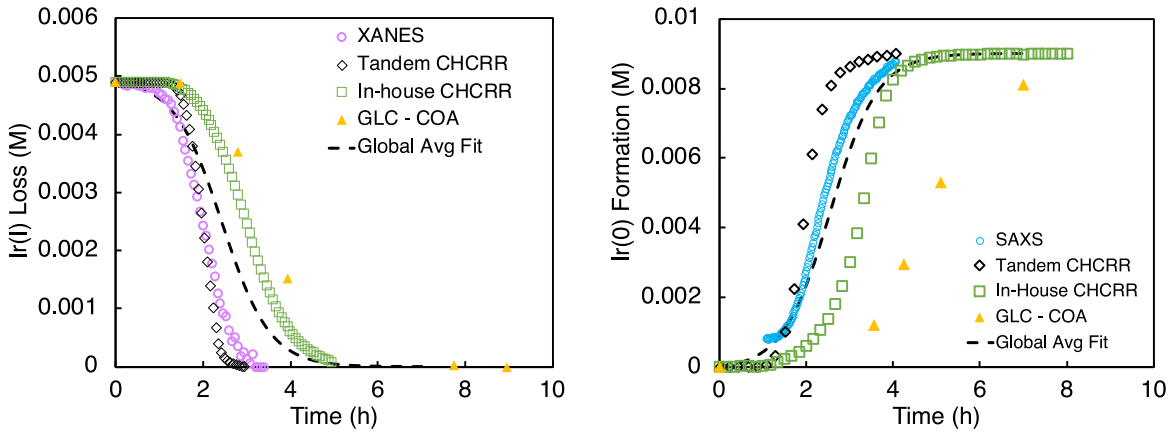

Figure 4.6. **(A)** Data reproduced from main text Figure 4.3A. A global fit of the data was performed and is given as a dashed black line. Resultant rate constants are $k_{1obs(avg,Table4.1)} = (2.2 \pm 0.3) \times 10^{-2}$ h^{-1} and $k_{2obs(avg,Table4.1)} = (3.7 \pm 0.1) \times 10^{2}$ h^{-1} M^{-1}. **(B)** Data reproduced from main text Figure 4.5A. A global fit of the data was performed and is given, again, as a dashed black line. Resultant rate constants are $k_{1obs(avg,Table4.2)} = (1.7 \pm 0.2) \times 10^{-2}$ h^{-1} and $k_{2obs(avg,Table4.2)} = (2.0 \pm 0.1) \times 10^{2}$ h^{-1} M^{-1}.

Table 4.3. Summary of the $k_{1obs,avg}$ and then $k_{2obs,avg}$ Values from a Global Fitting of the Kinetics Data in Table 4.1, Table 4.2, and Then Tables 4.1 and 4.2 Combined

Data Source	**$k_{1obs,avg}$ (h^{-1}) (% std deviation)**	**$k_{2obs,avg}$ (h^{-1} M^{-1}) (% std deviation)**
Table 4.1 Data[a] (XANES + Other Methods)	$(2.2 \pm 0.3) \times 10^{-2}$ (±14%)	$(3.7 \pm 0.1) \times 10^{2}$ (±3%)
Table 4.2 Data[b] (SAXS + Other Methods)	$(1.7 \pm 0.2) \times 10^{-2}$ (±12%)	$(2.0 \pm 0.1) \times 10^{2}$ (±5%)
All the Data (i.e., Tables 4.1 and 4.2 Data Combined)[c]	$(1.5 \pm 0.1) \times 10^{-2}$ (±7%)	$(2.4 \pm 0.1) \times 10^{2}$ (4%)

[a] As detailed in the Experimental Section, these experiments refer to the specific conditions of 5 mM $[\{[(COD)Ir^{I}\bullet HPO_4]_2\}^{2-}]$ and 2.5 added equivs of HPO_4^{2-}, as well as the initial ~1.65 M cyclohexene and ~55 psig H_2 of the experiment and associated CHCRR.

[b] As detailed in the Experimental Section, these experiments refer to the specific conditions of 9 mM $[\{[(COD)Ir^{I}\bullet HPO_4]_2\}^{2-}]$ and 3.6 added equivs of HPO_4^{2-} as well as the initial ~1.65 M cyclohexene and ~40 psig H_2 of the experiment and associated CHCRR.

[c] Combining these data, given their slightly different reaction conditions, is another zeroth-order approximation that effectively assumes that there is minimal further dependence of either k_{1obs} and k_{2obs} within the 5-9 mM range of initial $[\{[(COD)Ir^{I}\bullet HPO_4]_2\}^{2-}]$ and minimal further dependence of either k_{1obs} and k_{2obs} within the 2.5-3.6 range of added equivs of HPO_4^{2-}. However, evidence that these assumptions are acceptable for the purposes of the present work and within the reported error bars of the resultant rate constants is provided by Figures 4, 5, and S8 available in a 2019 publication.[64]

Combining all the kinetics data (1,178 total data points) overlooks possible issues of different precision or errors or amounts of data for the various methods—that is, is truly a zeroth-order approximation. However, combining the data does yield an average curve that visually accounts for the (average) data, and does have the expected effect of lowering the resultant error bars while

yielding the global-average estimates of $k_{1obs,global\ avg} = (1.5 \pm 0.1) \times 10^{-2}\ h^{-1}$ and $k_{2obs,global\ avg} = (2.4 \pm 0.1) \times 10^{2}\ h^{-1}\ M^{-1}$ of relative estimated precisions ±7% and ±4%, respectively. A section in Appendix III contains details on how the composite data were combined and treated, as well as Figure S4.9 that shows the fitted, global-average kinetics curve vs all of the input data. These $k_{1obs,global\ avg}$ and $k_{2obs,global\ avg}$ values are presently our most precise, and given the multiple (four) monitoring sources employed arguably also our most accurate, estimates of the rate constants for the nucleation and autocatalytic surface-growth PESteps of the 2-step particle-formation mechanism.

Collection of Transmission Electron Microscopy-Determined Particle Size Distributions Versus Time

Under the same specific conditions as the XANES experiments, samples of the $Ir(0)_n$ nanoparticle product were collected at four times throughout the reaction and examined by STEM. The particle size distributions at 1.5, 3.25, 5.0, and 10.0 h are given in Figure 4.7. The average diameter, average nuclearity, and polydispersity at each time point are given in Table 4.4.

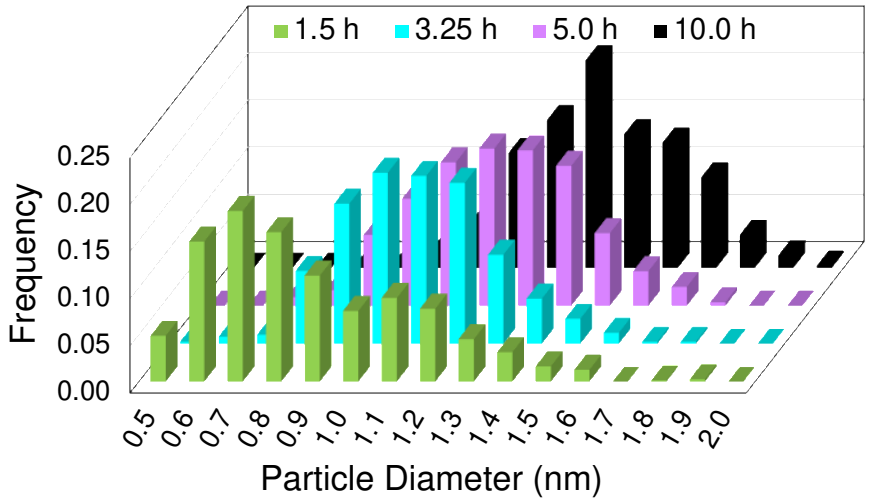

Figure 4.7. Particle size distributions for the formation of $Ir(0)_n$ nanoparticles at 1.5 h (green), 3.25 h (teal), 5.0 h (purple), and 10.0 h (black). At each time point, a new reaction solution was prepared of 5.0 mM $[(1,5\text{-COD})Ir^{I}(NCCH_3)_2][BF_4]$ in the presence of 2.25 molar equiv of $(Bu_4N)_2HPO_4$ in 3.33 mL acetone and 0.67 mL cyclohexene at 22.0 ± 0.1 °C. Each data point represents >450 measured particles; across the 4 samples >2700 particles were measured and binned in 0.1 nm bins.

Table 4.4. Summary of Time-Resolved STEM Under XANES Conditions, 5.0 mM Ir and 2.25 Molar Equivalents $(Bu_4N)_2HPO_4$

Time (hours)	Average Diameter (nm)	Average Nuclearity	Dispersity (%)
0.75	0.7 ± 0.4	13	56%
1.5	0.9 ± 0.3	26	30%
3.25	1.1 ± 0.2	55	19%
5.0	1.2 ± 0.2	68	17%
10.0	1.4 ± 0.2	150	14%

Ex situ STEM measurements show the rapid growth of particles past (i.e., larger than) the kinetics-determined Kinetically Effective Nucleus (KEN)[62] of $Ir(0)_2$. By 0.75 h, the average particle size is ~$Ir(0)_{13}$. At 1.5 h where the induction period is over (i.e., in most of the kinetics curves in Figures 4.3 and 4.5, regardless of the monitoring method used), the average particle nuclearity is ~26. Hence, one can say that a Catalytically Effective Nucleus (CEN)[92] of ≤26 is for sure formed by the end of the 1.5 h induction period that can perform the hydrogenation catalysis required for the CHCRR. Additionally, the finding of a KEN of just Ir_2[64] able to reduce / hydrogenate additional $(1,5\text{-COD})Ir^+$ moieties to Ir(0) and cyclooctane implies that the CEN starts with Ir_2.

The growth continues to, on average, the next magic number size, ~$Ir(0)_{55}$, at ~3.25 h. Growth stops at an average within error of the next, third (Ir_{147}) magic number, $Ir(0)_{\sim 150}$, with HPO_4^{2-} stabilizer ligand-capping as an almost surely important chemical component of attaining that relatively small, ~1.4 nm average-size particle that does not agglomerate to larger particles.

Importantly, as the *size increases*, the distribution *narrows with a size-focusing 4-fold decrease in polydispersity* from an initially observed ±56% to a final ±14%, near-monodisperse[88] (defined as ±≤15%)[88] PSD.

An interesting question when scrutinizing the STEM data in Figure 4.7 and Table 4.4 is if one can discern any evidence for initial "small" (B) particle agglomeration, B + B → C, as one might expect given the finding that "smaller particles are more reactive", at least in surface autocatalytic growth.[18,19] Intriguingly, the first, green-labeled PSD in Figure 4.7 shows a bimodal distribution of particles centering at ~0.75 nm ($Ir_{\sim 13}$ on average) and then at ~1.1 nm ($Ir_{\sim 55}$ on average), as well as substantial numbers of particles at ~0.9 nm ($Ir_{\sim 26}$ on average), for example. Hence, it is certainly possible that $Ir_{\sim 13}$ particles undergo aggregative dimerization to form ca. $Ir_{\sim 26}$ particles that themselves could dimerize to ca. $Ir_{\sim 55}$ particles. But, such "eye-ball" analysis of the data does not demand this, so that ME-PBM first without, and then with, aggregation à la B + B → C in the code will be needed to test if aggregation is a needed part of the mechanism. That said, one can reasonably infer that the ~0.75 nm, on-average $Ir_{\sim 13}$ could qualify as "B", smaller average-size particles while the ~1.1 nm, on-average Ir~55 might qualify as the "C", larger average-size particles in terms of the generalized "A, B, C" nomenclature of the minimal mechanisms summarized back in Scheme 4.2. This can be checked by the ME-PBM, that yields a B vs C cut-off parameter (M), that is predicted by the above analysis of the TEM to be between M = 13 to 55. Looking ahead, the best fitting ME-PBM to the PSD data reported herein yields M = 23, *vide infra.*

Fitting the Kinetics Data to the New, 2019 3-Step Mechanism Allowing Size-Dependent Surface Growth[18]

We know from published experience[45-64] (i) that the 2-step mechanism used so far is the best place to start to analyze and compare the kinetics data the various kinetics monitoring methods, consistent with (ii) statistical and mathematical considerations teaching that it is generally easier to determine precisely as well as accurately fewer compared to more parameters, for example 2- compared to 3- or 4- rate-constant parameters. And, in any rigorous approach to determining mechanism, (iii) one must always obey Ockham's razor and add more steps and details to the mechanism only as additional data and evidence demand (see section 2.6 elsewhere[65] for a discussion of a rigorous, stepwise approach to the mechanisms of more complicated reactions).

However, we can predict with confidence based on our 2019 and 2020 ME-PBM work[18,19] that the 2-step minimum mechanism employed to this point *will not be sufficient to account for the observed PSD*—a prediction confirmed in an upcoming ME-PBM section. We can also predict from that ME-PBM work[18,19] that the new, net 3-step mechanism discussed in the Introduction and shown which allows for size-dependent growth is the minimum mechanism that may be able to account for the observed PSD and, therefore, needs to be examined next.

Hence, we attempted fits of the Figure 4.3 and Figure 4.5 kinetics data form the XANES and SAXS studies, respectively, to the new 3-step mechanism, eq 4.19, employing as usual the numerical integration package COPASI[117], with the expectation that (i) a good if not better fit would result, but (ii) that determining precisely and additional, now 3 total rate constant parameters might prove challenging with the relatively limited amount of data from XANES or SAXS.

$$A \overset{k_1}{\rightarrow} B \qquad \text{(Eq 4.19-i)}$$

$$A + B \overset{k_2}{\rightarrow} C \qquad \text{(Eq 4.19-ii)}$$

$$A + C \overset{k_3}{\rightarrow} 1.5\ C \qquad \text{(Eq 4.19-iii)}$$

The fits using the new, 3-step mechanism to the XANES kinetics data (from Figure 4.3) and the SAXS kinetics data (from Figure 4.5) are shown in Figures 4.8A and 4.8B. The fits are very good, as expected since the 2-step mechanism fits these kinetics curves and we now have one additional rate-constant (fitting) parameter.

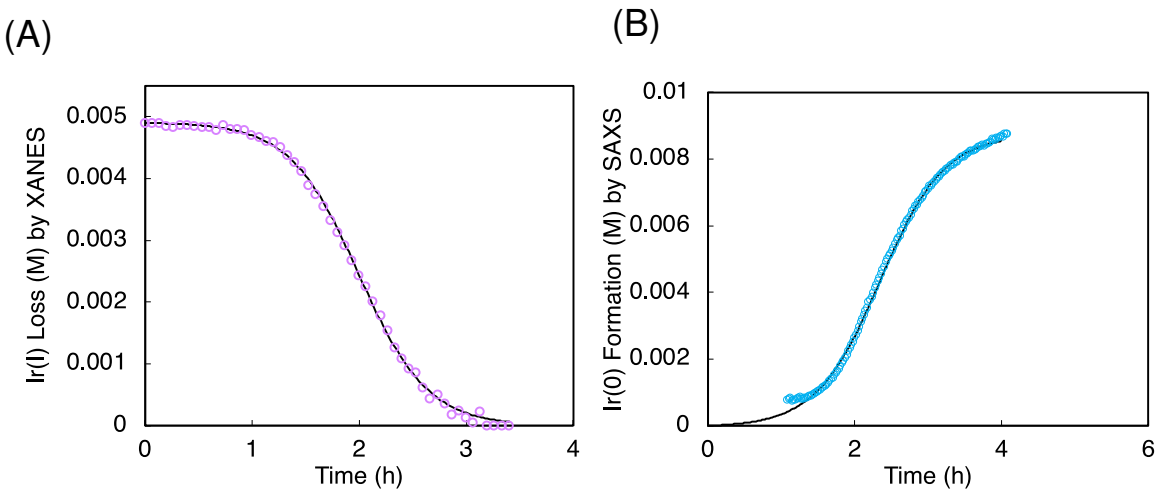

Figure 4.8. (A) Ir(I) concentration loss from XANES measurements (open purple circles) versus time data and fit using the new 3-step mechanism (solid black line). **(B)** Ir(0) concentration formation from SAXS measurements (open blue circles) versus time data and fit to the new 3-step mechanism (solid black line). The rate constants resulting from the fits are provided in the main text.

The resulting rate constants and fit error estimates for the XANES data are: $k_{1obs} = 0.0031 \pm 0.0002$ h^{-1}, $k_{2obs} \sim 3 \times 10^6\ h^{-1}\ M^{-1}$, and $k_{3obs} = 1270 \pm 20\ h^{-1}\ M^{-1}$. The resulting rate constants and fit error estimates for SAXS are: $k_{1obs} \sim 0.005\ h^{-1}$, $k_{2obs} \sim 6 \times 10^6\ h^{-1}\ M^{-1}$, and $k_{3obs} = 522 \pm 3\ h^{-1}\ M^{-1}$.

Several results from these fits merit noting: (i) the k_{1obs} value for the XANES data where there are data during the induction period is within 2-fold of the $k_{1obs,global\ avg} = 1.5 \times 10^{-2}\ h^{-1}$, a reassuring result; (ii) in both cases, the $k_{2obs} > k_{3obs}$ so that the "smaller grow faster than larger" finding[18,19] is once again observed / supported, a second noteworthy result; but (iii) that for both sets of data the k_{2obs} is not well determined to within even $10^{\pm1}$, a problem we have run into before once one has 3-4 rate constant parameters.[60] Nevertheless, a key result for the purposes of the present study is (iv) that the 3-step mechanism merits high priority for testing by ME-PBM, as will be done in the next section and after a look first at the ME-PBM for the 2-step minimum mechanism.

Mechanism-Enabled Population Balance Modeling Fitting of the TEM-Determined Particle Size Distribution: A Further, Demanding Test of the Proposed Mechanism

Although reported only in 2019,[18,19,94] Mechanism-Enabled Population Balance Modeling (ME-PBM) has already proved to be a critical new tool for testing any proposed mechanism of particle formation. Indeed, our prior work led to the preliminary conclusion as a working hypothesis that "no mechanism of particle formation should be published without testing of and input from the information-rich PSD via ME-PBM".[18]

Hence, it is of considerable interest to test, in at least an initial way, the proposed mechanism via ME-PBM-based fitting and rate constant extraction from the experimental TEM data back in Figure 4.8. The goal of the initial ME-PBM analysis that follows is primarily (i) to see if the 2-step minimum mechanism, which proved capable of fitting the CHCRR, GLC, XANES, and SAXS data, is, however and as expected[18,19], *not* able to account for the PSD because the 2-step mechanism does not allow size-dependent growth;[18,19] and then (ii) to see if the new 3-

step mechanism discovered in 2019 can fit the PSD, or (iii) will ME-PBM indicate that some additional step, for example agglomeration of "smaller" particles, B + B → C, as hinted at in an "eye-ball analysis" of the TEM-determined PSD, be required to fit the observed PSD? A full ME-PBM analysis, complete with Bayesian inversion statistical analysis and estimates of the reliability of and error bars on the ME-PBM-derived rate constants, is also underway and will be reported in due course.

2-Step Mechanism-Based ME-PBM.

To start, our expectation that the 2-step mechanism will *not* be able to generate the observed PSD was tested by an attempted ME-PBM fitting of the final PSD after 10.0 h shown in Figure 4.7. We employed the MATLAB code[18,19] developed from the 2-step mechanism shown back in Scheme 4.3, eqs 4.8 and 4.9, code which is archived and readily available to anyone that wants it via GITHUB, as detailed in the Experimental section.

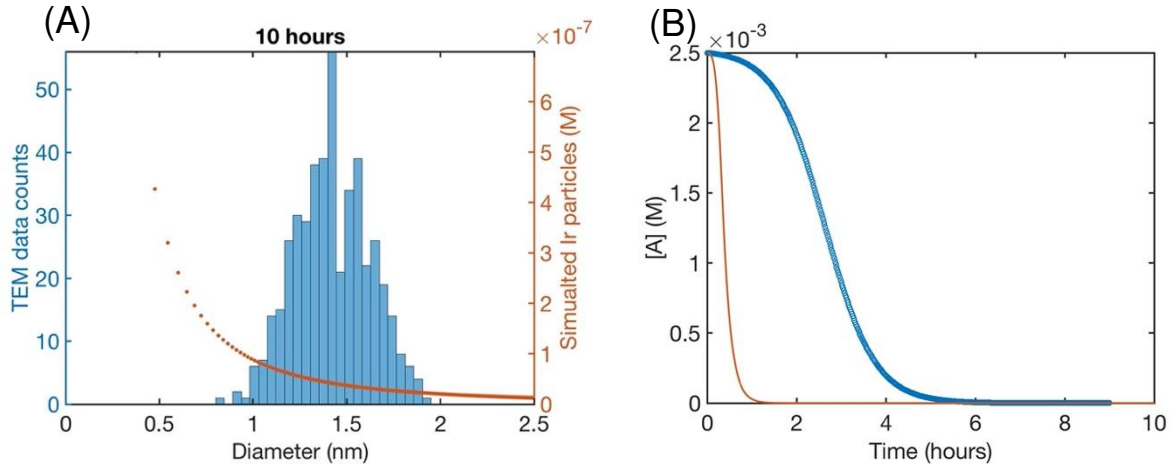

Figure 4.9. (A) Attempted fit to the end-time, 10.0 h histogram using ME-PBM built off of the 2-step mechanism, but while also including the experimentally determined nucleation mechanism in the code so as to give the attempted fit the best chance of succeeding. No fit that is even close to the data is seen; the Best Function Value (BFV)[18,19] is also a relatively high 90.0 indicating a poor fit (lower BFVs indicate better agreement between the fit and the experimental data[18,19]). The resultant fit-determined rate constants (that refer to Scheme S4.1) are as follows: $k_{+Diss} = 4.0 \times 10^{-1}$ h^{-1} M^{-2}, $k_{-Diss} = 3.7 \times 10^{4}$ h^{-1} M^{-1}, $k_1 = 6.6 \times 10^{-1}$ h^{-1}, $k_2 = 9.2 \times 10^{3}$ h^{-1} M^{-1}, meaningless rate

constants given the poor fit. However, the rate constants are provided here only because they are used to generate the predicted precursor loss curve discussed next. **(B)** Calculated precursor loss, $[A]_t$, using the "best-fit" rate constants parameters from the above attempted fit to the PSD, are co-plotted with the experimental $[A]_t$ data from the global fitting of all $[A]_t$ loss data (see Figure S4.9 of Appendix III). The attempted fit to the PSD (left) and the attempted simulation of the CHCRR curve (right) are both totally inadequate. The clear implication is that, as before,[18,19] the 2-step mechanism, while able to quantitatively account for all the kinetics data examined up to this point *including all of the synchrotron kinetics data*, is insufficient to be able to account in even a crude manner for the PSD.

Figure 4.9 confirms the anticipated result,[18,19] that the 2-step mechanism cannot fit the PSD at all, not even when including the experimentally determined nucleation mechanism. This is as expected[18,19], at a minimum one needs *size-dependent growth* as in the new 3-step mechanism to be able to fit PSDs of at least the $Ir(0)_n$ systems examined to date,[18,19] and in all probability more generally to fit PSDs in other systems as well.[18,19]

New 3-Step Mechanism-Based ME-PBM.

We quickly turned our attention next to trying a ME-PBM based on the recently discovered 3-step mechanism[18,19], while also including the experimentally determined nucleation mechanism shown back in eqs 4.8 and 4.9. Recall that the 3-step mechanism was able to fit closely the XANES and SAXS *kinetics* data as shown back in Figure 4.8.

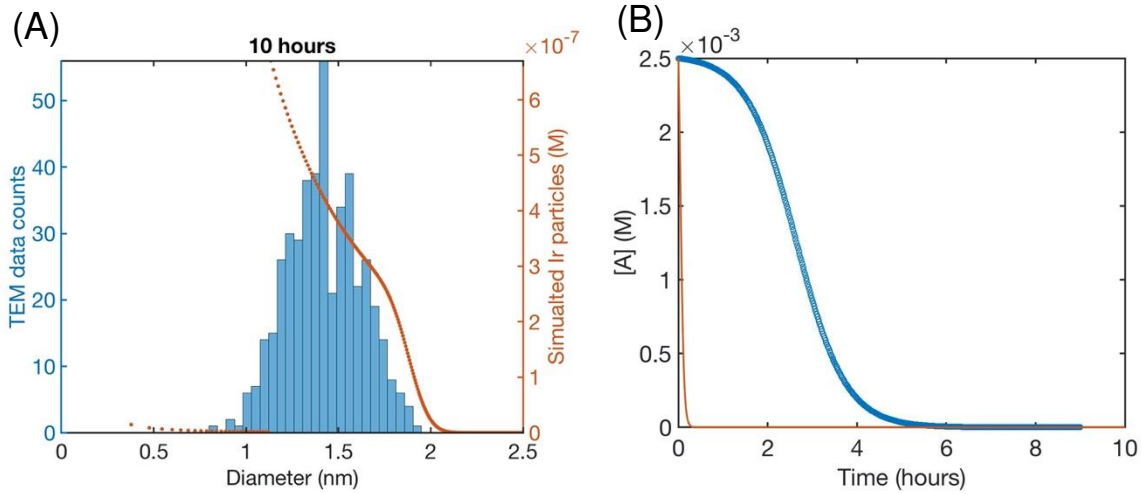

Figure 4.10. (A) Attempted fit to the end-time, 10.0 h histogram using ME-PBM encoded with the new 3-step mechanism plus the experimentally determined nucleation mechanism so as to give the attempted fit the best chance of succeeding. The fit is decent on the right side of the PSD, but this particular ME-PBM does not properly capture particles ≤ 1.2 nm. The BFV[18,19] is 54.8. The resultant fit-determined rate constants (that refer to Scheme S4.2) are as follows: $k_{+\text{Diss}} = 1.8 \times 10^{-1}$ h^{-1} M^{-2}, $k_{-\text{Diss}} = 1.2 \times 10^{4}$ h^{-1} M^{-1}, $k_1 = 6.3$ h^{-1}, $k_2 = 6.1 \times 10^{6}$ h^{-1} M^{-1}, $k_3 = 1.2 \times 10^{4}$ h^{-1} M^{-1}, and $M = 27$. **(B)** Calculated precursor loss, $[A]_t$, using the "best-fit" rate constants parameters from the above attempted fit to the PSD, are co-plotted with the experimental $[A]_t$ data from the global fitting of all $[A]_t$ loss data (see Figure S4.9 of Appendix III).

Figure 4.10 shows the attempted fit of the PSD using a ME-PBM code based on the new 3-step mechanism. While the right-most edge of the PSD is now reasonably accounted for, and the BFV has dropped considerably from 90.0 to a BFV = 37.2 indicating a better fit (as expected given the additional rate constant parameter in the 3-step mechanism), the fit to the left-hand side of the PSD is poor indicating that this ME-PBM yields too many small particles. Additionally, the predicted A-loss curve using the PSD-fitted rate constants is not even close to the experimental A-loss curve, taking off immediately without any observable induction period, indicating that a further revised mechanism and associated ME-PBM will need to somehow slow down the consumption of precursor A.

Overall, the ME-PBModel built off the new 3-step mechanism and including the experimentally determined nucleation mechanism is telling us that (i) yes, we have taken a step in the right direction with the 3-step mechanism and using the experimental nucleation pathway in the code, *but* that (ii) we still do not have the precisely correct mechanism. That mechanism (iii) needs a way to move smaller particles to larger particles more quickly while also slowing A loss and associated particle-growth steps somehow. These first two 2- and 3-step-based ME-PBModels strongly support our finding[18,19] that (iv) it is *not trivial* to find a ME-PBModel that will fit any given PSD. That is, ME-PBM attempted fittings of PSDs using MATLAB code developed for

each hypothesized mechanism are an important, *if not the most demanding, test of one's proposed mechanism of particle formation.*[18,19]

Exploration of a ME-PBModel Built Off the New 3-Step Mechanism, But With Added "Small-Small" Aggregation, B + B → C.

As the last ME-PBM examined as part of the present paper and initial ME-PBM studies, we explored the addition of a B + B → C, small-small aggregation step, as one rational way to move small particles "B" along while also slowing down precursor (A) loss by consuming B and, hence, kinetic competition with the A + B → C growth step of the 3-step mechanism. Indeed, this next ME-PBModel shows how one can logically and systematically use the results from even failed ME-PBModels and their input mechanisms to rationally guide one towards a more "correct" mechanism able to account quantitatively for all of the available data, including the kinetics-information-rich PSD.

Scheme 4.4. A 4-Step Mechanism Consisting of (i) Prior Equilibrium to Generate A_{solv}, (ii) Slow, Continuous Nucleation, (iii) Fast Small Particle Growth, (iv) Small Particle Agglomeration, and (v) Slow, Large Particle Growth

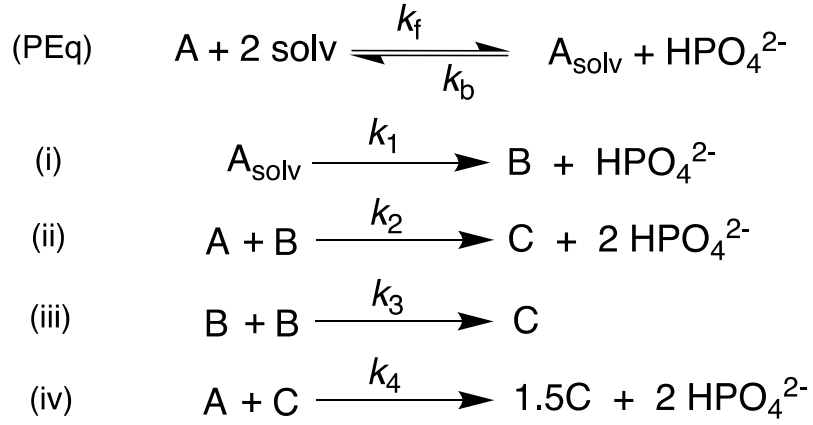

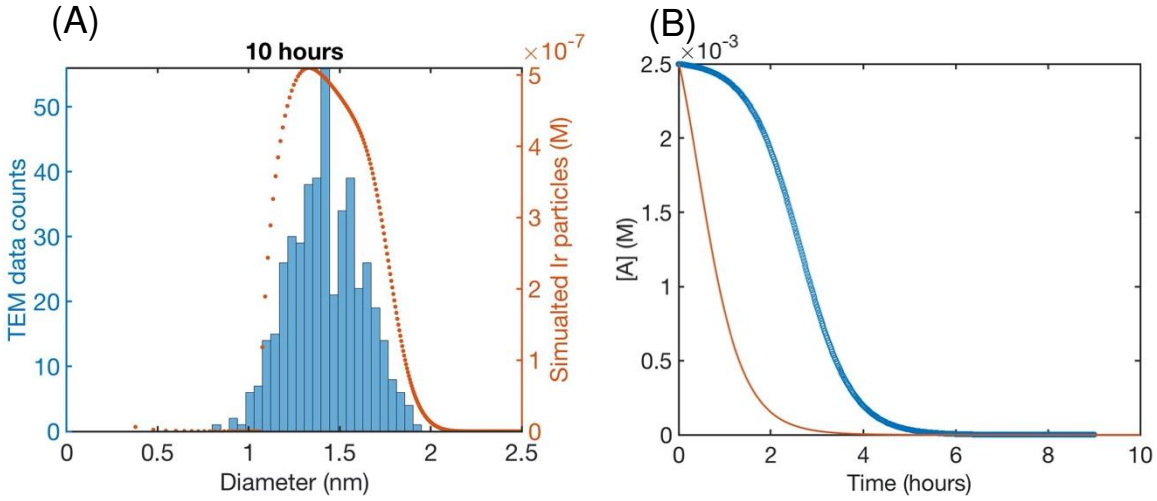

Figure 4.11. (A) Attempted fit to the end-time, 10.0 h histogram using ME-PBM encoded with the new 4-step mechanism plus the experimentally determined nucleation mechanism so as to give the attempted fit the best chance of succeeding. The general shape of the PSD is captured and the fit of the $[A]_t$ curve is improved from either the fit using the 2-step or 3-step mechanisms. The BFV[18,19] is 25.4. The resultant fit-determined rate constants (that refer to Scheme 4.6 above) are as follows: $k_{+Diss} = 2.6 \times 10^{-1}$ h^{-1} M^{-2}, $k_{-Diss} = 2.2 \times 10^{4}$ h^{-1} M^{-1}, $k_1 = 2.2$ h^{-1}, $k_2 = 5.4 \times 10^{4}$ h^{-1} M^{-1}, $k_3 = 1.6 \times 10^{6}$ h^{-1} M^{-1}, $k_4 = 1.0 \times 10^{3}$ h^{-1} M^{-1}, and $M = 23$. **(B)** Calculated precursor loss, $[A]_t$, using the "best-fit" rate constants parameters from the above attempted fit to the PSD, are co-plotted with the experimental $[A]_t$ data from the global fitting of all $[A]_t$ loss data (see Figure S4.9 of Appendix III).

While the PSD is better fit (and as it should be with one additional rate constant fitting parameter) and while the predicted [A]-loss curve to the right in Figure 4.11 now shows some delay, the match to the experimental CHCRR kinetics curve is poor, indicating we still have more work to do to uncover the more detailed, even closer to correct particle formation mechanism.

Several points are clear at this juncture: (i) ME-PBM analysis of the information buried in the PSD is critical to obtaining the more detailed, most reliable mechanism possible, and while getting closer (ii) we are not yet at that more detailed mechanism able to quantitatively account for all the kinetics and PSD data within experimental error. Hence, we have answered the question of: (iii) "can we fit the PSD and get the ostensibly correct mechanism in just three iterations of the ME-PBM (i.e., and given that the present, 2nd generation system is for a relatively well-understood

$Ir(0)_n$ nanoparticle formation system close to the example where ME-PBM was first developed[18,19]?)" The answer is "no", perhaps not surprisingly given that (iv) 11 known PEStep mechanisms were considered and ultimately disproved in our original ME-PBM on the first generation, $\{(1,5\text{-COD})Ir^{I}\bullet POM\}^{8-}$ precursor to $Ir(0)_n\bullet(POM^{9-})_x$ system en route to the new 3-step mechanism discovered there via ME-PBM.[18,19] Additionally, (v) the dimeric nature of the 2nd generation, $\{[(1,5\text{-COD})Ir^{I}\bullet HPO_4]_2\}^{2-}$ precursor introduces considerable more complexity into the ME-PBM analysis compared to the classic$\{(1,5\text{-COD})Ir^{I}\bullet POM\}^{8-}$ precursor system. In particular, (vi) it is conceivable the nucleation step involves dissociation from $\{[(1,5\text{-COD})Ir^{I}\bullet HPO_4]_2\}^{2-}$ to $(1,5\text{-COD})Ir^{I}(solv)_2^{+}$ (and $\{(1,5\text{-COD})Ir^{I}(HPO_4)_2\}^{3-}$), and conceivable that growth also involves either $(1,5\text{-COD})Ir^{I}(solv)_2^{+}$ or A(solv) (= $\{[(1,5\text{-COD})Ir^{I}]_2HPO_4]\}^{0}$) or conceivably both. Each of these pathways is expected to slow down the ME-PBM predicted [A]-loss kinetics curve. We are also (vii) performing full Bayesian inversion statistical analysis as part of the needed studies as a check on the resultant parameters, their reliability and error bars and as a further test of each possible mechanism and associated ME-PBM. Those coding and computer-time intensive studies are proceeding, will require their own substantial manuscript, and hence will be reported in due course.

Effects of Authentic *tetra*-Iridium-Hydride Cluster, $Ir^{I}_4H_4(1,5\text{-COD})_4$, On the Particle Formation Reaction: Does Addition of This Model of a Small, Kinetically Effective Nucleus (KEN)[62] Accelerate the Particle-Formation Reaction As Expected?

As we were writing up our studies, we realized that we were in a special position to be able to independently test if small, $(Ir\text{-}H)_n$ clusters, $n \leq 4$, could be kinetically competent intermediates for both the $Ir(0)_n$ formation reaction as well as a Catalytically Effective Nucleus

(CEN)[92] for the indirect monitoring by the CHCRR? Highly relevant here is that we have excellent kinetics evidence for an iridium-hydride-based Kinetically Effective Nucleus[62] of $\{\mathbf{Ir^{I}_{2}(H)_{2\mathit{x}}}\bullet(HPO_4)_n^{-2n}$ in the present system from our 2019 studies,[64] so that the discrete, *tetra*-Iridium-hydride cluster, $Ir^{I}_4H_4(1,5\text{-}COD)_4$ is just a dimer of that KEN (and once the 1,5-COD ligands are either replaced by added HPO_4^{2-} stabilizer that is present or removed by hydrogenation, i.e., as shown back in eq 4.7). The novel tests reported below are uniquely possible for the present Ir-based nanoparticle system because we previously synthesized and unequivocally characterized[51,52] by crystallography (and five additional methods, NMR, IR, mass spectrometry, UV-vis, and XAFS[51,52]) the discrete, *tetra*-Iridium-hydride cluster, $Ir^{I}_4H_4(1,5\text{-}COD)_4$ as it is a rare, close model of potential early nucleation intermediates in a particle-formation reaction.

We performed two sets of experiments, first with the $\{[(1,5\text{-}COD)Ir^{I}\bullet HPO_4]_2\}^{2-}$ precursor system and then with a second precursor system, so as to test the generality of the results, specifically $\{(1,5\text{-}COD)Ir^{I}Cl\}_2$ (plus 3 molar equivalents of $(Bu_4N)^+Cl^-$ to slow the reaction kinetics into a measurable range). Each set of particle formation experiments was done to start without, then with, 0.03 or 0.04 molar equivalents (=1.5% or =2.0% in added Ir) of added authentic $Ir^{I}_4H_4(1,5\text{-}COD)_4$ for the cases of $\{[(1,5\text{-}COD)Ir^{I}\bullet HPO_4]_2\}^{2-}$ and $\{(1,5\text{-}COD)Ir^{I}Cl\}_2$ (plus 3 molar equivalents of $(Bu_4N)^+Cl^-$), respectively.

The results provided in Figure S4.6 show that even just 0.03 molar equivalents (=1.5% in added Ir) of the reactive, discrete $Ir_4H_4(1,5\text{-}COD)_4$ cluster under H_2 accelerated the observed k_1 by *ca. an order of magnitude* in the case of the$\{[(1,5\text{-}COD)Ir^{I}\bullet HPO_4]_2\}^{2-}$ precursor. The case of the $\{(1,5\text{-}COD)Ir^{I}Cl\}_2$ / 3 $(Bu_4N)^+Cl^-$ precursor system proved even more interesting, the addition of the reactive, discrete $Ir_4H_4(1,5\text{-}COD)_4$ cluster under H_2 shortens the reaction time from >120 h (ca. 5 days) to ~1 h, an acceleration of nucleation and growth by over 10^2, Figure S4.6! The results

strongly and independently support the hypothesis that small $(Ir\text{-}H)_n$, $n \leq 4$ are both able KEN[62] as well able CEN[92] that can hydrogenate cyclohexene as required for the CHCRR to report with minimal delay on the $Ir(0)_n$ particle formation process.

4.4. DISCUSSION

The following discussion is organized by returning to the seven specific questions posed in the Introduction.

Question 1: *Are synchrotron-based methods alone, specifically XANES and SAXS, sufficient in the present example to obtain the ostensibly "correct" mechanism according to all the available data? Are synchrotron XANES and SAXS direct methods pretty much fool-proof, or do these generally powerful methods also have limitations?*

No, even the generally powerful, fairly direct methods of XANES and SAXS were not able to reveal the true underlying mechanism in the present example—ME-PBM analysis of the PSD vs time data was also required to get closer to the true, underlying mechanism. The synchrotron methods are also not absolutely fool-proof, and arguably best characterized as "fairly direct" as noted above due to precedented,[106,107,108,109,110] but underappreciated and underdiscussed, possibility of X-ray-induced radiolysis of solvent or other molecules (even the energetic process $Zn^{2+} \rightarrow Zn^{3+} + e^-$)[106] as a source of e^- and hence possible artifacts. Nucleation can be triggered by solvated e^- reduction to at least conceivably produce Ir(0), "B" in the present case. Autocatalytic growth following nucleation results in the exponential magnification of [A]-loss curve, why even trace nucleation due to solvated e^- need to be considered in studies employing the otherwise powerful synchrotron X-ray radiation-based methods.

Question 2: *Does the application of ME-PBM to the TEM-determined PSDs support or refute the best fitting mechanism? Is our recent conclusion, that ME-PBM is a "must use" tool[18,19] prior to publishing any particle formation mechanism, supported[18,19] or refuted?*

ME-PBM proved powerful and, overall, essential as before.[18,19,94] Quantitative fitting of the XANES, SAXS, CHCRR, and GLC-based kinetics proved possible, but did not by itself lead to a final mechanism able to account quantitatively for all the data, including the [A]-loss kinetics, at least in our hands. Overall, the results herein and those before[18,19,94] argue strongly that ME-PBM is a "must use" tool[18,19] before a reliable particle-formation mechanism can be claimed to be in-hand.

Question 3: *Will XANES and SAXS obtained kinetics data for the* $\{[(1,5\text{-COD})Ir^{I}\bullet HPO_4]_2\}^{2-}$ *precursor /* $Ir(0)_n\bullet(HPO_4^{2-})_x$ *nanoparticle system both be (i) sigmoidal as expected, (ii) well-fit by the 2-step mechanism as is found for the CHCRR and GLC-derived kinetics data? That is, will there (iii) be at least semi-quantitative agreement between the CHCRR, GLC and the more direct kinetic methods of XANES and SAXS?*

All XANES and SAXS kinetics data revealed the expected, sigmoidal curves. All the kinetics data herein were reasonably fit by the minimal 2-step mechanism as the recommended Ockham's razor obeying starting point. Then a good fit to an expanded, 3-step mechanism was demonstrated for the key XANES and SAXS kinetics data. Semi-quantitative agreement of the resultant pseudo-elementary step nucleation and autocatalytic surface growth rate constants (k_{1obs} and k_{2obs}, respectively) was observed for the four methods of kinetics data collection (the CHCRR, GLC, XANES, and SAXS) and within a factor of ≤ 2 for the raw resultant rate constants.

Question #4: *What level of quantitative agreement is there between the rate constants obtained by CHCRR, GLC, XANES and SAXS monitoring methods? What is the implied level of precision and, ideally, accuracy of the resultant rate constants?*

The rate constants for the four monitoring methods were in general agreement within a factor of ≤2 for separate comparisons of k_{1obs} and k_{2obs} rate constants, Tables 4.1 and 4.2, *vide supra*. Under the zeroth-order assumption that the small differences in conditions (of the XANES and SAXS experiments in particular) and that the data are all "equal" in validity, accuracy, and precision, a global-fit to the composite kinetics data provided the global rate constants cited earlier of $k_{1obs,global\ avg} = (1.5 \pm 0.1) \times 10^{-2}\ h^{-1}$ and $k_{2obs,global\ avg} = (2.4 \pm 0.1) \times 10^{2}\ h^{-1}\ M^{-1}$ of respective ±7% and ±4% estimated precisions. Given that these estimates cover the four different methods used to monitor the reaction, these global averages are also our best estimates and current working hypothesis of hopefully *accurate* rate constants for nucleation and autocatalytic surface growth in the 2nd generation system. What is perhaps noteworthy is the amount of time and effort it has taken to achieve these just two rate constants at the desired level of precision and perhaps also accuracy.

Question #5, part I: *When looking in more detail at the now well-established, prototype Ir^{I}(1,5-COD)$^{+}$-containing precursor systems,*[45-47,50-53,55-64,88-96] *what are the known, primary sources of experimental error in measuring accurate nucleation and growth rate constants?*

Effects of Common Dust on the classic {(1,5-COD)Ir^{I}•**POM**}$^{8-}$ precursor and Ir(0)$_n$•(**POM**$^{9-}$)$_x$ nanoparticle system.

There is little doubt that the presence of common room dust in solvents, on glassware and in reactors is a main source of approaching an order-of-magnitude error in nucleation rate measurements and hence rate constants.[63,64] In prior work on the first generation {(1,5-

COD)Ir^{I}•**POM**$\}^{8-}$ precursor and Ir(0)$_n$•(**POM**$^{9-}$)$_x$ nanoparticle system,[63] by using 0.20 μm microfiltered solvent (and then also washing the Fisher-Porter bottle reactor and any glassware used with that filtered solvent to lower the dust content) the $k_{1obs(bimolecular)}$ in that work was lowered by up to ~7.6-fold.[63] Interestingly, the absolute error seemed to remain constant as judged by the relative error in $k_{1obs(bimolecular)}$ being ±47% and hence larger compared to the smaller, ±27% relative error in the up to 7.6 fold faster $k_{1obs(bimolecular)}$ for the unfiltered solutions.[63] The $k_{2(obs)}$ rate constants were not changed within experimental error and serve as an "internal standard" of sorts arguing for the reliability of the results. Remarkably, the Ir(0)$_n$ PSD narrowed by a factor of 2.4 with the microfiltration treatment, from ±19% to a rather narrow ±8%,[63] not far off of the record minimum ~5% PSD from any nanoparticle self-assembly reaction as documented elsewhere.[63] The 2.4-fold narrowing of the PSD could be accounted for by a slowed nucleation rate constant, k_{1obs}, along with an unchanged autocatalytic growth rate constant, k_{2obs}, and with a Kinetically Effective Nucleus that includes dust, Ir$_3$H$_x$(**POM**)$_1$•dust.[63]

The Effects of Microfiltration on the Current $\{[(1,5\text{-COD})Ir^{I}\bullet\mathbf{HPO_4}]_2\}^{2-}$ Precursor and Ir(0)$_n$•(**HPO$_4^{2-}$**)$_x$ Nanoparticle Product System.

We have also examined the effects of incorporating the microfiltration protocol on the Ir(0)$_n$•(**HPO$_4^{2-}$**)$_x$ nanoparticle system,[64] with similar results to those described above. Specifically, the expected slowing of k_{1obs} with 0.2 μm filtration is seen, albeit at a somewhat lower, ~1.5–5-fold level in the $\{[(1,5\text{-COD})Ir^{I}\bullet\mathbf{HPO_4}]_2\}^{2-}$ precursor system of reduction in k_{1obs} for the $\{[(COD)Ir^{I}\bullet HPO_4]_2\}^{2-}$ system. Hence, the Kinetically Effective Nucleus in this system also includes dust, Ir$_2$H$_x$(**HPO$_4$**)$_1$•dust.[64] And, the studies reported herein by design include the presence of room dust[125] as those are the conditions that >99% of all reported particle syntheses are performed.

Literature Revealing Analogous Effects of Dust Removal by Microfiltration on Particle Formation Reactions.

Interestingly, both of the effects of an increase in the relative error[97] and a narrowing PSD have been observed before when using microfiltration as part of the experimental protocol. In the isonicotinamide crystallization study cited as part of Question #3, the authors report that the ±5% error bars in the J "nucleation" rates for the *filtered* solutions from 144 measurements[97] are reduced 3.6-fold to ±1.4% in the *unfiltered* solution, results that once again imply a relatively constant, absolute error source in the kinetics measurements. The effects of microfiltration were attributed to room dust by the authors although, direct evidence for dust, the size or type of the dust (i.e., "inorganic" and/or "organic"[63]), and hence compelling evidence for its removal by the filtration step, was not provided.

Also meriting mention is a seminal 1963 paper from Matijević and co-workers[126] studying the PSD of sulfur $(S)_n$ sols reports that careful attention to the purity of the starting reagents, the water solvent, efficient mixing, temperature control, *and the removal of dust by use of a 0.22 μm microfilter* are required to achieve a reproducible synthesis. Significantly, that careful experimental work narrowed the final size distribution 2-fold for 95% of the observed particles to 0.48±0.04 μm (i.e., ±8%)[124] from that seen of 0.51±0.08 μm (i.e., ±16%) in an earlier,[127] ostensibly closely analogous synthesis.[124] Intriguing is that the 2-fold narrowing in the $(S)_n$ system is nearly identical to the 2.4-fold narrowing we see for the $Ir(0)_n$•$(\mathbf{POM}^{9-})_x$ nanoparticle system when using the microfiltration treatment of the solvent and rinsing the reactor and glassware surfaces with microfiltered solvent.

The take home message is clear: dust is an omnipresent, kinetically important component of the nucleation process *and* the resultant particle-size and PSD. Nucleation is, indeed "almost

always heterogeneous" (see p. 542 of the proceedings of a 2015 workshop of experts on nucleation[128]). Relevant here is that common room dust has been known since the 1880s to be critical in vapor phase nucleation and particle formation processes,[129,130,131,132,133,134,135] yet to this day the effects of dust are not considered in most particle-formation reactions one finds in the literature. One can argue that valuable synchrotron time and radiation used in studies claiming to examine nucleation are being wasted presently until and unless the effects of omnipresent dust are taken into account.

Other Factors Affecting Nucleation and Growth in the Prototype $Ir(0)_n$ Nanoparticle Systems.

The other, often *adventitious* factors that we have found that influence the nucleation and growth of nanoparticles (i.e., factors other than the common, known ones of ligands, temperature, solvent, and so on) include the following, a growing list since 1994 studies that documenting such effects: acetone solvent impurities,[46] water,[46] O_2,[46] H^+,[46] trace residual solvents such as EtOAc[136] used in syntheses, dust[63,64], and additives such as the diprotonated $(Bu_3NH)_2(H_2P_2O_7)$.[64]

In summary, the $Ir^I(1,5\text{-COD})^+$-based 1st and 2nd generation systems provide well-studied systems that others can refer to about experimentally established factors that affect nucleation and growth rate constants. The above factors and the dominance of heterogeneous nucleation[126,135] over true homogeneous nucleation are among the reasons nucleation rate constants in particular are notoriously hard to measure reproducibly, precisely, and accurately.

Question #5, part II: *What more generally are the error bars on the nucleation and growth rate constants and how do those error bars compare to the most at least precise nucleation and growth kinetics in the literature?*[97,98]

Historically, agreement of specifically nucleation rates and rate constants within $\pm 10^{1\text{-}2}$ have been considered to be[63,137] "of great success".[135] That said, a good place to start en route to answering the above question more globally is the first generation $\{(1,5\text{-COD})Ir^{I}\bullet\mathbf{POM}\}^{8-}$ precursor and $Ir(0)_{\sim 300}\bullet(\mathbf{POM}^{9-})_x$ product system.[98] From over ~1500 kinetics runs to date using the CHCRR methodology by 11 researchers from studies that began before 1997,[53] the inter-investigator and intra-investigator error bars on the k_{1obs} and k_{2obs} for the 2-step mechanism are k_1 $\pm 10^{1.2}$ (i.e., ±15.9-fold)[98] inter- and ±50% intra-investigator, and k_2 ±50% inter- and ±15% intra-investigator, respectively. Even with great effort to eliminate sources of experimental variability (specifically those discussed in the first part of this question #5) and to reduce the error via 17 repeat experiments,[62] a single-investigator error of 21% was attainable after 17 repeat experiments focused on nucleation, a second-order rate constant $k_{1obs(bimolecular)} = 6.1 \pm 1.3\ h^{-1}\ M^{-1}$ in that particular study.[62]

For the second-generation $\{[(1,5\text{-COD})Ir^{I}\bullet\mathbf{HPO_4}]_2\}^{2-}$ precursor and $\{Ir(0)_{\sim 150}\bullet(\mathbf{HPO_4})_x\}^{-2x}$ product system studied in the present work, the inter-investigator error among 3 primary researchers over the ≥7 years since this study began in earnest prior to 2013 and among all the physical methods and synchrotron or in-house locations employed is the ≤2-fold variation in the individual k_{1obs} and k_{2obs} determinations detailed back in Tables 4.1 and 4.2. However, as detailed earlier, if one combines all the 1,178 total kinetics data points underlying Tables 4.1 and then fits that composite data set, global-average estimates of $k_{1obs,global\ avg} = (1.50 \pm 0.1) \times 10^{-2}\ h^{-1}$ and $k_{2obs,global\ avg} = (2.4 \pm 0.1) \times 10^{2}\ h^{-1}\ M^{-1}$ of respective estimated precisions of ±7% and ±4% are obtained—considerably lower error bars achieved, however, only post considerable experimental effort.

A state-of-the-art crystallization study by Kulkarni and co-workers[97] is summarized in a footnote for the reader interested, a study with high precision particle formation rates, albeit ones not adequately deconvoluted into separate nucleation and growth rate constants.[138] Of interest here is that the reported, apparent record ±1.4% precision in nucleation rates those authors report for 144 particle formation kinetics experiments is very close to the error expected if 144 experiments were performed in the present system instead of the net 11 experiments in Tables 4.1 and 4.2 (excluding the 5σ outlier), error that would then be expected to drop (if random)[139] to a nearly identical 1.1-1.9% (i.e., $(11)^{1/2}/(144)^{1/2}$•(4-7%) = 1.1-1.9%).

In summary, reproducible nucleation and growth rate constants of precision ≤10% are possible with sufficient experimental care and a sufficiently large amount of raw data from a sufficiently high number of repeat experiments. *Accurate* rate constants are another matter, requiring a suitable range of ideally complimentary physical methods according to all our evidence or knowledge of the literature.

Question #6: *What, then, is (are) deemed to be "best" physical method(s) for monitoring especially the notoriously hard to measure nucleation step(s)[62] and to obtain accurate rate constants? What are the strengths and weaknesses of each method, and how can they be used in a complimentary fashion? What roles do indirect, but in-house and hence convenient, methods such as the CHCRR have in comparison to the XANES and SAXS monitoring methods?*

Synchrotron XAFS and SAXS.

Based on the extensive use of synchrotron XAFS and SAXS to monitor particle formation reactions in the literature[140], as well as our own studies herein, the relatively direct methods of XAFS and SAXS will continue to be forefront methods for monitoring particle formation

reactions. That said, XANES is somewhat limited by both the precision and amount of data (as seen back in Figure 4.3) and SAXS is limited by the weaker scattering by smaller compared to larger particles. Both methods suffer in principle from possible X-ray radiation induced radiolysis[106-110] and, hence, the little tested effects of that radiolysis on nucleation and growth in all but a few important papers and systems.[106-110] The synchrotron methods do not provide large amounts of high precision kinetics data, nor are they "infinitely available" to any investigator. The latter is probably one reason that very basic studies such as measuring *the rate law for the particle formation process*, or the effects of dust on nucleation, are largely non-existent in the broader XAFS and SAXS literature. In this regard, machine learning – assisted analysis of XANES data[141,142,143,144,145] merits mention as a recently discovered way to improve the sensitivity of XANES, even in harsh conditions of low metal loadings, high temperatures and presence of reactor walls that complicate the use of the workhorse method for nanoparticle studies, EXAFS.[146,147,148] This advance has recently been applied to analyze the formation of metal nanoparticles under *in situ* conditions in ionic liquids[149,150] and ionic salt melts.[106]

In-House, Direct and Indirect Methods.

Over the years we have examined NMR, UV-visible, GLC, CHCRR, and TEM as in-house methods[45-64] to monitor the loss of precursor (NMR, UV-vis), cyclooctane reaction by-product formation (GLC) or particle formation (CHCRR and TEM). Only the CHCRR is *in situ* (actually *in operando*) due to the issue of H_2 gas also being a reactant so that the other methods require the removal and examination of reaction aliquots. Only NMR and, arguably, TEM are more direct, TEM bordering on being a "more direct" method due to multiple controls performed when we first used TEM in 1994.[45,46] Those key early controls demonstrate that third-row-metal $Ir(0)_n$ nanoparticles have high stability in the TEM beam, one of the multiple advantages[50,90] of the {(1,5-

COD)Ir^{I}•POM$\}^{8-}$ and $\{[(1,5\text{-COD})Ir^{I}\bullet HPO_4]_2\}^{2-}$precursor systems and one reason we picked $Ir(0)_n$ (and not $Rh(0)_n$ or $Au(0)_n$, for example) for emphasis >25 years ago.[45,46] Only the CHCRR gives continuous kinetics data and anything like >1500 data points of intrinsic ±0.01 psig precision and ~ ±0.5% precision as applied herein, the other aliquot-based methods giving ≤10 time-resolved data points of ~5-15% precision.

As nature would have it, the CHCRR monitoring method that is by far the most convenient, the most precise-data generating, as well as a continuous monitoring method is also the most indirect. The CHCRR kinetics method relies on the facile hydrogenation of cyclohexene, under experimental conditions where controls demonstrate the required zero-order dependence on cyclohexene[53] (i.e., so that it is not rate limiting in any way), by any and all the Ir-species from the $Ir^{I}_2(H)_{2x}\bullet(HPO_4)_n^{-2n}$ KEN forward, including $Ir(0)_n$. The choice of the so-called "structure-insensitive"[151] reaction of hydrogenation, that shows a minimal, often ≤ca.3-fold dependence on particle size[139], is an important, deliberate part of the design of the CHCRR.[45,46,53] The size $Ir(0)_n$ present by the end of the induction period is estimable by both TEM and GLC of aliquots taken before and after the induction period and has been defined as the Catalytically Effective Nucleus (CEN)[92]. The CEN was determined to start at Ir_2, be highly active at Ir_4 as modeled by a discrete $Ir_4H_4(ligand)_4$ cluster added to the reaction, and $Ir_{\leq 26}$ by the end of the observed induction period. The understanding and careful use of the PEStep method back in Scheme 4.1 and eqs 4.1-4.6 underlie the CHCRR as do critical controls done at the start[53] (and repeated for each new system[58-61,64]) showing that GLC monitoring yields the same kinetics and k_{1obs} and k_{2obs} rate constants within experimental error. Typically, only the first 1/3 to 1/2 of the CHCRR data are used to ensure the zero-order in [cyclohexene] conditions needed for the CHCRR. Earlier papers contain

additional details and discussions about the use of and approximations underlying the CHCRR.[53,55,57-64]

An issue since simulations done back in 2001[55] has been that the formation of even a $Ir_{\sim 13}$ Catalytically Effective Nucleus (CEN)[92] could lengthen the induction period (and thereby slow the apparent kinetics of the CHCRR) by as much as a factor of[55] 10 (a derivation plus discussion of how the formation of a CEN can influence the CHCRR kinetics is provided in Appendix III). However, compelling evidence small even $Ir_{2\text{-}3}$ KEN can both hydrogenate additional $Ir^{I}(1,5\text{-COD})^{+}$ (via surface autocatalytic growth) as well as hydrogenate cyclohexene in the CHCRR is now strongly supported by six lines of evidence (i) the agreement within a factor of[122] ≤ 2 of the k_{1obs} and k_{2obs} rate constants from the 4 kinetic methods back in Tables 4.1 and 4.2; (ii) the demonstration that the authentic, *tetra*-Iridium-hydride cluster, $Ir^{I}_{4}H_{4}(1,5\text{-COD})_{4}$, is able to both nucleate $Ir(0)_{n}$ particle formation as well as support the CHCRR; and (iii) that nothing even close to a factor of 10 that simulations indicate is possible for a putative Ir_{13} CEN is seen in Figures 4.3 or 4.5—at most a factor of ~2 in Figure 4.3b for example. Previous evidence that the CHCRR methodology was working largely as believed includes (iv) the GLC controls yielding roughly equivalent kinetics[53]; (v) the ability to determine nucleation kinetics via the CHCRR that yielded small, $Ir_{2\text{-}3}$ KENS[47,64]—something inconsistent with having to reach the experimentally determined CEN of $Ir_{\sim 26}$ before the CHCRR started "reporting" on the particle formation process; and that (vi) the CHCRR experimentally derived nucleation rate law and mechanism are at least generally supported by the ME-PBM—indeed are a required component of any ME-PBM able to fit PSD data.[18,19] The amplification of the signal (i.e., the amount of Ir product) by the CHCRR *catalysis* is another, valuable part of the CHCRR method. In short, six lines of evidence strongly

support the conclusion that the CHCRR is a valuable in-house tool for monitoring $Ir(0)_n$ and other $metal(0)_m$ nanoparticle-formation reactions.[45-64]

Complimentary Nature of the Direct and Indirect Methods.

The above discussion of the XANES, SAXS, GLC (or NMR, UV-vis, etc) and CHCRR methods makes apparent that each method has it strengths and weaknesses. Also apparent is that the more physical methods—and especially the more complimentary the multiple physical methods employed—the better, as is well known across the chemical sciences. SAXS is especially valuable as a relatively direct method[138] ("relatively", due to possibility of radiolysis[106-110] effects) if one can also obtain the number of particles vs time along with precursor conversion via standard radius vs time data—A. Karim's point that SAXS, then, counts as "two methods"[32].

However, in-house methods can be invaluable for scouting out experimental conditions for more direct, but less accessible and more expensive, methods such as trips to a synchrotron radiation source. The CHCRR is a case in point: over 1500 kinetics runs with 11 independent researchers over a 26-year period since[45,46] 1994 and accelerating after[53] 1997 have been performed with the CHCRR. Even for just the second-generation $\{[(1,5\text{-COD})Ir^{I}\bullet\mathbf{HPO_4}]_2\}^{2-}$ precursor system, the CHCRR and GLC methods have allowed one of us (CBW) to collect ~70 datasets per year over 3 yrs for a total of ~210 experimental datasets under a range of conditions. Without the CHCRR we would not have the minimum mechanisms in Scheme 4.2[46-53,56-64] nor any nucleation mechanisms[47,64] as working hypotheses for going forward, nor the paradigm shifting low molecularity, KENs of[47,64] $Ir_{2\text{-}3}$, nor the development of ME-PBM,[18,19] nor the important "smaller particles grow faster than larger particles"[18,19] insight. The total number of nanoparticle formation kinetics experiments we have performed using the CHCRR exceeds by nearly two orders of magnitude the number of synchrotron trips and associated kinetics studies (3

total) that at least we have been able to perform during the same time frame of this research. That said, access to synchrotron XANES and SAXS methods has been absolutely crucial to checking the fidelity of the CHCRR and other in-house methods and results.

Question #7. *Finally, what additional studies are recommended going forward en route towards an even more detailed understanding of particle formation nucleation, growth, and agglomeration across nature?*

The literature that at least we have assembled seems 100% clear on this point[65,66,95,138,152]: (i) more *experimental studies* of *especially nucleation* by multiple, complimentary physical methods, especially efforts to obtain experimental rate laws for nucleation of a variety of precursor systems and, hence, the Kinetically Effective Nucleus[47,62,64] for each system under consideration; (ii) the use of SAXS[138] while getting both radius data and the number of particles vs time[32] along with any controls possible to test for the effects of x-ray induced radiolysis[106,107,108,109,110]; and (iii) expansion of and testing all proposed mechanisms by Mechanism-Enabled Population Balance Modeling to see if the information-rich PSD supports or refutes the proposed particle-formation mechanism. (iv) *The combination of SAXS PSD data vs time with ME-PBM analysis and then alternative mechanism(s) construction is expected to prove especially powerful.* Depending on what other, in-house particle formation kinetics or, for example, TEM product vs time data are available, it may actually prove most efficient to perform initial Mechanism-Enabled Population Balance Modeling *before* going to the synchrotron in order to help plan and optimize the more expensive, less routine SAXS experiments. (v) XANES studies to have a separate look at the early, nucleation part of the kinetics and to check the SAXS results should continue to prove useful, all while (vi) following A. Karim's urgings[9,32,39] to vary conditions as widely as possible, especially

concentrations and the temperature, temperature-dependent kinetic studies of particle formation reactions being relatively rare to date. These capabilities will likely be dramatically enhanced by recently developed[144,145,146,147,148] applications of machine learning methods for nanoparticle structure characterization based on XANES data. Additionally, (vii) careful consideration of heterogeneous nucleation[126,135] and the role of impurities such as common room dust[63,64,94,127-133] in nucleation and growth studies of particle formation; and (viii) moving beyond—ultimately discarding—Classical Nucleation Theory (CNT) will be required to advance particle-formation science. CNT simply does not work for, nor was it intended to be used for, strongly bonding systems[66] where the monomer loses its identity in the nucleus in what is a kinetic process such as n M → $(M)_n$ (M = metals, for example) rather than a thermodynamic process as CNT postulates[66]. This is why CNT works best for gas phase systems aggregating with weak forces such as n RH ⇆ $(RH)_n$), the classic case where CNT *does* makes sense and *can be applied*[66]. Additionally, recommended is (ix) moving beyond—basically abandoning—the 70 year-old LaMer model of particle formation of putative "instantaneous / burst nucleation" and "diffusion-controlled growth" that has zero compelling support in nearly 2000 papers over 70 years as detailed in two, 2019 and 2020 reviews[65,66]; (x) moving beyond—effectively discarding—old, controversial, semi-empirical, non-mechanistic models for phase changes such as Avrami-based models for phase changes that do not treat nucleation in any physically real, reliable way, and that yield non-physical, convoluted parameters, the interpretation of which continue to confuse even experts that rely on those out-dated models[140]; and (xi) use of the available minimum, disproof-based mechanistic models for particle formation summarized in a table in a recent review[138]—including following A. Karim's lead using minimum mechanisms *that explicitly deal with added ligand, L, effects*[9,32,39]. (xii) The use of a time-tested, superior disproof-based[15,16,17] approach to the science,

including use of the 5 classes of ≥96 distinct particle-formation mechanisms now available elsewhere[138] that include ligand effects[9,32,39]; (xiii) applying those minimum mechanisms *and their associated mechanism-based differential equations* to the results of expert-obtained XAFS and SAXS kinetics data, rather than just presenting pictorial, schematic ("cartoon") representations and restatements of, often, the particle sizes vs time that are just a pictorial restatement of the raw data[138]; (xiv) emphasis on the minimum requirements of a reliable, minimum reaction mechanism of a balanced reaction stoichiometry plus kinetics[65,135]; (xv) consideration of and overlap with mechanisms of particle formation in the well-studied area of protein aggregation involving nucleation, growth and agglomeration processes[77]; and (xvi) greater reliance on modern methods of computation and theory (and *not CNT*) to better understand nucleation.[154,155]

We realize the above list is written from our personal, hence by definition biased, perspective. It is nevertheless our perspective based on, now, over a quarter century of effort including several older and more recent key contributions[18,19,47,53,62,63,64,65,66,95,138,140] striving to achieve a firmer, kinetics, mechanism, and ME-PBM-based approach and associated better understanding of particle formations across nature.

4.5. CONCLUSIONS

Herein, we have examined seven questions via the 2nd-generation, {[(1,5-COD)Ir^{I}•$\mathbf{HPO_4}$]$_2$}$^{2-}$ precursor to Ir(0)$_{\sim 150}$•($\mathbf{HPO_4^{2-}}$)$_x$ nanoparticle system. The reported studies achieve our goal of checking the kinetics and mechanism of Ir(0)$_n$ particle formation by more direct, synchrotron-based methods. Disproof-based experimentation that utilized a series of five experimental techniques (CHCRR, GLC, XAFS, SAXS, and TEM) plus ME-PBM revealed that Ir(0)$_{\sim 150}$•($\mathbf{HPO_4^{2-}}$)$_x$ nanoparticle formation kinetics are sigmoidal by all methods examined. Those

kinetics can be described quantitatively by a minimal 2-step mechanism of slow, continuous nucleation (A → B, k_{1obs}) followed by autocatalytic surface growth (A + B → 2B, k_{2obs}). The resultant k_{1obs} and k_{2obs} rate constants for all methods under XANES conditions were found to fall within a range of average values and error limits of ≤2-fold. A global-average fitting of all of the data yielded $k_{1obs,global\ avg} = (1.5 \pm 0.1) \times 10^{-2}\ h^{-1}$ and $k_{2obs,global\ avg} = (2.4 \pm 0.1) \times 10^{2}\ h^{-1}\ M^{-1}$ of respective ±7 and ±4 estimated precisions. A comparison of the sigmoidal curve corresponding to the global fit, Figure S4.9 in Appendix III, reveals that the separate XANES and SAXS kinetics curves are closest to and hence most representative (while actually spanning) the global average kinetics curve. However, ME-PBM was also required as before[18,19] to extract mechanistic information from the kinetics data information-rich PSD and as the best-available check on the proposed particle-formation mechanism.

The results were then used to go back and answer the seven questions raised in the Introduction. The seventh and final question of "what additional studies are recommended going forward en route towards an even more detailed understanding of particle formation nucleation, growth, and agglomeration across nature?" was answered with a list of 16 recommendations. Of note is that the combination of SAXS, XANES, complimentary monitoring methods even if indirect (along with suitable controls to check those methods) plus ME-PBM are expected to prove both most efficient and powerful *if* coupled with a proper, disproof-based approach and scientific method. Another recommendation worth emphasizing is that explicitly incorporating ligand, L, effects into kinetic models[9,32,39,138] merits much more attention and experimental effort. The 16 recommendations draw heavily from our recent reviews[65,66,95,138] and a Response to a Comment[140], hence are unavoidably infused with our opinions and any accumulated biases. But, those opinions and our recommendations are offered to the particle formation communities across nature with

the hope that they will stimulate the readers own critical thinking, improved experiments, improved experimental design, and then critical interpretation and analysis of the resultant data. We offer our best wishes to each and every one of those endeavors!

REFERENCES

1. Astruc, D.; Lu, F.; Aranzaes, J. R. Nanoparticles as Recyclable Catalysts: The Frontier between Homogeneous and Heterogeneous Catalysis. *Angew. Chem., Int. Ed.* **2005**, *44*, 7852-7872.

2. Chen, T.; Rodionov, V. O. Controllable Catalysis with Nanoparticles: Bimetallic Alloy Systems and Surface Adsorbates. *ACS Catal.* **2016**, *6*, 4025-4033.

3. Crooks, R. M.; Zhoa, M.; Sun, L.; Chechik, V.; Yeung, L. K. Dendrimer-Encapsulated Metal Nanoparticles: Synthesis, Characterization, and Applications to Catalysis. *Acc. Chem. Res.* **2001**, *34*, 181-190.

4. Zhao, S.; Jin, R.; Jin, R. Opportunities and Challenges in CO_2 Reduction by Gold- And Silver-Based Electrocatalysts: From Bulk Metals To Nanoparticles and Atomically Precise Nanoclusters. *ACS Energy Lett.* **2018**, *3*, 452-462.

5. Eguchi, D.; Sakamoto, M.; Teranishi, T. Ligand effect on the catalytic activity of porphyrin-protected gold clusters in the electrochemical hydrogen evolution reaction. *Chem. Sci.* **2018**, *9*, 261-265.

6. Cao, S.; Tao, F.; Tang, Y.; Li, Y.; Yu, J. Size- and shape-dependent catalytic performances of oxidation and reduction reactions on nanocatalysts. *Chem. Soc. Rev.* **2016**, *45*, 4747-4765.

7. Gabrielli, L.; Rosa-Gastaldo, D.; Salvia, M.-V.; Springhetti, S.; Rastrelli, F.; Mancin, F. Detection and identification of designer drugs by nanoparticle-based NMR chemosensing. *Chem. Sci.* **2018**, *9*, 4777-4784.

8. Webb, J. A.; Bardhan, R. Emerging Advances in Nanomedicine with Engineered Gold Nanostructures. *Nanoscale* **2014**, *6*, 2502.

9. Mozaffari, S.; Li, W.; Dixit, M.; Seifert, S.; Lee, B.; Kovarik, L.; Mpourmpakis, G.; Karim, A. M. The role of nanoparticle size and ligand coverage in size focusing of colloidal metal nanoparticles. *Nanoscale Adv.* **2019**, *1*, 4052-4066.

10. Ahmadi, T. S.; Wang, Z. L.; Green, T. C.; Henglein, A.; El-Sayed, M. A. Shape-Controlled Synthesis of Colloidal Platinum Nanoparticles. *Science* **1996**, *272*, 1924-1926.

11. Somorjai, G. A.; Park, J. Y. Colloid Science of Metal Nanoparticle Catalysts in 2D and 3D Structures. Challenges of Nucleation, Growth, Composition, Particle Shape, Size Control and Their Influence on Activity and Selectivity. *Top. Catal.* **2008**, *49*, 126-135.

12. Jin, R.; Qian, H.; Wu, Z.; Zhu, Y.; Zhu, M.; Mohanty, A.; Garg, N. Size Focusing: A Methodology for Synthesizing Atomically Precise Gold Nanoclusters. *J. Phys. Chem. Lett.* **2010**, *1*, 2903-2910.

13. Baek, J.; Allen, P. M.; Bawendi, M. G.; Jensen, K. F. Investigation of Indium Phosphide Nanocrystal Synthesis Using a High-Temperature and High-Pressure Continuous Flow Microreactor. *Angew. Chemie., Int. Ed.* **2011**, *50*, 627-630.

14. Hoffmann, R.; Minkin, V. I.; Carpenter, B. K. Ockham's razor and chemistry. *Bull. Soc. Chim. Fr.* **1996,** *133*, 117-130.

15. Chamberlin, T. C. Studies for students. The method of multiple working hypotheses. *J. Geol.* **1897**, *5*, 837-848.

16. Platt, J. R. Strong inference. *Science* **1964**, *146*, 347-353.

17. Scott, S. L. The Burden of *Dis*proof. *ACS Catal.* **2019**, *9*, 4706–4708.

18. Handwerk, D. R.; Shipman, P. D.; Whitehead, C. B.; Özkar, S.; Finke, R. G. Mechanism-enabled population balance modeling of particle formation en route to particle average size and size distribution understanding and control. *J. Am. Chem. Soc.* **2019**, *141*, 15827-15839.

19. Handwerk, D. R.; Shipman, P. D.; Whitehead, C. B.; Özkar, S.; Finke, R. G. Particle Size Distributions via Mechanism-Enabled Population Balance Modeling. *J. Phys. Chem. C* **2020**, *124*, 4852–4880.

20. Durán, N.; Nakazato, G.; Seabra, A. B. Antimicrobial activity of biogenic silver nanoparticles, and silver chloride nanoparticles: an overview and comments. *Appl. Microbiol. Biotechnol.* **2016**, *100*, 6555-6570.

21. Panfil, Y. E.; Oded, M.; Banin, U. Colloidal Quantum Nanostructures: Emerging Materials for Display Applications. *Angew. Chem., Int. Ed.* **2018**, *57*, 4274-4295.

22. Das, K.; Baruah, S. Quantum dots for solar energy harvesting. *Curr. Sci.* **2018**, *115*, 659-668.

23. Jing, L.; Kershaw, S. V.; Li, Y.; Huang, X.; Li, Y.; Rogach, A. L.; Gao, M. Aqueous Based Semiconductor Nanocrystals. *Chem. Rev.* **2016**, *116*, 10623−10730.

24. Wu, L.; Lian, H.; Willis, J. J.; Goodman, E. D.; McKay, I. S.; Qin, J.; Tassone, C. J.; Cargnello, M. Tuning Precursor Reactivity toward Nanometer-Size Control in Palladium Nanoparticles Studied by in Situ Small Angle X-ray Scattering. *Chem. Mater.* **2018**, *30*, 1127-1135.

25. Finney, E. E.; Finke, R. G. Nanocluster nucleation and growth kinetic and mechanistic studies: A review emphasizing transition-metal nanoclusters. *J. Colloid Interface Sci.* **2008**, 317, 351-374.

26. Polte, J. Fundamental growth principles of colloidal metal nanoparticles—a new perspective, *CrystEngComm*, **2015**, *17*, 6809-6830.

27. Turkevich, J.; Stevenson, P. C.; Hillier, J. A Study of the Nucleation and Growth Processes in the Synthesis of Colloidal Gold. *Discuss. Faraday Soc.* **1951**, *11*, 55-75.

28. Turkevich, J.; Stevenson, P. C.; Hillier, J. The Formation of Colloid Gold. *J. Phys. Chem.* **1953**, *57*, 670-673.

29. Drews, T. O.; Katsoulakis, M. A.; Tsapatsis, M. Mathematical Model for Crystal Growth by Aggregation of Precursor Metastable Nanoparticles. *J. Phys. Chem. B* **2005**, 109, 23879-23887.

30. Skrdla, P. J. Use of Dispersive Kinetic Models for Nucleation and Denucleation to Predict Steady-State Nanoparticle Size Distributions and the Role of Ostwald Ripening. *J. Phys. Chem. C* **2012**, *116*, 214–225.

31. Tong, F.; Hanson, M. P.; Bardeen, C. J. Analysis of reaction kinetics in the photomechanical molecular crystal 9-methylanthracene using an extended Finke-Watzky model. *Phys. Chem. Chem. Phys.* **2016**, *18*, 31936-31945.

32. Mozaffari, S.; Li, W.; Thompson, C.; Ivanov, S.; Seifert, S.; Lee, B.; Kovarik, L.; Karim, A. M. Colloidal nanoparticle size control: experimental and kinetic modeling investigation of the ligand–metal binding role in controlling the nucleation and growth kinetics. *Nanoscale* **2017**, *9*, 13772–13785.

33. McMurtry, B. M.; Qian, K.; Teglasi, J. T.; Swarnakar, A. K.; De Roo, J.; Owen, J. S., Continuous Nucleation and Size Dependent Growth Kinetics of Indium Phosphide Nanocrystals. *Chem. Mater.* **2020**, *32*, 4358-4368.

34. Harada, M.; Asakura, K.; Toshima, N. Structural Analysis of Polymer-Protected Platinum/Rhodium Bimetallic Clusters Using Extended X-ray Absorption Fine Structure Spectroscopy. Importance of Microclusters for the Formation of Bimetallic Clusters. *J. Phys. Chem.* **1994**, *98*, 2653-2662.

35. Calandra, P.; Giordano, C.; Longo, A.; Turco Liveri, V. Physiochemical investigation of surfactant-coated gold nanoparticles synthesized in the confined space of dry reversed micelles. *Mater. Chem. Phys.* **2006**, *98*, 494-499.

36. Harada, M.; Einaga, H. In Situ XAFS Studies of Au Particle Formation by Photoreduction in Polymer Solutions. *Langmuir* **2007**, *23*, 6536-6543.

37. Meneau, F.; Sankar, G.; Morgante, N.; Cristol, S.; Catlow, C. R. A.; Thomas, J. M.; Greaves, G. N. Characterization of zinc oxide nanoparticles encapsulated into zeolite-Y: An in-situ combined X-ray diffraction, XAFS, and SAXS study. *Nucl. Instrum. Meth. B* **2003**, *199*, 499-503.

38. Abécassis, B.; Testard, F.; Kong, Q.; Francois, B.; Spalla, O. Influence of Monomer Feeding on a Fast Gold Nanoparticles Synthesis: Time-Resolved XANES and SAXS Experiments. *Langmuir* **2010**, *26*, 13847-13854.

39. Karim, A. M.; Al Hasan, N.; Ivanov, S.; Seifert, S.; Kelly R. T.; Hallfors, N. G.; Benavidez, A.; Kovarik, L.; Jenkins, A.; Winans, R. E.; Datye, A. K. Synthesis of 1nm Pd nanoparticles: Insights on the synthesis mechanism using *in situ* XAFS and SAXS in a microfluidic reactor. *J. Phys. Chem. C* **2015**, *119*, 13257-13267.

40. Chen, X.; Schröder, J. H.; Hauschild, S.; Rosenfeldt, S.; Dulle, M.; Förster, S. Simultaneous SAXS/WAXS/UV-Vis Study of the Nucleation and Growth of Nanoparticles – A Test of Classical Nucleation Theory. *Langmuir* **2015**, *31*, 11678-11691.

41. Yang, L.; Cheng, H.; Jiang, Y.; Huang, T.; Bao, J.; Sun, Z.; Jiang, Z.; Ma, J.; Sun F.; Liu, Q.; Yao, T.; Deng, H.; Wang, S.; Zhu, M.; Wei, S. *In situ* studies on controlling an atomically-accurate formation process of gold nanoclusters. *Nanoscale* **2015**, *7*, 14452-14459.

42. Cormary, B.; Li, T.; Liakakos, N.; Peres, L.; Fazzini, P.-F.; Blon, T.; Respaud, M.; Kropf, A. J.; Chaudret, B.; Miller, J. T.; Mader, E. A.; Soulantica, K. Concerted Growth and Ordering of Cobalt Nanorod Arrays as Revealed by Tandem in Situ SAXS-XAS Studies. *J. Am. Chem. Soc.* **2016**, *138*, 8422-8431.

43. Sandoe, H. E.; Watzky, M. A.; Diaz, S. A. Experimental probes of silver metal nanoparticle formation kinetics: Comparing indirect versus more direct methods. *Int. J. Chem. Kinet.* **2019**, *51*, 861-871.

44. Georgiev, P.; Bojinova, A.; Kostova, B.; Momekova, D.; Bjornholm, T.; Balashev, K. Implementing atomic force microscopy (AFM) for studying kinetics of gold nanoparticle's growth. *Colloid Surf. A.* **2013**, *434*, 154-163.

45. Lin, Y.; Finke, R. G. Novel Polyoxoanion and Bu_4N^+ Stabilized, Isolable, and Redissolvable, 20-30 Å $Ir_{\sim 300\text{-}900}$ Nanoclusters: The Kinetically Controlled Synthesis, Characterization, and Mechanism of Formation of Organic Solvent-Soluble, Reproducible Size, and Reproducible Catalytic Activity Metal Nanoclusters. *J. Am. Chem. Soc.* **1994**, *116*, 8335-8353.

46. Lin, Y.; Finke, R. G. A More General Approach to Distinguishing "Homogeneous" from "Heterogeneous" Catalysis: Discovery of Polyoxoanion- and Bu_4N^+-Stabilized, Isolable and Redissolvable, High Reactivity $Ir_{\sim 190\text{-}450}$ Nanocluster Catalysts. *Inorg. Chem.* **1994**, *33*, 4891-4910.

47. Özkar, S.; Finke, R. G. Nanoparticle Nucleation Is Termolecular in Metal and Involves Hydrogen: Evidence for a Kinetically Effective Nucleus of Three $\{Ir_3H_{2x}\bullet P_2W_{15}Nb_3O_{62}\}^{6-}$ in $Ir(0)_n$ Nanoparticle Formation From $[(1,5\text{-COD})Ir^{I}\bullet P_2W_{15}Nb_3O_{62}]^{8-}$ Plus Dihydrogen. *J. Am. Chem. Soc.* **2017**, *139*, 5444-5457. Please also see the references therein.

48. Edlund, D. J.; Saxton, R. J.; Lyon, D. K.; Finke, R. G. Trisubstituted Heteropolytungstates as Soluble Metal Oxide Analogs, IV. The Synthesis and Characterization of Organic Solvent Soluble $(Bu_4N)_{12}H_4P_4W_{30}Nb_6O_{123}$ and $(Bu_4N)_9P_2W_{15}Nb_3O_{62}$ and Solution Spectroscopic and Other Evidence for the Supported Organometallic Derivatives $(Bu_4N)_7[(C_5Me_5)Rh{\bullet}P_2W_{15}Nb_3O_{62}]$ and $(Bu_4N)_7[(C_6H_6)Ru{\bullet}P_2W_{15}Nb_3O_{62}]$. *Organometallics* **1988**, *7*, 1692. Please also see the references cited therein.

49. Starkey-Ott, L.; Finke, R. G. Transition-Metal Nanocluster Stabilization for Catalysis: A Critical Review of Ranking Methods and Putative Stabilizers. *Coord. Chem. Rev.* **2007**, 251, 1075-1100.

50. Five advantages of the $\{(1,5\text{-COD})Ir^{I}{\bullet}\mathbf{POM}\}^{8-}$ nanoparticle formation system are: (i) it starts from a compositionally precisely characterized, reproducible precursor,[45,46] $\{(1,5\text{-COD})Ir^{I}{\bullet}POM\}^{8-}$ that also has a simple 1:1 ratio of Ir to stabilizing (POM^{9-}) anion; (ii) the resultant $Ir(0)_n{\bullet}POM$ stabilized nanoparticles are reproducibly formed and well-stabilized by the "Gold Standard" POM^{9-} stabilizer;[49] (iii) the kinetics of nanoparticle formation occur at a convenient rate at room temperature, under an initial 40 psig of H_2, and exhibit relatively reproducible kinetics; (iv) the nanoparticle formation kinetics can be monitored (indirectly, but in real time) by the CHCRR and (a bit more directly) by the evolution of cyclooctane by gas chromatography or NMR; and (v) the $\{(1,5\text{-COD})Ir^{I}{\bullet}POM\}^{8-}$ system operates via a POM^{9-} dissociative K_{eq} that allows the $[POM^{9-}]$ dependence of the kinetics to be studied en route to unraveling a more detailed nucleation mechanism.[47,62,63] Significantly, the 5 advantages of the $\{(1,5\text{-COD})Ir^{I}{\bullet}POM\}^{8-}$ system allowed the mechanisms in Scheme 4.2 to be uncovered as working hypotheses—a considerable advance given that only LaMer's 1950 model[67] was available before 1997[53]. The pseudo-elementary-step[54] based mechanisms become even more significant when one realizes that *5 classes of 96 distinct mechanisms* now exist compared to zero prior to 1997[53] (i.e., and if one works through the combinations of the pseudo-elementary steps[54] in Scheme 4.2 plus the new 3-step mechanism[18,19] as well as A. Karim's two ligand-based mechanisms[9,32,39] combined with precedented unimolecular[53,64], second-order / bi-molecular[62,64], ter-molecular,[47] or dissociative ligand dependent alternative-termolecular[47] nucleation as mentioned in our ME-PBM papers[18,19]). This arrangement of the mechanisms into 5 classes of 96 mechanisms replaces our prior, initial classification (into "19 classes of 48 distinct mechanisms"[19]) cited in our 2019 paper.[19]

51. Yih, K.-H.; Hamdemir, Isil K.; Mondloch, J. M.; Bayram, E.; Özkar, S.; Vasic, R.; Frenkel A. I.; Anderson, O.; Finke, R. G. Synthesis and Characterization of [(1,5-Cyclooctadiene)Ir(μ-H)]$_4$: A Multipurpose, Tetrametallic, Coordinatively Unsaturated Ir_4-Based Precatalyst and Synthon. *Inorg. Chem.* **2012**, *51*, 3186-3193.

52. Laxson, W. W.; Özkar, S.; Folkman, S.; Finke, R. G. The Story of a Mechanism-Based Solution to an Irreproducible Synthesis Resulting in an Unexpected Closed-System Requirement for the $LiBEt_3H$-Based Reduction: the Case of the Novel Subnanometer Cluster,

[Ir(1,5-COD)(μ-H)]$_4$, and the Resulting Improved, Independently Repeatable, Reliable Synthesis. *Inorg. Chim Acta.* **2015**, *432*, 250-257.

53. Watzky, M. A.; Finke, R. G. Transition Metal Nanocluster Formation Kinetic and Mechanistic Studies. A New Mechanism When Hydrogen Is the Reductant: Slow, Continuous Nucleation and Fast Autocatalytic Surface Growth. *J. Am. Chem. Soc.* **1997**, *119*, 10382–10400. This and a number of our later papers[53-61] also check the precursor, A = $\{(1,5\text{-COD})Ir^{I}\bullet POM\}^{8-}$ conversion by GLC monitoring of the cyclooctane produced due to hydrogenation of the 1,5-COD ligand in the precursor, A, under the reaction conditions.

54. Field, R. J.; Noyes, R. M. Oscillations in chemical systems. 18. Mechanisms of chemical oscillators: Conceptual bases. *Acc. Chem. Res.* **1977**, *10*, 214-221.

55. Widegren, J. A.; Aiken, J. D., III; Özkar, S.; Finke, R. G. Additional Investigations of a New Kinetic Method To Follow Transition-Metal Nanocluster Formation Including the Discovery of Heterolytic Hydrogen Activation in Nanocluster Nucleation Reactions. *Chem. Mater.* **2001**, *13*, 312-324. In the main text of this reference, see Figure 7 and Scheme 2 in comparison to SI Figure E to see the simulated effect of introducing a hypothetical Ir_{13} Catalytically Effective Nucleus[92] before the CHCRR could begin or, presumably, before cyclooctane evolution as monitored by GLC could begin.

56. Özkar, S.; Finke, R. G. Transition-Metal Nanocluster Stabilization Fundamental Studies: Hydrogen Phosphate as a Simple, Effective, Readily Available, Robust, and Previously Unappreciated Stabilizer for Well-Formed, Isolable, and Redissolvable Ir(0) and Other Transition-Metal Nanoclusters. *Langmuir* **2003**, *19*, 6247-6260.

57. Hornstein, B. J.; Finke, R. G. Transition-Metal Nanocluster Kinetic and Mechanistic Studies Emphasizing Nanocluster Agglomeration: Demonstration of a Kinetic Method That Allows Monitoring All Three Phases of Nanocluster Formation and Aging. *Chem. Mater.* **2004**, *16*, 139-150. (See also the addition / correction: *Chem. Mater.* **2004**, *16*, 3972.)

58. Besson, C.; Finney, E. E.; Finke, R. G. A Mechanism for Transition-Metal Nanoparticle Self-Assembly. *J. Am. Chem. Soc.* **2005**, *127*, 8179-8184.

59. Besson, C.; Finney, E. E.; Finke, R. G. Nanocluster Nucleation, Growth and Then Agglomeration Kinetic and Mechanistic Studies: A More General, Four-Step Mechanism Involving Double Autocatalysis. *Chem. Mater.* **2005**, *17*, 4925-4938.

60. Finney, E. E.; Finke, R. G. The Four-Step, Double-Autocatalytic Mechanism for Transition-Metal Nanocluster Nucleation, Growth and Then Agglomeration: Metal, Ligand, Concentration, Temperature, and Solvent Dependency Studies. *Chem. Mater.* **2008**, *20*, 1956-1970.

61. Kent, P. D.; Mondloch, J. E.; Finke, R. G. A Four-Step Mechanism for the Formation of Supported-Nanoparticle Heterogeneous Catalysts in Contact with Solution: The Conversion of Ir(1,5-COD)Cl/γ-Al_2O_3 to Ir(0)$_{\sim 170}$/γ-Al_2O_3. *J. Am. Chem. Soc.* **2014**, *136*, 1930-1941.

62. Laxson, W. W.; Finke, R. G. Nucleation is Second Order: An Apparent Kinetically Effective Nucleus of Two for Ir(0)$_n$ Nanoparticle Formation From $[(1,5\text{-COD})Ir^{I}\bullet P_2W_{15}Nb_3O_{62}]^{8-}$ Plus Hydrogen. *J. Am. Chem. Soc.* **2014**, *136,* 17601-17615. Please also see the references therein to the importance of nucleation to particle formation reactions across nature, the difficulties in measuring nucleation kinetics and their rate constants, hence the rarity of detailed nucleation *mechanisms*, and now also the emerging paradigm of low-molecularity nucleation in at least strong-bonding chemical systems. The emerging importance of and references to prenucleation clusters are provided in a recent review,[66] along with a discussion of the issue of if such clusters are on vs off the kinetically dominant pathway.[66]

63. Özkar, S.; Finke, R. Dust Effects On Nucleation Kinetics and Nanoparticle Product Size Distributions: The Illustrative Case Study of a Prototype Ir(0)$_n$ Transition-Metal Nanoparticle Formation System. *Langmuir* **2017**, *33*, 6550-6562. See also the references in this paper to the history and prior key literature on the effects of dust on particle formation and nucleation kinetics.

64. Whitehead, C. B.; Finke, R. G. Nucleation Kinetics and Molecular Mechanism in Transition-Metal Nanoparticle Formation: The Intriguing, Informative Case of a Bimetallic Precursor, $\{[(1,5\text{-COD})Ir^{I}\bullet HPO_4]_2\}^{2-}$. *Chem. Mater.* **2019**, *31*, 2848-2862.

65. Whitehead, C. B.; Özkar, S.; Finke, R. G. LaMer's 1950 Model for Particle Formation of Instantaneous Nucleation and Diffusion-Controlled Growth: A Historical Look at the Model's Origins, Assumptions, Equations, and Underlying Sulfur Sol Formation Kinetics Data. *Chem. Mater.* **2019**, *31*, 7116-7132.

66. Whitehead, C. B.; Özkar, S.; Finke, R. G. LaMer's 1950 Model of Particle Formation: A Review and Critical Analysis of Its Classical Nucleation and Fluctuation Theory Basis, of Competing Models and Mechanisms for Phase-Changes and Particle Formation, and then of Its Application to Silver Halide, Semiconductor, Metal, and Metal-Oxide Nanoparticles. *Mater. Adv.* **2020**, *2*, 186-235. See also the extensive list of references therein.

67. LaMer, V. K.; Dinegar, R. H. Theory, production and mechanism of formation of monodispersed hydrosols. *J. Am. Chem. Soc.* **1950**, *72*, 4847−4854.

68. Patakfalvi, R.; Papp, S.; Dékány, I. The kinetics of homogeneous nucleation of silver nanoparticles stabilized by polymers. *J. Nanopart. Res.* **2007**, *9*, 353-364.

69. Kytsya, A.; Bazylyak, L.; Simon, P.; Zelenina, I.; Antonyshyn, I. Kinetics of Ag_{300} nanoclusters formation: The catalytically effective nucleus via a steady-state approach. *Int. J. Chem. Kinet.* **2019**, *51*, 266-273.

70. Moiraghi, R.; Douglas-Gallardo, O. A.; Coronado, E. A.; Macagno, V. A.; Pérez, M. A. Gold nucleation inhibition by halide ions: a basis for seed-mediated approach. *RSC Adv.* **2015**, *5*, 19329-19336.

71. Munnik, P.; de Jongh, P. E.; de Jong, K. P. Recent Developments in the Synthesis of Supported Catalysts. *Chem. Rev.* **2015**, *115*, 6687-6718.

72. Scheeren, C. W.; Machado, G.; Dupont, J.; Fichtner, P. F. P.; Texeira, S. R. Nanoscale Pt(0) Particles Prepared in Imidazolium Room Temperature Ionic Liquids: Synthesis from an Organometallic Precursor, Characterization, and Catalytic Properties in Hydrogenation Reactions. *Inorg. Chem.* **2003**, *42*, 4738-4742.

73. Jaska, C. A.; Manners, I. Heterogeneous or Homogeneous Catalysis? Mechanistic Studies of the Rhodium-Catalyzed Dehydrocoupling of Amine-Borane and Phosphine-Borane Adducts. *J. Am. Chem. Soc.* **2004**, *126*, 9776-9785.

74. Desforges, A.; Deleuze, H.; Mondain-Monval, O.; Backov, R. Palladium Nanoparticle Generation within Microcellular Polymeric Foam and Size Dependence under Synthetic Conditions. *Ind. Eng. Chem. Res.* **2005**, *44*, 8521-8529.

75. Borgia, M. B.; Nickson, A. A.; Clarke, J.; Hounslow, M. J. A Mechanistic Model for Amorphous Protein Aggregation of Immunoglobulin-like Domains. *J. Am. Chem. Soc.* **2013**, *135*, 6456-6464.

76. Gillam, J. E.; MacPhee, C. E. Modelling amyloid fibril formation kinetics: mechanisms of nucleation and growth. *J. Phys.: Condens. Matter* **2013**, *25*, 373101.

77. Morris, A. M.; Watzky, M. A.; Finke, R. G. Protein aggregation kinetics, mechanism, and curve-fitting: a review of the literature. *Biochim. Biophys. Acta, Proteins Proteomics* **2009**, *1794*, 375-397.

78. Chen, D. P.; Fu, J.; Skrabalak, S. E. Towards Shape Control of Metal Oxide Nanocrystals in Confined Molten Media. *ChemNanoMat* **2015**, *1*, 18-26.

79. Salzillo, T.; Zaccheroni, S.; Della Valle, R. G.; Venuti, E.; Brillante, A. Micro Raman Investigation of the Photodimerization Reaction of 9-Cyanoanthracene in the Solid State. *J. Phys. Chem. C* **2014**, *118*, 9628-9635.

80. Avinash, M. B.; Sandeepa, K. V.; Govindaraju, T. Emergent Behaviors in Kinetically Controlled Dynamic Self-Assembly of Synthetic Molecular Systems. *ACS Omega* **2016**, *1*, 378-387.

81. Oladoja, N. A. A critical review of the applicability of Avrami fractional kinetic equation in adsorption-based water treatment studies. *Desalin. Water Treat.* **2015**, *57*, 15813-15825.

82. Randolph, A. D. A population balance for countable entities. *Can. J. Chem. Eng.* **1964**, *42*, 280-281.

83. Hulburt, H. M.; Katz, S. Some problems in particle technology. A statistical mechanical formulation. *Chem. Eng. Sci.* **1964**, *19*, 555-574.

84. Randolph, A. D.; Larson, M. A. The Population Balance. *Theory of Particulate Processes. Analysis and Techniques of Continuous Crystallization*; Academic Press: New York and London, 1971; p 46 for McCabe's law, which states that the growth rate is independent of diameter (length) of the particles.

85. Ramkrishna, D. The status of population balances. *Rev. Chem. Eng.* **1985**, *3*, 49-95.

86. Ramkrishna, D. Population Balances. *Theory and Application to Particulate Systems in Engineering*; Academic Press: New York, 2000.

87. Ramkrishna, D.; Mahoney, A. W. Population balance modeling. Promise for the future. *Chem. Eng. Sci.* **2002**, *57*, 595-606.

88. Aiken, J. D., III; Lin, Y.; Finke, R. G. A Perspective on Nanocluster Catalysis: Polyoxoanion and $(n\text{-}C_4H_9)_4N^+$ Stabilized $Ir(0)_{\sim 300}$ Nanocluster "Soluble Heterogeneous Catalysts". *J. Mol. Catal. A: Chem.* **1996**, *114*, 29-51. See p. 33 for the definition of "near-monodisperse" particle-size distributions.

89. Özkar, S.; Finke, R. G. The hydrogenphosphate complex of (1,5-cyclooctadiene)iridium(I), $\{[Bu_4N][(1,5\text{-COD})Ir{\bullet}HPO_4]\}_n$: synthesis, spectroscopic characterization, and ES-MS of a new, preferred precursor to HPO_4^{2-} and Bu_4N^+ stabilized $Ir(0)_n$ nanoclusters. *J. Organomet. Chem.* **2004**, *689*, 493–501.

90. Paraphrasing from our 2019 paper[64], the advantages of {[(1,5-COD)Ir^{I}•HPO_4]$_2$[Bu_4N]$_2$} as a nanoparticle precatalyst and for kinetic and mechanistic studies, include: (i) $(Bu_4N)_2HPO_4$ is readily prepared from commercially available, inexpensive $(Bu_4N)H_2PO_4$ by the addition of $Bu_4N^+OH^-$; (ii) HPO_4^{2-} has a valuable, direct ^{31}P NMR handle; (iii) HPO_4^{2-} ranks only slightly below the "Gold Standard"[49] $P_2W_{15}Nb_3O_{62}^{9-}$ polyanionic system as a stabilizer so that (iv) clean, reproducible $Ir(0)_n$ nanoparticle formation, with no bulk-metal formation, is seen using ≥ 2 equivalents of $(Bu_4N)_2HPO_4$; (v) reproducible, sigmoidal kinetics of nanoparticle formation are exhibited that occur at convenient rates using an easily implemented, *in situ* generation of {[(1,5-COD)Ir^{I}•HPO_4][Bu_4N]}$_2$; and (vi) this *in situ* synthesis and system allows kinetics studies wherein the Ir^{I}/HPO_4^{2-} ratio can be readily changed to optimize both the stability of the system and the nanoparticle formation kinetics. Additionally (vii) the existence of a HPO_4^{2-} dissociative equilibrium, K_{Diss}, allows one to probe the [HPO_4^{2-}] dependence on the particle formation kinetics en route to a more detailed nucleation mechanism.[64] Further, (viii) the {[(1,5-COD)Ir^{I}•HPO_4]$_2$}$^{2-}$ system has permitted successful synchrotron SAXS and XAFS experiments as well as ME-PBM studies of TEM-determined PSD data vs time reported as part of the present work. The above advantages so noted, also noteworthy is the extended effort since 2003[56] that has been required to complete the present particle formation kinetics and mechanistic studies.

91. Mondloch, J. E.; Finke, R. G. Kinetic Evidence for Bimolecular Nucleation in Supported-Transition-Metal-Nanoparticle Catalyst Formation in Contact with Solution: The Prototype Ir(1,5-COD)Cl/γ–Al_2O_3 to $Ir(0)_{\sim 600-900}/\gamma$–$Al_2O_3$ System. *ACS Catal.* **2012**, *2*, 298-305.

92. Watzky, M. A.; Finke, R. G. Nanocluster Size-Control and "Magic Number" Investigations. Experimental Tests of the "Living-metal Polymer" Concept and of Mechanism-Based Size-Control Predictions Leading to the Syntheses of Iridium(0) Nanoclusters Centering about Four Sequential Magic Numbers. *Chem. Mater.* **1997**, *9*, 3083-3095.

93. Mondloch, J. E.; Finke, R. G. Supported-Nanoparticle Heterogeneous Catalyst Formation in Contact with Solution: Kinetics and Proposed Mechanism for the Conversion of Ir(1,5-COD)Cl/γ–Al_2O_3 to $Ir(0)_{\sim 900}/\gamma$–Al_2O_3. *J. Am. Chem. Soc.* **2011**, *133*, 7744-7756.

94. Handwerk, D. R.; Shipman, P. D.; Özkar, S.; Finke, R. G. Dust Effects on $Ir(0)_n$ Nanoparticle Formation Nucleation and Growth Kinetics and Particle Size-Distributions: Analysis by and Insights from Mechanism-Enabled Population Balance Modeling. *Langmuir* **2020**, *36*, 1496-1506.

95. Whitehead, C. B.; Watzky, M. A.; Finke, R. G. Burst Nucleation vs Burst Growth in Near-Monodisperse Particle Formation Reactions: A Perspective. *J. Phys. Chem. C* **2020**, *124*, 24543-24554.

96. Özkar, S.; Finke, R. G. Transition-Metal Nanocluster Stabilization Fundamental Studies: Hydrogen Phosphate as a Simple, Effective, Readily Available, Robust, and Previously Unappreciated Stabilizer for Well-Formed, Isolable, and Redissolvable Ir(0) and Other Transition-Metal Nanoclusters. *Langmuir* **2003**, *19*, 6247-6260.

97. Kulkarni, S. A.; Kadam, S. S.; Meekes, H.; Stankiewicz, A. I.; ter Horst, J. H. Crystal Nucleation Kinetics from Induction Times and Metastable Zone Widths. *Cryst. Growth Des.* **2013**, *13*, 2435-2440.

98. Widegren, J. A.; Bennett, M. A.; Finke, R. G. Is It Homogeneous or Heterogeneous Catalysis? Identification of Bulk Ruthenium Metal as the True Catalyst in Benzene Hydrogenations Starting with the Monometallic Precursor, Ru(II)(η^6-C_6Me_6)$(OAc)_2$, Plus Kinetic Characterization of the Heterogeneous Nucleation, Then Autocatalytic Surface-Growth Mechanism of Metal Film Formation. *J. Am. Chem. Soc.* **2003**, *125*, 10301-10310. This work documents the level of error in k_{1obs} and k_{2obs} one can see when heterogeneous, vs homogeneous, nucleation is involved.

99. Day, V. W.; Klemperer, W. G.; Main, D. J. Niobotungstate, $Nb_2W_4O_{19}^{4-}$ and triphosphate, $P_3O_9^{3-}$, complexes of (cyclooctadiene)-iridium(I): synthesis, structure, and stability of tetra-*n*-butylammonium salts of $\{[(C_8H_{12})Ir]_5(Nb_2W_4O_{19})_2\}^{3-}$, $\{[(C_8H_{12})Ir]_2H(Nb_2W_4O_{19})_2\}^{5-}$, and $[(C_8H_{12})Ir(P_3O_9)]^{2-}$. *Inorg. Chem.* **1990**, *29*, 2345-2355.

100. Guthrie, J. P. Hydration and dehydration of phosphoric acid derivatives: free energies of formation of the pentacoordinate intermediates for phosphate ester hydrolysis and of monomeric metaphosphate. *J. Am. Chem. Soc.* **1977**, *99*, 3991-4001.

101. Van Wazer, J. R.; Griffith, E. J.; McCullough, J. F. Hydrolysis of Condensed Phosphates. *J. Am. Chem. Soc.* **1952**, *74*, 4977-4978.

102. Cotton, F. A.; Wilkinson, G. *Advanced Inorganic Chemistry*, 5th ed.; John Wiley & Sons: New York, 1988.

103. Ramirez, F.; Marecek, J. F. Oxyphosphorane and monomeric metaphosphate ion intermediates in phosphoryl transfer from 2,4-dinitrophenyl phosphate in aprotic and protic solvents. *J. Am. Chem. Soc.* **1979**, *101*, 1460-1465.

104. We greatly appreciate and acknowledge Patrick Kent for his contributions beginning back in 2014 and then providing us with his work cited herein, so this longstanding effort could finally be published without further delay. We further offer our most sincere condolences to Patrick on the tragic passing of his wife.

105. Newville, M. IFEFFIT: interactive XAFS analysis and FEFF fitting. *J. Synchrotron Radiat.* **2001**, *8*, 322-324.

106. Frenkel, A. I.; Kleifeld, O.; Wasserman, S.; Sagi, I. Phase speciation by extended x-ray absorption fine structure spectroscopy. *J. Chem. Phys.* **2002**, *116*, 9449-9456.

107. Wang, Q.; Hanson, J. C.; Frenkel, A. I. Solving the structure of reaction intermediates by time-resolved synchrotron x-ray absorption spectroscopy. *J. Chem. Phys.* **2008**, *129*, 234502.

108. Dias, E. T.; Gill, S. K.; Liu, Y.; Halstenberg, P.; Dai, S.; Huang, J.; Mausz, J.; Gakhar, R.; Phillips, W. C.; Mahurin, S.; Pimblott, S. M.; Wishart, J. F.; Frenkel, A. I. Radiation-Assisted Formation of Metal Nanoparticles in Molten Salts. *J. Phys. Chem. Lett.* **2021**, *12*, 157-164.

109. Ma, J.; Zou, Y.; Jiang, Z.; Huang, W.; Li, J.; Wu, G.; Huang, Y.; Xu, H. An in situ XAFS study—the formation mechanism of gold nanoparticles from X-ray-irradiated ionic liquid. *Phys. Chem. Chem. Phys.* **2013**, *15*, 11904-11908.

110. Bharti, A.; Bhardwaj, R.; Agrawal, A. K.; Goyal, N.; Gautam, S. Monochromatic X-Ray Induced Novel Synthesis of Plasmonic Nanostructure for Photovoltaic Application. *Sci. Rep*. **2016**, *6*, 22394.

111. Grand, J.; Ferreira, S. R.; de Waele, V.; Mintova, S.; Nenoff, T. M. Nanoparticle Alloy Formation by Radiolysis. *J. Phys. Chem. C* **2018**, *122*, 12573-12588.

112. Quinson, J.; Jensen, K. M. Ø. From platinum atoms in molecules to colloidal nanoparticles: A review on reduction, nucleation and growth mechanisms. *Adv. Colloid Interface Sci.* **2020**, *286*, 102300.

113. Remita, S.; Fontaine, P.; Lacaze, E.; Borensztein, Y.; Sellame, H.; Farha, R.; Rochas, C.; Goldmann, M. X-ray radiolysis induced formation of silver nano-particles: A SAXS and UV-visible absorption spectroscopy study. *Nuc. Instr. Meth. B* **2007**, *263*, 436-440.

114. Bondaz, L.; Fontaine, P.; Muller, F.; Pantoustier, N.; Perrin, P.; Morfin, I.; Goldmann, M.; Cousin, F. Controlled Synthesis of Gold Nanoparticles in Copolymers Nanomolds by X-ray Radiolysis. *Langmuir* **2020**, *36*, 6132-6144.

115. Yamaguchi, A.; Fukuoka, T.; Okada, I.; Ishihara, M.; Sakurai, I.; Utsumi, Y. Caltrop Particles Synthesized by Photochemical Reaction Induced by X-Ray Radiolysis. *J. Synchrotron Radiat.* **2017**, *24*, 653-660.

116. Stachowski, T. R.; Snell, M. E.; Snell, E. H. SAXS studies of X-ray induced disulfide bond damge: Engineering high-resolution insight from a low-resolution technique. *Plos One* **2020**, *15*, 0239702. DOI: 10.1371/journal.pone.0239702.

117. The ~10^{15} solvated electrons results from the rough estimation reported in the Supporting Information of reference 106. Therein, it is calculated that 1 photon of 8 keV energy results in the formation of ~300 absorbed electrons. Hence, given the observed complete absorption of radiation in the system examined, it was calculated that (300 absorbed electrons / photon) x (~$3x10^{13}$ photons / second) = ~10^{15} solvated electrons per second are produced.

118. Aiken, J. D. III; Finke, R. G. Nanocluster Formation Synthetic, Kinetic and Mechanistic Studies. The Detection of, and then Methods to Avoid, Hydrogen Mass-Transfer Limitations in the Synthesis of Polyoxoanion- and Tetrabutylammonium- Stabilized, Near Monodisperse 40 ± 6 Å Rh(0) Nanoclusters, *J. Am. Chem. Soc.* **1998**, *120*, 9545.

119. Hoops, S.; Sahle, S.; Gauges, R.; Lee, C.; Pahle, J.; Simus, N.; Singhal, M.; Xu, L.; Mendes, P.; Kummer, U. COPASI-a COmplex PAthway SImulator. *Bioinformatics* **2006**, *22*, 3067-3074.

120. Li, T.; Senesi, A. J.; Lee, B. Small Angle X-ray Scattering for Nanoparticle Research. *Chem. Rev.* **2016**, *116* 11128-11180.

121. Sun, Y.; Ren, Y. In Situ Synchrotron X-Ray Techniques for Real-Time Probing of Colloidal Nanoparticles Synthesis. *Part. Part. Syst. Charact.* **2013**, *30*, 399-419.

122. Woehrle, G. H.; Hutchison, J. E.; Özkar, S.; Finke, R. G. Analysis of Nanoparticle Transmission Electron Microscopy Data Using a Public- Domain Image-Processing Program, Image. *Turk. J. Chemistry* **2006**, *30*, 1-13.

123. Bentea, L.; Watzky, M. A.; Finke, R. G. Sigmoidal Nucleation and Growth Curves Across Nature Fit by the Finke–Watzky Model of Slow Continuous Nucleation and Autocatalytic Growth: Explicit Formulas for the Lag and Growth Times Plus Other Key Insights. *J. Phys. Chem. C* **2017**, *121*, 5302–5312.

124. Limiting explanations for the quantitative differences in the k_{1obs} and k_{2obs} values between the XANES vs Tandem CHCRR, in-house CHCRR, and in-house GLC include: (i) that precedented,[106,107,108] X-ray-induced radiolysis yields e^- that reduce small amounts of the Ir^I precatalyst to (autocatalytic[53]) Ir(0), thereby artifactually accelerating nucleation and subsequent exponential, autocatalytic growth[46,53] in the synchrotron x-ray dependent experiments; or that (ii) differences in reaction conditions are present for the synchrotron vs in-house experiments, for

example in the dust content or adventitious impurities (i.e., despite every effort being made to control the solvent, precursor and other variables so as to make all the kinetics experiments as comparable as possible). As for the CHCRR, (iii) a somewhat lengthened induction period in the CHCRR and GLC methods is possible if not likely because the CHCRR and GLC methods depend on the development of small, $\geq Ir_{2\text{-}3}$ clusters or particles that are able to do hydrogenation catalysis which, in turn, simulations[55] show that an assumed / model Catalytically Effective Nucleus (CEN)[92] of just $Ir_{\sim 13}$ could lead to a ~10-fold increase in the simulated[55] induction time and, then, differences in the correlated k_{1obs} and k_{2obs} rate constant variables[121]. A derivation and additional discussion provided in Appendix III of the possible effects of a CEN of $B_{\leq 26}$ on the kinetics of the CHCRR.

125. The reader might ask "Why, then, wasn't the microfiltration protocol used as part of the present studies"? The answer is simple; we deliberately did not try to exclude dust from the present studies because: (i) dust is a common component of nearly all current nanoparticle syntheses and, hence, we wanted to answer the questions posed in the Introduction for the most common reaction conditions, that is, when dust is present. Second, (ii) since we have already documented the effects of lowering the dust content in the $\{[(1,5\text{-COD})Ir^{I}\bullet\mathbf{HPO_4}]_2\}^{2-}$ precursor system, further knowledge of the effects of dust is not needed to answer any of the questions posed in the Introduction. And third, as we have pointed out elsewhere[63], (iii) what is needed next is the control of dust at, ideally, the level of a Class 9 Clean Room, studies that become very challenging to impossible depending on what physical method is being employed and whether or not it involves synchrotron radiation,[106,107,108,109] including at different sources across the world with several collaborators as we have employed.

126. Kerker, M.; Daby, E.; Cohen, G. L.; Kratohvil, J. P.; Matijevic, E. Particle size distribution in LaMer sulfur sols. *J. Phys. Chem.* **1963**, *67*, 2105-2111.

127. Petro, A. J. Particle size distribution in monodisperse sulfur hydrosols. *J. Phys. Chem.* **1960**, *64,*1508-1511.

128. Nucleation—a Transition State to the Directed Assembly of Materials. *Faraday Discussions*; Royal Society of Chemistry: U.K., **2015**; Vol. *179*, 9–557.

129. Spurny, K. R. Atmospheric Condensation Nuclei P. J. Coulier 1875 and J. Aitken 1880 (Historical Review). *Aerosol Science and Technology*, **2000**, *32*, 243-248.

130. Coulier, P. J. Note sur une nouvelle propriete de l'air. *J. de Pharmacie et de Chimie*, *Paris*, *Ser.* **1875**, *4*, 165-173.

131. Aitken, J. On the dust, fog, and clouds. *Proc. Roy. Soc.* **1882**, *11*, 14-18.

132. Aitken, J. On the numbers of dust particles in the atmosphere in certain places in Great Britain and on the continent, with remarks on the relation between the amount of dust and meteorological phenomena. *Transactions of the Royal Society of Edinburgh* **1889**, *35*, 1-19.

133. Aitken, J. On improvements in the apparatus for counting the dust particles in the atmosphere, *Proc. Roy. Soc.* **1890**, *16*, 135-172.

134. Aitken, J. On a simple pocket dust-counter. *Proc. Roy. Soc.* **1892**, *18*, 39-52.

135. Wilson, C. T. R. Condensation of water vapour in the presence of dust-free air and other gases. *Phil. Trans. Royal Soc. London*, **1897**, 189, 265-307.

136. Kent, P.; Mondloch, J. E.; Finke, R. G. Synthesis of Heterogeneous $Ir^0_{\sim 600\text{-}900}/\gamma\text{-}Al_2O_3$ in One Pot From the Precatalyst Ir(1,5-COD)Cl/γ-Al_2O_3: Discovery of Two Competing Trace "Ethyl Acetate Effects" on the Nucleation Step and Resultant Product. *ACS Catal.* **2016**, *6*, 5449–5461.

137. Oxtoby, D. W. Homogeneous nucleation: theory and experiment. *J. Phys.: Condens. Mat.* **1992**, *4*, 7627-7650.

138. Precise, albeit not necessarily accurate, *particle-formation rate* measurements are reported in the state-of-the-art crystallization study by Kulkarni and co-workers.[97] Briefly (and as discussed in more detail elsewhere[63] for the interested reader), the organic compound isonicotinamide at supersaturating concentrations was heated, then cooled, while a loss from "100% Transmissivity" of the initially-clear-when-hot solution was monitored as crystallization ensued (with an implied ±3% error in the "Transmissivity" from examining Figure 1 in that work[97]). The heating-cooling cycle was repeated 144 times for each solution, yielding as much and as precise crystallization kinetic data as one will find in the literature—albeit not for 144 independent experiments. The data were analyzed by assuming nucleation is stochastic (i.e., probabilistic) and then analyzing the data with a non-mechanistic, empirical "nucleation rate", J, model, $J(S) = A * S * \exp\left(\frac{-B}{ln^2 S}\right)$, where S is the supersaturation and A and B are "kinetic and nucleation rate parameters".[97] The empirical "nucleation rate, J" monitored by a decrease in the intensity of transmitted light and error bars were J = 631 ± 9 m^{-3} s^{-1}, that is, ±1.4%. Unfortunately, one issue with this otherwise very precise and noteworthy work is that the "J nucleation rate" may well be monitoring both nucleation and growth, not to a true nucleus such as the Kinetically Effective Nucleus,[62] but instead to the First Observable Cluster[62], reported however as a "nucleus size" of between 11-50 atoms. Further kinetics and especially a rate law for nucleation and growth will be required to obtain the particle-formation mechanism underlying this noteworthy, high-precisions crystallization system.

139. Skoog, D. A.; Holler, F. J.; Crouch, S. R. Evaluation of Analytical Data. In *Instrumental Analysis*. Cengage Learning: New Dehli, 2007.

140. Whitehead, C. B.; Finke, R. G. A Review of Metal, Metal-Oxide, and Semiconductor Nanoparticle Formation Based on In Situ Synchrotron XAFS and SAXS Investigations En Route to Reliable Minimum Mechanisms. **2021**, *submitted for publication (herein Chapter II).*

141. Timoshenko, J.; Frenkel, A. I. "Inverting" X-ray Absorption Spectra of Catalysts by Machine Learning in Search for Activity Descriptors. *ACS Catal.* **2019**, *9*, 10192-10211.

142. Timoshenko, J.; Lu, D.; Lin, Y.; Frenkel, A. I. Supervised Machine-Learning-Based Determination of Three-Dimensional Structure of Metallic Nanoparticles. *J. Phys. Chem. Lett.* **2017**, *8*, 5091-5098.

143. Marcella, N.; Liu, Y.; Timoshenko, J.; Guan, E.; Luneau, M.; Shirman, T.; Plonka, A. M.; van der Hoeven, J. E. S.; Aizenberg, J.; Friend, C. M; Frenkel, A. I. Neural network assisted analysis of bimetallic nanocatalysts using X-ray absorption near edge structure spectroscopy. *Phys. Chem. Chem. Phys.* **2020**, *22*, 18902-18910.

144. Liu, Y.; Marcella, N.; Timoshenko, J.; Halder, A.; Yang, B.; Kolipaka, L.; Pellin, M. J.; Seifert, S.; Vajda, S.; Liu, P.; Frenkel, A. I. Mapping XANES spectra on structural descriptors of copper oxide clusters using supervised machine learning. *J. Chem. Phys.* **2019**, *151*, 164201.

145. Timoshenk, J.; Halder, A.; Yang, B.; Seifert, S.; Pellin, M. J.; Vajda, S.; Frenkel, A. I. Subnanometer Substructures in Nanoassemblies Formed from Clusters under a Reactive Atmosphere Revealed Using Machine Learning. *J. Phys. Chem. C* **2018**, *122*, 21686-21693.

146. Frenkel, A. I.; Hills, C. W.; Nuzzo, R. G. A View from the Inside: Complexity in the Atomic Scale Ordering of Supported Metal Nanoparticles. *J. Phys. Chem. B* **2001**, *105*, 12689-12703.

147. Frenkel, A. I. Solving the structure of nanoparticles by multiple-scattering EXAFS analysis. *J. Synchrotron Rad.* **1999**, *6*, 293-295.

148. Frenkel, A. I. Applications of extended X-ray absorption fine-structure spectroscopy to studies of bimetallic nanoparticle catalysts. *Chem. Soc. Rev.* **2012**, *41*, 8163-8178.

149. Roese, S.; Kononov, A.; Timoshenko, J.; Frenkel, A. I.; Hövel, H. Cluster Assemblies Produced by Aggregation of Preformed Ag Clusters in Ionic Liquids. *Langmuir* **2018**, *34*, 4811-4819.

150. Timoshenko, J.; Roese, S.; Hövel, H.; Frenkel, A. I. Silver clusters shape determination from in-situ XANES data. *Radiat. Phys. Chem.* **2020**, *175*, 108049.

151. Che, M.; Bennett, C. O.; The Influence of Particle Size on the Catalytic Properties of Supported Metals, *Adv. Catal*. **1989**, *36*, 55-172. See p. 110, Figure 9 for example.

152. Finke, R. G.; Watzky, M. A.; Whitehead, C. B. Response to: Particle Size is a Primary Determinant for Sigmoidal Kinetics of Nanoparticle Formation: A "disproof" of the Finke-Watzky (F-W) nanoparticle nucleation and growth mechanism. *Chem. Mater*. **2020**, *32*, 3657-3672.

153. Briefly, the four criteria discussed more in one of our recent reviews[65] are: (i) complete mass- and charge-balanced reactions that sum to the proposed mechanism; (ii) kinetics data; (iii) (pseudo)-elementary step reactions that present the stepwise mechanism with well-defined rate constants; and (iv) disproof of competing, possible, alternative mechanisms en route to an Ockham's razor-obeying, deliberately minimalistic mechanism that, however, can explain all of the available data.

154. Kathmann, S. M.; Schenter, G. K.; Garrett, B. C. Understanding the Sensitivity of Nucleation Kinetics. *J. Chem. Phys.* **2002**, *116*, 5046-5057.

155. Kathmann, S. M.; Schenter, G. K.; Garrett, B. C.; Chen, B.; Siepmann, J. I. Thermodynamics and Kinetics of Nanoclusters Controlling Gas-to-Particle Nucleation. *J. Phys. Chem. C* **2009**, *113*, 10354-10370. See also the references 16 and 25-37 therein concerning DFT studies that strive to go beyond Classical Nucleation Theory.

V. SUMMARY

This dissertation has centered on reliable, disproof-based minimum mechanisms for nanoparticle formation. In Chapter II, a critical review of the relevant metal, metal-oxide, and semiconductor/quantum dot literature demonstrated the progress made in using synchrotron techniques to elucidate particle formation mechanisms. Then, in Chapters III and IV, the molecular mechanism of the second-generation $\{[(1,5\text{-COD})Ir^{I}\bullet HPO_4]_2\}^{2-}$ precursor to $Ir(0)_{\sim 150}(HPO_4^{2-})_x$ nanoparticle system is thoroughly investigated by 2 direct methods and 4 indirect methods for a total of 6 physical methods, plus mechanism-enabled population balance modeling (ME-PBM). The preliminary ME-PBM results further support the claim that ME-PBM must be applied to any particle formation mechanism as a final test of the hypothesized mechanism.

There are several potential avenues for continued research based on the results described herein. They include: (i) the study of greatly applicable metal-oxide or semiconductor/quantum dot systems by the series of 6 physical methods described *vide supra* to elucidate their minimum mechanisms of formation, which have the potential to improve modern technologies and industrial processes; (ii) the use of ME-PBM on the large swath of particle-size distributions available in the literature to test their proposed mechanisms of particle formation, and (iii) the combination of small-angle X-ray scattering (SAXS) and ME-PBM to enable a comprehensive test of the hypothesized minimum mechanism at each time point to observe the contribution of each pseudo-elementary step throughout a given particle-formation process.

APPENDIX I: SUPPORTING INFORMATION FOR CHAPTER II

Contents of this Supporting Information Section

Following additional information for case studies, there are four literature summary tables. These tables, S2.1–S2.4, contain the 69 papers that were analyzed for this review. The following is provided for each paper: (i) a presentation of the system and techniques used to study it; (ii) a synopsis of the reported results; and (iii) a critical analysis of the conclusions. A complete list of abbreviations may be useful and can be found as Appendix IV at the end of this dissertation. Common abbreviations for some of the models and mechanisms discussed in the tables are: AE = Avrami-Erofe'ev[1,2,3]; CNT = Classical Nucleation Theory[4,5,6]; FW = Finke-Watzky (2-Step Mechanism)[7]; and LSW = Liftshitz-Slyozov-Wagner[8,9]. Additionally, disproof-based[10,11] critical analysis is used when assessing the conclusions of the 69 papers. Finally, every attempt was made to remain unbiased and present only the details of the paper and provide a critical analysis of those results; the same approach as my three recent reviews[12,13,14] of the 1950 LaMer model[15].

Case Study #2: Additional Figures and Information

Below as Figures S2.1–S2.3, the accompanying MALDI-TOF mass spectra of the EXAFS experiments (Figure 2.7, Chapter II) on the $RhCl_3$–TTAB–PVP–EG system are given.[16]

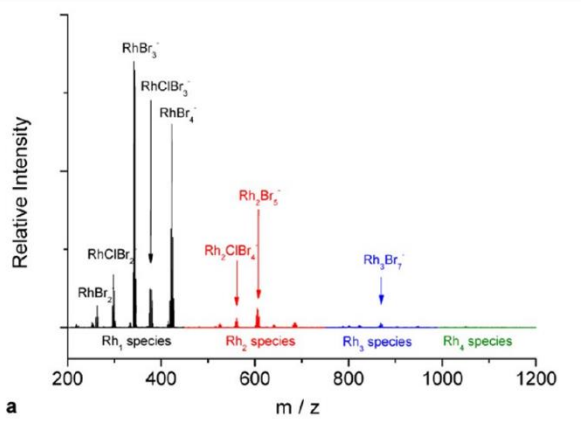

Figure S2.1. Negative ion MALDI-TOF mass spectra of the same $RhCl_3$–TTAB–PVP–EG system as shown in Figure 2.7 (Chapter II) at 3 min after reduction. Figure reproduced in part with permission from ref 16. Copyright 2012 American Chemical Society.

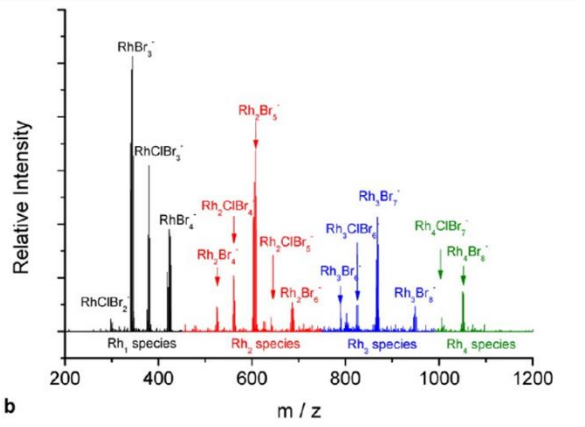

Figure S2.2. Negative ion MALDI-TOF mass spectra of the same $RhCl_3$–TTAB–PVP–EG system as shown in Figure 2.7 (Chapter II) at 15 min after reduction. Figure reproduced in part with permission from ref 16. Copyright 2012 American Chemical Society.

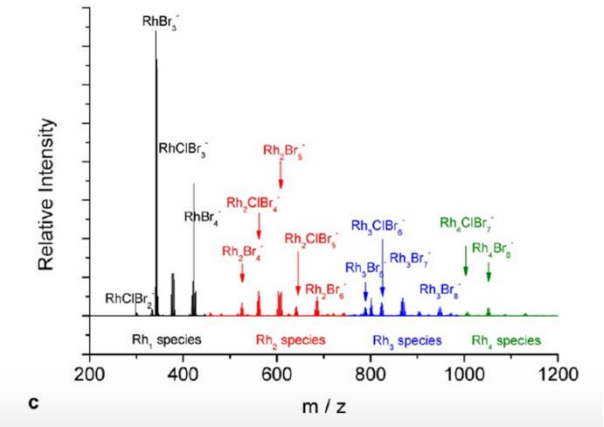

Figure S2.1. Negative ion MALDI-TOF mass spectra of the same $RhCl_3$–TTAB–PVP–EG system as shown in Figure 2.7 (Chapter II) at 20 min after reduction. Figure reproduced in part with permission from ref 16. Copyright 2012 American Chemical Society.

Differential Equations for the Karim 4-Step Mechanism

Set of differential equations (Eqs S2.1-S2.5) that accompany the Table 2.1 entry on the Karim 4-step. These differential equations result from the mechanism given in both Table 2.1 and earlier in Scheme 2.1 in Chapter II.

$$\frac{\mathrm{d}[A]}{\mathrm{d}t} = -k_{1-nuc}[A] - k_{2-growth}[A][B] - k_{3-f}[A][L] + \frac{k_{3-f}}{K_{5-eq}}[AL] \qquad \text{(Eq S2.1)}$$

$$\frac{\mathrm{d}[B]}{\mathrm{d}t} = k_{1-nuc}[A] + k_{2-growth}[A][B] - k_{4-f}[B][L] + \frac{k_{4-f}}{K_{6-eq}}[BL] \qquad \text{(Eq S2.2)}$$

$$\frac{\mathrm{d}[L]}{\mathrm{d}t} = -k_{3-f}[A][L] + \frac{k_{3-f}}{K_{5-eq}}[AL] - k_{4-f}[B][L] + \frac{k_{4-f}}{K_{6-eq}}[BL] \qquad \text{(Eq S2.3)}$$

$$\frac{\mathrm{d}[AL]}{\mathrm{d}t} = k_{3-f}[A][L] - \frac{k_{3-f}}{K_{5-eq}}[AL] \qquad \text{(Eq S2.4)}$$

$$\frac{\mathrm{d}[BL]}{\mathrm{d}t} = k_{4-f}[B][L] - \frac{k_{4-f}}{K_{6-eq}}[BL] \qquad \text{(Eq S2.5)}$$

Table S2.1. Summary of Reviews on Synchrotron XAFS and/or SAXS.

Entry	Title	Topic of the Review	Valuable Insights from the Review for the Scientific Community	Specific Points We Wish to Highlight from the Review	Ref.
1	Characterization of nanoparticles by scattering techniques	The review is focused on scattering techniques for characterization of nanoparticles. "The emphasis is on specific applications to determine the size, shape, and structure of particles, especially nanoparticles, by using the scattering techniques."[17]	The review has excellent background sections covering the theoretical foundation of SLS versus DLS and SAXS versus SANS. Next, the authors have provided guidance to researchers using angular dependence techniques to determine nanoparticle (i) size, (ii) shape, and (iii) internal structure. Then, the authors provide guidance to researchers re: determining the nanoparticle (i) hydrodynamic radius, (ii) particle size distribution, and then for anisotropic particles (iii) rotational diffusion coefficient.	This review article has an excellent section of derivations for "basic scattering functions". Next, the review covers the specific differences between time-averaged scattering techniques and intensity–intensity time correlation techniques. Finally, the review concisely concludes that "using a combination of different scattering techniques can provide much richer and complementary information on the specific systems."[17]	17
2	Use of SANS and SAXS in study of nanoparticles	The review is focused on the use of SANS, SAXS, or tandem SANS/SAXS to study nanoparticles. The review covers background knowledge of SANS and SAXS, the concept of Contrast Factor, and a case study of researching micelles using SANS/SAXS.	The two different techniques, SANS and SAXS, both have great value when researching micellular species. "For example SAXS experiments on gold nanoparticles will give information about the size of the core"[18] Whereas, "neutrons are largely scattered from hydrogenous material of the capping which constitutes the outer shell of Au nanoparticles."[18] Conversely, for micelles composed of hydrogenous materials, "neutrons see the core of the micelle and X-rays give information about the shell of counterions around the micelle."[18]	Of particular note, the two techniques are highly sensitive. The authors cover a case study where micelles were prepared from 100 mM solutions of sodium dodecyl suphate (SDS) and cetryltrimethylammonium chloride/bromide (CTAC / CTAB). The micelles prepared from SDS/CTAC exhibited similar SANS and SAXS patterns. However, the micelles prepared from SDS/CTAB were dramatically different. The techniques (SANS and SAXS) are extremely "sensitive to even small changes in the thickness of the shell" of the micelle.[18]	18
3	Combining *in situ* characterization methods in one set-up: looking with more eyes into the intricate chemistry of the synthesis and working of	The review by Dr. Ursula Bentrup is focused on the tandem use of several *in situ* characterization techniques to monitor the formation and activity of heterogeneous catalysts. She provides a "*tutorial*	Dr. Bentrup presents numerous excellent points about the use of tandem *in situ* techniques to monitor particle formation and reaction progress. First, is that each method used "has its own potentials, limitations, and special requirements."[19] Hence, it is necessary to understand what the technique's capability is and only apply	In particular, we wish to highlight Table 1 (Overview of available *in situ* techniques together with the specific information to be obtained) and Table 2 (Overview of existing combinations of *in situ* techniques and selected studied reactions). These are a *must read* for anyone preparing to use	19

	heterogeneous catalysts	*review*…of currently available set-ups equipped with multiple techniques for *in situ* catalyst characterization, catalyst preparation, and reaction monitoring."[19]	it to that. Second, from "looking at the specific information available from…different techniques it is evident that only a combination or coupling of different methods enables a comprehensive picture of the working catalysts in the particular reaction" of interest.[19] And third, "it has to be realised that no universal multitechnique set-up exists solving all problems because each applied *in situ* method has specific technical requirements, advantages and disadvantages, and provides definite information."[19]	direct *in situ* techniques to monitor their reaction. Furthermore, it is imperative that one remains vigilant of the limits of a given technique and not interpret their results beyond what the data allows.	
4	In Situ Synchrotron X-Ray Techniques for Real-Time Probing of Colloidal Nanoparticle Synthesis	The review by Y. Sun and Y. Ren provides foundational information on a series of X-ray techniques (XAFS, SAXS, XRD, PDF, TXM, WAXS, and X-ray Raman) for the in-situ study of solution nanoparticle formation. The authors include a series of case studies and *personal* perspectives on the use of the different X-ray techniques.	First, in section 3, TXM is understood to best work with particles between 50-2000 nanometers and "is capable of controlling image contrast of different elements by tuning X-ray energy".[20] In section 4, different variations of XAFS are analyzed. Of note, when dealing with *fast* reaction kinetics, DXAFS is most advisable, but one will lose some energy resolution due to the speed of the measurements. A final, important section to highlight is section 5.3 "In Situ Total Scattering Pair Distribution Function (PDF)"[20]. If PDF is appropriate for one's system, the PDFs "control structural information beyond the first few coordination shells that represents the major information of the XAFS data." Further, "the bond length between atoms derived from the PDFs are the absolute values while the distances extracted from the XAFS measurements are always subject to an offset or derived from a structural model."[20]	We wish to point the reader to Table 1, Figure 6, and Figure 12 within ref 20. Table 1 is a "summary of the in situ synchrotron X-ray techniques for studying colloidal nanoparticle synthesis".[20] Figure 6 shows SAXS scattering patterns for "particles with ideal geometries."[20] Figure 12 presents a "summary of possible processes involved in the growth of shaped nanoparticles made of face-centered cubic metals in liquid solutions as well as the potential capabilities of different in situ techniques for probing different process."[20] Finally, the reader should be mindful when going over ref 20 because it is an excellent source to obtain a foundational understanding for a series of different X-ray techniques, it is not recommended for understanding mechanistic investigations.	20
5	Small Angle X-ray Scattering for Nanoparticle Research	The review by Lee and co-workers is one of the most extensive in the literature today. It covers the majority of topics with the		We recommend this review to anyone that is interested in SAXS and would like to learn from this important review.	21

	primary sections being on the following: (1) Introduction, (2) Data Measurement and Processing, (3) Particle Scattering, (4) Correlation Function Approach, (5) Combination of Scattering with Model Simulations, (6) GISAXS, (7) Applications, and (8) Conclusions and Outlook.	

Table S2.2. Summary of Papers Using SAXS to Collect Kinetics Data.

Entry	Title	System & Techniques Used to Monitor the Kinetics	Results and Proposed Chemical Mechanism	Conclusions, Insights, and Critical Analysis	Ref.
1	Small-angle x-ray scattering analysis of polymer-protected platinum, rhodium, and platinum/rhodium colloidal dispersions	The authors studied the formation of three types of colloidal dispersions: platinum, rhodium, and 1:1 platinum/rhodium; all as polymer-protected dispersions. Aqueous metal salt solutions of hexachloroplatinic(IV) acid and rhodium(III) chloride were prepared. Next, ethanol solutions of PVP were prepared. The two solutions were mixed at 100 ºC, with stirring, and under N_2 gas. Measurements were collected using SAXS, and final particle size and size-distributions were determined using TEM.	Based on their results, the authors hypothesized the formation of their particles follows "three fundamental process… (I) formation of polymer–metal ion complexes, (II) reduction of metal ion complexes and formation of metal atoms, and (III) association of the metal atoms to form the elementary metal clusters."[29] The elementary metal clusters for the three systems are composed of magic number clusters, "i.e., Pt_{55}, Rh_{13}, and $[(Pt/Rh)_{55}]$."[29] "In addition to the processes described above, there is a process leading to formation of the higher-order organization of the superstructure; (IV) agglomeration of the elementary metal clusters into the superstructures and their higher-order organizations."[29] Finally, "[t]he hierarchy observed in the order of decreasing size is as follows: higher-order organization of superstructures>superstructure of fundamental metal clusters>fundamental metal cluster>elementary metal cluster composed of magic number of atoms."[29]	The results presented by the authors are fascinating. They demonstrate the application and benefit of using SAXS on a nanoparticle, colloidal-metal system. Of note, the authors have not attempted to *claim* a mechanism, but rather have presented a hypothesized reaction pathway with pseudo-elementary steps. The mass-balance and kinetics have not been determined, nor have alternative, competing hypotheses been disproven, but, again, the authors have not made claims beyond what the data allow. Intriguingly, with 22 years of hindsight one can now say that the authors have presented fascinating evidence for polymer–metal ion complexation indicative of "prenucleation clusters".[22,23,24,25,26,27,28] This growing concept necessitates additional study while including this paper as recommended background literature.	29
2	Small-Angle X-ray Scattering Study of Platinum-Containing Hydrogel/Surfactant Complexes	Platinum nanoparticles were prepared from a series of different platinum-containing starting materials, reducing agents, and stabilizers. The platinum compounds were	The authors found that $N_2H_4•H_2O$ was a slower reducing agent and "yielded much larger nanoparticles than the fast $NaBH_4$."[30] The $PtCl_4^{2-}$ starting material yielded smaller particles with narrower size	The authors of this study have presented an excellent *proof of concept*, where the use of SAXS and ASAXS are shown to provide excellent, direct, quantitative experimental results and details. These authors have investigated the effects of different variables	30

		$PtCl_4$, Na_2PtCl_6, $(NH_4)_2PtCl_4$, and H_2PtCl_6. The two reducing agents were $NaBH_4$ and $N_2H_4•H_2O$. The cation gel was poly(diallyldimethylammonium chloride) (PDADMACl) with either sodium dodecyl sulfate (SDS) or sodium dodecylbenzene sulfonate (SDBS), both anionic surfactants. The anionic gel / cationic surfactant combination was poly(methacrylic acid) and cetylpyridinium chloride (PMA/CPC). Reactions were run in water under argon. Characterization was done with SAXS and elemental analysis. SAXS measurements were collected using the Pt L_3-edge.	distributions than $PtCl_6^{2-}$, all in the cationic gel/anionic surfactant. Meanwhile, in the anionic gel/cationic surfactant, much larger particles were observed "where the particle growth is not controlled by the internal gel structure."[30] The authors conclude "that the highly ordered zones in the hydrogels concentrate around the growing nanoparticles."[30] Finally, the authors claim "the obtained results illustrate the potential of the SAXS and ASAXS methods allowing systematic selection of metal compounds and reducing agents for the preparation of metal nanoparticles with desired size distributions as well as quantitative characterization of the ordering phenomena in the gel/surfactant complexes."[30]	on the final nanoparticles size distribution. Most importantly, the authors have not attempted to claim results beyond what the data have shown. They suggest reaction pathways, that can now be investigated for the additional evidence (fitting of kinetics data and complete speciation/known stoichiometry) needed before a reliable mechanism can be claimed.	
3	Synthesis of Ultra-small ZnS Nanoparticles by Solid-Solid Reaction in the Confined Space of AOT Reversed Micelles	Small ZnS nanoparticles were prepared in reverse micelle synthesis. AOT (sodium bis(2-ethylhexyl)sulfosuccinate) and *n*-heptane were used to prepare the reverse micelles. The ZnS nanoparticles were made from the solid-solid mix of zinc sulfate and sodium sulfide. The reaction occurred at 22 ºC and studied by UV spectroscopy and SAXS.	The formation reaction was observed to occur on a fast time scale. The resulting nanoparticles were seen to be small, ~2 nm in diameter. In depth investigation revealed that "the coupled analysis of SAXS and UV spectra suggested that the energy gap does not uniquely depend on the nanoparticle size, but one more factor such as atomic arrangement could be involved."[31]	This study is not on the mechanism of the particle formation, but rather on demonstrating a new approach to preparing two-component nanoparticles using a solid-solid synthetic approach. Of note, the authors are careful to not overstate what their data means. In fact, in several instances, they recognize the limitations of their instrumentation and the need for addition investigations using WAXS, EXAFS, XPS, and so on. This is a fundamental, proof-of-concept study, one that does not strive to provide kinetics or mechanistic insights.	31
4	From Pt molecules to nanoparticles: *in-situ* (anomalous) small-angle X-ray scattering studies	Platinum colloids were prepared from $Pt(acac)_2$ in toluene under argon at 333 K. Over 4 hours, $Al(CH_3)_3$, also in toluene, was slowly added. The	The authors present ASAXS results of their $Pt_{\sim 53}$ nanoparticle system stabilized by what they call an organic shell. ASAXS data was collected on quenched reactions	Of note, the authors have used the "anomalous scattering from the metal atoms [to separate] the superimposed small angle scattering contributions from particles and the organic molecules in the solvent."[32] However, the	32

		reaction ran for ~24 hours until the solution changed from yellow to black and gas evolution had stopped. Characterization was done ex situ by quenching the aliquot to 195 K with liquid nitrogen. Measurements were taken using NMR (^{1}H, ^{13}C, and coupled to ^{195}Pt), XANES, ASAXS, TEM, and DFT. This report was focused on the ASAXS studies.	between 0.8 and 63 hours at room temperature. The authors found that "with increasing reaction time, the scattering intensity increases by half an order of magnitude, whereas the overall shape of the scattering curves remains essentially unchanged."[32] Then, they authors attempted to fit their kinetics data with an exponential power function. Finally, they claim "the nucleation of Pt nanoparticles with a rather narrow size distribution."[32]	analysis of the results are plagued by attempted *proof*-based and confirmation-bias laden experimentation, in which the experiments are designed to try to *prove* the author's conclusions—rather than the needed disproof of multiple alternative hypotheses. Further, the claim of a "narrow size distribution"[32] is not substantiated with any direct TEM images, size distributions, or even error associated with the average particle size. Finally, the kinetics data were 'fit' using a semi-empirical exponential function, that in essence is just the Avrami-Erofe've equation. Yet, there was no explanation for the use of the exponential function, nor did its use provide any valuable information on the mechanism or potential reaction pathways for the formation of $Pt_{\sim 53}$. Hence, considerable caution is recommended when reading this paper or using its contents or conclusions.	
5	Physicochemical investigation of surfactant-coated gold nanoparticles synthesized in the confined space of dry reversed micelles	Gold nanoparticles were synthesized inside of two dry reversed micelles, AOT (sodium bis(2-ethylhexyl)sulfosuccinate) and lecithin. The gold precursor used was tetrachloroauric acid and the reductant was hydrazine. The systems were characterized by UV-vis, FT-IR, WAXS, and SAXS.	FT-IR analysis of the dry reversed micelles with gold precursor revealed no distinguishable presence of water. UV-vis was used to show the loss of the d-d transition at 320 nm, indicative of $AuCl_4^-$, and the appearance of the signal at 528 nm, indicative of small-sized Au(0) nanoparticles. WAXS analysis suggests, that by either method, nanoparticles were formed with a radius of 1.4 ± 0.2 nm. SAXS results produced a size equivalent within experimental error. Overall, the authors claim to have "shown that a simple treatment with ethanol is able to eliminate the excess of surfactant not directly bound to the nanoparticle surface" and that	The authors have demonstrated the value of X-ray scattering techniques (SAXS and WAXS). Importantly, they have not attempted to draw conclusions beyond the data that they have collected. In addition, they state further investigations are required.	33

			"nanoparticle size does not seem to be modified by this treatment."[33]		
6	Synthesis of Ruthenium Nanoparticles Stabilized by Heavily Fluorinated Compounds	Ruthenium nanoparticles were prepared under H_2 from Ru(COD)(COT) in THF and stabilized by heavily fluorinated compounds, where COD = 1,5-cyclooctadiene and COT = 1,3,5-cyclooctatriene. The resulting $Ru(0)_n$ nanoparticles were characterized by FT-IR, elemental analysis, HR-TEM, WAXS, SAXS, and SEM-FEG.	The $Ru(0)_n$ nanoparticles were found by TEM and SAXS to be 2.9 nm in size with a dispersity of ca. 20%. These particles were found to aggregate into larger 50-100 nm spherical clusters. Of note, they are not observed to coalescence into a giant particle. The authors hypothesis that "[t]he coalescence of the particles may be prevented by the presence of the fluorinated stabilizer acting as a coating protective barrier."[34]	This system is of particular interest for mechanistic study as it has several direct as well as indirect physical handles and also produces stable, reproducible particles. Two main things that are needed are (i) kinetics data for the formation of the $Ru(0)_n$ nanoparticles, and (ii) differential equations to describe the pseudo-elementary step reactions.	34
7	Probing in situ the Nucleation and Growth of Gold Nanoparticles by Small-Angle X-ray Scattering	Gold nanoparticles were prepared by combining gold(III) chloride in toluene with tetrabutylammonium borohydride in the presence of either decylamine or decanoic acid. The cationic surfactant, didodecyldimethylammonium bromide, was used. The gold salt and the reducing agent (with ligands—either amine or acid) were combined using a stopped flow device. The reaction was monitored in real time using either UV-vis, SAXS, or WAXS.	The authors "observe that the final radius strongly depends on the chemical nature of the ligand (3.5 nm for the acid, 1.4 nm for the amine)."[38] The authors interpret the reaction kinetics data, collected using both UV-vis and SAXS, by applying CNT. Furthermore, they use "a generic differential equation"[38] to calculate the rate of growth of the particles. Finally, they conclude that "the final size of the particles is thus controlled by the very first instant of the reaction that these experiments are able to probe: the higher the nucleation rate, the smaller the final particle size. [Their] results thus unambiguously prove the pioneering hypothesis[35] of Frens."[38]	The authors have concluded, from their size versus time data, the chemical nature of the gold nanoparticle and ligand interactions. The authors have investigated the aspects of their data that support their hypothesis—whereas with mechanism, one needs to consider all reasonable alternative hypotheses.[10,11] Ligands, for example, are known to contribute *greatly* to controlling the *growth step*.[21] Additionally, the kinetics have been analyzed on the basis of CNT, which is unable to encapsulate the strong bonding in metal nanoparticle nucleation.[36,67] Therefore, reliable mechanistic understanding is not forthcoming from the kinetics analysis provided.	38
8	In Situ Small-Angle X-ray Scattering Observation of Pt Catalyst Particle	The size of catalytically active Pt nanoparticles was monitored by SAXS during potential cycling. The system used was	Over the 16 hours of testing, the particles are observed to grow continuously. The authors present a plot of the Pt nanoparticle size as	The authors have presented a fascinating study of the effects of potential cycling on the growth of nanoscale electrocatalysts. They have proposed a preliminary "potential	39

	Growth During Potential Cycling	Pt on carbon (20 or 40 weight % platinum on XC-72 Vulcan carbon). The electrode was placed in 0.1 $HClO_4$ against a carbon counter electrode and Ag/AgCl reference electrode. Potentials were cycled from 0.4 to 1.4 V.	a function of time over three potential cycles, where the particle growth appears to be "cycling with reversible and irreversible components."[39] The growth with potential cycling is observed to be small and "attribute[d] to oxide formation."[39]	mechanism for potential cycling-induced particle growth."[39] Unfortunately, this proposed mechanism has not been tested by the authors in this communication. The kinetics data need to be fit using the full integrated form of the differential rate equation based on the balanced stoichiometry.	
9	Characterization of metal nanoparticles prepared by photoreduction in aqueous solutions of various surfactants using UV-vis, EXAFS, and SAXS	Au and Pt colloids were prepared from eterachloroauric(III) acid and hexachloroplatinic(IV) acid in water. The stabilizers DTAC (dodecyltrimethylammonium chloride) and PEG (polyethylene glycol lauryl ether) were used in varied concentrations. Colloidal dispersions were made by irradiated the solutions with a 500 W super-high-pressure mercury lamp. Primarily, the colloidal products were characterized by SAXS. Additional, ex situ measurements were collected using EXAFS, UV-vis, and TEM.	The UV-vis display that the Au colloids are formed rapidly without about 15 minutes, while the Pt colloid formation takes longer. The TEM of Pt and Au colloids in the presence of 151x DTAC concentration resulted in an average diameter of 4.1 nm. The TEM of Pt and Au colloids in the presence of 151x PEG concentration resulted in an average diameter of 3.3 and 3.4 nm, respectively. No error range was given with the TEM results. The TEM results are in agreement with the SAXS results. No mechanism for particle formation is given. None of the kinetics data are fit.	The authors claim that "photoreduction formation mechanisms of metal particles in aqueous surfactant solution…were successfully investigated."[40] However, no mechanisms were proposed, and no kinetics data were fit. Furthermore, the authors claim in their conclusions that "the SAXS analysis indicated that the structure of surfactant micelles could be fitted by the hard-sphere model with the interaction radius R_{HS} and the spherically shaped core-shell structure."[40] While the authors are proposing this hypothesis based on their experimental results, they do not directly test or attempt to disprove this hypothesis. Hence, this statement remains just that, an untested hypothesis.	40
10	In Situ Observations of Nanoparticle Early Development Kinetics at Mineral—Water Interfaces	Iron oxide nanoparticles were prepared in water from a solution of ~0.1 mM $Fe(NO_3)_3$ at 1, 10, and 100 mM $NaNO_3$ at pH 3.6. The heterogeneous nucleation and growth of the iron oxide particles on a quartz surface were studied. The quartz surface was chemically and mechanically polished to an approximate roughness of 2.5 Å. The formation process	The authors used simultaneous SAXS/GISAXS to try and separate heterogeneous and homogeneous nucleation. They found that "the amount of homogeneously formed nanoparticles increased with increasing [ionic strength] and leveled off at 10 mM [ionic strength] and above"[41]. The reasoning behind these results is based on electrostatic repulsive forces. Furthermore, the observed	*Importantly and quantitatively*, this paper demonstrates the inapplicability of CNT to a nanoparticle formation system. The authors have presented their "mechanistic and morphological understanding"[41], but have not provided any kinetics analysis to support their claim. The rigorous kinetics data has been collected, but no differential equations have been written for the nucleation and growth processes.	41

		was studied by simultaneous SAXS/GISAXS.	smallest nanoparticle radii, at [$NaNO_3$] = 1 and 10 mM, were 1.7 ± 0.3 nm and 1.8 ± 0.2 nm, respectively. Meanwhile, at the same [$NaNO_3$], CNT predicted sizes of 21.1 and 31.5 nm. Finally, in Figure 5 within the paper[41], the authors present their proposed mechanism for the nucleation and growth behavior on the quartz surface.		
11	Nucleation and Growth of Metal Nanoparticles during Photoreduction Using In-Situ Time-Resolved SAXS Analysis	Palladium and rhodium nanoparticles were prepared from their metal-chloride salts in aqueous ethanol, in the presence of PVP and benzoin, and reduced by photoirradiation. The reaction was monitored by in situ time-resolved SAXS and ex-situ TEM.	The authors claim their analysis of the SAXS measurements "[show] that the mechanism underlying the formation of metal nanoparticles in the photoreduction process is constituted of three elementary phases: 'autocatalytic reduction—nucleation', 'nucleation—growth', and 'diffusion-limited Ostwald ripening-based growth'."[42] Furthermore, the authors concluded that "increased time resolution enables one to understand the nucleation and growth process at the beginning of the formation reaction, and it facilitates the evaluation of the kinetics of elementary steps to provide a complete quantitative description of nanoparticle formation processes in the near future."[42]	The authors have collected excellent synchrotron data and have specifically recognized the importance of increased time resolution at the early times of particle formation studies. However, there are numerous cases of scientific missteps and confirmation bias in this paper. First, the mathematical basis for their data analysis was LSW theory and classical nucleation, which has been shown to *not* be suitable for strong-bonding systems like metal nanoparticle formation. Second, the authors routinely claim to be "confirming" their hypothesis and mechanism with additional experiments, but they do not take into account other possible explanations or alternative hypotheses—that is, there is little attempt to disprove in this paper. Third, the words used to describe their 'mechanism' (cited in the column to the left) are not well supported. Overall, the authors have collected excellent, commendable data. But, they fail to analyze it appropriately, for example by taking disproven theories and applying them to their system. The authors did not determine the reaction stoichiometry for their system nor the (pseudo) elementary	42

				steps applicable to their particle formation reaction.	
12	In Situ UV/Vis, SAXS, and TEM Study of Single-Phase Gold Nanoparticle Growth	Gold nanoparticles (Au NPs) were prepared following the Stucky method.[43] Specifically, $(P(Ph)_3)Au^{I}Cl$ was reduced in toluene using the mild reductant, *tert*-butylamine-borane. The authors investigated the formation of Au NPs by UV-vis, SAXS, and TEM. Size versus time data were collected using SAXS and TEM, whereas volume fraction versus time was reported using UV-vis.	Depending on the conditions, the authors report an average particle diameter between 4.0 and 6.0 nm, with a best polydispersity of 7%. The TEM and SAXS data agree within experimental error. The particle formation process is reported by the authors to occur in four stages: (1) "early NP formation by the borane reaction is consistent with CNT. NP growth starts via a fast nucleation event of small clusters"; next, (2) Ostwald Ripening occurs "up to a critical particle radius. However, once particles reach this critical size—and, therefore, a critical surface energy—the mechanism changes."; (3) "excess Au(0) monomers present in the solution, and apparently stabilized by the alkyl thiol molecules, react directly with the NP surface"; and finally, (4) "termination of NP growth when the concentration of Au(0) monomer is in equilibrium with the size of the existing Au NPs."[44]	The strength of this study is that the authors have done a commendable job of using several direct techniques to collect kinetics data on their system. Unfortunately, the authors state that "the underlying mechanism is based on Ostwald ripening (OR), where the reaction kinetics is described with LSW theory."[44] However, the authors also note that the LSW kinetic model "only qualitatively describes the overall growth process and does not capture the discontinuity in dr/dt."[44] If true, then it follows that the full, correct formation mechanism cannot be described as claimed using LSW. What is missing from this work are the steps of: (i) writing out the (pseudo) elementary steps for each possible mechanism, (ii) writing down the corresponding differential equations for each mechanism, and then (iii) attempting to fit the kinetics data—which mechanisms can be ruled out? Which fit the data? None of these key steps underlying a reliable mechanism have been done in this study.	44

13	In Situ Small-Angle X-ray Scattering from Pd Nanoparticles Formed by Thermal Decomposition of Organo-Pd Catalyst Precursors Dissolved in Hydrocarbons	Palladium nanoparticles were prepared from solutions of either $Pd(acac)_2$ or $Pd(acetate)_2$ in toluene via the heat-up process, whereby the reaction solution was heated to 150 °C and 190 °C, respectively. The nanoparticle formation process was monitored using synchrotron SAXS. Independent repeat experiments were performed and monitored by TEM, XANES, and X-ray PDF analysis. Complete kinetics data were not reported.	The authors report a final size of 4.1 ± 0.1 nm for the particles formed from the precursor $Pd(acac)_2$. However, the particle size distribution in Figure 5 of the paper[45] suggests the size is much greater than ±0.1 nm, likely between ±1.0 - 1.5 nm. The SAXS and XANES data are in agreement with each other. Larger particles are observed at higher temperature, which the authors claim is due to "the additional thermal energy [that] should help marginally break Pd-ligand bonding."[45] Models were presented to describe the growth process of the two palladium systems.	The authors present high-quality synchrotron data. They have not attempted to overinterpret their data beyond qualitative models. However, they end their discussion section by saying that the "two different models can be used to interpret the growth patterns of the particles in $Pd(acac)_2$ and $Pd(acetate)_2$ toluene solutions".[45] No direct evidence supporting their cartoon drawings, presented as models, are provided. Missing are the pieces and steps to a reliable mechanism of determining the balanced chemical equation corresponding to their synthesis, collecting the needed kinetics data, postulating alternative mechanistic hypotheses, and the key step of determination of the (pseudo) elementary reactions that constitute the proposed mechanism.	45

14	Effect of Surfactant Concentration and Aggregation on the Growth Kinetics of Nickel Nanoparticles	Nickel nanoparticles were prepared from $Ni(acac)_2$, oleylaminne, and trioctylphosphine (TOP) with H_2 (g) as the reductant. The reaction was rapidly heated to 200 ºC, and the reaction time zero began once the temperature reached 200 ºC. Syntheses with varying molar equivalents of TOP were investigated. The reaction was studied by SAXS. Nanoparticles were characterized, after the reaction had finished, by ex situ HR-TEM.	The authors report four time-resolved experiments at 0.5, 1.0, 1.0, and 2.0 molar equivalents of TOP to Ni(II). Based on the SAXS results, they were able to determine volume of particles, particle radius, and dispersion, all with respect to time. Hence, time-resolved size distributions could be reported for each of the four experiments. Next, the authors analyzed the growth kinetics for the reaction. "The growth mechanism was reported to occur in two stages: first nucleation by a continuous reduction which keeps the process far from the solution's monomer supersaturation point."[46] Then, in 'phase 2', "fast autocatalytic decomposition of the metal precursor on the nanoparticles' surfaces, promoting growth at the particle surface."[46] Next, "once there is a sufficient number of particles with a radius larger than the critical radius for forming ferromagnetic particles (approximately 7.5 nm), the particles start to aggregate through magnetic attraction. This is phase 3."[46] Finally, "[i]n phase 4, large aggregates settle out of solution, evidenced by a decrease in the total volume of particles."[46]	The authors of this study have collected outstanding SAXS data and performed excellent, commendable initial analysis of the data. Next, the authors report fascinating results, particularly for samples (D) and (E), which are reported to both have TOP/Ni ratios of 1.0. Yet, the two samples display quite different kinetics. The authors have fit all of their data with the FW 2-step mechanism, which fits well until there is precipitation, or "settling" as the authors refer to it. It is clear that in all of the samples there is continuous nucleation and autocatalytic surface growth, as the kinetics data are well fit well with the integrated rate law corresponding to the two pseudo-elementary steps of the 2-step mechanism. However, the claims concerning 'phase 3' and 'phase 4' are not substantiated by the kinetics analysis provided. The exact composition of the nanoparticle surface after the reaction remains to be analyzed, and the exact products being formed have not been—but need to be— definitely determined. Overall, however, a noteworthy study that is recommend reading.	46

15	Time-Resolved, in Situ, Small- and Wide-Angle X-ray Scattering To Monitor Pt Nanoparticle Structure Evolution Stabilized by Adsorbed $SnCl_3^-$ Ligands During Synthesis	Platinum nanoparticles coated with inorganic $SnCl_3^-$ ligands were synthesized in 7.5 M HCl, with excess Sn-ligand at 106 ºC. Reaction progress was monitored using SAXS and WAXS. Additional, ex situ, measurements were performed using EXAFS.	The authors used in situ SAXS and WAXS "to monitor the dynamic evolution of nanoparticle size and structure during the autoreduction of Pt-Sn complexes."[47] They observed an induction period, followed by a "burst generation of Pt primary particles", then a growth period.[47] The authors claim they are observing a "LaMer-type growth by primary particle diffusion."[47]	The authors have studied an intriguing Pt-Sn system and have collected impressive, high-quality SAXS and WAXS data. However, their data analysis has not taken into account any alternative hypotheses and states contradictory phrases. First, the authors claim that their kinetics data show a burst of nucleation, yet they see an induction period characteristic of slow, continuous nucleation and then autocatalytic growth—in essence disproving the LaMer model of putative "burst" nucleation and "diffusion-controlled" growth that they say applies to their data. Relevant here is that a comprehensive look at the literature claiming the LaMer model shows no compelling experimental support even in 70 years for that model.[12,13] Additionally, no alternative hypotheses have been disproven en route to the authors' conclusions. If the authors had attempted to *fit their kinetics data including its induction period,* then, in our opinion, they very likely would have disproven the applicability of the LaMer model and their subsequent diffusion-controlled growth conclusion. In short, the data analysis needs further study.	47
16	Mesoscale Effects in Electrochemical Conversion: Coupling of Chemistry to Atomic- and Nanoscale structure in Iron-Based Electrodes	A series of iron compounds with differing amounts of oxygen and fluorine were studied. The compounds were as followed: Fe_2O_3, FeO, FeF_2, FeF_3, and $Fe^{II}_{(1-x)}Fe^{III}_xO_xF_{(2-x)}$, x = 0.5, 0.6. The synchrotron-based technique of SAXS and	The authors claim that "by combining PDF and SAXS, [they] can understand the link between chemistry and structure across multiple length scales."[48] While they did not study the mechanism of formation, the primary insight gained is that "the formation of unusual nanostructures in the	While the study is not explicitly about the mechanism of particle formation, it does produce high-quality synchrotron data on an interesting system, data of the type of interest to and needed by the nanoparticle formation community.	48

	then PDF analysis were used to characterize the compounds.	mixed anion phases, without an interconnected network of Fe nanoparticles, may be attributed to the competitive growth of Fe nanoparticles nucleated in different anion environments, with different defect concentrations."[48] The authors also found that the defect level is only loosely correlated to the particle size. Instead the authors found that the composition of the precursor substrate to be a bigger indicator, where they hypothesize that increasing the reaction temperature would likely decrease the concentration of defects due to increased restructuring or annealing.	

17	Resolving Early Stages of Homogeneous Iron(III) Oxyhydroxide Formation from Iron(III) Nitrate Solution at pH 3 Using Time-Resolved SAXS	Iron oxide clusters were prepared using a stopped-flow system with three injection lines containing: $Fe(NO_3)_3$, HNO_3, and pH 3 buffer with NaOH, respectively. The reaction was monitored by SAXS over approximately the first 1000 seconds. In addition, TEM and DLS measurements were obtained at different times. The majority of kinetics data were analyzed between 0 – 300 seconds.	The authors conclude that "the mechanism of FeO_x formation from 1 mM $Fe(NO_3)_3$ at pH 3 can be described by" four steps.[49] The four steps are: (i) "rapid (<1 s) polymerization reactions between multiple monomeric Fe hydrolysis species"; (ii) "formation of low dimensionality and/or polydisperse primary particles from 1 to 10 s after formation that evolve through a predominantly cluster-cluster addition mechanism to yield larger primary particles"; (iii) "ongoing growth of primary particles through a monomer addition mechanism…from 10 to 300 s to yield colloidal primary particles with radii of 3–10 nm"; and (iv) "aggregation (most likely reaction-limited) of colloidal primary particles through a cluster–cluster addition mechanism from 20 to 300 s to yield secondary particles with radii of gyration from 25 to 40 nm".[49]	The authors have collected generally outstanding SAXS data. That said, they do not have the sensitivity in their system to monitor nucleation—and, instead. have claimed that nucleation is 'instantaneous' (occurring in <1 second). This of course seriously hinders experimental investigation of the true particle formation mechanism—instantaneous nucleation having been thoroughly *disproved*.[12,13] The authors have concluded that their findings "are generally consistent with previously developed general models for FeO_x formation" and "provides further understanding of the mechanisms of FeO_x formation and transformation."[49] Yet, these statements from their Conclusions are not supported by their results which do not provide new insights into the field of FeO_x formation. Instead, their discussion of 'mechanism' is entirely based on the literature and *not* their data. Their particular FeO_x formation system is complex and does not yield a well-determined, balanced reaction stoichiometry. The authors are also unable to write out the (pseudo)-elementary steps for their particle formation reaction. Overall, the primary contribution of this study is *excellent* SAXS growth data. But, a reworking of the analysis and conclusions from this work are in order, in our opinion.	49

18	In Situ Probing Calcium Carbonate Formation by Combining Fast Controlled Precipitation Method and Small-Angle X-ray Scattering	Calcium carbonate ($CaCO_3$) clusters were formed from aqueous solutions of $Ca(HCO_3)_2$ at pH 5.2–5.5 with bubbling CO_2. Solutions were filtered through a 0.45 micron filter to remove dust. Reaction solutions were stirred at 850 rpm to decrease CO_2 concentration, raise the pH, and initiate precipitation of $CaCO_3$. The reaction started with either $[Ca^{2+}]$ = 200 mg/L or 100 mg/L, both at 30 ºC. The reaction was monitored by synchrotron SAXS and resistivity.	Based on their results, the authors conclude the precipitation process takes places in two 'domains'. "The first domain, called domain 1, is a metastable one…which could correspond to a prenucleation stage. The second domain called domain 2…is dominated by a rapid precipitation process."[50] The two methods, SAXS analysis and volume fraction of formed calcium carbonate as determined from the resistivity curve, were shown to be in agreement.	Overall, the authors have presented a fascinating, valuable study of the formation of $CaCO_3$ clusters. Impressively, they have presented the complete mass- and charge-balanced reaction. Further, they have collected kinetics data at different precursor starting concentrations, and they have studied their reaction with multiple physical handles. The intent of the work is to provide evidence for the presence of prenucleation clusters and provide a proof of concept for their SAXS, pH, and resistivity techniques—mission accomplished. The study of $CaCO_3$ presented here is intriguing and deserves further investigation. Needed are a deeper kinetics and mechanistic investigation into the nucleation and growth processes of this interesting system and by the methods used, en route to a pseudo-elementary step based, proposed mechanism where at least several alternative mechanisms are tested and, ideally, disproved.	50

19	*In situ* investigation of two-step nucleation and growth of CdS nanoparticle from solution	Cadmium sulfide nanoparticles were prepared using a free-jet setup to combine aqueous solutions of Na_2S and $CdCl_2$ in a micro mixer. SAXS and WAXS data were collected at different reaction times by moving the positions of the monochromatic X-ray beam and related by the expression $t_{react} = d/v$, where d is the distance to the mixing point and v is the flow velocity. Additional controls using DFT were performed with the Gaussian03 program package and the basis set HF-DGDZVP.	The authors collected data at four reaction times (150, 290, 530, and 1000 μs) and three jet velocities (10.6, 21.2, and 31.8 m^1 s^{-1}). Based on their SAXS/WAXS experiments, the authors proposed a two-step formation mechanism of (i) nucleation of clusters and (ii) coexistence of nucleation and diffusion driven growth. They claim "this first nucleation process is driven by diffusion of the cadmium and sulfur ions and further nucleation continuously takes place in the regions of the interfaces of turbulent mixing. From these primary clusters larger particles develop."[51] From here, the authors claim the growth is by agglomerations of clusters and not by atomic, monomer attachment. Of note, the authors cite that "after 2.5 ms the median of the particle diameter of the growing population has reached a value of about 5 nm."[51] Finally, based on their data, and their quantum calculations suggesting a structural prenucleation cluster model of $Cd_{13}S_4(SH)_{18}$, the conclude their study provides "direct experimental proof of a 2-step nucleation process for the very early stages of CdS formation and growth."[51]	The authors have presented an impressive, commendable experimental approach, especially on an important but difficult quantum dot system. That key positive so noted, the data do not support the overall conclusions, certainly not the paper's claim to have direct experimental *proof* of a nucleation *mechanism.* Not only is such proof impossible—one disproves instead[10,11]—the authors admit that their data are limited by early time sensitivity issues. No kinetics data are fit by a differential rate equation to *experimentally test* the proposed mechanism. No direct, experimental evidence is given for the Kinetically Effective Nucleus. With regard to the four criteria for a reliable mechanism detailed in the main text, the authors have only partially satisfied two of those requirements: they have collected kinetics data and mostly, but not completely, determined the reaction stoichiometry. Hence, additional work and data analysis are needed on this interesting system before reliable mechanistic conclusions can be claimed to be in hand.	51

20	Colloidal nanoparticle size control: experimental and kinetic modeling investigation of the ligand–metal binding role in controlling the nucleation and growth kinetics	Palladium nanoparticles were prepared from Pd(II) acetate and either pyridine or toluene. Then, a mixture of TOP (trioctylphosphine) and 1-hexanol was added, the solution heated to 100 ºC, and stirring initiated. Characterization was done by STEM. Kinetics data was collected using *in situ* SAXS.	The authors constructed a ligand-based model to fit their kinetics data consisting of 4 steps: (1) A → B; (2) A + B → 2B; (3) A + L ⇌ A•L; and (4) B + L ⇌ B•L. This model was used to successfully fit the *in situ* SAXS kinetics data and provide mechanistic insights into the Pd nanoparticle formation process. The paper's results "demonstrate that the binding of ligands with both the metal precursor and nanoparticles surface kinetically controls the rates of nucleation and growth and as a result the duration of their overlap."[52]	The report by the Karim Group is an illustrative case, which is covered in detail in the main text, for how one *should approach* kinetics and mechanism in particle formation reactions. Karim and coworkers wrote out the proposed pseudo-elementary steps, obtained quantitative kinetics data, used more than one observable, and disproved alternative hypotheses. While the exact speciation of the Pd precursor is not exactly known, this and the limitations of their model are stated upfront. This paper is highly recommend reading for anyone conducting nanoparticle formation mechanistic research, especially when an excess of good binding ligand is present.	52
21	Mild Homogeneous Synthesis of Gold Nanoparticles through the Epoxide Route: Kinetics, Mechanisms, and Related One-Pot Composites	Gold nanoparticles were prepared using tetrachloroauric acid in aqueous glycerol solution. PVP or CTAC was used as a stabilizer. Kinetics data were collected using UV-Vis, SAXS, and pH. Resultant nanoparticles were characterized by TEM. The reaction was run at 25 °C for 1000 min. A final experiment was run on the formation of gold nanoparticles in an Al-hydrogel formed from $AlCl_3$ and glycerol.	The authors claim to have a new methodology for obtaining gold nanoparticles. They use the controlled hydrolysis of glycidol to steadily release OH^- to alkalize the solution until the pH reaches ~10 and reduced Au^{III}. The authors directly monitored the pH, conductivity, and UV-Vis absorbances at 315 and 400 nm as a function of reaction time. The in situ SAXS and ex situ TEM are shown to be in agreement.	The authors have carefully investigated a new method for synthesizing gold nanoparticles in an aqueous glycerol solution. They have not yet determined the complete stoichiometry of the reaction. Primarily, they have investigated the glycerol to glycidol process, and they have characterized the final product. The authors collected kinetics data following the overall reaction from *n* Au(III) to $Au(0)_n$. The possible pseudo-elementary steps have not been hypothesized yet, but the authors note that they are not claiming a mechanism. Instead, they offer potential next steps as well as kinetic and mechanistic studies one could do to investigate the mechanism of formation for gold nanoparticles using the synthetic method investigated.	53

22	Insights into the Formation Mechanism of CdSe Nanoplatelets Using in Situ X-ray Scattering	Two-dimensional CdSe nanoplatelets (NPLs) were prepared using a heating up procedure. A mixture of cadmium oleate, cadmium acetate, and trioctylphosphine-selenide was heated to between 170-200 °C. SAXS and WAXS were used to monitor the NPL formation.	The authors provide experimental data for the formation of 3 monolayers thick CdSe NPL via a heating up and one-pot procedure. The reaction was monitored from 0 to 2250 s where at least 3 different processes were observed. The data disproved "a templating effect or an oriented attachment formation mechanism."[54] The data were consistent with lateral growth of NPLs from a small number of initial seeds. These data were also consistent with previous studies done by the authors with a UV-vis probe[55] and a recent kinetic pathway proposed by others.[56]	The authors have presented a fascinating study on the formation of CdSe NPLs. First, their kinetics data are direct and high-quality. Next, these authors have applied a disproof-based method to the presentation of their results. They were careful not to claim more than the data revealed and address all possible hypotheses. With further experiments, the authors will be able to determine the complete reaction stoichiometry and the pseudo-elementary steps. Regardless, we recommend this paper for its excellent kinetics data and approach to experimental investigation!	54

Table S2.3. Summary of Papers Using XAFS to Collect Kinetics Data.

Entry	Title	System & Techniques Used to Monitor the Kinetics	Results and Proposed Chemical Mechanism	Conclusions, Insights, and Critical Analysis	Ref.
1	Structural Analysis of Polymer-Protected Platinum/Rhodium Bimetallic Clusters Using Extended X-ray Absorption Fine Structure Spectroscopy. Importance of Microclusters for the Formation of Bimetallic Clusters	Platinum/Rhodium bimetallic clusters were prepared from aqueous solutions of $RhCl_3$ and H_2PtCl_6. PVP was used a protecting polymer in the aqueous/ethanol metal solutions. The reaction solution was stirred and refluxed at 100 °C for 2 hours under N_2. Reactions were run using 1:1, 4:1, and 1:4 ratios of platinum:rhodium. Clusters were characterized using TEM, STM, and EXAFS.	The authors found by STM and TEM "that the cluster particle is composed of several small microclusters, less than 10 Å in diameter".[57] To investigate this finding, the authors used EXAFS in order to better determine the structure and composition of the clusters and microclusters. They found direct EXAFS evidence of small, Rh_{13} microclusters, which were corroborated by STM. As the reaction continues, the microclusters aggregate together and "serve as building blocks for pseudo-close-packed superstructures."[57]	The authors have presented fascinating, early EXAFS data for the observation of small, less than 1.0 nanometer, sized clusters of strong-bonding metal nanoparticles. They have not proposed any chemical mechanism for the nucleation or growth of the Pt/Rh bimetallic clusters, but rather just present the data they were able to collect. Then, they only proposed the possible pathways based on the data collected, known thermodynamics, and other literature available at the time—a cautious, commendable approach that sets the stage for detailed kinetics and mechanistic studies on this classic PVP stabilizer, aqueous/alcohol reductant, bimetallic Pt/Rh particle formation system.	57
2	Genesis of Pt Clusters in Reverse Micelles Investigated by in Situ X-ray Absorption Spectroscopy	Platinum nanoclusters were synthesized from H_2PtCl_6 inside of AOT reverse micelles, where AOT = sodium bis(2-ethyl hexyl) sulfosuccinate. The microemulsion system was prepared in a mixture of *n*-heptane and water. Platinum was reduced using hydrazine (N_2H_4). The reaction was monitored using XAFS, and the particles were visualized using TEM.	The authors monitored the Pt L_{III}-edge with increasing concentration of N_2H_4. The authors claim to observe "six distinguishable steps…for the formation of Pt clusters at the early stage."[58] These steps include a reduction reaction from Pt^{4+} to Pt^{2+}, ligand exchange from $PtCl_4^{2-}$ to $Pt(OH)_4^{2-}$, a further reduction reaction from Pt^{2+} to Pt^0, and then particle growth. All the steps are found to be a function of the hydrazine concentration. Furthermore, the authors claim that the TEM micrograph "shows that the size distribution of the clusters is monodisperse."[58]	The authors have produced high-quality XAFS data but have not analyzed it in a way or at a level that can produce reliable mechanistic insights. First, the authors have not determined the complete mass and charge balanced reaction. Second, they have not produced the kinetics (concentration versus time) data needed to test proposed mechanisms by attempted fits to that data. Additionally, no disproof of alternative mechanistic hypotheses is provided.	58

3	Aggregated structure analysis of polymer-protected platinum/ruthenium colloidal dispersions using EXAFS, HRTEM, and electron diffraction measurements	Platinum/ruthenium colloidal dispersions were prepared from hexachloroplatinic(IV) acid in water combined with ruthenium(III) chloride in ethanol. PVP was added to the 1:1 ethanol:water mixture. The solution was refluxed at 100 ºC for 2 hours under atmospheric air with a subsequent control conducted under nitrogen. The colloidal dispersions were characterized by ex situ HR-TEM, EXAFS, and electron diffraction.	The authors characterized the Pt and Ru colloids separately, as well as combined. From EXAFS, the author report that "the aggregation occurs between small monometallic Pt clusters (diameter ca. 15 Å) and partially oxidized Ru microclusters (diameter less than 10 Å)."[59] It was concluded that a Pt/Ru alloy was not present in colloidal dispersion. The authors state that "an agglomerate, with more than 50 Å in diameter, consists of several partially oxidized Ru microclusters and small monometallic Pt clusters, not consisting of Pt/Ru alloyed clusters."[59] For platinum, it is most likely that 3 to 4 clusters of Pt_{55} are present, whereas, for ruthenium, the microclusters are likely Ru_{13}.	The authors have expertly used EXAFS in order to extract direct, valuable information on the particle synthesis. This system is, therefore, ripe for the design of appropriate kinetics and other experiments that can lead to a reliable mechanism for this mixed metal system.	59
4	Formation Mechanism of Pt Particles by Photoreduction of Pt Ions in Polymer Solutions	Platinum nanoparticles were prepared from $H_2PtCl_6 \cdot 6H_2O$ in aqueous ethanol with PVP. Solutions were bubbled with N_2 to remove dissolved O_2. Particles were prepared by irradiating dilute (0.66 mM) or concentrated (9.65 mM) solutions using a 500 W super-high-pressure mercury lamp. Characterization was done using UV-vis and TEM. In situ measurements were carrying out by EXAFS of the Pt L_3 edge.	Based on the EXAFS and XANES analyses, the authors propose the formation mechanism for Pt particles in this system to be "the following steps: (1) reduction of $PtCl_6^{2-}$ to $PtCl_4^{2-}$, (2) dissociation of Cl from $PtCl_4^{2-}$, followed by reduction of Pt^{2+} ionic species to Pt^0, (3) formation of a Pt^0–Pt^0 bond and particle growth by the association of Pt^0–Pt^0."[60] Aging experiments, where particles after irradiation were allowed to sit for 24 hours in the dark, with and without PVP revealed that PVP is needed to stabilize particles. Without PVP, particles agglomerated over the 24-hour, dark period.	The authors of this study have collected excellent XAFS data and have investigated the importance of using the stabilizer PVP for the long-term stability of their particles. The authors additionally have identified important *qualitative* trends in the appearance or disappearance of platinum species, Pt^{4+}, Pt^{2+}, and Pt^0 and proposed pseudo-elementary steps have been written out for this reaction. Missing and hence possible targets for future research are: writing differential equations corresponding to the proposed pseudo-elementary steps, collecting kinetics data, and then testing the proposed mechanisms by attempting *quantitative fits* to each proposed mechanism, all in a disproof-based manner.	60

5	In Situ XAFS Studies of Au Particle Formation by Photoreduction in Polymer Solutions	Gold nanoparticles were prepared from $HAuCl_4 \bullet 4H_2O$ in aqueous ethanol with PVP. Solutions were bubbled with N_2 to remove dissolved O_2. Particles were prepared by irradiating dilute (0.66 mM) or concentrated (12.2 mM) solutions using a 500 W super-high-pressure mercury lamp. Characterization was done using UV-vis and TEM. In situ and ex situ measurements were carrying out by XAFS.	UV-vis measurements at 545 nm reveal the formation of gold nanoparticles over the course of 10 hours with a peak growing in as early as 15 minutes. By XAFS, only three gold species were present through the reaction, Au^{3+}, Au^{+}, and Au^{0}. Based on the XANES and EXAFS results, the authors proposed a 3-step formation mechanism. "(1) The bond of Au–Cl rapidly dissociates until the reduction time reaches up to 30 min."[61] "(2) During the reduction time of 30–360 min, the peak intensity of the Au–Cl bond gradually decreases with time, while the peak attributed to the Au^0–Au^0 metallic bond appears around 2.8 Å and its intensity increases with time."[61] "(3) On the prolonged photoirradiation (the reduction time longer than 360 min), $AuCl_2^-$ is completely consumed, and the growth process of Au metal particles is obviously observed despite the [coordination number]s remaining nearly constant."[61]	The authors have collected excellent in situ UV-vis and XAFS data. The Fourier transformed XAFS data have been presented, but not analyzed or interpreted at a quantitative level. The authors have done valuable *qualitative* analysis of their data, corroborated their analysis by TEM, and hypothetical reaction steps have been produced. Remaining to be done are: (i) writing out the experimentally supported pseudo-elementary steps for their proposed mechanism; and (ii) *fitting* their kinetics data to the proposed mechanism(s), all in a disproof-based fashion so as to lead to more reliable mechanistic conclusions.	61
6	In Situ Time-Resolved XAFS Studies of Metal Particle Formation by Photoreduction in Polymer Solutions	Rhodium and palladium nanoparticles were prepared in aqueous ethanol solutions with PVP and benzoin (photoactivator) and studied by UV-vis, TEM, and in situ DXAFS. The starting metal salts were $RhCl_3 \bullet 3H_2O$ and $PdCl_2$. Solutions were degassed using N_2. Particles were formed by irradiation from a 500 W	By UV-vis, the loss of metal precursors is quantitatively monitored. Particle size distributions were determined by counting > 200 particles observed by TEM. Most importantly, in situ DXAFS measurements were collected for Rh and Pd every 36 and 40 seconds, respectively. In Scheme 1 of the paper,[62] the	Overall, this study[62] by Harada and Inada is a classic in the literature. The authors have collected excellent, direct kinetics data on the formation of Rh and Pd nanoparticles. They have successfully written out the pseudo-elementary steps, written differential equations for their reaction, and fit the data. They have corroborated these findings with a separate physical	62

		super-high-pressure mercury lamp.	pseudo-elementary steps of the proposed mechanism were explicitly written out. Differential rate equations were derived from these pseudo-elementary steps and the kinetics data for both Rh and Pd were fit with those proposed steps. The authors report, "the reduction rate of Rh(III) aqua chloro complexes in PVP solutions was found to be slower than that of Pd(II)."[62]	technique (UV-vis). The primary, still-needed experiment is the complete understanding of the reduction process, starting with the balanced reaction. Does Rh(III) immediately reduce to Rh(0) or does it reduce to Rh(I) first? What species does are form in solution? What is the exact composition of the Kinetically Effective Nucleus (KEN) for $Rh(0)_n$ and $Pd(0)_m$? This classic metal-chloride plus aqueous alcohol reductant system merits further investigation as do the other aqueous alcohol reductant systems already mentioned.	
7	Insights into Initial Kinetic Nucleation of Gold Nanocrystals	Gold nanoparticles were synthesized from an aqueous solution of $AuCl_4$ with citric acid as the reductant, and PVP as a stabilizing polymer. The reaction was stirred and heated to 70 ℃, and the reaction was run for 260 minutes. Ex situ characterization was done by UV-vis and TEM. In situ QXAFS were collected at the Au L_{III}-edge using a peristaltic pump set-up.	Based on their QXAFS data, the authors have "propose[d] a kinetic three-step mechanism involving the initial nucleation, slow growth, and eventual coalescence for the Au [nanocrystals] formation."[63] The three-step mechanism was divided up into three stages. "Stage I can be considered as the initial nucleation step, exhibiting a faster process compared with stage II which stands for the growth step. In Stage III, however, $N_{Au\text{-}Au}$ increases quickly along with the decreased $N_{Au\text{-}Cl}$, indicating the rapid increase in size of Au [nanocrystals]."[63]	The authors have collected outstanding in situ synchrotron data. Their time resolved data is shown in their[63] Figure 2. The data presented there is an excellent example of what the field as a whole should be striving to collect, in our opinion. That said, the authors claim of a 'mechanism' for the nucleation of Au nanocrystals is premature. They have yet to derive the differential equations or fit their kinetics data based on their pseudo-elementary steps—only then will they be able to claim a more reliable mechanism. The language used in their[63] Figure 4 is proper in this regard where they claim just "[a] schematic representation of the formation process"[63] that *qualitatively* describes their system and its kinetics data.	63
8	In Situ Observation of Nucleation and Growth Process of Gold Nanoparticles	Gold nanoparticles (AuNPs) were synthesized from $HAuCl_4$ in toluene with the addition of tetraoctylammonium bromide	The authors found that, in the presence of 2 or more equivalents of DT, the gold precursor was reduced from Au^{3+} to Au^{1+}. At 1	The authors have conducted a valuable study that includes a number of careful controls to characterize and determine the speciation of their starting reaction.	64

	by Quick XAFS Spectroscopy	(TOAB) and dodecanethiol (DT). Then, a solution of $NaBH_4$ in DMF was added. The reaction was studied by QXAFS. Characterization was done using XAFS, TEM, and UV-vis.	molar equivalent of DT to gold, fifty percent of the gold was Au^{3+} fifty percent was Au^{1+}. The resulting AuNPs were reported to be 3.3 ± 0.5 nm in diameter and covered with DT (as the surface ligand). The authors report that their "in situ analysis showed a different mechanism" (than what is typically cited/reported in the literature; e.g., often the LaMer model or the FW 2-step mechanism) "namely the reduction of all of Au ions, nucleation, and aggregation of the nuclei causing the particles to grow larger."[64] Most notably, the authors report direct XAFS data supporting the formation of a Au_4 cluster at 4.6 seconds after the addition of $NaBH_4$.	Next, they collected excellent, direct synchrotron data on the transformation of Au^{3+} / Au^{1+} to AuNPs. These positives so noted, the authors claim for a 'new mechanism' is not substantiated by their present data. They have yet to determine the exact pseudo-elementary steps for the reaction nor use those to define the differential equations required to fit kinetics data—that also needs to be acquired. Additionally, disproof of all reasonable alternative mechanisms remains to be done. Such studies would be welcome on this AuNP formation system with its specific of Au, DT, and TOAB components.	
9	*In Situ* Au L_3 and L_2 edge XANES spectral analysis during growth of thiol protected gold nanoparticles for the study on particle size dependent electronic properties	Gold nanoparticles were prepared from a toluene solution of $AuCl_4^-$ and dodecanethiol. (Auric acid was neutralized by tetraoctylbutylammonium bromide, which then transferred the $AuCl_4^-$ into the organic-toluene phase from the aqueous.) $NaBH_4$ in DMF was used as a reducing agent. QXAFS were used to monitor the nanoparticle formation process with 100 millisecond resolution.	XANES data suggests that the reduction of Au^{3+} and Au^+ in solution to Au^0 occurs by time = 3.6 seconds. From there and based "on the average state of the absorption atom"[65] determined by XAFS, the "results suggested that [gold nanoparticles] grow via the aggregation of [gold nanoparticles] themselves. As a result, we can estimate the particles size from the fraction of surface atoms, or, in other words, the dispersion."[65] By the end of the reaction time, the authors have calculated a dispersion of 28.3 percent. Most compelling, the authors have observed, *in situ*, the formation of gold nanoparticles at *both* the L_3-	The authors deserve to be commended for their impressive, high-quality QXAFS data. Remaining studies needed to obtain a mechanism for this interesting system include: (i) complete characterization of the precursor solution and resulting particles; (ii) proposing and testing plausible mechanisms of formation via their associated differential equations, all (iii) with an eye on a disproof- and Ockham's razor-based approach so as to yield a reliable, minimum proposed mechanism.	65

			and L_2-edges, and they have produced consistent, comparable results. No mechanism for the gold nanoparticle formation has been proposed, however.		
10	An *in situ* quick XAFS spectroscopy study of the formation mechanism of small gold nanoparticles supported by porphyrin-cored tetradentate passivants	Gold nanoparticles were prepared from $HAuCl_4$ in DMF using the reductant $NaBH_4$ and in the presence of a passivant. The two passivants used were: (**1**) α,α,α,α-5,10,15,20-(*o*-bisdisulfidepropylamidophenyl)-porphyrin and (**2**) 2,2'-dithiobis(*N*-(4-methyphenyl). Time-dependent studies of the gold particle formation were done using QXAFS. Further characterization was performed using UV-vis and TEM.	The authors collected time-resolved XANES and EXAFS. Their XANES suggest "that the size of Au nuclei is kinetically controlled by the speed with which the passivants trap the growing Au nuclei."[66] Their EXAFS analysis supports their XANES conclusions as the authors found "that **1** suppresses the particle growth more efficiently than **2** to provide smaller gold nanoparticles."[66] Furthermore, their end-time TEM reports smaller average size and narrow size distribution for Au nanoparticles formed in the presence of passivant **1**, than for passivant **2**. Overall, the authors conclude "the size of the Au nuclei is kinetically controlled."[66]	The authors have presented a cartoon scheme for the "formation mechanism of gold nanoparticles."[66] The scheme is based off of the broad conclusions determined from the (time-resolved) QXAFS data. Unfortunately, the authors have not defined the exact stoichiometry or derived the kinetics, so their proposed scheme for gold nanoparticle formation is *not* a mechanism. It is just a proposed reaction scheme. It is worth noting that the authors have good kinetics data, and they have completed a number of well thought out controls, but the authors have not performed a rigorous mechanistic analysis.	66
11	*In situ* XAFS experiments using a microfluidic cell: application to initial growth of CdSe nanocrystals	CdSe nanocrystals were synthesized by heating $Cd(CH_3COO)_2$, oleic acid, and octadecene (ODE) at 453 K under Ar using a microfluidic cell. Ligand, dodecylamine ($(CH_3(CH_2)_{11}NH_2$, DDA) in ODE, was added and the reaction solution was heated to 513 K. The reaction was monitored from 0.0 s to 8.1 s using XAFS, UV-Vis, and photoluminescence (PL).	The formation of $(CdSe)_n$ particles was observed by XANES, while simultaneously UV-Vis and PL spectroscopies were able to monitor the particle formation and crystallinity. Given the combined, XANES, EXAFS, UV-Vis, and PL results, the authors present preliminary insights into the initial formation of $(CdSe)_n$ particles.	The authors have presented a fascinating study and have keenly utilized a microfluidic device to probe the early time points of the reaction. Further, they have independently determined the Se-Cd coordination number three ways as a function of time. As we stated in the main text, further studies will allow them to (i) elucidate the exact reaction stoichiometry and (ii) write the complete pseudo-elementary steps for the particle-formation mechanism. These authors have already collected excellent kinetics data and incorporated	67

				disproof-based methods into their experimentation. Their study is, in our opinion, intriguing and a must-read.	
12	Nucleation and Aggregative Growth Process of Platinum Nanoparticles Studied by in Situ Quick XAFS Spectroscopy	Platinum nanoparticles were prepared from either $H_2PtCl_6 \cdot 6H_2O$ or K_2PtCl_4 in aqueous ethanol with PVP and benzoin. TEM was used to determine the average diameter of 200 particles. In situ QXAFS and data analysis are reported, along with UV-vis.	The authors report that their "quantitative in situ QXAFS analysis" reveal "the mechanism underlying the formation of Pt nanoparticles in the photoreduction process of three elementary stages, reduction-nucleation, autocatalytic surface growth on nucleates, and Ostwald ripening-based growth."[68] Kinetic rate equations have been written for the nucleation and growth steps. Then, the Ostwald ripening contribution is included with a "logistic 'turn-on' function to activate Ostwald ripening at a time τ_{OR}".[68] The LaMer model has been described as *not* applicable to this system.	The authors of the study have collected excellent, direct kinetics data. They write out proposed pseudo-elementary steps, and they use the associated differential equations for fitting their data, specifically the FW 2-step mechanism of slow, continuous nucleation and then autocatalytic surface growth. The authors also fit their data with the semi-empirical Avrami-Erofe've equation, although it is known not to yield mechanistic insights since balanced equations are not involved in such physical-chemistry models. Ostwald ripening is added along with a k_{OR} rate parameter as part of the fitting. Several areas of investigation are recommended for this system, including: (i) fuller investigation of the more intimate rate law for nucleation; (ii) the effect(s) of added ligand, including on agglomeration; and (iii) more evidence for or against Ostwald ripening vs Particle migration and coalescence, for example.	68
13	Formation and oxidation mechanisms of Pd–Zn nanoparticles on a ZnO supported Pd catalyst studied by *in situ* time-resolved QXAFS and DXAFS	PdZn nanoparticles were prepared from ZnO substrate with Pd particles formed on the surface from $PdCl_2$ under basic aqueous conditions at 353 K and then calcined at 773 K. The result was a precipitate of 3 wt% Pd/ZnO. This was used under 20 kPa H_2 (reductive) or O_2 (oxidative) conditions at 673 K to form PdZn particles. Kinetics data was	The two processes measured were: (1) the reduction of PdO on the surface of ZnO to Pd nanos and then PdZn; and (2) the oxidation of PdZn to Pd/Zn on ZnO and then PdO/ZnO on ZnO. The study demonstrated the direct monitoring of the full redox process of Pd/ZnO. The authors concluded that the "PdZn nanoparticles were formed on ZnO through a two-step	The authors have worked on an intriguing system with important implications in the catalytic conversion of methanol. They have collected excellent time-resolved data. However, the balanced stoichiometry needed en route to a reliable mechanism has not been determined. The fitting of their data to a single, pseudo-first-order 'rate' equation is not explained nor is the equation used to fit their data	69

		collected using in situ DXAFS measurements. Characterization was done using XAFS and XRD.	scheme under a hydrogen atmosphere."[69] They found the initial reduction to be fast (< 1 s) and the formation of PdZn to be longer (> 10s of min). The authors for the two reduction steps and two oxidation steps to have single exponential, first-order rate constants. Based on their results, the authors proposed, as their Fig. 6, a "mechanism of the redox process of Pd/ZnO."[69]	explicitly reported in either the main text or the SI. Overall, the authors have not determined a *mechanism* yet report 'rates' for the 'steps' of their reaction scheme. Additional study of this system is both of interest as well as needed.	
14	*In situ* time-resolved DXAFS study of Rh nanoparticle formation mechanism in ethylene glycol at elevated temperature	Rhodium nanoparticles were prepared from rhodium(II) chloride hydrate in ethylene glycol with PVP. The ratio of Rh:PVP were 1:15, 1:30, and 2:15. Kinetics measurements were collected using DXAFS at 403 K. Further ex situ measurements were done using ICP-MS and TEM.	XANES spectra, with near perfect isosbestic points, are reported for the formation of Rh nanoparticles. The formation process is suggested to be pseudo-first order in Rh^{3+} concentration. While some issues were reported in the discussion of the EXAFS results, the findings suggest that the nucleation process involves the formation of $(Rh^0)_n$, were n is small, n = 1, 2, or 3 Rh^0 atoms. The TEM micrographs display multipod nanoparticles, suggesting that aggregation of small particles may contribute to their formation, something that merits additional investigation. Based on the experimental evidence, the authors hypothesis the following word-based "mechanism" for Rh nanoparticle formation in ethylene glycol with PVP at 403 K: (1) "Rh^{3+} precursor might be thermally reduced by [ethylene glycol] to nucleate to be Rh^0 monomer"[16]; (2) "the Rh [nanoparticles] formed very rapidly to be uniform size	The authors in this study have collected high-quality, direct XAFS kinetics data for the formation of Rh nanoparticles. They have defined pseudo-elementary steps for the formation process and produced a rate law for those steps. They have used multiple physical handles. Still missing and hence targets for future research include: the balanced reaction stoichiometry; fitting the kinetics data with the integrated form of the differential rate law; and a focus on achieving a disproof-based, minimum mechanism that can quantitatively explain all the observed data.	16

			[nanoparticles], which are stable under the reaction conditions"[16]; and then (3) "a repeat of the second step, which is the repeat of uniform Rh [nanoparticle] formation."[16]		
15	XAFS in the tracking of reactions in aqueous solution: a case of redox reaction between $[AuCl_4]^-$ complex ions and ethanol	Gold nanoparticles were prepared from the reduction of $AuCl_4^-$ in a basic ethanol solution (pH = 12) at 22.5 °C. The reaction was monitored using synchrotron XAFS.	The authors have presented a short summary of the benefits of using XAFS to collect kinetics data for gold particle formation in an aqueous medium. They have presented very nice kinetics data for the reduction process of Au(III) to Au(0). Finally, the authors have presented a net, balanced chemical reaction for the hydrolysis of $Au(OH)_4^-$ to Au(0).	The authors illustrate the benefits of using XAFS to collect high-quality, direct kinetics data. Unfortunately, the authors chose to fit their data with an empirical first-order rate function that, thereby, produced a *single* rate parameter (that is not a rate constant, as it is not defined by a balanced reaction) that is unable to even qualitatively describe the *two processes* of nucleation and growth. Hence, remaining to be accomplished are: (i) collecting the fuller experimental rate law; (ii) producing pseudo-elementary steps for their reaction with defined rate constants for each step that, overall, define their proposed mechanism; (iii) producing alternative mechanisms to also test, and (iv) testing all possible reasonable mechanisms by attempted fits to the full kinetics and rate law, all in a disproof-based, Ockham's razor obeying fashion.	70
16	Insights into the Formation Mechanism of Rhodium Nanocubes	Rhodium nanocubes were synthesized at 130 ºC from $RhCl_3 \cdot 3H_2O$ in ethylene glycol with tetradecyltrimethylammonium bromide (TTAB) and PVP. Direct formation kinetics data were collected using DXAFS. Ex situ measurements were performed	Kinetics data (concentration of precursor versus time) were monitored directly using XANES. They were fit with the FW 2-Step mechanism with A = Rh_0^{3+} and B = Rh_t^{3+}. Throughout the experiment, samples were collected and ex situ measurements were taken using MALDI-TOF MS, XRD, TEM, and UV-Vis to	The authors have presented an impressive study. Points of note include the: (i) collection of direct kinetics data; (ii) characterization of the reaction solution as a function of time; (iii) direct evidence of Rh_{2-4} clusters—*an important finding suggestive of low molecularity nucleation*; (iv) fitting of the kinetics data to appropriate mechanistic equations; and (v) attempts	71

		using MALDI-TOF MS, XRD, TEM, and UV-Vis.	determine the speciation, ex situ reaction progress, and particle size distributions. Strong evidence was proposed for their 4-step mechanism: "(1) exchange of Rh^{3+} ligand sphere, (2) formation of Rh [nanocrystal] nuclei,…(3) evolution of nuclei into Rh [nanocrystals], and (4) shape corrections."[71]	to disprove alternative hypotheses. Additional experimental work that would be welcome includes (a) the temperature dependence of this classic system and study; and (b) attempted disproof of all reasonable alternative mechanistic hypotheses Nevertheless, as it stands this study is *one of the best studies* we have found that uses XAFS to collect kinetics data en route to a particle formation mechanism. As such, it is recommend reading in our opinion to anyone looking to use XAFS to study metal nanoparticle formation.	
17	Formation mechanism of metal nanoparticles studied by XAFS spectroscopy and effective synthesis of small metal nanoparticles	Gold nanoparticles were prepared chemically from tetrachloroauric(III) acid in DMF using $NaBH_4$ as the reductant. Resulting particles were stabilized with a series of thiol-containing ligands. The three types were: (i) tetradentate, (ii) monodentate, and (iii) dodecanethiol. The Au nanoparticle formation mechanism was studied by using QXAFS and TEM. Second, rhodium nanoparticles were prepared by photodeposition on TiO_2 in solution. The Rh nanoparticle formation mechanism was studied by using DXAFS, XPS, EDX, and TEM.	The authors found the syntheses that used the tetradentate ligand (containing 4 thiol groups) consistently produced smaller Au nanoparticles than the syntheses with either the monodentate ligand or the dodecanethiol. This was consistent across a range of S:Au ratios (0.1:1 to 16:1). From the XAFS data, the authors observe by 4.6 seconds into the reaction that all of the Au^{3+} and Au^{+} has been reduced to form Au^0 nuclei. The authors claim "the structure of the Au nuclei is estimated to be an Au_4 cluster."[72] From this, they propose the mechanism of gold nanoparticle formation is "the reduction of all of [the] Au ions, formation of nuclei, aggregation of the nuclei, and then the particles to grow larger."[72] For the Rh nanoparticle formation by photodeposition on TiO_2, the authors claim that "the in situ	The effectiveness of QXAFS cannot be overstated. The authors have compiled an impressive dataset for the formation of Au nanoparticles. Of particular note, the direct identification of the Au_4 cluster is an important result of significant value to the particle formation community, one that argues strongly against Classical Nucleation Theory in at least this example. The authors do claim that they have elucidated the mechanism of gold nanoparticle formation based on their direct observation of the reaction at different times. What remains to be done to support their claim of knowing the mechanism includes: (i) obtaining an experimentally based balanced reaction; (ii) writing down differential equation for their proposed mechanism(s); (iii) fit their high-quality kinetics data to each and every reasonable mechanism; and critically (iv) disproof of at least a couple, primary alternative mechanisms.	72

			XAPS study suggested the photodeposition mechanism as followed; the Langmuir type adsorption of Rh^{3+} ions on TiO_2 to form Rh-O bonds; the reduction of Rh^{3+} ions to Rh metals on the surface of irradiated TiO_2; the constant appearance of Rh metal particles."[72] Furthermore, the deposited Rh nanoparticles were found to have abnormal morphologies due to interactions with the TiO_2.		
18	An *in situ* XAFS study—the formation mechanism of gold nanoparticles from X-ray-irradiated ionic liquid	Gold nanoparticles were prepared from the ionic liquid [BMIM][$AuCl_4$] at room temperature under hard X-ray irradiation (BMIM = 1-butyl-3methylimidazolium). The reaction solution and the resulting particles were characterized by XAFS (both EXAFS and XANES analyses). TEM and XRD measurements were taken and reported in the SI.	The authors collected XAFS measurements at 30-90 minute intervals over 11.5 hours, at which the solution color had completely changed. At 5.5 hours, the authors observe an *N* ratio of 1:2 and an N_{Au-Au} value of 1.18, which they determine is evidence for "a structure like Cl_2Au-$AuCl_2$."[73] Based on their XAFS analyses, the authors propose a new "formation mechanism of gold nanoparticles" where the precursor $AuCl_4^-$ slowly loses Cl^- until the dichloroaurate complex dimerizes. The final particle is assumed to be stabilized in the ionic liquid by chloride.	The authors have collected interesting, but limited, XAFS data. The paper is unfortunately rife with confirmation bias rather than the needed disproof-based scientific approach. For example, the exact species in solution are not known, and considering ionic liquids, there are *numerous* speciation possibilities. The authors have used only simulations to "confirm" the existence of the Cl_2Au-$AuCl_2$ in solution as one example. Second, no kinetics data (concentration versus time) have been obtained nor fit with any proposed mechanism-based differential equation. Third, no corroborating evidence by any other technique is provided, be it in situ or ex situ, for the conclusions or proposed mechanism. It follows that the mechanistic claims in this paper need to be treated with considerable caution.	73
19	An in situ X-ray absorption spectroscopy study of copper	Copper nanoparticles were prepared from copper sulfate hydrate and sodium borohydride in reverse micelles. The microemulsions were prepared as	The primary finding reported by the authors was that "the decrease in water content from 15% to 13% in the reverse micelles was concluded to produce a larger	The authors made several claims about the reduction reaction of copper and the formation of the copper nanoparticles that do not seem firm based on the experiments conducted. For example,	74

	nanoparticles in microemulsion	followed: oil phase of heptane; aqueous phase a mixture of butanol and cetyltrimethylammonium bromide. Four reactions were studied varying the percentage of aqueous phase, concentration of $NaBH_4$, and the reaction time. Characterization of the copper nanoparticles was done by XANES and EXAFS at the end of the reaction time.	amount of metallic copper in these microemulsions with a radius slightly smaller than the metallic copper nanoparticles obtained in the reaction with 15% water."[74] They further report that the lower water content resulted in a slower reduction of copper.	the authors claim to have a detailed understanding of the reaction system, but have not done any other characterization experiments outside of the 4 XAFS data sets. The authors further claim that the copper disproportionates at long, 8 hours, reaction time versus 2 hours, but this claim is drawn from just two data points, and not continuous monitoring throughout the reaction time, and hence seems ill-supported. Overall, none of the 5 criteria for a reliable mechanistic study have been fulfilled for this copper nanoparticle formation system that need, therefore, considerable additional study.	
20	Detection and characterization of sub-critical nuclei during reactive Pd metal nucleation by X-ray absorption spectroscopy	Palladium nanoparticles were prepared from $[NH_4]_2PdCl_2$ in water at the interface with an organic layer of ααα-trifluorotoluene containing the reducing agent ferrocene. The aqueous phase contained LiCl, and the organic phase contained [BTPPA][TFPB], bis(triphenyl-phosphoranylidene) ammonium and tetrakis[3,5-bis(trifluoromethyl)-phenyl]borate respectively, as supporting electrolytes. Time-resolved data was collected using QEXAFS in fluorescence-yield mode.	Depending on the initial concentrations of palladium and ferrocene, the authors claim to observe no nucleation, spontaneous nucleation and growth, or metastable states due to density fluctuations. The authors point to classical nucleation theory (CNT) literature to support their results as "CNT predicts a metastable pre-nucleation state with sub-critical nuclei or clusters in a dynamic equilibrium with solute monomers."[75] The authors find that their observation of 'sub-critical nuclei' are in line with recent investigations of Au nanoparticles that have a 'sub-critical nucleus' size of 25 ± 4 nm. Finally, the authors claim they have "provided evidence of the presence of sub-critical nuclei of Pd metal before a	The authors have a creative approach to the designed, controlled synthesis of palladium nanoparticles. Furthermore, they have collected direct, valuable XAFS data on the particle formation reaction. However, the application of CNT and its assumption of a 'critical sized nucleus' is not supported by their results—and is not consistent with other reports in the literature that need to be considered before reaching such conclusions.[42,45,52,62] Additionally, reports of stable Pd clusters *below the 1.0 nm size*[42,52] offer an alternative hypothesis to, if not suggestive disproof of, CNT for such Pd nanoparticle formation systems. Overall, this report[75] should be read with caution and skepticism towards the conclusions drawn. The experimental set-up remains intriguing so that further studies of this system and by the	75

			stable metal product is actually formed, as predicted by CNT."[75] A strength of this study is that numerous control experiments were conducted to ensure the synthesis at the interface between the organic and aqueous phases was not producing false XAFS results or that X-rays were induced artefacts.	methods employed would likely be welcomed by the nanoparticle formation community.	
21	In Situ Time-Resolved XAFS Studies on Laser-Induced Particle Formation of Palladium Metal in an Aqueous/EtOH Solution	Palladium(0) nanoparticles were formed from the reduction of $PdCl_2$ in an aqueous/ethanol solution containing NaCl and polyvinylpyrrolidone (PVP) under N_2. Particle formation was induced using a Nd:YAG laser (266 nm, 10 Hz, 8 ns). The laser fluence was adjusted from 19.9 to 59.7 mJ/cm^2. Kinetics data were collected using DXAFS, and TEM was used to collect particle sizes and size-distributions.	The authors found correlations between the fluence of the UV laser and the resultant particle size. Broadly, they concluded "that laser irradiation with a higher fluence promotes particle growth."[76] The DXAFS-based kinetics data were fit successfully using the FW 2-step mechanism. Analysis of rate constants, extracted from the kinetics data with the FW 2-step mechanism, the k_1' (apparent nucleation rate constant) and k_2' (apparent growth rate constant), revealed that the fluence of the laser impacted both the nucleation and growth processes.	The authors in this study have collected excellent kinetics data using XAFS. The exact, characterization of the palladium(II) in the reaction solution is not known nor is the balanced reaction stoichiometry. Hence, it remains unclear what Pd(II) species is being reduced. The authors were able to fit their data using the FW 2-step mechanism Remaining to be done include: (i) speciation studies on the forms of Pd(II) in solution, such as are Pd^{2+} or $PdCl_xOH_y^{(2-x-y);}$ (ii) deconvolution of the FW 2-step k_1' (apparent) rate constant (i.e., from their current kinetic treatment of the DXAFS data) into its fuller, underlying nucleation rate law and hence more intimate nucleation mechanism (i.e., as done elsewhere for $Ir(0)_n$ systems discussed in the main text).	76
22	Synthesis and formation mechanism of self-assembled 3D flower-like Bi/γ-Fe_2O_3 composite particles	Particles composed of a bismuth core and iron(III) oxide shell were prepared using a hydrothermal process. Metal nitrate salts, potassium hydroxide, ethylene glycol (solvent and reducing agent), and in some cases the surfactant PVP, were used to	The authors concluded that the Bi/γ-Fe_2O_3 composite was composed "of a Bi metal nucleus and a γ-Fe_2O_3 shell. The Bi metal nucleus is the aggregate of Bi nanoparticles, while the γ-Fe_2O_3 shell results from the intercrossing of γ-Fe_2O_3 nanoslices."[77] These	The authors have characterized their system at specific points throughout the reaction quite well. Remaining to be done en route to a supported mechanism for this system include: (i) the balanced reaction stoichiometry; (ii) collecting of the necessary kinetics data and overall rate law for particle	77

	prepare the particles. Particles were characterized using XAFS, XRD, SEM, HR-TEM, ICP-OES, TGA, DSC, and Raman. No kinetics data was collected, but particles were characterized at 7 points throughout the reaction.	results were determined from analyzing the HR-TEM, XAFS, and XRD data, collected at the 7 different sampling times (0.5, 0.75, 1, 2, 4, 8, and 12 h). In Figure 9 of the paper,[77] the authors report a (cartoon) schematic of their proposed growth mechanism. It consists of hydrothermal treatment of the reaction solutions, nucleation and agglomeration (between 30 min – 1 h), short petal formation (1 h – 2 h), self-assembly and nanopetal growth (2 h – 24 h) and then 3D flower-like composite formation.	formation; and (iii) use of a disproof-based[10,11] approach so as to reach more reliable mechanistic conclusions, especially since the present study tends towards a confirmation bias approach.

Table S2.4. Summary of Papers Using Tandem Techniques: Use of Synchrotron XAFS and/or SAXS in Combination with Another Technique.

Entry	Title	System & Techniques Used to Monitor the Kinetics	Results and Proposed Chemical Mechanism	Conclusions, Insights, and Critical Analysis	Ref.
1	Nanoscopic Pt Colloids in the "Embryonic State"	Platinum colloids were prepared from $Pt(acac)_2$ in toluene under argon at 333 K. Over 4 hours, $Al(CH_3)_3$, also in toluene, was slowly added. The reaction ran for ~24 hours until the solution changed from yellow to black and gas evolution had stopped. Characterization was done ex situ by quenching the aliquot to 195 K with liquid nitrogen. Measurements were taken using NMR (^{1}H, ^{13}C, and coupled to ^{195}Pt), XANES, ASAXS, TEM, and DFT.	The authors present NMR evidence of a $(CH_3)_4Pt$-μ-$(Al(CH_3))_2$-μ-$Pt(CH_3)_4$ "intermediate" complex. However, the exact stoichiometry that is suggested does not equal the NMR results. The XANES measurements and analysis provide evidence of the platinum average oxidation state changing over the first 80 minutes. The EXAFS analysis reveals that the final size particles (~1.2 nm) contain about 53 atoms. The authors claim the formation kinetics, based on their XAFS results, are fit well by a first-order rate equation.	For analysis and comments, see Entry 2 directly below. This 1st entry is the shorter communication, whereas Entry 2 reports the subsequent full paper.	78

2	In Situ Study on the Wet Chemical Synthesis of Nanoscopic Pt Colloids by "Reductive Stabilization"	Platinum colloids were prepared from $Pt(acac)_2$ in toluene under argon at 333 K. Over 4 hours, $Al(CH_3)_3$, also in toluene, was slowly added. The reaction ran for ~24 hours until the solution changed from yellow to black and gas evolution had stopped. Characterization was done ex situ by quenching the aliquot to 195 K with liquid nitrogen. Measurements were taken using NMR (^{1}H, ^{13}C, and coupled to ^{195}Pt), XANES, ASAXS, TEM, and DFT.	The authors present NMR evidence of a $(CH_3)_4Pt$-μ-$(Al(CH_3))_2$-μ-$Pt(CH_3)_4$ "intermediate" complex. They report the exact stoichiometry that is suggested is not equal to the NMR results. Their XANES measurements and analysis provide evidence of the platinum average oxidation state changing over the first 80 minutes. The EXAFS analysis reveals the final size particles (~1.2 nm) contain about 53 atoms. The authors claim the formation kinetics, based on their XAFS results, are fit well by a first-order rate equation.	Overall, the authors have presented valuable evidence for the formation of a Pt-μ-$(Al)_2$-μ-Pt species, but whether this is an on-path or off-path species is not known and will require pre- or post-steady state kinetics to address that challenging mechanistic question. However, before such studies, there are a few points of confusion and concern that need to be addressed. First, the actual versus proposed stoichiometries do not match. Next, there are inconsistencies between results from different techniques, specifically, the DFT calculations do not support the XAFS. More broadly and unfortunately, the study is plagued by attempted *proof*-based and confirmation biased experimentation, where experiments are designed to *prove* rather than to try and disproof alternative hypotheses. It follows that the conclusions from this work need to be viewed with considerable caution.	79
3	Characterization of zinc oxide nanoparticles encapsulated into zeolite-Y: An in-situ combined X-ray diffraction, XAFS, and SAXS study	Zinc oxide particles prepared inside zeolite Y were prepared by ion-exchange between sodium zeolite Y (Si/Al – 2.52) and aqueous zinc acetate at room temperature for 24 hours. Then, the zinc zeolite Y was treated with sodium hydroxide "to precipitate the oxide nano-particles inside the zeolite framework."[80] The authors performed both XAFS-XRD and SAXS-WAXS on the system by calcinating the particles from 25 ºC to 550 ºC and 25 ºC to 300 ºC, respectively, at a rate of 5 ºC/min.	Based on XRD, the authors found no large zinc oxide particles. By XAFS, the authors found "only minor changes take place during the heat treatment process", and they "estimated the particle size by calculating the variation in coordination number of Zn–Zn for different cluster sizes…and we obtained a value of ~18 ± 4 Å."[80] Finally, the authors report a particle size of ~15 ± 5 Å by SAXS. Both the EXAFS and SAXS values are consistent with the size of the zeolite Y cage.	The authors have demonstrated the usefulness of the various synchrotron techniques, namely tandem XAFS-XRD and SAXS-WAXS. Importantly, they have not attempted to make conclusions beyond the scope of their data and the techniques used. They claim to have characterized the material. Then, they characterize it and state further inferences will require additional study. Careful, thoughtful, proper science and conclusions, in our opinion.	80

4	Structure of assemblies of metal nanowires in mesoporous alumina membranes studied by EXAFS, XANES, X-ray diffraction and SAXS	The authors studied four different metal nanowires formed inside anodic aluminum oxide (AAO) membranes. The AAO membranes were prepared by anodizing aluminum foils in polyprotic acid using a lead plate cathode. The pore diameters were controlled by the anodizing voltage. The resulting pores used were 12, 24, 48, and 72 nm. Nanowires of iron, cobalt, tin, and gallium nitride were prepared. Iron, cobalt, and tin were prepared "by electrochemical AC plating from an aqueous solution of metal sulfate, with H_3BO_3 as a supporting electrolyte in the case of iron and cobalt, and H_2SO_4 in the case of tin."[81] Gallium nitride nanowires were prepared from thermally decomposing $Ga(NO_3)_3$ at 1000 °C to gallium oxide, and then reacting that with NH_3 at 1000 °C. Nanowires were studied using EXAFS, XANES, WAXS, HE-XRD, and SAXS.	The iron nanowires were found to retain the same structure as bulk iron. However, the electronic structure of the iron nanowires appears to be correlated to the size of the AAO pore diameter. The cobalt nanowires appear to form a convolution of hcp and fcc structures depending on the nanowire diameter. The exact dependence was unable to be elucidated, as it was found that the ratio of the two structure types (hcp:fcc) was not linear with nanowire diameter. The tin nanowires were found to "become superconducting at the same temperature as bulk tin: 3.7 K."[81] The GaN nanowires were found to have a hexagonal wurtzite structure. However, extra heating in the synthesis process to 1150 °C resulted in incorporation of some aluminum into the structure.	Of note, the authors state in their conclusion that their "philosophy is that detailed characterization of the structures of assemblies of metal and semiconductor nanowires within AAO membranes is an essential prerequisite to understanding and controlling their physical properties."[81] *Noteworthy is that this philosophy is the proper foundation from which to conduct mechanistic research by any scientist.* One must fully characterize a material before being able to design meaningful kinetics and mechanistic experiments. Why, one might ask? Because the proposed steps of the mechanism must add up to the observed, balanced reaction—otherwise, one is proposing a mechanism for some other reaction than the one at hand. Often, even trace products or by-products can provide detailed insight into the underlying mechanism. A good example is trace R-R, R-H and R(-H) (olefin) products: these are often definitive indicators of R• intermediates, each R• giving characteristic R-R, R-H and R(-H) that vary little from the gas phase to different solvents.	81

5	A Combined SAXS/WAXS/ XAFS Setup Capable of Observing Concurrent Changes Across the Nano-to-Micrometer Size Range in Inorganic Solid Crystallization Processes	The authors have presented a unique multi-technique (SAXS/WAXS/XAFS) set-up to study the crystallization process of an inorganic-aluminum phosphate solid. The authors have identified the stoichiometry as $Zn_xAl_{1-x}PO_4$, prepared from the combination of zinc nitrate hydrate, H_3PO_4, triethylamine, and pseudoboehmite alumina.	The extent of crystallization was determined as a function of the increase in temperature. Initial WAXS peaks were observed after the temperature reached 90 °C, and the peaks increased until 160 °C. At that point (160 °C), the reaction was determined to have reached completion. The final crystallite size was calculated (by Scherrer analysis) to be ~54 nm. Based on the SAXS/WAXS/XAFS results, the authors proposed "that growth occurred via a two-step aggregation/crystallization process."[82]	This paper demonstrates the power of combining several direct techniques. As the authors say, for many studies of crystallizations, workers "often focus on data acquired using a single technique, which rarely provides all of the necessary information from which new insight can be obtained."[82] Here, the authors have shown the crystallization and broader scientific communities that effectiveness of using tandem, direct techniques. Needed in the following case to upgrade the proposed two-step growth process to a more reliable mechanism include: (i) knowledge of the complete, balanced reaction stoichiometry; (ii) postulation of pseudo-elementary reaction steps for all possible reasonable alternative mechanisms; and (iii) testing those mechanisms by attempted fittings of the kinetics data, all with a disproof of alternative mechanistic hypotheses as the *modus operandi*.	82
6	XAFS, SAXS, and HREM characterization of Pd nanoparticles capped with *n*-alkyl thiol molecules	Palladium nanoparticles, capped by thiols, were prepared by combining $PdCl_2$ with *n*-alkyl thiol (n = 12, 16, or 18; hereafter, SC12, SC16, and SC18), and lithium triethylborohydride in THF. The reaction was run at 60 °C for 16 hours before purification in cold ethanol and toluene. Characterization was performed using HR-TEM, XAFS, and SAXS.	The resulting nanoparticles were observed, by HR-TEM and SAXS, to have "diameters of 1.2 ± 0.4 nm, 1.2 ± 0.4 nm and 1.3 ± 0.5 nm for Pd:SC12, Pd:SC16 and Pd:SC18, respectively."[83] The particles from the Pd:SC12 synthesis were found to retain a metallic Pd core, while the particles from the Pd:SC18 synthesis were found to have converted completely to a PdS structure. Restated, as the authors state, "[t]he volume sulfidation in total in nanoclusters capped with thiol with long carbon chains (n = 18) and only	This paper presents an excellent summary of the characterization for these tiny palladium nanoparticles. These contain the necessary experiments to understand the final product stoichiometry. While no mechanistic or kinetics data are collected, the techniques used (SAXS and XAFS) could easily be applied to monitor the formation process of the palladium nanoparticles.	83

			partial in nanoclusters with short carbon chains (n = 12), the core of the particles remaining in this case in metallic state."[83]		
7	*In situ* observation of formation of silver particles in water-in-$scCO_2$ emulsions	Silver nanoparticles were prepared by two methods: photoreduction by UV light and chemical reduction by hydrazine. Reaction solutions were made of silver perchlorate, AOT (di-2-ethylhexyl sodium sulfosuccinate), benzoin, small amount of F-pentanol (2,2,3,3,4,4,5,5-octafluoro-1-pentanol), ethanol, water, and CO_2. The experimental cell was kept at 35 ºC and 25 MPa for 5 hours with stirring to form the homogeneous emulsions prior to either irradiation with UV light or addition of hydrazine. The reaction was monitored by either EXAFS or tandem UV-vis and SAXS.	The authors found, by both TEM and SAXS, that the average diameter or the Ag particles "prepared by the photoreduction and by the hydrazine reduction in the microemulsions is estimated…to be 6.4 and 2.9 nn, respectively."[84] The analysis of the size distribution reveals a rather large error in average diameter, ca. 28-62%. However, the SAXS analysis revealed that the size of the water droplets have a negligible effect on the Ag particle formation. Furthermore, the authors found the EXAFS "demonstrate that Ag^+ ions were completely reduced to Ag^0 atoms and the formation of Ag-Ag bond occurred in the AOT-rich phase by the hydrazine reduction, followed by the subsequent formation of larger Ag particles, while these Ag^+ ions were not completely reduced in the photoreduction of the concentrated Ag colloidal dispersions."[84]	This study demonstrates how careful, *tandem* experimentation is quite powerful. The combination of two direct techniques (SAXS and UV-vis) to monitor the size and electronic evolutions can provide the necessary, rigorous kinetics from which to conduct mechanistic investigations. This study is a good foundation upon which to begin a mechanistic study. The needed additional studies en route to a disproof-based minimum mechanism include: (i) determination of the balanced stoichiometry; (ii) writing out the entire list of pseudo-elementary step based plausible mechanisms; (iii) fitting the data to those mechanisms—and where fits are not possible, thereby (iv) disproof of alternative mechanisms for the formation of silver nanoparticles in water-in-$scCO_2$ emulsions. What would likely be of fundamental interest is (v) determining, from control experiments leaving out components such as the $scCO_2$ if / where possible, what the roles of those components are in the Ag_n particle formation process.	84

8	Influence of Monomer Feeding on a Fast Gold Nanoparticles Synthesis: Time-Resolved XANES and SAXS Experiments	Gold nanoparticles were synthesized in toluene from $AuCl_3$ (7 mM) The ligand was either decanoic acid or decylamine. Didodecyldimethylammonium bromide (DDAB) was used as a cationic surfactant. Tetrabutylammonium borohydride (TBAB) was used as a reductant. Ligand was added in a 14:1 ratio to Au starting material. DDAB:Au and TBAB:Au were both 4:1. The authors performed kinetics experiments using XANES and separate kinetics experiments using SAXS.	The authors claim to have "assessed in situ and quantitatively the fast formation process of gold nanoparticles in solution."[85] "An important result of these experiments is that during the reduction of Au(I) a measurable amount of Au(0) appears in bulk which shows that the model of a supersaturation of bulk monomer can be used."[85] Further, when the authors studied the effect of the ligand, they found "that the stabilizing ligand controls the size of the nanoparticles by controlling the formation rate of monomers. However, the molecular mechanism at play which could yield these differences remains difficult to assess rigorously."[85] The authors also used CNT to fit their data and the "Lamer scheme"[85] to explain their concentration of Au(0) monomer versus time plot.	The authors have presented an intriguing study for the formation of Au nanoparticles. They have expertly chosen to study directly the particle formation using XANES (for the Au oxidation state) and SAXS (for the particle size and size distribution), both as a function of time. However, it should be noted that the SAXS and XANES measurements were taken at different times and different locations, so while they are under the same conditions, they were separate experiments. The authors claim that CNT can be used for their system, yet there is presently no evidence in the literature for CNT being able to successfully explain metal particle formation.[13] The authors cite "a burst of the number of particles is in direct agreement with the old Lamer scheme"[85], which is a claim that has been disproven in two recent reviews.[12,13] Finally, the authors claim that "three processes occur concomitantly: formation of new monomers through reduction of the precursors (either in bulk or at the surface), nucleation of new particles, and growth of the existing particles."[85] The authors miss that *if* reduction of metal, nucleation of kinetically effective nuclei, and growth are all taking place at the same time as they claim, *then* CNT and the LaMer model are disproven by the author's own data Overall, this study illustrates an excellent choice of instrumentations and the collection of excellent data, but	85

				the interpretation of the data needs further examination.	
9	Mechanism of Gold Nanoparticle Formation in the Classical Citrate Synthesis Method Derived from Coupled In Situ XANES and SAXS Evaluation	Gold nanoparticles were prepared according to the original procedure by Turkevich,[86] where an aqueous solution of $HAuCl_4$ and $Na_3Citrate$ were mixed at 75 ºC. Measurements were taken in situ by tandem SAXS/XANES using an acoustic levitator as the sample holder. Further characterization was done by UV-vis, SEM, and TEM.	The authors report high-quality tandem SAXS/XANES studies leading to time-resolved size, number of particles, polydispersity, and oxidation state data. From these data the authors propose a 4-step gold nanoparticle formation pathway consisting of the words of "fast initial formation of small nuclei, coalescence of the nuclei into bigger particles, slow growth of particles sustained by ongoing reduction of gold precursor, and subsequent fast reduction ending with the complete consumption of the precursor species."[87]	While the data presented is impressive, there are numerous points of discussion to some concerns with the analysis. First, one should realize that the data are not all collected in situ, but "at different reaction time, ca. 4 μL of the liquid samples were extracted from the catch of reaction solution and placed as droplets in an acoustic levitator".[87] Second, the authors did not quantitatively, nor even qualitatively, fit their high-quality kinetics data to any mechanism. They claim to have determined a 4-step "mechanism", but in fact have not done any of the necessary steps to get to such mechanism that goes beyond just words. Notably, the needed studies are: (i) determination of the balanced reaction stoichiometry; (ii) writing out pseudo-elementary steps for all reasonable mechanisms along with their associated differential equations, (iii) then attempted fitting the kinetics data to each mechanism, all with (iv) a disproof-and Ockham's razor approach as the history of chemical mechanisms from physical-organic chemistry teaches is required to reach a reliable mechanism. Furthermore, the authors have described "the initial step as burst nucleation"[87], which is a concept from the LaMer model that has been definitively disproven,[12,13] a critical insight that future studies need to take into account.	87

10	In Situ and Simultaneous UV—vis/SAXS and UV—vis/XAFS Time-Resolved Monitoring of ZnO Quantum Dots Formation and Growth	Zinc oxide quantum dots were prepared from the zinc tetramer, Zn_4OAc_6, in absolute ethanol at 40 ºC. The hydrolysis and condensation reactions were catalyzed by the addition of KOH. In situ tandem measurements were taken using UV-vis/XAFS and UV-vis/SAXS.	Based on time-resolved data, the authors proposed a four-step schematic for the temporal evolution of the zinc oxide quantum dots. The authors claim the formation of the ZnO quantum dots "is a step process composed of four main stages: (i) ZnO Qdot nucleation and growth; (ii) growth of compact ZnO Qdot aggregates; (iii) growth of fractal aggregates; and (iv) secondary nucleation and fractal aggregates growth."[88] The exact nucleation process was not able to be elucidated "due to the experimental time acquisition", as "too little information was collected in that period of time to be able to give a quantitative analysis of this initial nucleation process."[88]	The authors in this paper have expertly collected tandem, direct, time-resolved particle size data. As noted, they have recognized when they were unable to collect quantitative data and wisely have not attempted to make conclusions beyond their data. Unfortunately, the authors have relied only on equations from models that do not fit their data. Needed before a reliable mechanism can be obtained are once again just those exact steps and approach listed in entries 5, 7, and 9 in this Table S2.4.	88
11	Probing Nucleation Pathways for Morphological Manipulation of Platinum Nanocrystals	Platinum nanocrystals were synthesized from two reaction solutions. Both systems used tetrachloroplatinate(II) and the stabilizer PVP. The first system used ethylene glycol (EG) as the solvent and reducing agent. The second system used citric acid (CA) as the reducing agent and water as the solvent. Nanocrystal formation was monitored by tandem in situ QXAFS and UV-Vis. Specifically, the EXAFS were analyzed.	The authors report that the EG synthesis produced nanocrystals with a nanowire morphology. Meanwhile, the CA synthesis produced nanospheres. The XAFS and UV-Vis results support the morphologies observed by TEM. The authors postulate that EG is a "weak" reductant, compared to CA, and does not completely reduce the Pt(II). This produces $[Cl_3Pt—PtCl_3]^{4-}$ dimers that polymerize into "longer line 'Pt_nCl_x' complexes."[89] CA is believed to immediately reduce Pt(II) to Pt(0). Hence, a cartoon mechanism is proposed for each reductant. For EG, $[PtCl_4]^{2-}$ is partially reduced to form $[Cl_3Pt—PtCl_3]^{4-}$ dimers, then longer "dimer clusters", and finally, a "linear Pt_nCl_x complex".[89] For CA,	The concept of "reducing strength" is intriguing, but qualitative and hence impossible to test quantitatively. Numerous scientific questions arise from this work that additional studies will hopefully address: (i) what is the effect of having EG versus water as the solvent;? (ii) what direct evidence is there for the formation of $Pt(0)_{2-3}$ clusters?; (iii) what is the speciation of the reaction solution?; and (iv) what differential equations were used to fit the kinetics data that produced the (cartoon) mechanism shown in Figure 4 within of that paper?.[89] Overall, the authors have collected impressive, high-quality synchrotron data, but gaps in needed evidence and a lack of mechanistic analysis are issues that merit attention.	89

			$[PtCl_4]^{2-}$ is reduced to Pt(0) atoms, the $Pt(0)_2$ and $Pt(0)_3$ clusters, and finally "spherical $Pt(0)_n$ cluster".[89]		
12	Understanding Solvothermal Crystallization of Mesoporous Anatase Beads by In Situ Synchrotron PXRD and SAXS	The crystallization of TiO_2 beads was performed using three different amorphous precursor beads (between 0.3 – 1.1 microns), titanium(IV) isopropoxide (TIP), hexadecylamine (HDA), potassium chloride, ammonia, and water. The reaction was monitored using in situ synchrotron PXRD and SAXS. Ex situ measurements were conducted using SEM, TEM, and SAED.	The authors conclude the crystallization from the amorphous TiO_2 beads "to be a 3-dimensional crystallization process involving 4-steps. This process involves (1) an induction period for HAD (organic structure-directing agent) and amorphous TIO_2 dissolution, (2) anatase nucleation and growth at the expense of precursor dissolution, (3) coarsening in anatase crystals accompanied by continued precursor dissolution, and (4) reaching stable crystallite size with no significant Ostwald ripening."[90]	The authors have collected excellent data using the best techniques available, directly and in situ. They have attempted to provide alternative hypotheses throughout their study. The authors have constructed a "words-only" 4-step mechanism based on their qualitative results—so that an issue is that no significant quantitative results are given to support their claimed 'mechanism'. This study, too, needs the stepwise, disproof-based mechanistic approach outlined in entries 5, 7, 9 and 10 directly above in this Table S2.4.	90

13	Mechanisms of SnO_2 Nanoparticles Formation and Growth in Acid Ethanol Solution Derived from SAXS and Combined Raman–XAS Time-Resolved Studies	SnO_2 nanoparticles were prepared from $SnCl_4 \cdot 5H_2O$ in absolute ethanol at pH = 0.9. Water was added slowly over 9 minutes, and the solution was aged for 30 minutes at room temperature. Next, the solution was heated from 30 ºC to 70 ºC at a rate of 1 ºC/minute. Once the solution reached 70 ºC, it was aged a further 60 minutes. The reaction was monitored in situ by tandem QXAFS and Raman, and a separate in situ SAXS experiment. In addition, ex situ measurements were taken using XRD and HR-TEM.	The authors have thoroughly investigated the speciation of the water-ethanol-tin solution that occurs at room temperature. They have identified the three primary components as $[SnCl_x(H_2O)_{6-x}]^{4-x}$, where x = 3, 4, or 5. Next, the authors have presented numerous figures of XAFS or SAXS output versus time. Based on their results, the authors proposed "a five-step mechanism of formation"[91] for their system. "The first three steps…correspond to the prenucleation of low nuclearity species, followed by a monomer – tin oxo cluster aggregation growth and cluster-cluster growth, leading to the formation of double or triple chains structure further interconnected for form SnO_2 nanoparticles."[91] During the heating and aging at 70 ºC, "a densification process followed by an advanced nanocrystallite growth through the addition of mononuclear species to the surface of the nanoparticles has been identified."[91]	Overall, the authors have collected superb data on a fascinating system. Their thorough investigation into the solution speciation before nanoparticle formation is noteworthy and commendable. The issues with this work are: they claim a mechanism without having written out the integrated rate law. In their[91] Figure 3, they have fit the "two linear growth regimes…with two distinct kinetic rates k" from the rate function "$Rg - Rg_0 = kt$", which they claim "indicate behaviour consistent with the reaction-limited growth kinetics controlled by two different mechanisms."[91] Yet, they have not further investigated these claimed mechanisms. At the end of the paper, the authors claim "these five well time-defined stages can be used as a versatile way to control the growth processes in order to fine tune the size of SnO_2 nanocrystalline particles." This claim is not demonstrated or substantiated anywhere in their paper nor by any literature they have cited. Overall, this study has collected first-rate synchrotron data and performed noteworthy, due diligence on the solution speciation. That said, they *do not have a mechanism* by the established criteria of obtaining a reliable reaction mechanism.	91

14	Synthesis of 1nm Pd nanoparticles: Insights on the synthesis mechanism using *in situ* XAFS and SAXS in a microfluidic reactor	Palladium nanoparticles were synthesized from palladium acetate in a 1:1 mixture of toluene and alcohol, in the presence of either oleylamine (OLA) or trioctylphosphine (TOP). The OLA-stabilized particles were synthesized at 60 ºC in a toluene/methanol solution at an OLA:Pd molar ratio of 1:1. The TOP-stabilized particles were synthesized at 100 ºC in a toluene/hexanol solution at a TOP:Pd molar ratio of 1.5:1. Particle formation was done inside a microfluidic reactor and monitored by tandem in situ SAXS and XAFS. STEM measurements were done ex situ.	The authors found for both OLA and TOP that "nucleation proceeded continuously over the time period analyzed and was overlapped by an autocatalytic growth phase without causing a broad size distribution."[92] Furthermore, and despite there still being a significant amount of unreacted precursor in solution, "the growth rate was observed to slow considerably and the nanoparticles size reached a plateau with a narrow size distribution."[92] "The combined SAXS and XAFS results strongly suggest the ligands play an important role in affecting the nucleation and growth rates leading to the self-limiting nanoparticle size observed."[92]	The authors have presented an intriguing study of TOP- and OLA-stabilized Pd nanoparticles. Importantly, and as they state it, the "coupling of multiple in situ techniques is needed to provide a more detailed, near complete picture of the synthesis mechanisms."[92] The use of synchrotron-based X-ray scattering and spectroscopy techniques are of particular interest to obtain size, shape, chemical, and structural information. Of particular note, the authors have not attempted to draw conclusions beyond what the data has presented. The author has presented the available particle formation mechanisms in the literature and systematically ruled out each of them. The one that most closely matches their data is the FW 2-step mechanism, and significant is that the authors further illustrate how it is not entirely effective / limited for the case at hand because ligand effects—which are shown to significantly contribute to this system—go beyond the minimum FW 2-step mechanism. Overall, this paper is an important study headed in the proper direction, one that *does not* attempt to draw conclusions beyond what the data has shown. Items for future study include: (i) a complete reaction stoichiometry, (ii) kinetics derivation, and fitting of kinetics data to plausible mechanisms explicitly containing ligand effects.	92

15	Simultaneous SAXS/WAXS/ UV-Vis Study of the Nucleation and Growth of Nanoparticles – A Test of Classical Nucleation Theory	Gold nanoparticles were prepared from $AuPPh_3Cl$ in toluene with dodecanethiol (DDT) and *t*-butylamine borane (TBAB), sonicated together at room temperature. The Au solution was combined with the TBAB (also in toluene) using a stopped flow device for measurements by in situ, tandem SAXS, WAXS, and UV-vis. TEM was used to characterize the resultant Au nanoparticles.	The authors used their in situ SAXS/WAXS/UV-vis technique to "study the kinetics as a function of the most relevant parameters such as concentration, temperature, ligand ratio, and the addition of polar cosolvents."[93] The authors claim to have, for the first time, "numerically solved the complete set of reaction rate equations comprising precursor reaction, nucleation, growth, and Ostwald ripening to obtain the evolution of the full particle size distribution from the induction period to the late growth stage."[93] Finally, the authors have presented a schematic presentation of Au nanoparticles growth based on their results and the components they believe are involved in the formation mechanism.	Noteworthy are the authors' unique tandem in situ technique and excellent resultant data! Next, the authors claim their model fits their data well; however, in their Figure 2a, the model fails to fit the early time data. It may be that their growth model fits the growth-dominated portion of the kinetics data, but the majority of the nucleation data is missed. The authors report a "fast nucleation (LaMer mechanism)"[93], but the LaMer mechanism at least, especially at room temperature, has been thoroughly disproven.[12,13] Overall, the authors experimental approach is impressive, and the fitting of the growth data is well performed. Requiring attention are the overlooked assumptions used in the nucleation model that cause the model to not work for this system. Further investigations along the lines discussed for entries 5, 7, 9, 10, 12, and 14 are needed before a more complete, reliable mechanism for this particular Au nanoparticles system can be claimed to be in hand.	93

16	*In situ* studies on controlling an atomically accurate formation process of gold nanoclusters	Polydisperse gold nanoparticles were prepared by reduction of $Au_2(L_3)_2Cl_2$, where L_3 = 1,3-bis(diphenylphosphino)propane, with $NaBH_4$ in dichloromethane. The polydisperse Au_n clusters were re-dispersed in ethanol, where HCl was added to initiate the formation of monodisperse $Au_{13}(L_3)_4Cl_4$ clusters. The "size-convergence" "etching" process was monitored by tandem, in situ UV-vis and XAFS. Ex situ measurements were taken using MALDI-MS.[94]	The authors monitored the reaction over a 10-hour period, where they observed Au_n (n ~ 15–65) "size-converge" to Au_{13} clusters.[94] Within hour 1, new peaks appeared in the UV-vis spectrum indicating particles of Au_8–Au_{13} (primarily Au_{11}), corroborated by MALDI-MS. By hour 2, particles of size Au_{30}–Au_{40} had disappeared, and absorption data suggested the formation of Au_{13}. Overall, the authors "found that the cluster formation is achieved in an etching/growth manner including two distinct reaction steps. (1) The initial polydisperse Au_n clusters are etched by HCl."[94] And (2) "a secondary-growth step to form uniform $Au_{13}(L_3)_4Cl_4$ clusters, by incorporating the reactive Au(I)–Cl species in the solution."[94]	The authors present an intriguing study of the secondary growth/etching in polydisperse Au_n nanoparticles treated with HCl. They have collected solid XAFS, MS, and UV-vis data. Remaining for future study are a better mechanistic understanding for "the etching mechanism during nanocluster formation".[94] Primarily, the authors use MS and their "schematic illustration" to attempt the impossibility of "deducing" the correct mechanism—that is, vs the proper approach of offering solutions for the inverse problem where on gets to "cause" (here, the mechanism) from "effects / observables" by inductively disproving ones way there. Hence, in order to claim they have the "etching mechanism", the steps noted already for entries in this Table S2.4 (Entries 5, 7, 9, 10, 12, 14, and 15) will be required.	94

17	Time-resolved *in situ* studies on the formation mechanism of iron oxide nanoparticles using combined fast-XANES and SAXS	Iron Oxide nanoparticles were prepared from an equal mixture of $FeCl_3 \cdot 6H_2O$ and $FeCl_2 \cdot 4H_2O$ in water (total Fe concentration of 0.31 M) and mixed with triethanolamine (TREA). The reaction was run for 1.5 h at 115°C. The reaction was monitored using tandem XANES and SAXS with an acoustic levitator as a sample holder. Ex situ TEM and XRD were used to characterize the resultant iron oxide nanoparticles.	The authors collected time-resolved XANES and SAXS results, as well as characterized the "first intermediate species"[95]. Then, they characterized the final product using TEM and XRD. Based on their experimental results, the authors claim a formation mechanism consisting of four phases. Paraphrasing, the four phases are: (i) formation of akageneite as an intermediate Fe_xO_y species; (ii) formation of magnetite particles (~3 nm); (iii) growth of magnetite nanoparticles; and (iv) maghemite nanoparticles grow to "a radius of gyration of 4.2 nm".[95]	The authors have examined the case of FeO_x nanoparticle formation using a creative tandem XANES and SAXS set-up. The complete, balanced reaction stoichiometry has not been presented. Kinetics data have been monitored. However, the kinetics data is not in a form, yet, that can be fit by an analytic equation. No pseudo-elementary steps or corresponding differential equations have been written for the proposed mechanism. Finally, the authors have started the needed disproof-based experimentation with their assessment over HCl's role in the reaction; the disproof of additional plausible mechanisms would be most welcome. Overall, this system and is creative experimental set-up, warrants further use to elucidate a complete mechanism for FeO_x formation.	95

18	Concerted Growth and Ordering of Cobalt Nanorod Arrays as Revealed by Tandem in Situ SAXS-XAS Studies	Cobalt nanoparticles were synthesized from $[Co\{N(SiMe_3)_2\}_2(THF)]$, lauric acid (LA), and hexadecylamine (HDA) at 130 or 150 ºC and reduced under ~50 psi H_2. Particles were analyzed ex situ by TEM and SEM. Tandem XAS and SAXS experiments collected kinetics data on the formation of the nanorods.	Based on the authors tandem XAS-SAXS experiments, in conjunction with their ex situ TEM images, the authors propose "a qualitative nanorod growth mechanism, which consists of three main steps: a fast nucleation, a fast growth by monomer addition that takes place during reduction of Co(II) species to Co(0), and a slower ripening step that takes place after complete reduction, which most likely involves an oriented attachment process."[96] In addition, the authors have proposed a reaction pathway for the overall nanorod formation.	The authors have produced excellent *qualitative* evidence and analysis for their proposed reaction pathway (presented as Scheme 1 in the paper[96]). Of note, their use of tandem XAFS and SAXS displays the power of tandem, in situ techniques for monitoring particle formation and developing mechanistic insights. Further, they applied disproof (or at least consideration) of alternative hypotheses to their results. The only drawback, as the authors note, is that they were not able to collect particle volume (number) data with their current set-up. Hence, they were only able to collect *qualitative* data. With additional *quantitative* data, they may be able to determine what the mechanism of nucleation and/or growth is for cobalt nanorod arrays. Currently, they have proposed fast nucleation and fast growth by monomer addition, which based on their present data could also be interpreted as continuous nucleation and autocatalytic surface growth according to the FW 2-step mechanism. Overall, the authors have produced an excellent, intriguing piece of research that deserves further study and, then, more detailed mechanistic analysis and interpretation.	96

19	Nucleation and Growth Kinetics of ZnO Nanoparticles Studied by in Situ Microfluidic SAXS/WAXS/ UV–Vis Experiments	ZnO nanoparticles were prepared by mixing solutions of zinc oleate in THF and tetrabutylammonium hydroxide (1 M in methanol) in THF. A stopped-flow microfluidic capillary was used. The reaction was monitored *in situ* using a SAXS/WAXS/UV-Vis set-up with a copper heating tube integrated into the *in situ* capillary holder. Kinetics experiments were conducted at two zinc concentrations (160 and 53 mM) and two temperatures (40 and 50 °C).	The authors reported particle size (radius) as a function of time for the four experimental conditions. Data were collected across the first 1000 s of the reaction. A set of differential equations were written based on the net reaction of Zn^{2+} and 2 OH^{-}. Then, Classical Nucleation Theory (CNT) was applied to describe the nucleation process and incorporated into the final differential equations. The authors claim that their model was able to fit ca. 50% of the radius versus time data.	The authors have presented a fascinating study of ZnO formation, examined via a creative and effective *in situ* microfluidic set-up. However, they were unable to determine the exact reaction stoichiometry. Excellent kinetics data were collected using state-of-the-art synchrotron methods, but the differential equations that were written are based on a single, net ion chemical reaction combined with CNT rather than writing out a full set of pseudo-elementary step reactions. Hence, the set of studies discussed in Entries 5, 7, 9, 10, 12, 14 and 15 in this Table S2.4 are recommended for emphasis with this ZnO nanoparticle formation system.	97

20	The role of pre-nucleation clusters in the crystallization of gold nanoparticles	Gold nanoparticles or gold nanowires were synthesized from 20 mM $AuCl_4^-$, 1 M triisoprpylsilane (TIPS), and 50-400 mM oleylamine (OY) in hexane. The reaction was monitored *in situ* by SAXS, XAS, and HE-XRD (for PDF analysis). Ex situ TEM images were collected	First, the authors determined the balanced stoichiometry for the reduction reaction. Then, they monitored both particle size and gold oxidation species as a function of time. They observed that at high OY concentrations, nanowires formed, whereas at low OY concentrations, ordered nanoparticles formed. Finally, the authors report a series of differential equations that were used to fit the two kinetics datasets based on hypothesized kinetic models for nanowire or nanoparticle formation.	The authors have presented a compelling case for their proposed kinetic models. First, they have written out the balanced chemical reaction and determined the reaction speciation as best they could. Next, they have collected state-of-the-art kinetics data by multiple physical methods. Then, they hypothesized a kinetic model and wrote the differential equations. *Excellent!* These were then solved using numerical integration in MatLab, and they were shown to *fit the kinetics curves*. Finally, an attempt was made to consider at least one additional kinetic model from the literature[7]. Furthermore, the concept of a prenucleation cluster was introduced, although the exact speciation was unable to be determined. The authors note that future studies are needed, a correct statement that in no way diminishes the value of this first-rate study, its mechanistic insights, all of which are a great, recommended read, in our opinion!	98

REFERENCES

1. Avrami, M. Kinetics of Phase Change. I. General Theory. *J. Chem. Phys.* **1939**, *7*, 1103-1112.

2. Avrami, M. Kinetics of Phase Change. II. Transformation-Time Relations for Random Distribution of Nuclei. *J. Chem. Phys.* **1940**, *8*, 212-224.

3. Avrami, M. Kinetics of Phase Change. III. Granulation, Phase Change, and Microstructure. *J. Chem. Phys*. **1941**, *9*, 177-184.

4. Gibbs, J. W. On the Equilibrium of Heterogeneous Substances. *New Haven Transactions of Connecticut Academy of Arts and Sciences* **1874**, *III*, 343-523.

5. Volmer, M. *Kinetik der Phasenbildung*. Verlag von Theordor Steinkopff: Leipzig, 1939.

6. Becker, R.; Döring, W. Kinetische Behandlung der Keimbildung in übersättigten Dampfen. *Ann. Phys.* **1935**, *24*, 719-752.

7. Watzky, M. A.; Finke, R. G. Transition Metal Nanocluster Formation Kinetic and Mechanistic Studies. A New Mechanism When Hydrogen Is the Reductant: Slow, Continuous Nucleation and Fast Autocatalytic Surface Growth. *J. Am. Chem. Soc.* **1997**, *119*, 10382-10400.

8. Liftshitz; I. M.; Slyozov, V. V. The kinetics of precipitation from supersaturated solid solutions. *J. Phys. Chem. Solids* **1961**, *19*, 35-50.

9. Wagner, C. Z. Theorie der Alterung von Niederschlägen durch Umlösen. *Electrochem.* **1961**, *65*, 581-591.

10. Platt, J. R. Strong Inference. *Science* **1964**, *146*, 347-353.

11. Chamberlain, T. C. Studies for Students. The Method of Multiple Working Hypotheses. *J. Geology* **1897**, *5*, 837-848.

12. Whitehead, C. B.; Özkar, S.; Finke, R. G. LaMer's 1950 Model for Particle Formation of Instantaneous Nucleation and Diffusion-Controlled Growth: A Historical Look at the Model's Origins, Assumptions, Equations, and Underlying Sulfur Sol Formation Kinetics Data. *Chem. Mater.* **2019**, *31*, 7116-7132.

13. Whitehead, C. B.; Özkar, S.; Finke, R. G. LaMer's 1950 Model of Particle Formation: A Review and Critical Analysis of Its Classical Nucleation and Fluctuation Theory Basis, of Competing Models and Mechanisms for Phase-Changes and Particle Formation, and then of Its Application to Silver Halide, Semiconductor, Metal, and Metal-Oxide Nanoparticles. *Mater. Adv.* **2021**, *2*, 186-235.

14. Whitehead, C. B.; Watzky, M. A.; Finke, R. G. "Burst Nucleation" vs Autocatalytic, "Burst" Growth In Near-Monodisperse Particle Formation Reactions. *J. Phys. Chem. C* **2020**, *32*, 3657-3672.

15. LaMer, V. K.; Dinegar, R. H. Theory, Production and Mechanism of Formation of Monodispersed Hydrosols. *J. Am. Chem. Soc.* **1950**, *72*, 4847-4854.

16. Asakura, H.; Teramura, K.; Shishido, T.; Tanaka, T.; Yan, N.; Xiao, C.; Yao, S.; Kou, Y. *In situ* time-resolved DXAFS study of Rh nanoparticle formation mechanism in ethylene glycol at elevated temperature. *Phys. Chem. Chem. Phys.* **2012**, *14*, 2983-2990.

17. Chu, B.; Liu, T. Characterization of nanoparticles by scattering techniques. *J. Nanopart. Res.* **2000**, *2*, 29-41.

18. Goyal, P. S.; Aswal, V. K. Use of SANS and SAXS in study of nanoparticles. *Int. J. Nanosci. Ser.* **2005**, *4*, 987-994.

19. Bentrup, U. Combining *in situ* characterization methods in one set-up: looking with more eyes into the intricate chemistry of the synthesis and working of heterogeneous catalysts. *Chem. Soc. Rev.* **2010**, *39*, 4718-4730.

20. Sun, Y.; Ren, Y. In Situ Synchrotron X-Ray Techniques for Real-Time Probing of Colloidal Nanoparticle Synthesis. *Part. Part. Syst. Charact.* **2013**, *30*, 399-419.

21. Li, T.; Senesi, A. J.; Lee, B. Small Angle X-ray Scattering for Nanoparticle Research. *Chem. Rev.* **2016**, *116*, 11128-11180.

22. Eisele, F. L.; Hanson, D. R. First Measurement of Prenucleation Molecular Clusters. *J. Phys. Chem. A* **2000**, *104*, 830-836.

23. Gebauer, D.; Voelkel, A.; Coelfen, H. Stable Prenucleation Calcium Carbonate Clusters. *Science* **2008**, *322*, 1819-1822.

24. Pouget, E. M.; Bomans, P. H. H.; Goos, J. A. C. M.; Frederik, P. M.; de With, G.; Sommerdijk, N. A. J. M. The Initial Stages of Template-Controlled $CaCO_3$ Formation Revealed by Cryo-TEM. *Science* **2009**, *323*, 1455-1458.

25. Dey, A.; Bomans, P. H. H.; Muller, F. A.; Frederik, P. M.; de With, G.; Sommerdijk, N. A. J. M.; Will, J. The role of prenucleation clusters in surface-induced calcium phosphate crystallization. *Nat. Mater.* **2010**, *9*, 1010-1014.

26. Demichelis, R.; Raiteri, P.; Gale, J. D.; Quigley, D.; Gebauer, D. Stable prenucleation mineral clusters are liquid-like ionic polymers. *Nat. Commun.* **2011**, *2*, 590.

27. Gebauer, D.; kellermeier, M.; Gale, J. D.; Bergström, L.; Cölfen, H. Pre-nucleation clusters as solute precursors in crystallization. *Chem. Soc. Rev.* **2014**, *43*, 2348-2371.

28. Fermani, S.; Vettraino, C.; Bonacini, I.; Marcaccio, M.; Falini, G.; Gavira, J. A.; Garcia Ruiz, J. M. Heterogeneous crystallization of proteins: Is it a prenucleation clusters mediated process? *Cryst. Growth Des.* **2013**, *13*, 3110-3115.

29. Hashimoto, T.; Saijo, K.; Harada, M.; Toshima, N. Small-angle x-ray scattering analysis of polymer-protected platinum, rhodium, and platinum/rhodium colloidal dispersions. *J. Chem. Phys.* **1998**, *109*, 5627-5638.

30. Svergun, D. I.; Shtykova, E. V.; Kozin, M. B.; Volkov, V. V.; Dembo, A. T.; Shtykova, E. V.; Bronstein, L. M.; Platonova, O. A.; Yakunin, A. N.; Valetsky, P. M.; Kholkhlov, A. R. Small-Angle X-ray Scattering Study of Platinum-Containing Hydrogel/Surfactant Complexes. *J. Phys. Chem. B* **2000**, *104*, 5242-5250.

31. Calandra, P.; Longo, A.; Liveri, V. T. Synthesis of Ultra-small ZnS Nanoparticles by Solid-Solid Reaction in the Confined Space of AOT Reversed Micelles. *J. Phys. Chem. B* **2003**, *107*, 25-30.

32. Haubold, H.-G.; Vad, T.; Waldöfner, N.; Bönnemann, H. From Pt molecules to nanoparticles: *in-situ* (anomalous) small-angle X-ray scattering studies. *J. Appl. Cryst.* **2003**, *36*, 617-620.

33. Calandra, P.; Giordano, C.; Longo, A.; Turco Liveri, V. Physiochemical investigation of surfactant-coated gold nanoparticles synthesized in the confined space of dry reversed micelles. *Mater. Chem. Phys.* **2006**, *98*, 494-499.

34. Tristany, M.; Chaudret, B.; Dieudonné, P.; Guari, Y.; Lecante, P.; Matsura, V.; Moreno-Mañas, Philippot, K.; Pleixats, R. Synthesis of Ruthenium Nanoparticles Stabilized by Heavily Fluorinated Compounds. *Adv. Funct. Mater.* **2006**, *16*, 2008-2015.

35. Frens, G. Controlled Nucleation for the Regulation of the Particle Size in Monodisperse Gold Suspensions. *Nature-Phys. Sci.* **1973**, *241*, 20-22.

36. Rusyniak, M.; Abdelsayed, V.; Campbell, J.; El-Shall, M. S. Vapor Phase Homogeneous Nucleation of Higher Alkanes: Dodecane, Hexadecane, and Octadecane. 1. Critical Supersaturation and Nucleation Rate Measurements. *J. Phys. Chem. B* **2011**, *105*, 11866-11872

37. Rusyniak, M.; El-Shall, M. S. Vapor Phase Homogeneous Nucleation of Higher Alkanes: Dodecane, Hexadecane, and Octadecane. 2. Corresponding States and Scaling Law Analysis. *J. Phys. Chem. B* **2001**, *105*, 11873-11879.

38. Abécassis, B.; Testard, F.; Spalla, O.; Barboux, P. Probing in situ the Nucleation and Growth of Gold Nanoparticles by Small-Angle X-ray Scattering. *Nano Lett.* **2007**, *7*, 1723-1727.

39. Smith, M. C.; Gilbert, J. A.; Mawdsley, J. R.; Seifert, S.; Myers, D. J. In Situ Small-Angle X-ray Scattering Observation of Pt Catalyst Particle Growth During Potential Cycling. *J. Am. Chem. Soc.* **2008**, *130*, 8112-8113.

40. Harada, M.; Saijo, K.; Sakamoto, N. Characterization of metal nanoparticles prepared by photoreduction in aqueous solutions of various surfactants using UV-vis, EXAFS, and SAXS. *Colloids Surf. A: Physicochem. Eng. Asp.* **2009**, *349*, 176-186.

41. Jun, Y.-S.; Lee, B.; Waychunas, G. A. In Situ Observations of Nanoparticle Early Development Kinetics at Mineral—Water Interfaces. *Environ. Sci. Technol.* **2010**, *44*, 8182-8189.

42. Harada, M.; Tamura, N.; Takenaka, M. Nucleation and Growth of Metal Nanoparticles during Photoreduction Using In Situ Time-Resolved SAXS Analysis. *J. Phys. Chem. C* **2011**, *115*, 14081-14092.

43. Zheng, N.; Fan, J.; Stucky, G. D. One-Step One-Phase Synthesis of Monodisperse Noble-Metallic Nanoparticles and Their Colloidal Crystals. *J. Am. Chem. Soc.* **2006**, *128*, 6550-6551.

44. Koerner, H.; MacCuspie, R. I.; Park, K.; Vaia, R. A. In Situ UV/Vis, SAXS, and TEM Study of Single-Phase Gold Nanoparticle Growth. *Chem. Mater.* **2012**, *24*, 981-995.

45. Wang, J.; Winans, R. E.; Anderson, S. L.; Seifert, S.; Lee, B.; Chupas, P. J.; Ren, Y.; Lee, S.; Liu, Y. In Situ Small-Angle X-ray Scattering from Pd Nanoparticles Formed by Thermal Decomposition of Organo-Pd Catalyst Precursors Dissolved in Hydrocarbons. *J. Phys. Chem. C* **2013**, *117*, 22627-22635.

46. LaGrow, A. P.; Ingham, B.; Toney, M. F.; Tilley, R. D. Effect of Surfactant Concentration and Aggregation on the Growth Kinetics of Nickel Nanoparticles. *J. Phys. Chem. C* **2013**, *117*, 16709-16718.

47. St. John, S.; Hu, N.; Schaefer, D. W.; Angelopoulos, A. P. Time-Resolved, in Situ, Small- and Wide-Angle X-ray Scattering To Monitor Pt Nanoparticle Structure Evolution Stabilized by Adsorbed $SnCl_3^-$ Ligands During Synthesis. *J. Phys. Chem. C* **2013**, *117*, 7924-7933.

48. Wiaderek, K. M.; Borkiewicz, O. J.; Pereira, N.; Ilavsky, J.; Amatucci, G. G.; Chupas, P. J.; Chapman, K. W. Mesoscale Effects in Electrochemical Conversion: Coupling of Chemistry to Atomic- and Nanoscale structure in Iron-Based Electrodes. *J. Am. Chem. Soc.* **2014**, *136*, 6211-6214.

49. Rose, A. L.; Bilgh, M. W.; Collins, R. N.; Waite, T. D. Resolving Early Stages of Homogeneous Iron(III) Oxyhydroxide Formation from iron(III) Nitrate Solutions at pH 3 Using Time-Resolved SAXS. *Langmuir* **2014**, *30*, 3548-3556.

50. Chao, Y.; Horner, O.; Vallée, P.; Meneau, F.; Alos-Ramos, O.; Hui, F.; Turmine, M.; Perrot, H.; Lédion, J. In Situ Probing Calcium Carbonate Formation by Combining Fast Controlled Precipitation Method and Small-Angle X-ray Scattering. *Langmuir* **2014**, *30*, 3303-3309.

51. Schiener, A.; Margerl, A.; Krach, A.; Seifert, S.; Steinrück, H.-G.; Zagorac, j.; Zahn, D.; Weihrich, R. *In situ* investigation of two-step nucleation and growth of CdS nanoparticles from solution. *Nanoscale* **2015**, *7*, 11328-11333.

52. Mozaffari, S.; Li, W.; Thompson, C.; Ivanov, S.; Seifert, S.; Lee, B.; Kovarik, L.; Karim, A. M. Colloidal nanoparticle size control: experimental and kinetic modeling investigation of the ligand–metal binding role in controlling the nucleation and growth kinetics. *Nanoscale* **2017**, *9*, 13772-13785.

53. Oestreicher, V.; Huck-Irart, C.; Soler-Illia, G.; Angelomé, P. C.; Jobbágy, M. Mild Homogeneous Synthesis of Gold Nanoparticles through the Epoxide Route: Kinetics, Mechanisms, and Related One-Pot Composites. *Chem. Eur. J.* **2020**, *26*, 3157-3165.

54. Castro, N.; Bouet, C.; Ithurria, S.; Lequeux, N.; Constantin, D.; Levitz, P.; Pontoni, D.; Abécassis, B. Insights into the Formation Mechanism of CdSe Nanoplatelets Using in Situ X-ray Scattering. *Nano Lett.* **2019**, *19*, 6466-6474.

55. Ithurria, S.; Bousquet, G.; Dubertret, B. Continuous Transition from 3D to 1D Confinement Observed during the Formation of CdSe Nanoplatelets. *J. Am. Chem. Soc.* **2011**, *133*, 3070-3077.

56. Riedinger, A.; Ott, F. D.; Mule, A.; Mazzotti, S.; Knüsel, P. N.; Kress, S. J. P.; Prins, F.; Erwin, S. C.; Norris, D. J. An intrinsic growth instability in isotropic materials leads to quasi-two-dimensional nanoplatelets. *Nat. Mater.* **2017**, *16*, 743-748.

57. Harada, M.; Asakura, K.; Toshima, N. Structural Analysis of Polymer-Protected Platinum/Rhodium Bimetallic Clusters Using Extended X-ray Absorption Fine Structure Spectroscopy. Importance of Microclusters for the Formation of Bimetallic Clusters. *J. Phys. Chem.* **1994**, *98*, 2653-2662.

58. Tsai, Y. W.; Tseng, Y. L.; Sarma, L. S.; Liu, D. G.; Lee, J. F.; Hwang, B. J. Genesis of Pt Clusters in Reverse Micelles Investigated by in Situ X-ray Absorption Spectroscopy. *J. Phys. Chem. B* **2004**, *108*, 8148-8152.

59. Harada, M.; Toshima, N.; Yoshida, K.; Isoda, S. Aggregated structure analysis of polymer-protected platinum/ruthenium colloidal dispersions using EXAFS, HRTEM, and electron diffraction measurements. *J. Colloid Interface Sci.* **2005**, *283*, 64-78.

60. Harada, M.; Einaga, H. Formation Mechanism of Pt Particles by Photoreduction of Pt Ions in Polymer Solutions. *Langmuir* **2006**, *22*, 2371-2377.

61. Harada, M.; Einaga, H. In Situ XAFS Studies of Au Particle Formation by Photoreduction in Polymer Solutions. *Langmuir* **2007**, *23*, 6536-6543.

62. Harada, M.; Inada, Y. In Situ Time-Resolved XAFS Studies of Metal Particle Formation by Photoreduction in Polymer Solutions. *Langmuir* **2009**, *25*, 6049-6061.

63. Yao, T.; Sun, Z.; Li, Y.; Pan, Z.; Wei, H.; Xie, Y.; Nomura, M.; Niwa, Y.; Yan, W.; Wu, Z.; Jiang, Y.; Liu, Q.; Wei, S. Insights into Initial Kinetic Nucleation of Gold Nanocrystals. *J. Am. Chem. Soc.* **2010**, *132*, 7696-7701.

64. Ohyama, J.; Teramura, K.; Higuchi, Y.; Shishido, T.; Hitomi, Y.; Kato, K.; Tanida, H.; Uruga, T.; Tanaka, T. In Situ Observation of Nucleation and Growth Process of Gold Nanoparticles by Quick XAFS Spectroscopy. *ChemPhysChem* **2011**, *12*, 127-131.

65. Ohyama, J.; Teramura, K.; Shishido, T.; Hitomi, Y.; Kato, K.; Tanida, H.; Uruga, T.; Tanaka, T. *In Situ* Au L_3 and L_2 edge XANES spectral analysis during growth of thiol protected gold nanoparticles for the study on particle size dependent electronic properties. *Chem. Phys. Lett.* **2011**, *507*, 105-110.

66. Ohyama, J.; Teramura, K.; Higuchi, Y.; Shishido, T.; Hitomi, Y.; Aoki, K.; Funabiki, T.; Kodera, M.; Kato, K.; Tanida, H.; Uruga, T.; Tanaka, T. An *in situ* quick XAFS spectroscopy study of the formation mechanism of small gold nanoparticles supported by porphyrin-cored tetradentate passivants. *Phys. Chem. Chem. Phys.* **2011**, *13*, 11128-11135.

67. Oyanagi, H.; Sun, Z. H.; Jiang, Y.; Uehara, M.; Nakamura, H.; Yamashita, K.; Zhang, L.; Lee, C.; Fukano, A.; Maeda, H. *In situ* XAFS experiments using a microfluidic cell: application to initial growth of CdSe nanocrystals. *J. Synchrotron Rad.* **2011**, *18*, 272-279.

68. Harada, M.; Kamigaito, Y. Nucleation and Aggregative Growth Process of Platinum Nanoparticles Studied by in Situ Quick XAFS Spectroscopy. *Langmuir* **2012**, *28*, 2415-2428.

69. Uemura, Y.; Inada, Y.; Niwa, Y.; Kimura, M.; Bando, K. K.; Yagishita, A.; Iwasawa, Y.; Nomura, M. Formation and oxidation mechanisms of Pd–Zn nanoparticles on a ZnO supported Pd catalyst studied by *in situ* time-resolved QXAFS and DXAFS. *Phys. Chem. Chem. Phys.* **2012**, *14*, 2152-2158.

70. Paclawski, K.; Sikora, M. XAFS in the tracking of reactions in aqueous solution: a case of redox reaction between $[AuCl_4]^-$ complex ions and ethanol. *Arch. Metall. Mater.* **2012**, *57*, 1011-1020.

71. Yao, S.; Yuan, Y.; Xiao, C.; Li, W.; Kou, Y.; Dyson, P. J.; Yan, N.; Asakura, H.; Teramura, K.; Tanaka, T. Insights into the Formation Mechanism of Rhodium Nanocubes. *J. Phys. Chem. C* **2012**, *116*, 15076-15086.

72. Tanaka, T.; Ohyama, J.; Teramura, K.; Hitomi, Y. Formation mechanism of metal nanoparticles studied by XAFS spectroscopy and effective synthesis of small metal nanoparticles. *Catal. Today* **2012**, *183*, 108-118.

73. Ma, J.; Zou, Y.; Jiang, Z.; Huang, W.; Li, J.; Wu, G.; Huang, Y.; Xu, H. An *in situ* XAFS study—the formation mechanism of gold nanoparticles from X-ray-irradiated ionic liquid. *Phys. Chem. Chem. Phys.* **2013**, *15*, 11904-11908.

74. Gomes, W. C. M.; Neto, A. O. W.; Pimentel, P. M.; Melo, D. M. A.; Silva, F. R. G. An in situ X-ray absorption spectroscopy study of copper nanoparticles in microemulsion. *Colloids Surf. A: Physicochem. Eng. Asp.* **2013**, *426*, 18-25.

75. Chang, S.-Y.; Gründer, Y.; Booth, S. G.; Molleta, L. B.; Uehara, A.; Mosselmans, J. F. W.; Cibin, G.; Pham, V.-T.; Nataf, L.; Dryfe, R. A. W.; Schroeder, S. L. M. Detection and characterization of sub-critical nuclei during reactive Pd metal nucleation by X-ray absorption spectroscopy. *CrystEngComm* **2016**, *18*, 674-682.

76. Saeki, M.; Matsumura, D.; Yomogida, T.; Taguchi, T.; Tsuji, T.; Saitoh, H.; Ohba, H. In Situ Time-Resolved XAFS Studies on Laser-Induced Particle Formation of Palladium Metal in an Aqueous/EtOH Solution. *J. Phys. Chem. C* **2019**, *123*, 817-824.

77. Liu, Y.; Qian, L.; Zhao, X.; Wang, J.; Yao, L.; Xing, X.; Mo, G.; Cai, Q.; Chen, Z.; Wu, Z. Synthesis and formation mechanism of self-assembled 3D flower-like Bi/□-Fe_2O_3 composite particles. *CrystEngComm* **2019**, *21*, 2799-2808.

78. Angermund, K.; Bühl, M.; Dinjus, E.; Endruschat, U.; Gassner, F.; Haubold, H.-G.; Hormes, J.; Köhl, G.; Mauschick, F. T.; Modrow, H.; Mörtel, R.; Mynott, R.; Tesche, B.; Vad, T.; Waldöfner, N.; Bönnemann, H. Nanoscopic Pt Colloids in the "Embryonic State". *Angew. Chem. Int., Ed.* **2002**, *41*, 4041-4044.

79. Angermund, K.; Bühl, M.; Endruschat, U.; Mauschick, F. T.; Mörtel, R.; Mynott, R.; Tesche, B.; Waldöfner, N.; Bönnemann, H.; Köhl, G.; Modrow, H.; Hormes, J.; Dinjus E.; Gassner, F.; Haubold, H.-G.; Vad, T. Kaupp, M. In Situ Study on the Wet Chemical Synthesis of Nanoscopic Pt Colloids by "Reductive Stabilization". *J. Phys. Chem. B* **2003**, *107*, 7507-7515.

80. Meneau, F.; Sankar, G.; Morgante, N.; Cristol, S.; Catlow, C. R. A.; Thomas, J. M.; Greaves, G. N. Characterization of zinc oxide nanoparticles encapsulated into zeolite-Y: An in-situ combined X-ray diffraction, XAFS, and SAXS study. *Nucl. Instrum. Meth. B* **2003**, *199*, 499-503.

81. Benfield, R. E.; Grandjean, D.; Dore, J. C.; Esfahanian, H.; Wu, Z.; Kröll, M.; Geerkens, M.; Schmid, G. Structure of assemblies of metal nanowires in mesoporous alumina membranes

studied by EXAFS, XANES, X-ray diffraction and SAXS. *Faraday Discuss.* **2004**, *125*, 327-342.

82. Beale, A. M.; van der Eerden, A. M. J.; Jacques, S. D. M.; Leynaud, O.; O'Brien, M. G.; Meneau, F.; Nikitenko, S.; Bras, W.; Weckhuysen, B. M. A Combined SAXS/WAXS/XAFS Setup Capable of Observing Concurrent Changes Across the Nano-to-Micrometer Size Range in Inorganic Solid Crystallization Processes. *J. Am. Chem. Soc.* **2006**, *128*, 12386-12387.

83. Ramallo-López, J. M.; Giovanetti, L.; Craievich, A. F.; Vicentin, F. C.; Marín-Almazo, M.; José-Yacaman, M.; Requejo, F. G. XAFS, SAXS, and HREM characterization of Pd nanoparticles capped with *n*-alkyl thiol molecules. *Physica B* **2007**, *389*, 150-154.

84. Harada, M.; Kuramitsu, K.; Kimura, Y.; Saijo, K. *In situ* observation of formation of silver particles in water-in-scCO_2 emulsions. *Colloids Surf. A: Physicochem. Eng. Asp.* **2008**, *327*, 21-33.

85. Abécassis, B.; Testard, F.; Kong, Q.; Francois, B.; Spalla, O. Influence of Monomer Feeding on a Fast Gold Nanoparticles Synthesis: Time-Resolved XANES and SAXS Experiments. *Langmuir* **2010**, *26*, 13847-13854.

86. Turkevich, J..; Stevenson, P. C.; Hillier, J. A study on the nucleation and growth processes in the synthesis of colloidal gold. *Discuss. Faraday Soc.* **1951**, *11*, 55-75.

87. Polte, J.; Ahner, T. T.; Delissen, F.; Sokolov, S.; Emmerling, F.; Thünemann, A. F.; Kraehnert, R. Mechanism of Gold Nanoparticle Formation in the Classical Citrate Synthesis Method Derived from Coupled In Situ XANES and SAXS Evaluation. *J. Am. Chem. Soc.* **2010**, *132*, 1296-1301.

88. Caetano, B. L.; Santilli, C. V.; Meneau, F.; Briois, V.; Pulcinelli, S. H. In Situ and Simultaneous UV—vis/SAXS and UV—vis/XAFS Time-Resolved Monitoring of ZnO Quantum Dots Formation and Growth. *J. Phys. Chem. C* **2011**, *115*, 4404-4412.

89. Yao, T.; Liu, S.; Sun, Z.; Li, Y.; He, S.; Cheng, H.; Xie, Y.; Liu, Q.; Jiang, Y.; Wu, Z.; Yan, W.; Wei, S. Probing Nucleation Pathways for Morphological Manipulation of Platinum Nanocrystals. *J. Am. Chem. Soc.* **2012**, *134*, 9410-9416.

90. Xia, F.; Chen, D.; Scarlett, N. V. Y.; Madsen, I. C.; Lau, D.; Leoni, M.; Ilavsky, J.; Brand, H. E. A.; Caruso, R. A. Understanding Solvothermal Crystallization of Mesoporous Anatase Beads by In Situ Synchrotron PXRD and SAXS. *Chem. Mater.* **2014**, *26*, 4563-4571.

91. Caetano, B. L.; Meneau, F.; Santilli, C. V.; Pulcinelli, S. H.; Magnami, M.; Briois, V. Mechanisms of SnO_2 Nanoparticles Formaiton and Growth in Acid Ethanol Solution Derived from SAXS and Combined Raman–XAS Time-Resolved Studies. *Chem. Mater.* **2014**, *26*, 6777-6785.

92. Karim, A. M.; Al Hasan, N.; Ivanov, S.; Seifert, S.; Kelly R. T.; Hallfors, N. G.; Benavidez, A.; Kovarik, L.; Jenkins, A.; Winans, R. E.; Datye, A. K. Synthesis of 1nm Pd nanoparticles: Insights on the synthesis mechanism using *in situ* XAFS and SAXS in a microfluidic reactor. *J. Phys. Chem. C* **2015**, *119*, 13257-13267.

93. Chen, X.; Schröder, J. H.; Hauschild, S.; Rosenfeldt, S.; Dulle, M.; Förster, S. Simultaneous SAXS/WAXS/UV-Vis Study of the Nucleation and Growth of Nanoparticles – A Test of Classical Nucleation Theory. *Langmuir* **2015**, *31*, 11678-11691.

94. Yang, L.; Cheng, H.; Jiang, Y.; Huang, T.; Bao, J.; Sun, Z.; Jiang, Z.; Ma, J.; Sun F.; Liu, Q.; Yao, T.; Deng, H.; Wang, S.; Zhu, M.; Wei, S. *In situ* studies on controlling an atomically-accurate formation process of gold nanoclusters. *Nanoscale* **2015**, *7*, 14452-14459.

95. Kabelitz, A.; Guilherme, A.; Joester, M.; Renholz, U.; Radtke, M.; Bienert, R.; Schulz, K.; Schmack, R.; Kraehnert, R.; Emmerling, F. Time-resolved *in situ* studies on the formation mechanism of iron oxide nanoparticles using combined fast-XANES and SAXS. *CrystEngComm* **2015**, *17*, 8463-8470.

96. Cormary, B.; Li, T.; Liakakos, N.; Peres, L.; Fazzini, P.-F.; Blon, T.; Respaud, M.; Kropf, A. J.; Chaudret, B.; Miller, J. T.; Mader, E. A.; Soulantica, K. Concerted Growth and Ordering of Cobalt Nanorod Arrays as Revealed by Tandem in Situ SAXS-XAS Studies. *J. Am. Chem. Soc.* **2016**, *138*, 8422-8431.

97. Herbst, M.; Hofmann, E.; Förster, S. Nucleation and Growth Kinetics and ZnO Nanoparticles Studied by in Situ Microfluidic SAXS/WAXS/UV–Vis Experiments. *Langmuir* **2019**, *35*, 11702-11709.

98. Ramamoorthy, R. K.; Yildirim, E.; Barba, E.; Roblin, P.; Vargas, J. A.; Lacroix, L.-M.; Rodriguez-Ruiz, I.; Decorse, P.; Petkov, V.; Teychené, S.; Viau, G. The role of pre-nucleation clusters in the crystallization of gold nanoparticles. *Nanoscale* **2020**, *12*, 16173-16188.

APPENDIX II: SUPPORTING INFORMATION FOR CHAPTER III

Further Details on the Preparation of $(Bu_4N)_2HPO_4$ and Its Characterization by ^{31}P NMR Spectroscopy

As stated in Chapter III, $(Bu_4N)_2HPO_4$ was prepared using the simple acid-base reaction between $(Bu_4N)H_2PO_4$ and $Bu_4N^+OH^-$, in CH_3CN, to produce $(Bu_4N)_2HPO_4$ and H_2O. The reaction was stirred for 4 hours and dried. The drying step proved not unexpectedly to be crucial in the determining the purity and repeatability of the resultant $(Bu_4N)_2HPO_4$. Three approaches for removing H_2O were investigated: (i) drying the solution under vacuum for 12–24 hours—this first approach was what was employed for the $(Bu_4N)_2HPO_4$ used in the preparations and experiments described in Chapter III and its experimental section; (ii) drying the solution over mol. sieves for 5 hours; and (iii) drying the solution over mol. sieves for 5 hours followed by placing the solution under vacuum for 12–24 hours. The identity and purity of the primary product of the deprotoation reaction, $(Bu_4N)_2HPO_4$, was determined by ^{31}P NMR. When dried by methods (i) and (iii), a primary ^{31}P NMR peak was observed at δ = 3.9 ppm (vs 85% H_3PO_4 as an internal capillary), which matches the literature value of HPO_4^{2-} (and if minimal water is present).[1] Meanwhile, when dried by method (ii), with no vacuum drying, δ = ~5.6 ppm (vs 85% H_3PO_4 as an internal capillary) was observed, which matches the previous report by our group from 2004.[2] The literature as well as our own results suggest the presence of water will slightly affect the position and intensity of the signal in ^{31}P NMR.[1] Specifically, we observe this effect in the slight upfield shift of the HPO_4^{2-} chemical shift between the two different drying approaches: mol. sieves versus the more complete removal of water via vacuum drying.

However, when vacuum drying the final product, $(Bu_4N)_2HPO_4$, for >24 hours, the formation of an impurity of <3–8% $(Bu_4N)_4(P_2O_7)$ resulted, as characterized and discussed in the following section. As seen there, the HPO_4^{2-} chemical shift is δ = 2.4 ppm (vs 85% H_3PO_4 as an internal capillary) when low levels of $P_2O_7^{4-}$, δ = -8.7 ppm, are present. Obviously, the precise ^{31}P NMR chemical shift of HPO_4^{2} is sensitive to water and the amounts and identity of any other acids or bases present, *vide infra*.

Characterization of $\{[(1,5\text{-COD})Ir\bullet HPO_4]_2\}^{2-}$ by ^{31}P NMR Spectroscopy

The isolated dimer complex, $\{[(1,5\text{-COD})Ir\bullet HPO_4]_2\}^{2-}$, **3**, was directly observed by ^{31}P NMR and compared to previous published reports.[2,3] In these reports from 2003 and 2004, **3** was reported at δ = 14.6 ± 0.2 ppm as a singlet (121 MHz NMR, CD_3CN, 50 mM in **3**, and number of scans = 512, unreported acquisition and delay times).[2,3] Here, in this study, **3** was prepared by combining 0.2 mmols of dried $(Bu_4N)_2HPO_4$ with 0.2 mmols $[(1,5\text{-COD})Ir(NCCH_3)_2]^+$ in 2.0 mL CD_3CN, yielding a final solution concentration of 25 mM in **3**. One milliliter of the solution was transferred to an NMR tube, sealed, removed from the drybox, and sonicated for 20 minutes to ensure its maximum solubility prior to being examined by ^{31}P NMR. The singlet peak appeared at δ = 14.2 ppm (162 MHz NMR, CD_3CN, number of scans = 128, acquisition time = 5 seconds, and delay time = 1 second). Next, a 0.5 molar equiv of $(Bu_4N)_2HPO_4$ was added to the above NMR sample and a spectrum was collected using the same experimental parameters. The singlet peak at δ = 14.2 ppm remained unchanged, but a new singlet at δ = 3.3 ppm appeared, indicative of HPO_4^{2-}. An internal capillary of 85% H_3PO_4 was used as a reference (using the same experimental parameters as stated above) and revealed a systematic downfield shift of ~0.5-1.0 ppm vs our prior literature.[2,3] As has been reported by our group previously,[4] referencing ^{31}P NMR as is commonly

done with an internal capillary can lead to ±0.5 ppm chemical shift difference (see footnote 34 on p 1423 of ref 4). Hence, the signals we observe for **3** in this work at 14.2 and 3.3 ppm correspond to those at ~14.7 and ~3.7 ppm in our prior work.[2,3] The ^{31}P NMR results in turn confirm the identity of the *in-situ* prepared $\{[(1,5\text{-COD})Ir{\bullet}HPO_4]_2\}^{2-}$, **3**, to the *isolated* **3** made previously, as expected since both samples are made by the identical procedure of adding $(Bu_4N)_2HPO_4$ to $[(1,5\text{-}C_8H_{12})Ir^{I}(NCCH_3)_2][BF_4]$ as detailed in the experimental section of Chapter III.

Characterization of $(Bu_4N)_4(P_2O_7)$ as a Minor, ≤3–8% Impurity by ^{31}P NMR Formed in the Synthesis of $(Bu_4N)_2HPO_4$

The stabilizer, $(Bu_4N)_2HPO_4$, was characterized with ^{31}P, ^{1}H, and ^{13}C NMR spectroscopy, Figures S3.1a–c. A minor impurity of $(Bu_4N)_4(P_2O_7)$ can be detected as detailed more in the Figure caption.

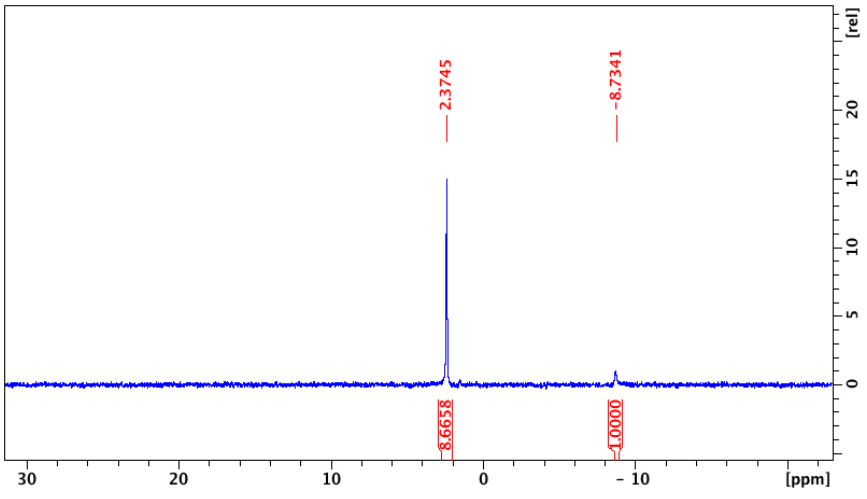

(a)

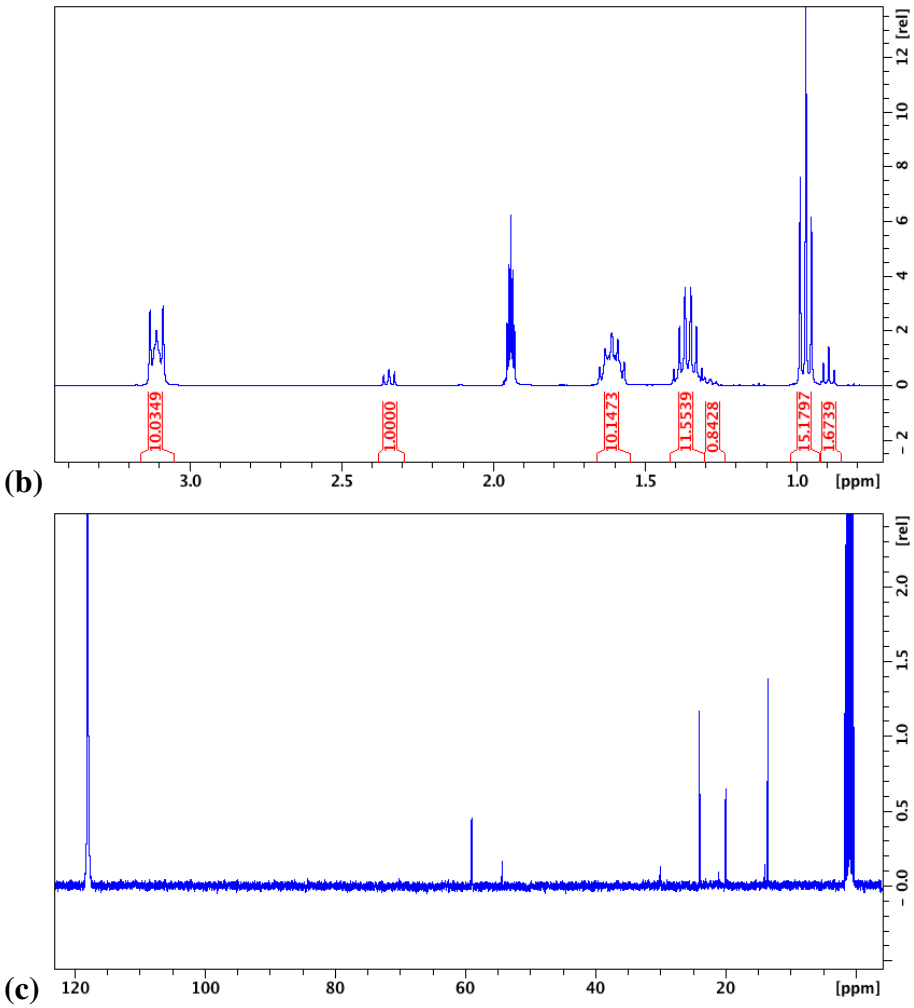

Figure S3.1. The ^{31}P, ^{1}H, and ^{13}C NMR spectroscopy characterization (in CD_3CN) of $(Bu_4N)_2HPO_4$, including evidence for a minor impurity of present. **(a)** ^{31}P NMR spectrum with signals integrated at δ: -8.73 (s, $P_2O_7^{4-}$) and 2.38 (s, HPO_4^{2-}) ppm (unoptimized acquisition and delay times of 1.0 and 2.0 seconds, respectively, were used for these ^{31}P NMR, compared to the preferred values of ~5 and ~1 seconds, respectively, used in the section just above). **(b)** ^{1}H NMR spectrum with signals integrated at δ: 0.90 (t, CH_3), 0.98 (t, CH_3), 1.33 (m, CH_2), 1.38 (m, CH_2), 1.62 (m, CH_2), 1.95 (br, solvent)[5], 2.35 (t, CH_2), and 3.15 (t, CH_2) ppm. The butyl groups of $(Bu_4N)_2HPO_4$ produce distinct signals at 0.98, 1.380, 1.62, and 3.15 ppm. The butyl groups of $(Bu_4N)_4(P_2O_7)$ produce signals at 0.90, 1.33, and 2.35 ppm. The fourth signal is obscured by the solvent peak at ~2 ppm. **(c)** ^{13}C NMR spectrum with signals at δ: 12.8 (s, CH_3), 13.4 (s, CH_3), 19.3 (s, CH_2), 20.3 (s, CH_2), 23.4 (s, CH_2), 29.3 (s, CH_2), 53.6 (s, CH_2), and 58.3 (t, CH_2) were identified. Solvent (acetonitrile) appears at 0.31 (m, CH_3) and 117.3 (s, CN).[5] The butyl groups of $(Bu_4N)_2HPO_4$ appear at 12.8, 19.3, 23.4, and 58.3 ppm, while the butyl groups of $(Bu_4N)_4(P_2O_7)$ appear at 13.4, 20.3, 29.4, and 53.6 ppm.

Further investigation into the synthesis of $(Bu_4N)_2HPO_4$ revealed that, upon vacuum drying for ≥20 hours at 25 °C, $(Bu_4N)_4(P_2O_7)$ is formed from the well-precedented dehydration reaction[6,7,8,9] between two $(Bu_4N)_2HPO_4$, Scheme S3.1, a reaction dependent on the temperature, vacuum, and drying time.

Scheme S3.1. Well Precedented Dehydration Reaction of Two $(Bu_4N)_2(HPO_4)$ to Form $(Bu_4N)_4(P_2O_7)$

$$2\ (Bu_4N)_2(HPO_4) \xrightarrow[vacuum]{heat} 1\ (Bu_4N)_4(P_2O_7) + 1\ H_2O\ (g)$$

A thorough examination of the relevant ^{31}P NMR literature revealed $P_2O_7^{4-}$ appears at c.a. -8 ppm depending on the solvent, the concentration and, in aqueous media, the precise pH.[10] In D_2O, the $P_2O_7^{4-}$ signal is a sharp singlet at -11.20, -8.17, and -6.57 ppm for pH 0.5, 6.0, and 10.2, respectively.[10] To assign the impurity peak is Figure S3.1c, a solution of $(Bu_4N)_2HPO_4$ was titrated with the *diprotonated* $(Bu_3NH)_2(H_2P_2O_7)$ because authentic material is commercially available and facile proton exchange between $P_2O_7^{4-}$ and $H_2P_2O_7^{2-}$ should still allow the observation of a single peak due, then, to $HP_2O_7^{3-}$. As seen in Figure S3.2a–c, the impurity peak quantitatively increases as well as shifts downfield with added (a) 0.0, (b) 0.2, and (c) 1.0 molar equivalents of $(Bu_3NH)_2(H_2P_2O_7)$. The ^{31}P NMR resonance for $(Bu_4N)_2HPO_4$ also shifts downfield, not unexpectedly given that the (at least aqueous) pK_a of $HP_2O_7^{3-}$ and $pK_{a2} = 8.0$;[11] while that of $H_2PO_4^-$ is similar, $pK_{a2} = 7.20$ (again *in H_2O*;[12] the relative pK_a *trends* are expected to be similar in organic solvents[13,14,15,16] such as acetone), so that some proton exchange between the two species is expected.

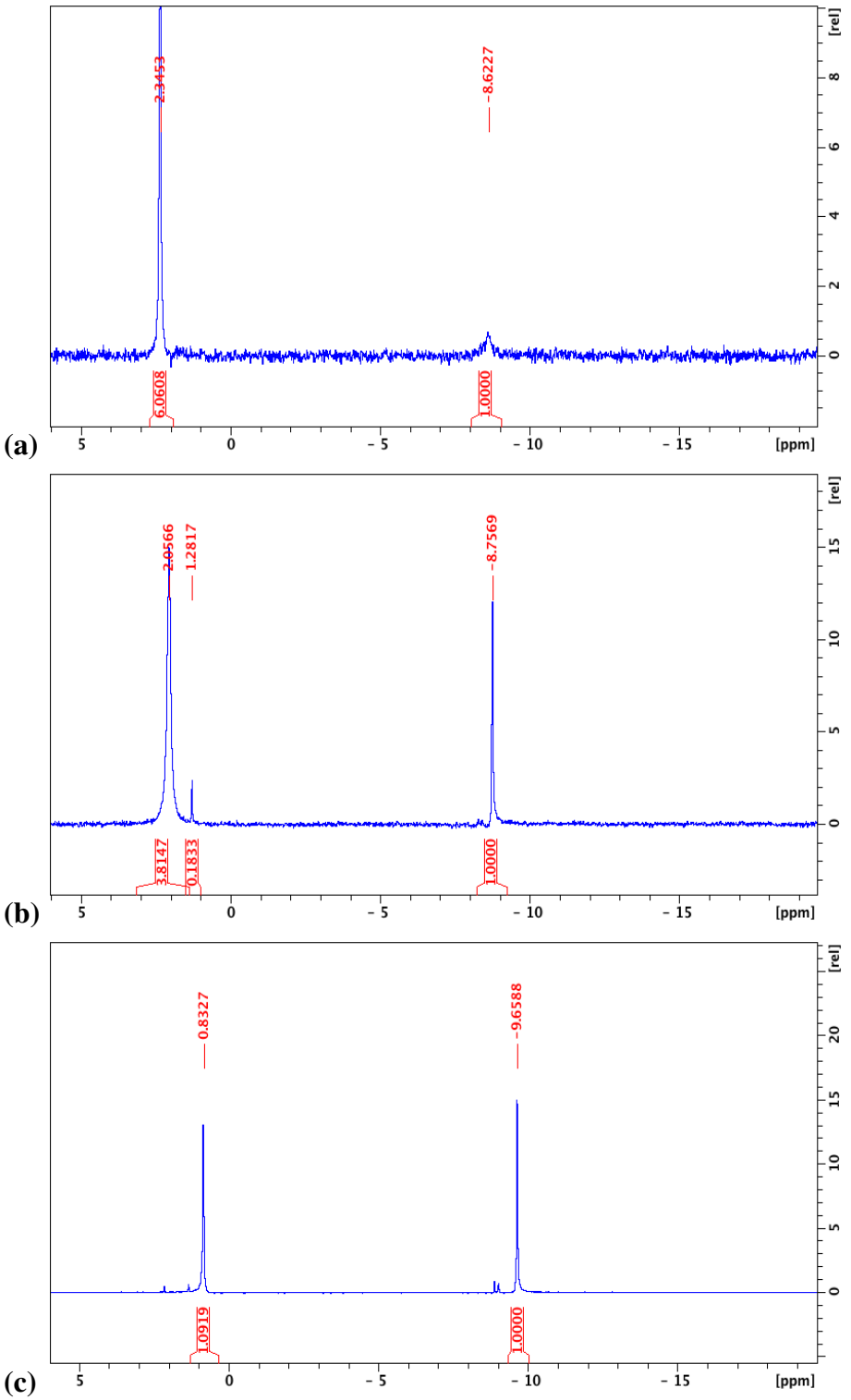

Figure S3.2. ^{31}P NMR spectra (in CD_3CN) for the titration of 19.9 mM $(Bu_4N)_2HPO_4$ with the **(a)** 0.0, **(b)** 0.2, and **(c)** 1.0 molar equivalents of commercially available $(Bu_3NH)_2(H_2P_2O_7)$. The

signals at 2.35, 2.06, and 0.83 ppm correspond to HPO_4^{2-} and the signals at -8.62, -8.76, and -9.66 ppm correspond to $HP_2O_7^{3-}$, for **(a)**, **(b)**, and **(c)** respectively.

In short, the ^{31}P NMR data, along with literature precedent for the dehydration reaction shown back in Scheme S3.1, are compelling in showing the minor, ≤3–8% impurity by ^{31}P NMR in the $(Bu_4N)_2HPO_4$ prepared and used herein is the expected dehydration side-product, $(Bu_4N)_4(P_2O_7)$. In a later section, evidence is provided that at the ≤10% level tested, no discernable effect on the nucleation kinetics, and hence no effect on any of the conclusions of this work, result from the ≤3–8% impurity of $(Bu_4N)_4(P_2O_7)$.

Evidence of *m*=2 in Solution, Revealing That the Kinetics Are Starting from a Dimer in Solution

(i) Investigation of Solution Speciation via ^{1}H NMR Spectroscopy

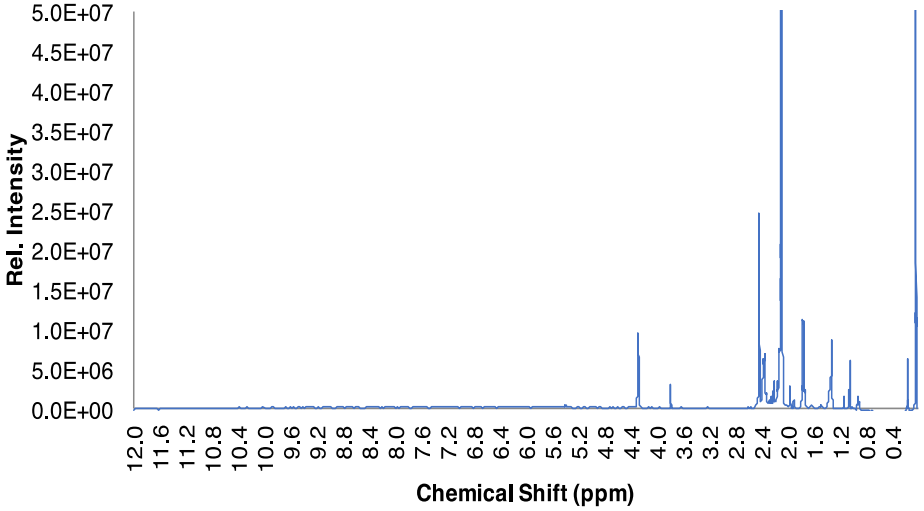

(a)

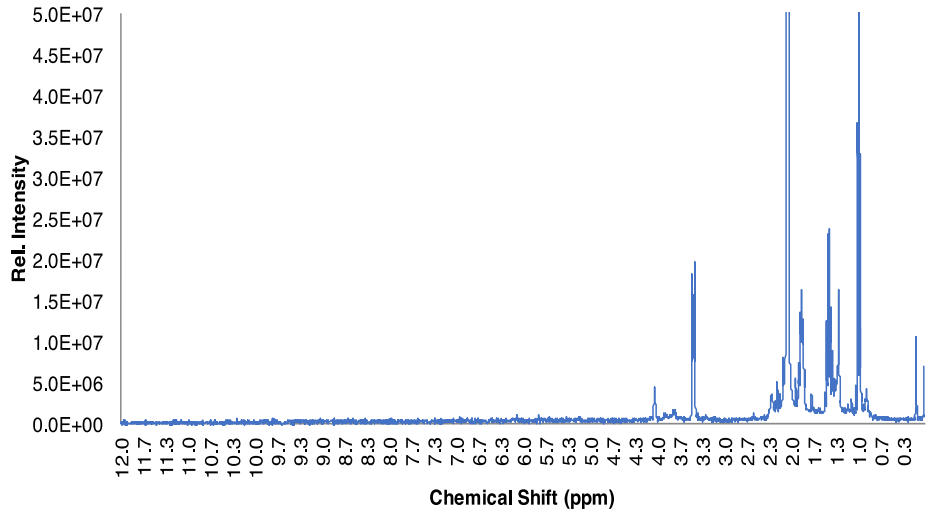

(b)

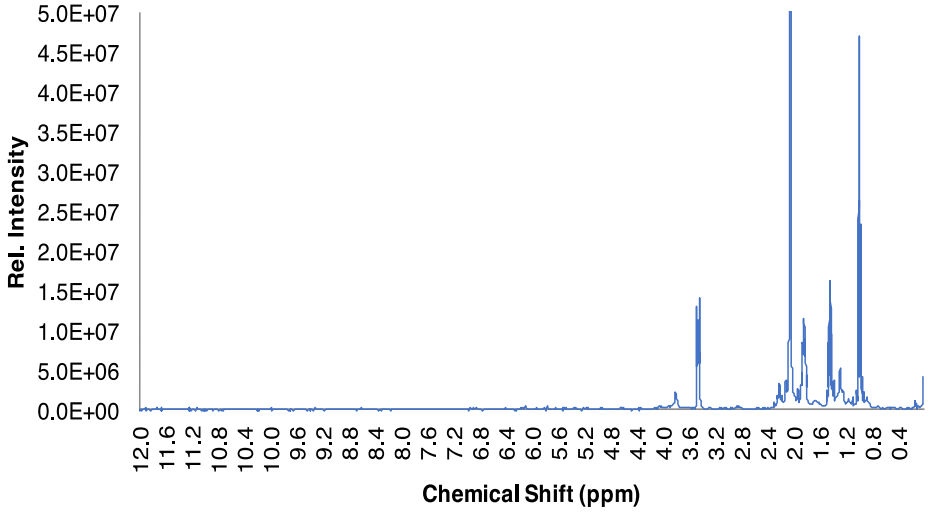

(c)

Figure S3.3. ^{1}H NMR spectra of 1.0 mM [(1,5-COD)Ir^{I}(NCCH$_3$)$_2$][BF$_4$] with **(a)** 0.0 molar equivalents of (Bu$_4$N)$_2$HPO$_4$, **(b)** 0.5 molar equivalents of (Bu$_4$N)$_2$HPO$_4$, and **(c)** 1.0 molar equivalents of (Bu$_4$N)$_2$HPO$_4$. The vinyl protons of the solvate complex, **1**, in **(a)** appear at 4.3 ppm. The vinyl protons of the iridium bridged species, **2**, in **(b)** appear at ~4.0 ppm. The vinyl protons of the iridium butyl phosphate dimer, **3**, in **(c)** appear at ~3.7 ppm.

As stated in Chapter III, in this initial ^{1}H NMR-monitored titration study, the loss of **1**, [(1,5-COD)Ir^{I}(NCCH$_3$)$_2$][BF$_4$], was monitored as a function of added molar equivalents of (Bu$_4$N)$_2$HPO$_4$. The ^{1}H NMR peak at 4.3 ppm, assigned to the vinyl protons of the bound cycloocta-1,5-diene, was integrated against the internal standard, benzene. Based on the rough break point at

1:2 HPO_4^{2-} / $[(1,5\text{-COD})Ir^I(NCCH_3)_2]^+$ ratio, a phosphate-bridged complex $\{[(1,5\text{-COD})Ir^I(NCCH_3)]_2{\bullet}HPO_4\}^0$, **2**, is postulated as an arguably expected intermediate species in the formation of the final product that has acquired (as one, again, might expect) a second HPO_4^{2-} to form $\{[(1,5\text{-COD})Ir^I{\bullet}HPO_4]_2[Bu_4N]_2\}$, **3**.

After the second titration was completed, data shown in Figure 3.2 in Chapter III, approximate values of $K_{Assoc,1}$ and $K_{Assoc,2}$ were calculated. Using the equilibrium expression defined in Scheme 3.1, along with the relative integrated amounts of **1** and **2** in Figure 3.2 and estimating the free HPO_4^{2-} by difference / mass balance, a *rough* estimate of $K_{Assoc,1} \approx 10^3\text{-}10^4\ M^{-1}$ for the formation of **2** was determined.

$$K_{Assoc,1} = \frac{\left[((COD)Ir^I(solv))_2(HPO_4)\right]}{[(COD)Ir^I(solv)_2]\left[{HPO_4}^{2-}\right]} \qquad \text{(Eq S3.1)}$$

The $K_{Assoc,2}$ for the conversion of **2** to **3** is defined in eq S3.2.

$$K_{Assoc,2} = \frac{\left[\left[\left((COD)Ir^I\right)(HPO_4)\right]_2^{\ 2-}\right]}{[((COD)Ir^I)_2(HPO_4)]\left[{HPO_4}^{2-}\right]} \qquad \text{(Eq S3.2)}$$

An analogously obtained, again *rough* estimate of $K_{Assoc,2}$ is $>10^2\ M^{-1}$. We emphasize that the $K_{Assoc,1}$ and $K_{Assoc,2}$ values are crude estimates only because the concentration of HPO_4^{2-} cannot be directly monitored during the experiment, but, instead, was estimated by difference via the mass balance equations, S3.3 and S3.4.

$$\left[{HPO_4}^{2-}\right]_{Free} = \left[{HPO_4}^{2-}\right]_{Added} - \frac{\left[((COD)Ir^I)_2(HPO_4)\right]}{2} \qquad \text{(Eq S3.3)}$$

$$\left[HPO_4{}^{2-}\right]_{Free} = \left[HPO_4{}^{2-}\right]_{Added} - \frac{\left[\left((COD)Ir^I\right)_2(HPO_4)\right]}{2} - \left[\left[\left((COD)Ir^I\right)(HPO_4)\right]_2{}^{2-}\right] \quad \text{(Eq S3.4)}$$

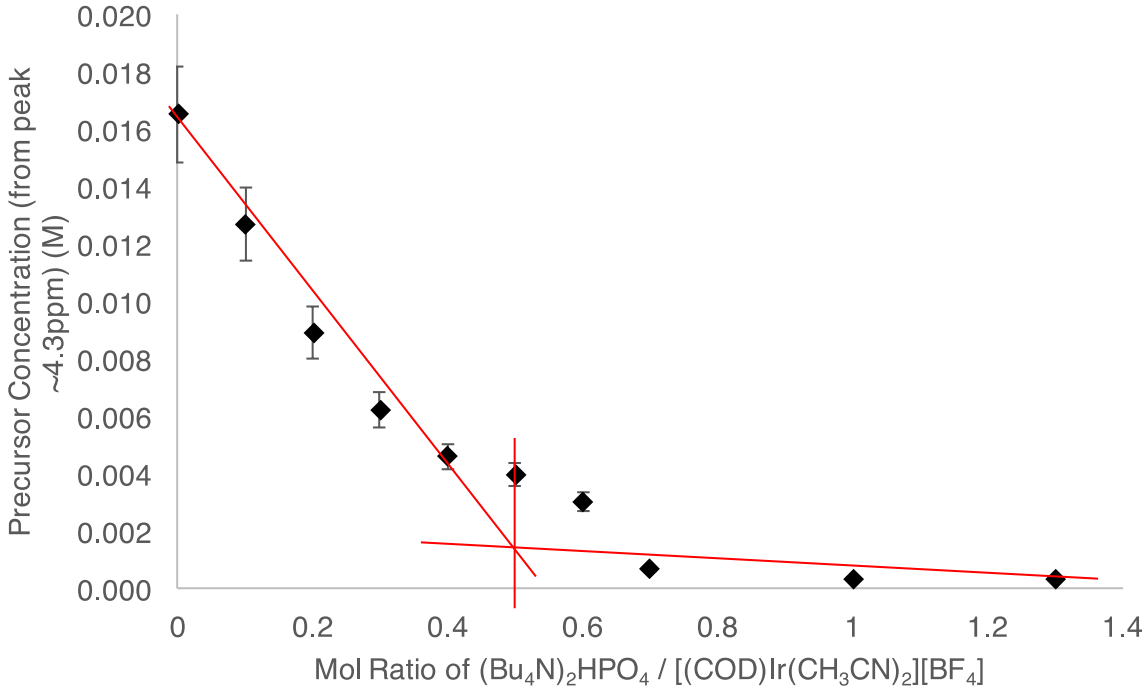

Figure S3.4. Graph of the titration of 0.0 – 1.3 molar equivalents of $(Bu_4N)_2HPO_4$ vs equivalents of $[(1,5\text{-COD})Ir^I(NCCH_3)_2][BF_4]$ in steps of 0.1 equivalents while monitoring the vinylic protons of the solvate complex, $[(1,5\text{-COD})Ir^I(NCCH_3)_2]^+$ at 4.3 ppm. Integrations were converted to concentration by use of benzene as an internal standard. The lines drawn are suggestive of the formation of an intermediate complex with a 1:2 HPO_4^{2-} / $[(1,5\text{-COD})Ir^I(NCCH_3)_2]^+$ ratio, namely the reasonable if not expected intermediate species, $\{[(1,5\text{-COD})Ir^I(NCCH_3)]_2{\bullet}HPO_4\}^0$, **2**.

(ii) Investigation of Solution Speciation via the Signer Molecular Weight Apparatus

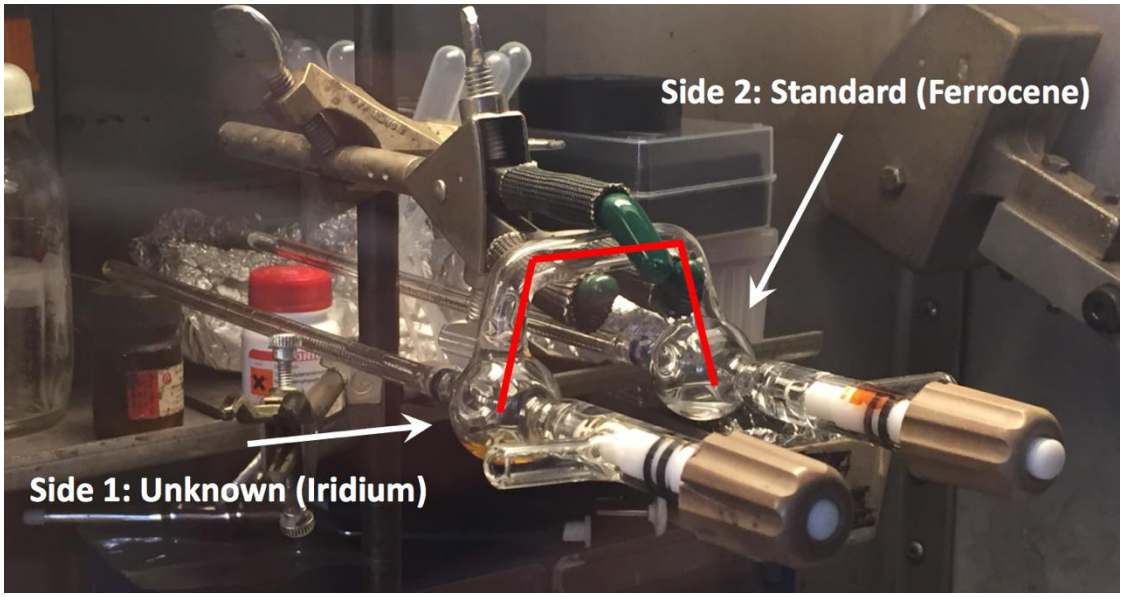

Figure S3.5. An image of the Signer molecular weight apparatus,[17] where the left bulb (Side 1) has the *in situ* formation of **3** in acetone and the right bulb (Side 2) has the chosen standard, ferrocene, also in acetone. The apparatus is in the horizontal position with the bridge, highlighted with the red line, up to allow the acetone solvent vapor to equilibrate. Attached to each bulb is a sealed pipet, so when the apparatus is in the vertical position the volume of each solution can then be quantitated. The entire apparatus is sealed to allow equilibration to take place at constant temperature in a ($\leq$ 1.0 ppm O_2) N_2 glovebox.

As stated in Chapter III, the Signer molecular weight apparatus[17] relies on the solution's colligative properties to determine the solution molecular weight of the unknown compound in the chosen solvent. For the formation of **3** from $[(1,5\text{-COD})Ir^{I}(NCCH_3)_2][BF_4]$ and $(Bu_4N)_2HPO_4$, the total number of species in solution has to be taken into account.

When the Signer reaches equilibrium and once the end volumes of the "unknown" solution and the "standard" (known) solution were recorded, eq 3.2a from Chapter III was used to calculate the *observed molecular weight* of **3**.

$$MW(\mathbf{3}) = \frac{mass(\mathbf{3}) * MW(stnd) * Volume(stnd)}{mass(stnd) * Volume(\mathbf{3})} \qquad \text{(Eq 3.2a)}$$

The observed molecular weight must then be divided by the sum of the *average molecular weights* of the species present in solution, multiplied by the number present in the solution, α, to determine the value for *m*, eq 3.3 from Chapter III. In addition, from the ^{1}H NMR data, it is clear that at a 1:1, [Ir]:[HPO_4^{2-}], molar equivalents yield a mixture of **2** and **3**.

$$m = \frac{MW_{Observed}}{\sum_i \alpha * MW_{avg,i}} \quad \text{(Eq 3.3)}$$

To obtain eq 3.3, specifically the MW_{avg} for both **2** and **3**, we used eq S3.5, which accounts for the number of the different species in solution, their molecular weights, and averages this total molecular weight over the total number of species in solution.

$$MW_{avg} = \frac{\sum_i n_i MW_i}{\sum_i n_i} \quad \text{(Eq S3.5)}$$

For example, in the case of a complete dissociation of all the species in solution, there would be the following for **3**: 1 $\{[(1,5\text{-COD})Ir^{I}\bullet HPO_4]_2\}^{2-}$, 2 BF_4^-, and 4 $Bu_4N\bullet(acetone)_6^+$. This results in eq S3.6.

$$MW_{avg,\mathbf{3}} = \frac{(1*792.7)+(2*86)+(4*591)}{1+2+4} = \frac{3328}{7} = 476 \quad \text{(Eq S3.6)}$$

Then, for the bridged species, the complete dissociation would result in the following: 1 $\{[(1,5\text{-COD})Ir^{I}(NCCH_3)]_2\bullet HPO_4\}^0$, 2 BF_4^-, and 2 $Bu_4N\bullet(acetone)_6^+$. This results in eq S3.7.

$$MW_{avg,\mathbf{2}} = \frac{(1*778.9)+(2*86)+(2*591)}{1+2+2} = \frac{2134}{5} = 427 \qquad \text{(Eq S3.7)}$$

Then, these values can be plugged into eq 3.3 to yield eq S3.8.

$$m = \frac{1070}{((0.7*476)+(0.3*427))} = 2.3 \qquad \text{(Eq S3.8)}$$

The same process was done for case / limiting assumption of complete tight-ion pairing, which yielded an *m* value of 1.8. Importantly, the $(Bu_4N)_2HPO_4$ used in this Signer MW experiment showed no detectable amount of $(Bu_4N)_4(P_2O_7)$ impurity by ^{31}P NMR, so any consideration of an addition to the apparent solution MW by the ≤3-8% $(Bu_4N)_4(P_2O_7)$ impurity common in the kinetics experiments was not needed nor, hence, made. The MW calculations above, eq S3.8 take into account that ca. 30% **2** as well as ~70% of **3** that are present at the 1:1 ratio of [(1,5-COD)$Ir^I(NCCH_3)_2$][BF_4] to $(Bu_4N)_2HPO_4$ examined.

The experimental, *apparent MW of 1070 g/mol* was then compared to the two extreme cases of: (i) assuming the tight-ion pairing of the anions and the Bu_4N^+ cations with a nominal mass of 1767 g/mol calculated from the 70% contribution of 1 $\{[(1,5\text{-COD})Ir{\bullet}HPO_4^-][Bu_4N^+]\}_2$ and 2 $[Bu_4N^+][BF_4^-]$, and the 30% contribution of 1 $\{[(1,5\text{-COD})Ir^I(NCCH_3)]_2{\bullet}HPO_4\}^0$ plus the presence of 2 $[Bu_4N^+][BF_4^-]$ from the synthesis stoichiometry; and then also (ii) assuming the full dissociation of all the anions from all the Bu_4N^+ cations. Doing so resulted in a calculated nominal mass of 2971 g/mol from the of the 70% contribution of 1 $\{[(1,5\text{-COD})Ir{\bullet}HPO_4]_2\}^{2-}$, its 2 BF_4^-, and 4 $Bu_4N{\bullet}(acetone)_6^+$ and the 30% contribution of 1 $\{[(1,5\text{-COD})Ir^I(NCCH_3)]_2{\bullet}HPO_4\}^0$, 2

Bu_4N^+, and 2 BF_4^-. These two cases, when entered into eq S3.8, result in *m* values of: *(i) 1.8 and (ii) 2.3—that is, again m ≈ 2 within experimental error.*

Next, simply as a control calculation, the case was considered where Scheme 3.1 lies 100% with **2** and 0% with **3**, and even though our NMR and other results tell us this case is not present (a calculation done just be confident in the conclusions from Signer MW experiments). In this calculation, the tight ion-pair (iii) and full dissociation (iv) calculations were conducted using eq 3.3 from the main text to yield: (iii) $m = 2.1$ for $\{[(1,5\text{-COD})Ir^I(NCCH_3)]_2 \bullet HPO_4\}^0$, 2 $[Bu_4N^+][BF_4^-]$, and 1 $[Bu_4N^+]_2[HPO_4^{2-}]$ for a calculated nominal mass of 2018 g/mol; and (iv) $m = 2.5$ for 1 $\{[(1,5\text{-COD})Ir^I(NCCH_3)]_2 \bullet HPO_4\}^0$, 2 BF_4^-, 1 HPO_4^{2-}, and 4 $Bu_4N \bullet (acetone)_6^+$ for a calculated nominal mass of 3412 g/mol. Hence, the range under this control calculation is $2.1 \leq m \leq 2.5$.

In short, all the results from the Signer MW experiment under all of the different calculations performed support an *m* value of ~2, revealing that of **3** is present to a large extent *as a dimer in acetone solution* at room temperature. We were also able to obtain mass spectrometry data consistent with this $m = 2$ dimer formulation, as detailed next.

(iii) Positive- and Negative-Ion Electrospray Ionization Mass Spectrometry (ESI-MS)

In situ preparations of **3** were prepared from 1:1 molar equivalents of $[(COD)Ir^I(NCCH_3)_2][BF_4]$ and $(Bu_4N)_2HPO_4$. These samples were prepared at ~5.0-6.0 mM in 1.0 mL of acetone and sealed in a septum-topped vial. The sample was introduced into the instrument using an gas-tight syringe and a syringe direct-injection method. The mobile phase for the instrument was MeOH. Spectra were collected in both the positive and negative modes. In the negative mode, peaks primarily appeared at 339.23, 416.29, and 1033.97 m/z. In the positive mode,

the only significant peak was at 242.28 m/z, assigned to Bu_4N^+ (Table S3.1). The results and the assignments made are summarized in Table S3.1.

Table S3.1. Summary of ESI-MS Results for the in situ Formation of **3** in Acetone

Mode	Positive (+)		Negative (-)		
Assignment	$(Bu_4N)^+$	$[(Bu_4N)_2(BF_4)]^+$	Unknown	$[BF_4)_2(Bu_4N)]^-$	$[(COD)Ir^I(HPO_4)]_2[Bu_4N]^-$
Peak (m/z)	242.28	571.56	339.23	416.29	1033.98
Calculated (m/z)	242.5	571.7	N/A	416.1	1035.2

The predominant signals observed in this work are the counter ion-pairs of BF_4^- and Bu_4N^+ for both the positive and negative modes. The only iridium species observed was in the negative mode for the mono-bridged complex, $\{[(1,5\text{-COD})Ir^I{\bullet}HPO_4]_2[Bu_4N]\}^-$, derived from **3**, a result which, however, supports and confirms the $\{[(1,5\text{-COD})Ir^I{\bullet}HPO_4]_2\}^{2-}$ core formulation underlying **3**.

Interestingly, none of the ESI-MS signals from the 2004 paper[2] of *preisolated material*,[2] m/z = 491, 493, 789, and 791, were observed from the current *in situ* prepared **3**. (The 2004 ESI-MS data were collected on the isolated version of **3**,[14] in comparison to the use of *in situ* formed **3** in this present work, the latter because we needed to be able to readily vary the HPO_4^{2-} to $Ir^I(1,5\text{-COD})^+$ ratio as part of the current kinetics studies performed.) The relatively low signal to noise, and perhaps also the solution speciation of **3**, as well as differences in the ESI-MS and injection methods, are possible contributing issues that come to mind for the lack of signals seen previously[14] in the ESI as part of an earlier study.[2]

Finke-Watzky (FW) 2-Step Mechanism of Slow, Continuous Nucleation Followed by Autocatalytic Surface Growth

Originally formulated in 1997 by Finke and Watzky,[18,19] what has become known in the literature as the FW 2-step mechanism successfully describes the phenomenon of nanoparticle formation through the use of two pseudo-elementary steps: (1) *slow, continuous nucleation,* followed by (2) typically fast *autocatalytic surface growth*, as shown in Scheme S3.2 below. The deliberately minimalistic, disproof-based, FW 2-step mechanism has been expanded to account for aggregation, agglomeration, and particle formation in oxide-supported heterogeneous catalysts.[20,21,22] As described in the experimental of the main text, kinetics data on the formation of $Ir(0)_n$ nanoparticles were collecting using the Catalytic Reporter Reaction (CRR), which exploits the ability of the $Ir(0)_n$ nanos to catalyze facile cyclohexene hydrogenation to cyclohexane, a catalysis-based amplification of the amount of $Ir(0)_n$ present at any given time. By monitoring the loss of hydrogen pressure in the Fischer-Porter reaction bottle, one is able to indirectly—but in real time and with thousands of ±0.05 psig high-precision data points—follow the formation process of the iridium nanoparticles, as shown in Scheme S3.2 under "Catalytic Reporter Reaction".

Scheme S3.2. The Finke-Watzky (FW) 2-Step Mechanism and Its Accompanying Catalytic Reporter Reaction

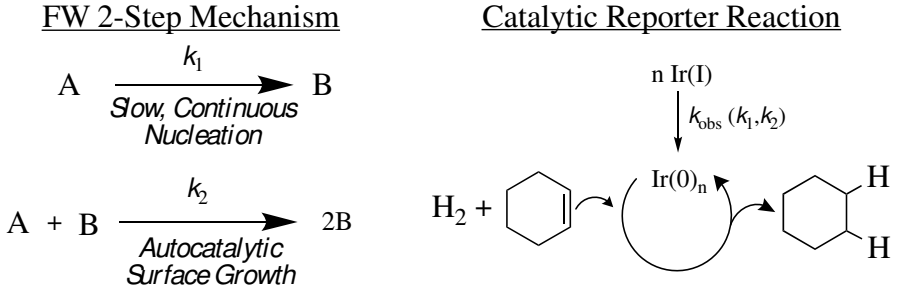

From the mechanism, the differential rate equation can be written, eq S3.9.

$$-\frac{d[A]}{dt} = k_{1obs}[A] + k_{2obs}[A][B] \qquad \text{(Eq S3.9)}$$

Next, eq S3.9 can be integrated into its usable form for particle formation kinetics as eq S3.10.

$$[A]_t = \frac{\left(\frac{k_{1obs}}{k_{2obs}}\right)+[A]_0}{1+\left(\frac{k_{1obs}}{k_{2obs}[A]_0}\right)*e^{\left[(k_{1obs}+k_{2obs}*[A]_0)*t\right]}} \qquad \text{(Eq S3.10)}$$

The additional details and assumptions needed to connect the H_2 loss to the loss of [A] and thereby process the kinetics data, are well documented and available in earlier publications.[18,19,20,21,22,23,24,25] Note that, as discussed in the experimental section of Chapter III, the k_{2obs} values provided below have been corrected by the [cyclohexene] / [Ir] ratio as the mathematics of the reporter reaction require.[15]

Control Experiment to Account for the Impact of Laboratory Dust on the Nucleation Kinetics

The effect of lowering the dust content (by 0.20 μm syringe filtration, including using filtered solvent to wash all glassware, as detailed in the experimental section of Chapter III) is seen in Figure S3.6 below. These control experiments to establish the effect(s) of dust were carried out on duplicate measurements of $[(1,5\text{-COD})Ir^{I}(NCCH_3)_2][BF_4]$ at 3.6, 6.0, and 9.6 mM with 5.4 molar equivalents of $(Bu_4N)_2HPO_4$, the results then being compared to the k_{1obs} rate constants from the same unfiltered experiments. The filtered reaction has an extended induction period, compared to the unfiltered reaction (Figure 3.3, Chapter III), consistent with the anticipated[27] slower nucleation rate constant (k_{1obs}) in the filtered solution. The effect of dust removal is, interestingly, more pronounced at lower iridium concentrations.

Also of interest is that the average values of the autocatalytic surface-growth rate constant, k_{2obs}, plotted against starting concentration of **3** remain the same within experimental error, as seen for the $\{(1,5\text{-COD})Ir\bullet POM\}^{8-}$ system.[27] This is consistent with the sigmoidal kinetics curves shown in Figure S3.6, where the latter, largely (albeit not exclusively[26]) growth segment of the curve does not appear to be significantly altered. A summary of these rate constants (k_{1obs} and k_{2obs}) is provided in Table S3.2.

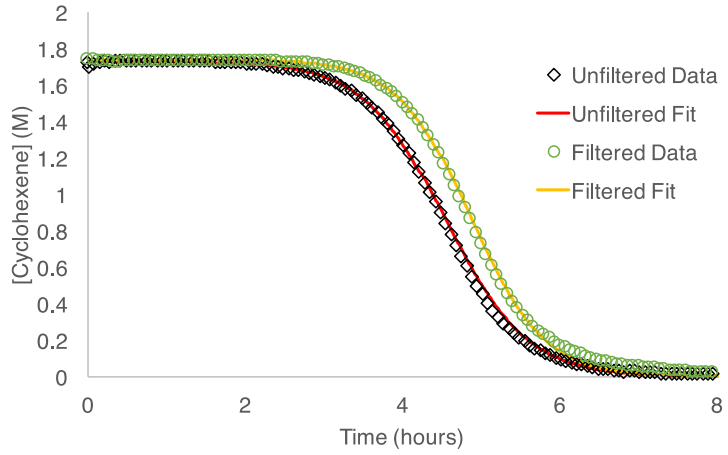

Figure S3.6. Representative sigmoidal kinetics for the catalytic reporter reaction (Scheme S3.2) of the *in situ* formed $\{[(1,5\text{-COD})Ir^{I}\bullet HPO_4][Bu_4N]\}_2$, **1**, in acetone under an initial 40 psig H_2 with [Ir] = 6.0 mM, 5.4 molar equivalents $(Bu_4N)_2HPO_4$, and 1 molar equivalent of Proton Sponge®. The two kinetics curves represent a control unfiltered (black diamonds with a red fit line) reaction solution and a 0.2 μm filtered (green circles with a yellow fit line) reaction solution. Each solution has a volume of 3 mL consisting of 2.5 mL acetone and 0.5 mL of 1.65 M cyclohexene. Shown is every fourth data point and the curve-fit of the data to the FW 2-step mechanism, eq S3.10.

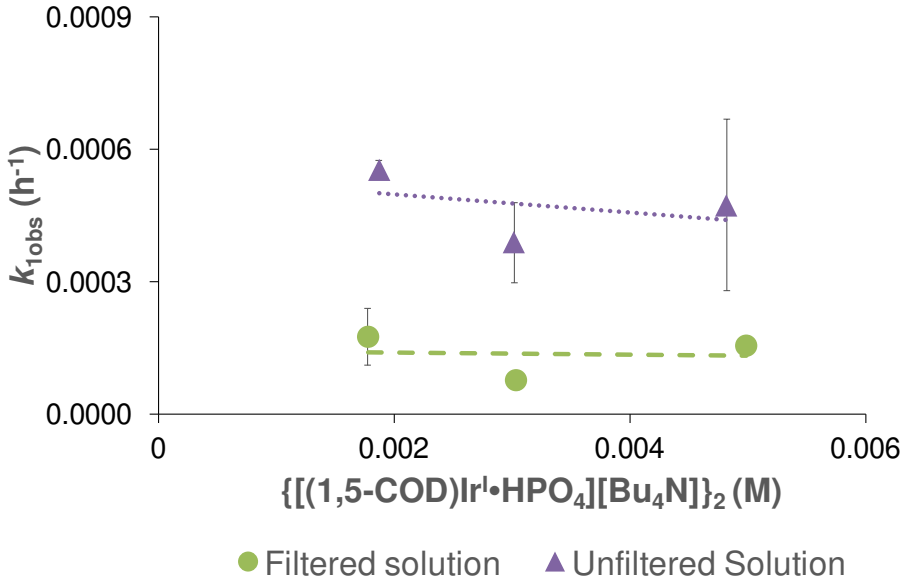

Figure S3.7. A plot of k_{1obs} (h^{-1}) vs $\{[(1,5\text{-COD})Ir^{I}\bullet HPO_4][Bu_4N]\}_2$ (M) obtained by curve-fitting each kinetics run to the integrated rate eq S10 for the unimolecular nucleation step of the FW 2-step mechanism. Solutions were prepared in situ from 6.0 mM $[(1,5\text{-COD})Ir^{I}(NCCH_3)_2][BF_4]$ and 5.4 molar equivalents of $(Bu_4N)_2HPO_4$. The purple triangles represent data from standard

hydrogenation conditions as described in the experimental section of Chapter III. Green circles represent hydrogenation experiments that were conducted after the reaction solution was passed through a 0.20 μm filter and the reaction tube was rinsed with filtered solvent prior to being filled with the reaction solution. All measurements were conducted ≥ 2 times leading to the error estimates shown.

The data in Figure S3.7 demonstrate that removal of dust from the reaction solution does cause a slowing of the nucleation rate constant, k_{1obs}. While the slowing effect is not to the same degree (a factor in Figure S3.7 of 1.5 to 5.0) as was previously observed for the {(1,5-COD)Ir•**POM**}$^{8-}$ system (a factor of 5-7.6 there)[27], the difference in k_{1obs} in Figure S3.7 between filtered and unfiltered solutions is greater than experimental error. However, the k_{2obs} value is not changed within experimental error by filtering the solution, Figure S3.8.

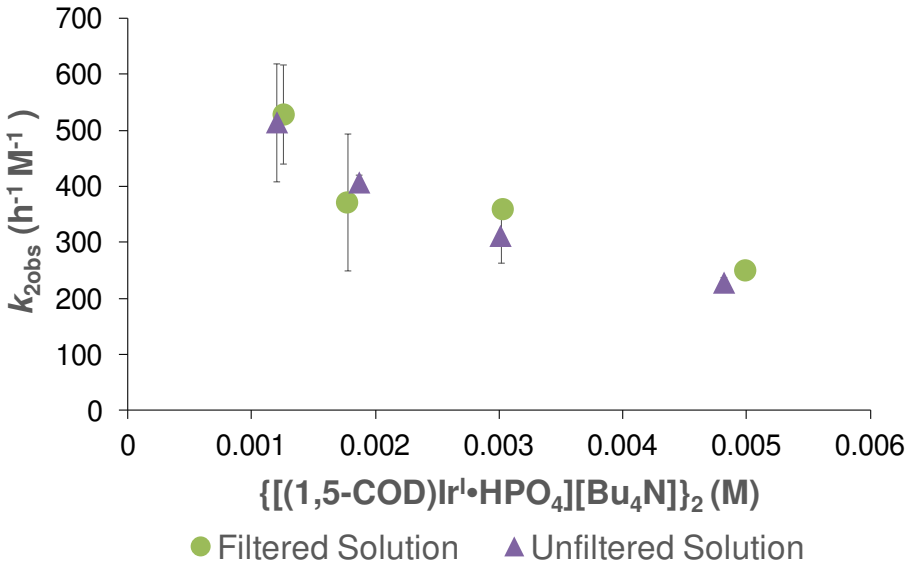

Figure S3.8. A plot of k_{2obs} (h^{-1} M^{-1}) vs {[(1,5-COD)Ir^{I}•HPO$_4$][Bu$_4$N]}$_2$ (M) obtained by curve-fitting each kinetic run to the integrated rate equation, eq S3.10, for the unimolecular nucleation step. Solutions were prepared in situ from 6.0 mM [(1,5-COD)Ir^{I}(NCCH$_3$)$_2$][BF$_4$] and 5.4 molar equivalents of (Bu$_4$N)$_2$HPO$_4$. The purple triangles represent data from standard hydrogenation conditions as described in the experimental section of Chapter III. Green circles represent hydrogenation experiments that were conducted after the reaction solution was passed through a 0.20 μm filter and the reaction tube was rinsed with filtered solvent prior to being filled with the reaction solution. All measurements were conducted ≥2 times leading to the error estimates shown. The decrease of k_{2obs} with $[A]_0$ implies either a dissociative step preceding the autocatalytic growth

step, or a HPO_4^{2-} ligand-binding effect masked in $k_{2(apparent)}$, or both (or some other explanation), but was not analyzed in further detail as part of the present work focusing on the initial, nucleation step.

Table S3.2. Comparison of Nucleation and Growth Rate Constants Between Filtered and Unfiltered Reaction Solutions

[Ir] (mM)	Rate Constant	Filtered	Unfiltered
3.6	k_{1obs} (h^{-1})	$(1.8 \pm 0.6)x10^{-4}$	$(5.5 \pm 0.2)x10^{-4}$
	k_{2obs} (h^{-1} M^{-1})	370 ± 120	406 ± 13
6.0	k_{1obs} (h^{-1})	$(0.8 \pm 0.2)x10^{-4}$	$(3.9 \pm 0.9)x10^{-4}$
	k_{2obs} (h^{-1} M^{-1})	359 ± 2	312 ± 48
9.6	k_{1obs} (h^{-1})	$(1.6 \pm 0.2)x10^{-4}$	$(4.7 \pm 1.9)x10^{-4}$
	k_{2obs} (h^{-1} M^{-1})	251 ± 9	228 ± 8

Importantly for the present work and its main conclusions, the kinetics in Figure S3.7 further demonstrate that k_{1obs} *is not dependent on the* $[A]_0 = \{[(1,5\text{-}COD)Ir^I \bullet HPO_4][Bu_4N]\}_2$*;* that is, $k_{1obs} = k_{1obs}[A]_0$; so that nucleation of the filtered solutions is still first order, in the dimeric complex, **3** (= A), A → B (k_{1obs}).

In short, the present results with the $\{[(1,5\text{-COD})Ir^I \bullet \mathbf{HPO_4}]_2\}^{2-}$ precursor, **3**, are consistent with previous investigations of $\{(1,5\text{-COD})Ir \bullet \mathbf{POM}\}^{8-}$ into the effects of laboratory dust on nucleation and growth studies, in that *only the nucleation rate constant* is affected by the presence of dust.[27]

Direct Time-Resolved Quantification of Cyclooctane (COA) By:

(i) ^{1}H NMR Spectroscopy & (ii) Gas-Liquid Chromatography (GLC)

The peak of cyclooctane (~1.4 ppm) was integrated and then normalized based on the relative intensity of the internal standard (~10 μL) of benzene (signal at 7.36 ppm). The data points were fit in COPASI[28] and produced the following rate constants: $k_{1obs} = 0.014 \pm 0.012$ h^{-1} and k_{2obs}

= 87 ± 29 h^{-1} M^{-1} (see elsewhere[18] for the correction term that has to do with the amount of cyclohexene used in the Catalytic Reporter Reaction (CRR)). From the same samples, GLC was conducted and the data points were fit in COPASI. The rate constants (by GLC) are as followed: $k_{1obs} \approx 0.02$ h^{-1} and $k_{2obs} \approx 67$ h^{-1} M^{-1} (while for comparison the rate constants produced by the CRR are: $k_{1obs} = 0.00041 \pm 0.00009$ h^{-1} and $k_{2obs} = 250 \pm 60$ h^{-1} M^{-1}). Important to note here is that rate constants obtained by the CRR result from fitting hundreds of relatively high precision (±0.05 psig) H_2 pressure data points, whereas both the GLC and NMR COA evolution-extracted rate constants come from only 6 data points and are, therefore, less well determined (the errors reported for the CRR are, themselves, just the fit errors). The main use of the COA evolution data in at least the present example is to tell when the reaction is over (for collection of samples for TEM, for example), and to confirm the sigmoidal shape of the curve.

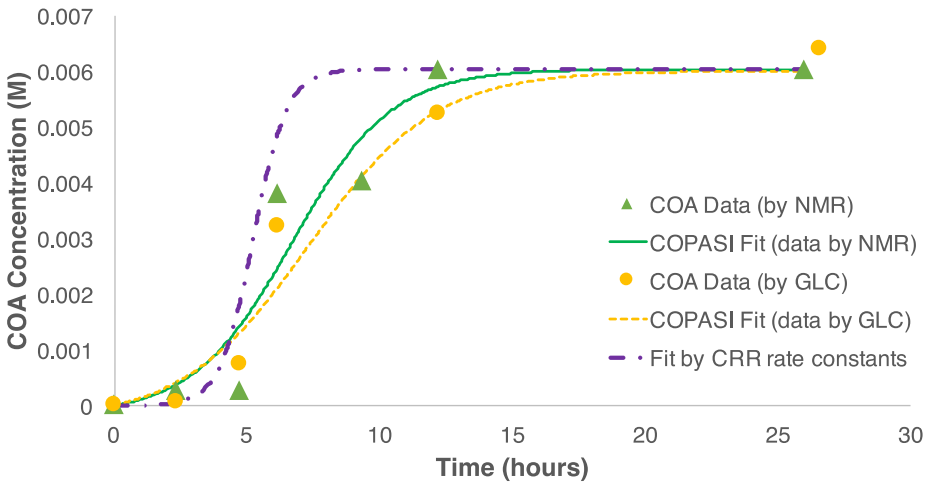

Figure S3.9. The concentration of cyclooctane (M) is plotted against time (hours). Each time point represents a new reaction mixture of 6.0 mM $[(1,5\text{-COD})Ir^{I}(NCCH_3)_2][BF_4]$ and 5.4 molar equivalents of $(Bu_4N)_2HPO_4$ in 3 mL of solvent (2.5 mL acetone and 0.5 mL cyclohexene). The reaction solution was collected at specific times and the concentration of cyclooctane was measured by ^1H NMR spectroscopy (green triangles) and gas-liquid chromatography (yellow circles). Fit lines and FW 2-step rate constants (k_{1obs} and k_{2obs}) were determined using COPASI. The green line is the COPASI fit for the NMR data and the dashed yellow line is the COPASI fit

for the GLC data. Finally, the dash-dot purple line is the simulated COA formation using the rate constants collected by the Catalytic Reporter Reaction (CRR).

(iii) UV-Visible Spectroscopy

The same samples that were analyzed by NMR and GLC were used to collect UV-Visible spectra. Samples were diluted by a rough 1:2 ratio to lower the absorbance into an observable range. All samples have the same starting concentration, but the dilution was not identical for each sample, so that the resultant spectra have an absorbance max range of 0.5 to 1.2 absorbance units.

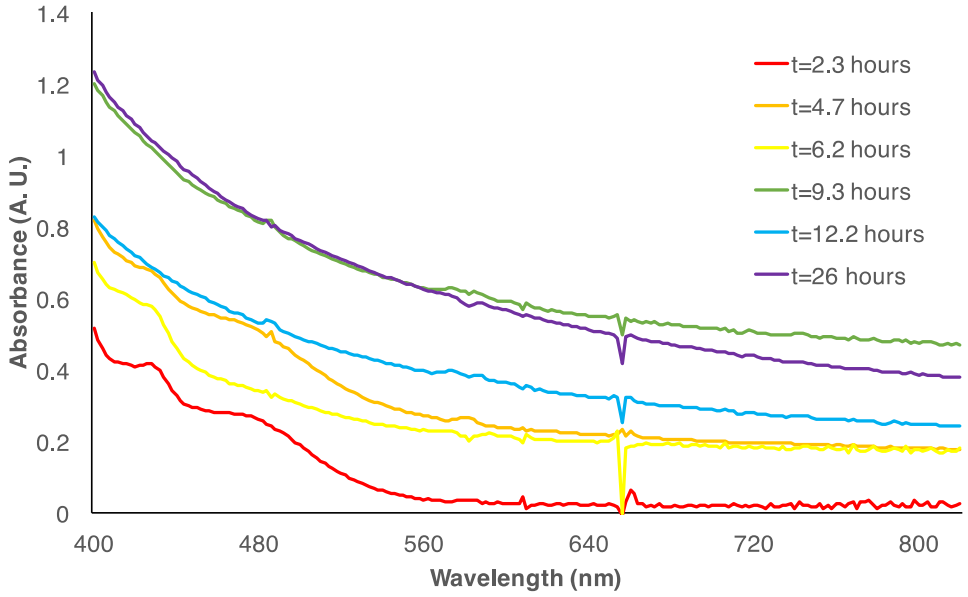

Figure S3.10. Samples from the ^{1}H NMR and GLC quantification of the cyclooctane were diluted by approximately half in order to collect UV-Vis spectra in an attempt to observe any useful changes in the plasmon resonance of $Ir(0)_n$ throughout the reaction. None were seen.

The main point of showing the UV-visible spectra given above is to demonstrate that the only signal observed is that assigned to the plasmon resonance for iridium nanoparticles.[29]

Time-Resolved Transmission Electron Microscopy (TR-TEM)

(a)

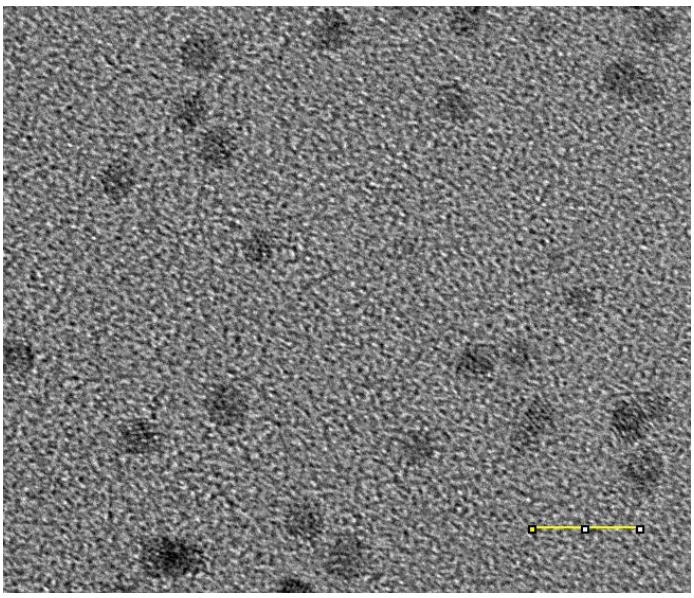

(b)

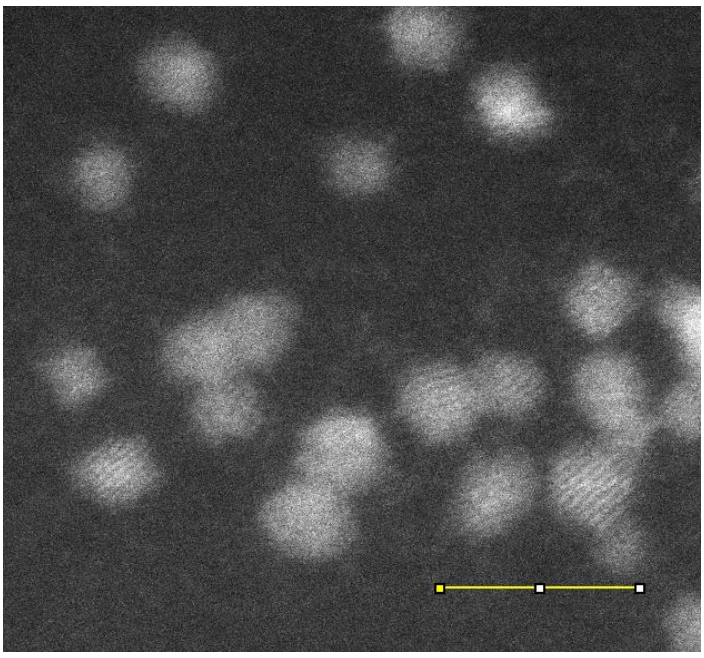

Figure S3.11. (a) TEM micrograph and **(b)** dark-field Scanning TEM (STEM) of $Ir(0)_n$ nanoparticles on silicon nitride. Nanoparticles were prepared from 6.0 mM [(1,5-COD)$Ir^{I}(NCCH_3)_2$][BF_4] and 5.4 molar equivalents of $(Bu_4N)_2HPO_4$. They were collected at the end of the reaction time (11.5 hours), as determined by concurrently COA evolution studies by GLC. Samples were prepared in a N_2-filled drybox by a 1:10 dilution of sample solution to 2-butanone. The yellow scale bar in both images represents 5.0 nm.

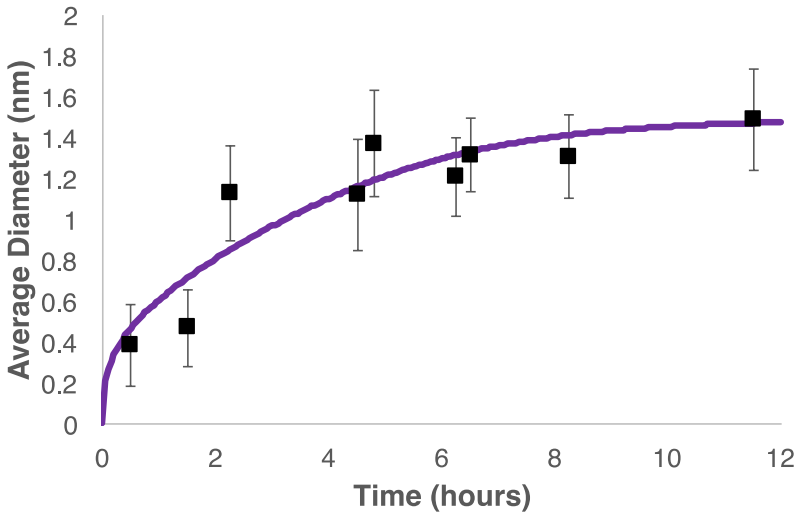

Figure S3.12. The particle size evolution across the full reaction time was determined by HR-TEM. A total of ~1900 non-touching particles were measured over the total ~12 h period. At each time point, a new reaction was prepared of 6.0 mM [(1,5-COD)$Ir^{I}(NCCH_3)_2$][BF_4] in the presence of 5.4 molar equivalents of $(Bu_4N)_2HPO_4$ and 0.5 mL of 1.65 M cyclohexene at 22.0 ± 0.1 ºC in acetone. The purple line represents a fit line using the FW 2-step mechanism via eq S3.11 to extract rough kinetic rate constants from the size versus time data.

Time-resolved study of the particle size evolution at 6.0 mM [(1,5-COD)$Ir^{I}(NCCH_3)_2$][BF_4] and 5.4 molar equivalents of $(Bu_4N)_2HPO_4$. The rate constants were obtained from using eq S3.11 which relates particle diameter (nm) vs time (h), an equation derived from the FW 2-step mechanism, plus assumptions, as detailed elsewhere:[30]

$$D_t = D_f * \left(\frac{k_{1obs} + k_{2obs}[A]_0}{k_{2obs}[A]_0 + k_{1obs} e^{(k_{1obs} + k_{2obs}[A]_0) * t}} \right)^{\frac{1}{3}} \qquad \text{(Eq S3.11)}$$

In eq S3.11, D_t is particle diameter at a given time, D_f is particle diameter at the end of the reaction, k_{1obs} and k_{2obs} are the nucleation and growth rate constants, respectively, from the FW 2-step mechanism, $[A]_0$ is the precursor concentration at zero hours, and t is time.[30] The fit yields the approximate rate constants k_{1obs} = 0.06 ± 0.03 h^{-1} and k_{2obs} = 70 ± 40 h^{-1} M^{-1}, interestingly more

comparable to the GLC-obtained rate constant, $k_{1obs} \approx 0.02$ h^{-1} and $k_{2obs} \approx 67$ h^{-1} M^{-1}, than to the Catalytic Reporter Reaction (CRR)–measured values of $k_{1obs} = 0.0004 \pm 0.0001$ h^{-1} and $k_{2obs} = 312 \pm 48$ h^{-1} M^{-1}. A quantitative comparison of the k_{1obs} and k_{2obs} rate constants for the {[(1,5-COD)Ir^{I}•**HPO$_4$**]$_2$}$^{2-}$ precursor obtained by the four methods of TEM, GLC, the CRR, and SAXS is in progress and will be reported in due course as part of a separate study (and even though in our original 1997 paper studying the {(1,5-COD)Ir^{I}•$P_2W_{15}Nb_3O_{62}$}$^{8-}$ system, the CRR- and GLC-derived k_{1obs} and k_{2obs} values agreed within experimental error for that system,[18] at least when just one equivalent of the $P_2W_{15}Nb_3O_{62}^{9-}$ is present). Such a study has been completed and can be found as Chapter IV.

The Effects of Added HPO_4^{2-} on the Nucleation Kinetics

From Chapter III, the data in Figure 3.5 was fit using eq 3.10, with [A_2] being the starting concentration of iridium as [(1,5-COD)Ir^{I}(NCCH$_3$)$_2$][BF$_4$], then dividing that value by 2, and using the resultant [A_2] as a fixed (known) parameter in the curve-fitting. Next, the *initial value* of k_{3obs} was set at ~100 h^{-1} (determined by previous fitting attempts). Then, K_{diss} and k_{3obs} were allowed to vary, with the fitting results reported in Table S3.3.

Table S3.3. Curve-Fit K_{Diss} and k_{3obs} Values for the (k_{1obs}) vs added $(Bu_4N)_2HPO_4$ Data in Figure 3.5 in Chapter III and fitted with eq 10 in Chapter III

Measured, Input [A_2] (M)	K_{diss} (M)[a]	k_{3obs} (h^{-1})[a]
(1.66 ± 0.05) x 10^{-2}	~4 x 10^{-6}	~33
(2.72 ± 0.06) x 10^{-2}	~2 x 10^{-6}	~108
(4.32 ± 0.06) x 10^{-2}	~7 x 10^{-6}	~46

[a] Points meriting mention here are as followed: (i) each pair of K_{diss} and k_{3obs} mathematically correspond to one another, that is, are the coupled results from curve-fitting the data; (ii) the

error estimates from the curve-fits show that these values could vary by even up to ~10^4, meaning the absolute values are poorly determined; however (iii) in the case of K_{diss}, we have another estimate from the ^{1}H NMR titration studies in the main text, namely $K_{diss(NMR)} = 1/(K_{Assoc,2}) = 1/(>10^2\ M^{-1})$ which yields $K_{diss(NMR)} < 10^{-2}$ M, consistent with the $K_{diss} \approx 10^{-6}$ M estimate in Table S3. Additionally, (iv) we know that complex **3** is mostly intact in the mM acetone solution, another fact consistent with a K_{diss} value in the roughly ~10^{-6} M range.

Three Control Experiments Testing for Effects of $P_2O_7^{4-}$ on the Nucleation Kinetics:

(i) Deliberately Increasing the Impurity $(Bu_4N)_4(P_2O_7)$ Through Excess Vacuum Drying

The dehydration product $(Bu_4N)_4(P_2O_7)$ has been shown to be present at ≤3–8% levels in the $(Bu_4N)_2HPO_4$ used in kinetics studies for this paper. Hence, it was important that controls were done to answer the question of if this ≤3–8% impurity has a detectable effect on the nucleation kinetics? To answer this question, the $(Bu_4N)_4(P_2O_7)$ impurity was deliberately increased by employing longer drying times under vacuum. The initial experimental preparation of $(Bu_4N)_2HPO_4$ was identical to that described in the main text, but then this product was dried under vacuum for an additional 48–72 hours at room temperature and checked by ^{1}H and ^{31}P NMR to determine the percentage of $(Bu_4N)_4(P_2O_7)$ present as a function of time. Additional nanoparticle formations were then performed using the Catalytic Reporter Reaction method with $(Bu_4N)_2HPO_4$ that contained 8% and 10% $(Bu_4N)_4(P_2O_7)$ according to ^{31}P NMR. Interestingly, attempts to dry the $(Bu_4N)_2HPO_4$ longer, up to 72 hours longer, resulted in no increase in the percentage of $(Bu_4N)_4(P_2O_7)$ beyond 10%. The results of these controls are summarized in Figure S3.13 and Table S3.4.

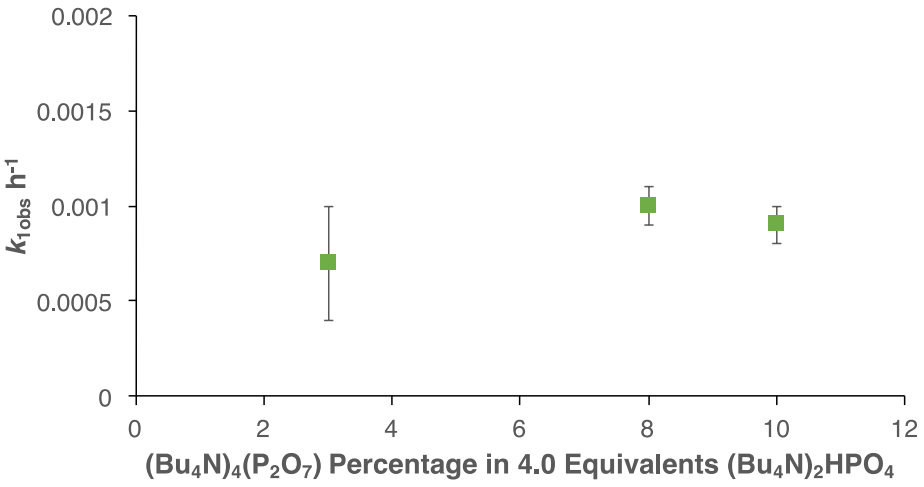

Figure S3.13. The measured nucleation rate constant (k_{1obs}) versus the percentage of $(Bu_4N)_4(P_2O_7)$ present in 4.0 molar equivalents of $(Bu_4N)_2HPO_4$ per mol of iridium for hydrogenation experiments prepared at [Ir] = 6.0 mM (18.0 μmols) with 4.0 molar equivalents $(Bu_4N)_2HPO_4$ (i.e., 3.6 equiv. $(Bu_4N)_2HPO_4$ and 0.4 equiv. $(Bu_4N)_4(P_2O_7)$). Nanoparticle formation reactions were run at the standard 3–8%, then at 8% and 10%. No bulk metal was observed from these experiments.

Table S3.4. Summary of Nucleation Rate Constants at Different Percentages of $(Bu_4N)_4(P_2O_7)$ Present in $(Bu_4N)_2HPO_4$ and the Observed Final Product

$(Bu_4N)_4(P_2O_7)$ Present in $(Bu_4N)_2HPO_4$	k_{1obs} (h^{-1})	Final Product
3 – 8 %	0.0007 ± 0.0003	Nanoparticles
8 %	0.0010 ± 0.0001	Nanoparticles
10 %	0.0009 ± 0.0001	Nanoparticles

From the results presented in Figure S3.13 and Table S3.4, there is no detectable effect on k_{1obs} of the $(Bu_4N)_4(P_2O_7)$ in $(Bu_4N)_2HPO_4$ within experimental error for even 2-4 times (10%) the 3–8% $(Bu_4N)_4(P_2O_7)$ present in the kinetics experiments—the k_{1obs} value at 3–8%, 8%, and 10% back *extrapolated* to 0% all yielding the same k_{1obs} value within experimental error. This result is as expected, since it is hard to imagine how a ≤3–8% level of $P_2O_7^{4-}$ would compete with the 10-20 fold higher level of $(Bu_4N)_2HPO_4$ present in the reaction and as a nanoparticle stabilizer. That

said, the controls needed to be done. And, the other controls and experiments reported below did uncover some interesting effects with either higher amounts of $P_2O_7^{4-}$ and probably what are acid / base effects with its diprotonated form, $H_2P_2O_7^{2-}$.

(ii) Effects of Adding the Tributylammonium Salt of $P_2O_7^{4-}$ / $HP_2O_7^{3-}$, $(Bu_3NH)_{4y+3x}(P_2O_7)_y(HP_2O_7)_x$

An attempt was made to produce authentic $P_2O_7^{4-}$ as its tributylammonium salt in order to spike the reaction mixture with >>25% of $P_2O_7^{4-}$. Hence, commercially available, diprotonated bis-tributylammonium salt, $(Bu_3NH)_2(H_2P_2O_7)$, was treated with 2 equivalents of Bu_3N in an attempt to make cleanly deprotonated $(Bu_3NH)_4(P_2O_7)$, but which actually likely yields $(Bu_3NH)_{4y+3x}(P_2O_7)_y(HP_2O_7)_x$. To start, a stock solution of $(Bu_3NH)_4(P_2O_7)$ was prepared by combining 137.0 mg (249.7 μmols) of $(Bu_3NH)_2(H_2P_2O_7)$ with 0.12 mL (500.8 μmols) Bu_3N in 1.88 mL of acetone. The respective, aqueous, pK_a's are the following, so that at least the first deprotonation in acetone should be complete: $H_2P_2O_7^{2-}$, $pK_{a1} = 5.8$ $pK_{a2} = 8.0$; while for Bu_3NH^+, the $pK_a = 9.05$,[11,31] so that the anticipated problem with this synthesis is that some singly protonated $HP_2O_7^{3-}$ is likely also present. Characterization was performed with ^{31}P NMR with signals at δ: -10.08 (s, $P_2O_7^{4-}$/ $HP_2O_7^{3-}$) ppm; and with ^1H NMR with signals at δ: 0.92 (t, CH_3), 1.36 (m, CH_2), 1.58 (m, CH_2), 2.01 (br, solvent)[5], and 2.72 (s, br, NH).

Next, and even though a mixture of $P_2O_7^{4-}$/ $HP_2O_7^{3-}$ was likely being employed, nanoparticle formation experiments were conducted by the Catalytic Reporter Reaction method at the standard conditions in the Experimental section of the main text for 6.0 mM [(1,5-COD)$Ir^I(NCCH_3)_2$][BF_4] with 4.0 molar equivalents of $(Bu_4N)_2HPO_4$ (i.e., containing 10% $(Bu_3NH)_4(P_2O_7)$) and spikes of $P_2O_7^{4-}$/ $HP_2O_7^{3-}$ as their Bu_3NH^+ salt were added at 10%, 50%,

and 100% molar equivalents as compared to the amount of HPO_4^{2-} present. All hydrogenation solutions were prepared with 3.0 mL of reaction solution. The data are summarized in Figure S3.14 and Table S3.5. They reveal that at levels of 20% $P_2O_7^{4-}$ plus $HP_2O_7^{3-}$ (i.e., 10% $(Bu_4N)_4P_2O_7$ and the 10% spike of $(Bu_3NH)_{4y+3x}(P_2O_7)_y(HP_2O_7)_x$, the nucleation kinetics *are* changed. Furthermore, with spikes of 50% and 100% of $(Bu_3NH)_{4y+3x}(P_2O_7)_y(HP_2O_7)_x$, the product is completely different (bulk metal) so that the rate constants reported for those two entries in Table S3.5 are not well determined.

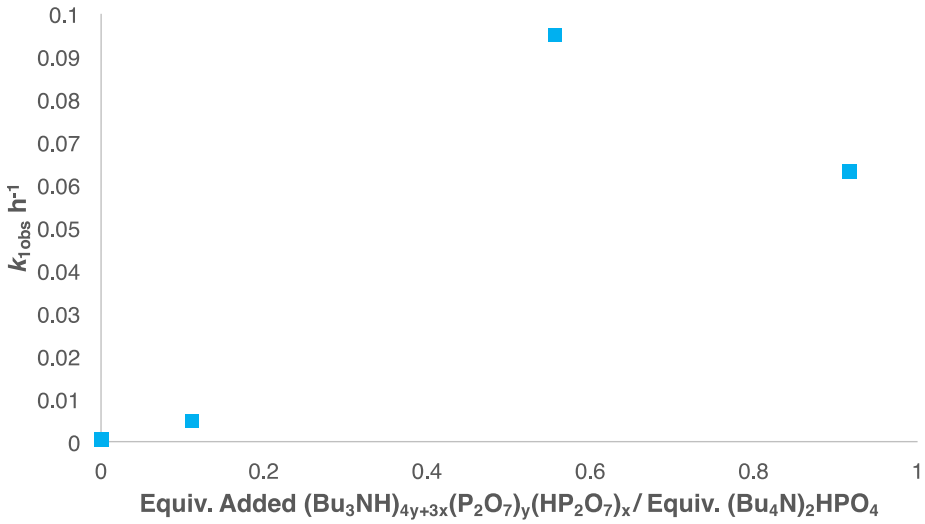

Figure S3.14. The nucleation rate constant (k_{1obs}) versus the ratio of $(Bu_3NH)_{4y+3x}(P_2O_7)_y(HP_2O_7)_x$ molar equivalents to $(Bu_4N)_2HPO_4$ molar equivalents per mol of iridium for hydrogenation experiments prepared at [Ir] = 6.0 mM (18.0 μmols) with 3.6 molar equivalents $(Bu_4N)_2HPO_4$ and 0.4 molar equivalents $(Bu_4N)_4(P_2O_7)$. The $(Bu_3NH)_{4y+3x}(P_2O_7)_y(HP_2O_7)_x$ was added in the following molar equivalents: 0.4, 2.0, and 3.3. The higher levels of added $(Bu_3NH)_{4y+3x}(P_2O_7)_y(HP_2O_7)_x$ result in the production of a different product, namely bulk metal, instead of Ir(0) nanoparticles.

Table S3.5. Summary of Nucleation Rate Constants at Different Ratios of $(Bu_3NH)_{4y+3x}(P_2O_7)_y(HP_2O_7)_x$ to $(Bu_4N)_2HPO_4$

$(Bu_3NH)_{4y+3x}(P_2O_7)_y(HP_2O_7)_x$ / $[(Bu_4N)_2HPO_4]$	k_{1obs} (h^{-1})	Final Product
0.00	0.0007 ± 0.0003	Nanoparticles

0.11	0.0048	Nanoparticles
0.56	(~0.1)	*Bulk Metal*
0.92	(~0.06)	*Bulk Metal*

The data presented in Figure S3.14 and Table S3.5 do reveal a sizable effect on the kinetics, although the effect extrapolates visually back to k_{1obs} ~0 in Figure S3.14 with zero added $(Bu_3NH)_{4y+3x}(P_2O_7)_y(HP_2O_7)_x$. At a ratio of greater than 0.5 ($(Bu_3NH)_4(P_2O_7)$ to $(Bu_4N)_2HPO_4$), there is a significant change in the reaction kinetics and the resulting products. Likely, $P_2O_7^{4-}$ is acting as a base and enhancing the nucleation rate, leading to more agglomeration, and bulk Ir(0) metal as the primary product. There is also the implication that at higher amounts, $P_2O_7^{4-}$ maybe replacing HPO_4^{2-} resulting in poorer nanoparticle stabilization, $P_2O_7^{4-}$ operating in a similar fashion as $P_3O_9^{3-}$, which is known to produce bulk Ir(0) metal when used as a nanoparticle stabilizer.[32]

(iii) Adding the Diprotonated, Bis-tributylammonium Salt of $P_2O_7^{4-}$, $(Bu_3NH)_2(H_2P_2O_7)$

Because the above results and because the effects of additives on nucleation are an understudied, but important[33,34] subject, the effects on the nucleation kinetics and products of adding preselected amounts of the commercially available *diprotonated* salt, $(Bu_3NH)_2H_2P_2O_7$, were also studied. The details of this experiment are as follows: nanoparticle formation runs were prepared with 6.0 mM $[(1,5\text{-COD})Ir^{I}(NCCH_3)_2][BF_4]$ (18.0 μmols) and 4.0 molar equivalents of $(Bu_4N)_2HPO_4$ (i.e., containing the 10% impurity of $P_2O_7^{4-}$, so having 3.6 molar equivalents of $(Bu_4N)_2HPO_4$ and 0.4 molar equivalents of $(Bu_4N)_4(P_2O_7)$). Next, commercial $(Bu_3NH)_2(H_2P_2O_7)$ was added to the reaction solution in each subsequent, independent kinetics run in increasing amounts of: 0.00, 0.10, 0.25, 0.35, 0.50, and 2.00 molar equivalents of $(Bu_3NH)_2(H_2P_2O_7)$. The

individual kinetics runs and a table of the resultant data are presented in Figures S3.15a-f and Table S3.6.

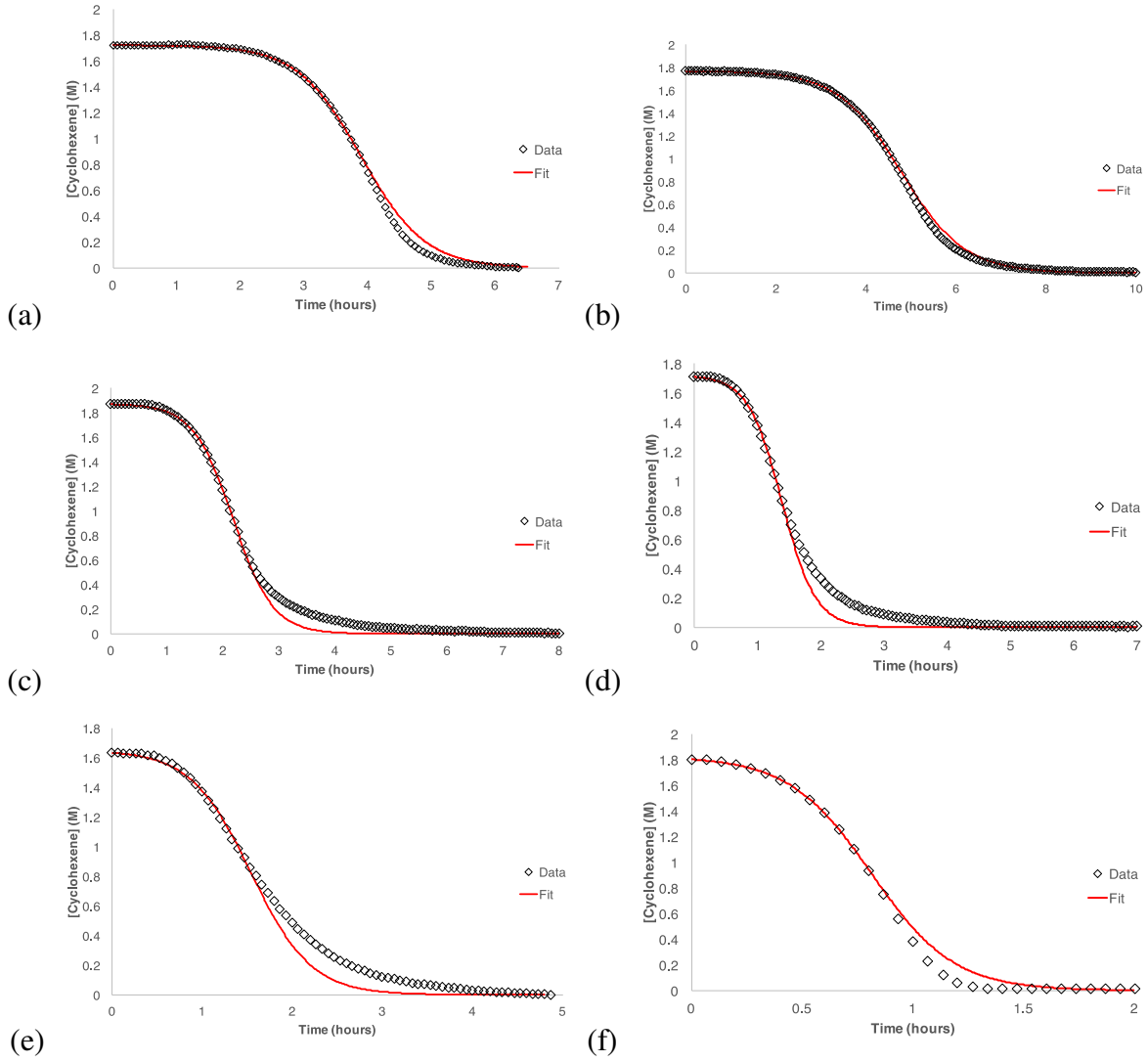

Figure S3.15. Sigmoidal kinetics for the formation of $Ir(0)_n$ from the *in situ* formed precatalyst, $\{[(1,5\text{-COD})Ir^{I}\bullet HPO_4][Bu_4N]\}_2$, in acetone under an initial H_2 pressure of 40 psig. All experiments were prepared at [Ir] = 6.0 mM (18.0 μmols) with 3.4 mol equivalents HPO_4^{2-} and 0.6 molar equivalents $P_2O_7^{4-}$. The commercially available $(Bu_3NH)_2(H_2P_2O_7)$ was added in the following molar equivalents: **(a)** 0.00, **(b)** 0.10, **(c)** 0.25, **(d)** 0.35, **(e)** 0.60, and **(f)** 2.00. This made the following molar equivalents of $P_2O_7^{4-}$ in the reaction solutions: **(a)** 0.60, **(b)** 0.70, **(c)** 0.85, **(d)** 0.95, **(e)** 1.10, and **(f)** 2.60. All the plots **(a)-(f)** are shown with a quarter of the data for visibility of the fit line. The nucleation and growth rate constants were extracted by curve-fitting the data with the integrated form of the FW 2-step mechanism rate equation.[18]

Table S3.6. Summary of Nucleation Rate Constants at Varying Equivalents of Added $H_2P_2O_7^{2-}$

Mol Equiv. $H_2P_2O_7^{2-}$	k_{1obs}
0.00 (Control)	0.0008 ± 0.0001
0.10	0.0016 ± 0.0001
0.25	0.0061 ± 0.0001
0.35	0.0212 ± 0.0007
0.5	0.030 ± 0.001
2.00	0.0671 ± 0.0008

The initial expectation was that the dianionic $H_2P_2O_7^{2-}$ might yield a decreased nucleation rate and rate constant as also seen for the dianionic stabilizer HPO_4^{2-}, Figure 3.5 in Chapter III. Figure S3.16 reveals that, instead, a dramatic, ca. exponential *increase* in the observed, apparent nucleation rate constant, k_{1obs}, is seen once ≥0.25 molar equivalent of $(Bu_3NH)_2(H_2P_2O_7)$ $H_2P_2O_7^{2-}$ per mol of Ir have been added, although the extrapolated intercept at 0 added $(Bu_3NH)_2(H_2P_2O_7)$ tends towards a small, k_{1obs} ~0.0007 h^{-1}.

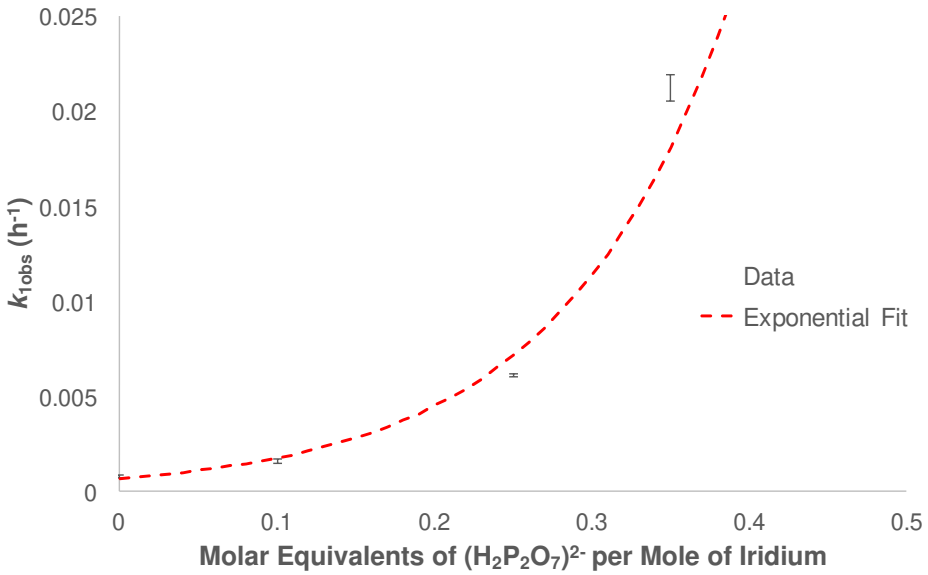

Figure S3.16. The nucleation rate constant (k_{1obs}) versus the total molar equivalents of $(Bu_3NH)_2(H_2P_2O_7)$ per mol of iridium for four hydrogenation experiments prepared at [Ir] = 6.0 mM (18.0 μmols) with 3.4 molar equivalents $(Bu_4N)_2HPO_4$ (that also contains 0.6 molar equivalents $(Bu_4N)_4(P_2O_7)$). The $(Bu_3NH)_2(H_2P_2O_7)$ was added in the following molar equivalents: 0.00, 0.10, 0.25, and 0.35. The data were fit with an exponential function, with an extrapolated value back to k_{1obs} ~0.0007 h^{-1} at 0 added $(Bu_3NH)_2(H_2P_2O_7)$.

As Figure S3.16 shows, the added $(Bu_3NH)_2(H_2P_2O_7)$ *increases* the nucleation apparent rate constant, k_{1obs}, exponentially by $10^{1\text{-}2}$ over the range of added $(Bu_3NH)_2(H_2P_2O_7)$ examined. The added $(Bu_3NH)_2(H_2P_2O_7)$ also changes the resultant product completely, with bulk Ir(0) being observed as the primary product (i.e., rather than the normal $Ir(0)_n$ nanoparticles) once ≥0.35 molar equivalents of $(Bu_3NH)_2(H_2P_2O_7)$ have been added.

Fortunately, and interestingly, knowledge of the nucleation mechanism presented herein in Scheme 3.2 allows a rational, leading *hypothesis* for the dramatic, nucleation rate accelerating effect of $H_2P_2O_7^{2-}$. Specifically, the dissociative equilibrium shown in eq 3.4 (and reproduced below as eq S3.12) should be shifted to the right by coupling to the protonation step in eq S3.13, in which $H_2P_2O_7^{2-}$ (pK_a = 5.80, *in* H_2O)[11] serves as an acid to protonate HPO_4^{2-} (conjugate acid, $H_2PO_4^-$, pK_a = 7.20, *in* H_2O)[11], $H_2P_2O_7^{2-}$, pK_{a1} 5.8 and pK_{a2} 8.0;[11] while for thereby causing the release of additional nucleation-enhancing $\{[(1,5\text{-COD})Ir^I(solv)]_2 \bullet HPO_4\}^0$ (estimated K_{eq} by eq 3.14 ~$10^{1.4}$ *in* H_2O). For reference, the aqueous Bu_3NH^+, the pK_a is 9.05[31] so that it should not be involved in the acid/base chemistry relevant to the results in at least Figure S3.16. It must be noted these pK_a values are all in aqueous solvents, and hence they will be different (higher) values in non-aqueous, organic solvents. However, a search of the literature shows that the pK_a values in acetone should increase at least roughly proportionally to one another,[13,14,15,16] although no specific pK_a values in any organic solvent, much less in acetone, were found for the above compounds.

$$\{[(COD)Ir^{I}\bullet HPO_4]\}_2^{2-} + 2\ solv \underset{}{\overset{K_{Diss}}{\rightleftharpoons}} \{[(COD)Ir^{I}(solv)]_2\bullet HPO_4\}^0 + HPO_4^{2-} \quad \text{(Eq S3.12)}$$

$$H_2P_2O_7^{2-} + HPO_4^{2-} \rightleftharpoons HP_2O_7^{3-} + H_2PO_4^- \quad \text{(Eq S3.13)}$$

$$\text{Sum: } \{[(COD)Ir^{I}\bullet HPO_4]\}_2^{2-} + 2\ solv + H_2P_2O_7^{2-} \overset{K_{eq}}{\rightleftharpoons} \{[(COD)Ir^{I}(solv)]_2\bullet HPO_4\}^0 + HP_2O_7^{3-} + H_2PO_4^- \quad \text{(Eq S3.14)}$$

A key point here is that (1,5-COD)Ir(solv)$_2^+$ is known to be reduced essentially immediately[18] under H_2 to form bulk Ir(0)$_n$ in the absence of sufficient good stabilizers. The data presented in the main text displays the same type of rapid reduction process for the {[(1,5-COD)Ir^I(solv)]$_2$•HPO$_4$}^{0} complex. The resultant faster nucleation gives rise to a higher concentration of nanoparticles,[18,19] which in turn is known to *accelerate bimolecular agglomeration steps* that lead to bulk Ir(0) formation[35], the observed product with ≥0.35 molar equivalent per Ir of added $(Bu_3NH)_2(H_2P_2O_7)$. Precisely why the curve in Figure S3.16 is exponential (i.e., and not linear in added $(Bu_3NH)_2(H_2P_2O_7)$ concentration as eq S3.13 alone implies) is not known, but likely has at least something to do with the bulk Ir(0) formation accelerating growth and an inability to then completely separate the nucleation from the growth rate constant.[36] However, the results demonstrate rather clearly (i) *the sensitivity of nucleation to the precise reaction conditions and components*,[27,33,34] as well as (ii) *the value of mechanistic understanding* in allowing the formation of at least rational initial hypotheses with some precedent to begin to explain such opposite-to-initially-expected results.

Control Experiment Ruling Out Any Effect of Added $(Bu_4N)^+(BF_4)^-$ on the Nucleation Kinetics

In the literature, BF_4^- is known as a weakly coordinating anion to metal nanoparticles,

specifically iridium nanoparticles.[37,38] It is also known that a very large excess of 50 and 100 molar equivalents of even the weak stabilizer BF_4^- will extend the stability of otherwise largely unstabilized $Ir(0)_n$ nanoparticles.[37] A third fact is that the balanced *in situ* reaction stoichiometry for the present system, $[(1,5\text{-COD})Ir^I(NCCH_3)_2][BF_4]$ plus $(Bu_4N)_2HPO_4$, produces one molar equivalent of $(Bu_4N)^+(BF_4)^-$. Hence, the question arose for one final set of control experiments of if the 1.0 equivalent of $(Bu_4N)^+(BF_4)^-$ is having any measurable effect on the observed nucleation kinetics. The expectation / hypothesis is that it is not, but this was tested with three controls experiments as described next.

Three control hydrogenations were performed starting with [Ir] = 6.0 mM, 4.0 molar equivalents of $(Bu_4N)_2HPO_4$ (where 3.6 molar equivalents are $(Bu_4N)_2HPO_4$ and 0.4 molar equivalents are $(Bu_4N)_4(P_2O_7)$), and then the following added amounts of $(Bu_4N)^+(BF_4)^-$: 2.0, 4.0, and 8.0 molar equivalents. No changes were observed in the nucleation rate constants within experimental error, k_{1obs}; k_{1obs} = 0.0011 ± 0.0002 h^{-1}, 0.0008 ± 0.0001 h^{-1}, and 0.0009 ± 0.0002 h^{-1} for 2.0, 4.0, and 8.0 molar equivalents of $(Bu_4N)^+(BF_4)^-$, respectively. Hence, as anticipated, there is *no measurable effect of $(Bu_4N)^+(BF_4)^-$ on the nucleation kinetics*, as one would expect for such a weak BF_4^- stabilizer and base.

REFERENCES

1. He, Z.; Honeycutt, C. W.; Xing, B.; McDowell, R. W.; Pellechia, P. J.; Zhang, T. Solid-State Fourier Transform Infrared and ^{31}P Nuclear Magnetic Resonance Spectral Features of Phosphate Compounds. *Soil Sci.* **2007**, *172*, 501–515.

2. Özkar, S.; Finke, R. G. The hydrogenphosphate complex of (1,5-cyclooctadiene)iridium(I), $\{[Bu_4N][1,5\text{-}COD)Ir{\bullet}HPO_4]\}_n$: synthesis, spectroscopic characterization, and ES-MS of a new, preferred precursor to HPO_4^{2-} and Bu_4N^+ stabilized $Ir(0)_n$ nanoclusters. *J. Organomet. Chem.* **2004**, 689, 493–501.

3. Özkar, S.; Finke, R. G. Transition-Metal Nanocluster Stabilization Fundamental Studies: Hydrogen Phosphate as a Simple, Effective, Readily Available, Robust, and Previously Unappreciated Stabilizer for Well-Formed, Isolable, and Redissolvable Ir(0) and Other Transition-Metal Nanoclusters. *Langmuir* **2003**, *19*, 6247–6260.

4. Pohl, M.; Lyon, D. K.; Mizuno, N.; Nomiya, K.; Finke, R. G. Polyoxoanion-Supported Catalyst Precursors. Synthesis and Characterization of the Iridium(I) and Rhodium(I) Precatalysts $[(n\text{-}C_4H_9)_4N]_5Na_3[(1,5\text{-}COD)M{\bullet}P_2W_{15}Nb_3O_{62}]$ (M = Ir, Rh). *Inorg. Chem.* **1995**, *34*, 1413–1429.

5. Gottlieb, H. E.; Kotlyar, V; Nudelman, A. NMR Chemical Shifts of Common Laboratory Solvents as Trace Impurities. *J. Org. Chem.* **1997**, *62*, 7512–7515.

6. Cotton, F. A.; Wilkinson, G. *Advanced Inorganic Chemistry, Fifth Edition*; John Wiley & Sons: New York, **1988**.

7. Van Wazer, J. R.; Griffith, E. J.; McCullough, J. F. Hydrolysis of Condensed Phosphates. *J. Am. Chem. Soc.* **1952**, *74*, 4977–4978.

8. Ramirez, F.; Marecek, J. F. Oxyphosphorane and monomeric metaphosphate ion intermediates in phosphoryl transfer from 2,4-dinitrophenyl phosphate in aprotic and protic solvents. *J. Am. Chem. Soc.* **1979**, *101*, 1460–1465.

9. Guthrie, J. P. Hydration and dehydration of phosphoric acid derivatives: free energies of formation of the pentacoordinate intermediates for phosphate ester hydrolysis and of monomeric metaphosphate. *J. Am. Chem. Soc.* **1977**, *99*, 3991–4001.

10. Mathieu, L.; Thivolle, P.; Delmau, M.; Berger, M. ^{31}P NMR spectroscopy of mixed aqueous Na pyrophosphate and stannous chloride solutions. Evidence for pyrophosphate–Sn complex formation. *J. Magn. Reson.* **1982**, *46*, 332–337.

11. McGilvery, J. D.; Crowther, J. P. The Hydrolysis of the Condensed Phosphates. II (A). The Role of the Hydrogen Ion in the Hydrolysis of Sodium Pyrophosphate. II (B). The Dissociation Constants of Pyrophosphoric Acid. *Can. J. Chem.* **1954**, *32*, 174–185.

12. Kumler, W. D.; Eiler, J. J. The Acid Strength of Mono and Diesters of Phosphoric Acid. The n-Alkyl Esters from Methyl to Butyl, the Esters of Biological Importance, and the Natural Guanidine Phosphoric Acids. *J. Am. Chem. Soc.* **1943**, *65*, 2355–2361.

13. Muckerman, J. T.; Skone, J .H.; Ning, M.; Wasada-Tsutsui, Y. Toward the accurate calculation of pK_a values in water and acetonitrile. *BBA–Bioenergetics* **2013**, *1827*, 882–891.

14. Kristjánsdóttir, S. S.; Loendorf, A. J.; Norton, J. R. Kinetics and Thermodynamic Acidity of Hydrido Transition-Metal Complexes. 9. A Sterically Hindered Cationic Hydride, $[H_4Re(PMe_2Ph)_4]^+$. *Inorg. Chem.* **1991**, *30*, 4470–4471.

15. Kaupmees, K.; Tolstoluzhsky, N.; Raja, S.; Rueping, M.; Leito, I. On the Acidity and Reactivity of Highly Effective Chiral Brønsted Acid Catalysts: Establishment of an Acidity Scale. *Angew. Chem. Int. Ed.* **2013**, *52*, 11569–11572.

16. Kolthoff, I. M.; Chantooni, M. K., Jr.; Bhowmik, S. Dissociation constants of uncharged and monovalent cation acids in dimethyl sulfoxide. *J. Am. Chem. Soc.* **1968**, *90*, 23–28.

17. Clark, E. P. Signer Method for Determining Molecular Weights. *Ind. Eng. Chem. Anal. Ed.* **1941**, *13*, 820–821.

18. Watzky, M. A.; Finke, R. G. Transition Metal Nanocluster Formation Kinetic and Mechanistic Studies. A New Mechanism When Hydrogen Is the Reductant: Slow, Continuous Nucleation and Fast Autocatalytic Surface Growth. *J. Am. Chem. Soc.* **1997**, *119*, 10382–10400.

19. Watzky, M. A.; Finke, R. G. Nanocluster Size-Control and "Magic Number" Investigations. Experimental Tests of the "Living-Metal Polymer" Concept and of Mechanism-Based Size-Control Predictions Leading to the Syntheses of Iridium(0) Nanoclusters Centering about Four Sequential Magic Numbers. *Chem. Mater.* **1997**, *9*, 3083–3095.

20. Mondloch, J. E.; Finke, R. G. Supported-Nanoparticle Heterogeneous Catalyst Formation in Contact with Solution: Kinetics and Proposed Mechanism for the Conversion of Ir(1,5-COD)Cl/γ-Al_2O_3 to $Ir(0)_{\sim 900}$/γ-Al_2O_3. *J. Am. Chem. Soc.* **2011**, *133*, 7744–7756.

21. Besson, C.; Finney, E. E.; Finke, R. G., A Mechanism for Transition-Metal Nanoparticle Self-Assembly. *J. Am. Chem. Soc.* **2005**, *127*, 8179–8184.

22. Mondloch, J. E. Finke, R. G. Kinetic Evidence for Bimolecular Nucleation in Supported-Transition-Metal-Nanoparticle Catalyst Formation in Contact with Solution: The Prototype Ir(1,5-COD)Cl/γ-Al_2O_3 to $Ir(0)_{\sim 900}$/γ-Al_2O_3 System. *ACS Catal.* **2012**, *2*, 298–305.

23. Harada, M.; Yosihiko, K. Nucleation and Aggregative Growth Process of Platinum Nanoparticles Studied by in Situ Quick XAFS Spectroscopy. *Langmuir* **2012**, *28*, 2415–2428.

24. Mozaffari, S.; Li, W.; Thompson, C.; Ivanov, S.; Seifert, S.; Lee, B.; Kovarik, L.; Karim, A. M. Colloidal nanoparticle size control: experimental and kinetic modeling investigation of the ligand-metal binding role in controlling the nucleation and growth kinetics. *Nanoscale* **2017**, *9*, 13772–13785.

25. Kent, P. D.; Mondloch, J. E.; Finke, R. G. A Four-Step Mechanism for the Formation of Supported-Nanoparticle Heterogeneous Catalysts in Contact with Solution: The Conversion of Ir(1,5-COD)Cl/γ-Al_2O_3 to $Ir(0)_{\sim 170}$/γ-Al_2O_3. *J. Am. Chem. Soc.* **2014**, *136*, 1930–1941.

26. Bentea, L.; Watzky, M. A.; Finke, R. G. Sigmoidal Nucleation and Growth Curves Across Nature Fit by the Finke-Watzky Model of Slow Continuous Nucleation and Autocatalytic Growth: Explicit Formulas for the Lag and Growth Times Plus Other Key Insights. *J. Phys. Chem. C* **2017**, *121*, 5302–5312.

27. Özkar, S.; Finke, R. G., Dust Effects On Nucleation Kinetics and Nanoparticle Product Size-Distributions: The Illustrative Case Study of a Prototype $Ir(0)_n$ Transition-Metal Nanoparticle Formation System. *Langmuir* **2017**, *33*, 6550–6562.

28. Hoops, S.; Sahle, S.; Gauges, R.; Lee, C.; Pahle, J.; Simus, N.; Singhal, M.; Xu, L.; Mendes, P.; Kummer, U. COPASI-a COmplex PAtheway SImulator. *Bioinformatics* **2006**, *22*, 3067–3074.

29. Creighton, J. A.; Eadon, D. G. Ultraviolet-Visible Absorption Spectra of the Colloidal Metallic Elements. *J. Chem. Soc. Faraday Trans.* **1991**, *87*, 3881–3891.

30. Watzky, M. A.; Finney, E. E.; Finke, R. G. Transition-Metal Nanocluster Size vs Formation Time and the Catalytically Effective Nucleus Number: A Mechanism-Based Treatment. *J. Am. Chem. Soc.* **2008**, *130*, 11959–11969.

31. Grechin, A. G.; Buschmann, H.-J.; Schollmeyer, E. Complexation of gaseous guests by solid host I. Quantitative thermodynamic approach for the reactions of β-cyclohextrin with amines using data in aqueous solution. *Thermochim. Acta* **2006**, *449*, 67–72.

32. Özkar, S.; Finke, R. G. Molecular insights for how preferred oxoanions bind to and stabilize transition-metal nanoclusters: A tridentate, C_3 symmetry, lattice size-matching binding model. *Coord. Chem. Rev.* **2004**, *248*, 135–146.

33. Lin, Y.; Finke, R. G. Novel Polyoxoanion- and Bu_4N^+-Stabilized, Isolable, and Redissolvable, 20—30-Å $Ir_{\sim 300\text{-}900}$ Nanoclusters: The Kinetically Controlled Synthesis, Characterization, and Mechanism of Formation of Organic Solvent-Soluble, Reproducible Size, and Reproducible Catalytic Activity Metal Nanoclusters. *J. Am. Chem. Soc.* **1994**, *116*, 8335–8353.

34. Kent, P.; Mondloch, J. E.; Finke, R. G. Synthesis of Heterogeneous $Ir^0_{\sim 600\text{-}900}/\gamma\text{-}Al_2O_3$ in One Pot From the Precatalyst Ir(1,5-COD)Cl/γ-Al_2O_3: Discovery of Two Competing Trace "Ethyl Acetate Effects" on the Nucleation Step and Resultant Product. *ACS Catal.* **2016**, *6*, 5449–5461.

35. Finney, E. E.; Finke, R. G. The Four-Step, Double-Autocatalytic Mechanism for Transition-Metal Nanocluster Nucleation, Growth, and Then Agglomeration: Metal, Ligand, Concentration, Temperature, and Solvent Dependency Studies. *Chem. Mater.* **2008**, *20*, 1956–1970.

36. Bentea, L.; Watzky, M. A.; Finke, R. G., Sigmoidal Nucleation and Growth Curves Across Nature Fit by the Finke-Watzky Model of Slow Continuous Nucleation and Autocatalytic Growth: Explicit Formulas for the Lag and Growth Times Plus Other Key Insights. *J. Phys. Chem. C* **2017**, *121*, 5302–5312.

37. Starkey Ott, L.; Finke, R. G. Nanocluster Formation and Stabilization Fundamental Studies: Investigating "Solvent-Only" Stabilization En Route to Discovering Stabilization by the Traditionally Weakly Coordinating Anion BF_4^- Plus High Dielectric Constant Solvents. *Inorg. Chem.* **2006**, *45*, 8382–8393.

38. Starkey Ott, L.; Finke, R. G. Transition-metal nanocluster stabilization for catalysis: A critical review of ranking methods and putative stabilizers. *Coord. Chem. Rev.* **2007**, *251*, 1075–1100.

APPENDIX III: SUPPORTING INFORMATION FOR CHAPTER IV

Cyclohexene Hydrogenation Catalytic Reporter Reaction (CHCRR) Methodology and the Pseudo-Elementary Step Treatment of the CHCRR Kinetics

The details of the pseudo-elementary-step (PEStep) treatment[1] of the kinetics[2] are provided in Scheme 4.1 of Chapter IV.[3] The essence of the PEStep treatment[1] is that one can, for example, write –d[cyclohexene]/dt/500 = –{d[A]/dt}/1 based on the PEStep eq 4.5 in Chapter IV, so long as the cyclohexene and other reagents are in excess and exhibit a zero-order dependence on $[Cyclohexene]^0$ throughout at least the initial part of the reaction[2]. For this reason, a zero-order dependence on [Cyclohexene] is checked experimentally in control experiments that are routinely performed.[2] One can, then and in turn, monitor the loss of cyclohexene (or, as actually done,[2] the loss of H_2) while actually monitoring kinetically the desired slow steps of particle nucleation (k_1) and autocatalytic growth (k_2) as confirmed by the sigmoidal shape of the curves. Advantages of the CHCRR method are: (i) the large amount of highly precise data readily available from monitoring the H_2 pressure loss vs time (≥1500 data points of ±0.01 psig precision[2]) in one's own lab; (ii) the catalytic amplification of the amount of catalytically active Ir produced by its turnover frequency; and (iii) an apparent sensitivity to smaller Ir species closer to the nucleation events (e.g., the Ir_3H_{2x}•POM^{6-} Kinetically Effective Nucleus (KEN)[3,4] and species just after it such as the smaller, catalytically more active[5,6] $Ir(0)_n$ nanoparticles).

The main *limitations* of the CHCRR methodology also need listing and are: (a) the indirect nature of the measurement, why since[7] 2003 we have been developing a second generation system that would allow XANES and SAXS checking and further testing of the CHCRR methodology as well as a better idea of the accuracy of the nucleation rate constants, and (b) the fact that the

reaction eventually runs out of cyclohexene at which time ca. 1/3 of the H_2 pressure is consumed, meaning that only the first 1/3–1/2 of the kinetics curve can typically be used for fitting purposes. (c) Using even that ca. 1/3 introduces a ~17% error in the resulting rate constants as previously discussed[2,8] (i.e., because one essentially has a $[H_2]_{avg} = \{[H_2]_{initial} + [H_2]_{final}\}/2$, hence a ~(1/3)/2 = ~17% systematic error, while the CHCRR method assumes the H_2 is constant, yet is actually being used to monitor the reaction in real time[2]).

Dust is another omnipresent complication in all nucleation and growth studies,[9] one reason nucleation rate constants[3] are notoriously hard to measure either precisely or accurately as discussed and referenced in the main text. Experimentally known sensitivities of nucleation and nanoparticle formation kinetics to water, O_2, H^+, an impurity in acetone solvent, and metal-contaminated reaction culture tubes and stir bars,[10] as well as to added ligand concentration[3,4,11,12] and H_2 gas-to-solution mass transfer limitations,[13] and hence to stirring rates[13] are all known and require attention by anyone trying to achieve reproducible nanoparticle formation reactions and associated kinetics. The correlated variable nature of the k_1 and k_2 variables are another known, complicating issue,[14] with k_1, k_2 and the starting $[A]_0$ value being part of each key region and feature of sigmoidal curves fit by the 2-step mechanism, as derivations in a 2017 paper demonstrate.[14]

EXAFS Analysis of the End-Time, Product Ir(0)$_n$ Nanoparticles

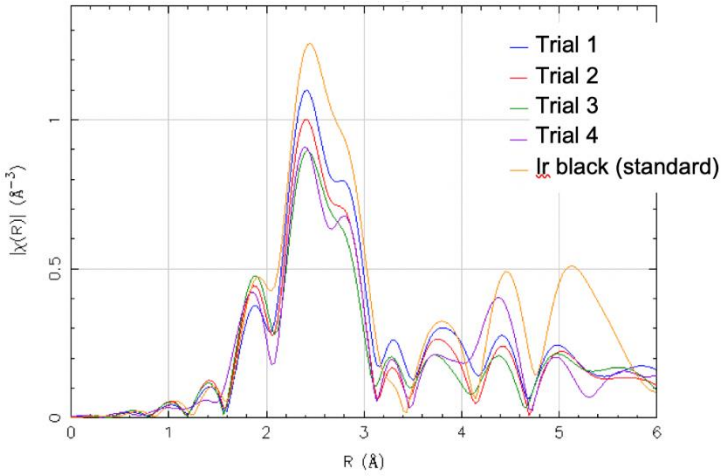

Figure S4.1. The end-time EXAFS spectra of resultant Ir(0)$_n$ nanoparticles from four standard kinetics experiments compared against an Ir black standard. The R-space spectra of final products are similar to that of Ir black.

The fitting procedure used two models. The first model contained two contributors, Ir–O and Ir-Ir. The second model contained only contributions from Ir-Ir. For experimental runs 1 and 3, the second model was capable and providing sufficient fits. For experimental runs 4 and 5, the first model was used due to the Ir-low Z contributions. The passive electron reduction factor (S_0^2) for Ir–Ir bond was obtained by fitting Ir black data and for the Ir–O bond by fitting the data of IrO_2. To improve uncertainties and stabilize fitting results, in fitting data of exps. 4 and 5, the disorder factor ($\square^2$) and the correction to the photoelectron energy origin (ΔE_0) were respectively constrained to be the same for Ir–O and Ir–Ir bond. Finally, the fitting range was set at 3.3-11.5 Å^{-1} in k space and 1.6-3.1 Å in R space.

Table S4.1. Fitting Result for EXAFS Experiments 1, 3, 4, and 5.

Exp.	bond	N	R (Å)	σ^2 (Å^2)	ΔE (eV)
1	Ir–Ir	5.2±0.6	2.697±0.006	0.0029±0.0007	8.9±1.2
3	Ir–Ir	5.0±0.6	2.696±0.006	0.0034±0.0007	8.6±1.3
4	Ir–O	0.8±0.4	2.02±0.04	0.003±0.001	10.4±2.4
	Ir–Ir	4.3±0.9	2.71±0.01	0.003±0.001	10.4±2.4
5	Ir–O	1.0±0.5	1.97±0.04	0.001±0.002	8.4±3.7
	Ir–Ir	3.0±1.0	2.70±0.02	0.001±0.002	8.4±3.7

Temperature Re-Equilibration and Acetone Solvent Plus Cyclohexene Vapor-Pressure Correction

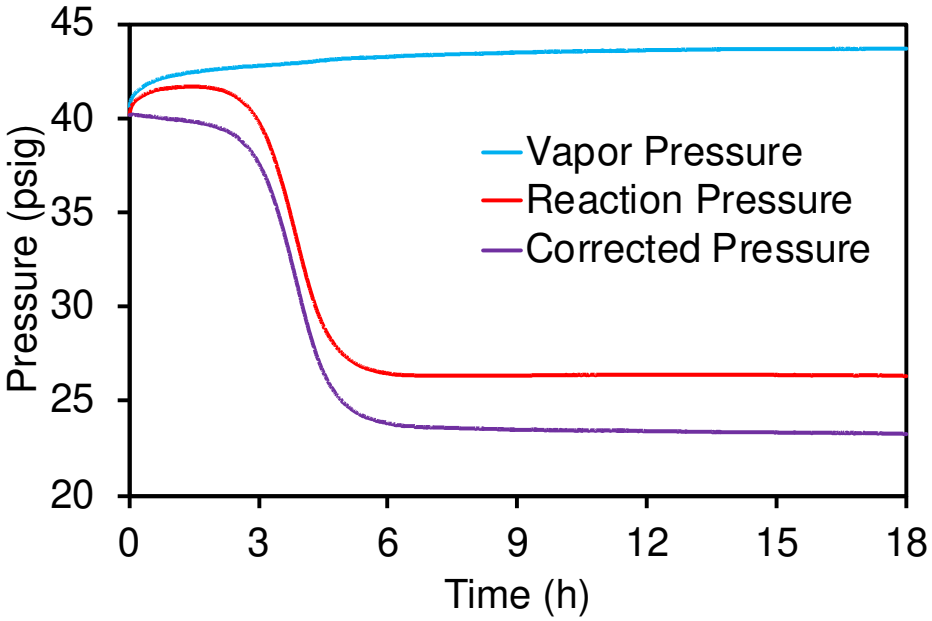

Figure S4.2. Solvent vapor pressure for 2.5 mL acetone and 0.5 mL cyclohexene were measured in triplicate over 18 h. The three runs were averaged to produce the blue, vapor pressure curve. A representative pressure curve for an $Ir(0)_n$ formation reaction with the $\{[(1,5\text{-COD})Ir^{I}\bullet HPO_4]_2\}^{2-}$ system is given in red. The point-by-point corrected pressure curve for H_2 loss is given in purple. The final purple curve data are then converted to cyclohexene concentration loss via the known stoichiometry of the CHCRR, that is, 1-to-1 H_2 to cyclohexene as reactants yield 1 cyclohexane as the product.

The Experimental section of Chapter IV provides additional details, as does reference 15.

SAXS Cell Constructed for Use at the Australian Synchrotron

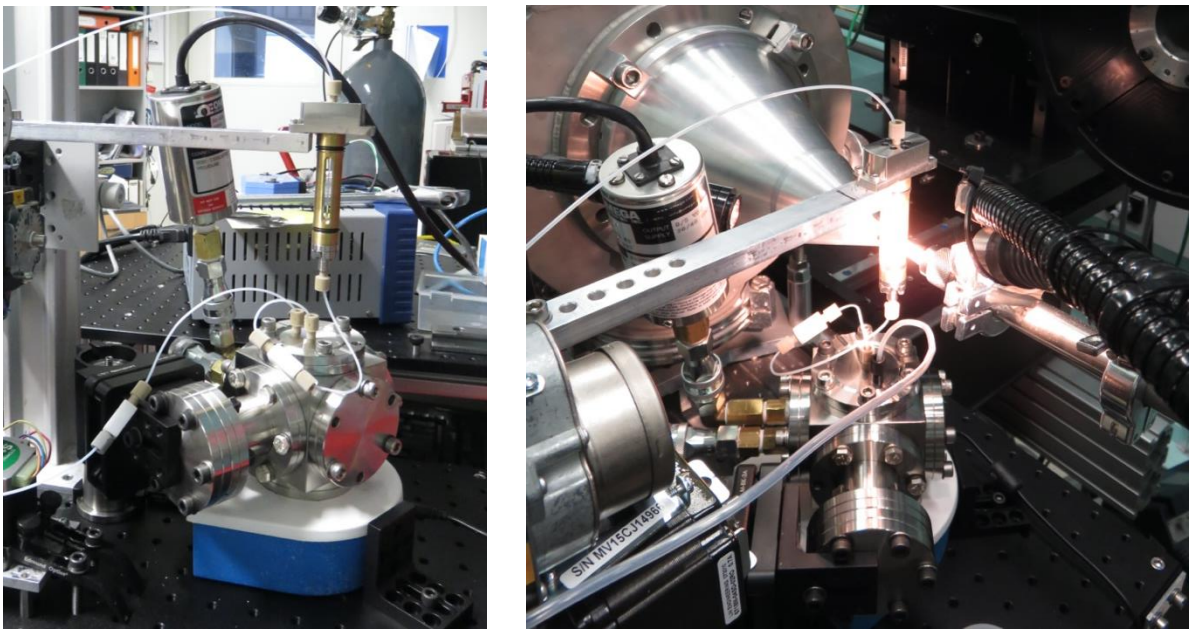

Figure S4.3. (**left**) The assembled SAXS cell off the beamline. The pressure cell is constructed of stainless steel using commercially available high-vacuum parts. Inside the cell, there is a standard 20 mL glass vial to contain the reaction solution. The pressure transducer is attached via a quick-connect fitting. The quartz capillary (into which the reaction solution is drawn upwards for measurements) is inside the brass housing directly above the cell and is connected via tubing. (**right**) The same cell mounted on the beamline with the capillary illuminated above the cell.

Additional Details of the SAXS Data Processing

Three distribution functions were compared: log-normal, Gaussian, and Schulz (Figure S4.4).

These have the following forms:

$$\text{Log normal:} \quad n(r) = \frac{\exp\left(-\frac{1}{2\sigma^2}\left(\ln\left(\frac{r}{r_0}\right)\right)^2\right)}{\sqrt{2\pi}r\sigma} \qquad \text{(Eq S4.1)}$$

Gaussian: $$n(r) = \frac{\exp\left(-\frac{(r-r_0)^2}{2w^2}\right)}{\sqrt{2\pi}w} \qquad \text{where } w = \sigma r_0 \qquad \text{(Eq S4.2)}$$

Schulz: $$n(r) = Z^Z X^{Z-1} \frac{\exp(-XZ)}{r_0 \Gamma(Z)} \qquad \text{(Eq S4.3)}$$

where $Z = \frac{1}{\sigma^2}$, $X = \frac{r_0}{r}$, and $\Gamma(x)$ is the gamma function.

The results show that there is relatively little difference between the three size distributions used (Table S4.2). In all cases the mode of the distribution lies at a radius of approximately 7.5 Å, and the distribution widths are similar. The log-normal and Schulz distributions have slightly more intensity in the tail at larger radius than the Gaussian distribution.

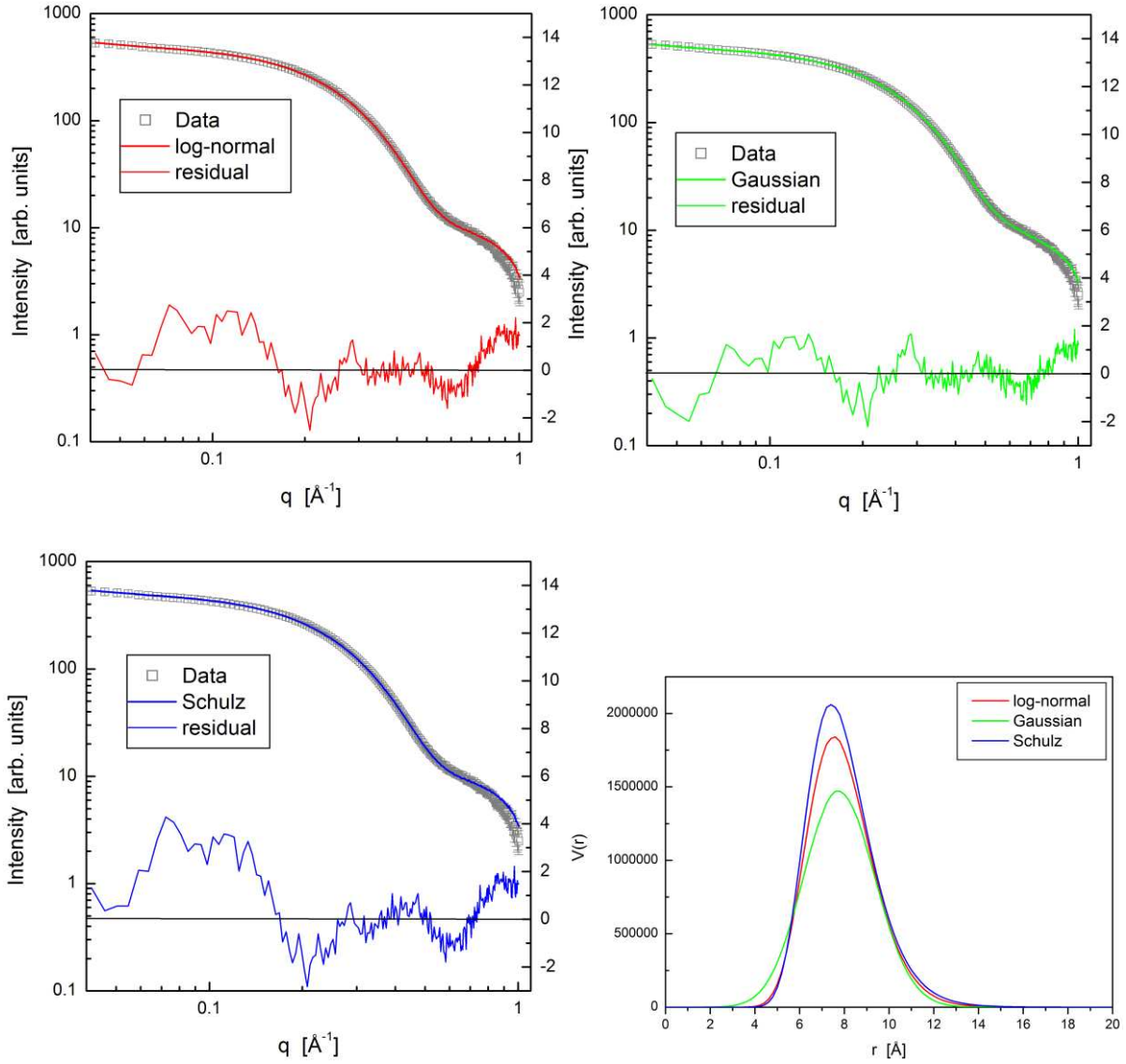

Figure S4.4. Fits to solution-subtracted final SAXS scan—of the data presented in Figure 4.4 of Chapter IV—using different size distribution functions: Log-normal (red), Gaussian (green), and Schulz (blue). The three resultant distributions are co-plotted as a function of particle radius (Å).

Table S4.2. Parameters Resulting from the Three Fits Shown in Figure S4.2.

Parameter	Log-normal	Gaussian	Schulz
r_0 [Å]	6.93 ± 0.02	6.64 ± 0.04	6.56 ± 0.02

σ	0.192 ± 0.002	0.255 ± 0.004	0.170 ± 0.001
N	1940 ± 20	1990 ± 30	1920 ± 10
background factor	0.677 ± 0.005	0.649 ± 0.006	0.691 ± 0.005
R^2	0.99992	0.99994	0.99988

Discussion of Which Of the Methods Employed Among CHCRR, GLC, XAFS, and SAXS Are Measuring $k_{2,\text{surface}}$ vs $k_{2,\text{Total}}$ (= $k_{2,\text{Volume}}$) Plus What the ME-PBM Reports

For the simplest, minimum mechanism, specifically the 2-step mechanism in eqs S4.4 and S4.5, these reactions are intrinsically "total" B (or "volume" of B; number of B) based reactions:

$$A \xrightarrow{k_1=k_{1,T}} B \qquad \text{(Eq S4.4)}$$

$$A + B \xrightarrow{k_2=k_{2,T}} 2B \qquad \text{(Eq S4.5)}$$

Hence $k_1 = k_{1,\text{T}}$ and $k_2 = k_{2,\text{T}}$ where T = total (alternatively $k_1 = k_{1,\text{V}}$ and $k_2 = k_{2,\text{V}}$, where V = volume) as shown. The associated differential equation is

$$-\frac{d[A]}{dt} = +\frac{d[B]}{dt} = k_{1,T}[A] + k_{2,T}[A][B]_T \qquad \text{(Eq S4.6a)}$$

However, up to a nuclearity of n = 13 (the first magic number cluster), n = 12 of those 13 atoms are on the surface (~92%), and even 42/55 (76%) of the atoms are surface atoms at the next, n = 55 magic number cluster, using magic number clusters as a model. Hence, for "small" nuclei defined as $n \leq 12$, $n_{\text{surface}} \approx n_{\text{Total}}$, so $k_{1,\text{surface}} \approx k_{1,\text{Total}} = k_1$, so that eq S4.6a becomes to a close approximation

$$-\frac{d[A]}{dt} = +\frac{d[B]}{dt} = k_1[A] + k_{2,T}[A][B]_T \quad \text{(Eq S4.6b)}$$

However, physically particle growth occurs by addition to the surface of the particles—that is, by surface Ir catalysis. Hence, while the nucleation step can continue to be represented by eq S4.4, growth in the simple 2-step kinetic model is more accurately accounted for by a $k_{2,s}$ (for surface growth) where the slower growth because not all B is on the surface. That is, surface autocatalytic growth *is modeled by taking up that slower growth (compared to the total volume or number of B) by the rate constant, $k_{2,s}$, where $k_{2,s} \leq k_{2,T}$*, eq S4.7. This allows us to continue to use the mass balance equation $[B]_t = [A]_o - [A]_t$ and, hence, get to the integrated rate equation eq 4.11 in the main text actually used to fit the kinetics data when the 2-step mechanism is being employed (and in the case where agglomeration is not also present).

$$A \xrightarrow{k_1} B \quad \text{(Eq S4.4)}$$

$$A + B \xrightarrow{k_{2,s}} B \quad \text{(Eq S4.7)}$$

Hence, the corresponding differential equation is

$$-\frac{d[A]}{dt} = k_1[A] + k_{2,s}[A][B]_T \quad \text{(Eq S4.8)}$$

A bit of reflection reveals that all of the monitoring methods used are monitoring growth that occurs by eq S4.8, hence are reporting $k_{2,s}$ (=$k_{2,\text{curve-fit}}$ from the COPASI[16] numerical integration-

based curve fitting; see the Experimental section in the main text). Table S4.3 summarizes the methods and what each measures along with explanatory comments.

Table S4.3. Summary of Monitoring Methods and What k_2, Growth Rate Constant They Measure, Plus ME-PBM.

Method	k_2 Measured (from fit to eqs S4.6a and S4.8)	Comment / Discussion
CHCRR	$k_{2,s}$	Only surface atoms are reactive, catalytically active
GLC (of cyclooctane evolution)	$k_{2,s}$	Cyclooctane produced by hydrogenation of 1,5-COD requires surface Ir catalysis
XANES	$k_{2,s}$	While XANES measures Ir(I) loss and Ir(0) formation, only $Ir(0)_{surface} = [B]_{surface}$ are involved physically in the growth step
SAXS	$k_{2,s}$	SAXS measure r (=radius) vs time (to be distinguished from our r(j) function used in the ME-PBM), that is, Ir(I) that gets converted to $Ir(0)_n$. But, again, only $Ir(0)_{surface} = [B]_{surface}$ are involved in the growth step.
ME-PBM	$k_{2,s}$ (via $k_{2,T}$r(j))	The ME-PBM is intrinsically a number balance, hence intrinsically $k_{2,T}$ ($=k_{2,volume} = k_{2,number}$). But, the ME-PBM code makes the conversion using the r(j) function so that $k_{2,s}$ is what is reported—for direct comparison to $k_{2,s}$ from the experimental measurements.

In short, all the physical methods employed (CHCRR, GLC, XANES, and SAXS) report $k_{2,s}$, while the ME-PBM intrinsically reports $k_{2,T}$ until and unless a correction for the number of surface monomer/number of total monomers is made. This function is

$$r(j) = \left(\frac{2.677 j^{0.72}}{j}\right) = \left(\frac{number\ of\ surface\ monomers}{total\ monomers}\right) \qquad \text{(Eq S4.9)}$$

where (j = number of monomers) as we have used in our ME-PBM[5].

As detailed in Footnote 50 of the cited 2019 paper[5], this $r(j)$ function, from Smirnov[17] and given as Figure 1 in our 2020 paper[6], artifactually has more surface atoms than total atoms for particles smaller than 34. Hence, a possibly more accurate function would be the piecewise function[5] $r = \begin{cases} j, & 1 < 34 \\ s(j), & j \geq 34 \end{cases}$, where $s(j)$ is the Schmidt and Smirnov equation/approximation[17] and j is the particle size in terms of total number of monomers.

But, even up to n = 55, 42/55 = 76% are still surface atoms by the magic number size analysis and approximation, so that only a ~24% error is present assuming $r(j) = 1$ up to even $j = 55$, an error likely within the experimental error of the kinetics measurements. Hence, in our ME-PBM we used the Schmidt and Smirnov $r(j)$ in eq S9 for all j values.

The approximation being made, then, at each j value is that shown in eq S4.10:

$$k_{2,s} = k_{2,T} r(j) \qquad \text{(Eq S4.10)}$$

Note here the general agreement of the form of eq S4.10 and the equation in footnote 46(a) on page 10396 of our 1997 paper[2] where we provided $k_{2(\text{calculated})}$ (= k_2 as used here) = $k_2((1 + x_{\text{Growth}})/2)$, where a "scaling factor", x, that is a non-continuous, magic-number-to-magic-number derived $x = (1 + x_{\text{Growth}})/2$ was used because the valuable continuous version of $r(j)$ from the work of Schmidt and Smirnov[17] was not yet available.

It follows that to be able to compare the intrinsically number (or total volume) ME-PBM to the $k_{2,s}[A][B]_s$ term measured by all the physical methods, a new function $\hat{r}(j) = k_i r(j)$ was defined as part of the ME-PBM to represent all growth processes for a particle of monomer-content-size j, where $\hat{r}(j)$ is called the *growth kernel*.[5] The key result is that the $k_{2,s}[A][B]$ term

measure by the physical methods is matched in the ME-PBM by a (summed) $k_i r(j)$ term.[18] Hence, the experimental kinetics curves, as well as the "k_2" values from the physical methods, can be compared directly with the computed curves and curve-fit "k_2" values of the ME-PBM.

Note, then, that the growth slows for larger clusters due to $r(j)$ getting smaller with higher j values. But, note that other factors are almost surely involved in the true growth kernel $\hat{r}(j)$ that have not yet been taken into account in the present, first-order treatment these factors include, (a) the anticipated, intrinsic decreased reactivity of clusters of increasing size, j, due to the energy of $j = \infty$ (bulk metal) dropping *ca.* 159 kcal/mol (=ΔH_{vap} of Ir(0) metal) from the j = 1; and (b) the effects of capping ligands as discussed and referenced in the main text.

Control Experiments of Examining Authentic, Crystallographically Characterized $Ir^{I}_4H_4$(1,5-COD)$_4$ Plus HPO_4^{2-}: Is This Discrete, *tetra*-Iridium-Hydride Cluster a Kinetically Competent CHCRR Catalyst and Perhaps Also a Good Model of the Kinetically Effective Nucleus?

Control Experiment Using Only $Ir^{I}_4H_4$(1,5-COD)$_4$. A standard hydrogenation was run using just the precursor $Ir^{I}_4H_4$(1,5-COD)$_4$ (1.2 mM in Ir) in 0.5 mL cyclohexene (~1.65 M) and 2.5 mL acetone (neat) and initially under 40 psig H_2 at 22 °C. Within 0.2 h, a clear brown solution with no visible precipitation of bulk metal was observed.

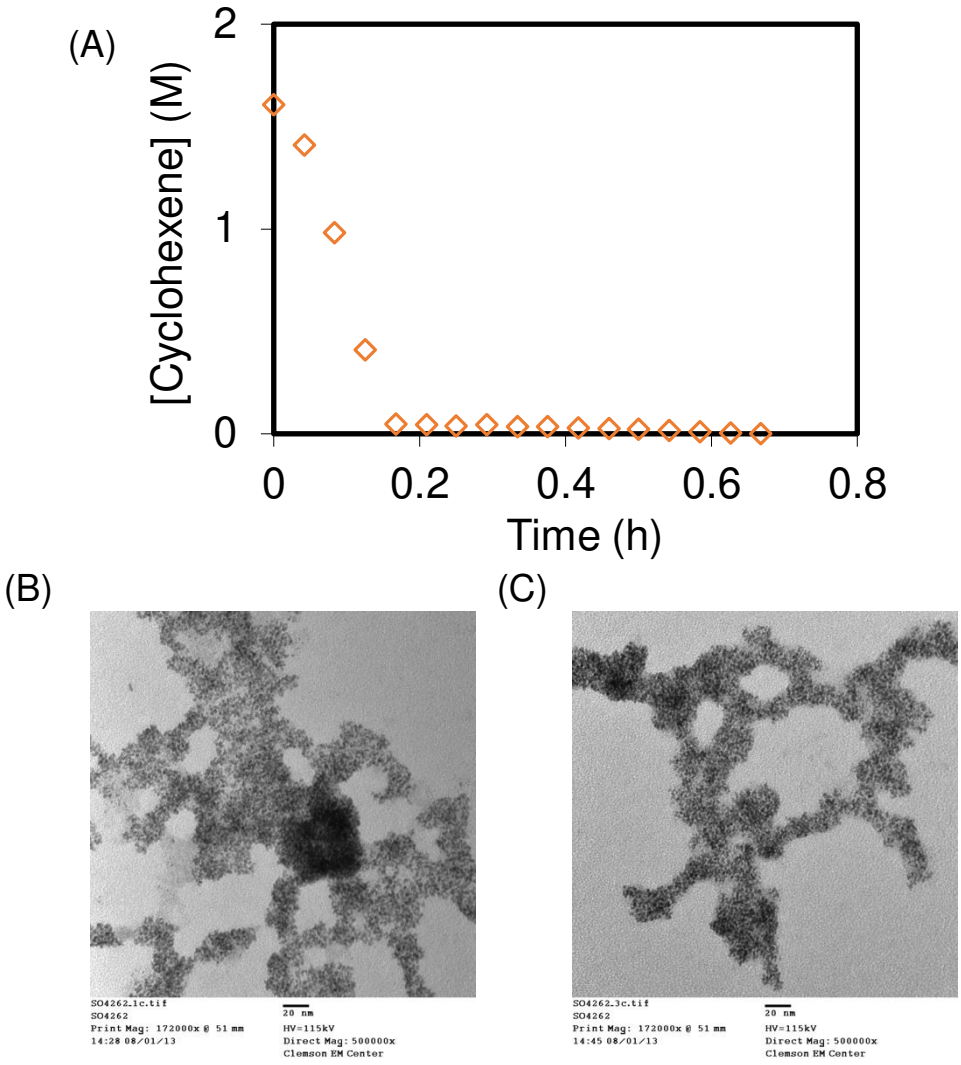

Figure S4.5. **(A)** The loss of cyclohexene versus time curve in the hydrogenation of 1.65 M cyclohexene and concomitant formation of Ir(0) nanoparticles starting with $[Ir(1,5\text{-COD})(\mu\text{-H})]_4$ (1.2 mM Ir) in acetone at 22.0 ± 0.1 °C. **(B)** and **(C)** TEM images of the sample harvested after cyclohexene hydrogenation.

Clearly, the discrete, isolable, crystallographically atomically characterized $Ir^{I}_4H_4(1,5\text{-COD})_4$ is able to serve as an efficacious Ir(0) nanoparticle precursor.

The next control experiment was performed because $Ir^{I}_4H_4(1,5\text{-COD})_4$[19,20] is essentially a dimer of the experimentally established Kinetically Effective Nucleus (KEN) in the

$\{[(COD)Ir^{I}\bullet HPO_4]_2\}^{2-}$ precursor system, that is a dimer of the bimetallic hydride KEN[21] of $Ir^{I}_2(H)_{2x}\bullet(HPO_4)_n^{-2n}$ (i.e., once the kinetically labile 1,5-COD ligands of $Ir^{I}_4H_4(1,5\text{-COD})_4$ are replaced by HPO_4^{2-} stabilizer and/or removed by hydrogenation under the CHCRR reaction conditions). The experiment that follows is a direct test of if an $Ir^{I}_4H_4(Ligand)_4$ species can accelerate the formation of $Ir(0)_n$ particles and support the CHCRR kinetics methodology in the $\{[(COD)Ir^{I}\bullet HPO_4]_2\}^{2-}$ precursor system.

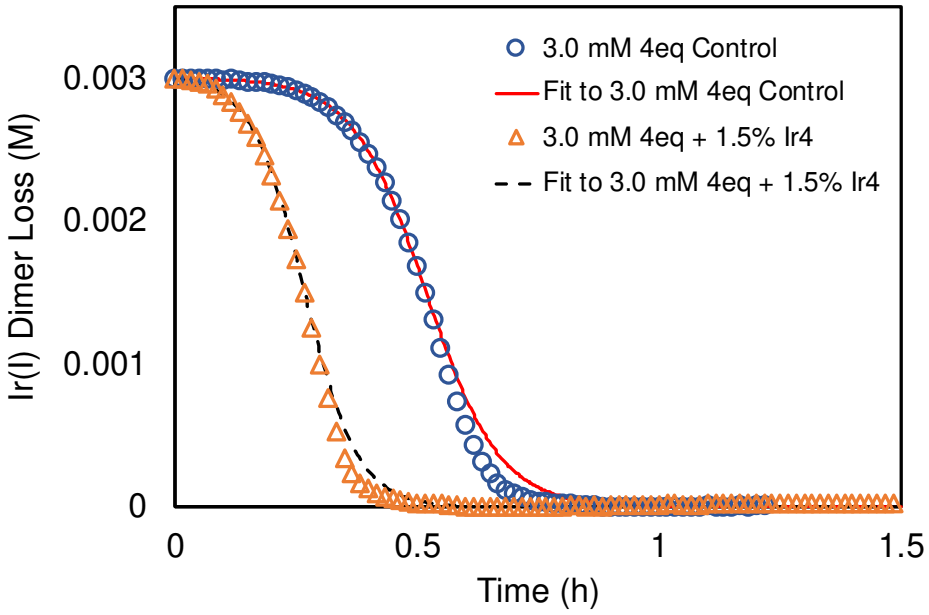

Figure S4.6. Iridium(I) loss data are plotted as a function of time (h) for reactions of $\{[(COD)Ir^{I}\bullet HPO_4]_2\}^{2-}$ (0.003 M) and ~4 molar equivalents of HPO_4^{2-} stabilizer without (blue circles) and then with (orange triangles) 1.5% by wt in Ir added $Ir^{I}_4H_4(1,5\text{-COD})_4$. Data were collected using the Cyclohexene Hydrogenation Catalytic Reporter Reaction and converted to Ir(I) loss data as detailed in the Experimental Section of Chapter IV. The resultant rate constants for the control without tetra-iridium (blue circles and solid red fit line) were: $k_{1obs} = 0.014 \pm 0.001$ h^{-1} and $k_{2obs} = (2.08 \pm 0.02) \times 10^3$ h^{-1} M^{-1}. The resultant rate constants for the control *with* tetra-iridium (orange triangles and dashed black fit line) were: $k_{1obs} = 0.14 \pm 0.01$ h^{-1} and $k_{2obs} = (3.00 \pm 0.03) \times 10^3$ h^{-1} M^{-1}.

The addition of 1.5% by wt in Ir of $Ir^{I}_{4}H_{4}(1,5\text{-COD})_{4}$ to a standard reaction solution of $\{[(COD)Ir^{I}\bullet HPO_{4}]_{2}\}^{2-}$ (0.003 M) resulted in a ~4-fold shortening of the induction period from ~0.4 h to ~0.1 h. The accompanying k_{1obs} increased by ~10^{1} compared to the reaction without the small, 1.5% by wt of added $Ir^{I}_{4}H_{4}(1,5\text{-COD})_{4}$. Clearly, $Ir^{I}_{4}H_{4}(Ligand)_{4}$ is able to serve as a nucleation species capable of supporting both nanoparticle growth and the CHCRR.

To test the generality of the acceleration by even a few percent of added $Ir^{I}_{4}H_{4}(1,5\text{-COD})_{4}$, another control experiment was performed in which 2% by wt in Ir of $Ir^{I}_{4}H_{4}(1,5\text{-COD})_{4}$ was added to a reaction solution of the commercial precursor $[(COD)Ir^{I}\mathbf{Cl}]_{2}$ (0.003 M), along with 3 molar equiv of $(Bu_{4}N)^{+}Cl^{-}$ added to slow the particle formation kinetics into an observable range. In this most interesting additional experiment, the induction period was shortened by over 10^{2} from more than 120 h (~5 days) to less than 0.1 h, Figure S4.7!

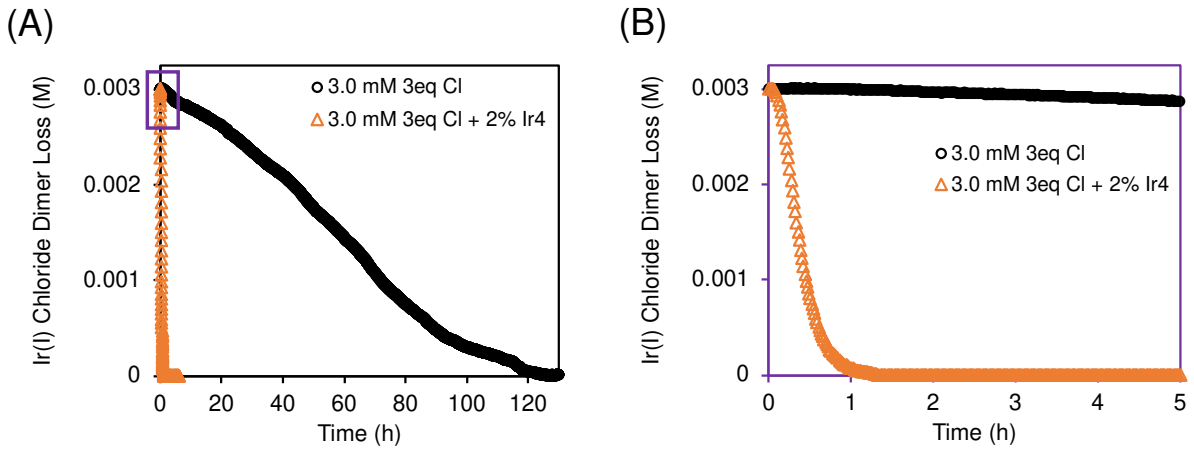

Figure S4.7. Iridium(I) loss data are plotted as a function of time (h) for reactions of $[(COD)Ir^{I}Cl]_{2}$ (0.003 M) and 3 molar equivalents of $Bu_{4}N^{+}Cl^{-}$ without (black circles) and then with (orange triangles) 2% by wt in Ir added $Ir^{I}_{4}H_{4}(1,5\text{-COD})_{4}$ **(A)** across the total reaction time (~120 h) and **(B)** during the first 5 h. Data were collected using the Cyclohexene Hydrogenation Catalytic Reporter Reaction and converted to Ir(I) loss data as detailed in the Experimental Section of the main text. The reaction without tetra-iridium (black circles) slowly reacted over 120 h, whereas the reaction with 2% by wt in Ir added tetra-iridium (orange triangles) reacted immediately within 1 h.

In short, the interpretation of these interesting experiments, exploiting the discrete, atomically characterized $Ir^{I}_{4}H_{4}(1,5\text{-COD})_{4}$ "nucleus model"[19,20], provide independent, compelling support that small, $Ir_{2\text{-}4}H_{x}$ clusters such as the bimetallic hydride KEN[21] of $Ir^{I}_{2}(H)_{2x}\bullet(HPO_{4})_{n}^{-2n}$ and the tetra-iridium hydride $Ir^{I}_{4}H_{4}(Ligand)_{4}$ (Ligands = HPO_{4}^{2-}, others) are kinetically competent species along the nucleation and growth as well as CHCRR monitoring pathways.

Fitting the XANES-type CHCRR Tandem Data with a Constrained k_{2obs} Rate Constant

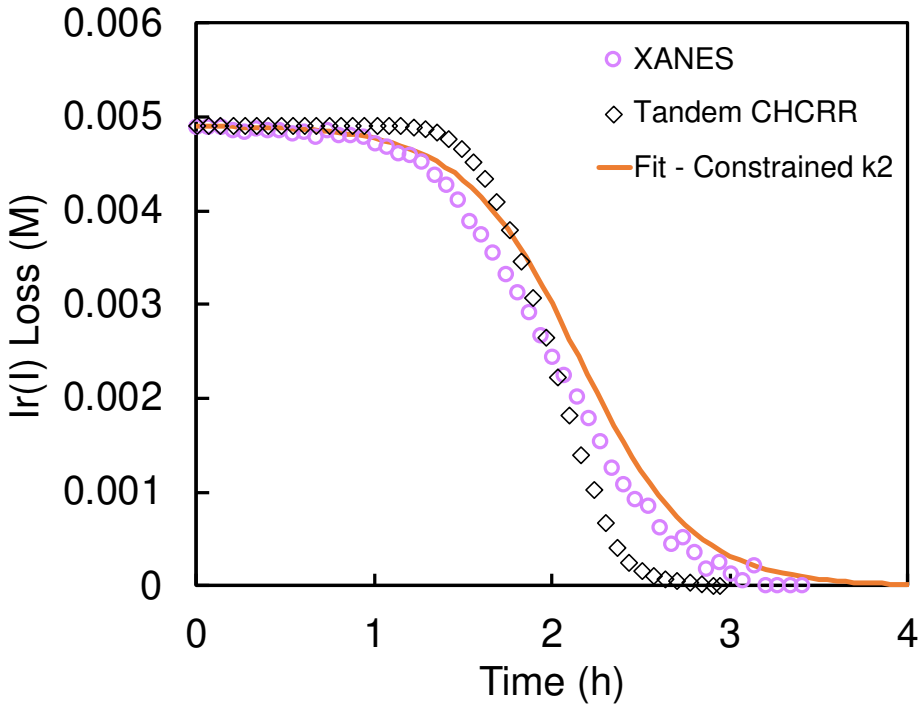

Figure S4.8. XANES (open purple circles) and Tandem CHCRR (black open diamonds) kinetics data are co-plotted with the constrained fit of the Tandem CHCRR data with the FW 2-step mechanism (orange solid line), where k_{2obs} is held to the XANES fit value ($k_{2obs(XANES)}$ = 634 h^{-1} M^{-1}) and k_{1obs} is allowed to vary. The result of trying to fit the Tandem CHCRR data with a constrained k_{2obs} is a line that is similar in shape to the XANES data with a resulting $k_{1obs} \approx 10^{-3}$ h^{-1}.

As stated in the main text, refitting the Tandem CHCRR kinetics data with a constrained k_{2obs} value equal to the XANES fit value of $k_{2obs(XANES)} = 634\ h^{-1}\ M^{-1}$ results in a k_{1obs} rate constant of *ca.* $10^{-3}\ h^{-1}$, thereby placing it in line with the rest of the data in Table 4.1 in Chapter IV. The fit to the Tandem CHCRR kinetics data in Figure S4.8 is poorer, but the reproduction of the XANES data is better. The correlated, compensating nature[22] of the k_{1obs} and k_{2obs} rate constants is apparent as well.

Composite, Global Fitting of all the Data (SAXS, XANES, CHCRR, and COA) Leading to the Reported Fits in Tables 4.1 and 4.2.

A global fit was performed of a composite of all of the kinetics data using COPASI and as discussed in the main text. The zeroth-order approximation being made is that every kinetics data point from each method is assumed to be lacking systematic errors and equally valid, accurate, and precise, assumptions necessary for combining the data in the absence of known weighting factors for the individual data. For this global fitting, the data were standardized at a middle-point concentration of 7.5 mM in Ir (i.e., between 5 and 9 mM, so (5+9)/2 = 7.5 mM Ir) given the concentration conditions in Figure 4.3 and Table 4.1 of Chapter IV (the XANES and accompanying CHCRR and COA experiments were conducted at 5 mM Ir and 2.5 molar equiv HPO_4^{2-}) vs those in Figure 4.5 and Table 4.2 of Chapter IV (the SAXS and accompanying tandem CHCRR, in-house CHCRR, and COA experiments were conducted at 9 mM Ir and 3.6 molar equiv HPO_4^{2-}). Evidence that these differences can be neglected without introducing larger errors is provided by examining Figures 4, 5, and S8 in a 2019 paper.[21]

The data were standardized by converting each concentration data point to the unitless extent of reaction (values of 0 to 1), then multiplying each data point by the concentration 7.5 mM.

This treatment was applied to all seven datasets. Then, all seven datasets were compiled and inputted as a single dataset (1,178 total data points) into COPASI. The data were fit with the 2-step mechanism of $A \overset{k_1}{\rightarrow} B$ and $A + B \overset{k_2}{\rightarrow} 2B$. All of the data and the simulated fit are given in Figure S4.9.

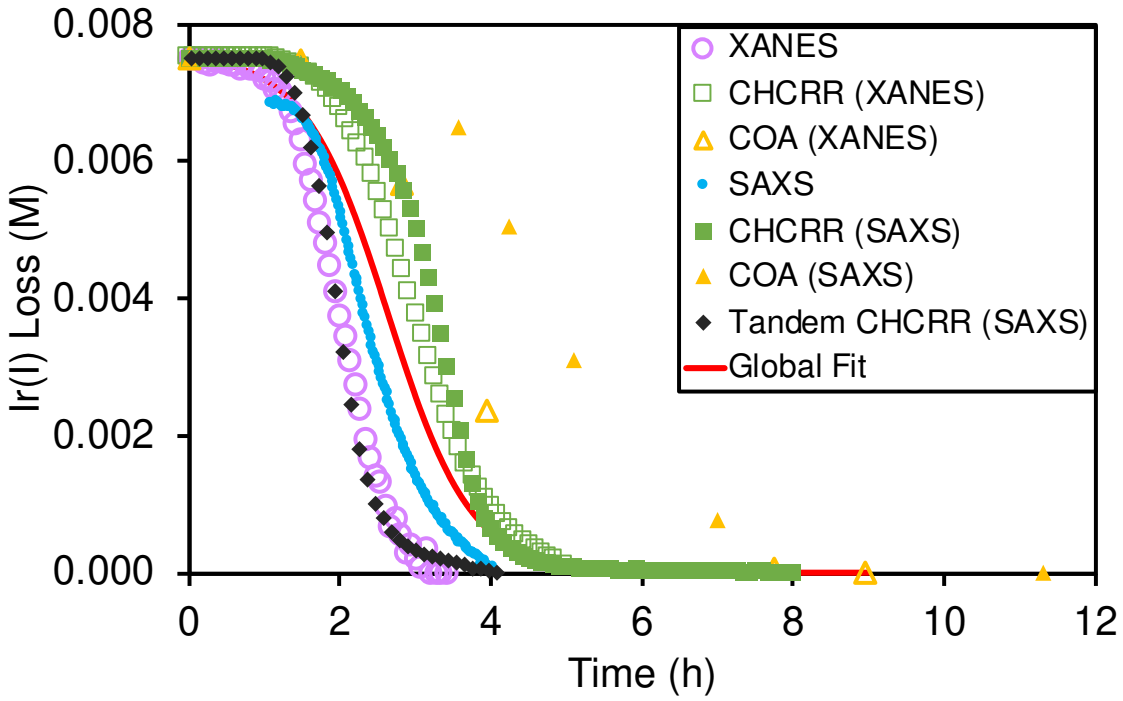

Figure S4.9. The seven datasets standardized to 7.5 mM in Ir^I are: XANES as hollow purple circles, in-house CHCRR (under XANES conditions) as hollow green squares, COA (under XANES conditions) as hollow yellow triangles, SAXS as solid blue circles, in-house CHCRR (under SAXS conditions) as solid green squares, COA (under SAXS conditions) as solid yellow triangles, and Tandem CHCRR (simultaneous with SAXS measurements) as solid black diamonds. The solid red line represents the global fit to all seven datasets.

The fit-determined rate constants and their fitting errors are $k_{1\text{obs,global avg}} = (1.5 \pm 0.1) \times 10^{-2}$ and $k_{2\text{obs,global avg}} = (2.4 \pm 0.1) \times 10^{2}$. Discussion of these results is provided in the main text, especially

in Table 4.3 in Chapter IV where a comparison of the k_{1obs} and k_{2obs} values from the XANES, SAXS, plus other methods vs this global analysis of the data are summarized and compared.

TEM-Determined Average Diameter versus Time Under XANES Conditions

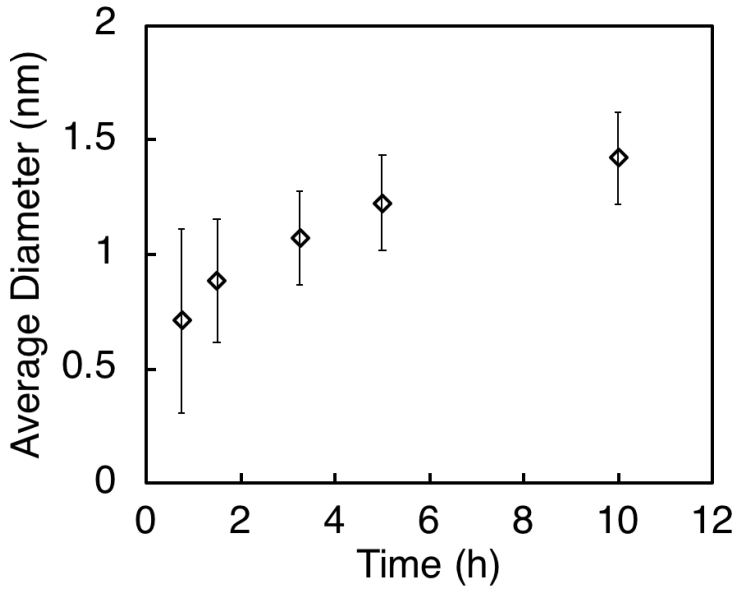

Figure S4.10. Dark Field Scanning-TEM-determined average nanoparticle diameter as a function of reaction time. Each time point represents a new sample prepared at 5.0 mM $[(COD)Ir^{I}(NCCH_3)_2][BF_4]$, 2.25 molar equiv of $(Bu_4N)_2HPO_4$ per Ir, 3.3 mL acetone, and 0.7 mL of 1.65 M cyclohexene at 22.0 ± 0.1 °C. Each data point represents >350 measured particles, and across all samples, >3000 particles were measured. The point at 1.5 hours corresponds with the turn-on of catalysis with an average particle nuclearity of 26 atoms, that is, $Ir_{\sim 26}$.

Consideration and Analysis of a Catalytically Effective Nucleus (CEN)[23] of B_n, $n \leq 26$.

Consider here is how a CEN[23] of B_n, $n \leq 26$, would length the induction period and change the k_{1obs} and k_{2obs} vs the known kinetically effective nuclei (KEN)[3] of Ir_2 in the $\{[(COD)Ir{\bullet}HPO_4]_2\}^{2-}$ system. For that system A = Ir_2 (i.e., A is the dimeric starting complex), and nucleation is given by[21]

$$A \xrightarrow{k_{1obs}} B \quad \text{(Eq S4.11)}$$

$$[B]_{t_1} = [A_o](1 - e^{-k_1 t_1}) \quad \text{(Eq S4.12)}$$

Now, for the postulated CEN of B_n, $n \leq 26$, the reactions are nucleation to Ir_2, followed by autocatalytic growth 2Ir at a time to $Ir_{\leq 26}$.

$$y\left(A \xrightarrow{k_{1obs}} B\right) \quad \text{(Eq S4.13)}$$

$$(n-y)\left(A + B \xrightarrow{k_{2obs}} 2B\right) \quad \text{(Eq S4.14)}$$

$$nA \xrightarrow{k_{appt\,(of\,k_1,k_2)}} nB, n_{max} \leq 26 \quad \text{(Eq S4.15)}$$

Equations S4.13 and S4.14 still obey the basic 2-step kinetics integrated equation[2] where we know experimentally that $t_{2(max)} = 1.5$ h.

$$[B]_{t_2} = [A_o]\left(1 - \frac{k_{1obs}+k_{2obs}[A_o]}{k_{1obs}[A_o]+k_{2obs}e^{(k_{1obs}+k_{2obs}[A_o]*t_2)}}\right) \quad \text{(Eq S4.16)}$$

Hence, we can ratio equations S4.12 and S4.16, plug in t_2, and solve for t_1. As part of this calculation, typically $[A_o] = 6.0 \times 10^{-3}$ M and we can use $k_{1obs(ave)} = 2.4 \times 10^{-3}$ h^{-1} and $k_{2obs(ave)} = 330$ h^{-1} M^{-1} from the main text for the purposes of this calculation / estimation. Note here that $k_{2obs(ave)} = 330$ h^{-1} $M^{-1} \times (3.0 \times 10^{-3}$ M$) = 0.99$ h^{-1}, so that $k_2[A_o]$ is >> k_1. By constructing the ratio of $[B]_{t1}$ / $[B]_{t2}$, one obtains

$$\frac{[B]_{t_1}}{[B]_{t_2}} = \frac{[A_o]\left(1-e^{-k_1 t_1}\right)}{[A_o]\left(1-\frac{k_{1obs}+k_{2obs}[A_o]}{k_{1obs}[A_o]+k_{2obs}e^{\left(k_{1obs}+k_{2obs}[A_o]*t_2\right)}}\right)} \qquad \text{(Eq S4.17)}$$

We know for the experimentally established[21] KEN = Ir_2 at t_1, and CEN ≤ 26 by time t_2, hence by plugging the numbers into eq S4.17 we have

$$\frac{2}{26} = \frac{1}{13} = \frac{\left(1-e^{-(0.0024)t_1}\right)}{\left(1-\frac{(0.0024)+(330)(0.003)}{(330)(0.003)+(330)e^{\left((0.0024)+(330)(0.003)*t_2\right)}}\right)} \qquad \text{(Eq S4.18)}$$

Solving eq S4.18, one finds that for t_2 = 1.5 h, $\boldsymbol{t_1}$ **= 0.06 h**.

In words, for the full development of a maximum size, CEN = B_{26} (= Ir_{26}) there would have been a ~25-fold increase in the induction time for the CHCRR vs the XANES data. However, examining the CHCRR vs XANES experimental data in Figure 4.3 in Chapter IV, the experimentally observed increase in the induction period for the CHCRR vs the XANES kinetics data is ca. ≤2-fold (and certainly ≤5-fold), possibly <<2-fold given that the XANES kinetics quite possibly contains a radiolysis-induced acceleration that artifactually shortens the observed induction period in the XANES studies.

Hence, as a bottom line to this section, the calculations compared to the experimental data are strongly suggestive of what one expects, chemically, namely that an Ir_2 KEN that can (by definition[21]) use H_2 to hydrogenate and thereby add $Ir^I(COD)^+$ is also able to hydrogenate cyclohexene + H_2 to cyclohexane along with later, larger $Ir_{>2}$ species. The implied CHCRR catalysis by Ir_n, $n \geq 2$, implies strongly that the average CEN is less than the $B_n \leq 26$. It follows that only a very short, relatively small, systematic delay/error in the CHCRR vs the direct XANES can be present in the CHCRR vs XANES monitoring kinetics methods.

A Comparison to the Results of Our 2001 Numerical Integration Simulation.[23]

In a 2001 numerical integration kinetics simulation[23], it was assumed that B_n, $n = 1$ species (denoted $M(0)_1$ in that work,[16] M = metal) and all later $n > 1$ species could grow, a series of educated guesses were used input rate constants for that growth,[23] and then to start it was assumed that all B_n, $n \geq 1$ species could also do the CHCRR at a rate much faster than the growth rate of each species. Then, a second, separate simulation was done examining what lengthened induction period would result if the CHCRR could not start until the first, Ir_{13} magic number cluster was formed[23] (i.e., and under an unchanged set of rate constants used as input[23]).

Under the assumptions made[23], a comparison of Figure 7 of the main text of the 2001 paper to Figure E of the SI of that 2001 paper[23], a ca. 7.5 h induction period results for the assumed CEN = Ir_{13} in comparison to a $\leq$1.5 h induction period apparent in Figure 7 of that 2001 paper.[23] The $k_{1(fit)}$ and $k_{2(fit)}$ to the two simulations are relisted below in Table S4.4.

Table S4.4. Fit Rate Constants from Figure 7 and Figure E of the 2001 Paper[23]

	$k_{1(fit)}$ (h^{-1})	$k_{2(fit)}$ (h^{-1} M^{-1})
No CEN	2.7×10^{-1}	300 (k_2, hydrogenation, corrected)
CEN = Ir_{13}	2.3×10^{-4}	540

While this simulation shows an up to 10^3 variation in k_1 and a ~2-fold variation in k_2 *could* result if a CEN of even Ir_{13} was the case and if the assumptions underlying the simulations hold, the consistency of the XANES, SAXS, and CHCRR $k_{1obs(avg)}$ in Tables 4.1 and 4.2 of Chapter IV to within a factor of ~2 indicate that nothing the size of even Ir_{13} is required before the CHCRR can

begin. Instead, the results once again imply that $Ir_{\geq 2}$ is both the KEN and the starting-point CEN for the CHCRR, consistent with the analysis in the section just above entitled "Consideration and Analysis of a Catalytically Effective Nucleus (CEN) of B_n, $n \leq 26$". Note here that even in 1997, a CEN (called a "critical nucleus" at the time[2]) of Ir_n, $n \leq 15$ was estimated based on experimental determination by GLC of how much cyclooctane had evolved from the (COD)Ir•POM^{8-} precatalyst by the end of the induction period (see the bottom of p 10,395)[2].

Mechanism-Enabled Population Balance Modeling (ME-PBM) and the Specific Mechanistic Models and Associated Ordinary Differential Equations (ODEs).

The ordinary differential equations (ODEs) employed in the three ME-PBMs reported in the main text were derived from the pseudo-elementary steps provided below. The 2-step mechanism with the experimentally determined nucleation mechanism at its start is given as Scheme S4.1.

Scheme S4.1. 2-Step Mechanism of (i) Prior Equilibrium to Generate A_{solv}, (ii) Slow, Continuous Nucleation and (iii) Autocatalytic Surface Growth

$$
\begin{aligned}
&[A + 2S \rightleftharpoons A_{solv} + {HPO_4}^{2-}],\ K_{Diss}\ \text{equilibrium constant}\\
&A_{solv} \xrightarrow{k_1} B + {HPO_4}^{2-}\\
&A + B \xrightarrow{k_2} 2B + 2{HPO_4}^{2-}
\end{aligned}
$$

The ODE system for the number of particles in this ME-PBM is

$$\frac{dn_1}{dt} = -k_f n_1 S^2 - k_2 n_1 \sum_{i=2}^{\infty} r\big(E(i)\big) n_i (i-1) + k_b A_{solv} HPO_4$$

$$\frac{dn_2}{dt} = k_1 A_{solv} - k_2 n_1 r\big(E(2)\big) n_2$$

$$\frac{dn_j}{dt} = k_2 n_1 (r(E(j-1)n(j-1)(j-2) - r(E(j))n_j(j-1))$$

$$\frac{dA_{solv}}{dt} = k_f n_1 S^2 - k_b A_{solv} HPO_4 - k_1 A_{solv}$$

$$\frac{dHPO_4}{dt} = k_f n_1 S^2 - k_b A_{solv} HPO_4 + 2k_2 n_1 \sum_{i=2}^{\infty} r\big(E(i)\big) n_i (i-1)\,.$$

(Eq S4.19)

Scheme S4.2. New 3-Step Mechanism[5,6] of (i) Prior Equilibrium to Generate A_{solv}, (ii) Slow, Continuous Nucleation, (iii) Fast Small Particle Growth, (iv) Slow, Large Particle Growth

$$[A + 2S \rightleftharpoons A_{solv} + {HPO_4}^{2-}],\ K_{Diss} \text{ equilibrium constant}$$
$$A_{solv} \xrightarrow{k_1} B + {HPO_4}^{2-}$$
$$A + B \xrightarrow{k_2} \mathrm{C} + 2{HPO_4}^{2-}$$
$$A + C \xrightarrow{k_3} 1.5C + 2{HPO_4}^{2-}$$

The ODE system for the number of particles in this ME-PBM is

$$\frac{dn_1}{dt} = -k_f n_1 S^2 - k_2 n_1 \sum_{i=2}^{M} r\big(E(i)\big) n_i (i-1) - k_3 n_1 \sum_{i=M+1}^{\infty} r\big(E(i)\big) n_i (i-1) + k_b A_{solv} HPO_4$$

$$\frac{dn_2}{dt} = k_1 A_{solv} - k_2 n_1 r\big(E(2)\big) n_2$$

$$\frac{dn_{j<M+1}}{dt} = k_2 n_1 (r(E(j-1)n(j-1)(j-2) - r(E(j))n_j(j-1))$$

$$\frac{dn_{j=M+1}}{dt} = k_2 n_1 r(E(j-1)n(j-1)(j-2) - k_3 n_1 r(E(j))n_j(j-1)$$

$$\frac{dn_{j>M+1}}{dt} = k_3 n_1 (r(E(j-1)n(j-1)(j-2) - r(E(j))n_j(j-1))$$

$$\frac{dA_{solv}}{dt} = k_f n_1 S^2 - k_b A_{solv} HPO_4 - k_1 A_{solv}$$

$$\frac{dHPO_4}{dt} = k_f n_1 S^2 - k_b A_{solv} HPO_4 + 2k_2 n_1 \sum_{i=2}^{\infty} r\big(E(i)\big) n_i (i-1).$$

(Eq S4.20)

Scheme S4.3. New 4-Step Mechanism Used in the Main Text of (i) Prior Equilibrium to Generate A_{solv}, (ii) Slow, Continuous Nucleation, (iii) Fast Small Particle Growth, (iv) Small Particle Agglomeration, and (v) Slow, Large Particle Growth

$$\begin{aligned}
&[A + 2S \rightleftharpoons A_{solv} + {HPO_4}^{2-}],\ K_{Diss} \text{ equilibrium constant} \\
&A_{solv} \xrightarrow{k_1} B + {HPO_4}^{2-} \\
&A + B \xrightarrow{k_2} C + 2{HPO_4}^{2-} \\
&B + B \xrightarrow{k_3} C \\
&A + C \xrightarrow{k_4} 1.5C + 2{HPO_4}^{2-}
\end{aligned}$$

The ODE system for the number of particles in this ME-PBM is

$$\frac{dn_1}{dt} = -k_f n_1 S^2 - k_2 n_1 \sum_{i=2}^{M} r\big(E(i)\big) n_i (i-1) - k_4 n_1 \sum_{i=M+1}^{\infty} r\big(E(i)\big) n_i (i-1) + k_b A_{solv} HPO_4$$

$$\frac{dn_2}{dt} = k_1 A_{solv} - k_2 n_1 r\big(E(2)\big) n_2 - k_3 r\big(E(2)\big) n_2 \sum_{i=2}^{M} r\big(E(i)\big) n_i (i-1) - k_3 \big(r\big(E(2)\big) n_2\big)^2$$

$$\frac{dn_{j<M+1}}{dt} = k_2 n_1 \left(r\big(E(j-1)\big) n_{j-1}(j-2) - r\big(E(j)\big) n_j (j-1) \right)$$

$$- k_3 r\big(E(j)\big)(j-1) n_j \sum_{i=2}^{M} r\big(E(i)\big) n_i (i-1) - k_3 \big(r\big(E(j)\big)(j-1) n_j \big)^2$$

$$+ k_3 \sum_{i+k=j} r\big(E(i)\big)(i-1) n_i r(E(k))(k-1) n_k$$

$$\frac{dn_{j=M+1}}{dt} = k_2 n_1 r(E(j-1)) n(j-1)(j-2) - k_4 n_1 r(E(j)) n_j (j-1)$$

$$+ k_3 \sum_{i+k=j} r\big(E(i)\big)(i-1) n_i r(E(k))(k-1) n_k$$

$$\frac{dn_{M+1<j\leq 2M}}{dt} = k_4 n_1 (r(E(j-1)) n(j-1)(j-2) - r(E(j)) n_j (j-1))$$

$$+ k_3 \sum_{i+k=j} r\big(E(i)\big)(i-1) n_i r(E(k))(k-1) n_k$$

$$\frac{dn_{j>2M+1}}{dt} = k_4 n_1 (r(E(j-1)) n(j-1)(j-2) - r(E(j)) n_j (j-1))$$

$$\frac{dA_{solv}}{dt} = k_f n_1 S^2 - k_b A_{solv} HPO_4 - k_1 A_{solv}$$

$$\frac{dHPO_4}{dt} = k_f n_1 S^2 - k_b A_{solv} HPO_4 + 2k_2 n_1 \sum_{i=2}^{M} r\big(E(i)\big) n_i (i-1)$$

$$+ 2k_4 n_1 \sum_{i=M+1}^{\infty} r\big(E(i)\big) n_i (i-1)$$

(Eq S4.21)

REFERENCES

1. Field, R. J.; Noyes, R. M. Oscillations in chemical systems. 18. Mechanisms of chemical oscillators: Conceptual bases. *Acc. Chem. Res.* **1977**, *10*, 214-221. The pseudo-elementary step approach utilized allows one to report a minimalistic mechanism of pseudo-elementary steps that are composites of the underling, true elementary steps. A valuable feature of the pseudo-elementary approach is that the pseudo-elementary steps and again their elementary step counterparts, possess well-defined words to describe the physical process occurring in that step and a corresponding, well-defined rate constant.

2. Watzky, M. A.; Finke, R. G. Transition Metal Nanocluster Formation Kinetic and Mechanistic Studies. A New Mechanism When Hydrogen Is the Reductant: Slow, Continuous Nucleation and Fast Autocatalytic Surface Growth. *J. Am. Chem. Soc.* **1997**, *119*, 10382–10400.

3. Laxson, W. W.; Finke, R. G. Nucleation is Second Order: An Apparent Kinetically Effective Nucleus of Two for $Ir(0)_n$ Nanoparticle Formation From $[(1,5\text{-COD})Ir^{I}\bullet P_2W_{15}Nb_3O_{62}]^{8-}$ Plus Hydrogen. *J. Am. Chem. Soc.* **2014**, *136,* 17601-17615.

4. Özkar, S.; Finke, R. G. Nanoparticle Nucleation Is Termolecular in Metal and Involves Hydrogen: Evidence for a Kinetically Effective Nucleus of Three $\{Ir_3H_{2x}\bullet P_2W_{15}Nb_3O_{62}\}^{6-}$ in $Ir(0)_n$ Nanoparticle Formation From $[(1,5\text{-COD})Ir^{I}\bullet P_2W_{15}Nb_3O_{62}]^{8-}$ Plus Dihydrogen. *J. Am. Chem. Soc.* **2017**, *139*, 5444-5457.

5. Handwerk, D. R.; Shipman, P. D.; Whitehead, C. B.; Özkar, S.; Finke, R. G. Mechanism-enabled population balance modeling of particle formation en route to particle average size and size distribution understanding and control. *J. Am. Chem. Soc.* **2019**, *141*, 15827-15839.

6. Handwerk, D. R.; Shipman, P. D.; Whitehead, C. B.; Özkar, S.; Finke, R. G. Particle Size Distributions via Mechanism-Enabled Population Balance Modeling. *J. Phys. Chem. C* **2020**, *124*, 4852–4880.

7. Özkar, S.; Finke, R. G. Transition-Metal Nanocluster Stabilization Fundamental Studies: Hydrogen Phosphate as a Simple, Effective, Readily Available, Robust, and Previously Unappreciated Stabilizer for Well-Formed, Isolable, and Redissolvable Ir(0) and Other Transition-Metal Nanoclusters. *Langmuir* **2003**, *19*, 6247-6260.

8. Lyon, D. K. Ph.D. Dissertation, University of Oregon, 1990; see pp 142-145.

9. Özkar, S.; Finke, R. Dust Effects On Nucleation Kinetics and Nanoparticle Product Size Distributions: The Illustrative Case Study of a Prototype $Ir(0)_n$ Transition-Metal Nanoparticle Formation System. *Langmuir* **2017**, *33*, 6550-6562. See also the references in this paper to the

history and prior key literature on the effects of dust on particle formation and nucleation kinetics.

10. Lin, Y.; Finke, R. G. A More General Approach to Distinguishing "Homogeneous" from "Heterogeneous" Catalysis: Discovery of Polyoxoanion- and Bu_4N^+-Stabilized, Isolable and Redissolvable, High Reactivity $Ir_{\sim 190\text{-}450}$ Nanocluster Catalysts. *Inorg. Chem.* **1994**, *33*, 4891-4910.

11. Özkar, S.; Finke R. G. Nanoparticle Formation Kinetics and Mechanistic Studies Important to Mechanism-Based Particle-Size Control: Evidence for Ligand-Based Slowing of the Autocatalytic Surface Growth Step Plus Postulated Mechanisms, *J. Phys. Chem. C* **2019**, *123*, 14047-14057. See also references 1-21 therein to ligand effects in nanoparticle chemistry.

12. Mozaffari, S.; Li, W.; Thompson, C.; Ivanov, S.; Seifert, S.; Lee, B.; Kovarik, L.; Karim, A. M. Colloidal nanoparticle size control: experimental and kinetic modeling investigation of the ligand-metal binding role in controlling the nucleation and growth kinetics. *Nanoscale* **2017**, *9*, 13772-13785.

13. Aiken, J. D., III; Finke, R. G., Nanocluster Formation Synthetic, Kinetic and Mechanistic Studies. The Detection of, and then Methods to Avoid, Hydrogen Mass-Transfer Limitations in the Synthesis of Polyoxoanion- and Tetrabutylammonium- Stabilized, Near Monodisperse 40 ± 6 Å Rh(0) Nanocluster. *J. Am. Chem. Soc.* **1998**, *120*, 9545.

14. Bentea, L.; Watzky, M. A.; Finke, R. G. Sigmoidal Nucleation and Growth Curves Across Nature Fit by the Finke-Watzky Model of Slow Continuous Nucleation and Autocatalytic Growth: Explicit Formulas for the Lag and Growth Times Plus Other Key Insights. *J. Phys. Chem. C* **2017**, *121*, 5302–5312. Note that that k_1 and k_2 (and $[A]_0$) are correlated in that they appear in the equation for each and every major phase and key point of the 2-step sigmoidal curves as detailed in the cited paper[13]. That k_1 and k_2 are correlated variables is easily recognized from their co-dependence on (correlation to) the loss of precursor A and hence $[A]_t$ in the primary kinetic equation for the 2-step mechanism[2], $-\frac{\mathrm{d}[A]_t}{\mathrm{d}t} = +\frac{\mathrm{d}[B]_t}{\mathrm{d}t} = k_1[A]_t + k_2[A]_t[B]_t$.

15. Widegren, J. A.; Aiken, J. D., III; Özkar, S.; Finke, R. G. Additional Investigations of a New Kinetic Method To Follow Transition-Metal Nanocluster Formation Including the Discovery of Heterolytic Hydrogen Activation in Nanocluster Nucleation Reactions. *Chem. Mater.* **2001**, *13*, 312–324. See Figure 7 and Scheme 2 of the main text in comparison to Figure E of the SI to see the simulated effect of introducing a hypothetical Ir_{13} Catalytically Effective Nucleus[23] before the CHCRR could begin or, presumably, before cyclooctane evolution as monitored by GLC could begin.

16. Hoops, S.; Sahle, S.; Gauges, R.; Lee, C.; Pahle, J.; Simus, N.; Singhal, M.; Xu, L.; Mendes, P.; Kummer, U. COPASI-a COmplex PAthway SImulator. *Bioinformatics* **2006**, *22*, 3067-3074.

17. Schmidt, A. F.; Smirnov, V. V. Concept of "magic" number clusters as a new approach to the interpretation of unusual kinetics of the Heck reaction with aryl bromides. *Top. Catal.* **2005**, *32*, 71–75.

18. For the interested reader, the explicit summation of the loss of monomer, n_1, is given as part of eq 4 on page 15832 of our 2019 paper[5]: $\frac{dn_1}{dt} = -\omega k_1 {n_1}^{\omega} - k_2 n_1 \sum_{j=\omega}^{\infty} r(j) * j * n_j$.

19. Yih, K.-H.; Hamdemir, I. K.; Mondloch, J. M.; Bayram, E.; Özkar, S.; Vasić, R.; Frenkel A. I.; Anderson, O. P.; Finke, R. G. Synthesis and Characterization of [Ir(1,5-Cyclooctadiene)(μ-H)]$_4$: A Tetrametallic Ir_4H_4-Core, Coordinatively Unsaturated Cluster. *Inorg. Chem.* **2012**, *51*, 3186–3193.

20. Laxson, W. W.; Özkar, S.; Folkman, S.; Finke, R. G. The Story of a Mechanism-Based Solution to an Irreproducible Synthesis Resulting in an Unexpected Closed-System Requirement for the $LiBEt_3H$-Based Reduction: the Case of the Novel Subnanometer Cluster, [Ir(1,5-COD)(μ-H)]$_4$, and the Resulting Improved, Independently Repeatable, Reliable Synthesis. *Inorg. Chim. Acta.* **2015**, *432*, 250–257.

21. Whitehead, C. B.; Finke, R. G. Nucleation Kinetics and Molecular Mechanism in Transition-Metal Nanoparticle Formation: The Intriguing, Informative Case of a Bimetallic Precursor, $\{[(1,5\text{-COD})Ir^{I}\bullet HPO_4]_2\}^{2-}$. *Chem. Mater.* **2019**, *31*, 2848–2862.

22. Bentea, L.; Watzky, M. A.; Finke, R. G. Sigmoidal Nucleation and Growth Curves Across Nature Fit by the Finke–Watzky Model of Slow Continuous Nucleation and Autocatalytic Growth: Explicit Formulas for the Lag and Growth Times Plus Other Key Insights. *J. Phys. Chem. C* **2017**, *121*, 5302–5312.

23. Watzky, M. A.; Finney, E. E.; Finke, R. G. Transition-Metal Nanocluster Size vs Formation Time and the Catalytically Effective Nucleus Number: A Mechanism-Based Treatment. *J. Am. Chem. Soc.* **2008**, *130*, 11959−11969.

LIST OF ABBREVIATIONS

AES	atomic emission spectroscopy
AFM	atomic force microscopy
DLS	dynamic light scattering
DSC	differential scanning calorimetry
DXAFS	dispersive X-ray absorption fine structure
EDX/EDS	electron-dispersive X-ray spectroscopy
EXAFS	extended X-ray absorption fine structure
FE-SEM	field-emission scanning electron microscopy
FE-TEM	field-emission transmission electron microscopy
FT-IR	Fourier-transform infrared spectroscopy
GATR	grazing angle attenuated total reflectance
GISAXS	grazing incidence small-angle x-ray scattering
GLC	gas-liquid chromatography
HAADF	high-angle annular dark-field
HE-XRD	high-energy x-ray diffraction
HR-TEM	high resolution transmission electron microscopy
ICP	inductively coupled plasma
LSA	laser scattering analysis
MALDI	matrix-assisted laser desorption/ionization
MS	mass spectrometry
NMR	nuclear magnetic resonance spectroscopy
OES	optical emission spectrometry
PDF	pair distribution function
QXAFS	quick X-ray absorption fine structure
SAED	selected area electron diffraction
SAXS	small-angle X-ray scattering
SEM	scanning electron microscopy
SEM-FEG	scanning electron microscopy with a field-emission gun
SQUID	superconducting quantum interference device
STEM	scanning transmission electron microscopy
TGA	thermogravimetric analysis
TEM	transmission electron microscopy
TOF	time-of-flight
TXM	Transmission X-ray Microscopy
UV-vis	UV-visible spectroscopy
XAFS	X-ray absorption fine structure
XANES	X-ray absorption near-edge structure

XPS	X-ray photoelectron spectroscopy
XRD	X-ray diffraction